

EVALUATION OF STRENGTH AND DUCTILITY OF A THREE-SPAN
EXTERNALLY POST-TENSIONED BOX GIRDER BRIDGE MODEL

by

Robert James Grierson MacGregor, BSCE, MSCE

DISSERTATION

Presented to the Faculty of the Graduate School of
The University of Texas at Austin
in Partial Fulfillment
of the Requirements
for the Degree of

DOCTOR OF PHILOSOPHY

THE UNIVERSITY OF TEXAS AT AUSTIN

August 1989

ACKNOWLEDGEMENTS

This dissertation is based on research conducted at the Phil M. Ferguson Structural Engineering Laboratory at the Balcones Research Center of The University of Texas at Austin. Financial support for the project was provided by the Texas State Department of Highways and Public Transportation, and the Federal Highway Administration. In addition, substantial financial support was provided by the National Science Foundation under Grant ECE-8419430.

This project was conducted under the direction of Dr. Michael E. Kreger and Dr. John E. Breen. Dr. Kreger provided almost daily support and guidance throughout the long and arduous process of constructing and testing a bridge in the laboratory. His enthusiastic approach and friendship helped to smooth over the many highs and lows along the way. His commitment and persistence have been instrumental to the successful completion of this project. It has been my pleasure and good fortune to have worked so closely with Dr. Breen. His technical skills have repeatedly challenged me to levels I had not previously thought possible. His wisdom, culture, and philosophy have helped me to understand and enjoy life beyond the "Ivory Towers" of academia. The support and guidance of Dr. Ned Burns and Dr. Ramon Carrasquillo are also gratefully acknowledged.

I would like to acknowledge the significant contributions by Mr. Alan Matejowsky of the TSDHPT who provided valuable suggestions and practical insight throughout all phases of the research project. In addition, I would like to acknowledge the guidance and assistance provided by local industry in development and construction of the model bridge structure. In particular, the assistance and cooperation of Prescon Corporation of San Antonio, Ivy Wire and Steel of Houston, and Cutler Gallaway of San Antonio were especially appreciated.

One of the components that makes a good school great is the quality of students that it attracts. Certainly by this standard The University of Texas at Austin ranks as one of the great schools of our time. The challenge, interaction, and friendship with an international contingent of students contributed immeasurably to my education experience. The friendship and support by the following people deserve special mention: Tommy Bush, Mike and Ellen Cyr, Greg Deierlein, Patricia Gaynor, David Hartmann, Eldon and Paula Kasl, Dominic Kelly, Leo Linbeck, Joe

Maffei, Vince Oue, David and Lisa Powell, Charles Quade, David Sanders, Dan Stoppenhagen, Paul Tikalsky, Gregor Wollman, and David Yates.

Construction of a segmentally precast box-girder bridge is a labor-intensive process requiring assistance from honest, hardworking people. The following undergraduate research assistants deserve special mention for their honest approach to hard work: Jose Arralega, Brian Booker, Chuck Crisman, Brian Elsasser, and Andy Irwin. In addition, the hard work and friendship of Mr. Elie Homsy were greatly appreciated. Elie provided definition by example to the phrase "an honest days work."

I would also like to express my gratitude for the assistance and cooperation of all the technical staff of the Ferguson Laboratory. The patient, helpful approach of Blake Stasney was greatly appreciated. Special thanks to Jean Gehrke and Sharon Cunningham for molding my work into a final comprehensible package. Very special thanks to Laurie Golding who approached all of my unusual purchases as a challenge and whose continuing friendship provided encouragement and support throughout my years at the lab. The memory of Mr. Gorham Hinckley, whose rough exterior concealed a kind and colorful gentleman, is an inspiration to all who knew him.

Finally, my deepest thanks to my family for providing their undying love and encouragement. To Anders and Eli Andersen, I extend my warmest thanks for their continued love and friendship. The constant love and support of my parents, Jim and Barbara MacGregor, have given me the background and strength to pursue my life to the fullest. Finally I would like to dedicate this work to my wife Mariann who has provided me with a quality home life, two little Texans, Lisanne and Anders, and her love and companionship. Her significant commitment and sacrifice during the often long and inconvenient hours were a constant source of strength and inspiration. I will spend a lifetime repaying her for her efforts.

List of Notation

- a = depth of the equivalent rectangular stress block
- A_p = area of prestressed reinforcement (general)
- A_{pe} = area of external (unbonded) prestressed reinforcement
- A_{pi} = area of internal (bonded) prestressed reinforcement
- A_s = area of the mild steel reinforcement in the tension side of the concrete section
- A'_s = area of the mild steel reinforcement in the compression side of the concrete section
- b = width of compression zone
- c = distance from extreme compression fiber to neutral axis
- c_u = distance from extreme compression fiber to neutral axis corresponding to ultimate flexural strength
- c_y = distance from the extreme compression fiber to the neutral axis assuming the tension reinforcement (mild and prestressed) has yielded
- C = resultant concrete compressive force
- d_e = effective depth of external (unbonded) tendons
- d_i = effective depth of internal (bonded) tendons
- d_p = distance from the extreme compression fiber to the center of the tension-flange prestressed reinforcement
- d_s = distance from the extreme compression fiber to the center of the tension-flange mild steel reinforcement
- e = eccentricity
- E = efficiency factor
- e_c = eccentricity of resultant compression force
- E_c = elastic modulus of the concrete

E_p	Elastic modulus of the prestressing tendon
f'_c	specified compressive strength of concrete
f_p	proportional limit of beam material for flexure
f_{pe}	effective stress in prestressed reinforcement after allowances for long-term losses
f_{pp}	maximum stress in prestressed reinforcement with assumed elastic-plastic behavior
f_{ps}	stress in prestressed reinforcement at nominal strength
f_{pse}	stress in external (unbonded) tendons corresponding to M_n
f_{psi}	stress in internal (unbonded) tendons corresponding to M_n
f_{pu}	specified tensile strength of prestressed reinforcement
f_{py}	yield strength of prestressed reinforcement
f_y	yield strength of mild steel reinforcement
G_c	shear modulus of concrete
I	impact factor
K_b	stiffness of beam system
K_s	stiffness of suspension system
K_θ	rotational stiffness at a plastic hinge
I_c	moment of inertia of concrete cross-section
L	span length
ℓ_b	bonded length of tendon
ℓ_d	development length of bonded tendon
ℓ_e	effective length of tendon for calculation of ultimate tendon stress, f_{ps}
ℓ_h	length of plastic hinge
ℓ_i	free length of tendon segment i

- LL = live load
- LL+I = live load with impact
- M = bending moment (general)
- M_d = decompression moment = applied moment that causes zero tension in the extreme fiber of the section where tensile stress is caused by applied load.
- M_n = nominal moment capacity of section
- M_o = moment at which the compressive forces concentrate in the top flange
- M_{si} = moment at which tendons begin to slip at the deviators
- M_{sf} = moment at which tendons are slipping over the entire length between anchor-ages
- M_p = applied moment that causes plastification of the prestressing tendons ($M_p = A_p * f_{pp} * Z_p$)
- P = concentrated load (force)
- q = uniformly distributed load (force/length)
- r = radius of gyration
- R = section forces (general)
- $T_e = A_p * f_{pe}$
- T_p = tension force in prestressing tendon
- v_p = proportional limit of beam material for shear
- y_t = distance from centroidal axis of the concrete cross-section to the top fiber
- y_b = distance from centroidal axis of the concrete cross- section to the bottom fiber
- Z_p = distance from the resultant compressive force to the center of the prestressed reinforcement on the tension side
- Z_s = distance from the resultant concrete compressive force to the center of the mild steel reinforcement on the tension side
- α = ratio of the areas of external (unbonded) and internal (bonded) prestressed reinforcement

- $\beta_1 = [0.85 - .05 * (f'c - 4.0)]$ with $f'c$ in ksi but not less than .65 or greater than .85
 $\Delta =$ deflection
 $\Delta M =$ change in moment
 $\Delta\theta =$ change in rotation
 $\Delta\sigma_p =$ change in tendon stress
 $\Delta T_j =$ change in tendon force at plastic hinge location
 $\Delta_{bp} =$ deflection corresponding to plastification of bonded prestressed reinforcement.
 $\Delta_{ubp} =$ deflection corresponding to plastification of unbonded prestressed reinforcement.
 $\Delta_m =$ maximum deflection limited by the rotation capacity at a concrete hinge.
 $\delta_h =$ elongation of tendon occurring at plastic hinge
 $\delta_j =$ elongation of tendon occurring at articulated joint
 $\varepsilon_c =$ concrete strain
 $\varepsilon_{cm} =$ limiting compressive strain in concrete
 $\varepsilon_{cu} =$ ultimate crushing strain of concrete
 $(\varepsilon_{ci})_c =$ initial concrete strain on flexural compression side of beam
 $\varepsilon_{cp} =$ change in concrete strain at the level of the unbonded prestressed reinforcement
 $\varepsilon_{sm} =$ limiting tensile strain in passive segment reinforcement
 $\gamma =$ material density (Force/Length³)
 $\Theta_h =$ concentrated rotation occurring at plastic hinge
 $\Theta_j =$ concentrated rotation occurring at articulated joint
 $\lambda =$ fraction defining any point on L
 $\rho_p =$ reinforcement ratio of prestressed reinforcement = $[A_p / (b * d_p)]$
 $\sigma_{pt} =$ tendon stress

- σ_t = lateral deviation stress applied to strands in contact with deviation hardware
- v_f = shear stress in strands in contact with deviation hardware
- Φ = curvature (general)
- Φ_h = magnitude of curvature at plastic hinge rotational strain component (curvature)
- Φ_m = maximum possible curvature at a plastic hinge
- ψ = ratio of plastic hinge length to neutral axis depth at ultimate (ℓ_h/c_u). Approximately equal to 10.5 (Determined experimentally in Reference 5)

TABLE OF CONTENTS

CHAPTER 1. INTRODUCTION	1
1.1 Background	1
1.1.1 Historical Development and Construction Methods	3
1.1.2 Rehabilitation of Existing Structures	4
1.1.3 Advantages and Disadvantages of External Post-Tensioning	4
1.2 Flexural Behavior of Girders with External Tendons	10
1.2.1 Before Cracking	10
1.2.1.1 Comparison between Bonded and Unbonded Systems	10
1.2.2 After Cracking or Joint Opening	11
1.2.2.1 Ideal Rigid Body Mechanism	11
1.2.2.2 Plastic Hinges in Concrete Structures	19
1.2.2.2.1 Rotation Capacity and Tendon Elongations	21
1.2.2.2.2 Multiple Hinges	25
1.2.2.3 Slip of Tendons at Deviators	27
1.3 Previous Studies on Externally Post-Tensioning Girders	28
1.3.1 Experimental Research	28
1.3.1.1 St. Remy Laboratory	28
1.3.1.2 Construction Technology Laboratory	29
1.3.2 Analytical Research	32
1.3.2.1 University of Texas	32
1.3.3 Additional Related Research	33
1.4 Object and Scope of Model Study	34

1.5	Summary	34
CHAPTER 2. DESIGN AND CONSTRUCTION OF BRIDGE MODEL		36
2.1	Development of Bridge Model	36
2.1.1	Dimensional Analysis	36
2.1.2	Scale Selection	38
2.1.3	Design Criteria	40
2.1.4	Description of Model Bridge Structure	52
2.2	Material Properties	56
2.2.1	Concrete	56
2.2.2	Prestressing Strands	62
2.2.3	Steel Reinforcement	64
2.3	Bridge Model Details	65
2.3.1	Typical Segment Details	65
2.3.1.1	Reinforcement	65
2.3.1.2	Fabrication of Typical Segments	68
2.3.1.3	Deviators	75
2.3.1.4	Shear Keys	75
2.3.1.5	Fabrication Tolerances of Typical Segments	76
2.3.1.6	Segment Repair Procedures	76
2.3.2	Pier Segment Details	80
2.3.2.1	Reinforcement	81
2.3.2.2	Anchorage Zone Pretest	85
2.3.2.3	Fabrication of Pier Segments	87
2.3.3	Bearings and Piers	89

2.4	Erection Procedures and Details	92
2.4.1	Span-by-Span Erection Method	92
2.4.2	Geometry Control	92
2.4.3	Temporary Post-Tensioning	94
2.4.4	Erection Falsework	95
2.4.5	Segment Joints	97
2.4.6	Cast-in-Place Closure Strips	99
2.4.7	Post-Tensioning Methods	100
2.4.8	Tendon Ducts and Grouting Details	103
CHAPTER 3. INSTRUMENTATION AND DATA ACQUISITION		107
3.1	General Requirements	107
3.2	Data Acquisition	107
3.3	Instrumentation Identification Code	107
3.4	Instrument Locations	109
3.5	Support Reactions	109
3.6	Measurement of Applied Loads	109
3.7	Deflection Measurements	113
3.8	Strand Strain Measurement	114
3.9	Joint-Opening Measurement	115
CHAPTER 4 BEHAVIOR OF STRUCTURE DURING CONSTRUCTION		118
4.1	Stressing Observations	118
4.2	Tendon Stress History	124
4.3	Deflections	126
4.4	Support Reactions	132
4.5	Summary of Observations Made During Erection	137

CHAPTER 5	ANALYSIS OF ERECTION STRESSES	138
5.1	Nonlinear Finite Element Analysis	138
5.2	Plastic Mechanism Analysis	138
5.3	Plane Frame Analysis	139
5.4	Estimate of Conditions in the Structure Before Testing	149
CHAPTER 6	LOAD TESTS	168
6.1	Loading Program	168
6.2	Description of Loading System	170
6.2.1	Reduced Scale Truck Loads	170
6.2.1.1	Location of Loads	170
6.2.1.2	Load Application Equipment	172
6.2.2	Equivalent Live Load with Impact	173
6.2.3	Factored Dead Load	174
6.3	General Test Procedure	174
6.4	Presentation of Test Data	175
6.5	Center-span Service Load Tests	177
6.5.1	Live Load Cycles for Center-span	177
6.5.2	Cracking Cycle for Center-span	177
6.5.3	Decompression Load Test of Center-Span.	182
6.6	North-span Load Tests (Dry Jointed)	188
6.6.1	Service Load Tests of North-Span.	188
6.6.1.1	Live Load Cycles of North-Span.	188
6.6.1.2	Decompression Load Cycles for North-Span	190
6.6.1.3	Torsional Load Cycles	193

6.6.2	Factored Load Cycles for North Span	194
6.6.3	Flexural Strength Tests of North Span	197
	6.6.3.1 Joint Opening Cycles for North Span	197
	6.6.3.2 Flexural Strength Cycles for North Span	208
6.6.4	Shear Strength Test of North Span	223
6.7	South-Span Load Tests (Epoxyed Joints)	232
	6.7.1 Service Load Tests of South-Span	232
	6.7.1.1 Live Load Cycles for South-Span	232
	6.7.1.2 Cracking Cycle for South-Span	233
	6.7.1.3 Decompression Load Cycles for South-Span	238
6.7.2	Factored Load Cycles for South-Span	245
6.7.3	Flexural Strength Tests Of South-Span	251
	6.7.3.1 Crack Opening Cycles for South-Span	251
	6.7.3.2 Flexural Strength Cycle for South-Span	259
6.7.4	Shear Strength Cycle for South-Span	270
CHAPTER 7. INTERPRETATION OF TEST DATA		283
7.1	Observations from Load Tests	283
	7.1.1 Service Load Behavior	283
	7.1.1.1 Live Load Response	283
	7.1.1.2 Comparison with Elastic Analysis	283
	7.1.1.3 Torsional Response	284
	7.1.1.4 Fretting Fatigue at Deviators	284
7.1.2	Factored Load Behavior	286
7.1.3	Ultimate Flexural Behavior	288

7.1.4	Shear Behavior	289
7.1.5	Ductility	292
7.2	Estimation of Insitu Forces	296
7.2.1	Insitu Dead Load Forces	296
7.2.2	Effective Prestress Forces at Critical Joints	296
7.2.3	Service Load Tendon Stresses	300
7.3	Effect of Epoxy on Model Behavior	303
7.3.1	Effect of Epoxy on Construction	303
7.3.2	Effect on Service Load Behavior	303
7.3.3	Effect on Factored Load Behavior	304
7.3.4	Effect on Flexural Strength	305
7.3.5	Effect on Shear Strength	305
7.3.6	Effect on Ductility	305
7.4	Flexural Strength Model	306
7.4.1	Observations from Load Tests	307
7.4.2	Factors Affecting the Unbonded Tendon Stress at Nominal Flexural Capacity	309
7.4.2.1	Effective Prestress Force	309
7.4.2.2	Ratio of Prestress Depth to Tendon Free Length	312
7.4.2.3	Neutral Axis Depth	312
7.4.2.4	Rotation Capacity at Precast Joints	312
7.4.2.5	Tendon Slip at Deviators	314
7.4.3	Prediction Equations for Tendon Stress in Unbonded Tendons Corresponding to Nominal Capacity	315
7.4.3.1	ACI	315

7.4.3.2	AASHTO	315
7.4.3.3	Tam and Pannell	315
7.4.3.4	Canadian Standards Association (CSA)	318
7.4.3.5	Virlogeux	318
7.4.3.6	Comparison of Prediction Equations with Test Data	318
7.4.4	Recommendation for Calculation of Flexural Strength	322
7.5	Load Rating Existing Structures	325
7.6	Secondary Prestress Forces at Ultimate Load Levels	327
7.6.1	Background Information	327
7.6.2	Secondary Prestress Forces from Construction	329
7.6.3	Redistribution of Secondary Prestress Forces	332
CHAPTER 8. CONCLUSIONS AND RECOMMENDATIONS		340
8.1	Fabrication Conclusions and Recommendations	340
8.2	Erection Process	341
8.3	Analysis	342
8.4	Behavior	343
8.5	Research Needs	348

LIST OF FIGURES

Figure		Page
1.1	External post-tensioning in Long Key Bridge	2
1.2	Concrete Truss with External Tendons	5
1.3	Mixed System with Steel Webs and Concrete Flanges	6
1.4	Mixed System with Internal and External Tendons	7
1.5	Calculation of Unbonded Tendon Stresses	12
1.6	Local Increase in Curvature at Plastic Hinge	13
1.7	Rigid Body Mechanisms	14
1.8	General Layout of Simple-Span Structure	15
1.9	Applied Moment vs. Deflection	15
1.10	Tendon Stress vs. Deflection	15
1.11	Stress-Strain Relationship for Prestressing Strand	16
1.12	Calculation of Tendon Elongation	17
1.13	Moment-Deflection Response for Bonded Tendons	18
1.14	Moment-Deflection Response for Unbonded Tendons	20
1.15	Tendon Elongation in the Plastic Hinge Region	22
1.16	Local Increase in Curvature at Opening Joint	24
1.17	Tam and Pannell Method	26
1.18	Saint-Remy Test Girders	29
1.19	Moment-Deflection Behavior	30
1.20	PCA Test Girders	31
2.1	Test Set-Up	40
2.2	Possible Model Cross-Sections	42

2.3	1/4 - Scale Truck Load	43
2.4	Design Loads	45
2.4	Design Loads	46
2.5	Scale Model of Externally Post-Tensioned Box Girder	53
2.6	Model Cross-Sections	54
2.7	Schematic Post-Tensioning Layout	55
2.8a	Theoretical Tendon Locations	57
2.8b	Theoretical Tendon Locations	58
2.8c	Theoretical Tendon Locations	59
2.8d	Internal and Auxiliary Tendons	60
2.9	Prestressing Strand Stress-Strain Relationship	64
2.10	Typical Segment Detailing Requirements	67
2.11	Typical Segment Reinforcing	68
2.12	Welded Wire Fabric Details	69
2.13	Deviator Force Components	70
2.14	Deviator Reinforcement	71
2.15	Methods for Precasting Segments	72
2.16	Typical Segment Formwork	73
2.17	Shear Key Details	77
2.18	Measured Dimensions	78
2.19	Repair Details	79
2.20	South Interior Pier Segment	81
2.21	Pier Segment Reinforcement	82
2.21	Pier Segment Reinforcement (continued)	83
2.21	Pier Segment Reinforcement (continued)	84

2.22	Pier Segment Reinforcement	86
2.23	Post-Tensioning Anchorage Pretest	88
2.24	Bearing Schematics	90
2.25	Pier Details	91
2.26	Span-by-Span Erection System	93
2.27	Temporary Post-Tensioning	96
2.28	Multistrand Stressing Methods	102
2.29	Monostrand Stressing Method	103
2.30	Tendon Grouting	106
3.1	Instrumentation Identification Code	108
3.2	Instrumentation Layout During Testing	110
3.3	Joint-Distortion Instrumentation	111
3.4	Locations of Deflection Instrumentation During Construction	112
3.5	Joint Opening Instrumentation	116
3.6	Joint Opening Instrumentation	117
4.1	Strain Gage Calibration Results	119
4.2	Measured Tendon Stress Corrections	120
4.3	Measured Data Corrections	121
4.4	Tendon Stress Profiles During Stressing	123
4.5	Tendon Stress History	125
4.6	Deflection Profiles	128
4.6	Deflection Profiles - continued	129
4.6	Deflection Profiles - continued	130
4.7	Resultant Deflected Shape after Construction	131
4.8	Measurement of North Exterior Reactions	133

4.9	Lift-Off Force Determination	133
4.10	Equalization of North Exterior Reactions	136
4.11	Equalization of South Interior Reactions	136
5.1	Plastic Mechanism Analysis	140
5.1	Plastic Mechanism Analysis-continued	141
5.1	Plastic Mechanism Analysis-continued	142
5.2	Possible Complex Mechanism in Dry Jointed Span	143
5.3	Plate Frame Elastic Analysis Models	145
5.4	One Span Configuration	150
5.4	One Span Configuration – continued	151
5.5	Two Span Configuration	152
5.5	Two Span Configuration – continued	153
5.6	Three Span Configuration	154
5.6	Three Span Configuration – continued	155
5.7	Theoretical Three Span Structure	157
5.7	Theoretical Three Span Structure – continued	158
5.8	Comparison of Extreme Fiber Stresses for As-Built and Theoretical Structures	160
5.9	Extreme Fiber Live Load Stresses	161
5.10	Service Stress Range	162
5.11	Test Load Forces	164
5.11	Test Load Forces – continued	165
6.1	Test Load Configurations	171
6.2	Load Frame	173
6.3	Center Span Service Load Test Deflection Profile	178

6.4	Center Span Cracking Cycle: Applied Load vs. Deflection	178
6.5	Center Span Cracking Cycle: Reactions and Joint Moments . . .	179
6.6	Center Span Cracking Cycle: Change in Tendon Stress vs. Applied Load	180
6.7	Center Span Decompression Cycles: Applied Load vs. Deflection .	183
6.8	Center Span Decompression Cycles: Reactions and Joint Moments	184
6.9	Center Span Decompression Cycles: Change in Tendon Stress vs. Applied Load	185
6.10	Change in Tendon Stress vs. Applied Load: Comparison Between First and Second Cycles	186
6.11	North Span Service Load Tests: Deflection Profile	189
6.12	North Span Decompression Cycles: Applied Load vs. Deflection .	191
6.13	North Span Decompression Cycles: Reactions and Joint Moments	192
6.14	North Span Factored Load Cycles: Applied Load vs. Deflection .	195
6.15	North Span Factored Load Cycles: Reactions and Joint Moments .	196
6.16	North Span Joint Opening Cycles: Applied Load vs. Deflection .	196
6.17	North Span Joint Opening Cycles: Reactions and Joint Moments .	199
6.18	North Span Joint Opening Cycles: Change in Tendon Stress vs. Applied Load	200
6.19	North Span Joint Opening Cycles: Joint Opening Potentiometer vs. Applied Load	201
6.20	North Span Joint Opening Cycles: Comparison of Tendon Stresses of Cycles 1 & 2	205

6.21	North Span Joint Opening Cycles: Tension Stress Profile	206
6.22	North Span Joint Opening Cycles: Comparison of Joint Moments for Cycles 1 & 2	207
6.23	North Span Flexural Strength Test: Applied Load vs. Deflection	209
6.24	North Span Flexural Strength Tests: Applied Load vs. Deflection	210
6.25	North Span Flexural Strength Tests: Reactions and Joint Moments	211
6.26	North Span Flexural Strength Tests: Change in Tendon Stress vs. Applied Load (North-Span Tendons)	212
6.27	North Span Flexural Strength Tests: Change in Tendon Stress vs. Applied Load (Center-Span Tendons)	213
6.28	South Span Flexural Strength Tests: Joint Opening Behavior	214
6.29	North Span Flexural Strength Test: Crushing on Top of Key at Joint	216
6.30	North-Span Flexural Test: Deflection Profile	221
6.31	Plastic Mechanism Rotations for Propped Cantilever	222
6.32	North Span Flexural Test: Cracking Summary	223
6.33	North Span Shgear Strength: Applied Load vs. Deflection	225
6.34	North Span Shear Strength Test: Reactions and Joint Moments	226
6.35	North Span Shear Strength Test: Change in Tendon Stress vs. Applied Load (North Span)	227
6.36	North Span Shear Strength Test: Change in Tendon Stress vs. Applied Load (Center Span)	228
6.37	North Span Shear Strength Test: Joint Opening Behavior	229

6.38	North Span Shear Test: Deflection Profiles	230
6.39	North Span Shear Test: Cracking Summary	232
6.40	South Span Service Load Tests: Deflection Profile	234
6.41	South Span Cracking Cycle: Applied Load vs. Deflection	235
6.42	South Span Cracking Cycles: Reactions and Joint Moments	236
6.43	South Span Cracking Cycle: Change in Tendon Stress vs. Applied Load	237
6.44	South Span Cracking Cycle: Joint Opening Potentiometer vs. Applied Load	239
6.45	South Span Decompression Cycles: Applied Load vs. Deflection	241
6.46	South Span Decompression Cycles: Reactions and Joint Moments	242
6.47	Comparison of South Span Cracking Cycle and Decompression Load Cycle Response for Tendon 4a	244
6.48	South Span-Tendon 4a Stress Profile	246
6.49	Comparison of South Span Cracking Cycle and Decompression Load Cycle Response for Tendon 5	247
6.50	Tendon Slip after Cracking Cycle	248
6.51	South span Factored Load Cycles: Applied Load vs. Deflection	249
6.52	South Span Factored Load Cycles: Reactions and Joint Moments	250
6.53	South Span Crack Opening Cycles: Applied Load vs. Deflection	253
6.54	South Span Crack Opening Cycles: Reactions and Joint Moments	254
6.55	South Span Crack Opening Cycles: Joint Opening Potentiometer vs. Applied Load	255

6.56	South Span Cracking Cycle: Joint Opening Potentiometer vs. Applied Load	257
6.57	South Span Crack Opening Cycles: Tendon 4a Stress Profile Before Cycles 1 & 2	258
6.58	South Span Flexural Strength Test: Applied Load vs. Deflection .	260
6.59	South Span Flexural Strength Test: Reactions and Joint Moments	261
6.60	South Span Flexural Strength Test: Change in Tendon Stress vs. Applied Load South Span Tendons	262
6.61	South Span Flexural Strength Test: Change in Tendon Stress vs. Applied Load South Span Tendons	263
6.62	South Span Flexural Strength Test: Crack Opening Behavior . .	264
6.63	South Span Flexural Strength Test: Deflection Profiles	269
6.64	South Span Flexural Strength Test: Cracking Summary	271
6.65	South Span Shear Test: Applied Load vs. Deflection	273
6.66	South Span Shear Test: Reactions and Joint Moments	274
6.67	South Span Shear Test: Change in Tendon Stress vs. Applied Load - South Span Tendons	275
6.68	South Span Shear Test: Change in Tendon Stress vs. Applied Load - Center Span Tendons	276
6.69	South Span Shear Test: Crack Opening Behavior	277
6.70	South Span Shear Test: Deflection Profile	280
6.71	South Span Shear Test: Cracking Summary	281
7.1	Beam and Suspension Systems	285
7.2	Deviator Force Components	286
7.3	Stress Condition for Strand in Contact with Deviator	287

7.4	Stages of Flexural Behavior	289
7.5	Ultimate Deflection Profile	290
7.6	Shear Mechanisms at Opening Joints	291
7.7	Bridge Collapse During Construction	294
7.8	Service Load Tendon Stresses	301
7.8	Service Load Tendon Stresses – continued	302
7.9	Flexural Model	307
7.10	Tendon Stress Response to Applied Load	308
7.11	Typical Tendon Stress Response	310
7.12	Comparison of Ultimate Flexural Behavior of Exterior Spans	311
7.13	Tendon Profile Slenderness Ratio	313
7.14	Methods for Calculating f_{ps}	316
7.14	Methods for Calculating f_{ps} – continued	317
7.15	Recommended Design Equation	323
7.16	Neutral Axis Depth, c_y	324
7.17	Free Tendon Length	326
7.18	Primary and Secondary Prestress Forces	328
7.19	Secondary Prestress Forces from the Construction Method	330
7.20	Staged Construction to Relieve Secondary Forces	331
7.21	Reactions and Joint Moments	333
7.22	Rotational Stiffness at an Opening Joint	335
7.23	Rotational Joint Stiffness vs. Moment	336
7.24	Applied Load vs. Bending Moment	338

LIST OF TABLES

Table		Page
2.1	AASHTO-83 Stress Limits	48
2.2	PTI Proposed Stress Limits for Segmental Construction	49
2.3	Load Combinations	50
2.3	Load Combinations - continued	51
2.4	Concrete Mix Types	62
2.5	Segment Concrete Properties	63
2.6	Reinforcement Properties	65
4.1	Summary of Tendon-Stress Losses	127
4.2	Exterior Reaction Corrections	135
5.1	Member Properties for Elastic Analysis	146
5.2	Dead Loads for Elastic Analysis	148
5.3	Concrete Stress Limits for Model Structure	163
5.4	Multiple of Live Plus Impact Loads Required for Joint Decompression	167
6.1	Loading Program	169
6.2	Center-span cracking cycle - maximum response values	181
6.3	Center-span Cracking Cycle - Change in Tendon Stress (ksi)	182
6.4	Summary of Center-span Cracking Cycle	182
6.5	Center-span Decompression Cycles - Maximum Response Values	187
6.6	Center-span Decompression Cycles - Change in Tendon Stress	187
6.7	Summary of Center-span Decompression Cycles	188
6.8	North-span Decompression Cycles - Maximum Response Values	190

6.9	North-span Decompression Cycles - Change in Tendon Stress (ksi)	193
6.10	Summary of North-span Decompression Cycles	193
6.11	North Span Factored Load Cycle - Maximum Response Values at Factored Load = $2.9(LL+I)$	197
6.12	North Span Factored Load Cycle - Change in Tendon Stress at Factored Load = $2.9(LL+I)$	197
6.13	Summary of North Span Factored Load Cycles	197
6.14	North Span Joint Opening Cycles - Maximum Response Values at Load = $4.7(LL+I)$	203
6.15	North Span Joint Opening Cycles - Change in Tendon Stress at Load = $4.7(LL+I)$	203
6.16	Summary of North Span Joint Opening Cycles	204
6.17	Instantaneous Stiffness During North-Span Tests (measured in ($LL+I$)/inch)	217
6.18	North span flexural strength cycles - maximum response values - flexural strength load = $6.8(LI+i)^2$	217
6.19	North Span Flexural Strength Cycles Change in Tendon Stress (ksi) - Flexural Strength Load = $6.8(LL+I)$	217
6.20	Summary of North Span Flexural Strength Cycle	218
6.21	North Span Shear Test - Maximum Response Values -Shear Strength Load = $7.2(LL+I)$	218
6.22	North Span Shear Test - Change in Tendon Stress -Shear Strength Load = $7.2(LL+I)$	219
6.23	Summary of North-Span Shear Test	220
6.24	South-span Cracking Cycle - Maximum Response Values	240
6.25	South-Span Cracking Cycle - Change in Tendon Stress	240
6.26	Summary of South-Span Cracking Cycle	240

6.27	South-Span Decompression Cycles - Maximum Response Values	243
6.28	South-Span Decompression Cycles - Change in Tendon Stress (ksi)	243
6.29	Summary of South-Span Decompression Cycles	243
6.30	South-span Factored Load Cycles - Maximum Response Values at Factored Load = $2.9(LL+I)$	245
6.31	South-span Factored Load Cycles - Change in Tendon Stress (ksi) at Factored Load = $2.9(LL+I)$	251
6.32	Summary of South-span Factored Load Cycles	251
6.33	South-span Crack-Opening Cycles - Maximum Response Values at Load = $4.8(LL+I)$	256
6.34	South-span Crack-Opening Cycles - Change in Tendon Stress (ksi) at Load = $4.7(LL+I)$ Cycle 1	256
6.35	Summary of South-span Crack-Opening Cycles	256
6.36	Tangent Stiffness During South-Span Tests – (measured in ($LL+I$)/inch)	266
6.37	South-Span Flexural Test - Maximum Response Values Flexural Strength Load = $7.7(LL+I)$	266
6.38	South-span Flexural Test - Change in Tendon Stress (ksi) Flexural Strength Load = $7.8(LL+I)$	267
6.39	Summary of South-span Flexural Strength Cycle	268
6.40	South-span Shear Test - Maximum Response Values Shear Strength Load = $8.0(LL+I)$	272
6.41	South-span Shear Test - Change in Tendon Stress (ksi) Shear Strength Load = $8.0(LL+I)$	278
6.42	Summary of South-Span Shear Strength Cycle	279
7.1	Service Load Deflections	284
7.2	Factor of Safety and Safety Margin Service and Ultimate Level Midspan Moments	295

7.3	Insitu Dead Load Forces	297
7.4	Calculation of Effective Prestress Forces	299
7.5	Cracking and Decompression Loads	304
7.6	Comparison Between Measured and Calculated Tendon Stress Response	320

1. INTRODUCTION

1.1 Background

The development of post-tensioned concrete box-girder bridges in the U.S. has progressed at a remarkable rate. The introduction of segmental technology, with its time saving and economic advantages, has resulted in widespread use of segmental prestressed box-girder construction for medium to moderately long-span bridges. An important recent development in U.S. box-girder construction is the use of external post-tensioning tendons (tendons external to the concrete cross-section), as opposed to traditional internal tendons which are contained within the webs or flanges. The United States' first externally post-tensioned concrete box-girder structure, the Long Key bridge, was completed in 1980. Long Key was one of four externally post-tensioned bridges linking the Florida Keys. Since 1980, a significant number of these structures have been built and many more are in design and planning stages. At the present time, the Texas Department of Highways and Public Transportation is involved in a four-part project to construct approximately 12 miles of elevated roadway through San Antonio. Segmental precast box-girders with external tendons were the low cost alternate bid by the contractors and are being used throughout that project.

“Internal post-tensioning” refers to the practice of embedding the tendon ducts, in straight or draped patterns as required by design, within the webs and flanges of the box girder section. This practice requires time-consuming placing and securing of the ducts inside the box-girder reinforcement cage. The presence of multiple ducts often results in congestion and interference with the reinforcing cage. After the concrete is placed and cured, or after the precast segments are assembled, the tendons are pulled through the embedded ducts and then stressed. After post-tensioning, the ducts are normally cement grouted. The grout bonds the tendon to the duct and the concrete along the full length of the tendon and, if the ducts are completely filled with a dense grout, should improve the corrosion protection for the tendon.

“External Post-tensioning” implies that the tendons are removed from the webs and flanges of the concrete section, and are relocated inside the void of the

box-girder or between the webs of parallel girders. The draped profile is maintained by passing the tendons through deviation devices cast monolithically with the webs and/or flanges at discrete locations along the span. These "deviators" vary in shape and size, though the most common form is a small block or saddle located at the junction of the web and the flange of the box-girder section. Anchorages for the external tendons are usually placed in thick diaphragms situated over the piers, although blister anchorages are sometimes used at intermediate points within the span. Tendons typically overlap at diaphragm anchorages for continuity. The cut-away view of the Long Key bridge in Fig. 1.1 clearly illustrates the concept of external post-tensioning. The only positive connection between the external tendon and the concrete section occurs at the anchorages and the deviators. Between attachment points, the exposed tendon is enclosed in sheathing; typically polyethylene tubing. The tendon is usually grouted along its entire length for protection against corrosion. External tendons are considered unbonded since the majority of the tendons is not bonded to the concrete section and the strains in the tendon are not compatible with the strains in the adjacent concrete section.

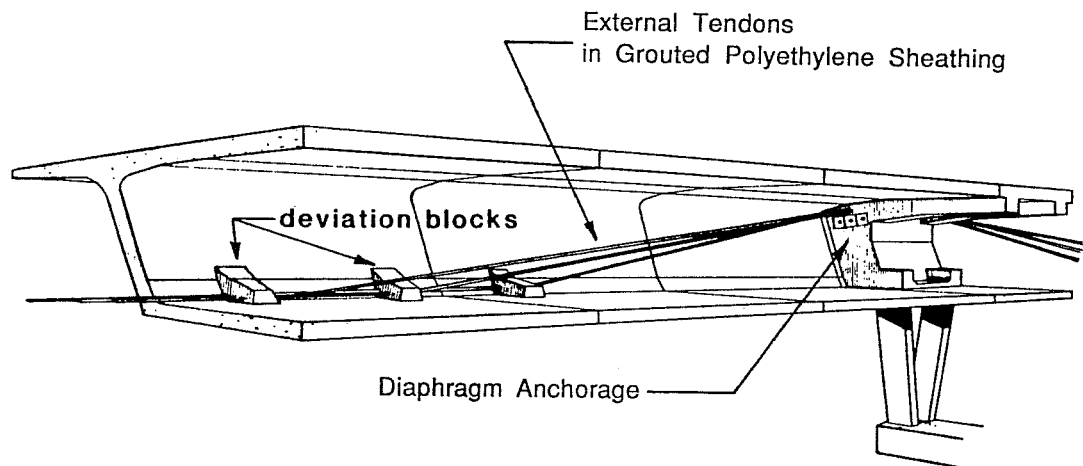


Figure 1.1 External post-tensioning in Long Key Bridge

Experimental research in the area of external post-tensioning for bridges is just beginning in this country, although research efforts in Europe, especially in France and Belgium, have been underway for some time. In fact, although external post-tensioning is a very recent development in the U.S., the concept has been incorporated in a number of European structures over the last several decades. A detailed literature review was presented by Powell et al. (1) which traces the development of the use of external tendons citing both successes and problems that have been experienced from the inception to the present. Such information provides insight to the current state of the art and points to uncertainties that could benefit from experimental investigation. Only a brief review of important and directly pertinent factors will be repeated in this report.

In this chapter the externally post-tensioned box-girder system is introduced and the ultimate flexural behavior examined. The historical development leading to the current usage of external tendons in new and existing structures will be presented, and advantages and disadvantages of the system will be discussed. The theoretical flexural behavior of unbonded externally post-tensioned bridge structures will then be discussed with reference made to modern mechanics-based prediction models. This will be followed by a brief review of related research programs in the United States and Europe. Finally, the scope and objectives of the research program will be summarized.

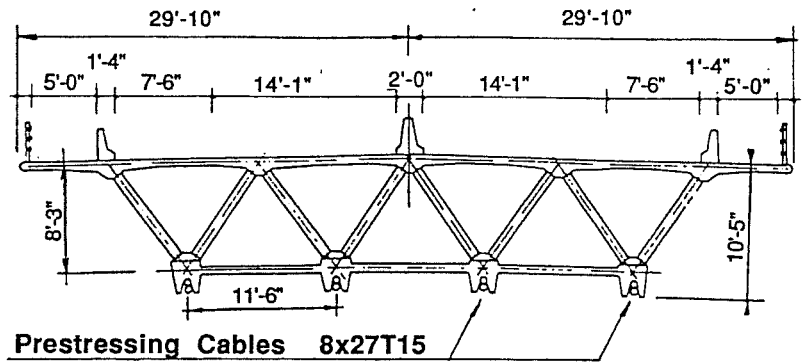
1.1.1 Historical Development and Construction Methods. Powell (1) has provided details on a large number of externally prestressed bridges. It becomes clear on studying her report that the external tendon bridges have developed as an evolution of the construction process. Very early structures were often cast-in-situ with external tendons provided for ease of fabrication and to relieve congestion problems in the webs. Relatively little consideration was given to the basic differences between bonded and unbonded tendons, and in a number of cases corrosion protection of the tendons was a problem. With further development of cast-in-situ bridges the trend moved to internal, grouted, and hence fully bonded tendons, which could develop most of the tendon strength at ultimate. With the advent of segmentally precast box-girder construction, the internal tendons caused severe congestion problems in webs and flanges, and external tendons were seen as a way of reducing such congestion. Similarly, for shorter-span bridges, the span-by-span process speeded the

construction rate and was very well suited to external tendons. Since service-level stress conditions, rather than ultimate conditions, tended to govern the design, the relative inefficiency at ultimate of unbonded external tendons (which cannot develop significantly higher tendon stress than the initial prestress level) was tolerable.

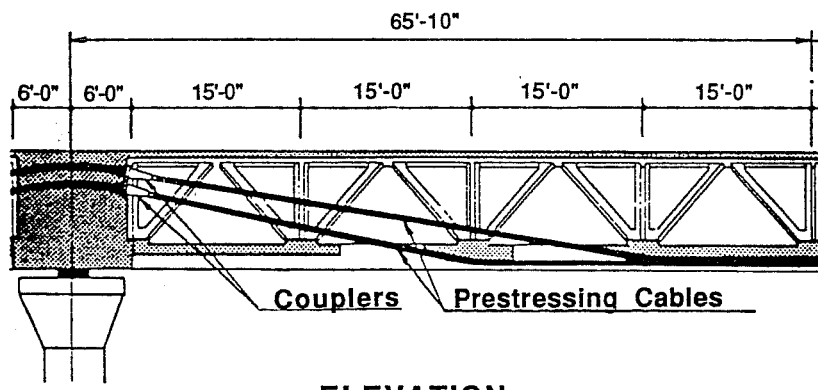
The rapid development in this area indicates that an ideal system is still evolving. There have been several impressive structures in which precast prestressed web elements have been used to fabricate concrete trusses which are post-tensioned with necessarily external tendons (Fig. 1.2). In addition, there is growing use of mixed systems in which combinations of concrete and steel have been used to form composite systems. An innovative example of a modern mixed system is shown in Fig. 1.3 in which external post-tensioning is used with concrete flanges in combination with corrugated steel webs to achieve a light structure capable of spans longer than conventional concrete box-girders (2). A logical extension for precast concrete box-girders is a mixed system of internal and external tendons which provides continuous bonded reinforcement across segment joints (Fig. 1.4). Long-span structures can be built with this method in which the structure is constructed in cantilever using internal tendons before additional strength is added for service loads by external post-tensioning.

1.1.2 Rehabilitation of Existing Structures. In addition to new construction, there has been wide use of external tendons for rehabilitating existing structures (1). Generally, external post-tensioning can be added to deficient structures to increase the axial stress component and, if deviators can be incorporated, to provide a small uplift to the structure. A large number of examples have been reported for rehabilitating both bridge and parking structures.

1.1.3 Advantages and Disadvantages of External Post-Tensioning. A comprehensive discussion of the advantages and disadvantages of external prestressing was presented by Powell (1). Powell's observations are presented in condensed form below.

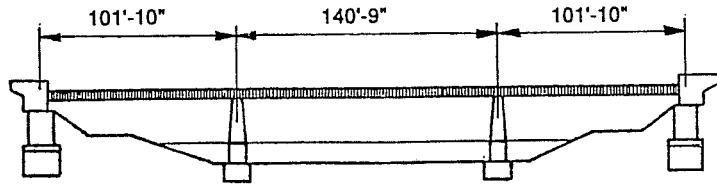


SECTION



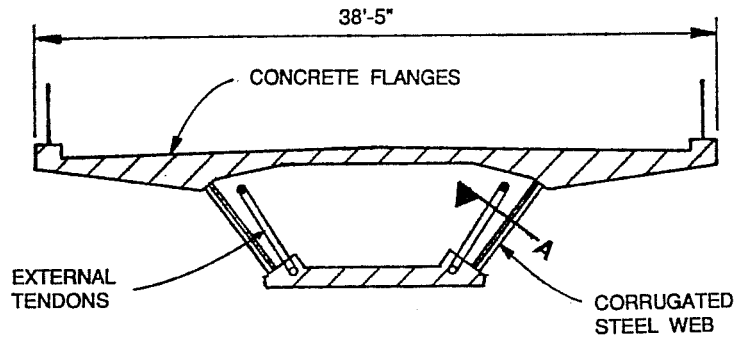
ELEVATION

Figure 1.2 Concrete Truss with External Tendons

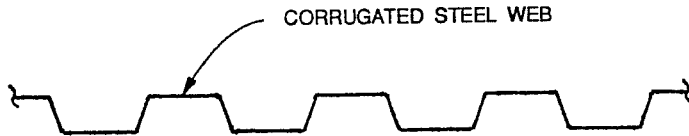


COGNAC BRIDGE

ELEVATION

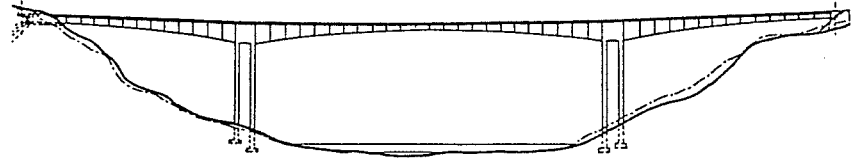


SECTION

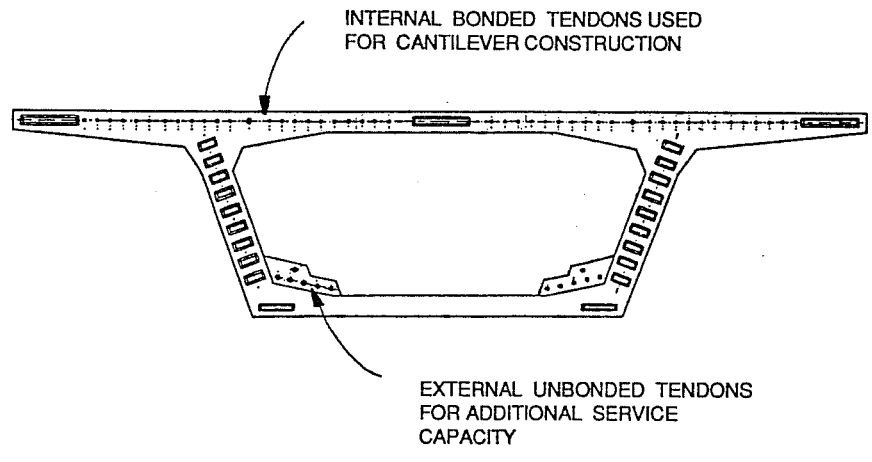


SECTION A

Figure 1.3 Mixed System with Steel Webs and Concrete Flanges



ELEVATION



SECTION

Figure 1.4 Mixed System with Internal and External Tendons

Advantages

- (1) Concrete cross-section is free of ducts:
 - (a) Thinner web sections can be used.
 - (b) There is no interference with the passive reinforcement which reduces the time required to assemble the segment cages. The segment cages can be assembled without worry of interference with the post-tensioning ducts, thus leading to "assembly line" efficiency.
 - (c) There is appreciably reduced congestion in the concrete cross-section which leads to better consolidation.
- (2) Access to the external tendon ducts is greatly improved. This eases the installation and grouting procedures and allows for possible tendon replacement.
- (3) The overall loss of prestress due to friction is reduced. The angular friction is approximately the same as for internal tendons, but the amount of horizontal angle change tends to be reduced. Wobble effects are almost non-existent.
- (4) Conventional fatigue is substantially eliminated because of the relatively low service load stress range in the unbonded external tendons.
- (5) The corrosion protection in a continuous external tendon duct can be made more certain than in an internal duct. Tendons are contained in a continuous sheath instead of epoxied joints where tendons pass between segments.
- (6) Misalignment of the internal tendon ducts is not a problem.
- (7) Very rapid construction is possible with the span-by-span erection system.

Disadvantages

- (1) Potential alignment problem of deviation hardware can lead to concentrated stress points in the external tendons and possibly decrease life due to fretting fatigue.

- (2) Vibrations of unrestrained lengths of external tendons have been noticed in several structures.
- (3) The external tendons are removed from the concrete section and extend through the inside of the box. The range of possible eccentricities is limited between the bottom of the top flange at the pier segment and the top of the bottom flange near midspan. This reduces the efficiency of the post-tensioning in two ways. First, the smaller eccentricities require larger tendon forces to achieve the desired service load stresses in the concrete section. Second, the smaller effective depth, from the extreme compression fiber to the tendon center-line, requires increased tendon forces to achieve the desired ultimate strength.
- (4) The external tendons are attached to the concrete section only at discrete locations along the span. Since the tendon strains are not compatible with the adjacent concrete strains, as in bonded construction, large tendon elongations must occur to achieve the increased tendon strains required for ultimate load conditions. This results in mechanism behavior with large concentrated rotations occurring at critical cracks or joints along the span. The ultimate tendon stress is a function of the effective tendon stress and develops considerably less stress than a similar bonded tendon.
- (5) The shear behavior of the system is changed because of mechanism behavior. At opening cracks or joints, the force is transferred across the joint by a local plastic truss mechanism. At regions between critical mechanism joints, the shear behavior is expected to be similar to monolithic construction. However, the shear strength at opening joints is limited by the tensile capacity of the web reinforcement crossing an inclined crack and is therefore expected to be less than that of monolithic construction.
- (6) The use of external tendons may result in reduced ductility since the failure is governed by the rotation capacity at a joint. In addition, the ultimate tendon stress is highly dependant on the end anchorage and deviation devices. Possible catastrophic failure may result if the tendons or diffusion elements are damaged.

- (7) Post-tensioning forces are applied to the structure at discrete locations inducing high local diffusion forces to the structure. Failure of any of the diffusion mechanisms could have serious consequences. The design of the deviator is covered in Reference (12) and is assumed to be fully adequate throughout this study.

1.2 Flexural Behavior of Girders with External Tendons

As outlined below, externally post-tensioned girders have two distinct ranges of behavior. The structure behaves linearly until cracking occurs or a dry joint begins to open. After joint or crack opening, the structure behaves as a mechanism with plastic hinges forming at critical cracks or joints. The flexural strength is reached when the rotation capacity is reached at the plastic hinge.

1.2.1 Before Cracking.

1.2.1.1 Comparison between Bonded and Unbonded Systems. In a fully bonded system where the tendon is completely encased in the concrete section and effectively grouted, changes in tendon strains are assumed to be the same as change in the concrete section at the level of the tendon. In an unbonded system (as with external tendons), the tendon strains are not compatible with the adjacent concrete strains. Assuming that no friction exists between the tendon and the surrounding duct, then tendon strain is constant over the full length between anchorages. The change in tendon strain due to applied loads is calculated from the total change in length of the tendon over its entire length. This is equal to the average accumulation of concrete strains at the level of the tendon between ends of the tendon. This leads to relatively low increases in tendon stress due to live load.

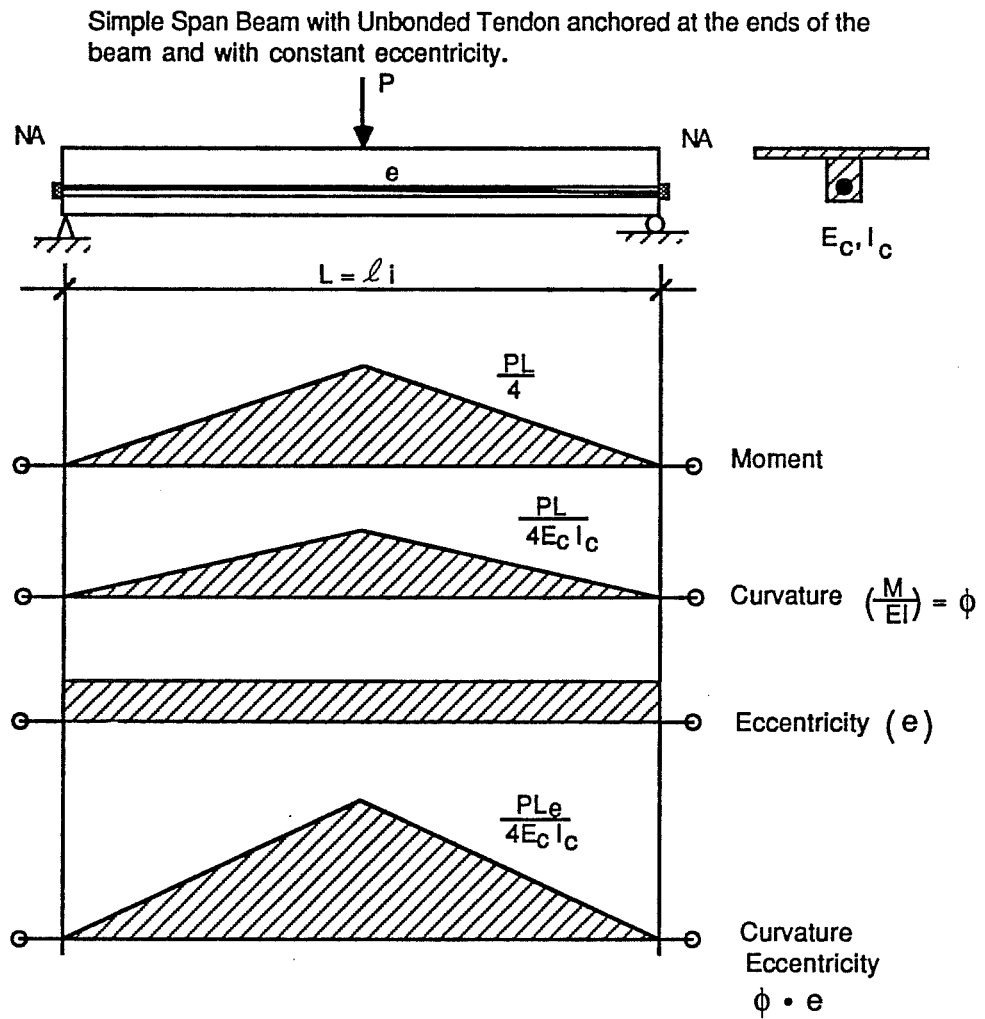
In an unbonded configuration the change in tendon stress, before cracking, can be calculated by integrating the product of the change in concrete section curvature (caused by the applied loads) and the eccentricity. This concept is shown graphically in Fig. 1.5. From the applied loads, the moments can be determined and the elastic curvature can be calculated directly. The curvature ordinate can then be multiplied by the eccentricity at each location along the beam. Note that the tendon eccentricity is considered positive when located below the centroid of the cross section. The change in tendon length can then be calculated directly by determining

the area under the curvature-eccentricity diagram between the ends of each tendon segment. The change in tendon strain is then calculated from the change in length divided by the free length of each tendon segment.

1.2.2 After Cracking or Joint Opening. In an externally prestressed girder, when a section cracks or a dry joint begins to open, the girder begins to “hinge” at that location. This causes local increases in the curvature and subsequently increased tendon stresses. This can be shown schematically in the curvature-eccentricity relationships shown in Fig. 1.6. Immediately prior to cracking the curvature is elastic and can be calculated directly from the moment and section properties. After the section cracks, the curvature increases over a finite hinge length causing a corresponding increase in the tendon strains for tendon segments crossing the plastic hinge.

1.2.2.1 Ideal Rigid Body Mechanism. The behavior of a multiple-span external tendon bridge structure can be simply modeled as a series of rigid members connected by hinges at the extreme compression fiber, and containing draped or straight tendons, as shown in Fig. 1.7. This model was first presented by Virlogeux (3) to illustrate the basic difference between bonded and unbonded systems for load levels higher than the cracking or joint opening load. A plastic mechanism analysis is first conducted to determine the critical mechanism joint locations. Although one generally thinks of mechanism analysis in terms of continuous structures, in this hybrid system it is very interesting to examine the simple case of a rigid body mechanism for a simple span structure with straight tendons. The general layout of the structure is shown in Fig. 1.8, and the load-deformation and tendon stress responses are shown in Figs. 1.9 and 1.10 respectively. The model consists of two rigid members that are hinged at the extreme top fiber and are prestressed with a tendon having an area, A_p , and an initial stress of f_{pe} . The stress-strain relationship for the prestressing strand is shown in Fig. 1.11. The actual behavior is replaced with an ideal elasto-plastic material model with elastic modulus of E_p and a limiting plastic stress of f_{pp} . The tendon is located at a constant lever arm of Z_p from the center of the plastic hinge.

In developing the load-deformation response, load is applied to the mechanism, and moment is plotted at the hinge location with respect to deflection. Because the structure consists of rigid bodies, no deflection occurs until the moment exceeds



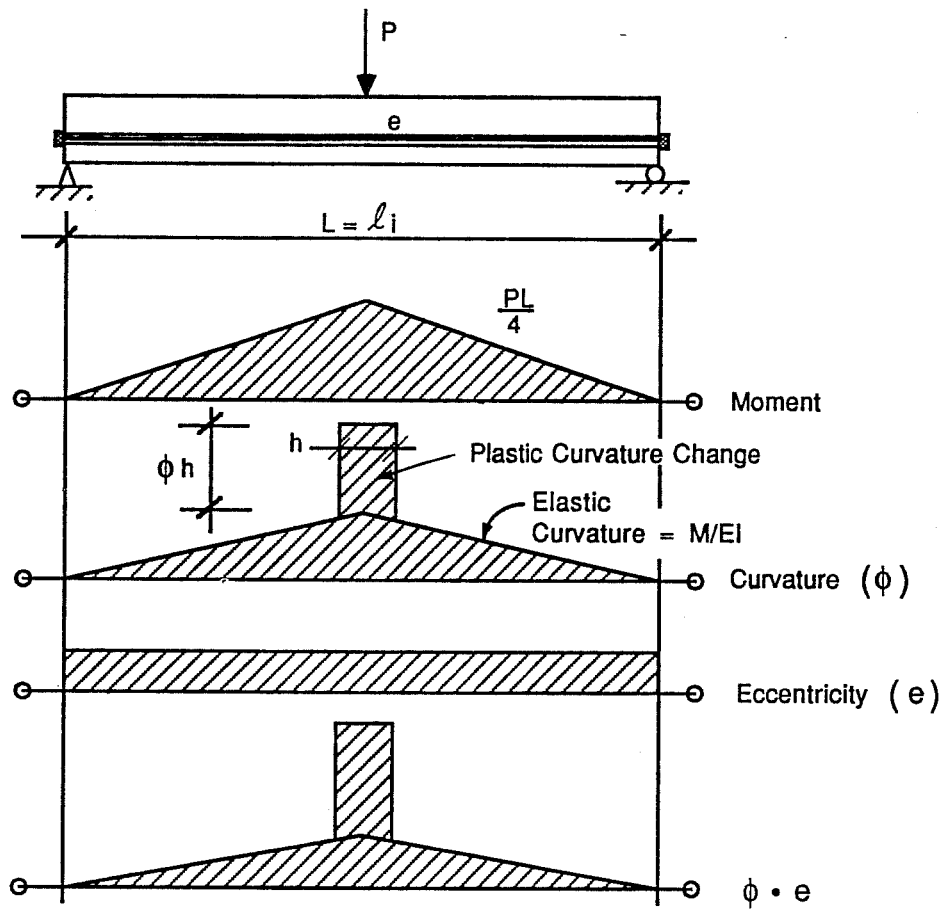
Elongation = area under $\phi \cdot e$ diagram

$$= \frac{PL^2 e}{8E_c I_c}$$

$$\Delta F_s = \text{Elongation} \left(\frac{E_p}{\ell_i} \right)$$

$$\Delta F_s = \frac{PLe}{8I_c} \left(\frac{E_p}{E_c} \right)$$

Figure 1.5 Calculation of Unbonded Tendon Stresses



$$\text{Elongation} = \frac{PL^2 e}{8E_c I_c} + \phi_h l_h e$$

$$\Delta F_s = \left[\frac{PL^2 e}{8E_c I_c} + \phi_h l_h e \right] \frac{E_p}{l_i}$$

Figure 1.6 Local Increase in Curvature at Plastic Hinge

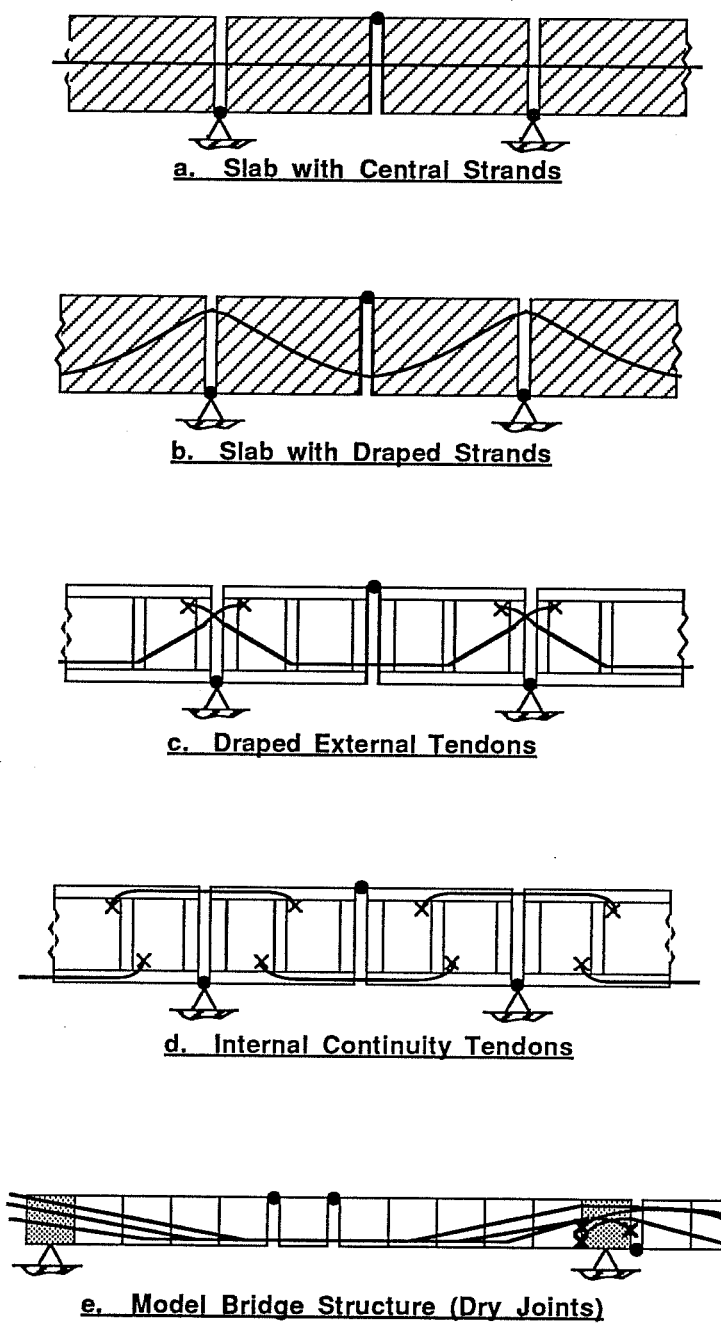


Figure 1.7 Rigid Body Mechanisms

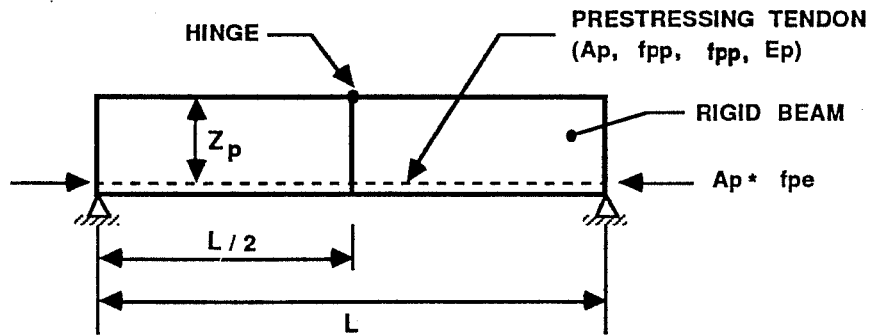


Figure 1.8 General Layout of Simple-Span Structure with Straight Tendons

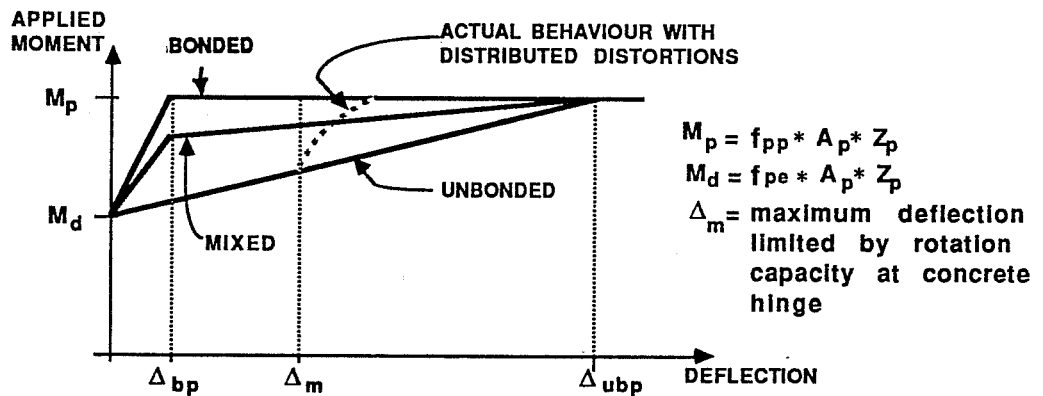


Figure 1.9 Applied Moment vs. Deflection

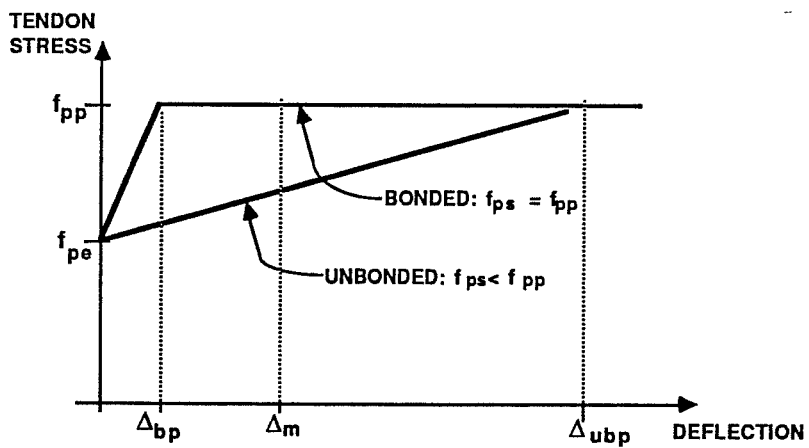


Figure 1.10 Tendon Stress vs. Deflection

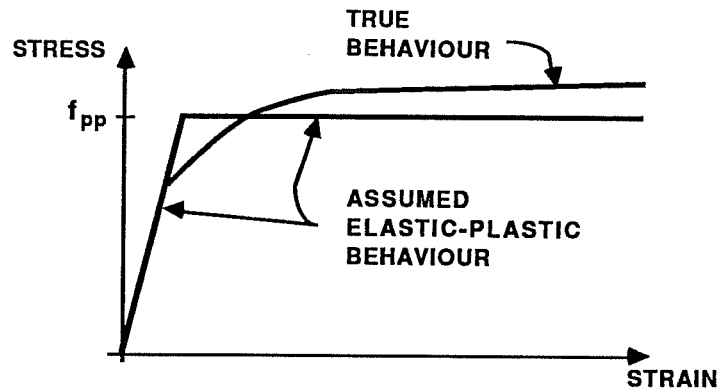


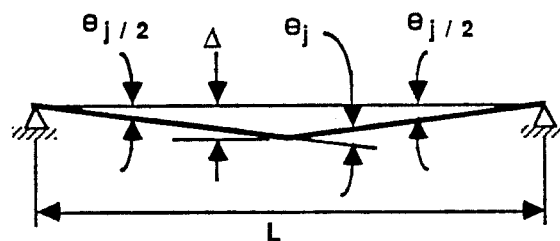
Figure 1.11 Stress-Strain Relationship for Prestressing Strand

the initial clamping moment due to the prestressing. The clamping moment, or decompression moment, M_d , equals the product of the initial prestress force ($A_p * f_{pe}$) and the lever arm, Z_p . Similarly, no elongations occur in the tendon until the hinge or joint begins to open. When the joint begins to open there is a geometric relationship between the midspan deflection and the elongation of the tendon. For rigid bodies, the tendon elongations occur entirely as the result of opening at the joint, with the magnitude of the elongation calculated as shown in Fig. 1.12. Note that the geometric relationships shown in Fig. 1.12 are specific for the simple-span mechanism with a centrally located hinge.

The corresponding tendon strains are calculated from the tendon elongation at the opening joint and the characteristic “free” length of tendon. Two cases must be considered:

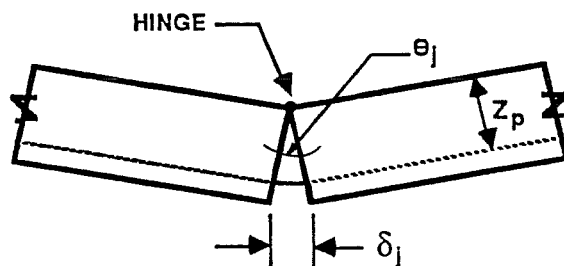
- (1) With bonded tendons:

The increase in tendon force is assumed to occur linearly over a development length, l_d . The total elongation can therefore be calculated as the area under the tendon-force curve as shown in Fig. 1.13. From moment

**MECHANISM GEOMETRY**

$$\frac{\theta_j}{2} = \frac{\Delta}{L/2}$$

$$\therefore \theta_j = \frac{4\Delta}{L}$$

**JOINT GEOMETRY**

$$\delta_j = \theta_j \cdot Z_p$$

$$\delta_j = \frac{4\Delta \cdot Z_p}{L}$$

Figure 1.12 Calculation of Tendon Elongation

equilibrium the change in tendon force is equal to the moment above the decompression moment divided by the distance, Z_p , between the resultant compressive force and the center of the tendon. Equating the two terms for elongation yields the expression relating applied moment and midspan deflection for a bonded-tendon girder.

- (2) With unbonded tendons:

In a similar manner an expression can be developed for unbonded tendons. In this case the strains are calculated from the elongations that occur at the opening joint averaged over the free length of the tendon segment, l_i . The resultant expression in terms of the tendon-segment length, l_i , and

the span length, L , is shown in Fig. 1.14. With anchorages provided at the end of the span, the equation can be further reduced with $l_i = L$.

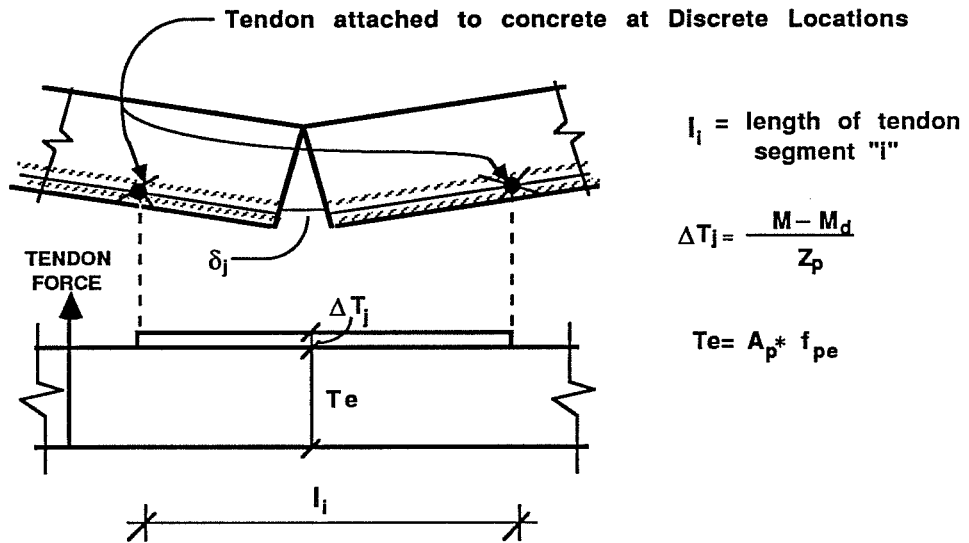
Assuming the tendons behave in an elasto-plastic manner, as shown in Fig. 1.11, the maximum plastic-moment capacity can be calculated as

$$M_p = A_{ps} * f_{pp} * Z_p$$

The deflections corresponding to plastification of the bonded and unbonded tendons can therefore be calculated and are shown on Fig. 1.9. Note that the deflection required to plastify the unbonded tendons is much greater than the deflection required to plastify the bonded tendons. With mixed systems, in which bonded and unbonded tendons are used, care must be made to ensure that the bonded tendons do not rupture before the unbonded tendons plastify.

The simple model outlined above describes the upper limit to behavior of prestressed systems and illustrates important considerations. A similar articulated rigid-member system can be developed for any prestressed system. Slab systems as well as draped externally prestressed systems can all be analyzed using this method, as shown in Fig. 1.7. Because perfect plastic behavior is assumed, this method represents an upper bound to the true strength.

1.2.2.2 Plastic Hinges in Concrete Structures. In order to extrapolate this simple plastic model to a real structure the concrete plastic hinge behavior must be included in the formulation. Instead of allowing unlimited rotation at an ideal hinge, the concentrated rotations must occur in the concrete adjacent to the critical opening joints or cracks. The plastic hinge occurs over some finite length, and the maximum rotation is limited by the curvature capacity of the reinforced segments. If we assume that the deflection is limited by the rotation capacity of the concrete section at the hinge, then the maximum deflection will be limited to Δ_m . With limited rotation, the ultimate moment capacity is limited for the unbonded and mixed systems, as shown in Fig. 1.9. Since plastification of the bonded tendons occurs at such an early stage, the ultimate capacity of the bonded-tendon girder is not seriously affected by the concrete hinge rotation capacity.



With Rigid Members: $\delta_j = \text{Tendon Elongation}$

$$\delta_j = \frac{\Delta T_j * l_i}{A_p E_p} \quad (\text{assumes } l_i \gg \delta_j)$$

From Mechanism and Joint Geometries

$$\Delta = \frac{l_i L}{4 A_p E_p Z_p^2} (M - M_d)$$

Deflection Causing Plastification of Unbonded Tendons, Δ_{ubp}

$$\Delta_{ubp} = \frac{l_i L}{4 E_p Z_p^2} (f_{pp} - f_{pe})$$

Figure 1.14 Moment-Deflection Response for Unbonded Tendons

Herein lies the primary difference between the ultimate flexural behavior of bonded and unbonded flexural members. In the bonded member the ultimate moment is primarily a function of the tendon properties, with the concrete properties being of only minor importance. In an unbonded member the flexural strength is governed by the rotation capacity of the concrete section adjacent to the hinge, and depends primarily on the concrete properties and reinforcing details adjacent to the hinge. Except for the initial prestress condition, the unbonded tendon properties have only minimum influence on the ultimate flexural strength since yielding does not occur.

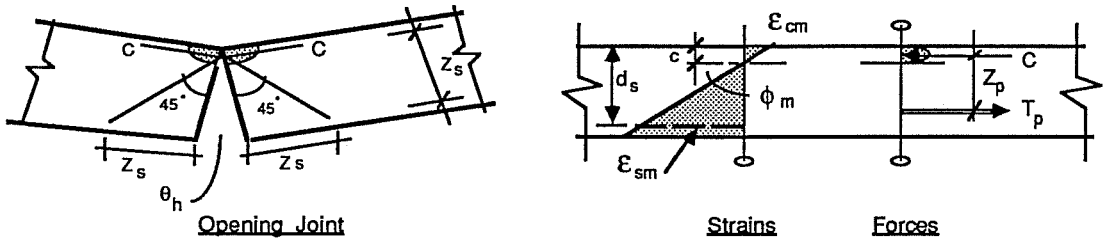
Two general methods have been presented for predicting the rotation capacity of a concrete hinge. The first method assumes that the length of the plastic hinge is approximately equal to the effective depth of the reinforced concrete section, and rotation occurs uniformly over this length. In the second method the length of the concrete hinge is assumed to be a linear function of the depth of the neutral axis, and rotation is assumed to occur equally along this length. These methods are described below.

1.2.2.2.1 Rotation Capacity and Tendon Elongations. Virlogeux (3) assumed that the concentrated rotations were distributed over a plastic hinge length equal to $2*Z_s$, (Z_s on either side of the critical crack or joint) where Z_s is the distance from the resultant concrete compressive force to the center of the passive reinforcement in the tension side of the reinforced concrete segment. This corresponds to a force diffusion angle of 45 degrees.

The curvature, ϕ_m , was assumed to be constant over the hinge length and was determined by limiting strains in the concrete compression zone and the passive segment reinforcement. The concrete compressive strains are ultimately limited by the crushing strain of the concrete, ϵ_{cu} , or conservatively for design by ϵ_{cm} (recommended to be .002 by Virlogeux). The tensile strain in the segment is limited by the maximum acceptable tensile strain in the passive segment reinforcement, ϵ_{sm} , and possibly depends on the anchorage characteristics of the tension-side reinforcement of the segment. Virlogeux suggested using a strain value of .010 for design.

If rotation is assumed to be centered about the resultant compressive force, and the curvature is assumed constant over the hinge region, then the tendon elongation within the concrete plastic hinge, δ_h , (shown in Fig. 1.15) can be determined

from the maximum curvature, ϕ_m , and the distances from the compressive force resultant to the prestressing tendon, Z_p , and to the passive segment reinforcement, Z_s . $Z_p(x)$ is Z_p as a function of x and is approximately constant over the short hinge length. Therefore, for constant eccentricity, the tendon elongation in the hinge region can be written as:



Z_s = distance from resultant compressive force to the segment reinforcement on the tension side

Concrete Hinge Length = $2 * Z_s$

ϵ_{cm} = maximum concrete strain = .002 for design (Virlogeux)
 ϵ_{sm} = Maximum strain in segment reinforcement = .010 for design (Virlogeux)
 $\phi_m = \frac{\epsilon_{cm} + \epsilon_{sm}}{d_s} = \text{maximum allowable curvature}$

Assume Curvature is Constant over Hinge Length

δ_h = Tendon Elongation occurring in Concrete Hinge region

$$\delta_h = \int_{-Z_s}^{Z_s} \left[\phi_m * Z_p(x) * \left(\frac{x}{Z_s} \right) \right] dx$$

with Constant eccentricity: $Z_p(x) = \text{Constant} = Z_p$

$$\delta_h = \frac{2\phi_m Z_p}{Z_s} \int_0^{Z_s} x dx \Rightarrow \underline{\delta_h = \phi_m Z_p Z_s}$$

Figure 1.15 Tendon Elongation in the Plastic Hinge Region

$$\delta_h = \phi_m * Z_p * Z_s$$

To calculate the change in tendon-stress that occurs at the hinge, the tendon hinge elongation must be divided by the free length of the tendon-segment

under consideration. With bonded tendons the increase in tendon stress occurs over a free length equal to the development length, ℓ_d as shown in Fig. 1.13. The maximum stress is also limited by the plastic stress of the tendon. Therefore the change in bonded-tendon stress caused by the elongation at a plastic hinge is:

$$\Delta f_{psb} = \left[\frac{\delta_h * E_p}{\ell_d} \right] < f_{pp} - f_{pe}$$

With unbonded tendons the increase in tendon stress occurs over the entire free length of the tendon-segment. The tendon-segment length, ℓ_i , can range from the length between the anchorages for friction-free systems to the length between deviators for slip-free systems. The change in unbonded tendon stress that occurs because of hinging is therefore calculated as:

$$\Delta f_{psub} = \left[\frac{\delta_h * E_p}{\ell_i} \right] < f_{pp} - f_{pe}$$

As was the case with bonded tendons, the maximum stress cannot exceed the plastic limit stress, although with unbonded tendons this limiting stress will seldom govern.

The rotation capacity at a hinge typically limits the plastic behavior of the system. Using the simple rigid-body plastic mechanism described above, the limiting midspan deflection can be determined. From the mechanism geometry, Fig. 1.12, the midspan rotation and deflection are related as:

$$\Theta = \frac{4 * \Delta}{L}$$

The maximum rotation that can occur at a plastic hinge is:

$$\Theta_m = \frac{\delta_h}{Z_p} = \phi_m * Z_s$$

Therefore, the limiting midspan deflection, Δ_m , is determined as:

$$\Delta_m = \frac{\phi_m * Z_s * L}{4}$$

This maximum deflection is shown schematically in the applied-moment vs deflection curve for the rigid body mechanism in Fig. 1.9. This illustrates how the rotation capacity at a plastic hinge limits the maximum attainable strength. The true situation is probably worse than this since bonded tendons will allow distribution of distortions and possibly higher total rotation. The true gradation of strengths may be more closely represented by the points of intersection of the dotted line and applied-moment vs deflection curves shown in Fig. 1.9.

The second method for estimating the limiting rotation capacity in a concrete plastic hinge was first proposed by Baker (4) in 1949. He made the assumption that "all changes in slope or curvature of a member can be related to and expressed in terms of the deformation in the concrete on the compression side of the neutral axis" (Fig. 1.16). In simple terms, the ultimate curvature in the concrete hinge region, shown in Fig. 1.16, can be determined from the ultimate strain gradient on the compressive side of the girder.

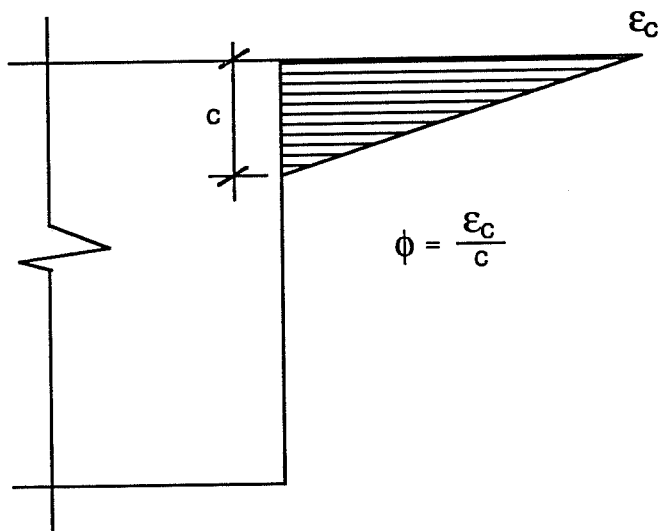


Figure 1.16 Local Increase in Curvature at Opening Joint

These assumptions form the basis for design recommendations first proposed by Tam and Pannell (5) in 1976. They assumed that the curvature was constant over a hinge region with length, ℓ_h , and could be determined from the ultimate concrete compressive strain, ε_{cu} , and the depth to the neutral axis, c_u , as shown in Fig. 1.17. They then conducted an experimental investigation to determine the relationship between the length of the hinge and the depth to the neutral axis, that is:

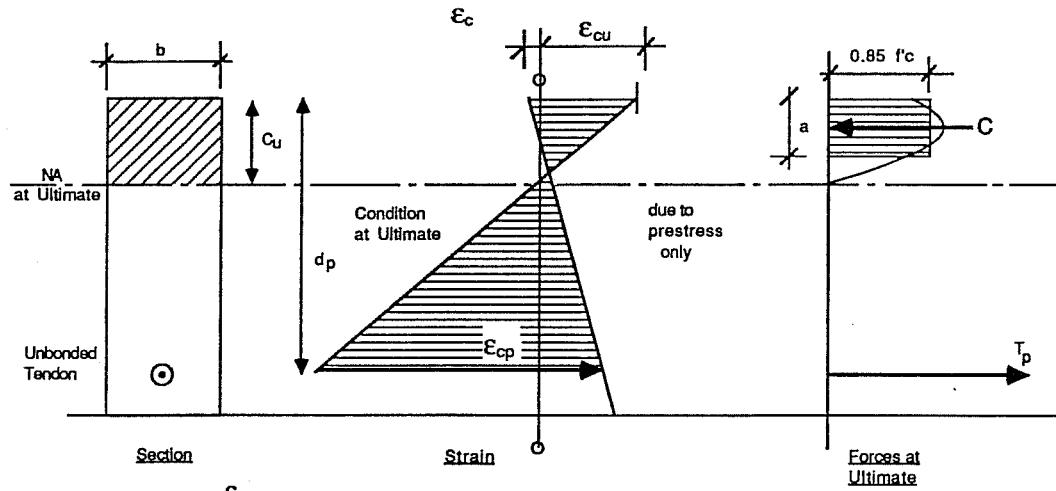
$$\ell_h = \psi * c_u$$

From their experimental study it was determined that the total length of the concrete hinge was approximately 10.5 times the depth of the neutral axis, ($\psi = 10.5$). Having determined the ultimate curvature in the hinge region and the length of the plastic hinge, they could calculate the maximum rotation and the ultimate elongation in the tendon as the structure was loaded to failure.

The derivation of an expression for the unbonded tendon stress when nominal strength is reached, f_{ps} , is presented in condensed form in Fig. 1.17. This expression is presented in its simplest form with only unbonded prestressed reinforcement considered. It is also possible to include the effects of bonded active and passive reinforcement in the formulation.

Ritz (6) used a similar mechanism analysis method as above and pointed out the importance of considering the deflection-to-span ratio limits in developing the dependable tendon stress that can be mobilized in unbonded tendons. He has indicated that the values for attainable tendon stress used in the ACI Building Code (7) are probably unrealistically high for longer-span members found in bridges.

1.2.2.2.2 Multiple Hinges. It is important to note at this stage that the load deflection response developed above is specific for a simple-span structure with a central plastic hinge. The elongation that occurs in a tendon which crosses several plastic hinges is a function of the overall geometry of the critical beam mechanism. A plastic mechanism analysis must be conducted on the structure to determine the locations of the critical opening hinges and the relative angle change that occurs at each hinge.



ϵ_{cu} = Ultimate crushing strain in concrete

ϵ_{ci} = Initial concrete strain on flexural compression side

ϵ_{cp} = Change in concrete strain at the level of the unbonded tendon

C = Compressive force in concrete at ultimate

$$C = 0.85f'_c b a = 0.85f'_c b \beta_1 c_u$$

T_p = Tension force in unbonded prestressed reinforcement at ultimate

$$T_p = f_{ps} A_p$$

f_{ps} = Stress in unbonded prestressed reinforcement at ultimate

$$f_{ps} = f_{pe} + \frac{\delta_h E_p}{\ell_i}$$

δ_h = Elongation in unbonded tendon occurring over the length of the plastic hinge (ℓ_h)

$$\delta_h = \int_{-\frac{\ell_h}{2}}^{\frac{\ell_h}{2}} (\epsilon_{cp}) dx = \epsilon_{cp} \ell_h$$

Assume ℓ_h = function of the neutral axis depth

$$\ell_h = \psi c_u$$

(ψ was determined experimentally to be approximately 10.5)

From Geometry of Strains

$$\epsilon_{cp} = \left(\frac{d_p - c_u}{c_u} \right) [\epsilon_{cu} + \epsilon_{ci}]$$

Assume $\epsilon_{ci} \ll \epsilon_{cu}$

$$\therefore \epsilon_{cp} = \left(\frac{d_p - c_u}{c_u} \right) \epsilon_{cu}$$

Therefore:

$$f_{ps} = f_{pe} + \psi E_p \epsilon_{cu} \left(\frac{d_p - c_u}{\ell_i} \right)$$

Figure 1.17 Tam and Pannell Method

Only tendons crossing an opening hinge will undergo the elongations, and the elongations will be limited by the amount of rotation that occurs at that joint. If a particular tendon crosses several opening hinges and friction is assumed to be zero between the hinges, then the tendon elongation is the sum of the elongations at each hinge. This is generally the case with slab structures in which individual strands are draped to the tension side and are contained in a greased duct.

However, the case of cumulative elongations may not be true for bridge structures, primarily for two reasons. First, in a bridge structure with external tendons that are deviated at discrete deviation points, the level of friction may resist free sliding of the tendons. In this case the elongation that occurs at each hinge may not be additive to elongations occurring at other hinges. This will depend on the magnitude of the friction and whether slip occurs at the deviators. The effect of deviator slip will be discussed in more detail in the next section.

Another reason that elongations are not necessarily additive is a result of the method of construction, and is illustrated by the model tendon configuration shown in Fig. 2.7. External post-tensioning tendons are typically stressed from the pier segments and are one full span in length. Since the interior spans have reduced flexural requirements they will often have reduced post-tensioning. This causes the critical support mechanism to form at the interior face of the first interior pier segment. If this is the case then the support mechanism involves a different set of tendons than the critical midspan mechanism. Clearly, for this case, the elongations occurring at one mechanism are not additive to the elongations occurring at the other.

1.2.2.3 Slip of Tendons at Deviators. One of the major unknowns in this area is the effect of friction between the tendons and the ducts, particularly at the deviators. Two basic assumptions are used for bounding the solution. First, the tendons are assumed to slip freely at all deviators thus providing the longest free lengths for the unbonded tendons. This assumption will produce a lower bound to the ultimate strength and an upper bound on structural flexibility. The second assumption that can be made is that the tendons will not slip relative to the deviators. In this case the solution will produce an upper bound to ultimate strength and a lower bound on structural flexibility. Obviously the true behavior lies somewhere between these two extremes.

A major point of interest in the experimental program is the amount of slip that might actually occur in the model between tendon and deviator during various load cycles. Instrumentation was provided to verify tendon strains and hence, forces along the span.

1.3 Previous Studies on Externally Post-Tensioning Girders

1.3.1 *Experimental Research*

1.3.1.1 *St. Remy Laboratory.* Under the combined auspices of the French organizations SETRA (Service d'Etude Technique des Routes et Autoroutes) and CEBTP (Centre Experimentale de Rechere et D'Etudes du Batiment et des Travaux Publics), engineers at the laboratory at Saint-Remy conducted tests of four externally post-tensioned segmental box-girders (8). The primary objective of the study was to examine the ultimate behavior of segmentally precast box-girders with external post-tensioning tendons.

The test girders were match cast and erected with dry joints. The reduced-scale cross-section used for all four tests was a simple, compact prismatic box-girder (Fig. 1.18). The girders differed in tendon profile and type of tendon protection (grouted, and hot wax injected). The fourth test girder also included some bonded internal tendons. The behavior of the deviators and their effect on the overall behavior was not a parameter in this study.

The simply supported girders were loaded symmetrically with point loads at the outer quarter points. All girders experienced the same failure mode, independent of tendon profile or protection. First, the central joints opened and continued to open to the level of the bottom surface of the top flange. A primary mechanism formed with large rotations occurring at the first joint to the outside of the load points. At the same time, diagonal cracks propagated upward from the shear keys in the compressed region. The stress in the tendon did not rise significantly until the mechanism formed. Failure was initiated by crushing in the webs in the region of the highly compressed top flange.

The experimental results agreed reasonably well with calculations performed according to methods presented previously by M. Virlogeux (3).

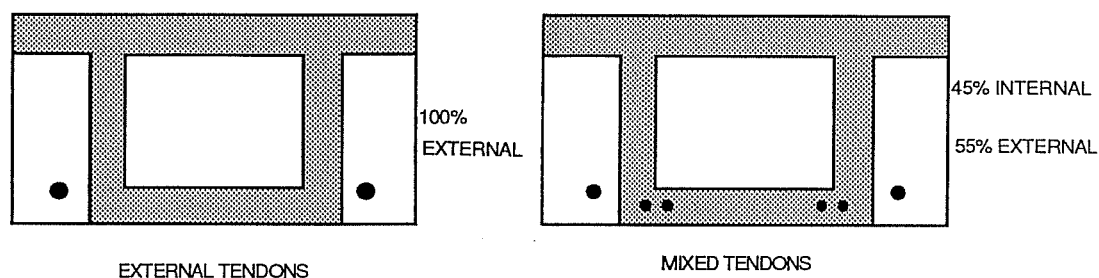
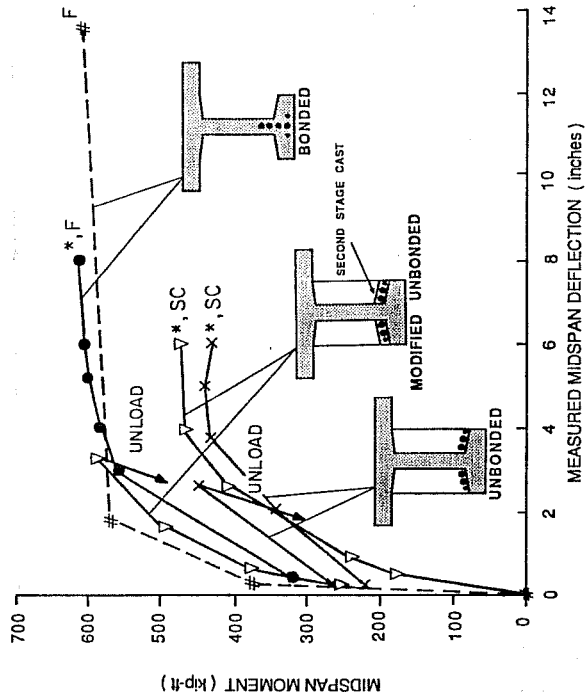


Figure 1.18 Saint-Remy Test Girders

Fig 1.19a shows a theoretical moment-deflection curve for a simple beam model similar to the St. Remy tests, analyzed assuming monolithic construction with internal bonded tendons. It also shows the test results for the same member with a mixture of internal bonded tendons and external unbonded tendons, as well as test results with external unbonded tendons alone. This comparison illustrates the loss of tendon strength development and possible reduction in ductility for the external tendon case.

1.3.1.2 Construction Technology Laboratory. At the request of Figg and Muller Engineers, Inc., Construction Technology Laboratories (CTL) conducted tests of three simply supported segmental girders with different post-tensioning systems. One girder had conventional bonded internal tendons, a second had unbonded external tendons, and a third included external tendons encased with a secondary cast, making them modified unbonded. The primary objectives were to verify the theoretical analyses and to compare the behavior of the three types of post-tensioning systems (9).

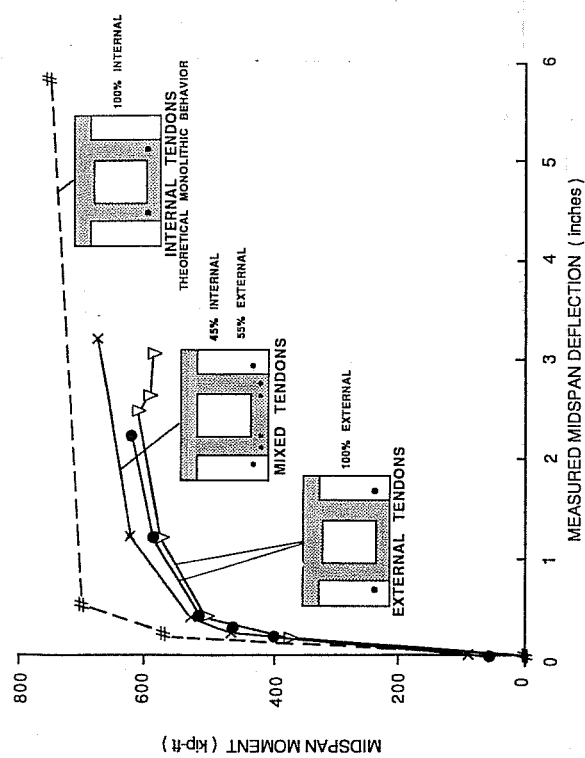


Notes:
 Midspan Moment = dead load moment + applied load moment
 Measured midspan deflection = deflection due to applied load only

- #-- Monolithic with bonded tendons (theoretical)
- Segmental with bonded tendons and dry joints
- x— Segmental with unbonded tendons and dry joints
- ▽— Segmental with modified unbonded tendons and dry joints

Failure modes: F = Flexural failure
 SC = Shear compression failure

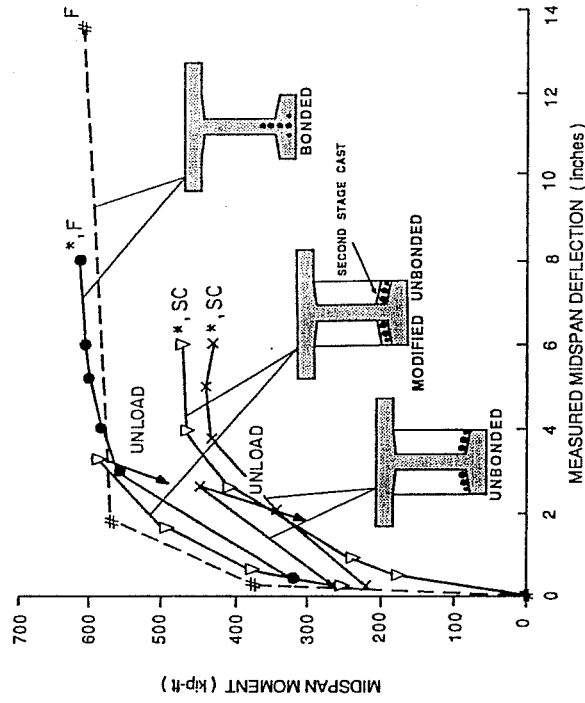
* Some anchorages burned before reloading.



Notes:
 Midspan Moment = dead load moment + applied load moment
 Measured midspan deflection = deflection due to applied load only

- #-- Monolithic, bonded internal tendons (theoretical)
- Segmental, external tendons, dry joints, cement grouted ducts
- ▽— Segmental, external tendons, dry joints, grease-injected ducts
- x— Segmental, mixed tendons, dry joints, cement grouted ducts

Figure 1.19 Moment-Deflection Behavior

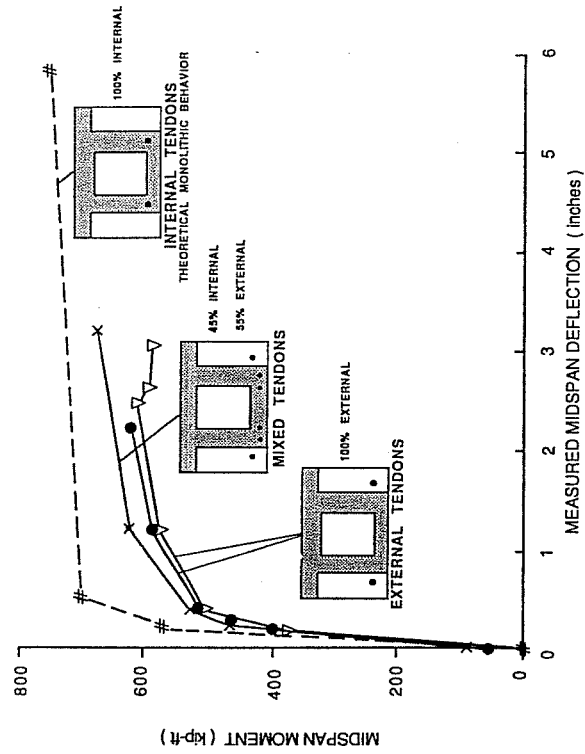


Notes:
 Midspan Moment = dead load moment + applied load moment
 Measured midspan deflection = deflection due to applied load only

- #-- Monolithic with bonded tendons (theoretical)
- Segmental with bonded tendons and dry joints
- × Segmental with unbonded tendons and dry joints
- ▽ Segmental with modified unbonded tendons and dry joints

Failure modes: F = Flexural failure
 SC = Shear compression failure

* Some anchorages burned before reloading.



Notes:
 Midspan Moment = dead load moment + applied load moment
 Measured midspan deflection = deflection due to applied load only

- #-- Monolithic, bonded internal tendons (theoretical)
- Segmental, external tendons, dry joints, cement grouted ducts
- ▽ Segmental, external tendons, dry joints, grease-injected ducts
- × Segmental, mixed tendons, dry joints, cement grouted ducts

Figure 1.19 Moment-Deflection Behavior

Fig. 1.20 shows the I-shaped cross-section used for each girder. Deviator behavior was not of interest in this test series, so deviators were conservatively designed. The match-cast segments were assembled with dry joints and the ducts containing all tendons were cement-grouted.

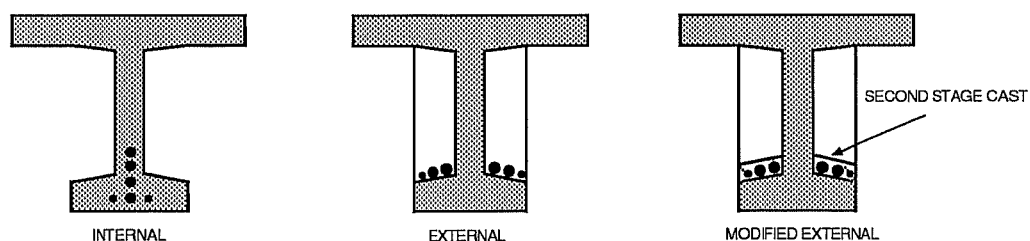


Figure 1.20 PCA Test Girders

The girders were statically loaded in two cycles. The first cycle loading increased incrementally until the girder reached a midspan deflection of about 3 inches or approximately $L/120$ (span length was 30 feet). The girders were subsequently unloaded and, in an attempt to simulate an anchorage loss in the case of an earthquake, the wedges for some of the strands were burned and removed. The girders were then reloaded incrementally to failure.

The failure mode for the bonded tendon girder was flexural, with the concrete in the compression zone crushing simultaneously with the fracturing of the strands in the tensile zone. The unbonded and modified unbonded tendon girders both experienced a shear compression failure in the web at the top flange interface. In these cases the joints opened and shear keys progressively broke, concentrating strain in the top flange.

Fig. 1.20 shows the I-shaped cross-section used for each girder. Deviator behavior was not of interest in this test series, so deviators were conservatively designed. The match-cast segments were assembled with dry joints and the ducts containing all tendons were cement-grouted.

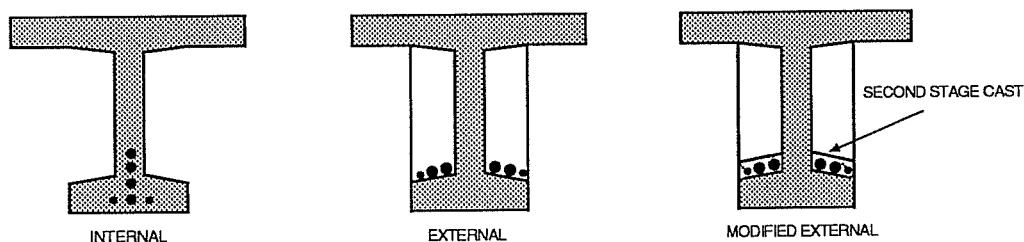


Figure 1.20 PCA Test Girders

The girders were statically loaded in two cycles. The first cycle loading increased incrementally until the girder reached a midspan deflection of about 3 inches or approximately $L/120$ (span length was 30 feet). The girders were subsequently unloaded and, in an attempt to simulate an anchorage loss in the case of an earthquake, the wedges for some of the strands were burned and removed. The girders were then reloaded incrementally to failure.

The failure mode for the bonded tendon girder was flexural, with the concrete in the compression zone crushing simultaneously with the fracturing of the strands in the tensile zone. The unbonded and modified unbonded tendon girders both experienced a shear compression failure in the web at the top flange interface. In these cases the joints opened and shear keys progressively broke, concentrating strain in the top flange.

When the CTL test results are compared with a theoretical moment-deflection curve for a monolithic, fully bonded girder, as shown in Fig. 1.19b, the reduced capacity of unbonded systems in both strength and deformation capacity is evident. Because of the test procedures used in the test, it is difficult to determine the insitu condition of the structure. Having the tendon anchors burnt at their ends, the tendons tend to distress in the end regions. In the bonded internal tendon girder the stress release affected the end regions only, and all of the tendons were effective in the midspan region. For the unbonded external tendon girders the stress release affected a larger portion of the girder. Because it is not known whether tendons slipped in the anchorage or deviator, the effective tendon area in the midspan region is unknown. It is therefore difficult to draw definitive conclusions from this test series.

1.3.2 Analytical Research

1.3.2.1 University of Texas. Several programs have been developed to analyze externally post-tensioned box-girders. Most of these programs are based on finite element formulations with generalized assumptions regarding the behavior near opening joints. Working in parallel with this project at The University of Texas at Austin, El Habir (10) coded and tested a program based on the following finite elements:

Fibrous Strip Beam Elements - The concrete segments were modeled with a fibrous strip beam element which accounted for the layering of the concrete and steel reinforcement. Inelastic material models were incorporated for the concrete, passive segment reinforcing steel, and any bonded active reinforcement. Program testing revealed that segment elements near critical mechanism joints required a finer strip selection to accurately model the large rotations that occur.

Joint Elements - Finite joint elements joined adjacent segments at a precast joint. The joint element transferred the compressive forces across the joint and could differentiate between dry and epoxy joints on the tension side of the joint.

External Tendon Elements - The external tendons were modelled with direct tension members which were attached to the concrete section by

rigid links. The initial tendon strains were input and then released on the unstressed structure. Several trials were therefore necessary to model known initial post-tensioning tendon forces.

The method was tested on segmental structures with external tendons and provided a reasonable estimate of behavior. The method needs improvements however to allow for tendon slip at the deviators, post-tensioned instead of pre-tensioned conditions, and a more convenient method for tackling complex construction sequencing.

Virlogeux (3) has shown promising comparisons with French tests using an analytic model developed in France by SETRA. At the recent International Symposium on Externally Post-Tensioned Bridges held in Houston, Texas in October 1988, Muller and Gauthier (11) reported on a computer program DEFLECT which showed very good agreement in modelling the CEBTP-SETRA and CTL test data.

1.3.3 Additional Related Research. The behavior of bridges constructed using external tendons and subjected to overloads has not been thoroughly documented. In addition to the global behavior studied by the scale-model project reported herein, uncertainties also exist concerning the proper design criteria and methodology for important details. A comprehensive investigation of deviator details was investigated in Ferguson Laboratory at The University of Texas at Austin by Powell and Beaupre (12). Contemporary deviation details as well as several proposed details (such as the use of epoxy coated reinforcement) were tested to failure in the laboratory. This study isolated components of deviator strength and presented behavioral observations and design methodology. Currently, the deviator test setup is being utilized to investigate the important problem of fretting fatigue at the deviators.

Another important aspect of behavior of externally post-tensioned segmental construction is the shear behavior at a critical mechanism joint. This was studied by Ramirez (13) at Ferguson Laboratory for segmentally precast girders with dry and epoxied joints and for various shear-span to depth ratios.

1.4 Object and Scope of Model Study

The objectives of this portion of the study for the Texas SDHPT, which is currently using this type of construction in several miles of elevated freeway in San Antonio, were to:

- (1) determine the level of strength and ductility that may be expected for segmentally precast bridges with external post-tensioning tendons, current tendon anchorages and joint details, and alternate joint details.
- (2) recommend changes in joint details and tendon patterns where changes will improve the behavior of the system without significantly reducing construction efficiency.
- (3) develop suitable analysis methods.
- (4) recommend methods for design and load rating criteria.

This phase of the study was restricted to the behavior of multi-span segmental box-girder bridges with external tendons, and focused on the results of a reduced scale model test. Another study now currently underway at Ferguson Laboratory will continue testing of this same model but will improve tendon bonding by physically connecting the tendons to each segment. In addition, the current test will study the effect of mixed external and internal tendons. Both of these subjects are outside the scope of the study reported herein. One of the most significant variables in the model test was the presence or absence of epoxy joints. One exterior span of the model was constructed with dry joints, while the other two spans had epoxy joints.

1.5 Summary

The body of this report is organized as follows:

Chapter 2 contains a summary of the design and construction of the reduced-scale bridge model. Chapter 3 gives technical details of the instrumentation and data acquisition systems. Observations made on the structure during the construction process are presented in Chapter 4, and Chapter 5 furnishes an analysis and interpretation of erection stresses. Chapter 6 outlines and discusses the

service level, factored design level, and ultimate load tests, and Chapter 7 evaluates the major findings of the study based on all test results. Finally, conclusions and recommendations developed from the model test are summarized in Chapter 8.

CHAPTER 2

DESIGN AND CONSTRUCTION OF BRIDGE MODEL

2.1 Development of Bridge Model

This chapter summarizes the design and construction of the scale model bridge. Model similitude requirements are determined and dimensionless behavioral parameters are formed. Design criteria are scaled from the prototype structure. Material, structural components, and erection procedures and details are described in detail.

2.1.1 Dimensional Analysis. The purpose for building a scale model is to conveniently simulate the behavior of a prototype structure. To construct a true structural model, from which behavioral observations can be directly extrapolated to the prototype structure, geometric, material, and loading conditions must be properly scaled. The Buckingham II theorem (Ref. 14) states that for true structural similitude, dimensionless parameters, γ , formed from behavior-affecting variables, must be equal for the model and the prototype structures.

$$\gamma_{model} = \gamma_{prototype}$$

In Appendix A, dimensionless parameters (Π_i) have been formed from variables that affect deflections and section forces (Ref. 15), the ultimate flexural strength and the associated bonded and unbonded strand stresses. The choice of dimensionless parameters is an arbitrary process in which behavior associated terms are grouped together. Considerable insight, as well as specific model requirements are gained through examination of these parameters.

The variables that affect deflections are presented in Appendix A.1. The variables include geometric relationships, section forces, and material and system properties. The dimensionless terms are expanded to give three basic requirements. The first requirement (Π_1) is that the dimensions and loading of the model structure be geometrically similar to prototype construction. The second term, Π_2 , illustrates an inherent problem in reduced scale prestressed concrete models. The Π_2 term indicates that section forces, and therefore tendon forces, vary with the square of

the scale factor. However, the tendons are anchored in the pier segments which have a volume that decreases by the cube of the scale factor. This means that a proportionally larger amount of force must be transferred per unit volume of pier segment. This causes severe congestion in the anchorage regions of reduced scale models of post-tensioned systems.

The final three Π terms require that the model be constructed with materials having similar properties as those used in the prototype structure. The stress-strain relationships for the concrete, prestressing strand, and mild steel reinforcement must be similar to those used in prototype construction.

The variables that affect section forces are presented in Appendix A.2. The variables include geometric relationships, loading information, and material properties. The first two Π terms are similar to the previously discussed deflection terms and require geometric and material similarity. The last three Π terms relate the prototype loading with the equivalent model loading. The first of these loading requirements involves the section forces resulting from the structural self weight. To achieve similar self-weight stresses in the model and in the prototype, the model must be constructed with a material having a density that scales inversely with the scale factor. Since it is not practical to construct the model with an increased density and still maintain material similitude requirements, dead load compensating weights are suspended from the structure. The next loading similitude requirement involves the section forces that result from uniformly distributed applied loads (Force/Length). To achieve the same stresses in the model and in the prototype, a uniformly distributed load must be scaled linearly with the scale factor. The final loading similitude requirement involves section forces resulting from concentrated applied loads. To achieve similar stresses in the model and in the prototype, a concentrated load must be scaled by the square of the scale factor.

Variables that affect the ultimate flexural strength of box-girder structures are presented in Appendix A.3. The variables include geometric and material properties for the concrete section and the prestressing tendons. Dimensionless parameters have been developed in Appendix A.3 to provide two types of similitude requirements. The first two dimensionless terms are the external and internal post-tensioning reinforcement ratios. These ratios and the ratio of external to internal

tendon area require geometric similarity. The last four dimensionless terms represent various limits of flexural strength. The first two terms are limited by the tensile forces in the external and internal tendons, while the last two are limited by the compressive strength of the concrete.

Possible variables that affect the stress in bonded internal tendons at ultimate flexural strength are presented in Appendix A.4. The variables include geometric and material information about the concrete section and the post-tensioning tendons. The dimensionless parameters provide geometric and material similitude requirements. An examination of the ACI Building Code formula for nominal strength tendon stress of bonded prestressing, also shown in Appendix A4, reveals that many of these parameters are included in the formulation.

Possible variables that affect the stress in unbonded external tendons at ultimate flexural strength are presented in Appendix A.5. The variables include geometric and material information about the concrete section and the post-tensioning tendons similar to the bonded tendons. In addition, several other parameters specific to unbonded tendons have been added. These include specific geometric properties of the external tendon, d_e and l_i , as well as an index of the effective prestress in the cross-section, M_d . Dimensionless parameters were expanded to provide three types of expressions. The external tendon reinforcement ratio, the ratio of external to internal tendon area, and the ratio of l_i/d_e provide geometric similitude requirements. The next four terms require material similarity. The last dimensionless term relates the moment that causes decompression of the extreme tension fibers in the cross-section with an effective prestress moment.

The dimensional analysis was undertaken for several reasons. The primary purpose was to establish the framework for constructing a true structural model. Every level of the dimensional study provided geometric and material similitude requirements. To achieve similitude of stresses, specific loading requirements must be followed. A second purpose for developing dimensionless parameters was to examine how variables interact with other variables on a dimensional basis. Arbitrary grouping of parameters can be very useful for understanding overall behavior.

2.1.2 Scale Selection. The selection of scale for a particular model involves the consideration of many interrelated factors. The costs, availability, and

limitations of components and materials must be examined. A preliminary design of the structure, loading, instrumentation, and fabrication systems should be carried out to ensure that research objectives can be met with the proposed model. Preliminary estimates of labor requirements should also be examined.

A study of fabrication and loading costs, as a function of scale factor, was performed by Breen (16) for a reinforced concrete skewed bridge system. He found that optimum economy was achieved for a scale of approximately $1/8$ with less than a 50% increase in cost for scales between $1/4$ and $1/32$. For scales larger than $1/4$, material and loading costs become excessive, and for very small models instrumentation and fabrication costs govern.

The availability of materials and model components, such as small-scale reinforcing bars, will often dictate a range of minimum and maximum scales. If conventional post-tensioning strands and anchorages are to be used, then minimum strand diameters and stressing hardware may dictate a minimum scale. Similarly, if "Ready-mix" concrete is to be used then the smallest locally available aggregate size, which affects reinforcement cover, will dictate a minimum scale. Budget limitations and the availability of test space may dictate a maximum scale.

Externally post-tensioned box-girder bridges are usually constructed continuous over several spans. The Phase 1a Development of the San Antonio Y project consists of 4 to 8-span continuous box-girders ranging in length between 390 and 720 feet. A multi-span model was therefore decided to be characteristic of prototype construction. A three-span structure was chosen with the interior span providing a realistic amount of restraint for the end spans. The interior span is also representative of an interior span of a multi-span structure. The continuity of the structure over the interior supports allow for investigation of negative-moment flexure and shear at an opening joint. The two similar end spans allow for direct comparison of the effects of epoxy joints on service and ultimate load behavior.

The detailed layout of precast segments was determined using the San Antonio Y structure as a guide. A large portion of the Phase 1 development consists of 100 ft spans with ten 9'-0" segments per span, 9'-0" pier segments, and 6 inch C.I.P. closure strips between the pier segments and the span segments. A $1/4$ scale was chosen to allow the use of multiple strands and conventional anchorage hardware

for the tendons and locally available ready-mixed concrete. The model layout is shown in Figure 2.1. The model has essentially the same segment layout as the prototype structure, except proportionately larger closure strips were used in the model to ensure proper concrete consolidation.

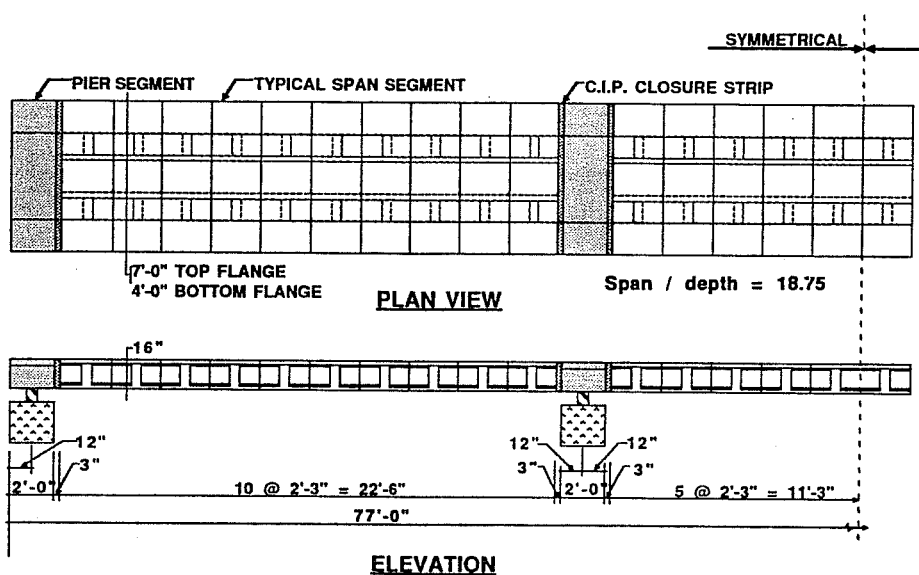


Figure 2.1 Test Set-Up

2.1.3 Design Criteria. For the model structure to be a good representation of prototype construction the design must follow the same general procedures and criteria. Cross-sectional requirements, loading and load combinations, and design allowable stress limits used in the model were appropriately scaled from prototype design requirements.

Podolny and Muller (17) suggest the use of an "Efficiency" factor for comparing similar cross-sections. This factor, E , uses the radius of gyration, r^2 , and the distances from the neutral axis to the top and bottom fibers (y_t and y_b).

$$E = \frac{r^2}{y_t * y_b} = \frac{I}{A * y_t * y_b}$$

This parameter compares the ability of the cross-section to resist applied moments to the cross-sectional area (a measure of concrete volume if integrated with length). An efficiency value of approximately 60% is considered optimum for box-girder construction.

Several types of cross-sections were considered for use in the model. A box-section, shown in Fig 2.2a, is geometrically similar to prototype construction and would provide the best representation. Difficulties in fabrication and instrumentation of the external tendons within the reduced scale box forced the use of other types of sections. An open box, with torsional bracing in the top flange, shown in Fig 2.2b, was briefly considered for its true tendon profile and open access for fabrication and instrumentation. This section was considered to be too different from actual construction to be a representative model. An "I" section (Fig 2.2c) was also considered for its ease of construction but was also regarded as not representative of box-girder bridge construction. Finally a modified box-section (shown in Fig 2.2d) was developed. The webs were shifted towards the center to provide space for the draped external tendons on the outside of the box. This section maintains a good representation of conventional box-girders as well as providing access to the primary external tendons. Differences in tendon deviation reinforcement and the cross-section's torsional response did not significantly affect the overall behavior of the system.

To obtain the same dead load stresses in the model as in the prototype structure, the model should have been constructed with a material having four times the density of the prototype structure. Because this was not practical, dead load compensating weights, equalling three times the structural weight, were suspended from the model structure.

Model Dead Load Calculations:

$$\text{Model Section Weight} = 433\text{in}^2 \times .150\text{kcf} \times 1/144 = .451\text{klf}$$

$$\text{Dead Load Compensating Weights} = 3 \times .451\text{klf} = 1.353\text{klf}$$

$$\text{Total Dead Load} = .451\text{klf} + 1.353\text{klf} = 1.804\text{klf}$$

The model structure was designed to carry its own dead weight plus superimposed live loads in conformance with the AASHTO Bridge Design Specification

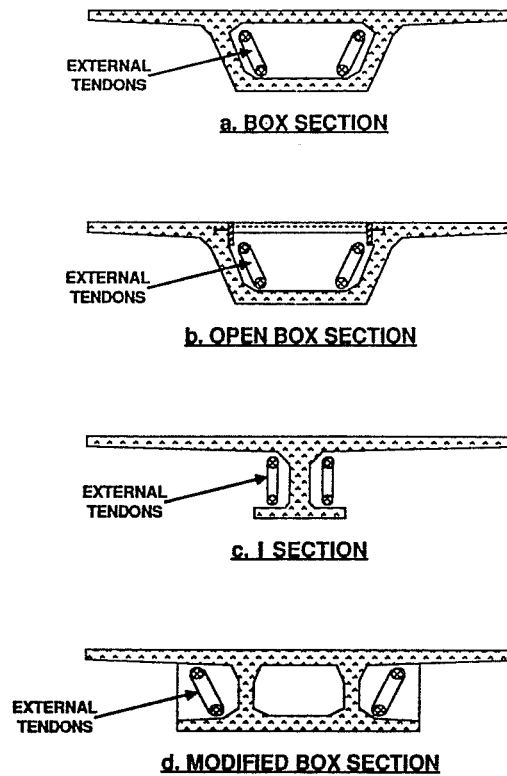
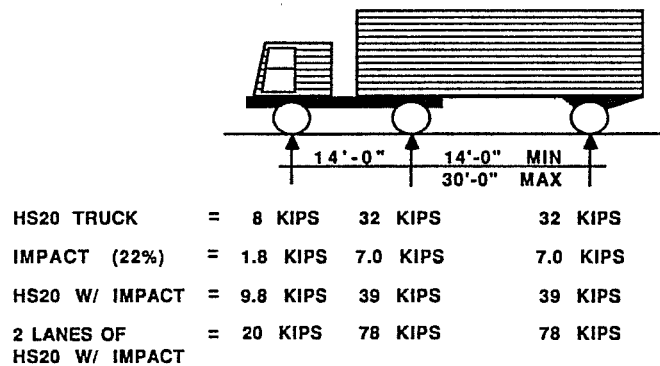


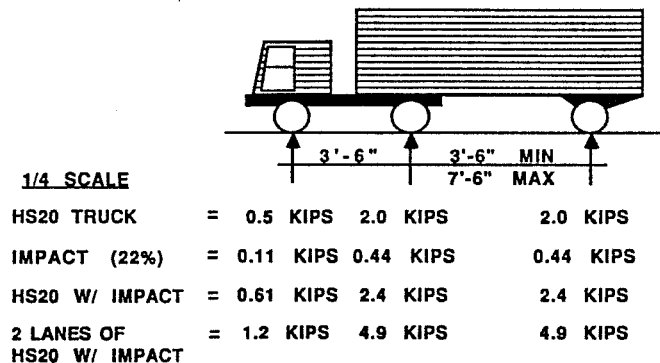
Figure 2.2 Possible Model Cross-Sections

(18). Since the primary objective of this research was to investigate in-plane flexural and shear behavior, and because the structure was constructed in a protected and controlled environment, only vertical traffic loads were considered during design. An HS-20 Truck load, shown in Fig 2.3, was adopted as the traffic loading for design of the model structure. The AASHTO specification requires design to be based on the maximum effect caused by either a uniformly distributed lane load or a set of concentrated truck axle loads. For a prototype structure with 100 foot spans the concentrated truck axle loads govern the design. Similarly, the impact factor was calculated using a prototype span length of 100 feet.

$$I = 50/(L+125) = 50/(100+125) = .22$$



a. AASHTO HS20 TRUCK LOAD



b. REDUCED SCALE HS20 TRUCK LOAD

Figure 2.3 1/4 - Scale Truck Load

The width of the top flange of the model structure was dictated by the 4-ft spacing of the bolt clusters in the test floor. A 7-ft top flange width was selected to fit within a load frame tied down to the test floor at bolt clusters 8 ft. apart. With a scale of 1/4 the corresponding prototype width would be 28 feet, and two lanes of traffic would be possible. Therefore, the loading on the model structure was appropriately scaled from two lanes of AASHTO HS-20 truck load with impact.

The structure was built in a sequential span-by-span manner similar to prototype construction (see section 2.4.1). In the prototype the completed spans are often used to support erection equipment or for delivery of segments, materials, and equipment. Each intermediate structural configuration must therefore carry the weight imposed during erection. Construction live loads can vary from small

traffic loads to the governing live load case depending on the specific method of construction.

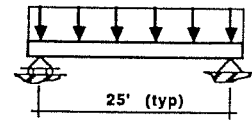
The tendon layout is affected by the magnitude of the erection loads. The structure is typically erected by stressing single-span tendons to support each erected span and then further stressing multispan "continuity" tendons to provide additional service load capacity. If continuity tendons are to be used then the erection loads must be less than the service loads to provide sufficient strength with only a portion of the tendons stressed. For the model structure, this erection load deficit was achieved by using two lanes of HS-20 truck load plus impact for service loads and two lanes of HS-20 truck load without impact for construction loads. Lower ultimate load factors were also used on construction live loads to increase this load difference.

The design loading for two lanes of the AASHTO HS20 Truck Load, including impact is shown in Fig 2.3a. To satisfy similitude requirements, the concentrated truck axle loads are reduced by the square of the scale factor ($1/16$) for application to the model structure. The axle spacing is a geometric property and scales directly with the scale factor ($1/4$). The reduced scale "HS20" truck load is therefore shown in Fig 2.3b.

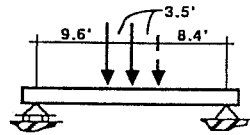
The load cases considered during design of the model structure are shown in Fig 2.4. As the structure evolved during construction, three structural configurations were apparent. In the one and two-span configurations, shown in Fig 2.4a and 2.4b, dead loads and construction live loads were considered. In the three-span configuration, shown in 2.4c, dead loads and service live loads were considered. All live load cases were chosen to produce maximum midspan and support moments. Shear and torsional load cases were also considered in determining the required web shear capacity.

The structure was erected, on falsework, in a sequential span-by-span manner. After stressing the falsework-supported first span, the falsework was advanced to the second span. The second span was erected on the falsework and matched with the first span with a cast-in-place closure strip (see Section 2.4.6). This erection procedure "locked in" the stresses and curvatures existing in the structure after stressing the previous span. When the second span was stressed onto the first span, the weight of the second span was carried by the current two-span structure. The

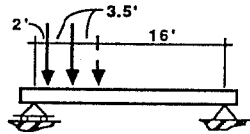
LOAD CASE DESIGNATION



DL1

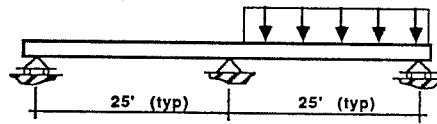


LC1-M1

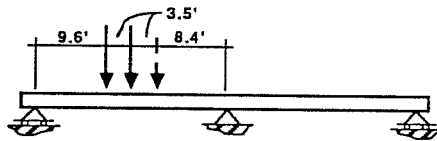


LC1-V

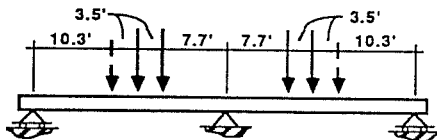
a) ONE SPAN CONFIGURATION



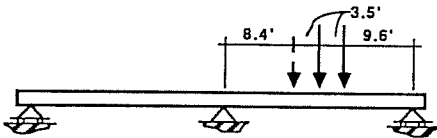
DL2



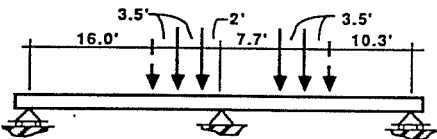
LC2-M1



LC2-M2



LC2-M3



LC2-V

b) TWO - SPAN CONFIGURATION

Figure 2.4 Design Loads

dead loads, live loads, and prestress forces must act on the current two-span structure. The loads for the second and third span are shown schematically in Figs. 2.4b and 2.4c respectively.

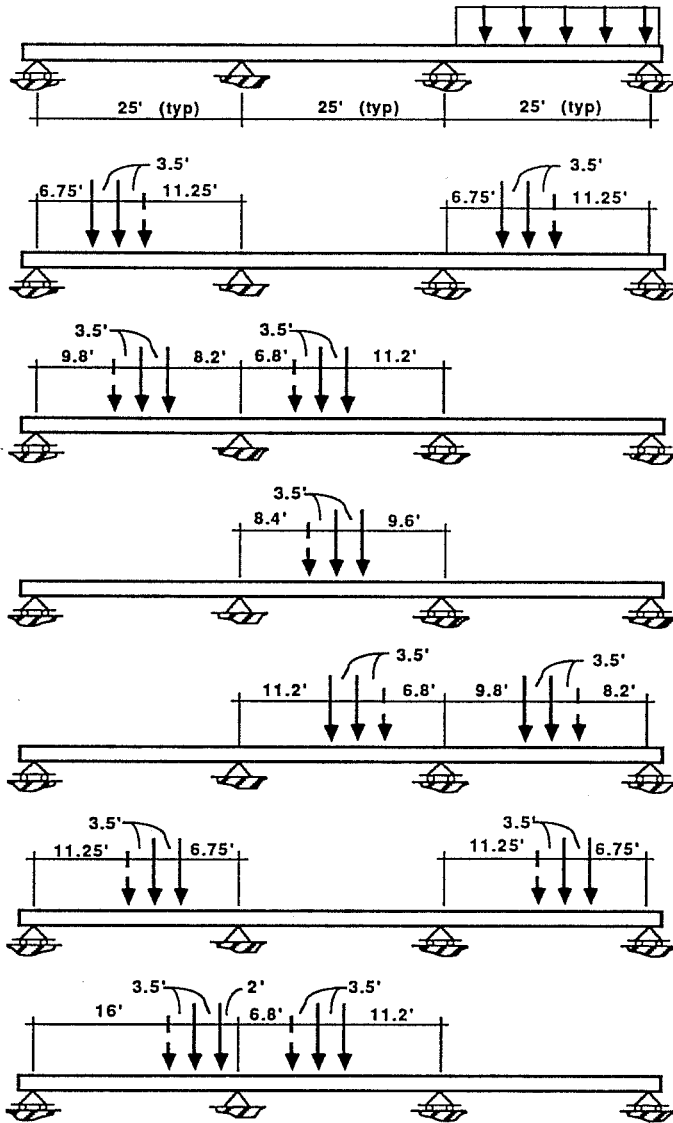
To ensure adequate behavior of a post-tensioned concrete structure it is necessary to consider two levels of behavior. The structure must meet serviceability requirements with respect to stresses and deflections and also must have sufficient strength to resist forces caused by factored ultimate loads. For each structural configuration of the evolving structure, service load stresses and deflections must be within certain limits and ultimate strength must be ensured.

The model structure was designed to meet the stress limits outlined in the 1983 AASHTO Bridge Design Specification (18). Table 2.1 summarizes the stress limits of the concrete and prestressing tendon, as outlined in the 1983 specification. This specification is intended for design of conventional prestressed and post-tensioned structures and does not specifically address the problems of segmental box-girders with external tendons. Recently, PTI (19) has proposed design requirements to AASHTO which are specifically for segmental construction. These requirements are outlined in Table 2.2 and provide specific stress limits for various types of segmental construction. An earlier draft proposal (20) was used in some of the design of the model. The concrete compressive stress limits have remained the same as in the current AASHTO specifications, while the tensile stress limits have been adjusted to reflect differences in segmental construction.

If the structure is segmentally cast-in-place, or segmentally precast with glued joints and has a minimum of 50% bonded tendons, then the tensile stress limit is chosen based on whether nonprestressed reinforcement is provided across segment joints. If less than 50 percent of total tendon area is bonded, then a residual compressive stress is required in the tensile zone. The amount of reserve compressive stress depends on whether the segment joints are epoxied or dry.

The model structure was designed for the service and ultimate load combinations outlined in the 1983 AASHTO specification. As described previously, only vertical self weight and traffic loads were considered for design. Table 2.3 summarizes the design load combinations considered at various stages of construction. At each stage of construction, service load combinations were considered with respect

LOAD CASE DESIGNATION



DL3

LS3-M1

LS3-M2

LS3-M3

LS3-M4

LS3-M5

LS3-V

e) THREE - SPAN CONFIGURATION

Figure 2.4 Design Loads

Table 2.1 AASHTO-83 Stress Limits

ALLOWABLE STRESSES AASHTO-83 (Ref. 18)

Material	Force Type	Specific	Monolithic	Limiting Stresses Segmental Epoxy Jointed	Segmental Dry Jointed
<u>Temporary Stresses Before Long Term Losses</u>					
Concrete	Compression	Post-Tensioned Members	.55*f _{ci}	.55*f _{ci}	.55*f _{ci}
	Tension	Precompressed Tensile Zone: Other Areas: with Bonded Reinf.*Crossing Joint without Bonded Reinf. Crossing Joint	Not Spec. $7.5*\sqrt{f'_c}$ 200 psi or $3*\sqrt{f'_c}$	Not Spec. $7.5*\sqrt{f'_c}$ 200 psi or $3*\sqrt{f'_c}$	Not Spec. $7.5*\sqrt{f'_c}$ Assume = 0 psi Not Spec.
Prestressing Steel	Tension	*reinforcement designed to resist total tension force in concrete computed with uncracked section During Stressing After Transfer	.60*fp _u .70*fp _u	.80*fp _u .70*fp _u	.80*fp _u .70*fp _u
<u>Stress at Service Load After Losses Have Occurred</u>					
Concrete	Compression	All Members	.40*f _c	.40*f _c	.40*f _c
	Tension	Precompressed Tensile Zone: With Bonded Reinf. Crossing Joint Normal Environments Corrosive Environments Without Bonded Reinf. Crossing Joint Other Areas: With Bonded Reinf. * Crossing Joint Without Bonded Reinf. Crossing Joint	$6*\sqrt{f'_c}$ $3*\sqrt{f'_c}$ 0 psi $7.5*\sqrt{f'_c}$ 200 psi or $3*\sqrt{f'_c}$	$6*\sqrt{f'_c}$ $3*\sqrt{f'_c}$ 0 psi $7.5*\sqrt{f'_c}$ 200 psi or $3*\sqrt{f'_c}$	$6*\sqrt{f'_c}$ $3*\sqrt{f'_c}$ 0 psi $7.5*\sqrt{f'_c}$ 200 psi or Not Spec.
Prestressing Steel	Tension	*reinforcement designed to resist total tension force in concrete computed with uncracked section At Service Load	.80*fp _y	.80*fp _y	.80*fp _y

Table 2.2 PTI Proposed Stress Limits for Segmental Construction
(Ref. 19)

Material	Force Type	Specific	Monolithic	Limiting Stresses Segmental Epoxy Jointed	Segmental Dry Jointed
<u>Temporary Stresses Before Long Term Losses</u>					
Concrete	Compression	Post-Tensioned Members Precompressed Tensile Zone:	0.55*f _{ci}	0.55*f _{ci}	Not Spec.
	Tension	With Min. 50% Bonded P.T. Tendons With bonded mild reinf. crossing joint Without bonded mild reinf. crossing joint Less Than 50% Bonded P.T. Tendons With bonded mild reinf. crossing joint Without bonded mild reinf. crossing joint Transverse Tension in Precompressed Tensile Zone Other Areas: With bonded reinf. * crossing joint Without bonded reinf. crossing joint	3*√f _c 0 psi Not Spec. N.A. 3*√f _c 7.5*√f _c 200 psi or 3*√f _c	3*√f _c 0 psi Not Spec. 3*√f _c 3*√f _c 7.5*√f _c 200 psi or 3*√f _c	Not Spec. Not Spec. Not Spec. 6*√f _c 3*√f _c Not Spec. 7.5*√f _c Assume = 0 psi Not Spec.
Prestressing Steel	Tension	*reinforcement designed to resist total tension force in concrete computed with uncracked section During Stressing After Transfer	.80*fpu .70*fpu	.80fpu .70*fpu	.80fpu .70*fpu
<u>Stress at Service Load After Losses Have Occurred</u>					
Concrete	Compression	All Members Precompressed Tensile Zone:	.40*f _c	.40*f _c	.40*f _c
	Tension	With Min. 50% Bonded P.T. Tendons With bonded mild reinf. crossing joint Without bonded mild reinf. crossing joint Less Than 50% Bonded P.T. Tendons With bonded mild reinf. crossing joint Without bonded mild reinf. crossing joint Transverse Tension in Precompressed Tensile Zone Other Areas: With Bonded Reinf.*Crossing Joint Without Bonded Reinf. Crossing Joint At Service Load	3*√f _c 0 psi Not Spec. N.A. 3*√f _c 7.5*√f _c 200 psi or 3*√f _c .82*fp (.74*fpu)	3*√f _c 0 psi Not Spec. 3*√f _c 3*√f _c 7.5*√f _c 200 psi or 3*√f _c .82*fp (.74*fpu)	Not Spec. Not Spec. Not Spec. 6*√f _c 3*√f _c Not Spec. 7.5*√f _c Assume = 0 psi Not Spec. .82*fp (.74*fpu)
Prestressing Steel	Tension				

Table 2.3 Load Combinations

A. Construction Load Combinations
One Scan Configuration

Load Case	DL1	P51A	2	P51B	2	LC1 M1	LC1 V1
Service Load Cases							
SUM1	1	1	1	1	1	1	1
CS1, M1	1	1	1	1	1	1	1
CS1, V1	1	1	1	1	1	1	1
Ultimate Load Cases							
CU1, M1	1.3		1*		1*	1.95	1.95
CU1, V1	1.3		1*		1*		1.95

Two Scan Configuration

Load Case	SUM1	DL1	DL2	P52	2	P53	2	LC2 M1	LC2 M2	LC2 M3	LC2 V1
Service Load Cases											
SUM2	1		1	1	1	1	1	1			
CS2, M1	1		1	1	1	1	1	1	1		
CS2, M2	1		1	1	1	1	1	1	1		
CS2, M3	1		1	1	1	1	1	1		1	
CS2, V1	1		1	1	1	1	1	1			1
Ultimate Load Cases											
CU2-M1		1.3	1.3		1*		1*	1.95			
CU2-M2		1.3	1.3		1*		1*	1.95			
CU2-M3		1.3	1.3		1*		1*		1.95		
CU2-V1		1.3	1.3		1*		1*				1.95

* Secondary prestress forces were included if additive to ultimate load combination.

Table 2.3 Load Combinations - continued

B. Service Load Combinations
Three Span Configuration

Load Case	SUM2	DL1	DL2	DL3	PS4a	PS4b	PS5	PSi	LS3 M1	LS3 M2	LS3 M3	LS3 M4	LS3 M5	LS3 V
Service Load Cases														
SUM3	1			1	1	1	1	1						
SS-M1	1			1	1	1	1	1	1					
SS-M2	1			1	1	1	1	1		1				
SS-M3	1			1	1	1	1	1			1			
SS-M4	1			1	1	1	1	1				1		
SS-M5	1			1	1	1	1	1					1	
SS-V	1			1	1	1	1	1						1
Ultimate Load Cases														
SU-M1		1.3	1.3	1.3	1*				1*	2.86				
SU-M2		1.3	1.3	1.3	1*				1*	2.86				
SU-M3		1.3	1.3	1.3	1*				1*		2.86			
SU-M4		1.3	1.3	1.3	1*				1*			2.86		
SU-M5		1.3	1.3	1.3	1*				1*				2.86	
SU-V		1.3	1.3	1.3	1*				1*					2.86

* Secondary prestress forces were included if additive to ultimate load combination.

to stress limits and deflections, and ultimate load combinations were considered for strength requirements.

As discussed previously, the magnitude of the erection loads must be minimized so that additional strength does not have to be provided for temporary conditions. For this reason impact factors were not included for construction live loads. The construction live load multipliers were also decreased to reduce the temporary structural requirements. Slightly higher risk was accepted for the short term, controlled construction period. A load factor of 1.5 was chosen for the construction live loads. This load factor combined with the load combination factor of 1.3 provides an ultimate load factor of 1.95 on construction live loads.

2.1.4 Description of Model Bridge Structure. The model structure was constructed in the Ferguson Structural Engineering Laboratory at the Balcones Research Center of the University of Texas at Austin. The model bridge, shown in Fig 2.5, was a three-span structure geometrically symmetrical about the center line. Figure 2.1 shows a plan and elevation of the structure. Each span consists of ten typical segments. Over each support is a pier segment which contains the anchorages for all post-tensioning tendons. Since the typical segments were precast separately from the pier segments a cast-in-place closure strip was provided at each end of the pier segments.

The model cross-sections are shown in Fig. 2.6. As was described in Section 2.1.1, the typical segment shape, shown in Fig. 2.6a, was chosen to give a span/depth ratio and efficiency rating typical of contemporary construction. At midlength of each typical segment was a full height diaphragm through which the external tendons were deviated. Flanges tapered towards the ends and had chamfers at each flange/web junction. The calculated transformed section properties of the section are also shown in Fig. 2.6a.

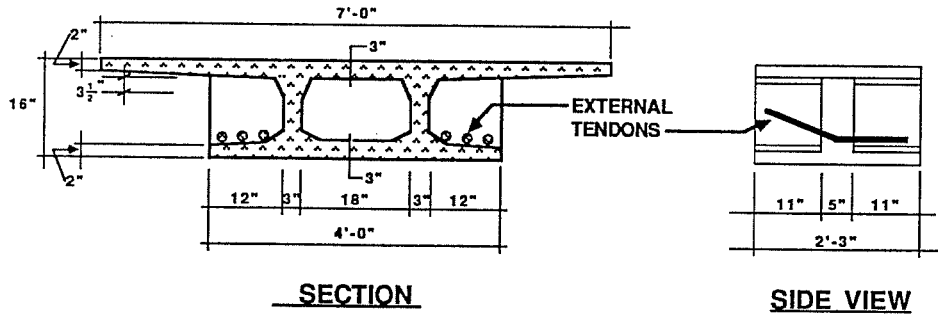
The shape of the pier segment, shown in Fig. 2.6b evolved from several requirements and considerations. The top and bottom flange widths, and the overall structural depth, were chosen to match the typical segments. The top flange thickness was increased to a constant 3.5" to meet cover and spacing requirements for larger size reinforcement. The external tendon anchorages were contained in the solid portion outside of the web interface. A stiff diaphragm beam was then added



Figure 2.5 Scale Model of Externally Post-Tensioned Box Girder

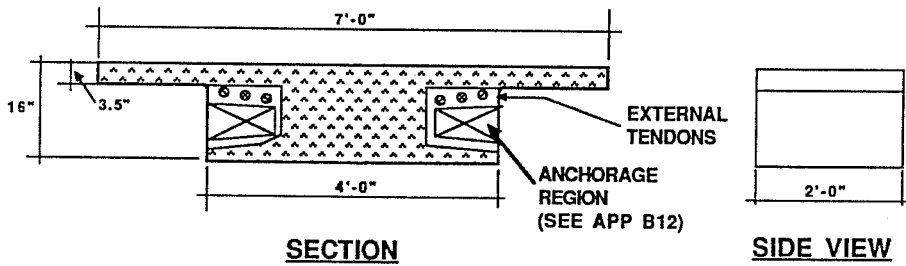
to concentrate torsional shear flow from the span to the reactions. The remainder of the box section was ultimately filled in to ease forming, congestion, and consolidation problems. The calculated transformed sectional properties of the concrete section are also shown in Fig. 2.6b.

A schematic of the post-tensioning tendons is shown in Fig. 2.7. The tendons are draped down from high points over the supports to low points near midspan. The tendon locations are shown for sections at the exterior support, midspan, and interior supports. These duct locations act as a work point from which all other tendon geometries are calculated. At the exterior support, the tendon locations were chosen to give approximately zero eccentricity of the resultant tendon forces. At midspan, the tendons were located to allow the external tendon ducts to be placed flush with the bottom flange. So that the primary vertical deviation forces were transmitted directly into the box webs, the tendons were draped down to the duct location closest to the web and then deviated vertically and horizontally away from the web. This allowed the next tendon to be vertically deviated close to the web also. This crossing tendon pattern can be seen in the plan view of Fig. 2.7. The theoretical tendon locations at the interior support were chosen to assure that the



NOTES:
 SPAN to DEPTH RATIO = 18.75 $A^* = 450 \text{ in}^2$
 EFFICIENCY FACTOR = .60 $I^* = 16540 \text{ in}^4$

a. TYPICAL SPAN SEGMENT



$A^* = 894 \text{ in}^2$
 $I^* = 20741 \text{ in}^4$

b. PIER SEGMENT

* Transformed Section Properties

FIG. 2.6 - MODEL CROSS-SECTIONS

Figure 2.6 Model Cross-Sections

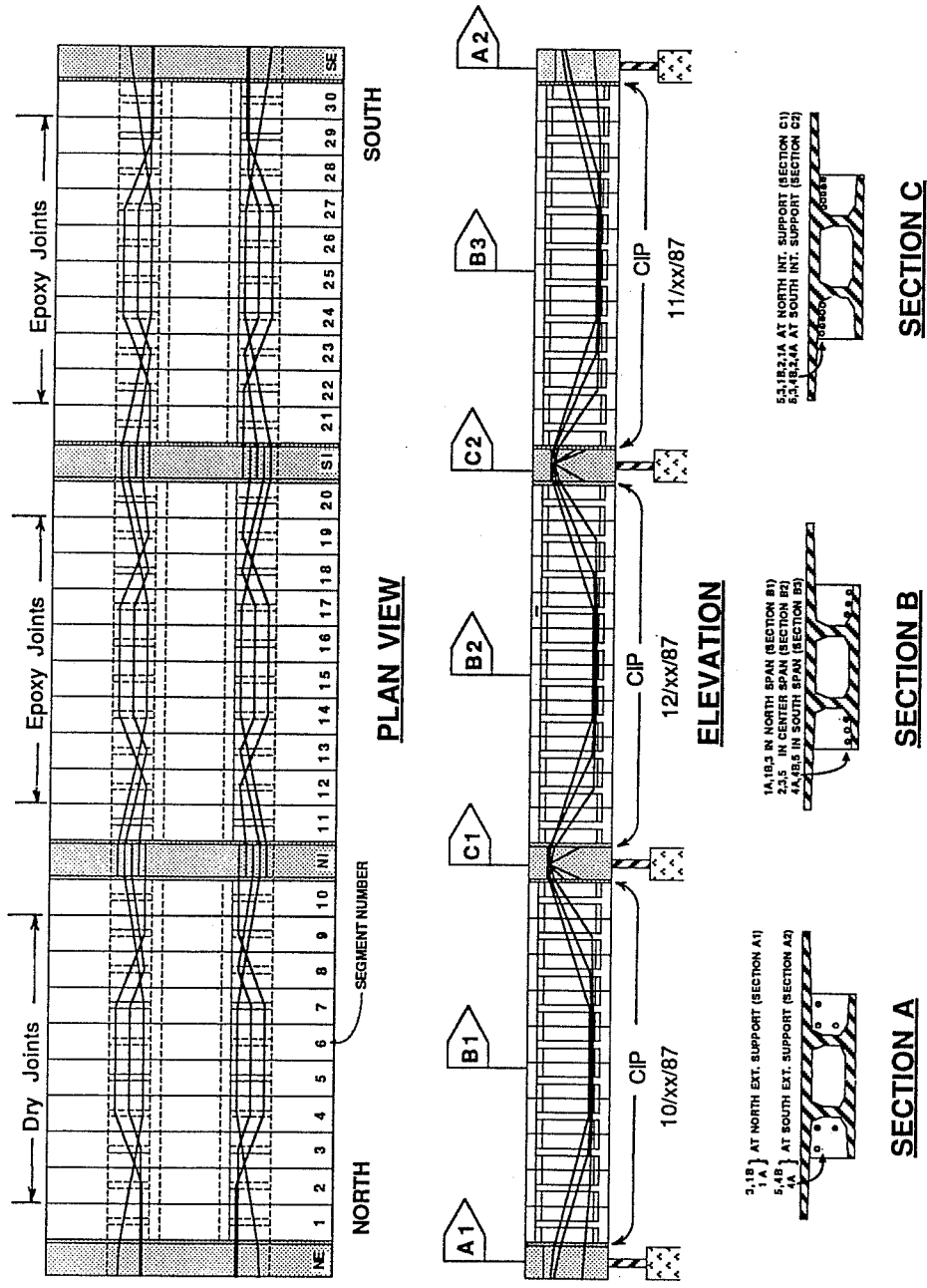


Figure 2.7 Schematic Post-Tensioning Layout

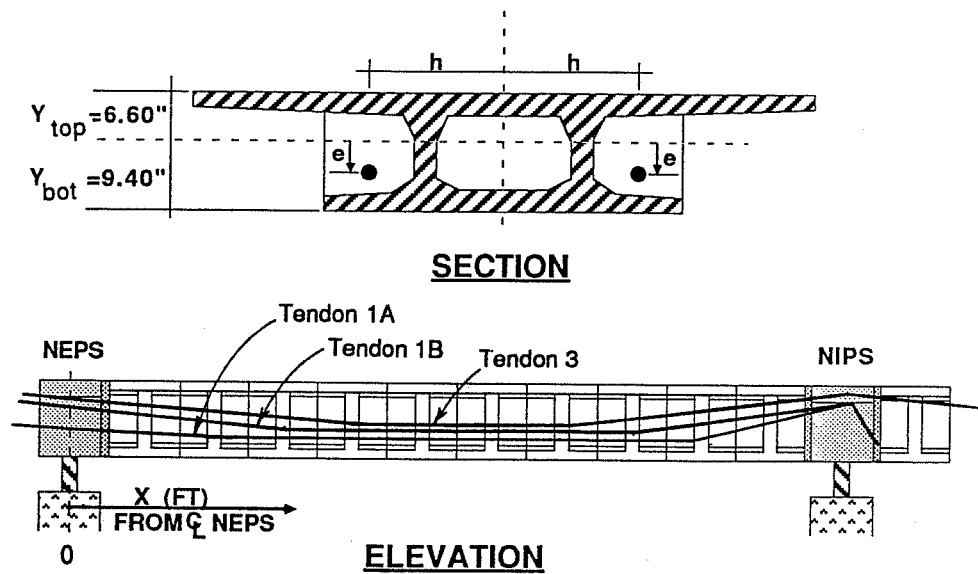
theoretical tendon locations at the interior support were chosen to assure that the external tendon ducts would penetrate the pier segment below the bottom of the top flange of the typical segments.

As previously described, the structure was constructed with single-span "erection" tendons and then additionally stressed with multispan continuity tendons. Tendon 1A, 1B, 2, 4A, and 4B all contained 10-3/8" diameter strands (5 each side) and were stressed as each span was erected. Tendons 3 and 5 contained 4-3/8" diameter strands (2 each side) and were stressed after erecting span 2 and span 3 respectively. Figure 2.8 gives the theoretical tendon locations for Tendons 1A, 1B, 2, 3, 4A, 4B, and 5. In addition to the external tendons described above, tendons were also provided within the concrete section. The internal tendons (Fig. 2.8d) were provided at the corners of the box to augment the flexural and torsional capacity, as well as at the ends of the thin top flange to control shear lag. All internal tendons had a straight profile and were anchored at the extreme ends of the structure. Two 3/8" diameter strands were provided at each corner of the box and in each top flange overhang. Only the top internal tendons were stressed for this test series. The internal tendons will also be grouted in a future test to investigate the effect of having bonded prestressed reinforcement crossing the joints.

The new PTI specification for segmental box-girder construction (19) requires that provision be made to add future post-tensioning if needed. This provides the ability to add additional prestress to the system for unexpected prestress losses or for serviceability considerations such as deflection adjustment or deteriorated external tendon replacement. Four 3/8" dia. straight strands (Fig. 2.8d) were provided for such contingencies within the box void, and anchorages were provided at the exterior pier segments.

2.2 Material Properties

2.2.1 Concrete. In order to match prototype construction the minimum 28 day compressive strength was chosen as 6000 psi. The reduced scale dictated a minimum concrete cover of 1/2", so a maximum aggregate size of 3/8 inches was required. To ensure that the webs and bottom flanges would be properly consolidated, the tops of the bottom flanges were left open during casting. This dictated



TENDON 1A : 2 x (5-3/8" dia. Grade 270 Strands)

x (ft)	-1	0	4.625	9.125	15.875	20.375	25	26
e (in)	2.9	3.4	5.65	6.23	6.23	5.65	-2.67	3.15
h (in)	15	15	15	22	22	15	14	15.25

TENDON 1B : 2 x (5-3/8" dia. Grade 270 Strands)

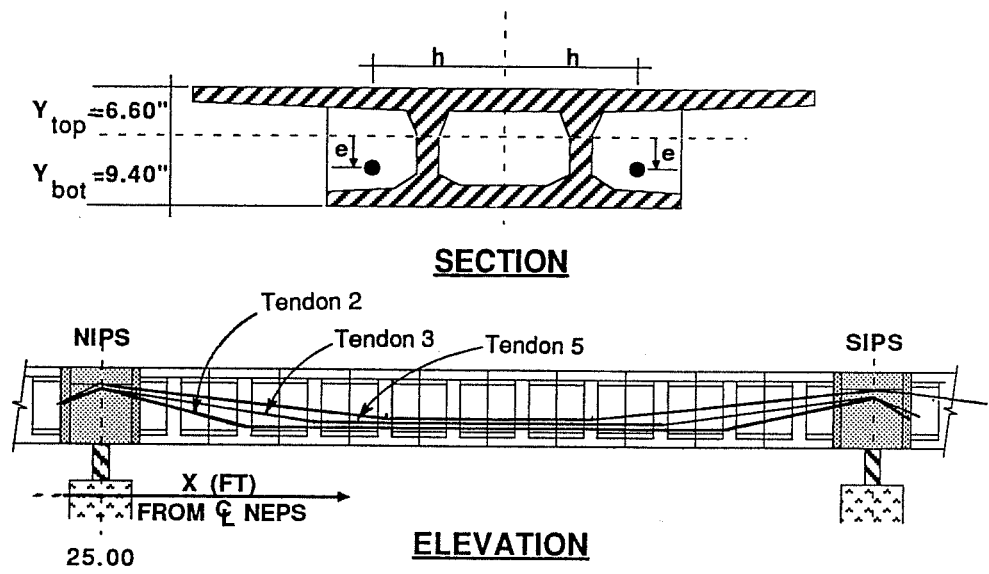
x (ft)	-1	0	6.875	9.125	15.875	18.125	25	26
e (in)	-2.48	-2.1	5.65	5.94	5.94	5.65	-2.81	3.15
h (in)	15	15	15	18.5	18.5	15	18.25	20.75

TENDON 3 : 2 x (2-3/8" dia. Grade 270 Strands)

x (ft)	-1	0	9.125	15.875	25	31.875	Continues	
e (in)	-2.6	-2.1	5.65	5.65	-2.88	5.65	In Center Span	
h (in)	21.5	21.5	15	15	20.38	15		

NORTH EXTERIOR SPAN

Figure 2.8a Theoretical Tendon Locations



TENDON 2 : 2 x (5-3/8" dia. Grade 270 Strands)

x (ft)	24	25	29.625	34.125	40.875	45.375	50	51
e (in)	2.65	-2.74	5.65	6.23	6.23	5.65	-2.74	2.65
h (in)	16	16.13	15	22	22	15	16.13	16

TENDON 3 : 2 x (2-3/8" dia Grade 270 Strands)

x (ft)*	15.875	25	31.875	34.125	40.875	43.125	50	51
e (in)	5.65	-2.88	5.65	5.94	5.94	5.65	-2.88	2.4
h (in)	15	20.38	15	18.5	18.5	15	20.38	22

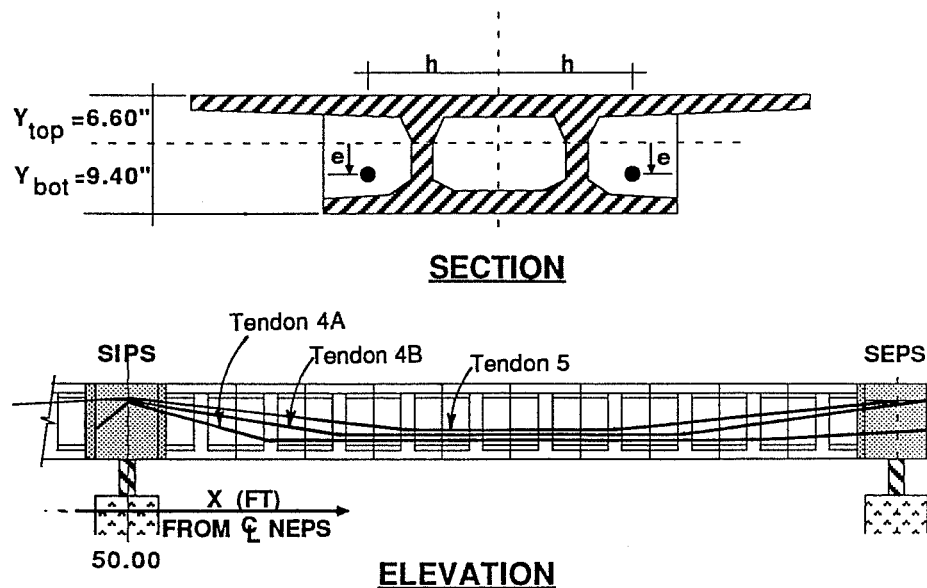
*continues in North Span

TENDON 5 : 2 x (2-3/8" dia. Grade 270 Strands)

x (ft)	24	25	34.125	40.875	50	59.125	Continues In South Span	
e (in)	1.4	-2.95	5.65	5.65	-2.95	5.65		
h (in)	22	22.5	15	15	22.5	15		

INTERIOR SPAN

Figure 2.8b Theoretical Tendon Locations



TENDON 4A : 2 x (5-3/8" dia. Grade 270 Strands)

x (ft)	49	50	54.625	59.125	65.875	70.375	75	76
e (In)	3.15	-2.67	5.65	6.23	6.23	5.65	3.4	2.9
h (In)	15.25	14	15	22	22	15	15	15

TENDON 4B : 2 x (5-3/8" dia Grade 270 Strands)

x (ft)	49	50	56.875	59.125	65.875	68.125	75	76
e (In)	3.15	-2.81	5.65	5.94	5.94	5.65	-2.1	-2.48
h (In)	20.75	18.25	15	18.5	18.5	15	15	15

TENDON 5 : 2 x (2-3/8" dia. Grade 270 Strands)

x (ft)	Continues	40.875	50	59.125	65.875	75	76
e (In)	In Center Span	5.65	-2.95	5.65	5.65	-2.1	-2.6
h (In)		15	22.5	15	15	21.5	21.5

SOUTH EXTERIOR SPAN

Figure 2.8c Theoretical Tendon Locations

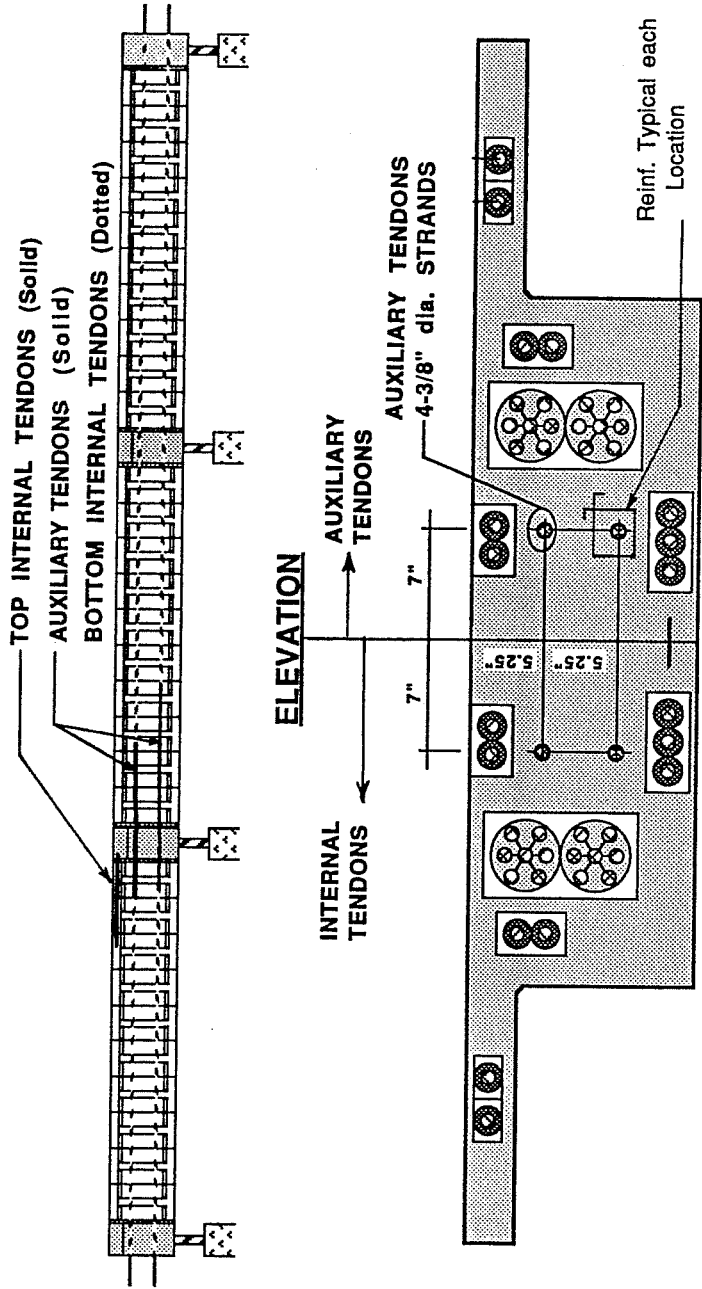


Figure 2.8d Internal and Auxiliary Tendons

out of the webs. A slump of 2 inches was chosen as a minimum based on placement considerations. The concrete mix was also required to remain workable, with high ambient air temperatures, for a minimum of 1 hour after it arrived on site. Additional retarding admixture was used during the hot summer months to provide the required workability period. The fine to coarse aggregate ratio was increased to allow for proper finishing of the exposed flanges.

Concrete batch control is critical for precasting of match-cast segments. A comprehensive inspection program, before, during, and after the casting operation should be utilized to ensure that the concrete strength and workability characteristics remain within acceptable limits. Trial batches were performed in advance to learn the strength gain and workability characteristics of the proposed mix. Batch control procedures, on-site approval methods, and post-casting testing procedures were established during trial batches.

The four general types of concrete that were used in the model structure are summarized in Table 2.4. The concrete strength and elastic modulus data is presented in Table 2.5. Preliminary trial batches indicated that the 6 sack mix, shown as Type 1, would yield concrete with the necessary characteristics. Several segments were cast using this mix until 28 day cylinder tests revealed low strengths. The cement content was then increased to 6.5 sacks to achieve the desired strength. This basic mix, Types 2 and 3, was used for all remaining typical segments.

Batch control problems at the first ready-mix company forced a change to a second company for 9 segments of the last span. The basic mix design, Type 3, is the same as Type 2. The piers were also cast using Type 3 mix with larger 3/4" aggregate replacing the 3/8" crushed stone.

To allow for higher bearing stresses behind the post-tensioning anchorages, high-strength concrete was used for the pier segments. This mix, Type 4, was batched by a third ready-mix supplier so that fly ash could be substituted for some of the cementitious material. This company also had quarry rights to hard Burnet Limestone which was necessary for very high-strength concretes. Hartman (21) provides a detailed description of high-strength concrete production.

Table 2.4 Concrete Mix Types

	<u>Concrete Mix Proportions</u> (per cubic yard)			
	Type 1	Type 2	Type 3	Type 4
Water (gal)	35	35	35	35
Cement (lbs)	564	611	611	691
Fly Ash (lbs)	—	—	—	298
Sacks	6	6.5	6.5	10.5
W/C	.52	.48	.48	.29 ^a
Sand (lbs) ^b	1355	1355	1355	1039
Rock ^b	1700	1700	1680	1821 ^c
Retarder (oz)	24	39	24	30
Superplast. (oz)	—	^d d	—	160 ^e
Ready Mix Co.	1	1	2	3
Segment #	(3-B)	(1, 2, 9-20, 25)	(21-24, 26-30)	(Pier Segments)

Notes

- a. W/C includes total cementitious material
b. Aggregate weights are for saturated surface dry condition
c. 3/8" crushed Burnet Limestone
d. Low dosage of superplasticizer was occasionally used to increase slump.
Approximate dosage rate: 12 oz per yd. per inch of slump increase.
e. Half of superplasticizer was added at the batch plant and half at the Laboratory
-
-

2.2.2 *Prestressing Strands.* All prestressing steel used in the model structure was 3/8" diameter Grade 270 low relaxation strands. The stress-strain relationship for the strand was furnished by the supplier and is shown as the solid line in Fig. 2.9. The strand has an area of .085 square inches, an ultimate strength of 279ksi at 5.47 percent elongation, and an elastic modulus of 28,400 ksi.

The dotted line in Fig 2.9 was determined by testing a 3/8 inch diameter strand in a test machine. Strand strain was measured with electronic strain gauges attached to opposite wires of the 7-wire strand. This curve has an apparent elastic modulus of approximately 30,300 ksi and provides a calibration between electronically measured strains and strand stresses.

Table 2.5 Segment Concrete Properties
Segment Information

Segment No.	Mix No.	Date Cast	f'_{c28} (psi)	$f'_{c_{test}}$ Cylinder (psi)	$f'_{c_{test}}$ Calc. (psi)	$E'_{c_{test}}$ Cylinder (ksi)	$E'_{c_{test}}$ Calc. (ksi)
NEPS	4	5/26/87	12746 ^a		13383		6594
1	2	7/31/86	5855		6558		3986
2	2	7/28/86	5094		5705		3718
3	1	6/30/86	4343		4864		3592
4	1	6/12/86	5355	6022		3997	
5	1	5/28/86	6006	6839			4260
6	1	6/12/86	5355	6022		3997	
7	1	6/30/86	4343		4864		3592
8	1	7/14/86	4744		5313		3755
9	2	7/28/86	5094		5705		3718
10	2	7/31/86	5855		6558		3986
NIPS	4	7/28/87	9652 ^b		10135		5738
11	2	9/10/86	6707		7512		4266
12	2	8/27/86	5930		6642		4012
13	2	8/21/86	5630		6306		3909
14	2	8/18/86	6429	7187			4173
15	2	8/14/86	6948	7777		4341	
16	2	8/18/86	6429	7187			4173
17	2	8/21/86	5630		6306		3909
18	2	8/27/86	5930		6642		4012
19	2	9/10/86	6707		7512		4266
20	2	9/16/86	6954		7788		4342
SIPS	4	3/12/87	12805 ^c		13445		6609
21	3	10/16/86	6498		7148		4495
22	3	10/10/86	6780		7458		4591
23	3	10/8/86	6709	7348			4557
24	3	10/6/86	7351	7409		4576	
25	2	9/25/86	7744	8769			4610
26	3	10/6/86	7351	7409			4576
27	3	10/8/86	6709	7348			4557
28	3	10/10/86	6780		7458		4591
29	3	10/16/86	6498		7148		4495
30	3	10/24/86	7848		8633		4940
SEPS	4	6/8/87	13270 ^d		13934		6728

Notes:
a. 94-day strength
b. 31-day strength
c. 35-day strength
d. 81-day strength

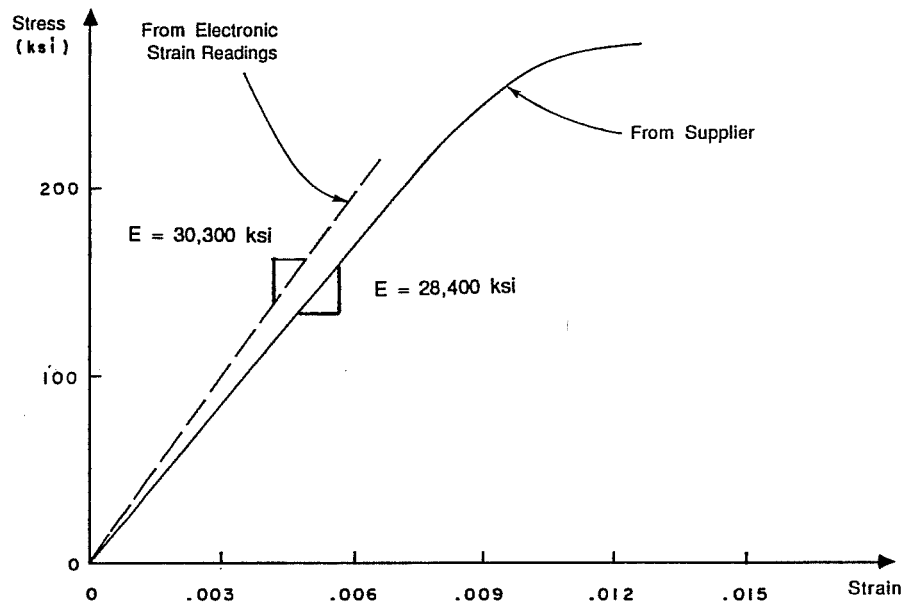


Figure 2.9 Prestressing Strand Stress-Strain Relationship

2.2.3 Steel Reinforcement. Several types of mild steel reinforcement were used in the model structure. Welded wire fabric formed the skeleton of the typical segment cages. Small diameter micro-reinforcing bars were used in the typical segments in the diaphragms and to tie together the welded wire mats. Normal size Grade 60 reinforcement was used in the typical segments for the primary tendon deviator reinforcement. The pier segment and pier cages were fabricated almost entirely from Grade 60 reinforcement.

The welded wire fabric had high yield and ultimate strengths, and limited ductility. The web mats were process annealed to improve ductility. The annealing process reduced the yield strength and reestablished the mild steel behavior. The yield and ultimate strengths for the welded wire is summarized in Table 2.6.

In addition to the welded wire reinforcement, small diameter micro-reinforcing bars were used in the typical segments. These bars exhibited erratic yield and ultimate strengths with very brittle behavior. The small reinforcing bars appeared to be cold-drawn steel wire with deformations stamped into the sides.

Table 2.6 Reinforcement Properties

	f_y	f_{ult}
Welded Wire Fabric (W5.5)		
Non-heat treated	82	88
Heat treated	75	79
Micro Reinforcing Bars		
#1.25 (non-heat treated)	83.0	92.5
#1.5 (heat treated)	42.5	61.3
#2 (heat treated)	44.5	65.7
Standard Reinforcing Bars		
#3	67.3	110
#4	85.3	128
#5	78.7	117

These bars were also process annealed to restore their mild steel behavior. The strength characteristics of this reinforcement are also shown in Table 2.6.

The pier segment and pier cages were fabricated from conventional Grade 60 reinforcing bars, ranging in size between #3 and #5 in the pier segments and #3 and #8 in the piers. The strength characteristics of all but the #8 bars are also shown in Table 2.6.

2.3 Bridge Model Details

2.3.1 Typical Segment Details.

2.3.1.1 Reinforcement. A typical span segment of a precast segmental box-girder structure must resist several types of forces. Longitudinal bending stress, caused by self weight and applied load, must be transmitted through the segment. Shear flow in the webs and flanges, resulting from shear and torsion, must be resisted by the segment. Bending in the transverse direction is also necessary to transfer eccentric loads to the load carrying box. Finally, an individual segment must be properly detailed to resist local forces within the segment.

In addition to the force components mentioned above the local forces at tendon deviation points must be superimposed. The reinforcement for a typical span segment consists of a basic cage that is typical for all segments plus special local reinforcement to transfer the tendon deviation forces to the box girder. The general design requirements for the typical reinforcing cage will be discussed first and then the special reinforcement required for tendon deviation is discussed second.

The typical reinforcing cage for a model segment was designed by considering shear flow in the webs and flanges plus transverse bending requirements. A particular load case will cause a symmetrical shear flow in the webs due to the vertical loads plus a nonsymmetrical shear flow in the webs and flanges caused by the vertical loads being applied at some eccentricity. Web and flange reinforcement from each of these effects was designed using a plasticity approach (22) and then superimposed to obtain the reinforcement required for shear and torsion.

The next stage of design considered local transverse bending stresses required to transfer the eccentric loading to the central box. Pucher curves (23) were used to calculate the fixed-end moments in the transverse direction in the flanges caused by concentrated wheel loads applied on the flanges. Reinforcement requirements from the transverse bending stresses were then superimposed with the shear and torsion requirements to obtain the total reinforcement required in the section.

So that global behavior would not be limited by a local weakness in a segment the segment cage had to be properly detailed. Figure 2.10 shows a possible plastic truss mechanism for a portion of a span with a tendon deviation and several opening joints. The primary load carrying mechanism is through arch action supported by the tendon deviations and supports. In a central segment, without tendon deviation, compressive struts form between the compressive zone and the free corner adjacent to the opening joint. Fully developed web reinforcement, as well as bottom chord reinforcement, is required to contain the inclined strut at the corner of the segment. These considerations lead to the use of hooked chord bars at the top and bottom of each web to contain the longitudinal inclined struts in the webs. The web reinforcement was also detailed with two welded cross-wires at each side on the top (24) and a continuous closed stirrup around the bottom to ensure complete anchorage at the top and bottom of the segment.

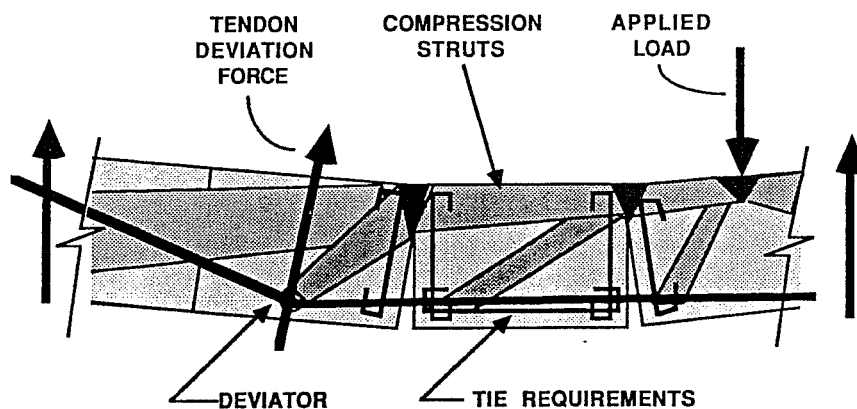
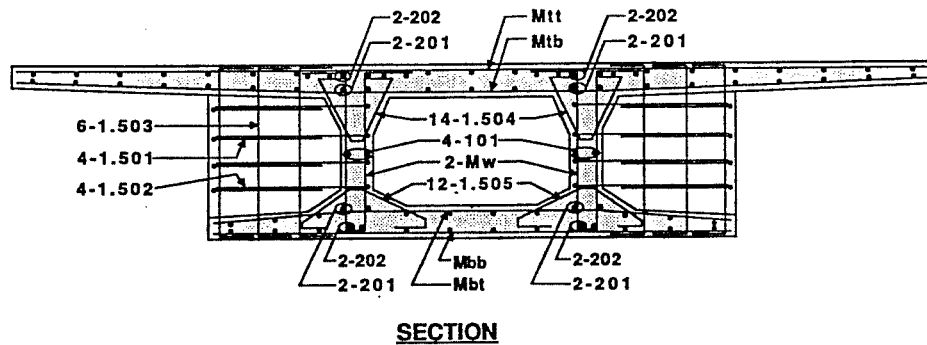


Figure 2.10 Typical Segment Detailing Requirements

The basic cage of a typical span segment is shown in Fig. 2.11. The cage consists of six specially fabricated mats of welded wire reinforcement, detailed in Fig. 2.12, tied together with micro reinforcing bars. The tendon deviation diaphragm is reinforced with basic wall reinforcement which was adjusted to mesh with the particular tendon duct configuration.

Superimposed with the basic reinforcement of a typical segment is the special reinforcement required to deviate the primary external tendons. Figure 2.13 shows the force components that are caused by deviating a tendon. The tendons are draped down from the ends of the span and are vertically and horizontally bent at the deviator. This results in vertical and horizontal force components applied to the segment at the deviator as shown in Fig. 2.13. Figure 2.14 illustrates the special deviation reinforcement for the four typical locations along each span. The horizontal deviation forces are resisted by transverse bars which confine the bottom of the diaphragm region (#401 bars). The vertical deviation forces are resisted by the "link" bars (#402) which are bent down and under the transverse confining bars. Additional confinement was also provided around the tendon ducts using bent #2 bars.

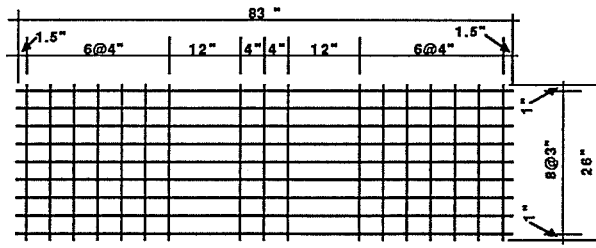


(see Fig. 2.12 for welded wire fabric details)

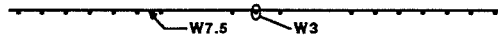
Figure 2.11 Typical Segment Reinforcing

2.3.1.2 Fabrication of Typical Segments. Two general methods are available for match-cast precasting of box-girder segments (17). The short line method, shown in Fig. 2.15a uses a single stationary set of forms to match-cast segments. After casting a particular segment it is slid forward and used to match-cast the next segment. Complex horizontal, vertical, and rotational alignments are possible by adjusting the position of the matching segment. The position of the matching segment must be set very accurately since a check of the alignment of a span is not made until final erection. Several stationary casting machines are commonly set-up on the casting yard providing high segment production with small space requirements.

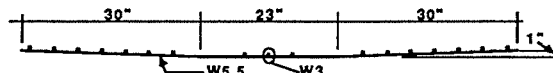
The long-line method, shown in Fig. 2.15b uses one or more traveling forms to match-cast a series of segments. After casting a particular segment the formwork is advanced to cast the next segment with the previous segment left in position for match-casting. Complex geometries are also possible with the long-line method by using an adjustable soffit form. A final check of the span alignment is made in the



PLAN VIEW

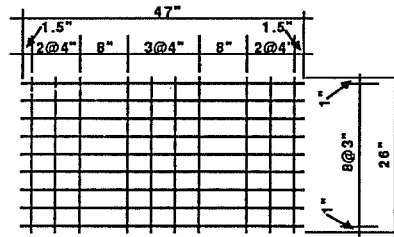


Mtt - TOP FLANGE/TOP MAT

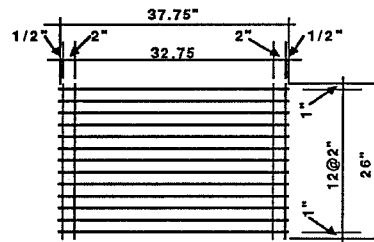


Mtb - TOP FLANGE/BOTTOM MAT

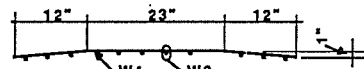
TOP FLANGE



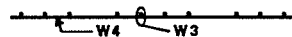
PLAN VIEW



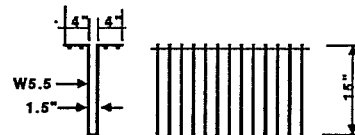
PLAN VIEW (UNBENT)



Mbt - BOTTOM FLANGE/TOP MAT



Mbb - BOTTOM FLANGE/BOTTOM MAT



END

ELEVATION

Mw - WEB MAT

BOTTOM FLANGE

WEBS

Figure 2.12 Welded Wire Fabric Details

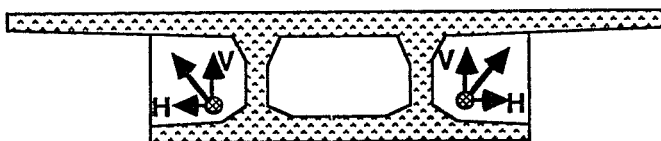
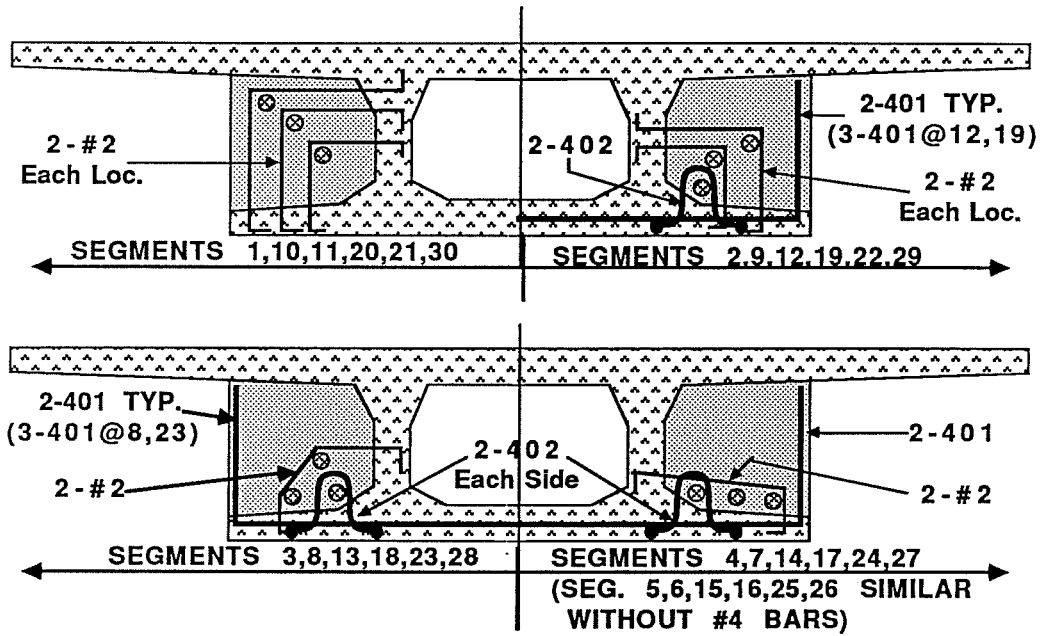


Figure 2.13 Deviator Force Components

casting yard with casting errors being corrected rather than accumulated. A major problem with the long-line casting method is the space required to set up the long casting beds. Also, foundation conditions for the casting bed must be firm at all locations to minimize settlement under the weight of the segments.

Since the model bridge structure had neither horizontal or vertical curvature the simpler long-line casting method was used. A long planar casting bed, 4'-6" wide by 30 feet long, was fabricated using a liquid Acrylic Polymer grout formed with carefully leveled side rails. The planar locations of the ten segments of one span were laid out on the casting bed with a transit and tape. Segments were cast directly on the casting bed with the top elevations set using a surveying level and rod. The ten typical segments of one span were precast by starting at a central segment and match-casting outward in both directions towards the ends of the span.

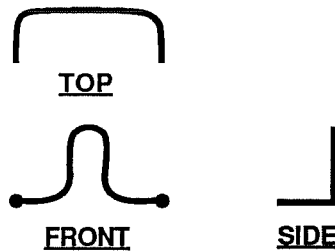
Two identical sets of forms were fabricated for precasting the segments. Figure 2.16 shows a cross-section and longitudinal section of the formwork. The web forms and top flange forms were made 6" longer than the new segment to overlap with the previously cast segment, and were supported at the front by a stiff end form.



TENDON DEVIATION AND DIAPHRAGM REINFORCEMENT

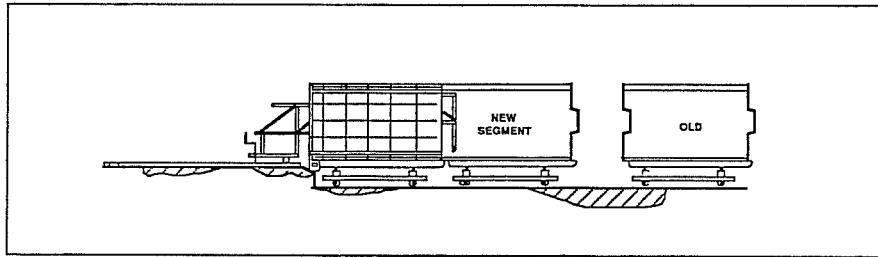
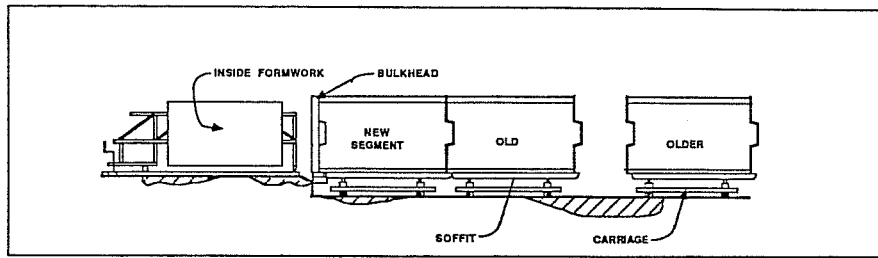


BAR TYPE 401

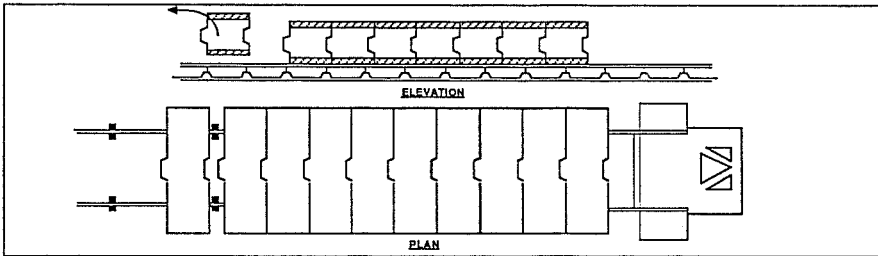
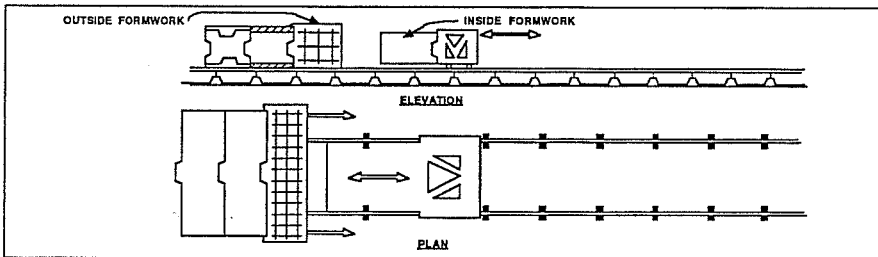


BAR TYPE 402

Figure 2.14 Deviator Reinforcement

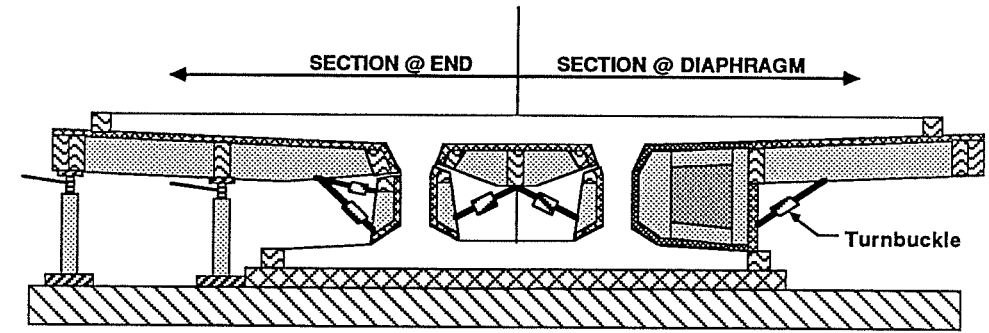


SHORT LINE CASTING METHOD

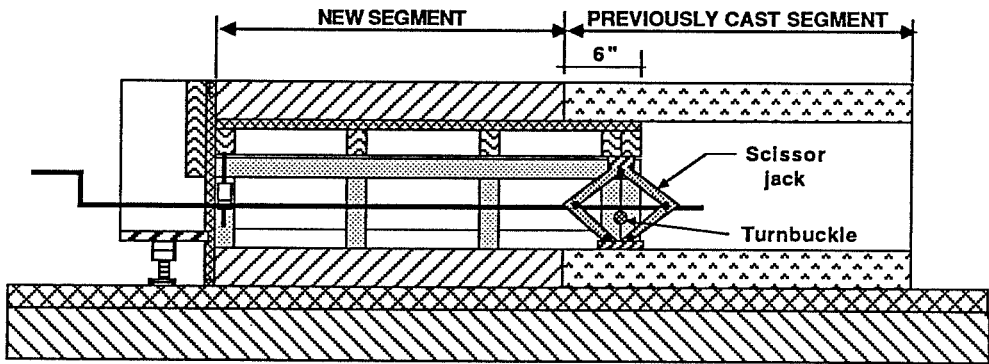


LONG LINE CASTING METHOD

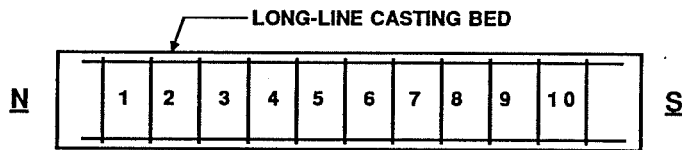
Figure 2.15 Methods for Precasting Segments



CROSS-SECTION



LONGITUDINAL SECTION



NORTH SPAN:	6	4,5	3	2	1	2	3	4	5	6
CENTER SPAN:	5	4	3	2	1	2	3	4	5	6
SOUTH SPAN:	5	4	3	2	1	2	3	4	5	6

CASTING SEQUENCE

Figure 2.16 Typical Segment Formwork

The end form contained the shear key block-outs and supported the internal tendon ducts. The top surface of the bottom flange was left open for proper consolidation.

The tendon deviation diaphragm form was suspended over the bottom flange with rods extending through the web and top flange forms. Since the tendons drape down at midspan, they penetrate each face of each diaphragm, at a different location. The diaphragm forms were therefore fabricated with lighter materials and used only once. Holes were drilled in the diaphragm forms to support the deviator conduit or the pass-through blockouts (2" diameter foam). A 1/2 inch foam strip was also provided on the top, inside, and bottom edges of this form to ease form removal.

A debonding agent consisting of flax Soap and talc (6:1 by volume) was applied to all match-cast faces and to the casting bed prior to concrete placement. This mixture was also used as a form release agent.

The concrete was placed by shovel from a wheel barrow and was consolidated using 1 inch diameter immersion vibrators. The webs and diaphragms were placed first and were consolidated in approximately four equal lifts. After placing concrete in the webs, the concrete had slumped out into the open bottom flange regions. Additional concrete was added to fill the bottom flange and then it was vibrated also. Consolidating the bottom flange caused the webs and diaphragms to slump a bit more, so they were vibrated additionally. The top flanges were then placed and consolidated by vibrating the mats of welded wire fabric. The top-flange/web junction was consolidated thoroughly to ensure complete mixing of the separate lifts of concrete.

After the segment was completely consolidated the flange surfaces were screeded and finished. The top flange was screeded with two passes of a vibrating screed. Excess concrete was removed from the bottom flange regions using small custom rakes and floats. All flange surfaces were then finished using a finishing trowel and specially made floats.

Once the concrete had achieved its initial set, wet burlap was applied to all exposed surfaces and the entire segment was shrouded with polyethylene sheets. The forms were removed after one day so that preparations could begin for the next

segment. After removal of the forms, the segments were then covered again with burlap and plastic for an additional two days.

2.3.1.3 Deviators. With externally post-tensioned box-girders, the tendons are draped down from the ends of the span and are horizontally and vertically redirected through the deviators. The deviator region is very important since it provides the only attachment between the concrete girder and the post-tensioning tendons. Since the model bridge was to be used to investigate the global behavior of the structural system, the action of the local deviator regions were studied separately by Powell and Beaupre (12). In the model bridge structure, the tendons were deviated through an oversized 5" thick diaphragm element to ensure that local effects at the deviator would not limit the global behavior.

In the prototype structure the external tendons are commonly deviated through a bent steel pipe that is cast into the concrete section. In the model structure, the tendons were deviated through an 8 inch length of 1-1/2 inch diameter thin wall electrical conduit. The conduit was bent to an angle equaling the calculated angle change plus 2 degrees. This was done to ensure that the tendon would bear on the edge of the deviator pipe. The deviator conduit was bent using a hydraulically assisted electricians conduit bender. Since the conduit bender had a fixed radius of curvature that was smaller than required, the total angle change was divided into three equal concentrated bends. These concentrated bends were spaced at the center of the diaphragm and at 1-1/2 inches on either side of center to produce the proper overall angle change.

2.3.1.4 Shear Keys. Shear keys are used on segment faces to transfer shear across segment joints and to provide an interlock between match-cast segments. Exploratory studies by Koseki and Breen (25) indicated that a multiple key pattern provided the most uniform shear transfer across a segment joint. A study of contemporary segmental structures provided approximate ranges of key dimensions.

The strength of a multiple key joint is determined as the sum of the direct friction across the prestressed joint and the concrete shear capacity through the bases of all the keys (25). The shear strength is also limited by the bearing capacity on the key faces and the flexural capacity of the unreinforced key. Short keys will be limited by bearing stresses on their faces and long keys by flexural cracking through

the base of the keys. These bearing and flexural modes of failure provide a lower and upper limit to key depth.

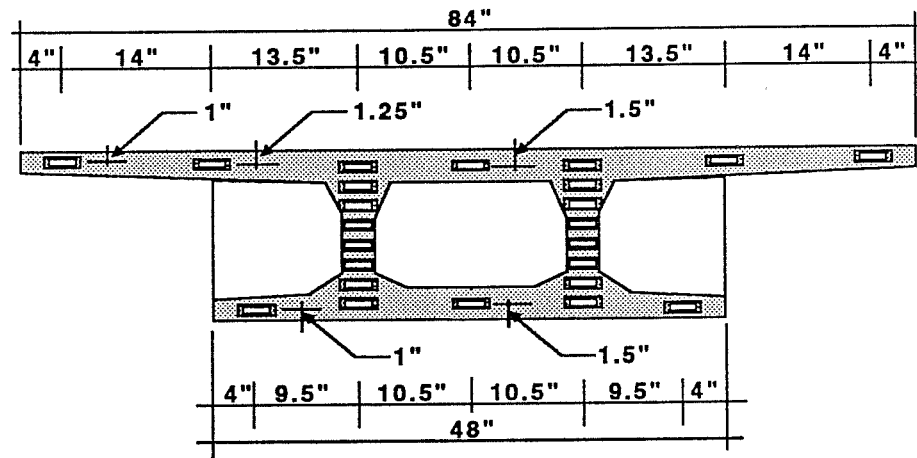
Keys were also provided in the flange regions to assist in realigning the segments during erection. Another purpose for flange keys is to transfer torsional shear flow that may exist in the flanges.

The shear keys were laid out on the end of the segment as shown in Fig 2.17. The blockouts had a trapezoidal shape and were cut from a sheet of 0.50 inch thick neoprene rubber. Rubber blockouts were used to provide a soft layer to minimize key damage during form removal.

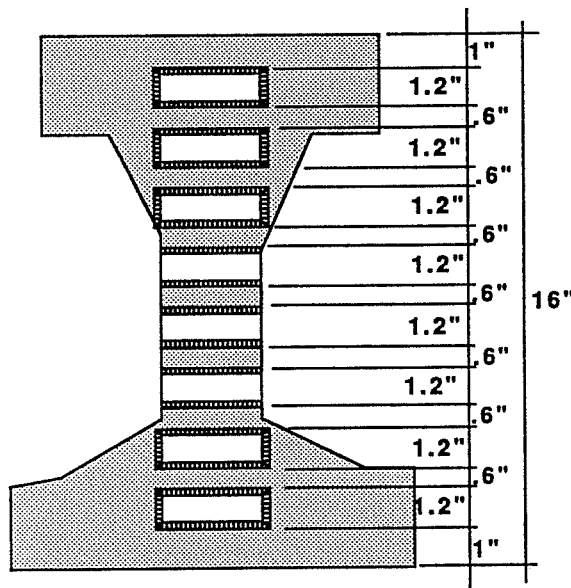
2.3.1.5 Fabrication Tolerances of Typical Segments. After casting and separating all the segments they were systematically measured at critical locations. Figure 2.18 shows the measurement locations on the north end of the cross-sections with the dimension numbers increasing from east to west. The segments were measured at the north and south ends and the average dimension is tabulated in Fig. 2.18. The mean and standard deviation of each measured dimension are also shown.

In most cases the match-cast face of a segment was wider than the new end because of the method of formwork. At the new end the formwork was adjusted to the proper position and held with turnbuckles. At the match-cast end of the segment the formwork overlapped the previous segment by 6 inches for closure. This distance and small irregularities in the concrete did not allow the forms to close completely against the previous segment.

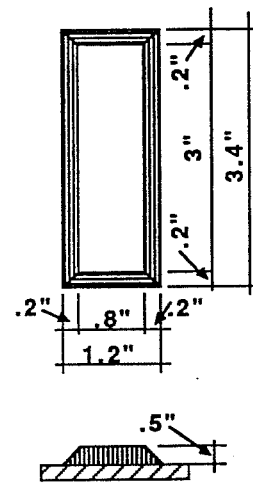
2.3.1.6 Segment Repair Procedures. As would be expected with an unexperienced contractor, several problems developed during precasting the model bridge segments. The hydraulic pressure, exerted by the concrete on the web forms, was not properly restrained and caused a problem in segment 4. The outside web form shifted out during the casting operation taking the diaphragm form with it. This caused the duct hole in the diaphragm to also shift to the outside. The forces exerted on the structure by this misalignment were insignificant but the outside duct hole was too close to the outside edge of the bottom flange. The diaphragm and bottom flange were chipped out, as shown in Fig 2.19a, the reinforcing and outside duct hole were realigned and the diaphragm and bottom flange were recast.



SEGMENT END ELEVATION

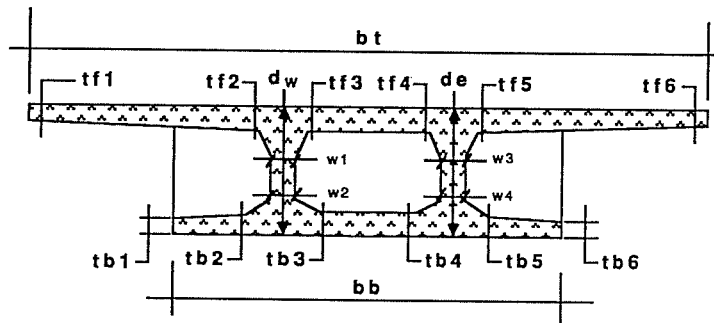


WEB DETAIL



SHEAR KEY DIMENSIONS

Figure 2.17 Shear Key Details

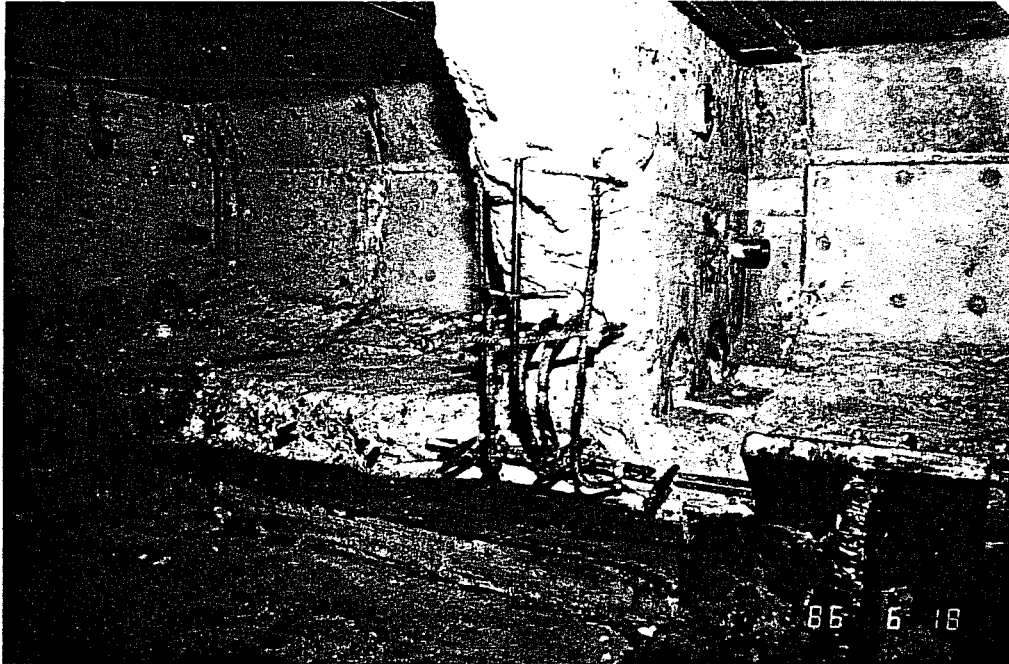


a. MEASURED LOCATIONS

Segment Inventory - Measured Dimensions

Segment #	bt avg	bb avg	de avg	dw avg	w1 avg	w2 avg	w3 avg	w4 avg	tf1 avg	tf2 avg	tf3 avg	tf4 avg	tf5 avg	tf6 avg	tb1 avg	tb2 avg	tb3 avg	tb4 avg	tb5 avg	tb6 avg
1	84.13	48.00	16.08	16.03	3.09	3.19	3.22	3.31	2.13	3.00	3.13	3.03	3.00	2.09	2.25	2.56	3.19	3.19	2.44	2.38
2	84.09	48.13	16.13	16.09	3.00	3.16	3.25	3.28	2.25	3.00	3.09	3.06	2.91	2.16	2.31	2.41	3.13	3.16	2.50	2.34
3	84.25	48.25	16.25	16.13	2.97	3.22	3.13	3.19	2.16	3.03	3.09	2.91	2.81	2.13	2.25	2.59	3.03	3.00	2.44	2.13
4	84.19	48.19	16.28	16.16	3.06	3.28	3.19	3.22	2.22	3.06	3.13	3.00	2.91	2.25	2.22	2.59	3.06	3.03	2.53	2.22
5	83.58	47.97	16.19	16.25	3.09	3.18	3.06	3.06	2.15	2.94	3.06	3.09	2.91	2.13	2.22	2.38	2.88	2.88	2.41	2.00
6	83.78	48.38	16.03	16.19	3.19	3.34	3.13	3.31	2.09	2.94	3.03	3.06	3.00	2.03	2.13	2.41	3.06	3.19	2.31	2.16
7	83.61	48.31	16.03	16.13	3.31	3.41	3.19	3.53	2.16	2.88	3.03	3.06	3.09	2.09	2.00	2.41	3.00	3.09	2.63	2.19
8	84.00	48.09	16.13	16.06	3.22	3.41	3.13	3.16	2.25	2.72	3.00	2.94	3.09	2.06	2.44	2.53	2.84	3.00	2.28	2.28
9	83.97	47.91	16.19	16.06	3.25	3.44	3.13	3.22	2.34	2.84	3.06	3.13	3.09	2.06	2.22	2.47	3.06	3.19	2.25	2.25
10	84.00	47.94	16.09	16.09	3.13	3.56	3.06	3.19	2.38	2.94	3.13	3.16	3.16	2.06	2.10	2.28	3.06	3.06	2.34	2.25
11	84.09	48.03	16.09	16.13	3.00	2.88	3.06	3.00	2.09	3.00	3.00	3.22	2.88	2.13	2.13	2.28	3.06	2.88	2.28	2.19
12	84.09	48.00	16.09	16.19	3.19	3.28	3.28	3.13	2.09	3.00	3.00	3.13	2.97	2.16	2.16	2.38	3.06	2.84	2.47	2.13
13	84.09	48.06	16.09	16.06	3.13	3.19	3.19	3.06	2.13	2.91	3.03	3.13	2.91	2.13	2.25	2.44	3.06	2.94	2.41	2.28
14	83.97	48.09	16.13	16.13	3.03	3.16	3.34	3.19	2.13	2.97	3.06	3.06	2.94	2.19	2.25	2.50	3.00	2.94	2.38	2.34
15	84.00	48.13	16.13	16.06	3.06	3.16	3.13	3.22	2.25	3.06	3.13	3.16	2.94	2.25	2.22	2.50	2.97	3.03	2.50	2.31
16	84.06	48.09	16.09	16.09	3.22	3.28	3.09	3.19	2.31	3.06	3.03	3.19	3.03	2.13	2.16	2.13	3.00	2.97	2.19	2.19
17	84.00	47.91	16.16	16.16	3.25	3.38	3.19	3.25	2.19	2.94	3.03	3.09	3.03	2.09	2.25	2.34	3.13	3.03	2.28	2.22
18	84.06	47.94	16.19	16.09	3.34	3.38	3.16	3.25	2.19	3.00	3.06	3.19	3.00	2.06	2.13	2.31	3.00	2.97	2.22	2.03
19	84.06	47.81	16.19	16.03	3.28	3.31	3.16	3.25	2.25	3.00	2.97	3.25	2.97	2.16	2.13	2.34	3.09	3.00	2.25	2.25
20	83.94	47.56	16.06	16.09	3.25	3.13	3.16	3.13	2.19	2.97	3.00	3.28	2.91	2.09	2.19	2.50	3.03	3.03	2.28	2.09
21	84.16	48.25	16.13	16.03	3.19	3.16	3.13	3.13	2.19	3.03	3.22	3.13	3.03	2.16	2.13	2.41	3.16	3.09	2.59	2.16
22	84.09	48.16	16.28	16.19	3.16	3.19	3.22	3.19	2.13	3.00	3.19	3.13	2.94	2.13	2.25	2.25	3.00	3.00	2.50	2.22
23	84.00	48.09	16.16	16.13	3.06	3.22	3.38	3.25	2.16	3.06	3.25	3.25	2.97	2.16	2.13	2.09	3.03	2.97	2.53	2.13
24	84.00	48.13	16.31	16.22	3.03	3.13	3.25	3.31	2.19	3.03	3.25	3.19	3.00	2.34	2.19	2.19	3.03	3.13	2.34	2.22
25	84.00	48.06	16.16	16.09	3.03	3.00	2.97	3.03	2.16	3.00	2.88	3.06	3.00	2.13	2.28	2.50	3.03	3.03	2.44	2.25
26	84.06	48.22	16.16	16.16	3.13	3.09	3.13	3.09	2.31	2.94	3.00	3.13	3.03	2.19	2.22	2.19	2.88	2.97	2.28	2.19
27	84.03	48.25	16.16	16.19	3.25	3.34	3.19	3.19	2.10	2.94	3.09	3.16	3.03	2.19	2.09	2.22	2.94	2.91	2.34	2.16
28	84.03	48.16	16.09	16.19	3.22	3.25	3.25	3.25	2.25	2.88	3.06	3.22	3.00	2.09	2.13	2.59	2.97	2.75	2.16	2.19
29	84.06	47.97	16.19	16.22	3.28	3.31	3.03	2.94	2.25	2.81	3.03	3.25	2.94	2.22	2.22	2.47	3.00	3.13	2.28	2.09
30	84.03	48.03	16.03	16.03	3.13	3.00	3.03	2.94	2.19	2.91	3.00	3.25	2.94	2.25	2.03	2.31	3.06	2.88	2.16	2.03
AVG	84.02	48.07	16.14	16.12	3.15	3.23	3.16	3.18	2.20	2.96	3.07	3.13	2.98	2.14	2.19	2.39	3.03	3.01	2.37	2.19
SD	.13	.16	.07	.06	.10	.15	.09	.12	.07	.08	.08	.09	.07	.07	.09	.14	.07	.11	.13	.09
SD/AVG	.0015	.0034	.0045	.0039	.033	.045	.029	.038	.034	.027	.027	.030	.025	.034	.039	.060	.024	.036	.054	.042

Figure 2.18 Measured Dimensions



a. Repair of diaphragm in Segment #4



b. Inadequate consolidation between casting lifts in Segment #2

Figure 2.19 Repair Details

In segment 2, the interface between the webs and the top flange was not consolidated and a layer of honeycombing occurred, as shown in Fig 2.19b. This was caused by incomplete mixing of the two lifts of concrete. Segment 2 was recast and care was subsequently taken to ensure proper consolidation at this critical joint.

The top flanges were too thin to be properly vibrated using immersion type vibrators. Therefore to consolidate the top flanges, the vibrator was hooked into the reinforcement so that the vibratory energy was transmitted to the concrete through the reinforcement. In segment 7, the vibrator was inadvertently hooked onto one of the internal tendon ducts and dislodged it from its support system. The concrete was chipped back approximately 2" on either side of the proper alignment and the duct was repositioned and cast-in-place. To ensure proper alignment, the adjacent segments (6 and 8) were matched and a nominal stress of 50 psi was applied to the matching face.

Another problem that was encountered during the casting operation was damage to the shear keys while separating the segments. Shear key damage was caused by two general problems. In some segments, the debonding agent was not completely applied to all surfaces causing the match-cast concrete to partially bond together. This caused generally minor damage local to the bonded area. A more serious problem was caused by overlapping lips in the match-cast keys which engaged when the segments were separated. These lips were caused by fresh concrete filling air voids and irregularities in the match-cast face. Depending on the size and location of the overlapping lips the key damage ranged from small corners breaking off to complete removal of keys. This problem can be minimized by carefully sealing around the edges of the forms and filling any air voids and irregularities with sealant prior to match-casting.

To ensure that the match-cast segments fit back together, repair of damaged keys must be done after the segments have been stressed together. Since key damage did not occur at critical joints they were not repaired for this test series.

2.3.2 Pier Segment Details. The pier segments for externally post-tensioned box-girders are the critical segments of the structure. They contain most, if not all, of the anchorages for the post-tensioning tendons. The tendon anchorage details were pretested to ensure adequacy. For interior pier segments, anchorages are

required on both faces with tendons crossing within the segment. In addition to the anchorage requirements, the bearing hardware is also required in the pier segments. A photograph of the south interior pier segment for the model structure is shown on the casting bed in Fig 2.20.

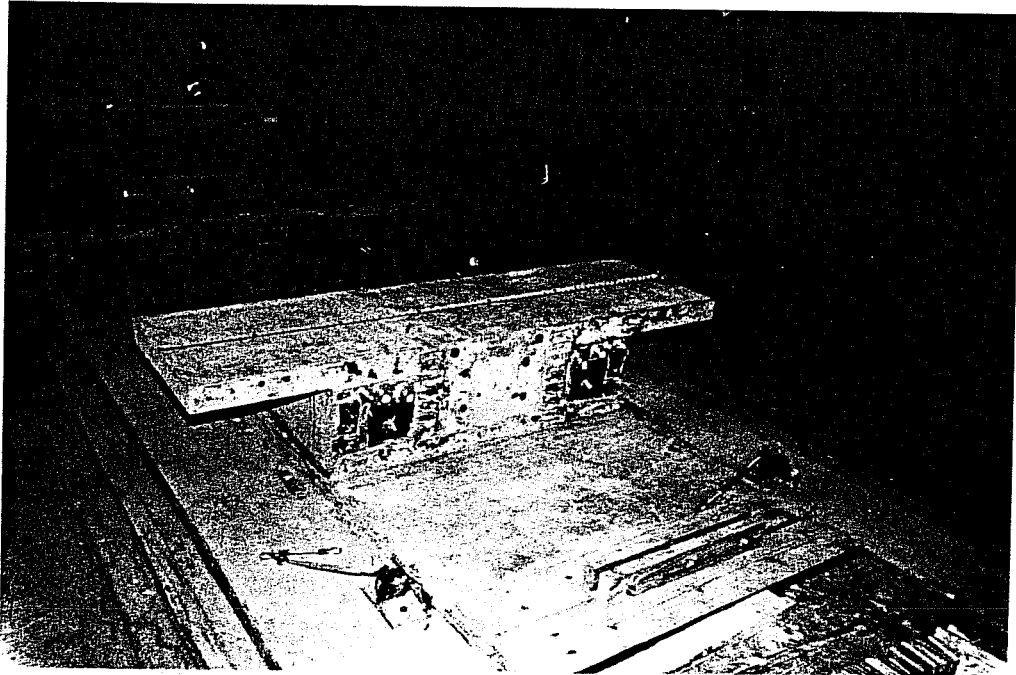
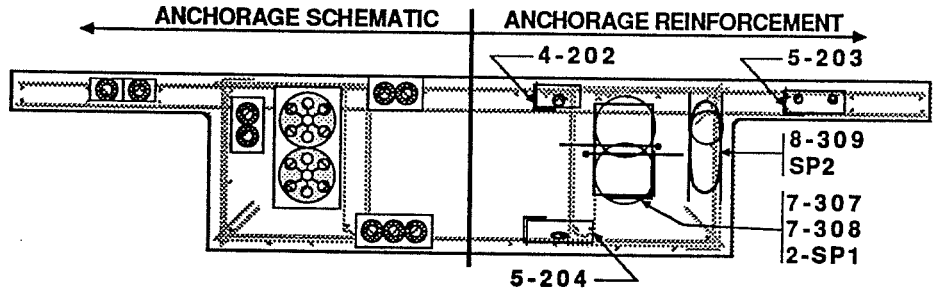


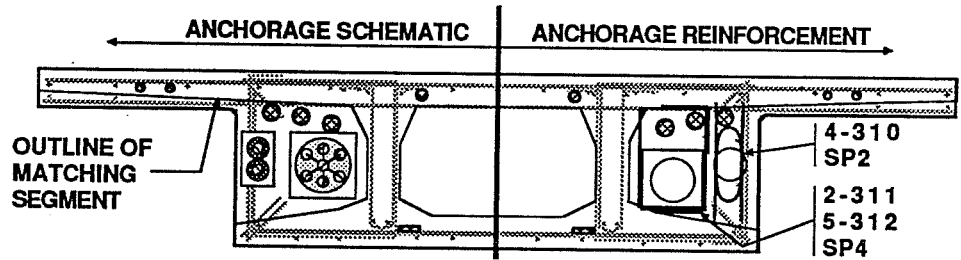
Figure 2.20 South Interior Pier Segment

2.3.2.1 Reinforcement. As was mentioned previously, severe congestion problems can be expected in the anchorage regions of reduced scale models of post-tensioned systems. The post-tensioning force varies with cross-sectional area as the square of the scale factor ($1/16$), while the volume of concrete in the pier segment varies as the cube of the scale factor ($1/64$). If the amount of confining reinforcement behind the anchorage is proportional to the post-tensioning force then there will be 4 times the amount of confining reinforcement per volume of concrete in the model as in the prototype. This leads to severe congestion in the model.

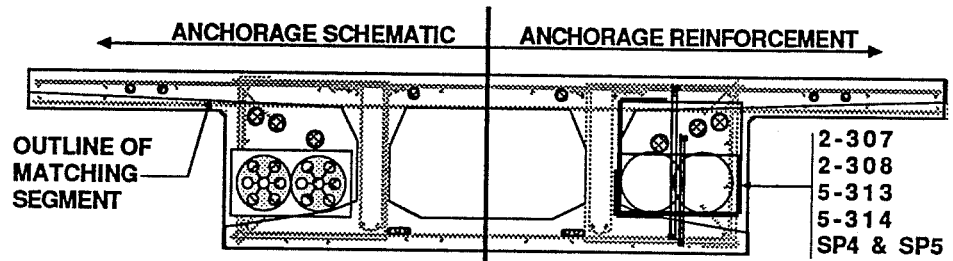
The basic cage of the pier segments, shown in Fig. 2.21 was designed to resist several types of forces. In line with the span webs, the shear forces must be transferred to the bearings. Each web was reinforced with the welded-wire mats used



c. EXTERIOR FACE OF EXTERIOR PIER SEGMENT



d. EXTERIOR FACE OF INTERIOR PIER SEGMENT



e. INTERIOR FACE OF INTERIOR PIER SEGMENT

SEE Fig. 2.21 f FOR REINFORCEMENT DESCRIPTION

Figure 2.21 Pier Segment Reinforcement (continued)

Bar No.	Type	Bar Size	Dimensions (inches)		
			A	B	C
201	Straight	2	23		
202	B1	2	2	4	2
203	B1	2	2	5.5	2
204	B1	2	2	6	2
301	Straight	3	83		
302	B2	3	47	4	
303	Straight	3	47		
304	B3	3	14	14.5	4
305	B4	3	14.5	2.5	4
306	Straight	3	23		
307	B1	3	5.5	11	4
308	B5	3	1.75	10	
309	B5	3	2.25	9	
310	B5	3	1.75	9	
311	B1	3	5.5	5.5	4
312	B1	3	6	9	4
313	B1	3	10	11	4
314	B5	3	1.75	14	
315	B1	3	6.5	14.5	4
401	Straight	4	83		
402	B2	4	47	4.5	
403	Striaght	4	47		
501	B2	5	47	12	
SP1	SP	1/4"	5	11	1
SP2	SP	1/4"	3	6	1
SP3	SP	1/4"	1.5	4.5	.75
SP4	SP	1/4"	4	4	.75
SP5	SP	1/4"	2.5	18	1
SP6	SP	1/4"	4	6	.75
SP7	SP	1/4"	2.5	20	1

f. REINFORCEMENT SCHEDULE

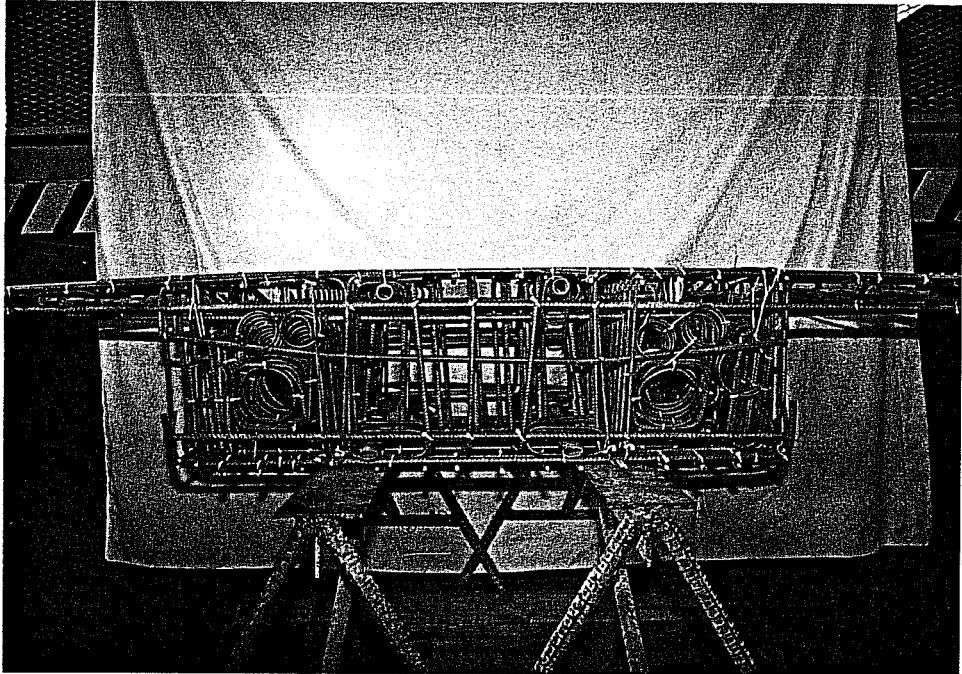
Figure 2.21 Pier Segment Reinforcement (continued)

in the webs of the typical segments, M_w , shown in Fig. 2.12. The external tendons are draped up from the span and deviated and anchored in the pier segments. The anchorage region was enclosed with stirrups to confine the entire region and resist the high shears from the anchorages and curvatures. With the anchorages outside the line of the webs, transverse reinforcement was required to direct the forces to the webs. The transverse flange reinforcement was therefore bundled near the edges. Longitudinal reinforcement was designed to resist the longitudinal moments over the bearing. Finally, a stiff shear diaphragm was provided over the bearings to concentrate torsional shear flow from the span. The basic cage reinforcement and typical bar bend types are described in Fig. 2.21a and 2.21b respectively. The anchorage zone reinforcement is shown in Figures 2.21c, 2.21d, and 2.21e. The reinforcement types are scheduled in Fig. 2.21f.

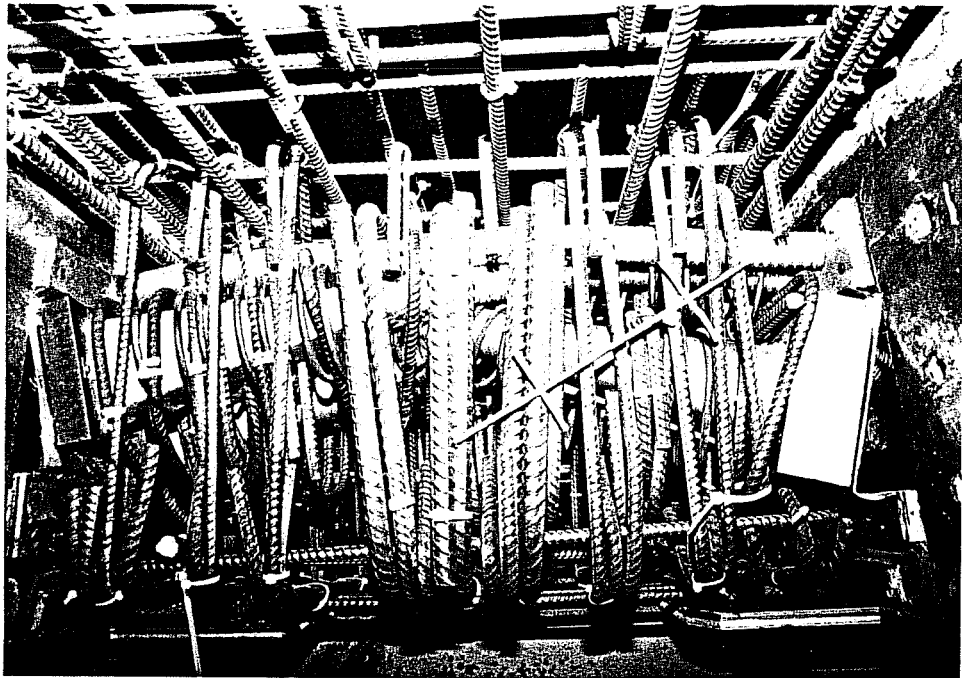
The reinforcement for the anchorage regions was designed to resist the bursting stresses that occur behind the anchorage (26). An equivalent triangular stress prism was calculated using the Rhodes Turner Method (27). Reinforcement was provided at 20 ksi to resist the maximum of the vertical or horizontal force requirements. A spiral was then added behind the bearing plate for confinement (28). Spirals were also provided at locations of high tendon curvature to resist the multi-strand tendon splitting forces (28). A photograph of the completed cage for an interior pier segment is shown in Fig 2.22a. The extreme congestion of the anchorage region, as viewed from under the top flange, after partial form assembly, is shown in Fig 2.22b.

Bearing stresses behind the anchorage bearing plates were limited to those recommended by the ACI 318.83 Building Code (7) with a loaded area to total area ratio of 1.0. High-strength concrete with a minimum 28 day compressive strength of 10 ksi was used to reduce overall plate dimensions.

2.3.2.2 Anchorage Zone Pretest. Before casting the pier segments it is prudent to pretest the anchorage zone configurations. This can be done by testing each pier segment for a proof load greater than the expected anchorage load. This does not give any indication of the ultimate safety factor and involves considerable wasted effort if found to be deficient. Sometimes a better method of investigating the strength of the anchorage zone region is to construct a simplified mock-up that includes the critical bearings, reinforcement, and tendon inclinations and curvatures.



a. Reinforcement for south interior pier segment



b. Congestion in anchorage region

Figure 2.22 Pier Segment Reinforcement

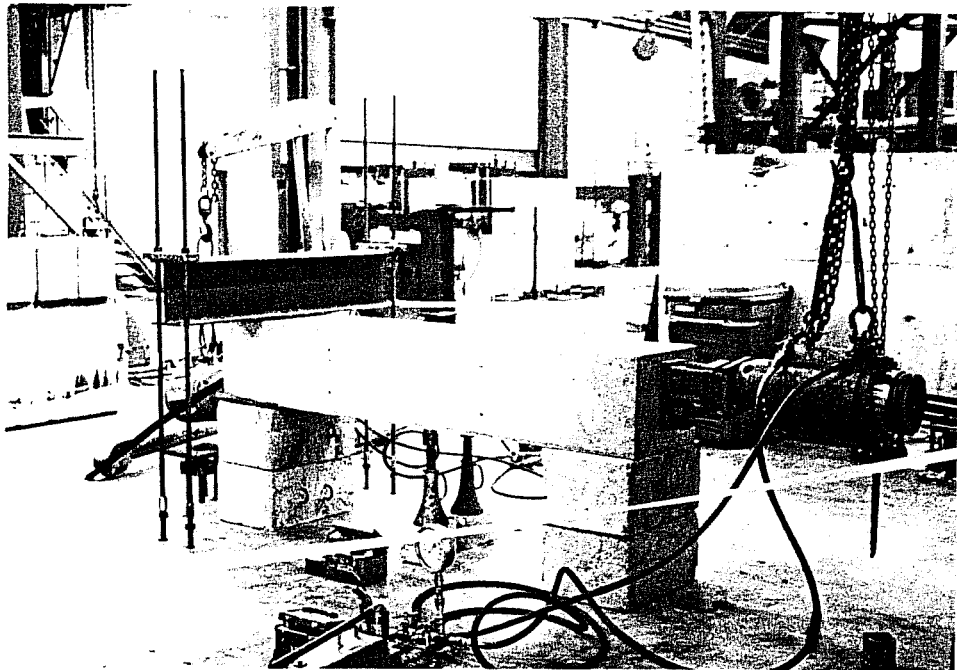
The mock-up can then be loaded to higher loads providing design information for cracking and possibly ultimate strength.

An anchorage zone pretest was designed with a critical anchorage assembly at each end of a rectangular prism. The layout of the test is shown in Fig 2.23a with reinforcing details shown in Fig 2.23b. The prism was reinforced with the same reinforcement that was used to confine the pier segment anchorage zone regions. The east end of the prism contained the horizontally oriented double tendon anchorage, and the west end of the prism contained the vertically oriented double tendon anchorage. To allow higher anchorage forces to be reached without overstressing the strands, 7-1/2" diameter strands were used instead of the model structures 5-3/8" diameter strands ($A_{mockup}/A_{model}=2.5$). Larger tendon ducts were used to allow the increased tendon area. For a similar test for prototype structures, larger tendon configurations can be substituted with the same reinforcement scheme.

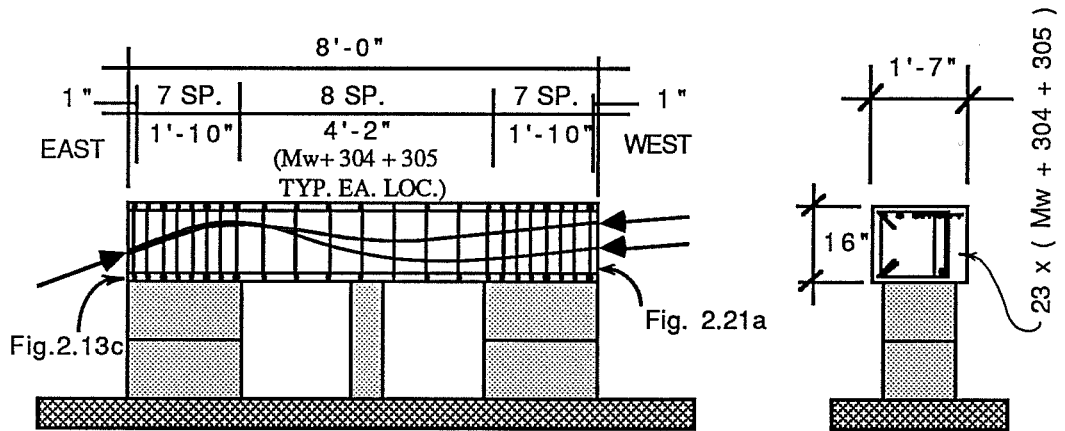
The mock-up was tested by alternately stressing tendons from each end of the concrete prism. Tendons were stressed in equal increments to a maximum load level of approximately 200% of the load that the model structure will be subjected to, (ie. $2.0 \cdot 0.8 \cdot f_{pu} \cdot (A_{ps})_{model}$). No external cracking was evident, although sounds at approximately 188% of the maximum model load indicated some internal cracking probably occurred. The test was discontinued, before visible surface cracking or ultimate anchorage strength was reached, when the increased tendon area reached approximately 70% of its ultimate strength.

2.3.2.3 Fabrication of Pier Segments. Because of the complexity of the pier segments they were precast separately from the typical span segments and joined with a cast-in-place closure strip. This was similar to the Phase 1a portion of the San Antonio project in which the pier segments were set independently or incorporated into the face of the straddle bents.

The pier segments were cast on the casting bed using the end forms from the typical span segments plus a new top flange and edge face form. The end form contained the shear key blockouts and internal tendon support systems. The forms were modified by cutting holes to accept the anchorage bearing assemblies and external tendon extensions. Anchorage bearing assemblies were fabricated for all faces of the pier segments and attached to the end forms at a standard location.



a. Anchorage zone pretest set-up



b. Reinforcing details

Figure 2.23 Post-Tensioning Anchorage Pretest

The anchorage bearing assemblies consisted of a steel bearing plate attached to a stainless steel tendon transition trumpet, which was in turn attached to the tendon duct. The end forms with attached anchorage assemblies were simultaneously fed into the reinforcing cage from both sides to mesh the ducting into the congestion of reinforcement (Fig. 2.22b).

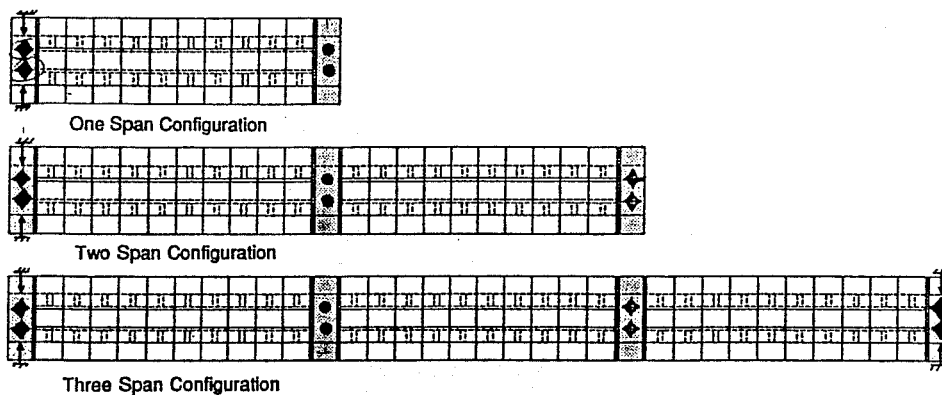
To ensure the external tendon ducts would not have concentrated curvatures at the face of the pier segments they had to extend from the segment face at the proper inclination. This was accomplished by extending dowels from tendon ducts at the segment face at the correct inclination, and attaching them to a plywood jig located 36 inches from the face of the segment.

2.3.3 Bearings and Piers. The arrangement of lateral and longitudinal restraint used in the model structure is shown schematically in Fig. 2.24. To satisfy erection and testing requirements the translationally-fixed bearing was located on the north interior pier. With the span-by-span construction method each intermediate structural configuration must be fully restrained. This required lateral restraint at both ends of the first span erected, the north span. In addition, longitudinal restraint was also required at one of these two supports. The longitudinal restraint was located at the north interior pier to reduce longitudinal movements at the far end and to provide the same exterior support condition for the two end spans.

Both exterior support reactions were measured with load cells. A third reaction at the south interior pier was also measured to provide a statical check. The exterior pier support reactions were measured under each web with a 100-kip capacity load cell. Rotational and longitudinal movements were allowed for by using neoprene bearing pads on top of each load cell. So that the measured reactions would not be affected, the lateral restraint at the exterior piers was provided with angle bracing which beared against the sides of the pier segment.

The support reaction at the south interior pier was measured with a 200 kip load cell under each web. Neoprene bearing pads were used to allow unrestrained movement at this support. Lateral restraint was not provided at this location.

So that reactions could be equalized under each web at a particular support, provisions were made for jacking and setting all the measured reactions. After completing erection, each support was individually lifted from its bearings, the load



- LEGEND:
- ◆ - 100 kip Load Cell Assembly
-Allows translational and rotational movements
 - ◆ - 200 kip Load Cell Assembly
-Allows translational and rotational movements
 - - Fixed Bearing Assembly
-Restrains Translational movement; Allows rotational movements
 - ↑ External Lateral Restraint to pier

Figure 2.24 Bearing Schematics

cells were zeroed, and then the structure was set back down. The structure was again lifted and shims were placed under the web of the lowest reaction. Several layers of aluminum foil shims were used to provide a fine adjustment capability. This process was continued until the reactions under each web were measured to be equal within 10% of each other.

The structural bearings at the north interior pier were fabricated from a spherical machine bearing set into a heavy steel plate. The pier segment was adjusted to its final elevation by tightening nuts on rod anchors set in the top of the pier and then the space between the top of the pier and the bottom of the steel bearing plate was filled with a liquid grout.

The piers were proportioned conservatively as shown in Fig. 2.25. All the piers were tied down to the test floor with 12 in. steel wide flanges on each side and were cast in their final position. A 32 in. by 21 in. opening was provided in each pier to allow movement of the erection girder to the next span erected. Both exterior piers were identical and had a stepped top to provide additional space for jacking

(adjustment of end reactions). The interior piers had different top elevations to correspond to the two types of interior bearings used. Sufficient space was provided within the bearing height to jack up on the structure.

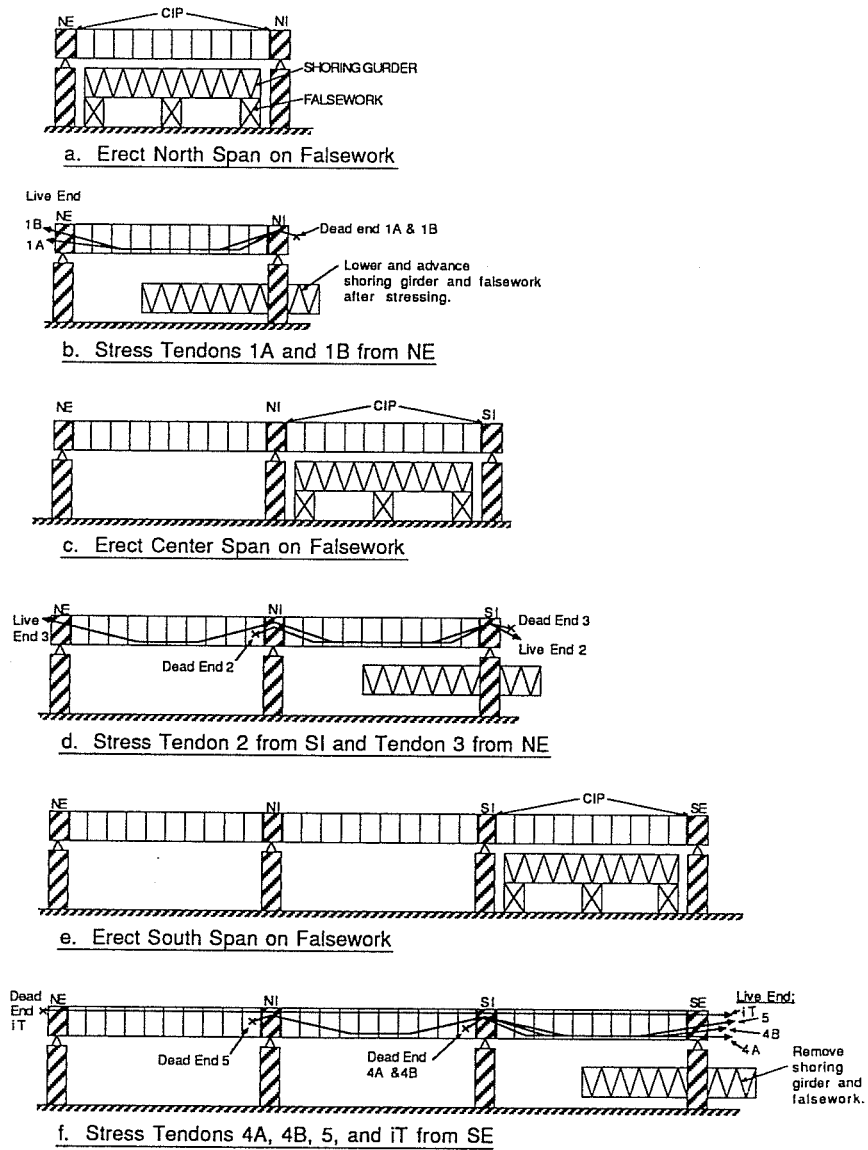
2.4 Erection Procedures and Details

2.4.1 Span-by-Span Erection Method. Although other methods of construction can be used with external post-tensioning, the majority of existing structures have been built using the sequential span-by-span method. For medium span elevated highway viaducts with approximately equal spans, the repetitive nature of this method leads to good economy. Erection equipment is fabricated once and used to erect many similar spans.

The model was therefore erected in a sequential span-by-span manner similar to prototype construction. The sequence of erection is shown schematically in Fig. 2.26. Erection began at the north exterior span and progressed towards the south. Falsework was erected in the north span to support all the segments for the entire span. The span segments were erected onto the falsework and drawn together with temporary post-tensioning. The pier segments were then erected and matched with the span segments with a cast-in-place closure strip. The dead load compensating blocks were suspended and the entire span was stressed to make it self-supporting. The falsework was then lowered and moved under the pier to the center span.

The center span was erected in the same manner as the north span. The span segments and pier segment were erected and then matched with the north span with a cast-in-place closure strip. After suspending the dead load blocks, the second span was then stressed to make the structure continuous over two spans. The falsework was then moved to the south span which was erected in a similar manner.

2.4.2 Geometry Control. An instrument stand, fabricated from a hollow structural tube, was erected on top of the south exterior pier. A theodolite was attached to the top of this stand and was positioned directly over the longitudinal bench-mark at Station 75'. A target at the same elevation as the instrument, and in line with the centerline of the structure, was marked on the wall to the north of



- STEPS:
- a. Erect North Span Segments on Falsework
 - b. Stress Tendons 1A, 1B
 - c. Erect Center Span Segments on Falsework
 - d. Stress Tendons 2 & 3
 - e. Erect South Span Segments on Falsework
 - f. Stress Tendons 4A, 4B, 5 and Top Internal Tendon

Figure 2.26 Span-by-Span Erection System

the structure. Initial sightings were taken on this target to set zeros on the instrument. Vertical elevations were surveyed using a surveying rod with the theodolite in the level position. Longitudinal alignment was sighted directly. The instrument stand remained in position until just prior to erecting the south exterior pier segment. Alignment of the south exterior pier segment was achieved using a temporary instrument setup on the bridge structure.

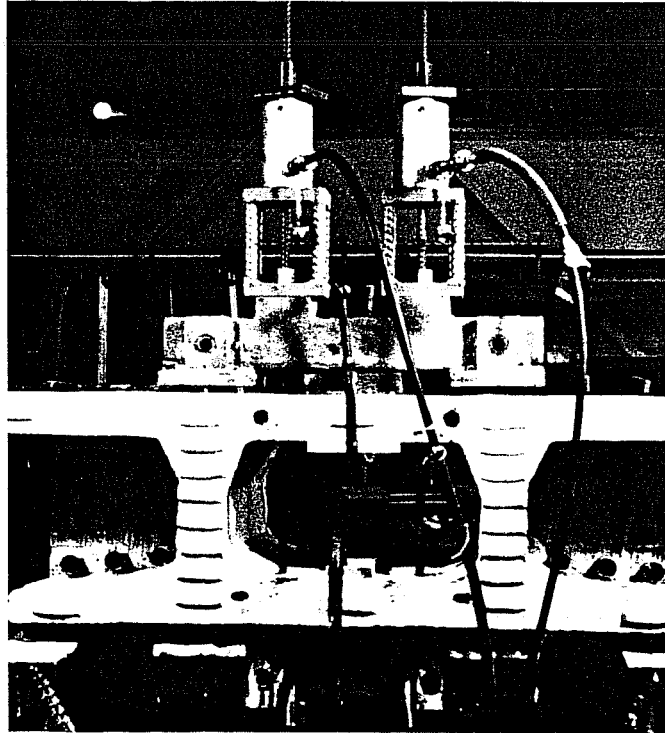
2.4.3 Temporary Post-Tensioning. During erection, the segments are positioned on the falsework, carefully drawn together, and if epoxy is used, stressed together. To pull the segments into their match-cast position and to provide a contact pressure for the epoxy to cure under, temporary post-tensioning is required. This stress must remain in position until the permanent tendons have been stressed.

To ensure that joints will not open before the permanent tendons have been stressed, a residual compressive stress is desirable. Minimum specified residual compressive stresses range between 50 and 75 psi (20) and are dependant on the segment weight, and exposure condition. A value of 50 psi was used for design of the temporary post-tensioning and supporting falsework.

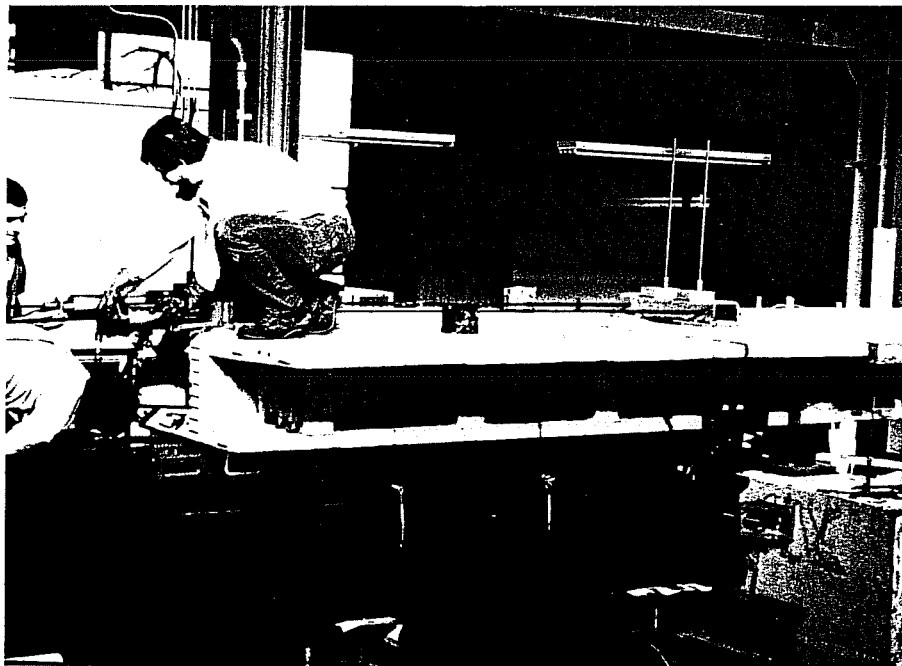
The layout of the temporary post-tensioning is controlled by the workable life of the epoxy joining material. The pot-life of the epoxy joining material ranges between 30 minutes (for standard set) and 24 hours (for slow set). The epoxy must be applied to all matching surfaces, the segments must be closed and the contact pressure applied all within the usable life of the epoxy. This maximum time period may limit the number of joints that can practically be joined in one operation.

A further consideration in choosing the layout of temporary post-tensioning is the weight of segments being joined. Because of slight errors in setting the elevations of segments on the falsework prior to closing, one or more of the joining segments may have to lift slightly to return to their match-cast position. If very heavy segments are being joined, then this lifting force may be substantial and could even change the uniform clamping stress. For this reason, prototype segments are usually closed and clamped one segment at a time.

The amount of temporary stress that is needed is a function of the stiffness of the supporting falsework. As the segment weight is added, the shoring and the segments deflect to carry the load. If the shoring is more flexible than the stressed



a. Application of vertical clamping force



b. Application of longitudinal stress

Figure 2.27 Temporary Post-Tensioning

stressed segments, then the segments will span independently between the ends of their current configuration. With stiffer falsework, the weight of the segments and the falsework, is shared by the two systems in proportion to their stiffnesses. Temporary post-tensioning is required to provide a compressive stress in the concrete segments to counter the bending stresses induced by deflecting with the falsework.

The temporary post-tensioning is applied to the segments in two stages. After applying the epoxy to the segment joints the segments must be drawn back into their original match-cast position. This first stressing stage requires side to side adjustment so that segment joints can be closed evenly. After full contact is achieved, the second stage of stressing is applied to induce a minimum residual compressive stress at all epoxied joints. To achieve the desired stress distribution in the segments, it is necessary to have top to bottom adjustment. The total time period available for stressing (Stage 1 and Stage 2) is limited by the pot-life of the epoxy jointing material. A complex valve assembly was used to change quickly from horizontal to vertical adjustment.

The temporary stress was applied to the concrete segments through a heavy steel bracket (Fig. 2.27a). These brackets were clamped to the top and bottom of the segments by vertically stressing 2-5/8" diameter DYWIDAG bars. To increase the frictional force between the steel bracket and the concrete segment a hydrastone layer was cast at the interface. The brackets were clamped to segments at four locations along the span. With nine joints between ten segments, three joints were closed in each stressing operation. This was considered to be the maximum number of joints that could be epoxy coated, closed, and stressed within the usable life of the epoxy.

The longitudinal stress was applied by stressing 4-5/8" diameter DYWIDAG bars between the brackets as shown in Fig 2.27b. The segment at the north end was held in position on the shoring and segments were added and stressed three at a time. DYWIDAG rod couplers were used to extend the rods for the full span length.

2.4.4 Erection Falsework. As described above, a stiff shoring girder consisting of two 18 inch steel wide flange sections supported at approximately 5 feet on center, was chosen in conjunction with the temporary post-tensioning system. The

two 18 inch steel beams were centered under the webs of the concrete box section and were braced together to act as a single shoring girder. The heavy shoring girder was supported on narrow gauge shoring and was continuous between faces of adjacent piers.

The concrete segments were erected on wooden blocks resting on variable-height steel spacers which were bolted to the heavy shoring girder. The steel spacers were necessary to allow the temporary post-tensioning hardware to slide forward during closing of the segments. The concrete segments were also laterally restrained.

2.4.5 Segment Joints. A primary interest of this test program was to investigate the effect the epoxy jointing material had on the girder behavior. Its use has been prescribed in bridge structures to provide a reserve against joint openings caused by unusual load cases or calculation inaccuracies. The possible benefit to ultimate load behavior is unknown and will be examined herein.

To study the effects of epoxy on service, moderate overload, and ultimate load behavior, one exterior span was constructed with dry joints and the other with epoxy joints. This provided two otherwise identical spans in which behavior could be compared directly. The interior span was constructed with epoxy joints to provide the possibility for additional testing of epoxy-jointed segments. The layout of epoxy and dry joints is shown in Fig. 2.7.

The epoxy joining material must meet three general requirements: adequate tensile and compressive strength, minimum usable time, and viscosity (25). The epoxy must transmit compressive stresses across the joint plus provide a tensile capacity between match-cast segments. Ideally, the epoxy should develop a tensile capacity higher than the adjacent concrete. This forces the segmental girder to behave more as a monolithic beam. The second requirement of the epoxy involves the method of segment erection and epoxy application. The epoxy must remain workable for a minimum time period, for a certain range of ambient air temperature, to enable organized assembly of the segments. The epoxy must be applied to all matching surfaces, and the joints must be closed and temporarily stressed, all within the working life of the epoxy. The epoxy application process was practiced on the dry north span to ensure time limits could be met. Finally the epoxy must

have the proper consistency to be properly applied and the necessary viscosity to not drip onto the area below the bridge.

Several brands of segmental application epoxies were investigated prior to use in the model structure. The epoxy was tested by comparing modulus of rupture tests for monolithic and match-cast specimens. A 6"x6"x20 concrete prism was match-cast in two halves. Characteristic monolithic prisms were cast from the concrete used for each beam half. The debonding agent used on the typical segment faces was used on the match-cast face. A central duct was cast in the specimens to enable stress to be applied during closing. The matching faces of the specimens were cleaned and prepared in the same way as the segment faces and epoxy was applied to both matching faces. A uniform stress of 50 psi was applied to the joined face which remained in place for a minimum of four days to ensure the epoxy had fully cured.

A standard modulus of rupture test was conducted on all specimens. A third point loading system was used to minimize shear forces across the joint and to provide a constant moment region so that specimens could break away from the joint. For approval, the modulus of rupture of the joined specimen was required to be greater than 90% of the monolithic prisms. Pot-life and workability characteristics were also assessed.

The epoxy was delivered to the laboratory in two components (resin and hardener) with mix proportions labeled on the container. Two types of epoxies were approved for use depending on the ambient air temperature. The mix proportions were preweighed and mixed in a large bowl using a T shaped extension on an electric hand drill. After mixing for a minimum of 3 minutes, the epoxy was applied to both matching faces of a segment joint using rubber gloves. After closing the joints, the internal tendons were cleaned of epoxy by inserting a rod with attached cloth into the internal tendon ducts. The cloths were replaced several times until they came out of the duct clean.

To ensure proper bonding of the epoxy with the underlying concrete, matching surfaces were lightly sandblasted prior to joining the segments. This cleaned off all the residue left from the casting operation, such as bond-breaker,

cement laitance, and form deterioration debris, as well as removed loose or soft concrete resulting from consolidation or form sealant problems. A light duty sandblaster was purchased from a local retailer and was used to sandblast all the segments. All matching faces of the typical span segments and pier segments were sandblasted prior to erection. All segments were sandblasted whether they were to be epoxied or not. Preliminary trials revealed that the severity of the sandblasting was related to the air pressure, the size of blasting sand used, and the distance from the nozzle to the treatment surface. Proper blasting provided a clean porous surface without removing excessive amounts of the fine concrete aggregates.

2.4.6 Cast-in-Place Closure Strips. At each end of each span, between the pier segment and the first span segment, a 3 inch thick cast-in-place (CIP) strip was provided. This CIP closure strip joined the separately precast pier and span segments and corrected fabrication and erection errors.

In the prototype structure, the closure strip is an unreinforced strip ranging in width between 6 and 10 inches. The web reinforcement was sized and spaced so that the closure strip width was contained approximately within one spacing of the web reinforcement. In this way, web reinforcement was not required in the CIP closure strips. In the model structure, a 3 inch CIP width was chosen as a practical minimum for proper consolidation of this critical joint. The web reinforcement of the typical span segments was spaced at 2 inches to reduce bar sizes and allow for the tight bar-bend diameters required in the 3 inch thick webs. A layer of reinforcement was therefore required in the CIP strip to maintain a constant web reinforcement spacing. A wire was cut from each of the mats of welded wire reinforcement used for the typical segments, shown in Fig. 2.12. These wires were tied together to form a layer of reinforcement within the 3 inch CIP closure strip.

The closure strips were fabricated using plywood forms which closed the space between the span segments and the pier segments. The end of the box void of the last span segment was filled with an expansive polyurethane foam to act as a blockout during casting. The top of the bottom flanges outside the web interface were left open to ensure proper consolidation of the critical bottom flange regions.

The internal tendon ducts were supported during casting using threaded pipe nipples. These pipe nipples were welded to the side of the internal tendon ducts

and bolted to the plywood for support. The pipe nipples extended from the face of the finished concrete segment and can also be used for grout injection (see Section 2.4.8). The strands of the internal tendon ducts were fed through prior to casting the CIP closure strip. The auxiliary tendons were sheathed through the CIP region to prevent bonding.

The concrete was mixed in a 9 cubic foot mixer using a mix similar to the Type 3 mix shown in Table 2.4. A small dosage of super-plasticizer was used to increase the slump to approximately 8 inches. With the high surface to volume ratio in the pour strips it is important to moisten the forms and matching segment faces to reduce water loss due to absorption. The super-plasticizer is beneficial in providing concrete with a high workability that is independent of water loss to absorption.

The concrete was delivered and placed using 5 gallon plastic buckets. The concrete was consolidated, with a 1 inch diameter immersion vibrator, from the top and also from the sides in the bottom flange regions. After initial set was achieved, all exposed surfaces were covered with burlap and plastic sheet. The burlap was kept continuously moist for a minimum of 4 days and then the forms were removed.

2.4.7 Post-Tensioning Methods. Three general types of post-tensioning tendons exist in the model bridge structure. The external tendons consist of single span five-strand tendons used for erecting each span, and double span two-strand continuity tendons used to increase service load strength. The final type of tendons used in the model are the internal tendons which were stressed from the extreme ends after the structure was fully constructed.

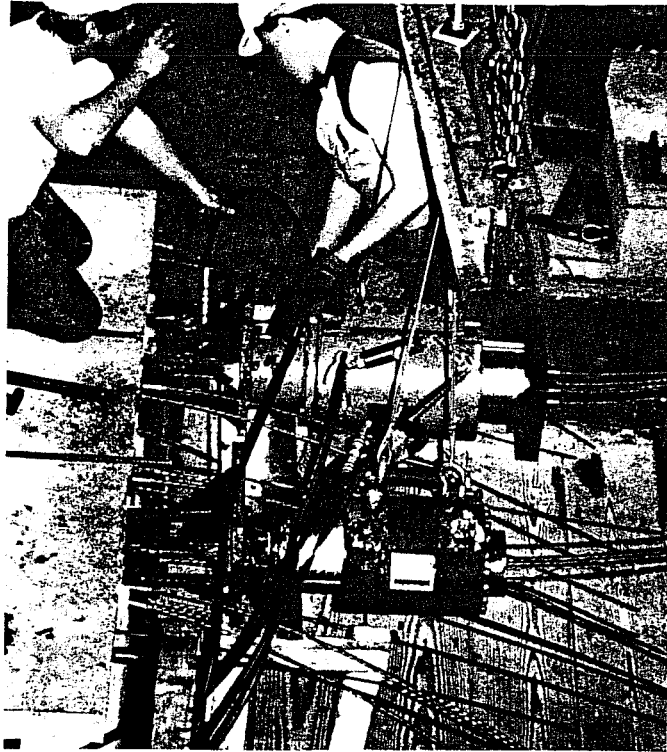
The jacking force was controlled for all stressing operations by using a visual pressure gauge and an electronic pressure transducer. Approximate force changes during stress increments were controlled visually by reading the pressure gauge. Exact jacking forces were measured with the pressure transducer connected to a strain indicator box. Each hydraulic setup (rams, hoses, pumps, pressure gauges and transducers) used during construction of the model was calibrated prior to applying force to the tendons. This is recommended since it acts as a pressure check of the hydraulic system as well as providing a condition check of the pressure gauges and transducers.

Two basic setups were used for stressing the five-strand external tendons. For tendons 1a and 1b of the north span, the tendons were stressed using two 200 ton rams that were pressurized by the same pump in parallel. This is not a recommended setup since the hydraulic oil went to the location of least resistance. The piston movement on both rams was erratic with the pistons stopping and starting as resistances in the rams and tendons changed. Also, ram travel was exceeded on one of the rams while stressing tendon 1a and was not immediately noticed because oil kept feeding to the other ram.

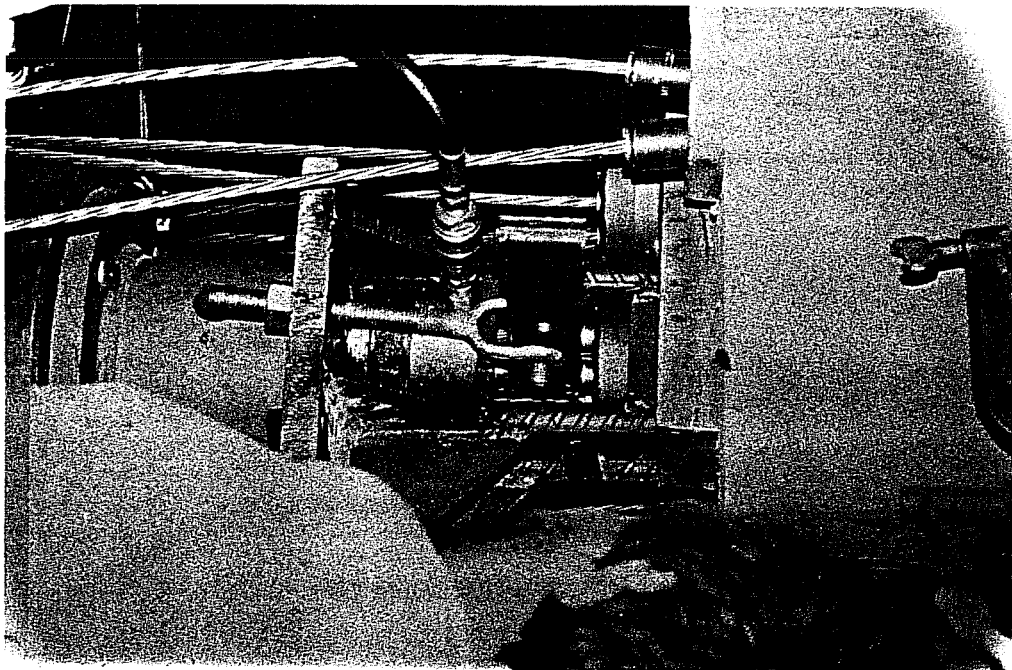
For stressing the remaining five-strand tendons (2, 4a, and 4b) a 100 ton ram and a 200 ton ram were operated simultaneously. Each ram was operated separately with its own pump and pressure control system. Far better control was achieved by using the two separate setups. Differences between the two sides were noticed immediately by the pump operator, and jacking forces were known at all times for both rams. Side to side control of jacking force was achieved automatically. Figure 2.28a shows the symmetrical stressing operation for the multistrand tendons.

To reduce the prestress losses due to wedge set in the anchor head, a special chair was designed to incorporate a hydraulic seating device. A photograph of the multistrand anchorage seating mechanism is shown in Fig. 2.28b. A small 25 kip hydraulic ram was used to apply force to a lever bar. The lever bar was tied up to the chair at the back and beared against the anchor wedges at the front. A force of 4.5 kips was applied to each wedge prior to releasing the tendons. This hydraulic seating device was tested prior to use in the structure and the anchorage set after hydraulically seating the wedges was measured to be approximately 1/8 inch.

For the first tendon stressed the wedges were hydraulically seated and the tendons released. In an attempt to reduce anchorage set even more, the tendons were restressed to the jacking force and the power seater was applied again. This applied a local surface shear to the previously seated strands which caused a wire to break in one of the strands. Because it was not possible to destress the anchored system the tendons had to be cut. The tendons were cut in a controlled manner using an 1/8 inch thick cutting wheel on a small hand grinder. Four wires were cut alternately on each side of the structure until all five strands (35 wires) had been cut.



a. Multistrand stressing operation



b. Hydraulic seating device

Figure 2.28 Multistrand Stressing Methods

The two-strand external tendons were stressed using a monostrand ram with internal seating device. Figure 2.29a is a photograph of the monostrand jack in operation. The power seating mechanism is shown schematically in Fig. 2.29b. During the seating process, the internal seating cone extends forward until the ram force bears against the wedges. This forces the wedges into the anchor barrel and reduces the subsequent seating loss.

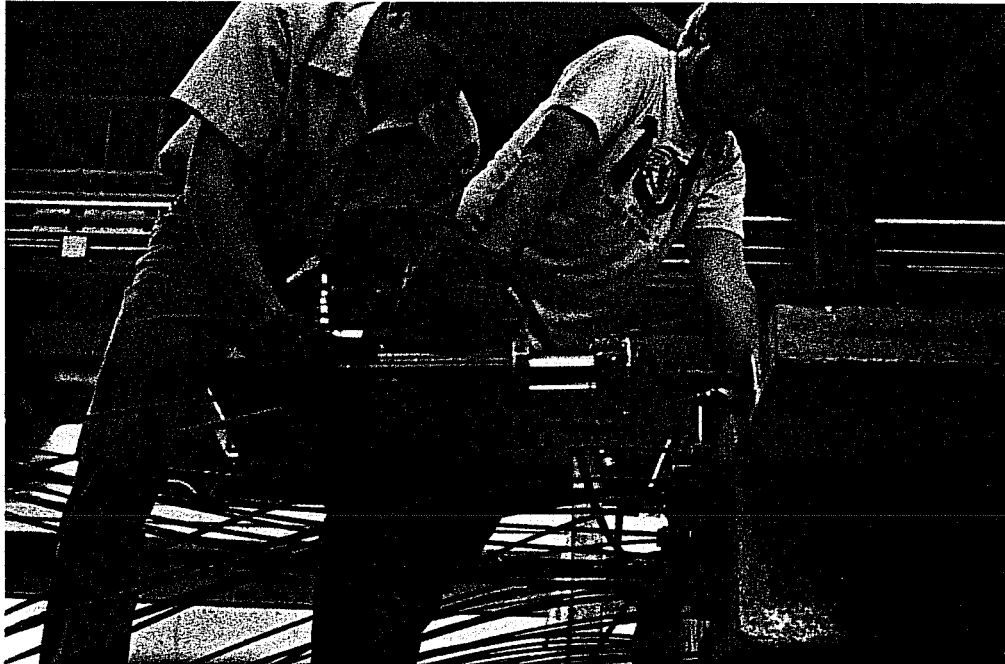


Figure 2.29 Monostrand Stressing Method

The two-strand external tendons were stressed by alternately stressing each strand in small increments. This was done to ensure that a stressed strand would not bear against, and bind up, an unstressed strand.

The top interior tendons were also stressed using the monostrand equipment described previously. Because crossing and binding of these strands was not possible they were all stressed in one operation to the full jacking force.

2.4.8 Tendon Ducts and Grouting Details. Considerable effort was spent in locating suitable ducting for tendons in the model bridge structure. Since standard post-tensioning ducts were not locally available in the small sizes required it

was necessary to examine other avenues of supply. The ducting consists of two basic types. The locations where tendons were within the concrete section (internal tendons) ideally required a duct with a ribbed profile for interlock, water tight for casting, and rigid enough to hold alignment during casting. In the locations where tendons were external to the concrete section, the duct was required to withstand an internal pressure of approximately 100 psi to avoid splitting during grouting.

There were two types of tendons that were internal to the concrete section. At the corners of the box and at the ends of the flanges were internal tendons with a straight profile between the ends of the structure. To facilitate feeding of the strands through these long continuous tendons it was critical to have a rigid duct that would hold its alignment in the forms. A profiled duct with sufficient rigidity was not located so a smooth thin-walled electrical conduit was used. The bottom internal tendon ducts were flattened to fit through the layering of reinforcement in the bottom flange.

The second location where tendons were internal to the concrete section was where the external tendons passed through and were anchored to the pier segments. In these locations, the tendons have sharp curvature, and a ribbed profile was desirable to improve the stress development of the strands to the concrete section. In these locations a water tight flexible electrical conduit was used as ducting. This ducting had a coiled metal profile similar to conventional post-tensioning ducts, only with a relatively larger rib profile.

The external tendon ducts consisted of two basic types. In the inclined portions of the draped tendons a polyethylene pipe was used. This pipe is similar to the pipe used in prototype construction. In the midspan regions, where the external tendons are parallel to the bottom flange, a flexible electrical conduit was used as ducting. This profiled ducting was used to facilitate the possibility of bonding the external tendons to the midspan regions of the bottom flange for a possible future test.

At the locations where the external tendons pass through the segment diaphragms, a short length of thin walled electrical conduit was used. This conduit

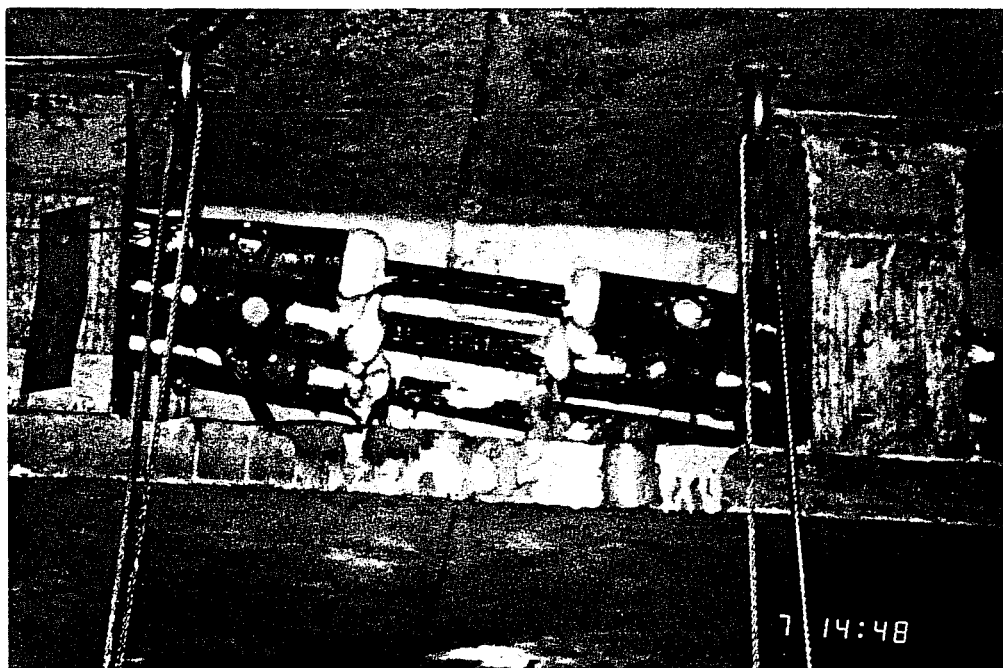
was spliced with the external tendon duct and was provided to allow for the possibility of bonding the tendons to intermediate diaphragms. This could possibly reduce the free length of the external tendon and perhaps improve ductility of the system.

All tendons were provided with injection nozzles for grouting the ducts. Grouting is done to bond the internal tendons to the concrete section and to provide protection against corrosion for the exposed external tendons. So that instrumentation could be attached to the external tendons, the tendon duct was made discontinuous at three locations on each side of each span. This provided a short length of exposed tendon to which strain gages could be attached. Grout nozzles were provided on both sides of this instrumentation blackout as shown in Fig. 2.30a. The open ends of the ducts were sealed for grouting by injecting an expansive roofers foam into the end.

Grout ports for the internal tendon ducts were provided at the cast-in-place closure strips at each end of each span (see Sec. 2.4.6.). Figure 2.30b shows the completed closure strip with grout injection nozzles protruding from the concrete section.

The grout mixture used was the standard Texas State Department of Highways and Public Transportation grout mixture used for post-tensioning ducts. It consists of 1 part cement to 1/2 parts water (by weight) with 1 oz expansive admixture per hundred pounds of cement. The grout was mixed in a large grout mixer and then dispensed into a 10 gallon pressure canister. Compressed air was pumped into the pressure canister which forced the grout into the tendon ducts. A compressed air system was used so that excessive pressures would not build up within the tendon ducts.

All the external tendons were grouted after erecting the entire structure. The top internal tendon ducts were left ungrouted so that pure unbonded behavior could be investigated.



a. External tendon grout injection port



b. Internal tendon grout injection port

Figure 2.30 Tendon Grouting

CHAPTER 3 INSTRUMENTATION AND DATA ACQUISITION

3.1 General Requirements

The reduced-scale bridge model was instrumented to measure the structural response to applied loads ranging from service level to ultimate strength. Several types of measurements were made to monitor the behavior of the structure during construction and load tests. Applied loads were monitored and reactions were measured to provide a check of static equilibrium as well as to provide information regarding load distribution in the continuous structure. Deflections were measured at key locations, and when combined with the applied loads provided important load-deflection information. Local deformations, such as external tendon strains and joint openings, were also measured to determine internal forces and local joint distortions at all levels of loading.

3.2 Data Acquisition

Since a large number of measurements were required to record the behavior of the model, the majority of the data was measured with an electronic data acquisition system. Reactions, applied loads, deflections, and joint-opening behavior were all recorded with the electronic system. Manual readings for deflections and joint distortions were also made to verify and augment electronically recorded data.

3.3 Instrumentation Identification Code

To avoid confusion during testing and data reduction a systematic data identification method was employed. The instrumentation identification code is illustrated in Fig. 3.1. The general form of the code is TYPE-LOCATION-SPECIFIC. The reactions are designated as Type RX and are located at each of the supporting piers (NE, NI, SI, SE) on either the west or east side. The deflections were measured with either potentiometers, designated as Type DP, or with dial gauges, designated as Type DG, and were located under a particular segment, either on the longitudinal centerline or symmetrically located on the west and east side. The external

Basic Form: TYPE - LOCATION - SPECIFIC

TYPE -

RX	Reaction Load Cell
DP	Vertical Deflection Measured with Potentiometer
DG	Vertical Deflection Measured with Dial Gauge
T	Tendon Strain Gauge
JP	Joint Opening Potentiometer
JC	Joint Opening Crack Monitor

LOCATION -

SUPPORT DESIGNATION	Particular Support e.g. NE = North Exterior
SEGMENT DESIGNATION	Particular Segment e.g. 5 = Segment 5
JOINT DESIGNATION	Particular Joint Specified e.g. (N. Seg., S. Seg.) where N. Seg. and S. Seg. are the segments on the North and South sides of the joint, respectively

SPECIFIC -

Reactions Form:	RX - SUPPORT DESIGNATION - SIDE Side = West or East
Deflections Form:	D? - SEGMENT DESIGNATION - SIDE Side = West, Center or East
Tendon Strains Form:	T - JOINT DESIGNATION - TENDON Tendon = Tendon #, West or East, #1 or #2 e.g. T - (5,6) - (1A.W1)
Joint Opening Form:	JP - JOINT - SIDE Side = West or East JC - JOINT - DEPTH Depth = TF, TW, BW, BF TF = Top Flange TW = Top Web BW = Bottom Web BF = Bottom Flange

Figure 3.1 Instrumentation Identification Code

tendon strains are designated as Type T and are located at a particular segment joint where the tendon strains are measured in a specific tendon on either the west or east side. Joint distortions were measured with either linear potentiometers, designated as Type JP, or with a grid crack monitor, designated as Type JC. Type JP measurements were made at a particular segment joint on either the west or east side. Type JC measurements were made at a specific depth of a particular joint on the west side only.

3.4 Instrument Locations

The layout of the permanent instrumentation used during testing of the structure is shown in Fig. 3.2. This instrumentation was the same for all tests and included the instrumentation for reactions, tendon strains, and deflections. The joint distortion instrumentation, shown in Fig. 3.3, was assembled differently for each test. During construction, deflections were measured at the temporary locations shown in Fig. 3.4. The choice of instrumentation type and location is described in detail in the following sections.

3.5 Support Reactions

Reactions were measured at three of the four supporting piers. Web reactions were measured at the two exterior supports as well as at the south interior support (See Fig. 3.2). At each location, two calibrated load cells were used to measure the reaction in each of the segment webs. At the exterior supports, two 100-kip load cells were used, and at the south interior support, two 200-kip load cells were used. The complete bearing assembly was compressed in the testing machine during calibration, and the overall compressive deformations were measured. This measured stiffness of the load cell bearing assembly was used for analytical modeling of the supports, (see Section 5.3).

3.6 Measurement of Applied Loads

The loads were applied to the structure with two 60-kip capacity hydraulic rams. Hydraulic line pressure was measured using two 10 ksi pressure transducers which were used to control hydraulic line pressure during testing.

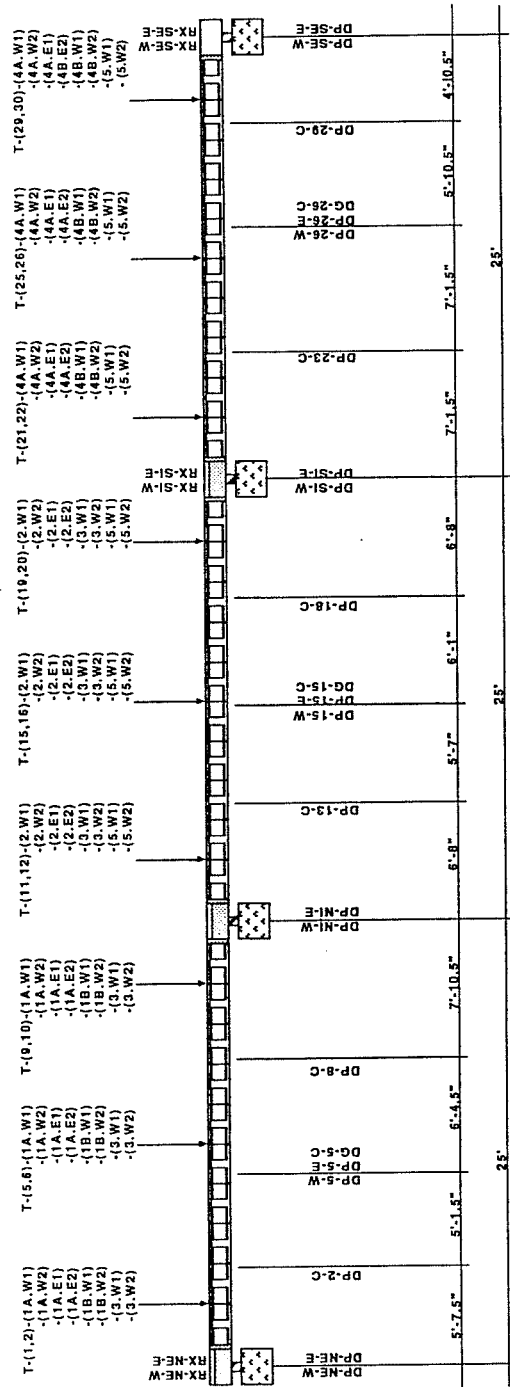


Fig. 3.2 Instrumentation Layout During Testing

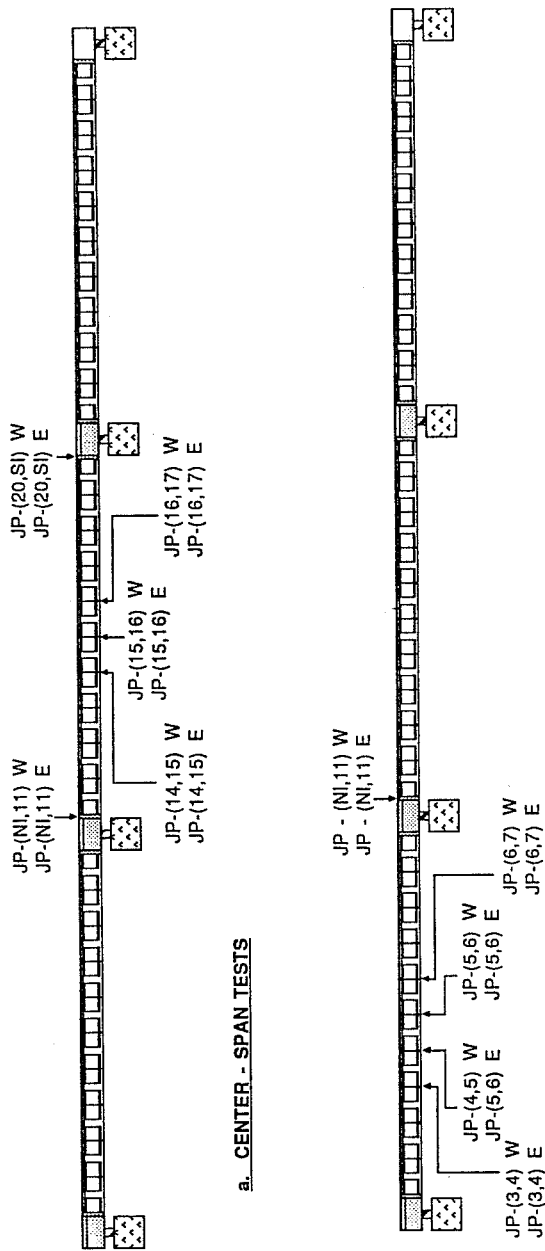


Fig. 3.3 Joint-Distortion Instrumentation

3.7 Deflection Measurements

The location of the vertical deflection instrumentation during all load tests is shown in Fig. 3.2. Vertical deflections were measured at each support plus three locations in each span. The center measurements in each span were situated at approximately the location of maximum deflection. The other measurement locations were approximately equidistant from the maximum deflection location and the bearing.

All vertical deflections during testing were measured under the bottom flange, either along the centerline or at two points equidistant from the centerline. At the maximum deflection location, vertical deflections were measured under both of the box-girder webs. At the quarter points, vertical deflections were measured under the centerline of the structure. The vertical deflections of the pier segments were measured at locations 22 in. each side of the centerline, in line with the bearings.

During the three stages of construction, vertical deflections were measured at the temporary locations shown in Figure 3.4. Measurements were taken at each support and at three locations along each span. In the span under construction, the longitudinal locations of the measurements were dictated by the instrumentation-stand configuration and the location of the tie-down rods in the test floor. Vertical deflections were measured approximately 6 in. from the edges of the top flange. In the completed north span of the two-span configuration, vertical deflections were measured under the bottom flange along the centerline of the structure at longitudinal locations corresponding to the test locations described above. Vertical deflections of the pier segment were measured as described earlier. To provide additional information related to the torsional response of the structure during erection of the third span, deflections of the completed north and center spans were measured at midspan under the box-girder webs.

Vertical movements of the model were monitored using linear voltage displacement transducers (LVDT, also called potentiometers) and dial gauges which were also used to verify electronic data. The vertical deflection instrumentation was mounted on frames set in a hydrastone bed to ensure firm support.

Horizontal displacements were also monitored during construction and load testing. During construction, the horizontal deflections were measured using dial

gauges at each pier segment. A theodolite was also used with a measuring tape to record movements from the theoretical alignment. Horizontal movements were monitored during load tests at the supports and at the center of the span being tested. At the supports, dial gauges measured the horizontal displacement of one side face of the pier segments. At the center of the span being tested, horizontal movements were monitored by hanging a plumb-line from the edge of the top flange to a steel measuring-tape epoxied to the test floor.

3.8 Strand Strain Measurement

The external tendon strains were measured at nine locations on each side of the three-span structure. The tendon layout is described in detail in Section 2.1.4. In general terms, the tendons drape down from high points over the supports and are horizontal in the midspan regions. Strains were measured in each tendon in the inclined portions near the supports and also in the horizontal region at midspan. Since knowledge of tendon stresses is critical for determination of internal forces, two strain gages were attached to each tendon at each location. To reduce the total number of strain gages, all three tendons were instrumented at each location on the west side while only one tendon was instrumented at each location on the east side.

The strain in the post-tensioning strand was measured by attaching a small 0.16 in. by 0.24 in. resistance-type strain gauge to a single wire of a strand in a multistrand tendon. The strain gage was chosen to fit cleanly on a single wire of a 3/8 in. diameter, 7-wire post-tensioning strand. The strain gages were mounted on the strands after the multistrand tendon had been pulled through the duct, and before the tendons were stressed. At a particular location, strain gages were attached to two randomly selected, accessible wires from different strands of a particular multistrand tendon. Strain gages were not necessarily attached to the same wire (or strand) along the length of the tendon.

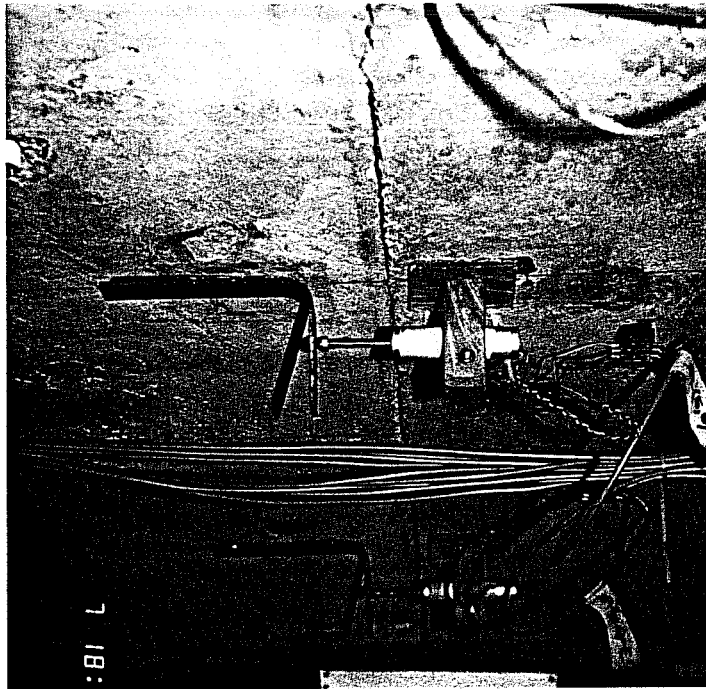
3.9 Joint-Opening Measurement

Distortions along the height of segment joints were measured during load tests. Critical joints were determined for each test-load case using both an elastic analysis and a plastic mechanism analysis, as described in Chapter 5. The critical joints for center-span tests, shown in Fig. 3.3a, include three joints in the midspan region and two joints in the support regions. The critical joints for the north exterior-span tests, shown in Fig. 3.3b, include four midspan joints and one joint near the support. The critical joint in the support region is on the interior side of the north interior pier-segment, as discussed in Section 5.2. The critical joints for south exterior-span tests appear as the mirror image to the north span.

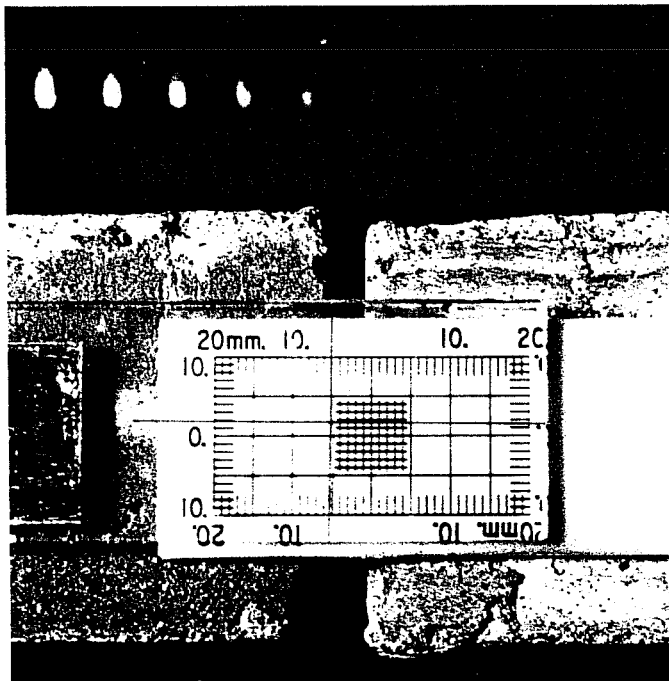
Two types of instrumentation were used to measure the behavior of joint regions at higher load levels. Linear voltage displacement transducers were mounted on the flange of the tension side of critical joints using a plexiglass bracket. The bracket, shown in Fig. 3.5a, was epoxied to the concrete segment, and held the potentiometer parallel to the concrete surface. The potentiometer extended across the joint to a light-gauge steel angle epoxied to the adjacent segment.

To measure distortions at various depths of the joint, a grid-type crack monitor was used. This device, shown in Fig. 3.5b, consists of overlapping planes of plexiglass, each with a matching grid. Relative displacement of the centers of matching grids reflected the amount of joint opening at the level of the crack monitor. Close-up views were obtained by sighting through a telescopic instrument. Very small movements could be recorded by averaging the relative movements of the grids at the extreme edges of the crack monitor. Approximate joint rotations were also calculated from the relative grid movements.

The crack monitors were attached at several locations along each joint. For bottom-opening joints, crack monitors were provided at the top and bottom of the vertical portion of a web as well as on the end of the bottom flange, as shown in Fig. 3.6a. The locations of each of the crack monitors and bottom-flange potentiometers for critical joints are tabulated in Fig. 3.6a. For top-opening joints the inclined tendons did not allow access to the web regions, so a single crack monitor was used on an end of the top flange, as shown in Fig 3.6b.

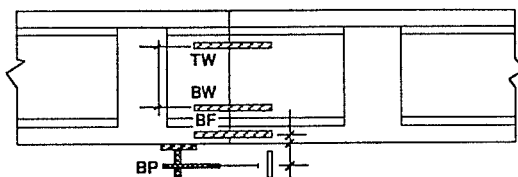


a. Joint Opening Potentiometers



b. Crack Monitor

Figure 3.5 Joint Opening Instrumentation

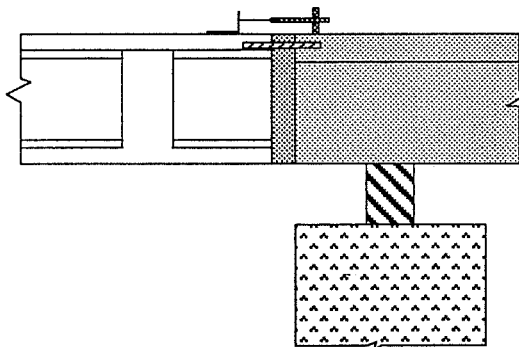


Distance
from Top (inches) *

LOCATION	JOINT				
	(3,4)	(4,5)	(5,6)	(25,26)	(26,27)
Top Web	6.95	7.00	7.05	7.11	7.12
Bottom of Web	11.01	11.06	11.11	11.17	11.18
Bottom of Flange	15.12	15.18	15.19	15.10	15.15
Bottom Potentiometer	17.65	17.71	17.72	17.63	17.68

*Calculated from measured segment dimensions

a. Bottom Opening Joints



b. Top Opening Joints

Figure 3.6 Joint Opening Instrumentation

CHAPTER 4

BEHAVIOR OF STRUCTURE DURING CONSTRUCTION

The model structure was instrumented during construction, and measurements were taken during the erection process. This construction data provided vital erection control information and a history of behavior of the structure for determination of the final in-situ condition. The construction data also provided important practical information regarding construction of segmental structures of this type.

This chapter summarizes observations made during the construction process. Tendon stresses were determined from strand strain measurements, and observations were made regarding friction losses. Model deflections were monitored throughout erection, and observations were made concerning the interaction of the shoring system with the bearings. Finally, web reactions were measured at the end of construction, and the unequal web reactions are discussed.

4.1 Stressing Observations

The tendons were stressed using the methods and equipment described in Chapter 2. The tendon designation, eg. Tendon 1a, refers to a pair of multi-strand tendons located symmetrically on each side of the structure. The two tendons were stressed simultaneously so that lateral bending stresses would not be excessive. Stress was applied slowly to the tendons while constantly advancing the wedge anchors. The tendons were stressed to a jacking force, P_j , of approximately 75 to 80 percent of the nominal tendon capacity. Data was recorded at the following ram force increments: 0, $0.1*P_j$, $0.25*P_j$, $0.40*P_j$, $0.60*P_j$, $0.80*P_j$, and P_j . Ram travel was also measured at each of these load stages.

In spite of the careful stressing procedures and the use of strain gages on some strands, two problems exist that make the estimation of average tendon stress difficult. The first problem was investigated by Yates (29), who found that in a stressed 7-wire prestressing strand the individual wires have appreciably different stresses. In Fig. 4.1, nominal strand stress is plotted against measured strain in the 6 exterior wires of a 7-wire strand. Initially, as the strand gripping system engaged wires of the strand, each wire picked up load at a slightly different rate. Once all

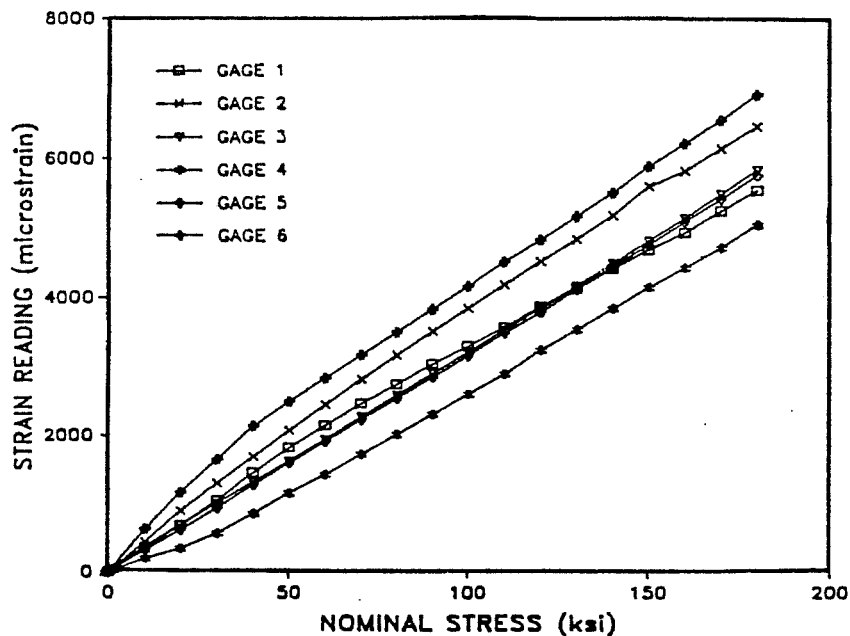


Figure 4.1 Strain Gage Calibration Results

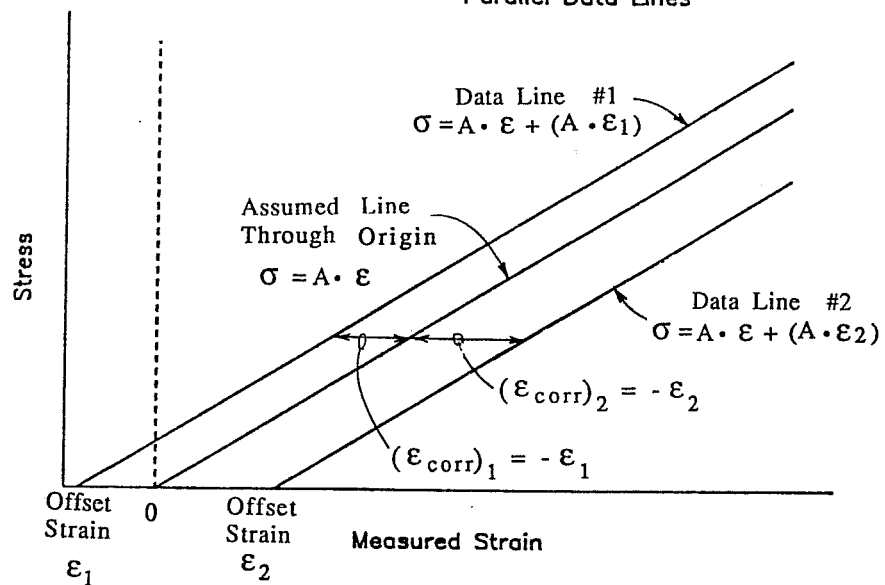
wires were fully anchored, all wires strained at an equal rate. The average of the six measured strains was linear and passed through the origin. However, results from a single gage could give a misleading value of tendon stress.

A second problem in estimating the average tendon stress is similar to the above, since each strand within a multistrand tendon could have slightly different stress. The temporary anchorage system of the stressing ram fully engages each strand at a slightly different force level. After all the strands are fully engaged, they should exhibit similar stress strain behavior, with the average of all the strands providing the average tendon stress that lies on a line passing through the origin.

The correction of both of these problems is achieved by applying a linear transformation to each data line. This process transforms each data line to a line passing through the origin, with each line having a slope equal to the average of all data-line slopes. Ideally all lines are parallel, so the linear transformation reverts to the addition of an offset, as shown in Fig. 4.2a. If the data lines are not exactly parallel, then the linear transformation also includes a slope correction, as shown in Fig. 4.2b.

NOMINAL TENDON STRESS vs MEASURED STRAIN

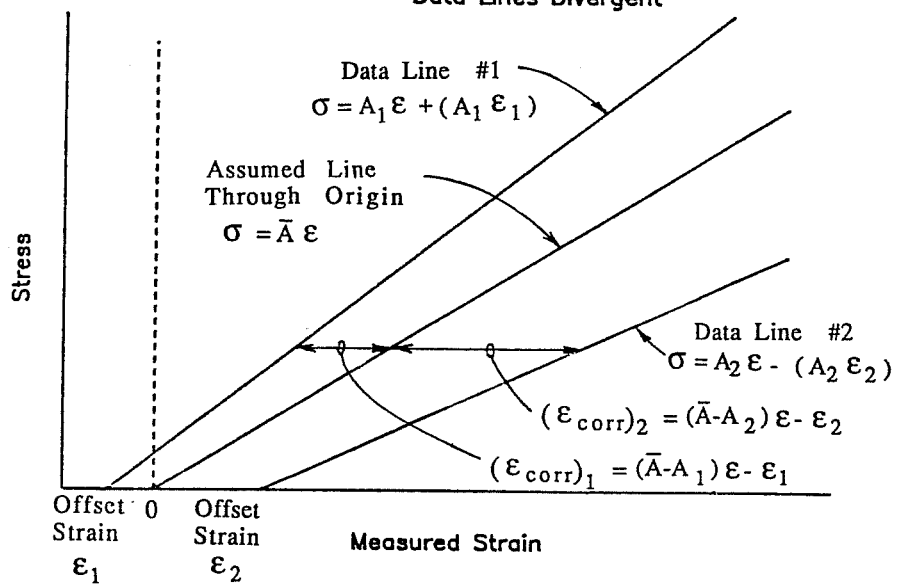
Parallel Data Lines



a) Case with Parallel Data Lines

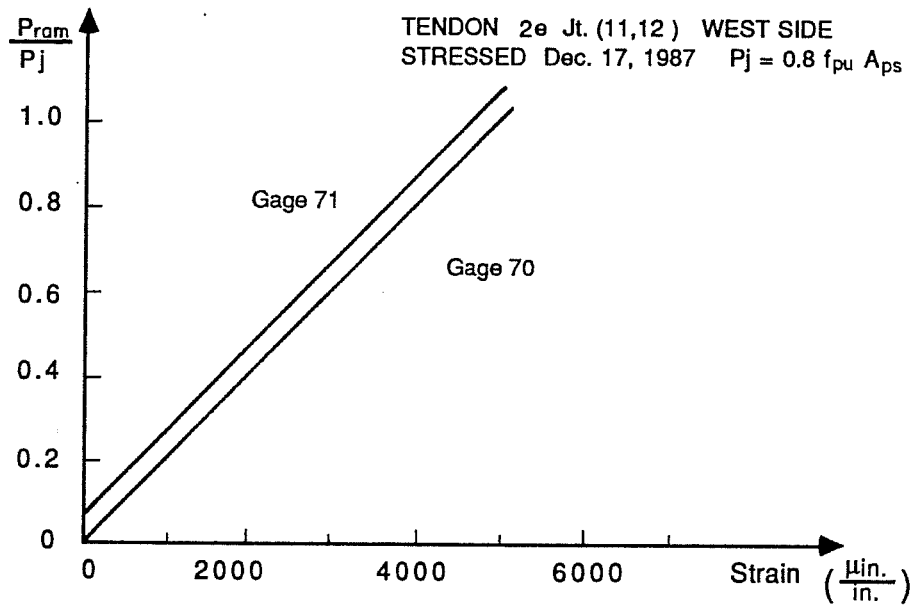
NOMINAL TENDON STRESS vs MEASURED STRAIN

Data Lines Divergent

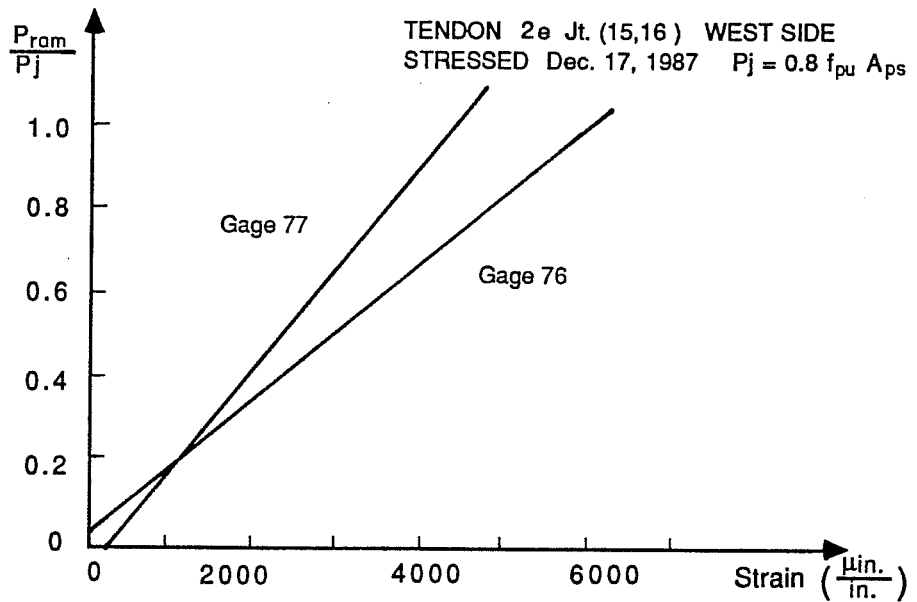


b) Case with Divergent Data Lines

Figure 4.2 Measured Tendon Stress Corrections



a. Typical Case with Approximately Parallel Data



b. Worst Case with Divergent Data

Figure 4.3 Measured Data Corrections

The method used to estimate the average tendon stress from the measured strand strains follows this general procedure. A comparison was made between the jacking force at the live end of the tendon and the measured strains from two gages attached to wires in a tendon at a particular location. In most cases, this yielded two approximately parallel lines, as shown in Fig. 4.3a, with the lines offset from the origin by some initial strain. The corrected average tendon strain was assumed to lie on a line passing through the origin and having a slope equal to the average slope of the two data lines. A linear transformation algorithm was then developed to transform each data line to the assumed average line. The average tendon stress was then calculated using the apparent elastic modulus of 30,300 ksi determined during calibration and described in Chapter 2.

In a few cases the two data lines were divergent. The worst case is shown in Fig. 4.3b. It is unknown why this happened, but may have partially been caused by incorrect application of the gages to the strands. The average tendon stresses for these strands were calculated using the same procedure as above.

Tendon elongations were measured during stressing by recording the travel of the prestressing ram. The measured elongations ranged from 95 to 108 percent of the calculated elongations (using an apparent elastic modulus of 27500 ksi).

Typical tendon stress profiles (here during stressing of Tendons 4a and 1a) are shown in Fig. 4.4. Similar plots for the remainder of the tendons are contained in Appendix B. In these plots the tendon stress is plotted at locations along the span. The solid lines represent the theoretical tendon stresses for a jacking load, P_j , at the live end. These lines were determined from the tendon angle changes, α , and an angular friction coefficient, μ , using the exponential reduction equation in the AASHTO Bridge Specification (18). The upper and lower lines represent the calculated tendon stresses with angular friction coefficients of 0.20 and 0.40, respectively. Because the majority of the tendons are external to the concrete, wobble effects were assumed as zero during calculation of frictional losses.

The measured tendon stresses are also plotted for jacking forces of $0.40 \cdot P_j$, $0.80 \cdot P_j$, P_j , and after releasing the tendon. Several observations can be made from the tendon stress profiles. First, there appears to be a reduction in stress at the live end of the tendons. In all but one case the measured stress closest to the live

end was lower than calculated considering friction. This reduction could be caused by a number of factors including high friction in the pier-segment ducting, friction at the tendon-duct/anchorage transition, or friction between strands and wedges, or strand and the anchor-head at the live-end anchor. These problems were possibly aggravated by model details, but similar reductions were also noticed by Quade (30) using standard industry hardware. Research is needed to quantify friction losses within standard industry anchorage hardware as well as at locations of high duct curvature.

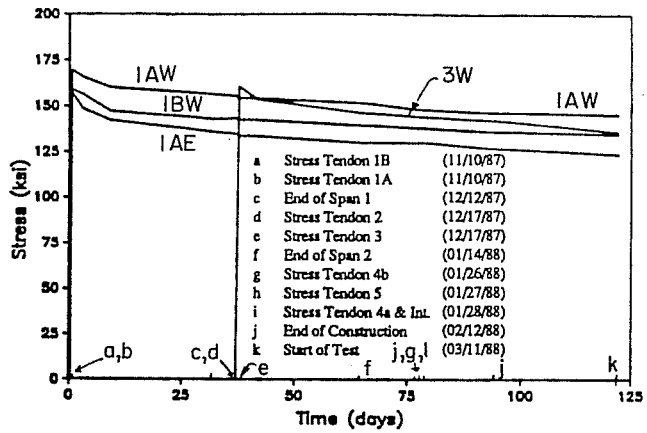
A second observation that can be made from the tendon stress profiles is the apparently low friction between the tendons and deviators. In most cases, after the initial loss at the live-end anchorage, tendons exhibited small losses along the remainder of the span. The angular friction losses through the deviators in most cases were less than predicted using $\mu = 0.20$. Additional research is needed to quantify friction losses through concentrated angle changes at deviators.

Tendon 1a was stressed by simultaneously pressurizing two rams with one pump. After the tendons were stressed to their full jacking force, the load was held while the anchor wedges were hydraulically seated. This process took almost an hour, during which time the stress in the west-side tendon, shown in Fig. 4.4, reduced to approximately 93 percent of the original stress. Even though the hydraulic line pressure was maintained, the ram force did not remain constant. The reason for this drop in stress is unknown, but may likely be attributed to the interaction of hydraulically-linked rams and the friction in the individual rams. All subsequent tendons were stressed using an independent system for stressing each of the two multistrand tendons.

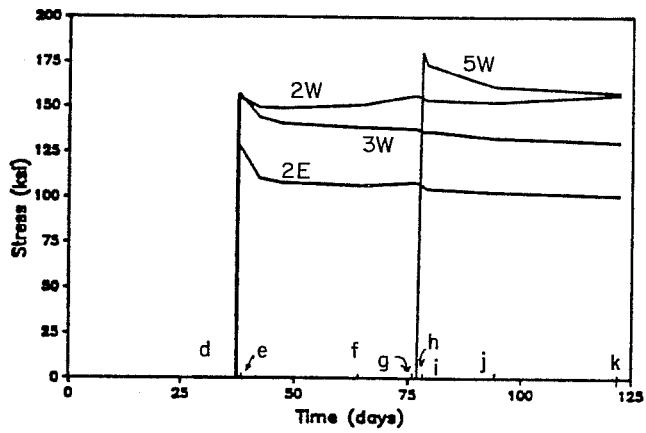
4.2 Tendon Stress History

The measured tendon stresses at the center joint of each span during the three stages of construction are shown in Fig. 4.5. The time scale was chosen to correspond with the construction time of 122 days between stressing the first tendon, Tendon 1b on November 10, 1987, and starting the load tests, on March 11, 1988. Key times during the erection process are shown on the time scale and are described

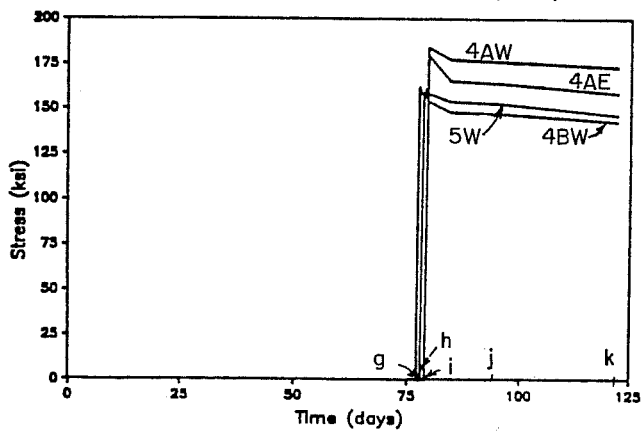
TENDON STRESS vs TIME



a) North Span Tendons at Joint (5,6)



b) Center Span Tendons at Joint (15,16)



c) South Span Tendons at Joint (25,26)

Figure 4.5 Tendon Stress History

in the figure notes. The measured prestress losses at 3 days, 7 days, 28 days, and before initiation of testing are shown in Table 4.1 for all tendons.

Measured prestress losses for the north and center spans were approximately the same at 28 days. Because of erratic data in center span tendon 2W at the time testing began, averages could not be compared. Losses in the south span were typically smaller than in the other two spans. This difference may have been caused by reduced creep in the concrete of the south span. Also, a different concrete supplier was used for the segments in the south span.

4.3 Deflections

The deflections of the model structure were monitored during all stages of construction with the instrumentation described in Section 3.7. The measured deflections, at key times during construction, are shown in Fig. 4.6. The deflections are plotted for each structural configuration with the initial deflections in each case equal to zero. The deflections that are shown are therefore the deflections occurring during the particular structural configuration. The final deflections from each of the three construction stages were then superimposed. The deflected shape of the completed structure is shown in Fig. 4.7. Time dependent deflections continued to occur while testing procedures were being finalized. The final pretest deflected shape is also shown in Fig. 4.7. The results from an elastic analysis are also shown for each stage of construction and for the final pre-test condition.

In each stage of construction the elastic analysis underestimated the camber caused by stressing the external tendons. This may indicate that tendon stresses were actually higher than the corrected stresses used for the analysis, (see Section 5.4).

Before stressing the tendons, the unstressed span is supported uniformly along the entire span length. As the tendons are stressed, the center regions are first lifted off the shoring. With unyielding supports, the structure eventually lifts off the shoring and spans between the supports. With relatively flexible supports, as with neoprene bearing pads, the structure remains in contact with the stiff shoring close to the flexible support. This phenomenon was evident in all the spans erected. In the north span, the north end was supported on the flexible bearing assembly

Table 4.1 Summary of Tendon-Stress Losses

Location	Tendon	Stress at Release (ksi)	3 Days Loss (ksi)	% fsi	7 Days Loss (ksi)	Losses % fsi	28 Days Loss (ksi)	% fsi	Start Test Loss (ksi)	% fsi	Age (days)
North Span Joint (5,6)	1aW	169.63	4.03	2.38	7.68	4.53	13.01	7.67	24.29	14.32	122
	1aE	157.17	8.95	5.69	13.11	8.34	20.72	13.18	33.39	21.24	122
	1bW	164.75	8.72	5.29	14.77	8.97	21.69	13.17	29.99	18.20	122
	3W	160.36	5.34	3.33	8.08	5.04	14.64	9.13	24.54	15.30	85
	AVG.			4.17		6.74		10.79		17.27	
Center Span Joint (15,16)	2W	156.27	4.78	3.06	7.46	4.77	5.23	3.35	*	*	85
	2E	130.85	12.64	9.66	21.70	16.58	24.72	18.89	30.07	22.98	85
	3W	156.84	7.32	4.67	14.54	9.27	18.73	11.94	26.60	16.96	85
	5W	179.98	8.35	4.64	19.10	10.61	20.53	11.41	22.43	12.46	44
	AVG.			5.51		10.31		11.40		*	*
South Span Joint (25, 26)	4aW	184.06	4.00	2.17	6.91	3.75	7.11	3.86	6.24	3.39	43
	4aE	179.79	8.00	4.45	14.63	8.14	18.52	10.30	21.71	12.08	43
	4bW	162.21	6.94	4.28	14.27	8.80	17.24	10.65	20.20	12.45	45
	5W	158.26	.05	.03	4.58	2.89	8.67	5.48	12.61	7.97	44
	AVG.			2.73		5.90		7.57		8.97	

*Obviously flawed data omitted

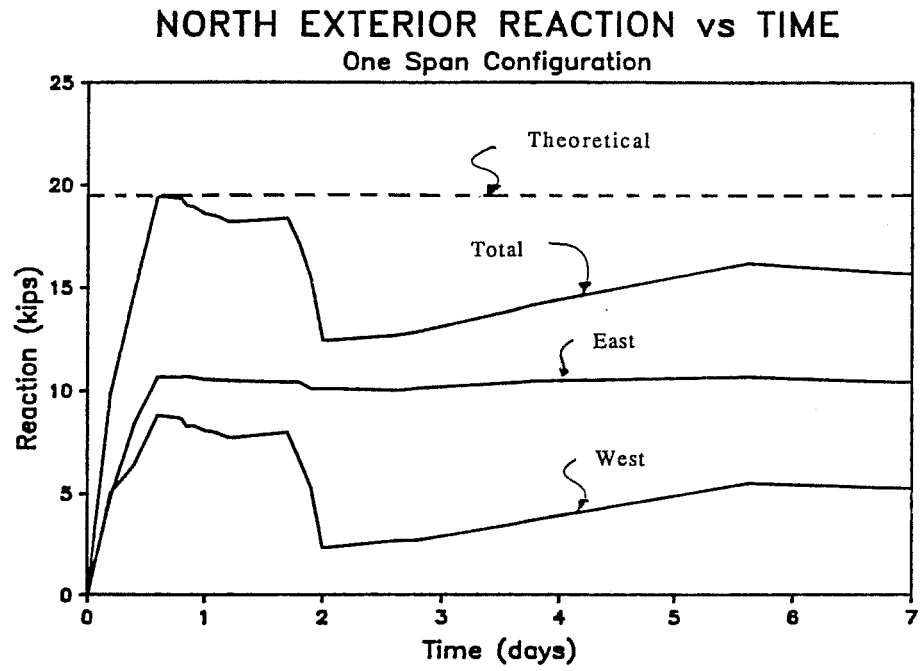


Figure 4.8 Measurement of North Exterior Reactions

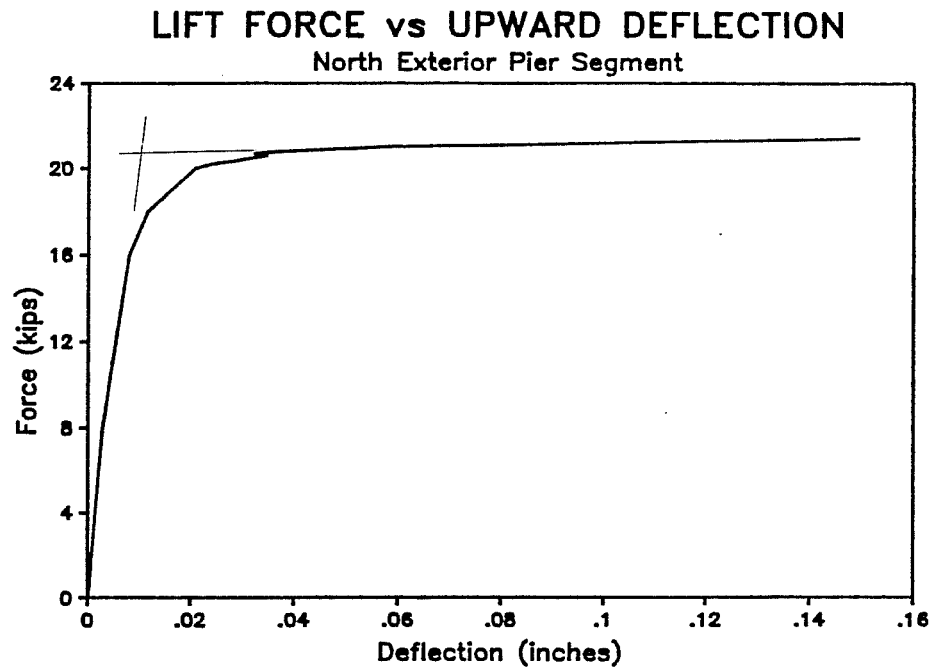


Figure 4.9 Lift-Off Force Determination

The drift in the load cell measurements occurred under sustained loads with small deviations occurring in the first day. It was therefore believed that short-term changes in reactions during testing could be adequately measured with the load-cells.

As was discussed in Chapter 2, the measured reactions were modified by hydraulically lifting the pier segments and inserting shims at supports during construction. This was done to equalize reactions under each web at a particular support as well as to equalize the total reactions at the two ends of the structure. Starting at the North Exterior support and proceeding southward, each of the measured reactions were set. Because of the long-term drift in the load cells, each reaction was initialized by lifting the structure from the bearing, taking a zero reading for each of the load cells, and then setting the structure back onto the bearing. This provided an initial reading of the as-constructed condition.

Determination of the force at which the structure lifted from the bearings provided an additional calibration for the measured reactions at the two exterior supports. At the exterior supports the lift-off force was easily determined. As the lifting force is applied to the underside of the pier segment, the reaction force shifts from the bearings to the hydraulic system. Upward movement during this stage is limited to the compressive deformation of the bearing assembly under the reaction force. When the reactive force is finally exceeded, the response changes dramatically. The additional lifting forces are then acting on the end of a long cantilever with a length equal to one span. The structure becomes very flexible, with small changes in lift-force causing relatively large upward movements at the pier segment. The dramatic change in load response is clearly seen in Fig. 4.9 for lift-off at the north exterior support.

The lift-off force at an interior support is not as easily determined. Once the reactive force is exceeded, then the lifting force is resisted by the structure spanning in both directions. This continuous system is considerably stiffer than the cantilever. Therefore an exact determination of the lift-off force was not determined for the interior pier.

The lift-off forces and measured total reactions (after setting the structure down) are tabulated in Table 4.2 for the two exterior supports. At the north exterior

The lift-off forces and measured total reactions (after setting the structure down) are tabulated in Table 4.2 for the two exterior supports. At the north exterior support the lift-off force was measured to be approximately 5 percent more than the measured reactions in the load cells. At the south exterior support the lift-off force was measured to be approximately 80 percent of the reactions measured by the load cells. Since the lift-off force was measured precisely with rams calibrated immediately before the procedure, this force was believed to be accurate. Reactions at the north and south exterior piers were therefore corrected by the factors of 1.05 and 0.80 respectively.

Table 4.2 Exterior Reaction Corrections

Location	Lift-off Force	Load-Cell Measurement	Correction	Corrected Reaction
North Exterior	20.40	19.40	1.05	20.40
South Exterior	22.40	28.03	.80	22.40

$$(N.E.)_{corrected} = 1.05 * [(N.E.) \text{ load cell }]$$

$$(S.E.)_{corrected} = 0.80 * [(S.E.) \text{ load cell }]$$

This correction was subsequently checked for symmetrical load cases and found to give accurate results. The cause of this discrepancy is not known.

The corrected web reactions at the north exterior and south interior piers during the adjustment process are shown in Figs. 4.10 and 4.11, respectively. The reactions in each of the webs at the north exterior pier after initializing the load cells are shown in Fig 4.10a, with the east side carrying 55 percent of the total reaction. The structure was then lifted and a 0.008 inch thick shim was placed under the west side. This caused the west side reaction to increase excessively, as shown in Fig. 4.10b. The pier segment was lifted again, and a 0.004 inch shim was placed under the west web. This provided approximately equal reactions under each of the webs, as shown in Fig. 4.10c. The reactions under each of the webs at the south interior

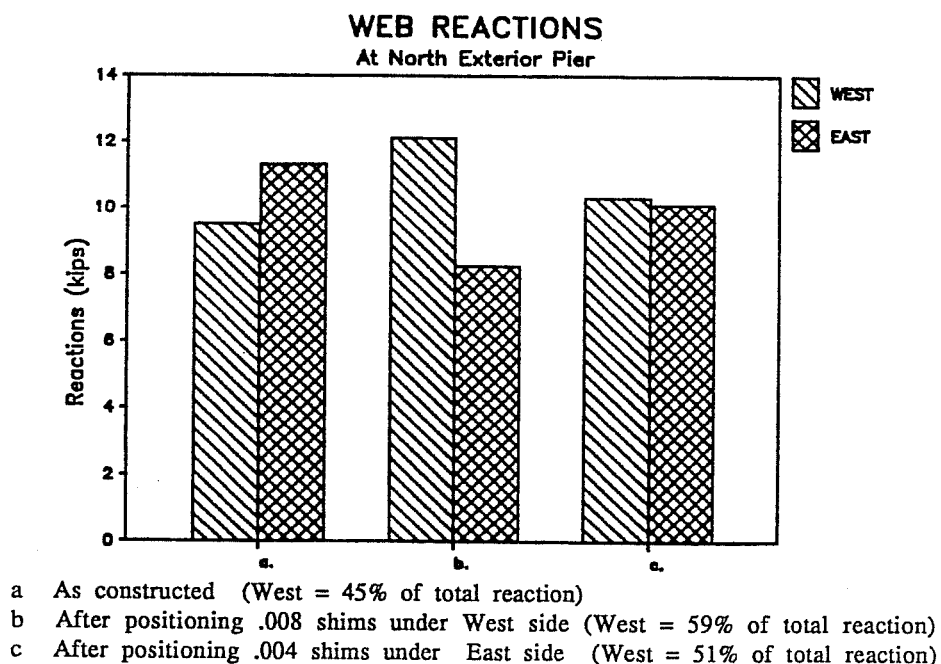


Figure 4.10 Equalization of North Exterior Reactions

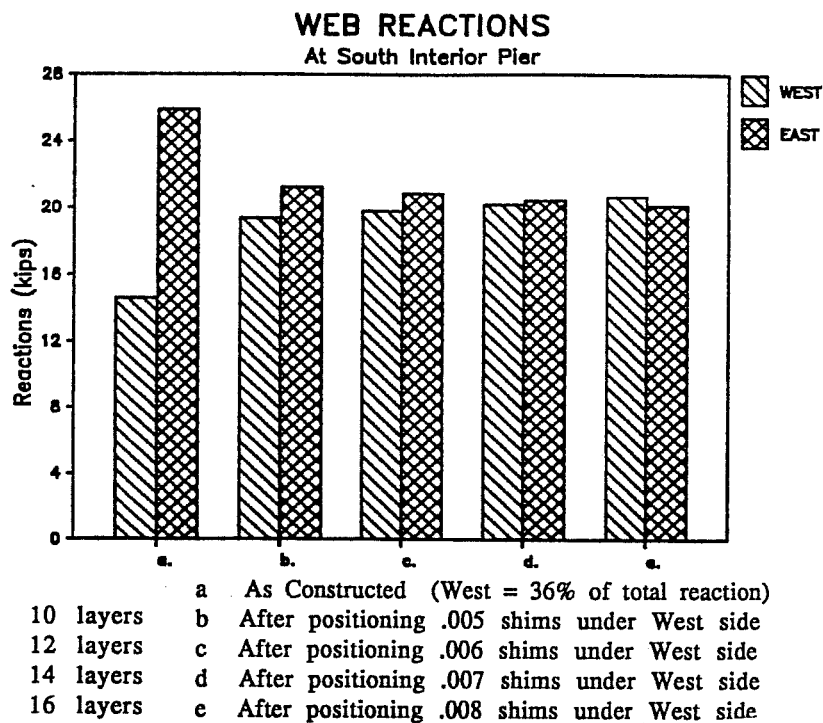


Figure 4.11 Equalization of South Interior Reactions

pier, after initialization, are shown in Fig. 4.11a. The web reactions after positioning various thicknesses of shims are shown in Figs. 4.11b-e.

Figs. 4.10 and 4.11 illustrate the importance of providing the ability to equalize the web reactions after erection. In the constructed condition, the web reactions were not necessarily equal, and in some cases were considerably different. If the web reactions at the south interior pier were left as they were constructed, the east web would carry approximately 25 percent more vertical shear than the usual design value of half the total vertical shear. Additionally, very thin shims were required to equalize the reactions under the webs, or conversely, very small deformations are necessary to unbalance the web reactions. Unequal web reactions can therefore be expected for construction of this type, and provisions should be made for equalizing reactions after erection.

4.5 Summary of Observations Made During Erection

Several important observations were made from the erection data. Higher-than-expected friction losses were measured at the live end of the post-tensioning tendons. Research is needed to quantify friction losses that occur using standard industry hardware and stressing equipment. Lower than expected friction losses were measured at the deviators. Research is also needed to determine the friction losses that occur through concentrated angle changes at deviators.

As the primary tendons are stressed, the structure lifts off the shoring at midspan regions first. If flexible supports are used, then the stressed structure will remain in contact with the shoring. This load path must be considered for design of the shoring system and segment reinforcement.

Finally, unequal web reactions can be expected in segmental systems erected on shoring. Provision should be made to equalize web reactions after erection.

CHAPTER 5

ANALYSIS OF ERECTION STRESSES

Several analysis methods were used during design, construction, and testing of the model structure. Preliminary sizing and serviceability checks were made using moment distribution techniques. After the geometry of the model was established, a plane frame elastic analysis was used to finalize design and to investigate the in-situ condition of the completed structure. The “in-situ” structure was also analyzed to estimate the limits of elastic behavior. A nonlinear finite element program was developed to estimate the full range of flexural behavior of the structure. Finally an upper-bound plastic mechanism analysis was conducted to design the testing apparatus and to predict the location of critical joint mechanisms.

5.1 Nonlinear Finite Element Analysis

In conjunction with this research project, a nonlinear finite element program was developed, by El Habr (10). The program uses several types of structural elements, material models, and an iterative solution technique to estimate the full range of flexural behavior of externally post-tensioned box-girders. The finite elements and solution technique were summarized in Chapter 1 and described in detail in Ref. 10.

5.2 Plastic Mechanism Analysis

An upper-bound plastic mechanism analysis was conducted to obtain forces for the design of the testing apparatus, and to predict which joints would open during testing. Several plastic mechanisms were considered for each test-load location. Hinge locations were assumed to occur at segment joints, and ultimate moment capacities were calculated at key joints along the structure. Two cases were considered to bound the solution. As an upper limit, the ultimate moment capacities were calculated assuming yield of the tendons, or for low relaxation strands

$$f_{ps} = f_{py} = 0.9f_{pu} = 243 \text{ ksi}$$

As a lower limit, the mechanism load was determined from the effective prestress, f_{se} , the specified concrete compressive strength, f'_c , and the unbonded post-tensioning reinforcement ratio, ρ_p , using the ACI formula for unbonded tendons (7)

$$f_{ps} = f_{se} + 10,000 + ((f'_c)/(100*\rho_p))$$

$$< f_{py}$$

$$< f_{se} + 60,000$$

to predict the stress in the tendons corresponding to nominal flexural strength. This second solution used the measured tendon stresses at the start of testing as the effective prestress force, f_{se} .

The critical mechanism loads for each test load, and for each ultimate tendon stress assumption, are summarized in Fig. 5.1. For testing the exterior spans, two mechanisms displayed approximately equal strengths. For testing the interior span, one mechanism was critical.

The mechanism analysis revealed important information regarding the behavior of the structure near ultimate loads. Because mechanisms gave almost equal strengths for testing of the exterior spans, “complex” mechanisms with several joints opening, as shown in Fig. 5.2, could be expected in the dry-jointed span. The mechanism analysis also revealed the location of the critical joints in the support regions. For loading in the exterior spans, the negative-moment hinge was found to occur at the interior face of the first interior pier segment, as shown in Fig 5.1. This occurred because the interior span had reduced flexural requirements and therefore less tendon area.

5.3 Plane Frame Analysis

A plane frame elastic analysis, PFT, was used during all stages of design, construction, and testing to predict the elastic behavior of the structure. Dead loads, equivalent prestress forces, and construction live loads were considered for each structural configuration during construction. The completed structure was further analyzed to reflect measured dead loads, concrete properties, support stiffness, and external tendon forces. Design live-load cases were checked for conformance with

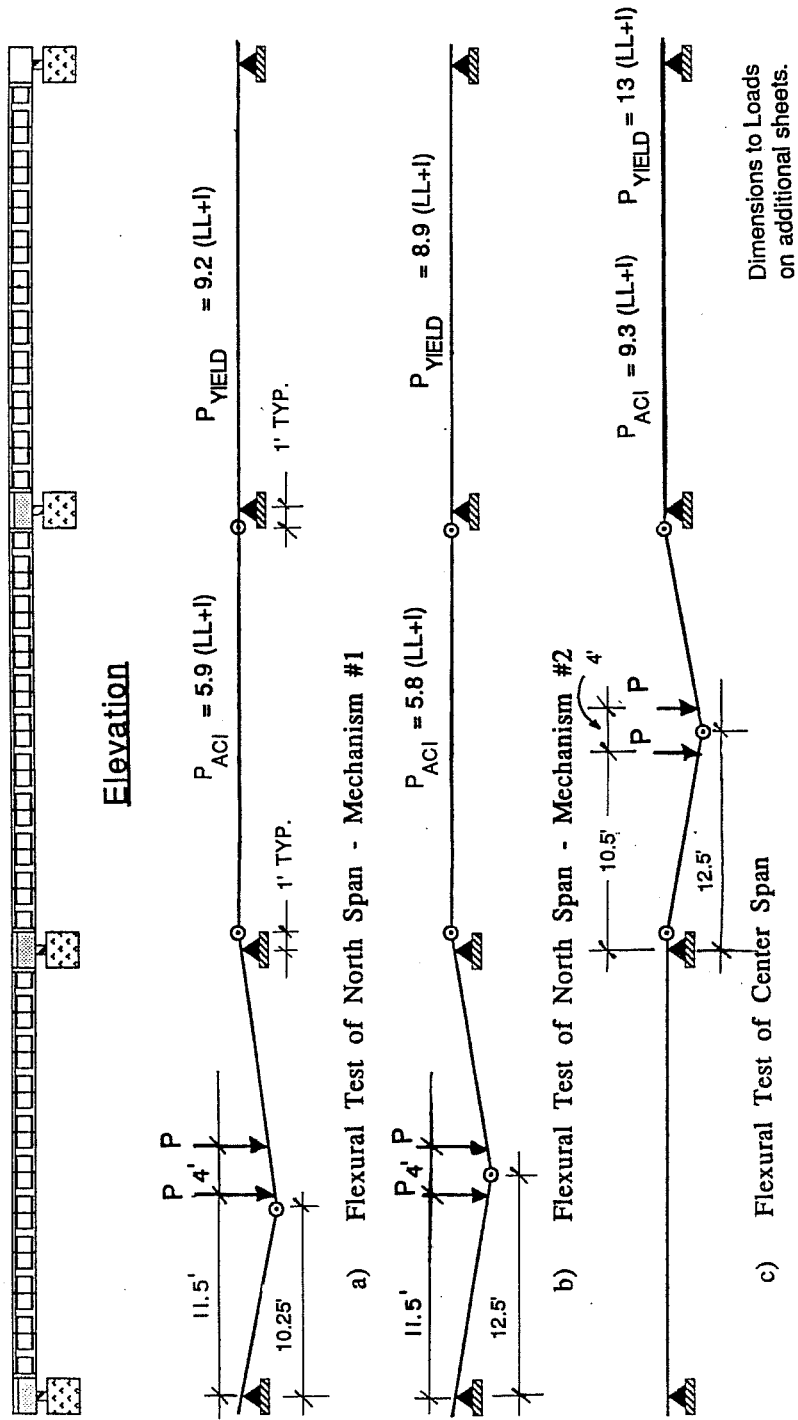


Fig. 5.1 Plastic Mechanism Analysis

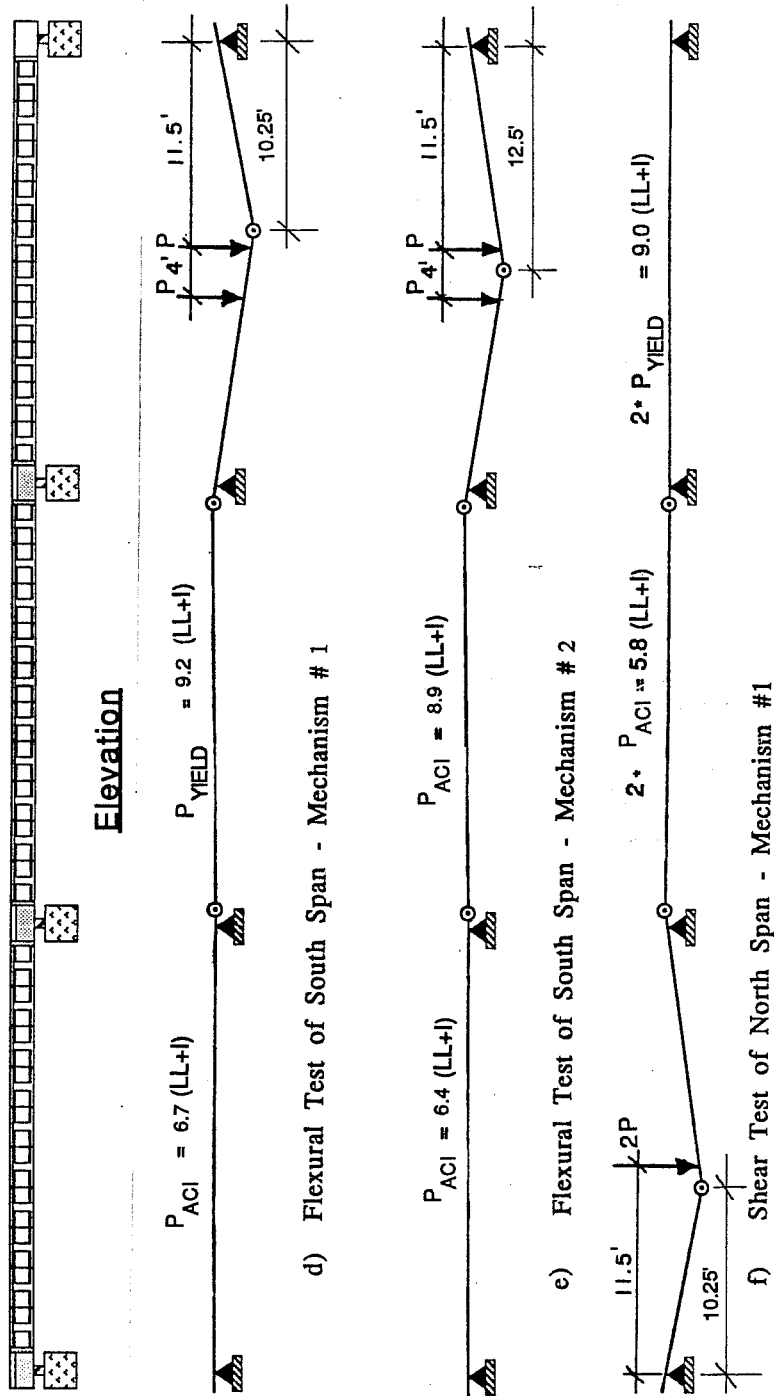


Fig. 5.1 (con't) Plastic Mechanism Analysis

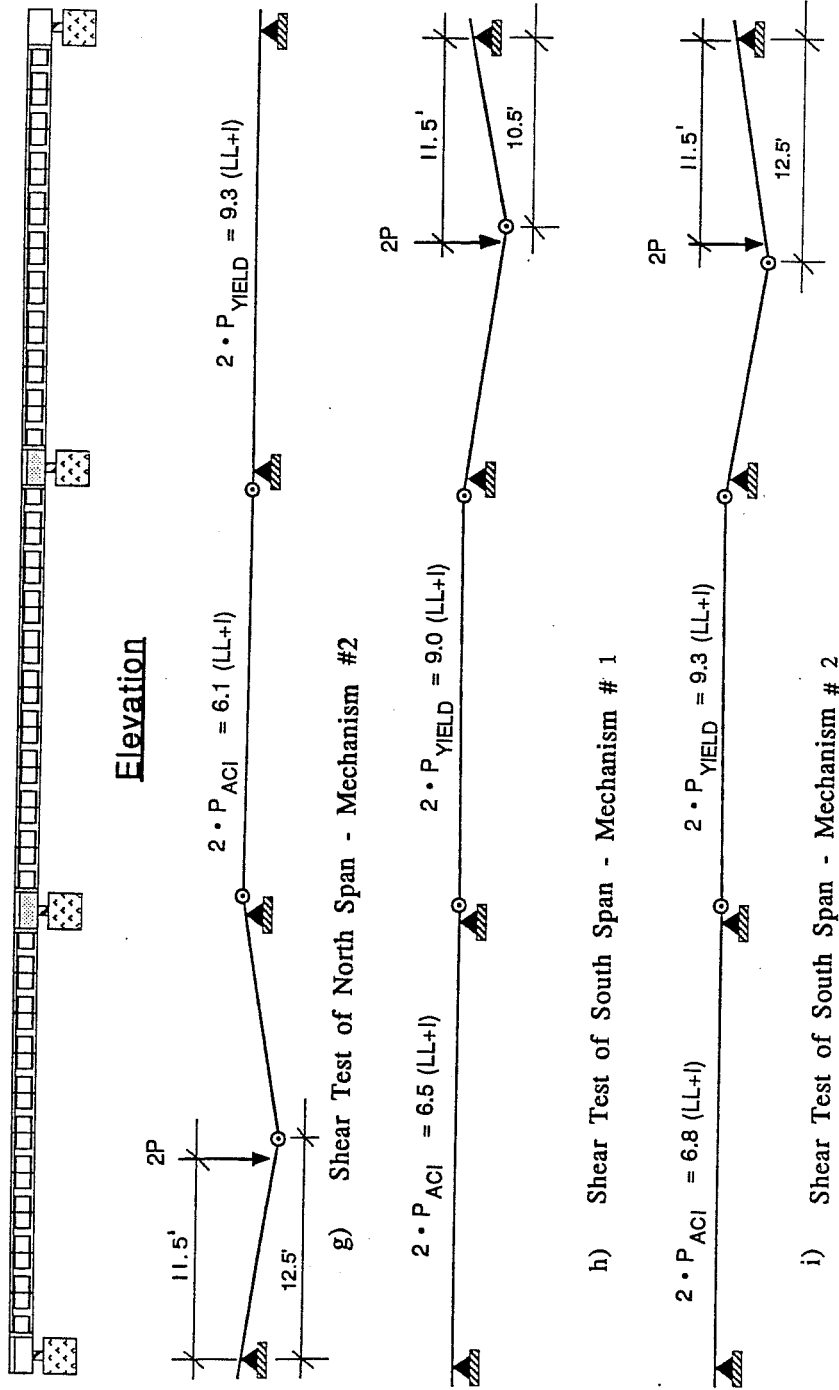


Fig. 5.1 (cont) Plastic Mechanism Analysis

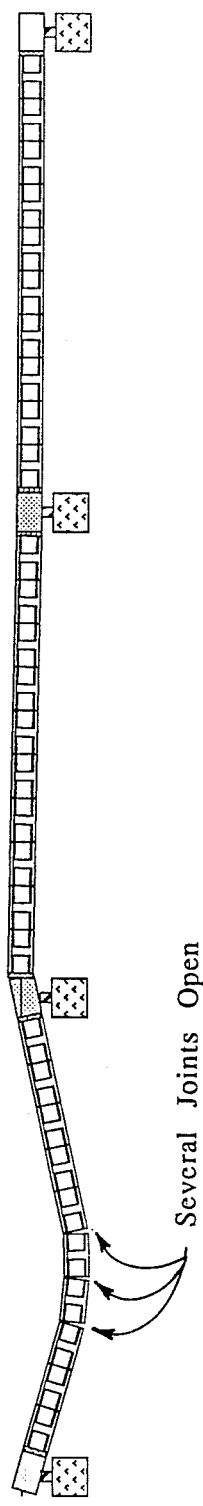


Fig. 5.2 Possible Complex Mechanism in Dry Jointed Span

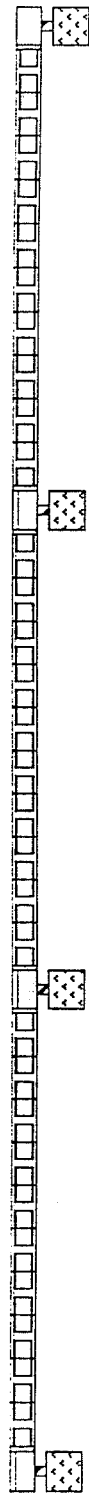
design serviceability limits. Finally, test load cases were analyzed for comparison with measured behavior.

An elevation of the completed three-span structure is shown in Figure 5.3a. The analytical models used for the three phases of construction are shown in Figures 5.3b-d. The analytical models consist of a linear “frame” with nodes located at every segment joint. The members are continuous through the nodes to form a long continuous beam. An additional node was also provided at the center of each “pier-segment” to correspond with the bearing location. For simplicity the closure strip width (3 in.) was added to the adjacent span-segment at each location. To model the flexible bearing assemblies, additional nodes and members were added at each measured reaction location.

The properties of the members were determined from the measured properties of the model structure. The cross-sectional properties of the span and pier-segments were calculated from a transformed section analysis which included the longitudinal reinforcement and measured dimensions. The concrete modulus was measured for representative cylinders from each type of concrete and an elastic modulus was determined for each segment. The products of the measured modulus and the moment of inertia for each segment, determined from measured section dimensions, were then grouped into five sets for span-segments and two sets for pier-segments. An average value of $E_c I_c$ was then determined for each group of segments. The product of E_c and I_c used for each segment in the analysis is tabulated in Table 5.1.

The flexibility of the load-cell bearing assemblies was modeled with short, axially stiff members. The cross-sectional area of these members was determined from the axial stiffness of the load-cells as measured during calibration. These members were assigned a low moment of inertia so that longitudinal restraint was not added to the model structure. The “load-cell” members also had a hinge at the structure/load-cell interface, so that rotational restraint would not be added to the superstructure.

Several types of loadings were applied to the analytical model. Dead loads consisting of segment self weight, dead load compensating weight, and factored dead loads were applied as uniformly distributed loads on each member. Construction



a) Elevation of Completed Structure



b) One Span Configuration



c) Two Span Configuration



d) Three Span Configuration

Figure 5.3 Plane Frame Elastic Analysis Models

Table 5.1 Member Properties for Elastic Analysis

Model Segment No.	P.F.T. Member No.	i Mode	j Mode	Length (ft)	Area (in ²)	$\frac{E_c I_c (meas)}{10^6}$ (k-in ²)	Type	Comment:
N.E.	1	1	2	1.00	894	137.8	Pier Segment	
N.E.	2	2	3	1.00	894	137.8	Pier Segment	
1	3	3	4	2.50	450	65.76	Span Segment	Include Pour Strip
2	4	4	5	2.25	450	60.78	Span Segment	
3	5	5	6	2.25	450	60.78	Span Segment	
4	6	6	7	2.25	450	65.76	Span Segment	
5	7	7	8	2.25	450	70.48	Span Segment	
6	8	8	9	2.25	450	65.76	Span Segment	
7	9	9	10	2.25	450	60.78	Span Segment	
8	10	10	11	2.25	450	60.78	Span Segment	
9	11	11	12	2.25	450	60.78	Span Segment	
10	12	12	13	2.50	450	65.76	Span Segment	Includes Pour Strip
N.I.	13	13	14	1.00	894	119.0	Pier Segment	
N.I.	14	14	15	1.00	894	119.0	Pier Segment	
11	15	15	16	2.50	450	70.48	Span Segment	Includes Pour Strip
12	16	16	17	2.25	450	65.76	Span Segment	
13	17	17	18	2.25	450	65.76	Span Segment	
14	18	18	19	2.25	450	70.48	Span Segment	
15	19	19	20	2.25	450	70.48	Span Segment	
16	20	20	21	2.25	450	70.48	Span Segment	
17	21	21	22	2.25	450	65.76	Span Segment	
18	22	22	23	2.25	450	65.76	Span Segment	
19	23	23	24	2.25	450	70.48	Span Segment	
20	24	24	25	2.50	450	70.48	Span Segment	Includes Pour Strip
S.I.	25	25	26	1.00	894	137.8	Pier Segment	
S.I.	26	26	27	1.00	894	137.8	Pier Segment	
21	27	27	28	2.50	450	75.44	Span Segment	Includes Pour Strip
22	28	28	29	2.25	450	75.44	Span Segment	
23	29	29	30	2.25	450	75.44	Span Segment	
24	30	30	31	2.25	450	75.44	Span Segment	
25	31	31	32	2.25	450	75.44	Span Segment	
26	32	32	33	2.25	450	75.44	Span Segment	
27	33	33	34	2.25	450	75.44	Span Segment	
28	34	34	35	2.25	450	75.44	Span Segment	
29	35	35	36	2.25	450	75.44	Span Segment	
30	36	36	37	2.50	450	81.71	Span Segment	Includes Pour Strip
S.E.	37	37	38	1.00	894	137.8	Pier Segment	
S.E.	38	38	39	1.00	894	137.8	Pier Segment	
N.E.B.	39	2	40	.83	20510	1.0	Bearing	2 - 100 kip load cells
S.I.B.	40	26	41	.83	34920	1.0	Bearing	2 - 200 kip load cells
S.E.B.	41	38	42	.83	30510	1.0	Bearing	2 - 100 kip load cells

on members. The post-tensioning forces were applied to members and nodes as a series of vertical and horizontal forces, and concentrated moments.

The model structure was erected in a sequential span-by-span manner. The internal forces and curvatures that exist after erecting a span are additive to the forces and curvatures induced by erecting subsequent spans. To properly predict the in-situ condition of the structure it is necessary to analyze each structural configuration of the evolving structure. Dead loads, equivalent prestress forces, and construction or service live loads were applied to each intermediate structure. The resultant internal forces and deflections from a particular configuration were then superposed with subsequent configurations using a spread sheet.

Several types of dead loads existed during construction and testing of the model structure, and are tabulated in Table 5.2. Self weight of the segments was calculated from the measured segment dimensions. The weight of the cast-in-place closure strip was calculated from its measured dimensions and added to the weight of the adjacent span segment. The dead load compensating blocks comprised a large portion of the total dead load (approximately 75 percent), so each dead load block was weighed prior to erection. The weights ranged from 360 to 396 pounds. Finally, additional dead weight was placed on the structure for application of the factored dead load during testing.

The effect of the post-tensioning was applied to the analytic model by calculating an equivalent prestress force for each tendon and applying this force to the appropriate structural configuration. The equivalent prestress forces were calculated from the measured tendon strains and theoretical tendon geometries. Vertical, lateral, and longitudinal forces, and moments were calculated for each tendon deviation point and anchorage location. To simplify the analysis, and to ensure that vertical, longitudinal, and rotational equilibrium were maintained, all tendon deviations were assumed to occur at a point.

For each structural configuration, two types of equivalent prestress forces were applied. The equivalent prestress forces for tendons stressed during a particular structural configuration were calculated from the measured stresses at the completion of that configuration. In addition, the losses that occurred in tendons that were stressed during previous configurations were applied as the difference between the

Table 5.2 Dead Loads for Elastic Analysis

Model Segment No.	P.F.T. Member No.	Length (ft)	Calc. Segment Weight (lbs)	Pour Strip Weight (lbs)	Dead Load Comp. Weights (lbs)	Total Weight (lbs)	Uniform Distrib. Load (pH)
N.E.	1	1.00	1000			1000	1000
N.E.	2	1.00	1000			1000	1000
1	3	2.50	1055	153	3078	4286	1714
2	4	2.25	1054		2961	4015	1785
3	5	2.25	1037		3009	4046	1798
4	6	2.25	1057		3007	4064	1806
5	7	2.25	1021		3059	4080	1813
6	8	2.25	1040		3072	4112	1828
7	9	2.25	1050		3097	4147	1843
8	10	2.25	1037		3065	4102	1823
9	11	2.25	1054		3077	4131	1836
10	12	2.50	1056	153	2972	4181	1672
N.I.	13	1.00	1000			1000	1000
N.I.	14	1.00	1000			1000	1000
1	15	2.50	1022	153	2991	4166	1666
12	16	2.25	1039		3075	4114	1828
13	17	2.25	1035		3022	4057	1803
14	18	2.25	1041		3069	4110	1827
15	19	2.25	1054		2955	4009	1782
16	20	2.25	1045		3093	4138	1839
17	21	2.25	1046		3079	4125	1833
18	22	2.25	1041		3087	4128	1835
19	23	2.25	1048		3089	4137	1839
20	24	2.50	1036	153	3006	4195	1678
S.I.	25	1.00	1000			1000	1000
S.I.	26	1.00	1000			1000	1000
21	27	2.50	1057	153	3074	4284	1714
22	28	2.25	1046		3051	4097	1821
23	29	2.25	1051		3055	4106	1825
24	30	2.25	1061		3059	4120	1831
25	31	2.25	1033		3087	4120	1831
26	32	2.25	1037		3088	4125	1833
27	33	2.25	1043		3049	4092	1819
28	34	2.25	1035		3090	4125	1833
29	35	2.25	1043		3066	4109	1826
30	36	2.50	1025	153	3057	4235	1694
S.E.	37	1.00	1000			1000	1000
S.E.	38	1.00	1000			1000	1000

equivalent prestress forces calculated at the beginning of construction of the current configuration and end of construction of the previous configuration. These forces were applied to the current structure, and act in a direction opposite to the original equivalent prestress forces.

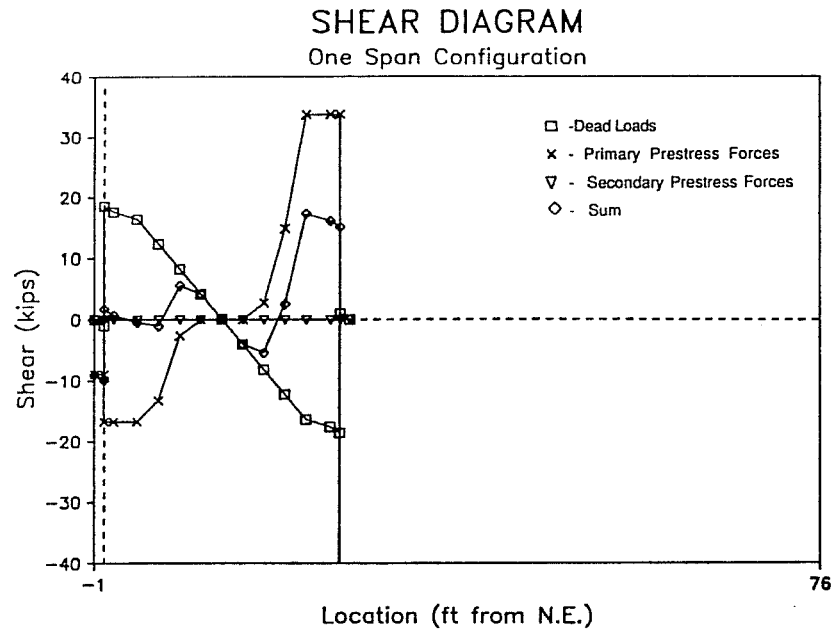
The top internal tendons were not instrumented, so in-situ stresses are not known. These tendons were stressed to a jacking force of $0.74 \cdot f_{pu}$, and the wedge anchors were seated with the internal seating device of the monostrand stressing ram. With approximately $3/8$ inch loss due to anchorage set averaged over 77 feet between anchors, the stress in the internal tendons was assumed to be approximately $0.70 \cdot f_{pu}$ (189 ksi) after seating. With approximately 10 percent time-dependant losses occurring between the end of construction and the start of the test, the effective prestress force in the internal tendons at the start of testing was assumed to be $.63 \cdot f_{pu}$ (170 ksi).

5.4 Estimate of Conditions in the Structure Before Testing

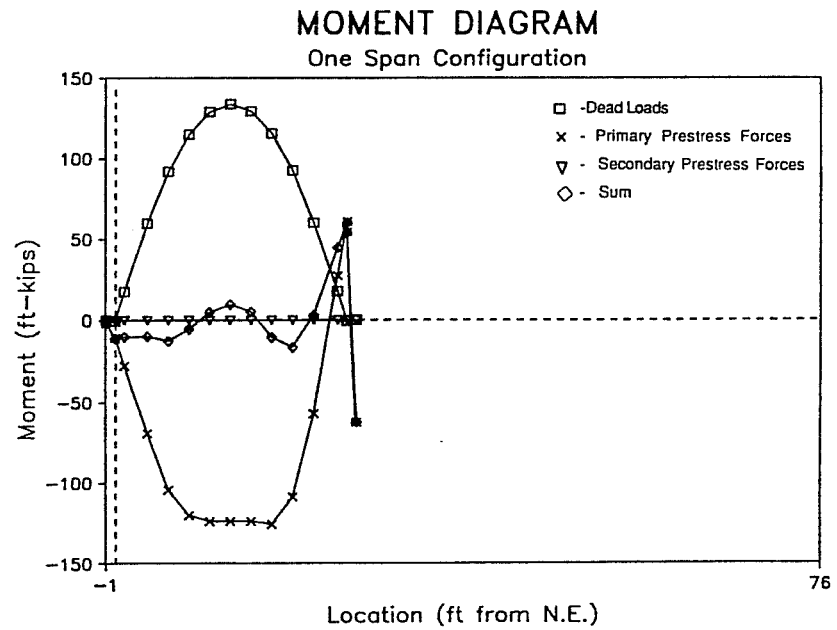
The structure was analyzed using the plane frame model and loading conditions described above. Each structural configuration was analyzed for forces occurring during that stage of construction, and internal forces (shears, moments, and axial forces) and deflections were determined for each case. The forces and deflections from each stage were added to subsequent stages to determine the in-situ condition of the structure. Top and bottom stresses were also determined from calculated internal forces and cross-sectional properties.

Shears, moments, and top and bottom fiber stresses are plotted for each structural configuration in Figures 5.4 through 5.6. The sign convention for stresses assumes compression stress as positive. Each force type is divided into components caused by dead loads, primary prestress forces, and secondary prestress forces. In each case the forces represent the total from each component at the end of the current stage of construction. The sum of the three components is also shown in each case.

The forces existing in the one-span configuration are shown in Fig. 5.4. The dead-load shears and moments are counteracted by the prestress forces, with some reserve provided for shear at the south end. The extreme fiber stresses range from 450 to 700 psi in the middle portion of the span, providing reserve stress

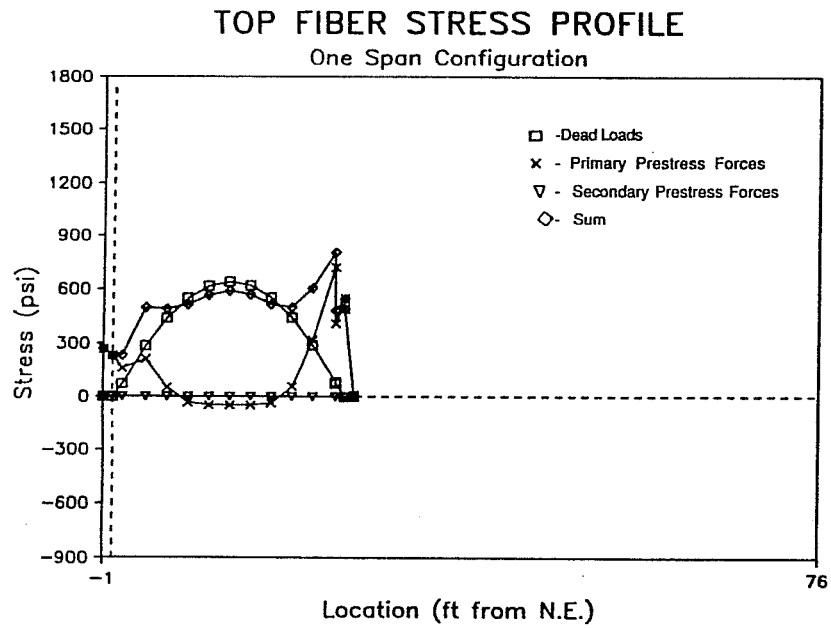


a) Shear Force Diagram

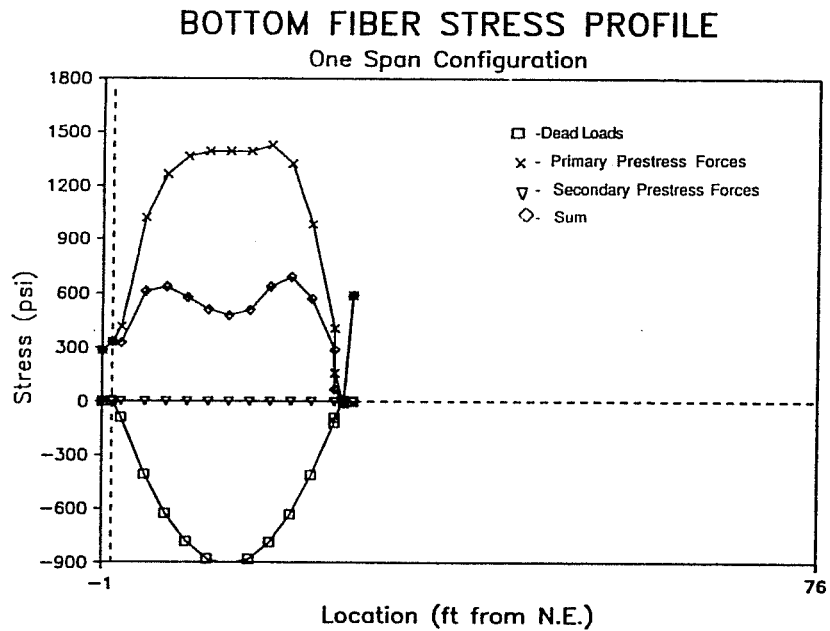


b) Bending Moment Diagram

Figure 5.4 One Span Configuration

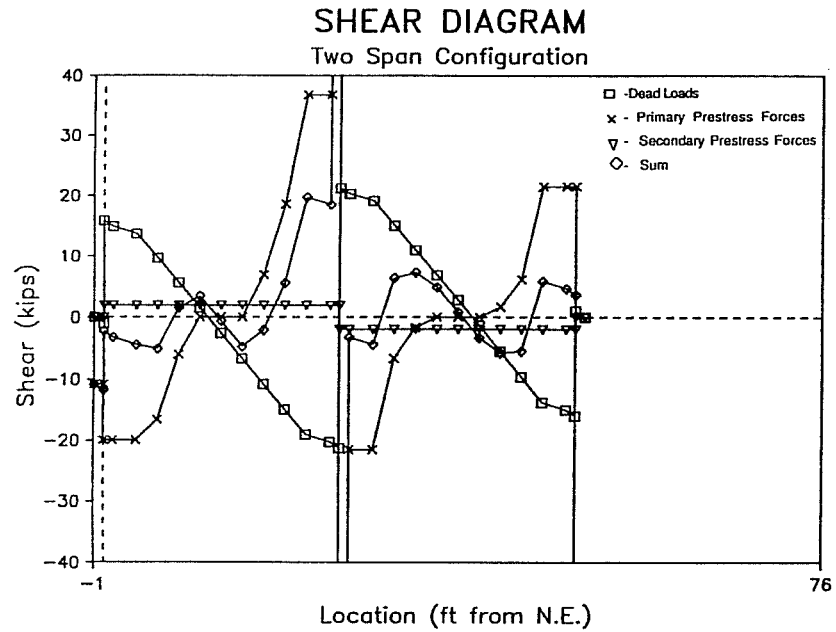


c) Top Fiber Stress Profile

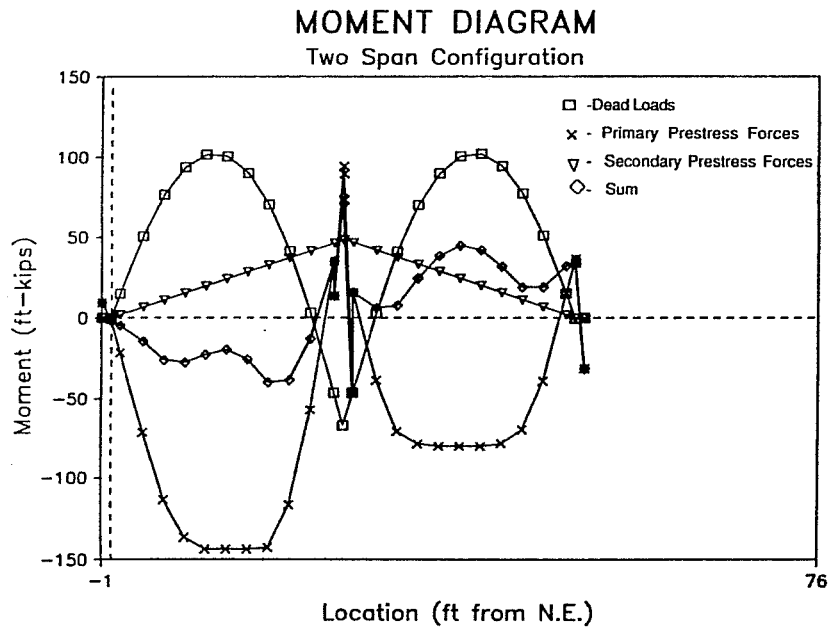


d) Bottom Fiber Stress Profile

Figure 5.4 One Span Configuration – continued



a) Shear Force Diagram

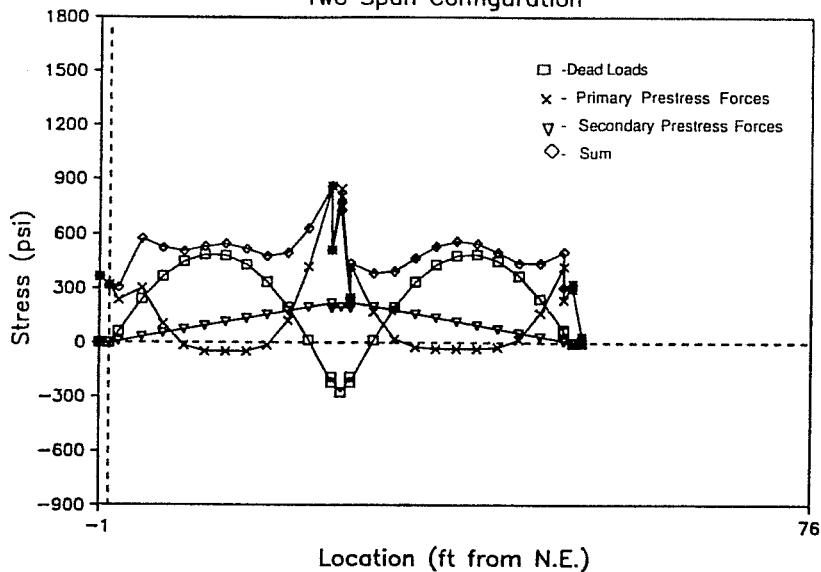


b) Bending Moment Diagram

Figure 5.5 Two Span Configuration

TOP FIBER STRESS PROFILE

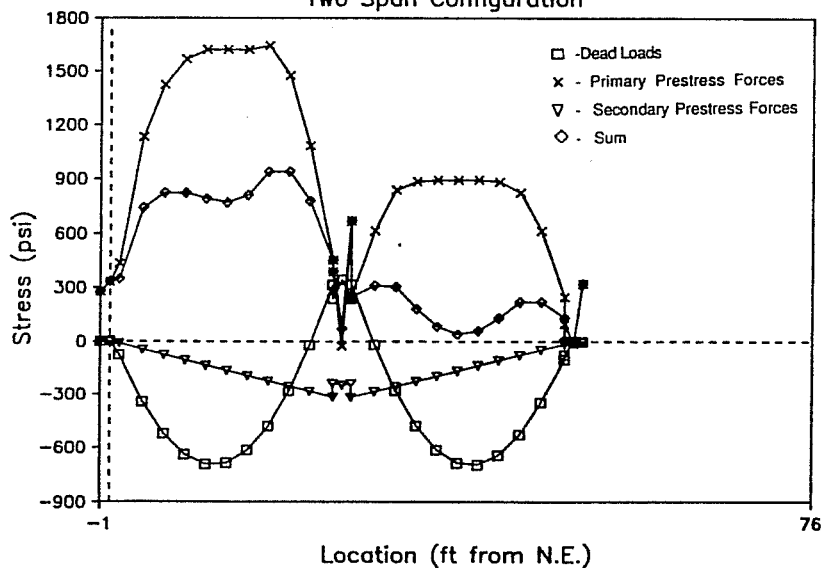
Two Span Configuration



c) Top Fiber Stress Profile

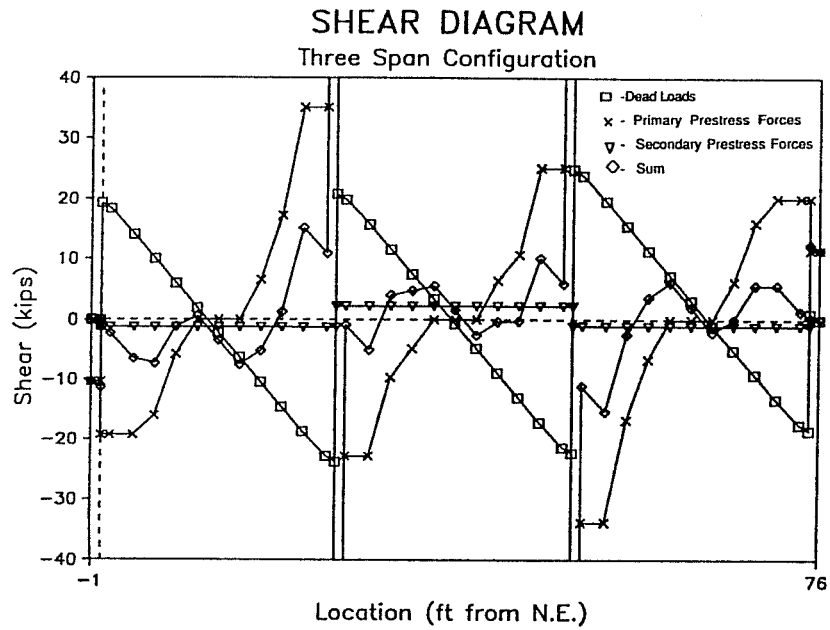
BOTTOM FIBER STRESS PROFILE

Two Span Configuration

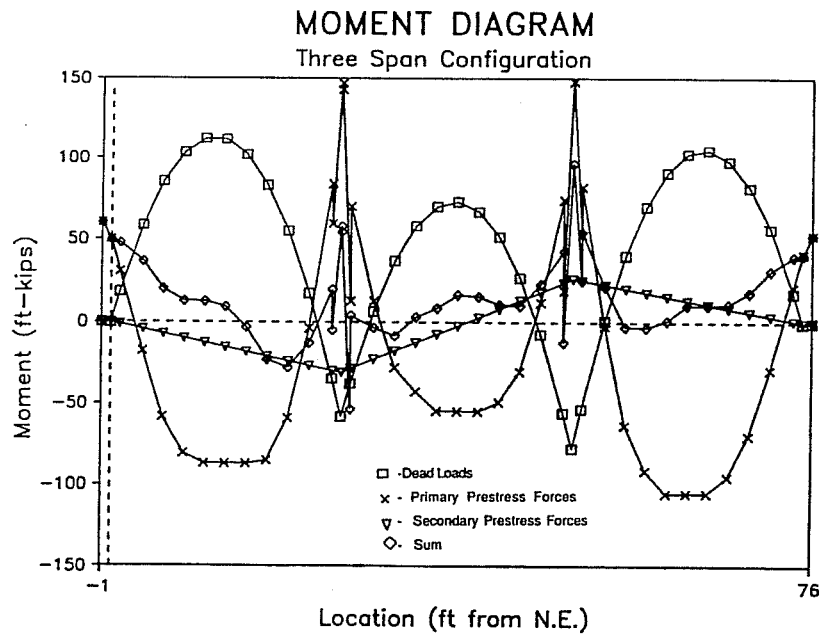


d) Bottom Fiber Stress Profile

Figure 5.5 Two Span Configuration – continued



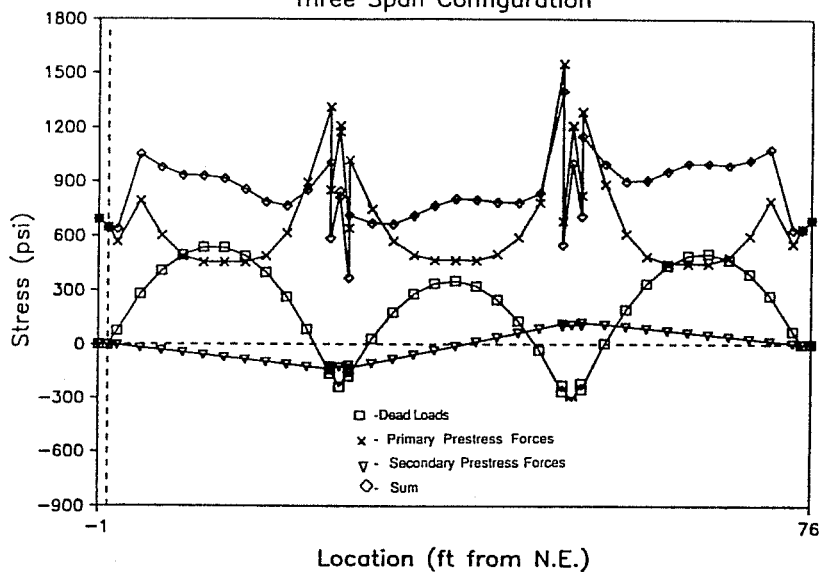
a) Shear Force Diagram



b) Bending Moment Diagram

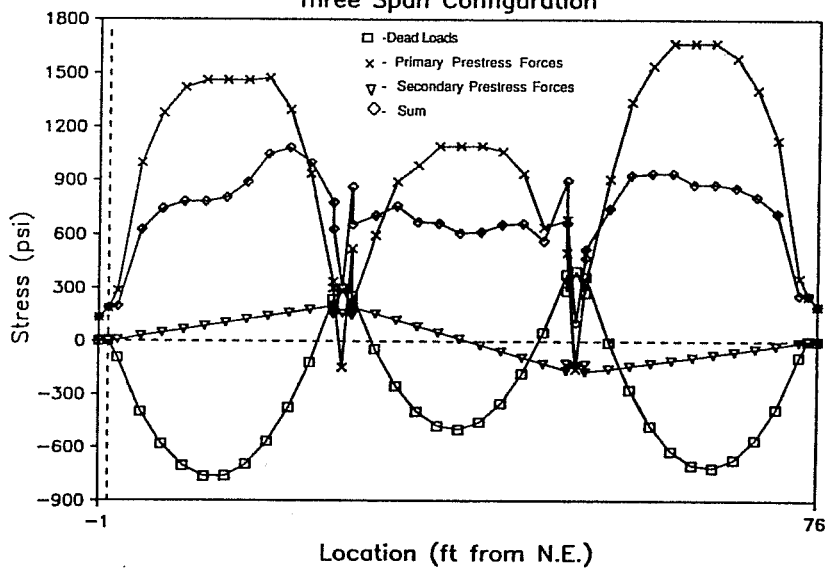
Figure 5.6 Three Span Configuration

TOP FIBER STRESS PROFILE
Three Span Configuration



c) Top Fiber Stress Profile

BOTTOM FIBER STRESS PROFILE
Three Span Configuration



d) Bottom Fiber Stress Profile

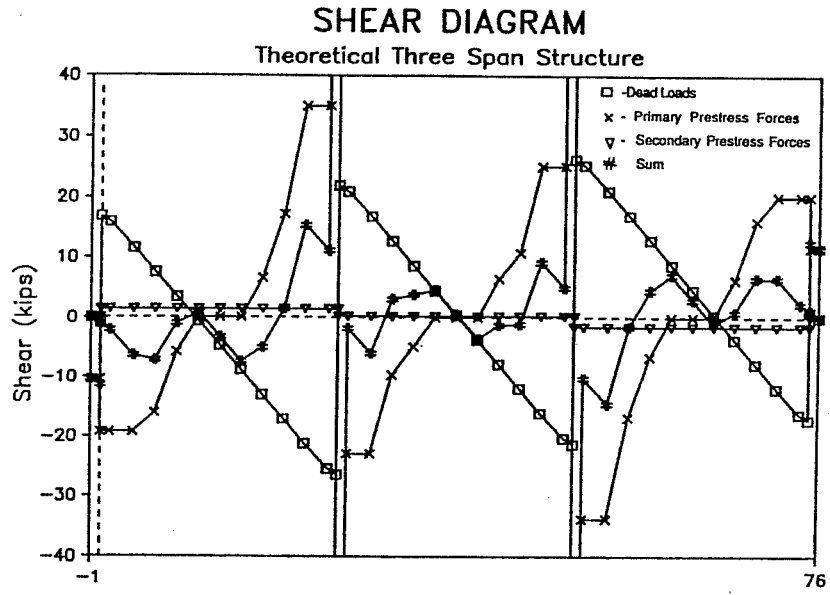
Figure 5.6 Three Span Configuration – continued

for application of construction live load. In this statically determinate system, the secondary prestress forces are zero.

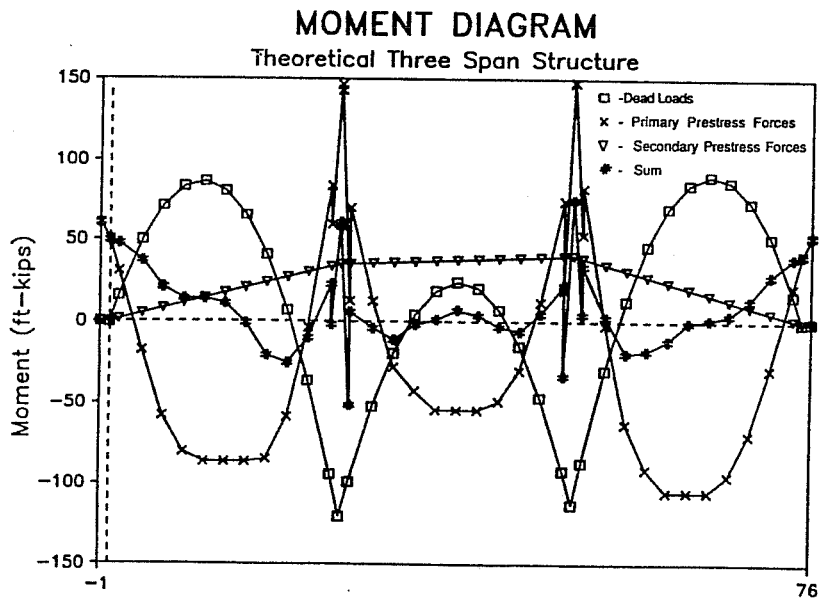
The forces existing in the two-span configuration are shown in Fig. 5.5. In the north span the dead load forces are balanced by the prestress forces with reserve for construction live-loads at all locations. In the "center" span the prestress forces only partially offset the dead load forces leaving almost no reserve for construction live loads. The top fiber stresses range from approximately 400 to 600 psi compression in both spans while the bottom fiber stresses are almost zero in the midspan region of the "center" span. The low stresses in the "center" span at this stage are a result of the construction sequence in which a portion of the "center" span tendons are not stressed until after erection of the south span. High friction losses also occurred in the primary "center" span tendon 2. Also, the secondary prestress forces in the continuous structure contribute to the low combined stresses in the "center" span.

The estimated forces that exist in the structure at the beginning of testing are shown in Fig. 5.6. The dead load shears are more than offset by the prestress forces with some reserve provided for service live loads. The resultant moments at all midspan locations are less than 20 percent of the corresponding dead load moments. The extreme-fiber stresses in the center of all spans range between 600 and 1100 psi compression.

The "Span-by-Span" construction method causes hyperstatic forces to be locked into each structural configuration. A three-span structure with post-tensioning forces applied simultaneously to all spans was analyzed for comparison with results of the true sequential construction method. The resultant forces for this structure are shown in Fig. 5.7. The primary difference between the two structures is the distribution of secondary forces. In the sequentially constructed structure, shown in Fig. 5.6, the secondary prestress forces are anti-symmetric about the center of the structure. This results from stressing each span individually, and causes reduced shears at the north end and increased shears at the south end. In the structure that is post-tensioned in one operation, the secondary prestress forces are approximately symmetrical about the center line. This causes both exterior reactions to increase by approximately the same amount.



a) Shear Force Diagram

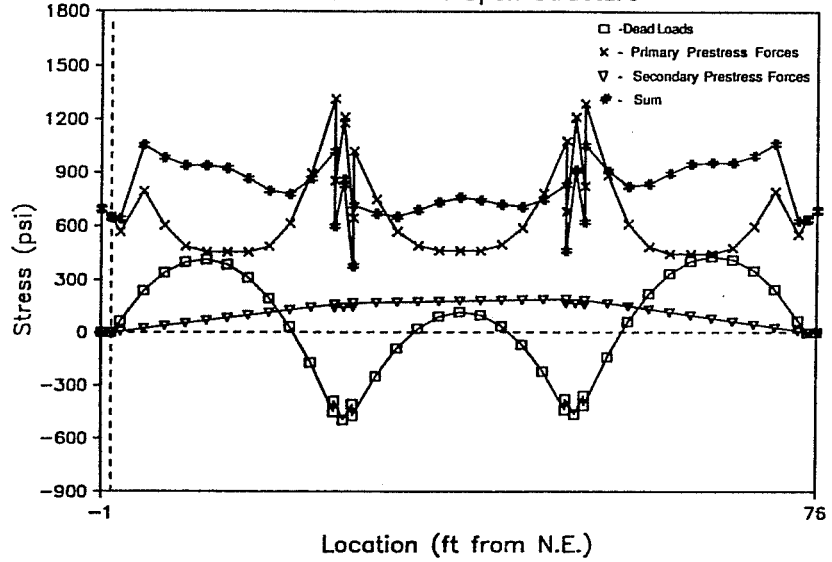


b) Bending Moment Diagram

Figure 5.7 Theoretical Three Span Structure

TOP FIBER STRESS PROFILE

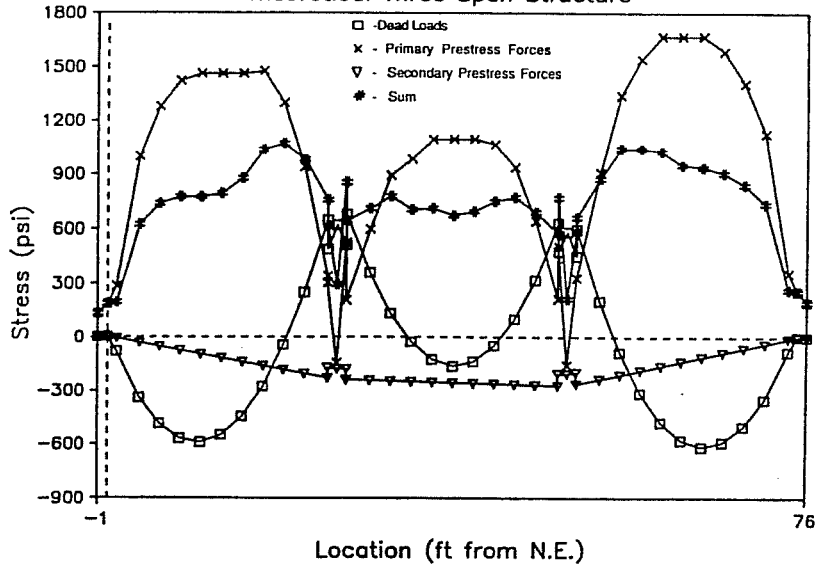
Theoretical Three Span Structure



c) Top Fiber Stresses

BOTTOM FIBER STRESS PROFILE

Theoretical Three Span Structure



d) Bottom Fiber Stresses

Figure 5.7 Theoretical Three Span Structure – continued

The resultant dead load forces are also distributed differently in the two structures. In the sequentially constructed structure the dead loads are resisted primarily by positive-moment bending with a ratio of positive to negative moments in the exterior spans of approximately two. In the three-span structure that is post-tensioned in one operation, the dead load forces are carried by a more equal distribution of positive and negative moments, with a positive-to-negative moment ratio of approximately one.

The resultant extreme-fiber stresses from the two structures are compared in Fig. 5.8. In the north span, the differences in secondary-force distribution are offset by the differences in dead-load force distribution to yield almost no change in extreme fiber stress. In the center and south spans the differences in dead load and secondary-force distributions lead to reduced top fiber stresses and increased bottom fiber stresses for the simultaneously post-tensioned structure. Changes in stress as high as 10 percent were computed.

The service live loads were input to the completed analytical model to check conformance with design serviceability criteria. The design concrete stress limits for all types of segmental construction are also described in Chapter 2. For externally post-tensioned precast segmental box-girders, the newly proposed PTI stress limits (19, 20) are summarized in Table 5.3. The table shows the initial proposal of Jan. 1987 (20) as well as the finally agreed on values of Feb. 1988 (19). When the bridge model was designed and constructed, the values used in design were those of the Jan. 1987 proposal. These provided that if bonded reinforcement is not provided across segment joints (as is the case in the model), then a residual compression is required in flexural tension zones. The required amount of residual compression depends on whether the segment joints are dry or epoxied. The allowable concrete compressive stress is independent of the type of construction.

The extreme-fiber stresses that result from only the design service loads are shown in Fig. 5.9. The service load stress envelopes were then superimposed on the calculated in-situ stresses to yield the range of service level stresses in the completed structure. The service load stress range and the design stress limits for the top and bottom fibers are shown in Fig. 5.10. The service stresses in the completed structure are all within the specified limits. The maximum compressive stresses are well below the limiting stress of 2400 psi, shown in Table 5.3. In the flexural tension

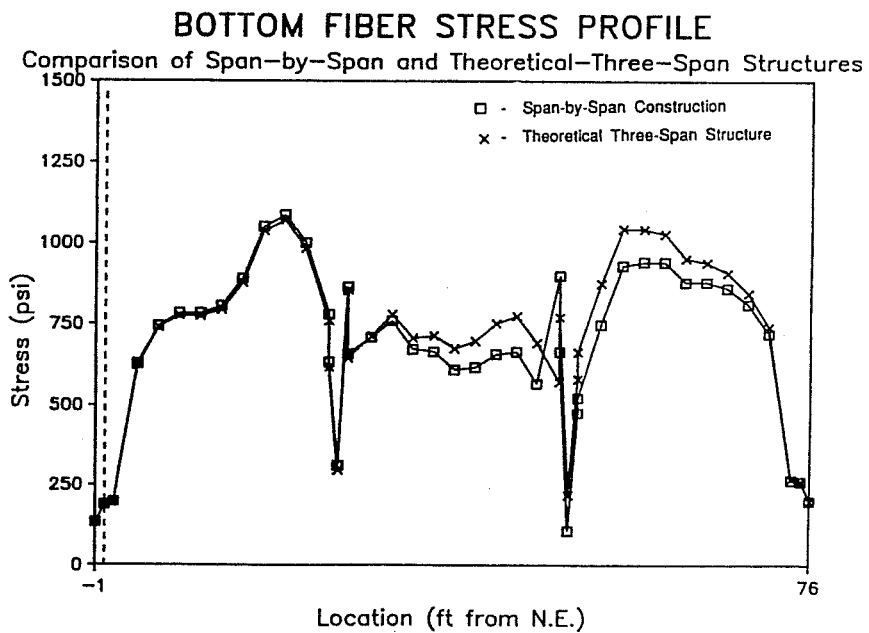
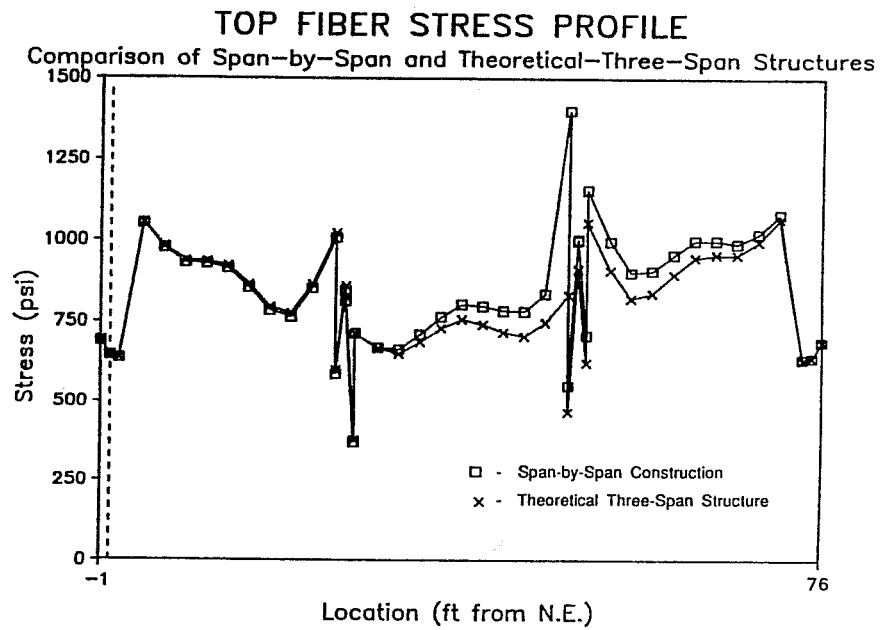
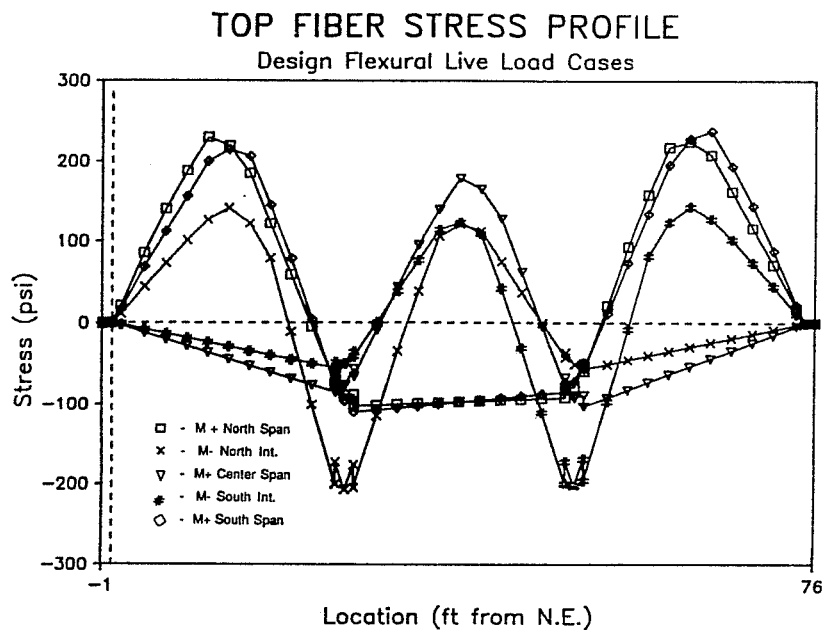
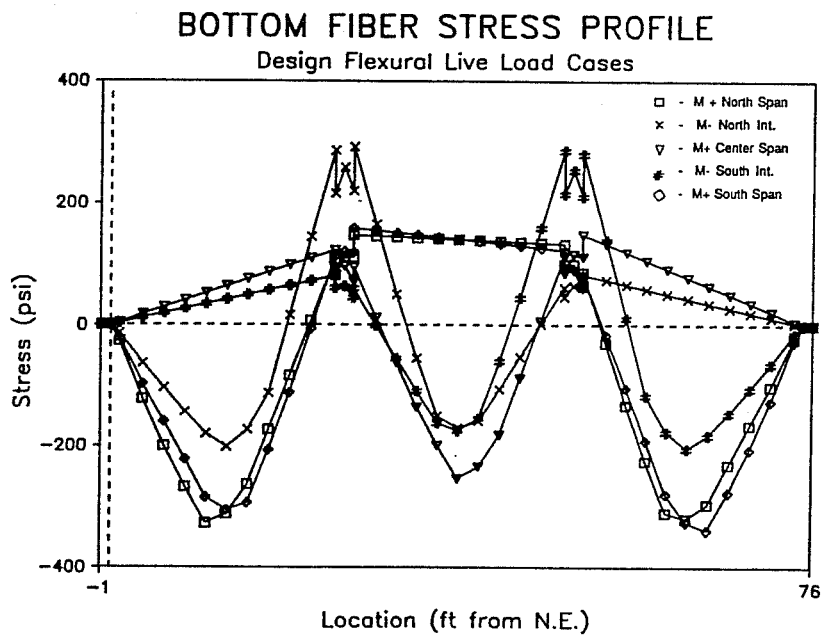


Figure 5.8 Comparison of Extreme Fiber Stresses for As-Built and Theoretical Structures

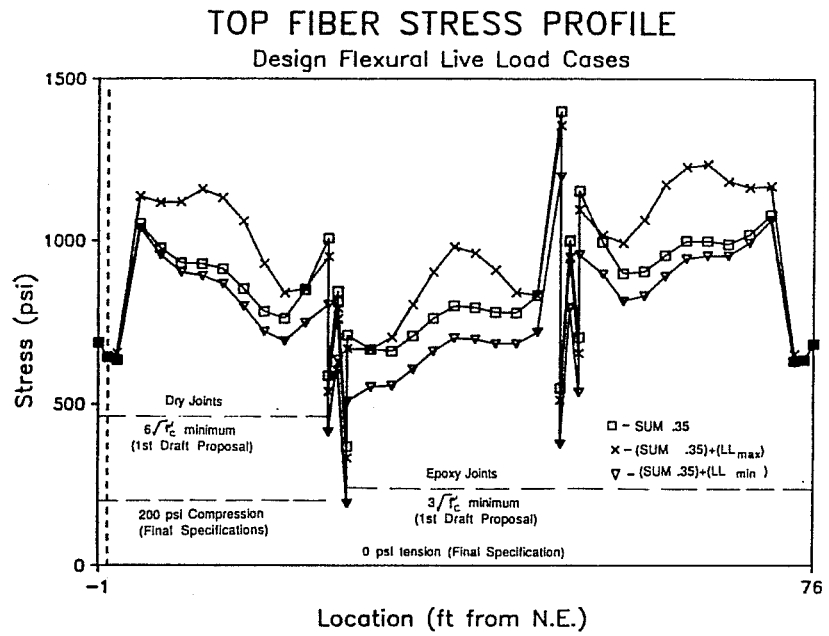


a) Top Fiber Stresses

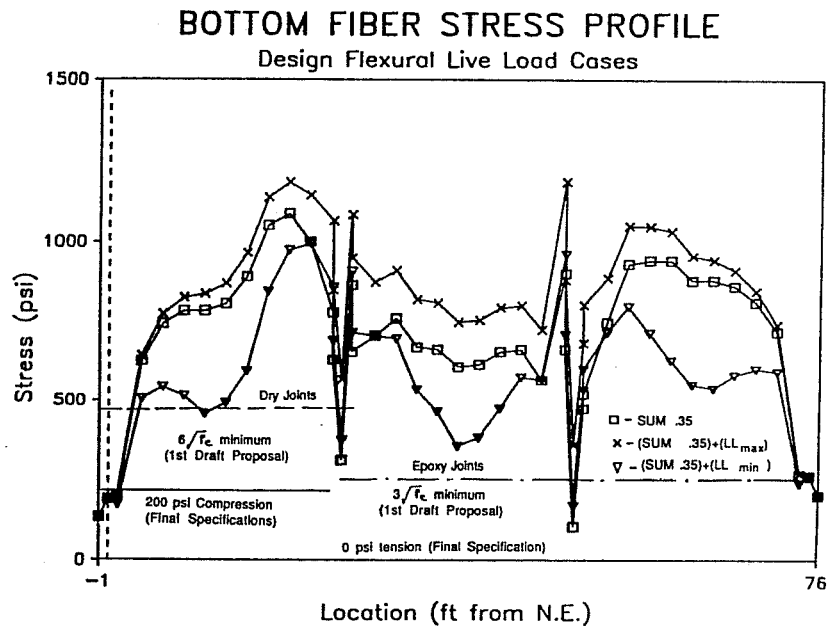


b) Bottom Fiber Stresses

Figure 5.9 Extreme Fiber Live Load Stresses



a) Top Fiber Stresses

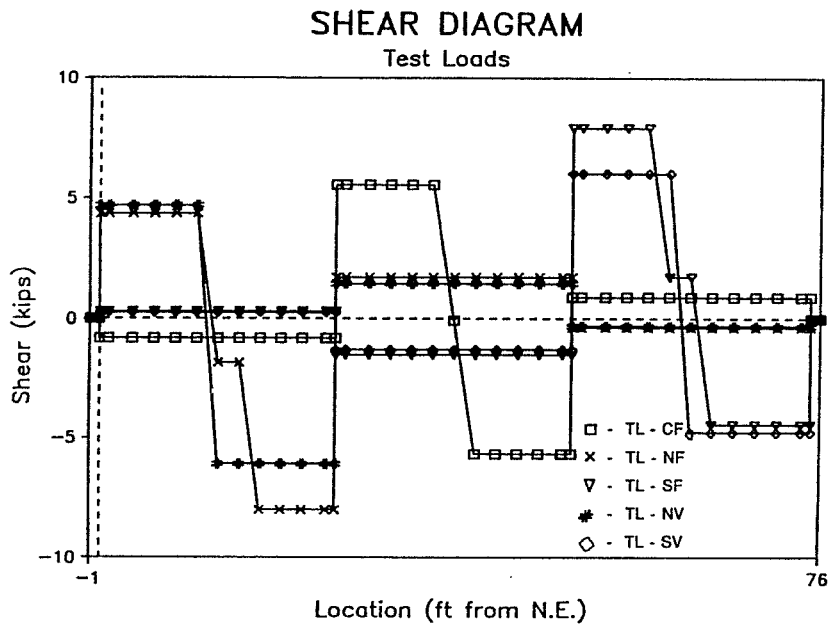


b) Bottom Fiber Stresses

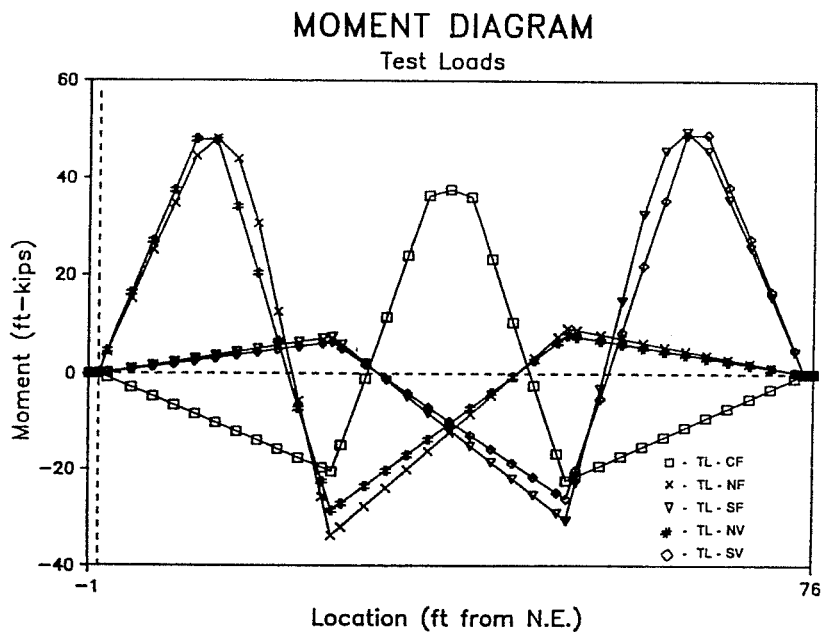
Figure 5.10 Service Stress Range

Table 5.3 Concrete Stress Limits for Model Structure

<p>Condition:</p> <ul style="list-style-type: none"> - Segmental Construction - Stresses at Service Loads after Losses have Occurred - Less than 50% bonded Prestressed Reinforcement - Without bonded mild reinforcement crossing joints - Design Specified Concrete Strength (f'_c) of 6000 psi 	<p>Jan. 1987 Draft (20) Limit:</p>	<p>Feb. 1988 Final Report(19) Limit:</p>
<p>Compression All Members Tension Precompressed Tensile Zones: Dry Joints: Epoxied Joints:</p>	<p>0.40f'_c</p> <p>6.0 $\sqrt{f'_c}$ (Comp.) 3.0 $\sqrt{f'_c}$ (Comp.)</p>	<p>0.40f'_c</p> <p>200 psi compression 0 tension</p>

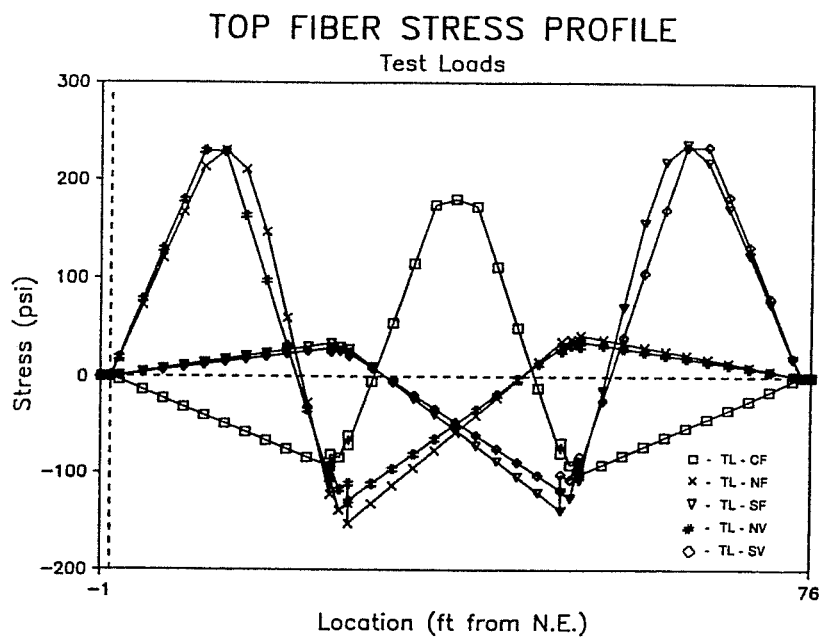


a) Shear Force Diagram

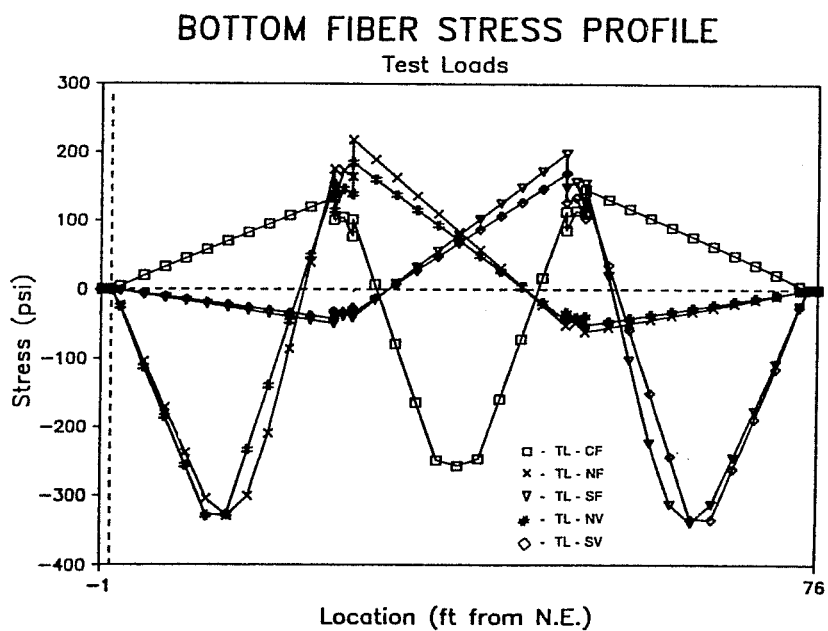


b) Bending Moment Diagram

Figure 5.11 Test Load Forces



c) Top Fiber Stresses



d) Bottom Fiber Stresses

Figure 5.11 Test Load Forces – continued

zones, the PTI initial draft minimum allowable residual concrete compression is 465 psi ($6.0 \sqrt{f'_c}$) in the dry span and 232 psi ($3.0 \sqrt{f'_c}$) in the epoxied exterior span. These values were used in the model design and are more conservative than the final proposal.

Examination of the service load stress range in Fig. 5.10 reveals that the dry exterior span meets the 1st Draft (20) residual compression requirement almost exactly and has a residual compression about 2.4 times the recent PTI recommendations (19), the epoxy joint span has a residual compression of approximately 2.4 times the 1st Draft (20) required residual compression and has a residual compression almost 500 psi above the new PTI recommendations (19). This extra over-design in the epoxy span was required in the model to provide similar exterior spans. Note both exterior spans are designed quite conservatively. The smallest compression stress at an extreme fiber in the center span is approximately 1.6 times the required compression for epoxy spans. Critical placements of the test load cases corresponding to the equivalent model live load plus impact factor were determined for each case (N=North, C=Center, S=South) for flexure (F) and for shear (V). These test load cases were also applied to the completed structure to determine the internal force distribution and the onset of joint opening assuming no tensile strength at the joint.

The shear forces, bending moments, and extreme fiber stresses resulting from the five different test loads are shown in Fig. 5.11. The level at which joints would open (neglecting the tensile capacity of the epoxy) were estimated by determining the multiple number of test loads required to overcome the precompression and induce tensile stress at critical joints. Table 5.4 summarizes the estimates for the joint decompression load levels for each test load case. From this table it is seen that no joint opening would be expected until approximately 2.4 (L+I) load in the dry-jointed north span and substantially higher load levels in the epoxy-jointed center and south spans. Elastic deflections for each test load case were also determined and compared with deflections recorded during testing (see Chapter 6).

Table 5.4 Multiple of Live Plus Impact Loads Required for Joint Decompression

Test Load Case	Span Loading	Critical Joint No.	Construction Joint Stress (psi)	Joint Stress from Test Load (psi)	Multiple of Test Loads Required for Joint Decompression
TL-CF	Center Flexure	(15, 16)	609	257	2.37
TL-NF	North Flexure	(4, 5)	783	304	2.57
		(5, 6)	805	329	2.45
TL-SF	South Flexure	(25, 26)	878	339	2.59
		(26, 27)	879	313	2.81
TL-NV	North Shear	(4, 5)	783	329	2.38
		(5, 6)	805	327	2.46
TL-SV	South Shear	(25, 26)	878	335	2.62
		(26, 27)	879	335	2.62

CHAPTER 6 LOAD TESTS

6.1 Loading Program

The model structure was load tested to investigate the complete range of flexural behavior and to conduct preliminary tests of shear and torsional behavior. The test program, shown in Table 6.1, consisted of three distinct phases:

Phase 1 - structural characterization

Phase 2 - factored load tests

Phase 3 - ultimate strength tests

The first phase of testing involved loading the structure to the design service-level live loads and then increasing loads to higher levels to establish the decompression loads at critical joints along the structure. In the second phase of testing, the structure was loaded with the increased factored loads used for strength design. In the final phase of testing, the structure was loaded until the ultimate strength was reached. The initial failure tests were flexural. Exploratory tests were then carried out on the partially damaged structure to investigate shear behavior at an opening joint. Phase 1 testing was conducted on all three spans, while Phases 2 and 3 were conducted on the exterior spans only. At all levels of loading, comparisons were made between the dry-jointed and epoxy-jointed exterior spans.

The structural characterization phase of testing, summarized in Table 6.1a, was designed to define and characterize the in-situ condition of the structure. Each of the three spans was tested in a similar manner on the dates shown in Table 6.1a. First, four cycles of service live load were applied to each span. A cracking cycle was then conducted on the epoxy jointed spans (center and south), and then three additional load cycles were applied on all spans to determine the decompression load. The decompression load is the applied load that is necessary to reduce the initial compressive stress to a zero stress level in the extreme flexural-tension fiber, and was determined by a subtle change in stiffness as indicated by load deflection curve. Three additional decompression cycles were applied with an unacceptable pair of rams to the north-span (see Section 6.2.1.2). The data from these load cycles are

Table 6.1 Loading Program

	North Span (Dry)	Center Span (Epoxy)	South Span (Epoxy)
A. Phase 1 - Structural Characterization			
Design Service Load Cycles			
4 Cycles:	3/15/88	3/11/88	3/11/88
Cracking Cycle			
1 Cycle:	N/A	3/11/88	3/11/88
Decompression Load Cycles			
3 Cycles:	3/17/88*	3/14/88	3/16/88
Torsional Load Cycles			
Cycles:	3/18/88	N/A	3/18/88
B. Phase 2 - Factored Load Tests			
Design Factored Load Cycles			
3 Cycles:	3/29/88/**	N/A	3/31/88
C. Phase 3 - Ultimate Strength Tests			
Flexural Strength Test - Joint Opening Cycles			
3 Cycles:	4/5/88	N/A	4/18/88
Flexural Strength Test - Ultimate Cycle			
1 Cycle:	4/12/88***	N/A	4/19/88
Shear Strength Test			
1 Cycle:	4/21/88	N/A	4/26/88

*Three additional cycles on 3/15/88 with bad rams

**Three additional cycles on 3/25/88 with restraining load system

***Testing conducted on 4/5/88 and 4/7/88 also

not presented here. Finally, three cycles of eccentrically applied service load were applied to the two exterior spans to investigate service level torsional behavior.

After completing the first phase of testing, all spans of the structure were loaded with additional dead weight to provide the design factored dead load. Each exterior span was then subjected to three cycles of the factored design loads. Three additional factored load cycles were applied to the north-span with a loading system that offered restraint to the structure, (see Section 6.2.1.2). These data are also not presented here.

The ultimate strength phase of testing, shown in Table 6.1c, is divided into two stages, flexural strength and shear strength. Each exterior span of the structure was initially subjected to three cycles of load large enough to cause visible opening at a segment joint(s). After completing the “joint-opening” cycles, the load was then continuously increased until the flexural strength was reached. Three separate load cycles were applied to the north-span before flexural strength was achieved. Larger low-level load increments were used on the south-span, and ultimate strength was achieved on the first “ultimate” cycle. The flexural-strength test was discontinued when the stiffness of the span being loaded had reduced to a very small fraction of the initial elastic stiffness. Both exterior spans experienced approximately the same maximum deflection.

After completing the flexural strength stage of testing, an exploratory test was conducted on each exterior span in which significant shear was transferred across an opening joint. Only one cycle of load applied to each exterior span. Loading was applied to each span until the measured stiffness reached approximately the same stiffness as measured at the conclusion of the flexural strength test.

6.2 Description of Loading System

6.2.1 Reduced Scale Truck Loads.

6.2.1.1 Location of Loads. The reduced-scale representation of two lanes of AASHTO HS20 truck load with impact, derived in Section 2.1.3, consists of a series of three concentrated loads spaced at 42-in. on-center, as shown in Fig. 2.3. To simplify the load frame, rams were provided only at locations in-line with the

rod-clusters in the test floor. Also, two identical rams were used and were operated on the same hydraulic system. These two requirements lead to the use of two equal loads spaced at 48-in. on-center. The rams were attached to heavy steel cross-beams which were tied down to the test floor with 1-in. diam. rods at each end (see Section 6.2.1.2).

With the basic test-configuration described above there were only a few possible locations for the test load. For flexural tests, two rams were spaced at 48-in. measured along the longitudinal axis of the structure. For the shear tests, to increase the shear transfer across an opening joint, the two rams were located at one section along the length of the structure. For the torsion tests, the rams were spaced 48-in. apart along the longitudinal axis of the structure, and were located directly over the west web of the box-girder model. The three types of test load configurations are shown schematically in Fig. 6.1.

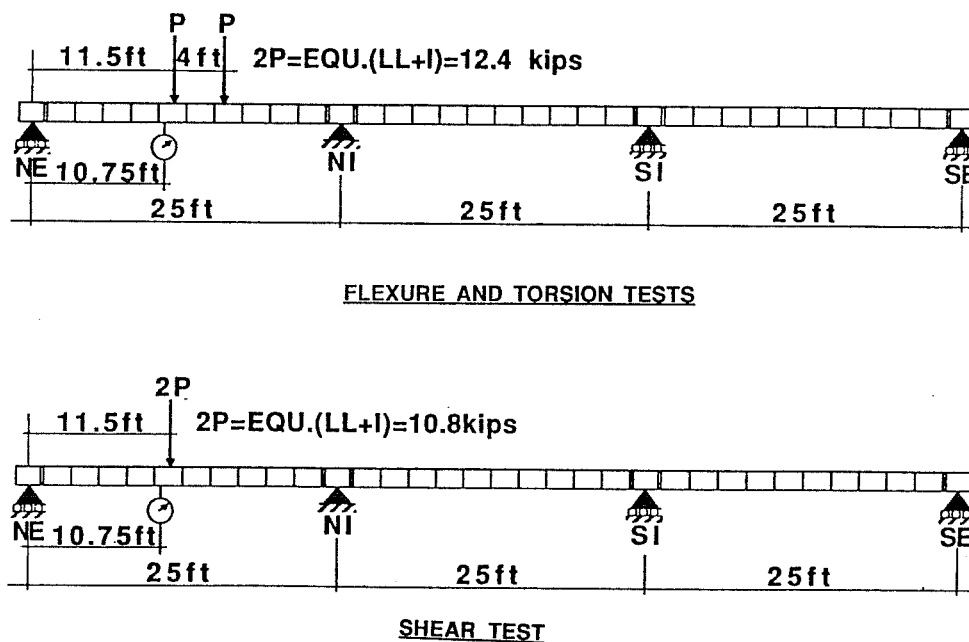


Figure 6.1 Test Load Configurations

The flexural test load configuration provides a reasonable representation of the design AASHTO truck load. The model design load has three loads spaced at 3.5 feet on center, with a percent distribution of total load to the axles of 12%, 44%, and 44%, respectively, and a radius of gyration of force equal to 2.33 feet. The actual flexural test load has two loads spaced at 4.0 feet on center, with 50 percent of the total load distributed to each ram, and a radius of gyration of force equal to 2.0 feet. The radius of gyration of force provides a measure of the global distribution of force within the load case. A smaller value indicates the load group is more concentrated and will result in higher shears and larger peak moments in the critical midspan flexure region.

Each possible load configuration was analyzed using a plastic mechanism analysis (Section 5.2) to determine the locations of critical joints. Each test load configuration was also analyzed using an elastic analysis (Section 5.4) to determine the elastic internal forces at the critical mechanism joints. The flexural and shear test load locations were chosen so that the same joints were critical for both tests. If a different joint was critical for the flexure test of the cracked epoxied space, then the desired critical shear mechanism may not have developed properly. The final test load locations were therefore chosen so that flexure and shear test mechanisms involved the same critical joint with the largest shear transfer across the joint.

6.2.1.2 Load Application Equipment. The load frame consisted of a rectangular tension structure that was tied down to the test-floor at its four corners (see Fig. 6.2). The cross-beams were braced to each other with two secondary beams. In the unloaded condition the frame was supported at each corner with adjustable post shores and was tied to the model for stability.

The rams were placed between the load frame and the structure. For all flexural tests the centrally located rams applied load to the webs of the box girder located through a spherical bearing and spreader beam. For the torsion and shear tests the rams were positioned directly above the box-girder webs and located through spherical bearings.

Two types of bearing conditions were used to transfer the applied ram force to the concrete model. During low load-level testing, the spreader beam was seated with hydrastone to the top of the model to ensure uniform bearing. After several

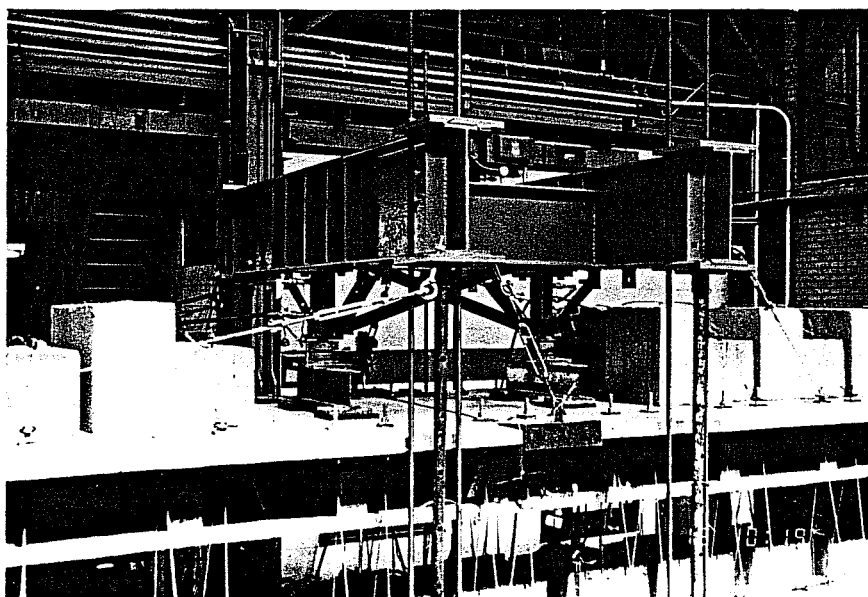


Figure 6.2 Load Frame

tests it was found that the stiff hydrastone was providing a load path through the load frame which was restraining the top flange of the structure. For all subsequent tests (all factored load and ultimate strength tests) the spreader beam bore on a 1/2-in. thick layer of neoprene. This provided a flexible support between the load frame and the structure so that longitudinal restraint of the top flange of the structure was not induced.

Two double-action 30 ton rams were operated in parallel using a single pump. The applied test force was controlled manually with a pressure transducer connected to a strain indicator box and monitored by a second pressure transducer which was connected to the electronic data acquisition system.

6.2.2 Equivalent Live Load with Impact. So that comparisons could be made with the AASHTO service truck load, it was necessary to determine the magnitude of test load that was equivalent to the reduced-scale service live load. Since the tests were planned to primarily examine flexural behavior, the joint moments were used as the conversion between the service design loads and test loads. The "Equivalent Live Load with Impact" was chosen to provide the same moment at

the critical joint as the maximum design service load moment determined at any location. Maximum design moments were determined from the design service loads using influence diagrams developed for each joint. Then, using the influence line for moments at the critical joint, the magnitude of the test load was calculated to give the same moment at the critical joint. The “Equivalent Live Load with Impact [Equivalent (LL+I)]” is defined as the test load that causes the maximum design live-load moment to occur at the critical joint.

6.2.3 Factored Dead Load. Additional dead weight blocks were added on top of the structure as shown in Fig. 6.2 to simulate the factored dead load for loading above normal service levels. The extra factored dead load consists of 30% of the model dead weight (segment weight plus weight of dead-load compensating blocks). A space was left between adjacent segment-blocks to ensure arching did not occur. Because of interference with the load frame, the factored dead load blocks were left off three central segments. This deficit was made up during testing by applying a small ram load prior to application of additional service live loads.

6.3 General Test Procedure

All tests were conducted with the same equipment and the same general procedure. At the start of each test, ram force was zeroed and reaction load cells, deflection potentiometers, joint opening potentiometers, and pressure transducers were all initialized. Initial readings were also taken on all manually-recorded instrumentation. Using this procedure, the data from the test measurements represented the structural response due to test loads only. The tendon strains were never zeroed, so the measured strain data represented the actual tendon strain.

Test loads were applied in small increments until the desired maximum level was reached. If the maximum level was defined by a specific load, as for service and factored load tests, then the range of force was divided into approximately equal increments. If the maximum level was defined by the model behavior, as for cracking, decompression, and ultimate strength tests, then the load increments were chosen to highlight important observations. An attempt was made, although not always successful, to use the same load increments for testing of both of the exterior spans, so that direct behavioral comparisons could be made.

The first load cycle was started immediately after zeroing the instrumentation. A small load was applied (approximately 2 kips total load) to stabilize the load frame, and then the temporary restraining brackets for the load frame were loosened. The loads were then increased to the first load increment.

The load was increased to the desired level and then held for approximately 5 seconds to enable scanning of all channels by the data acquisition system. The hydraulic line pressure was allowed to equalize until all other manual readings had been made. Midspan deflections were manually read and plotted with applied load during the test to provide information for control of the test.

6.4 Presentation of Test Data

For comparison, most of the data has been presented as a function of the applied test load. In all figures, and for discussion purposes the applied test load is expressed in terms of its reduced-scale equivalent, including impact (i.e., the Equivalent (LL+I), as described in Section 6.2.2). The data are plotted against multiples of equivalent (LL+I), with the origin located to reflect the unloaded state. For the service level tests the unloaded state corresponds with the actual dead load (DL). For the factored and ultimate load tests the unloaded state corresponds approximately with the factored dead load (1.3DL). Because the concrete blocks comprising the additional 30% load for the factored dead load could not be positioned on the segments near the test frame, a small load of about $0.30(LL+I)$ was necessary to bring the loading up to the factored dead load condition. This load was applied prior to application of the live load. Therefore, the applied load starts with this small negative value for all factored and ultimate strength data.

The test data is presented in several standard figures which are described below. In most cases only the loading portion of a complete load cycle is shown.

Applied Load vs Deflections: The deflection represents the net deflection of the structure at the location shown on the schematic after adjustment for support deflections.

Reaction vs Applied Load: The reaction represents the total force measured by the two load cells at a particular support, corrected as described in Section

4.4. Each of the four reactions of the structure are plotted. The reaction at the north interior pier was calculated from the other three reactions and the applied loads.

Joint Moment vs Applied Load: Joint moments were calculated from the corrected reactions and applied loads. The calculated joint moments are presented for all opening joints for a particular test.

Change in Tendon Stress vs Applied Load: The change in the tendon stress represent the average change in stress in two strands of the tendon, corrected as described in Section 4.1. The values indicate the change in stress resulting from the applied test load, and are shown for all measurement locations.

Joint Opening vs Applied Load: The relative movement between points on the bottom flange of adjacent segments at a joint was measured using potentiometers crossing the segment joints, as described in Section 3.9. Relative movements are presented for all opening joints for a particular test.

Joint Opening Profiles: The relative movements between points at various depths of adjacent segments at a joint were measured using grid crack monitors as described in Section 3.9. The relative movements are presented as a profile at a particular joint with the measured displacements plotted as a function of depth. The joint profiles are presented for only the ultimate strength tests for specific joints which exhibited large openings extending into the webs.

The test data and observations will be presented in the following general format. First, a brief description of the test series outlines general observations and specifies load increments and maxima. Then, all the figures illustrating important information about the test will be introduced at once. A representative cycle of the test series will then be described chronologically in detail making reference to any of the figures designated previously. Finally each test will be summarized in tabular form highlighting important behavioral observations. The figures for each test will be grouped together and located after the summary tables.

6.5 Center-span Service Load Tests

The interior span was subjected to service level loads so that the three span structure could be fully characterized for service conditions. Data from the live load cycles provide a measure of service stiffness, as well as a comparison with analytical results. The cracking and decompression loads provide an indication of the level of effective prestress for the center-span.

6.5.1 Live Load Cycles for Center-span. Four cycles of service live load were applied to the center-span using the load set-up shown on the schematic in Fig. 6.3. In the first cycle the applied force was increased from zero to the service live load in $0.09(LL+I)$ increments in the first cycle and in $0.18(LL+I)$ increments in the last three cycles. Each of the four cycles provided approximately the same response to the applied loads.

The measured deflected shape of the three-span structure is shown in Fig. 6.3 for a typical service load cycle. The midspan deflection of 0.040 inches corresponds to a deflection/span ratio of $L/7500$. Also shown is the calculated deflected shape from the elastic analysis (see Section 5.4). The elastic analysis overestimates the measured deflection by approximately 20 percent. The tendon data indicated a live-load stress range of about 1 ksi. No tendon slip was noticed at this load level.

6.5.2 Cracking Cycle for Center-span. After completing the live load cycles it was necessary to initially crack the epoxied center-span in order to determine the decompression load. The applied load was increased from zero to a maximum load level of almost $6.0(LL+I)$ in increments of $0.18(LL+I)$. The structure cracked in two stages at approximately 5.2 and $5.7(LL+I)$.

The applied load-deflection response during the cracking cycle is shown in Fig. 6.4. The measured reactions and the calculated joint-moments are plotted with respect to the applied load in Fig. 6.5. The change in tendon stress due to applied load is shown for all center-span tendons in Fig. 6.6.

2.6(LL+I): The structure exhibited linear behavior up to a level of approximately $2.6(LL+I)$. As loading was increased beyond this level the deflection response remained linear but had a slightly lower stiffness.

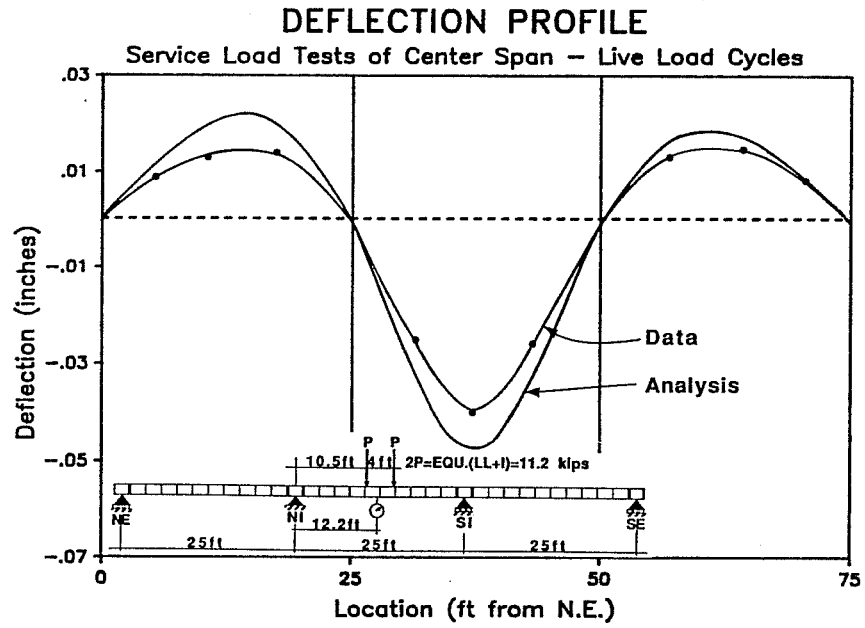


Figure 6.3 Center Span Service Load Test Deflection Profile

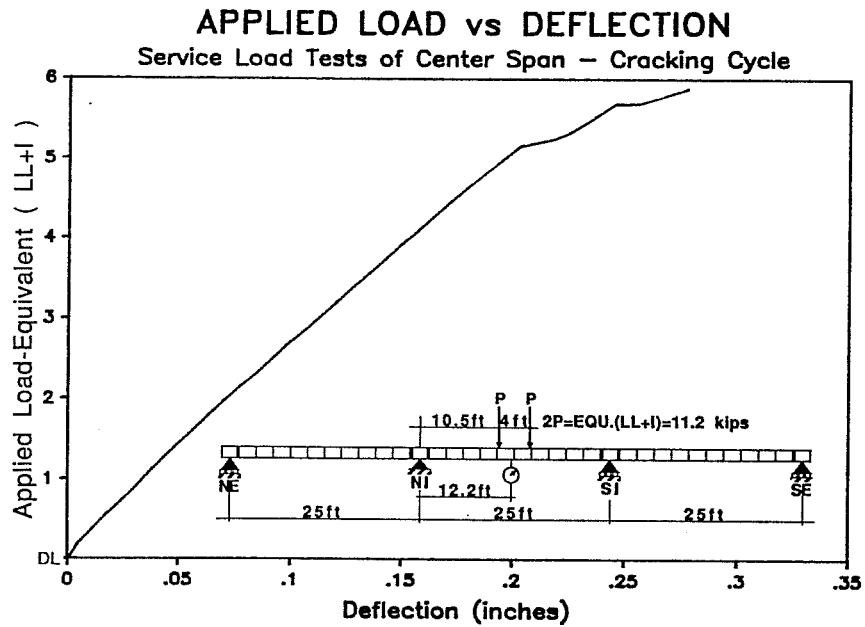


Figure 6.4 Center Span Cracking Cycle: Applied Load vs. Deflection

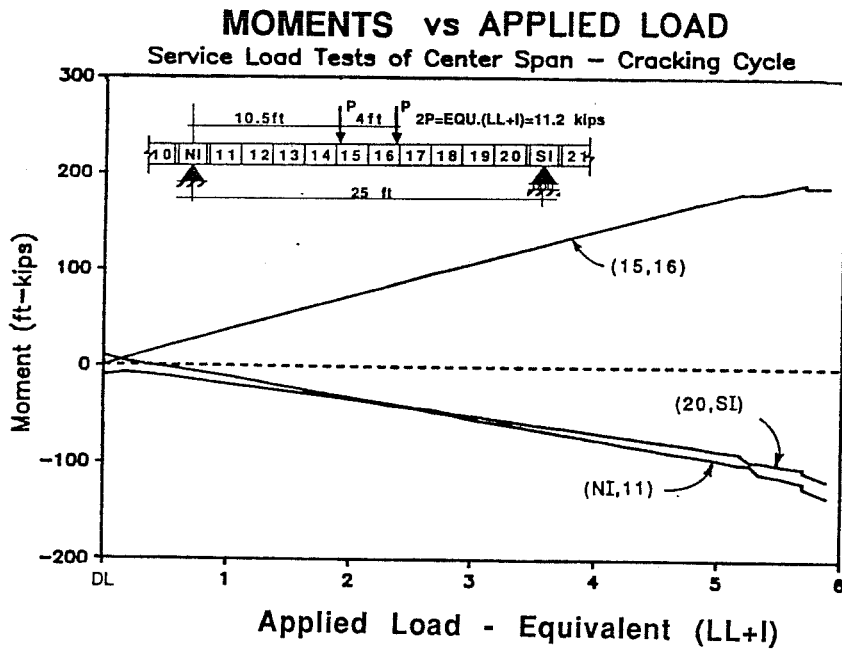
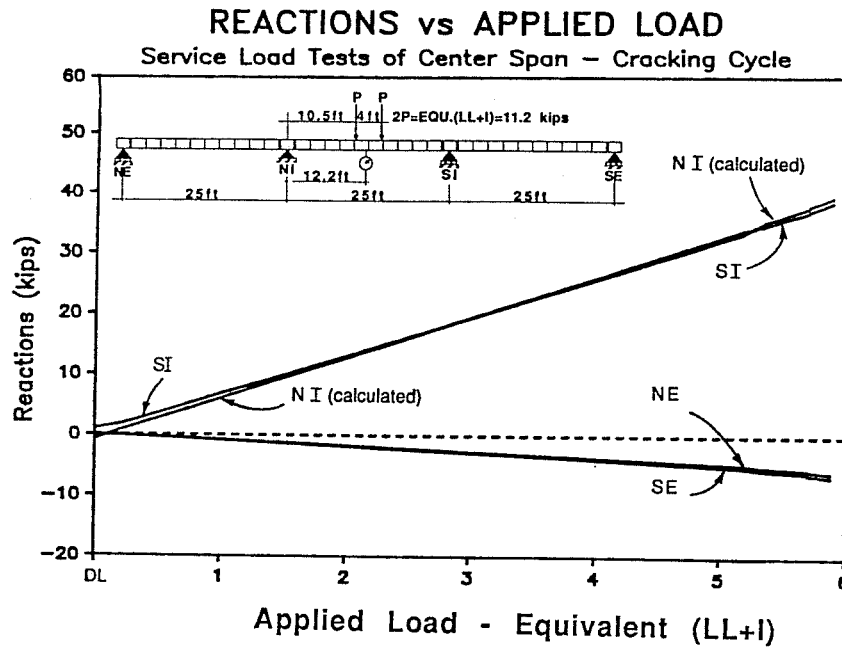


Figure 6.5 Center Span Cracking Cycle: Reactions and Joint Moments

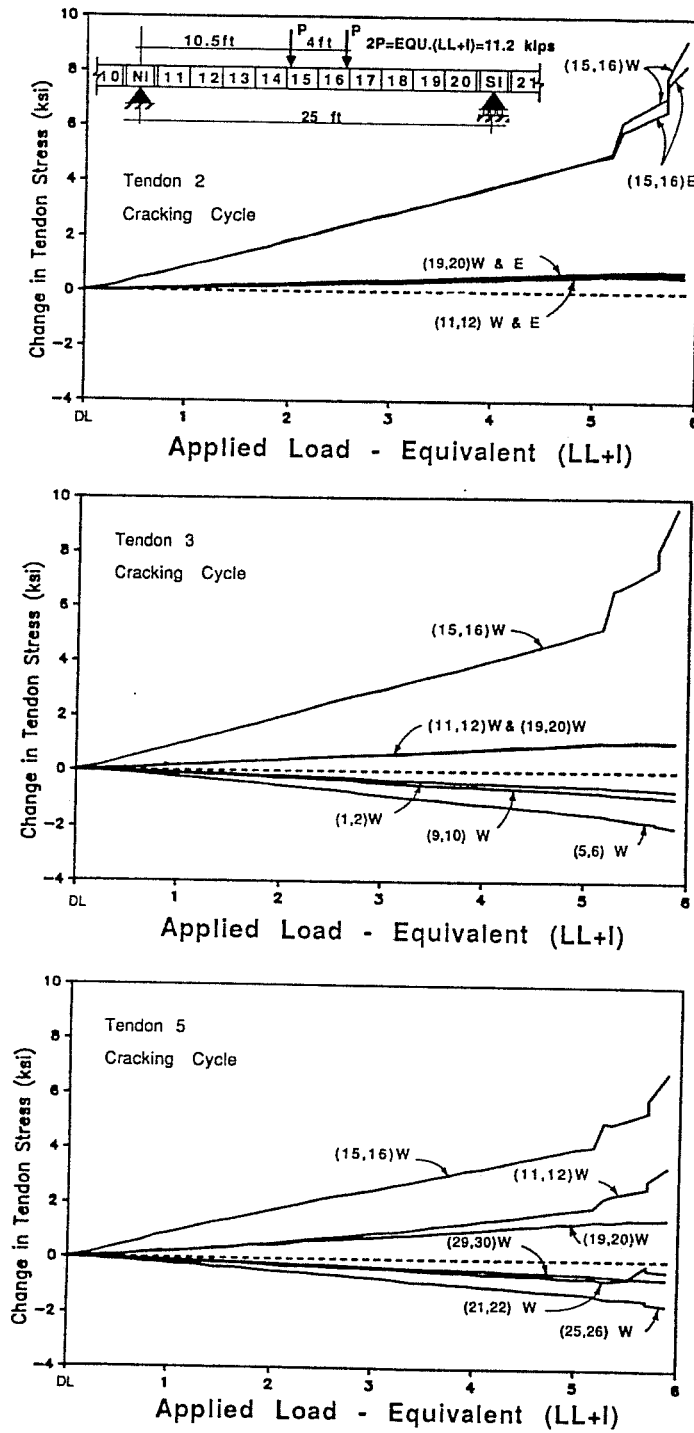


Figure 6.6 Center Span Cracking Cycle: Change in Tendon Stress vs. Applied Load

5.2(LL+I): The applied load was increased until visible cracking occurred in the concrete in segment 16, adjacent to joint (15,16) at approximately 5.2(LL+I). Cracking at joint (15,16) of the center-span reduced the stiffness at that point and caused the internal forces to redistribute. After cracking, a larger portion of the load was carried at the interior reactions as the applied load tended to cantilever from the stiff uncracked support region.

The midspan tendon stresses remained linear with applied load up to the point that the concrete section cracked. As cracking occurred, the tensile force that was previously carried by the concrete was transferred to the post-tensioning tendons. This caused a sudden increase in tendon stresses and corresponding strains to equilibrate these forces. With unbonded tendons, considerable elongation was necessary to develop the increased tendon forces. This caused concentrated rotations to occur at the midspan and subsequently increased vertical deflection.

Tendon 5 began slipping from the north end towards the midspan region of the center-span. Tendon 5 also began slipping from the north end of the south-span (21,22) through the pier segment to the south end of the north-span (19,20).

5.7(LL+I): As loads were increased further, additional cracking occurred at approximately 5.7(LL+I).

5.9(LL+I): The test was discontinued when a hydraulic fitting sprung a leak and pressure reduced rapidly. The cracking cycle is summarized in Tables 6.2, 6.3, and 6.4.

Table 6.2 Center-span Cracking Cycle - Maximum Response Values

	Cracking 5.2(LL+I)	5.9(LL+I)
Deflections	.20 (L/1500)	.28 inches (L/1071)
Reactions	35 kips at NI and SI	39 kips at NI and SI
Moments M+ve	180 ft-kips at (15,16)	190 ft-kips at (15,16)
M-ve	-100 ft-kips at (NI,11)	-130 ft-kips at (NI,11)

Table 6.3 Center-span Cracking Cycle - Change in Tendon Stress (ksi)

	Before Cracking 5.2(LL+I)	5.9(LL+I)
Tendon 2:	.5 / 5 / 0.5	1 / 9 / 1
Tendon 3:	1 / 5 / 5	1 / 10 / 1
Tendon 5:	2 / 4 / 2	3 * 7 / 2

* denotes slip towards midspan
 key = (11,12)/(15,16)/(19,20)
 = north-end/midspan/south-end

Table 6.4 Summary of Center-span Cracking Cycle

$P_{applied}$:	Description:
DL only	-Start Test ($P_{rams}=0$)
DL+2.7(LL+I)	-Stiffness reduces slightly in P-delta curve
DL+5.2(LL+I)	-Cracking occurs in Segment 16 adjacent to joint (15,16) -Tendon 5 (center-span) begins to slip from the north end towards the midspan region -Tendon 5 (south-span) begins to slip from the north end of the south-span (21,22) through the pier segment to the south end of north-span (19,20).
DL+5.7(LL+I)	-Cracking propagates further
DL+5.9(LL+I)	-Test discontinued

6.5.3 Decompression Load Test of Center-Span. After initially cracking the center joint, three load cycles were applied to the center-span to determine the magnitude of the decompression load. The applied load was increased in $0.54(LL+I)$ increments up to a load level of approximately $2.1(LL+I)$, and then in $0.18(LL+I)$ increments up to a maximum load of $4.1(LL+I)$, or approximately 70 percent higher than the measured decompression load, $2.4(LL+I)$.

The applied load-deflection response was almost identical for all three decompression cycles, and cycle 1 is shown in Fig. 6.7. The measured reactions and the calculated joint-moments are plotted with respect to the applied load in Fig. 6.8. The change in tendon stress due to applied load is shown for all center-span tendons in Fig. 6.9.

APPLIED LOAD vs DEFLECTION

Service Load Tests of Center Span - Pd Cycles

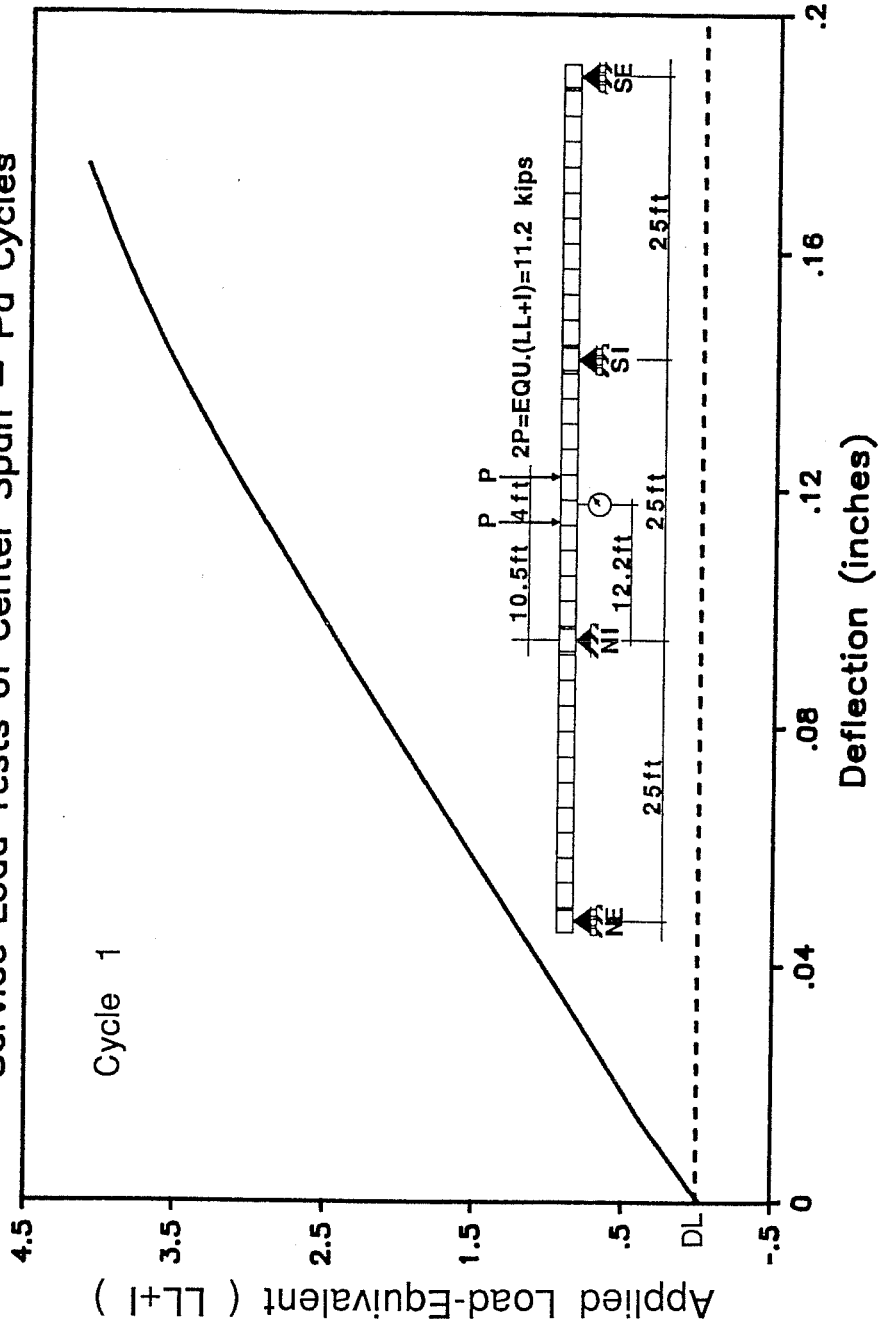


Figure 6.7 Center Span Decompression Cycles: Applied Load vs. Deflection

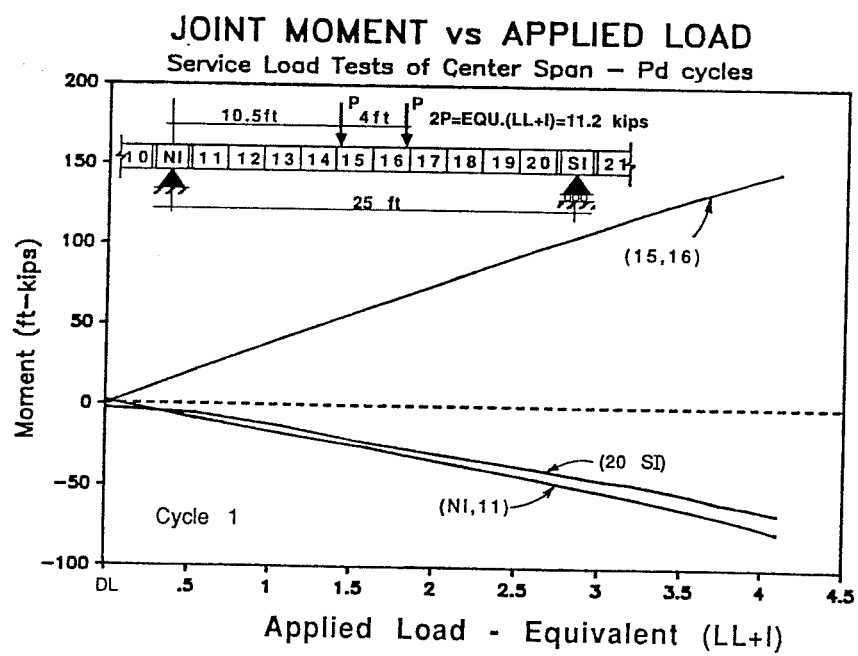
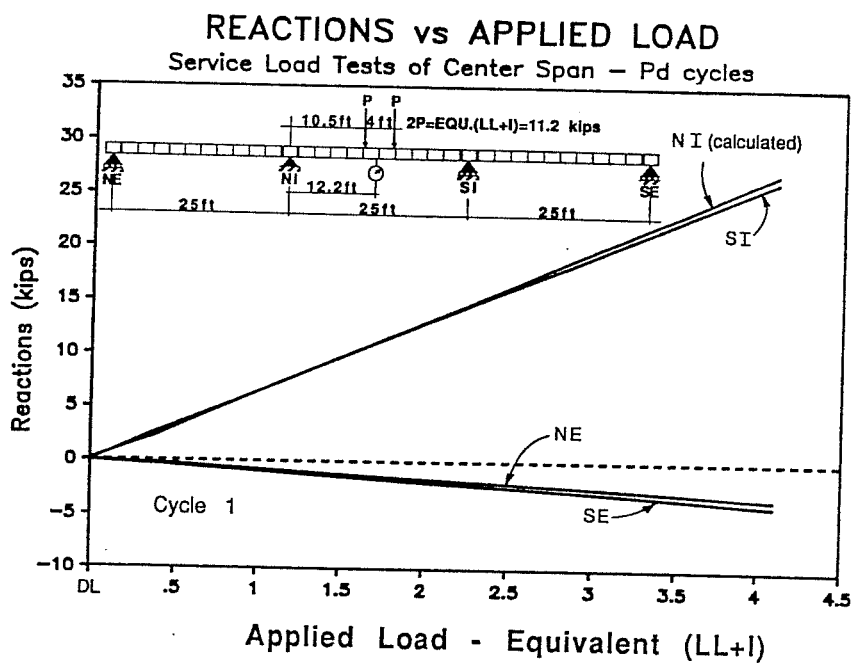


Figure 6.8 Center Span Decompression Cycles: Reactions and Joint Moments

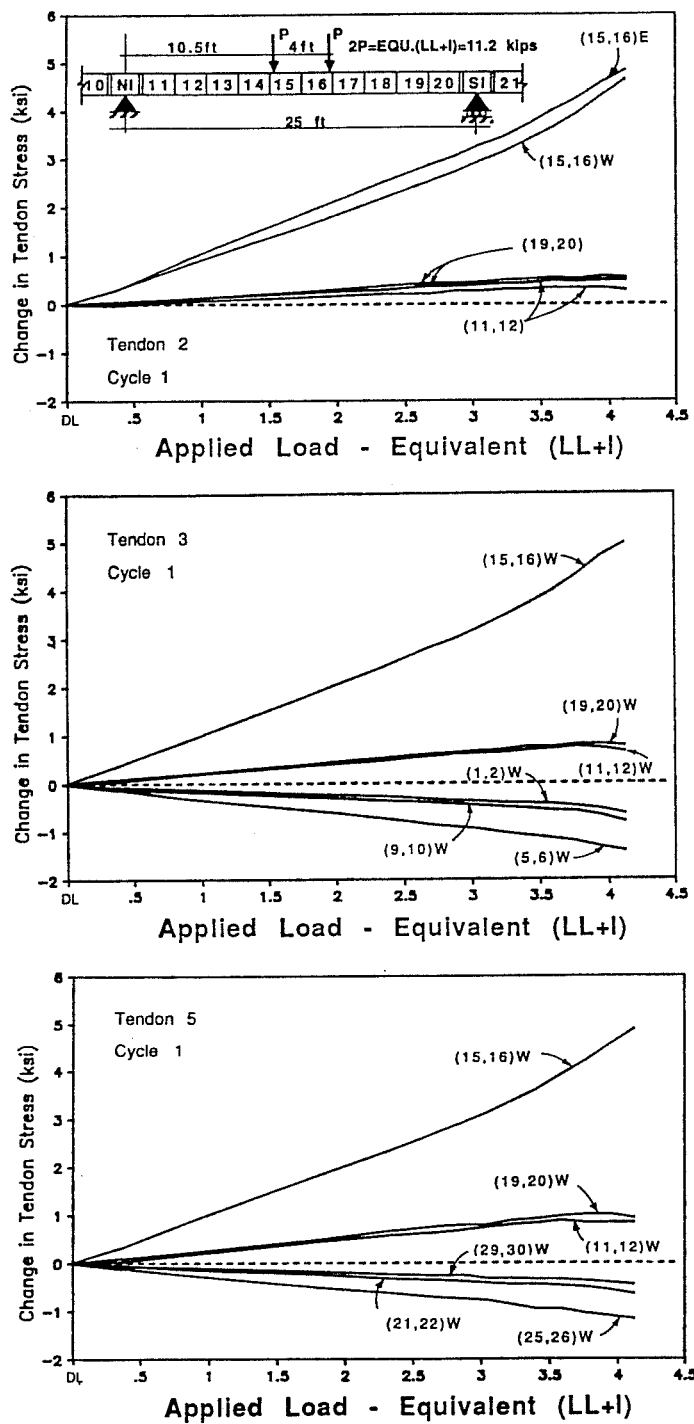


Figure 6.9 Center Span Decompression Cycles: Change in Tendon Stress vs. Applied Load

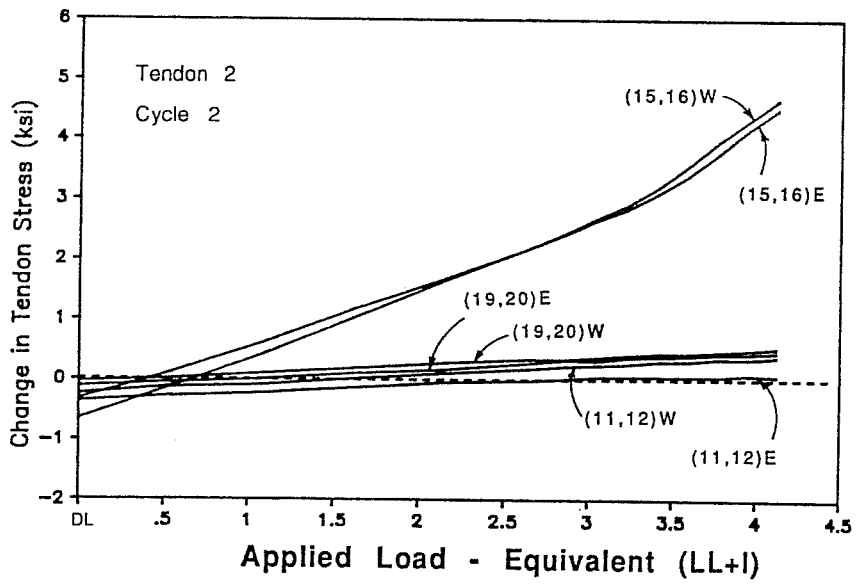
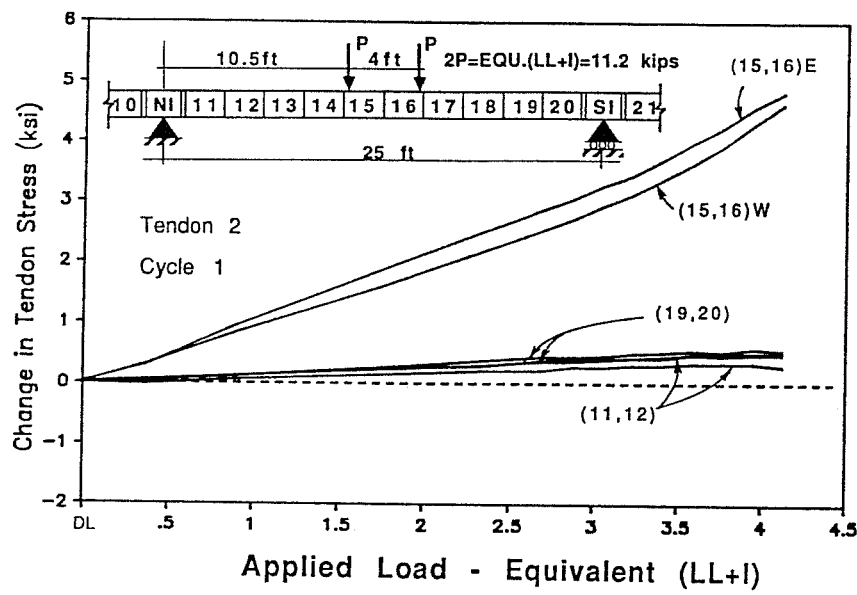


Figure 6.10 Change in Tendon Stress vs. Applied Load: Comparison Between First and Second Cycles

2.4(LL+I) Decompression Load: The structure exhibited linear behavior up to the level of the decompression load, at 2.4(LL+I). Beyond this load, the load-deflection, response reactions, and joint-moment response all diverge from linear behavior. The midspan stiffness reduces as the joint opens under increased loading, causing a larger portion of the load to be carried by negative bending at the supports.

2.8(LL+I): The midspan tendon stresses remained linear up to approximately 2.8(LL+I). Beyond this load level the tendon stresses began to diverge from the linear response at an increasing rate.

4.1(LL+I): The maximum load level reached during the decompression load cycles for the center-span was 4.1(LL+I). The decompression load cycles for the center-span are summarized in Tables 6.5, 6.6, and 6.7.

Table 6.5 Center-span Decompression Cycles - Maximum Response Values

	Decompression Load 2.4(LL+I)	4.1(LL+I)
Deflections	0.09 in. L/3333	0.17 inches L/1764)
Reactions	16 kips at NI and SI	27 kips at NI and SI
Moments M+ve	90 ft-kips at (15,16)	150 ft-kips at (15,16)
M-ve	-40 ft-kips at (NI,11)	-70 ft-kips at (NI,11)

Table 6.6 Center-span Decompression Cycles - Change in Tendon Stress

	Decompression Load 2.4(LL+I)	4.1(LL+I)
Tendon 2:	0 / 2 / 0	.5 / 5 / 0.5
Tendon 3:	.5 / 2 / 0.5	1 / 5 / 1
Tendon 5:	.5 / 2 / 0.5	1 / 5 / 1

key = (11,12)/(15,16)/(19,20)
= north end/midspan/south end

Table 6.7 Summary of Center-span Decompression Cycles

$P_{applied}$:	Description:
DL only	-Start Test ($P_{rams}=0$)
DL+2.4(LL+I)	-Decompression Load
DL+2.8(LL+I)	-The midspan tendon stresses began to deviate from initially linear behavior
DL+4.1(LL+I)	-Maximum applied load

In all tendons of the center-span there appeared to be a small change in stress between the first and second decompression cycles, as shown in Fig. 6.11 for tendon 2. After unloading from the first load cycle there was a net reduction in tendon stress of approximately 0.5 ksi. When the load was reapplied, the tendon stress still increased to the same level as the first cycle. It appears that slip may have occurred at the pier segments during the first cycle causing a reduction of tendon force in cycle 2.

6.6 North-span Load Tests (Dry Jointed)

The north-span was subjected to all levels of loading ranging from design service loads to loads producing ultimate flexural and shear strength.

6.6.1 Service Load Tests of North-Span.

6.6.1.1 Live Load Cycles of North-Span. Four cycles of service live load were applied to the north-span using the load set-up shown in the schematic on Fig. 6.11. The load was applied in 0.16(LL+I) increments for all four cycles. Each of the four cycles provided approximately the same response to the applied loads.

The measured deflected shape of the three span structure is shown in Fig 6.11 for a typical service load cycle. The midspan deflection of 0.053 inches corresponds to a deflection/span ratio of $L/5660$. Also shown is the calculated deflected shape from the elastic analysis (see Section 5.4). The elastic analysis overestimates the measured deflection by approximately 28 percent. The tendon data indicated a live load stress range of about 1 ksi. No tendon slip was noticed at this load level.

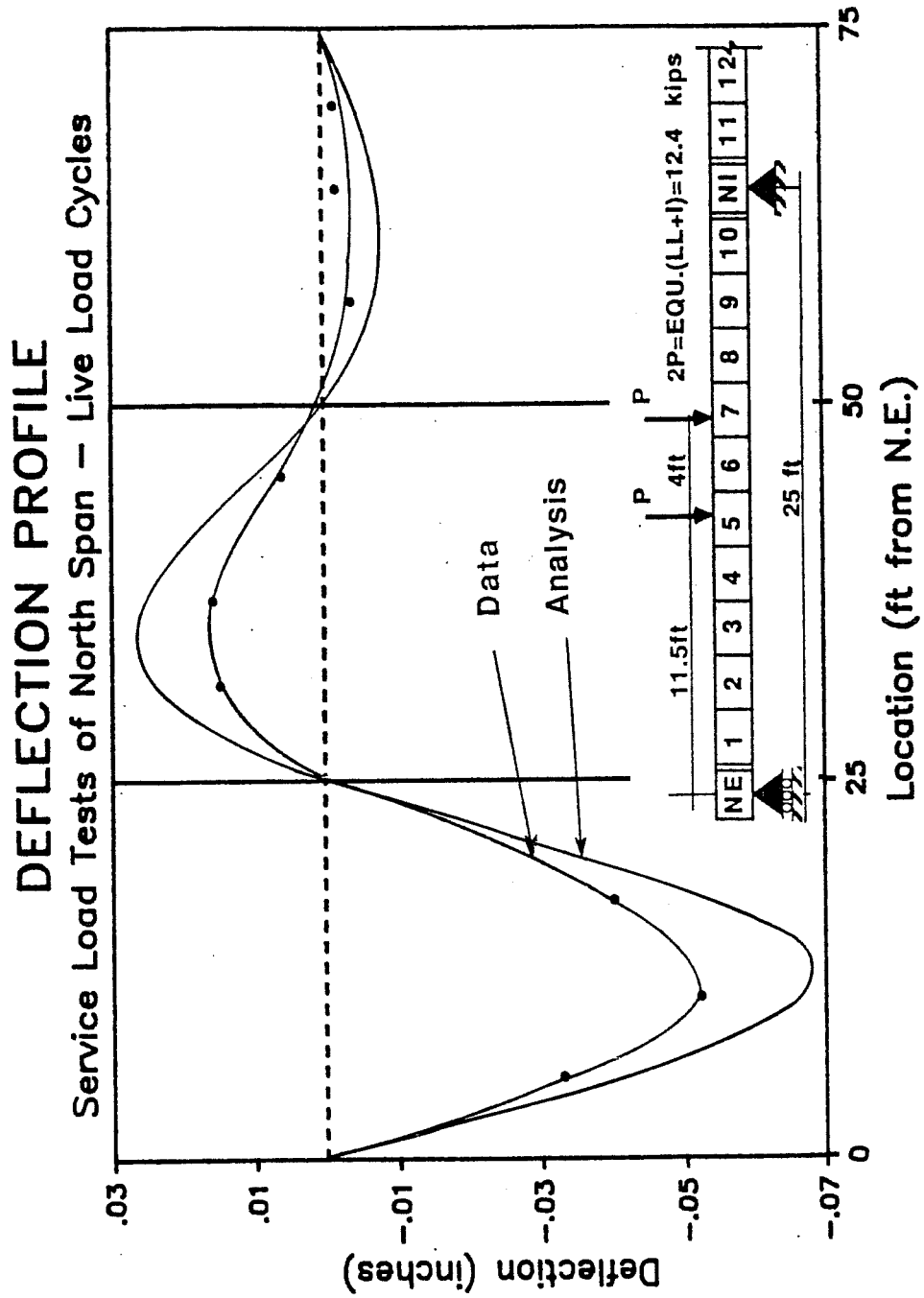


Figure 6.11 North Span Service Load Tests: Deflection Profile

6.6.1.2 Decompression Load Cycles for North-Span. Because the north-span was erected with dry joints it was not necessary to initially crack the span prior to conducting the decompression load tests. A total of six decompression cycles were applied to the north-span. For the first three cycles, a pair of rams was used which displayed erratic behavior possibly caused by higher ram friction. A different pair of rams were used for subsequent tests.

The final three decompression cycles produced more consistent results. The load was applied in $0.32(LL+I)$ increments up to $1.6(LL+I)$, and then in $0.16(LL+I)$ increments up to a maximum load of $2.6(LL+I)$, or approximately 37 percent higher than the measured decompression load of $1.9(LL+I)$.

The applied load-deflection response was identical for all three decompression cycles, and cycle 1 is shown in Fig. 6.12. The measured reactions and the calculated joint-moments are plotted with respect to the applied load in Fig. 6.13.

1.9(LL+I) Decompression Load: The decompression load was estimated to be approximately $1.9(LL+I)$. The structure exhibited bi-linear elastic behavior with a very slight reduction in stiffness for loads above the decompression load.

The reaction and joint moment data show very slight redistribution of internal forces towards the interior support for load levels above the decompression load.

2.6(LL+I): The maximum load level reached during the decompression load cycles for the north-span was $2.6(LL+I)$. The decompression load cycles are summarized in Tables 6.8, 6.9, and 6.10.

Table 6.8 North-span Decompression Cycles - Maximum Response Values

	Decompression Load $1.9(LL+I)$	$2.6(LL+I)$
Deflections	0.10 in. (L/3000)	0.14 inches (L/2143)
Reactions	18 kips at NI	25 kips at NI
Moments M +ve	92 ft-kips at (5,6)	120 ft-kips at (5,6)
M -ve	-56 ft-kips at (NI,11)	-79 ft-kips at (NI,11)

APPLIED LOAD VS DEFLECTION

Service Load Tests of North Span - Pd Cycle

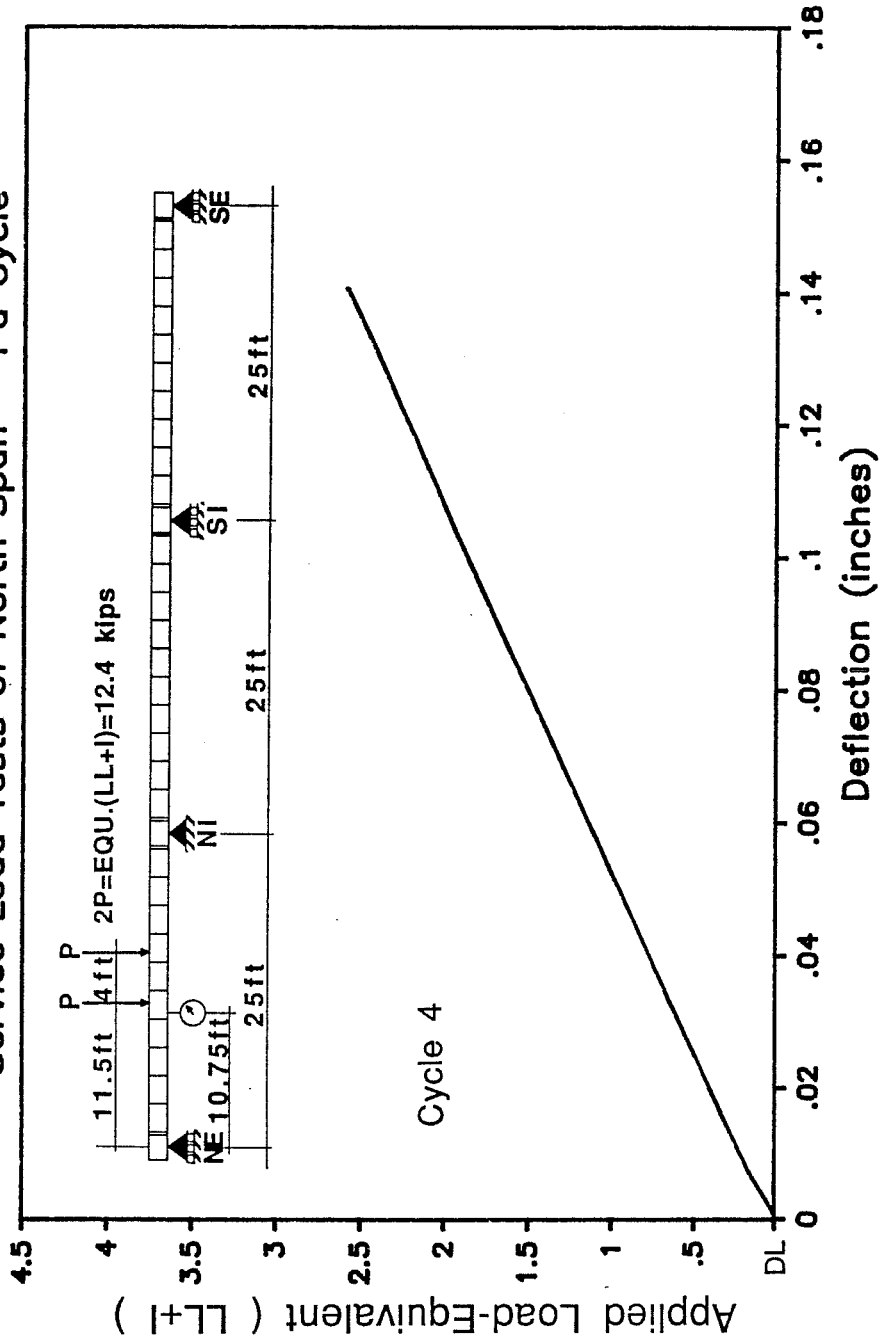


Figure 6.12 North Span Decompression Cycles: Applied Load vs. Deflection

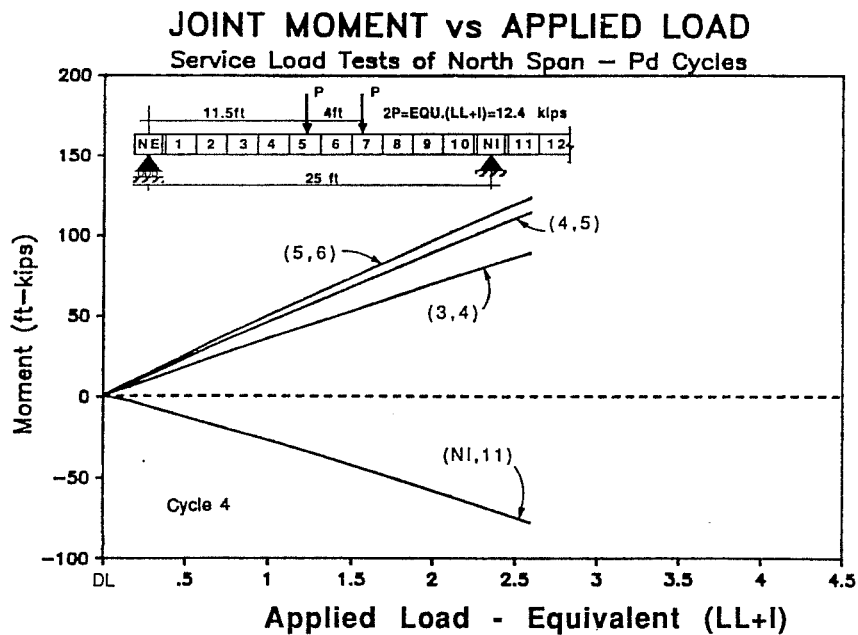
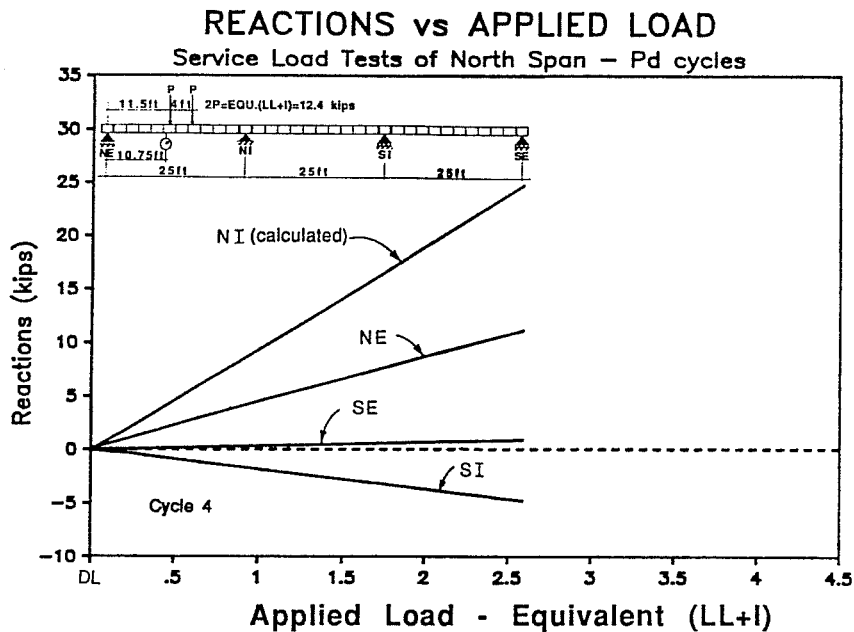


Figure 6.13 North Span Decompression Cycles: Reactions and Joint Moments

Table 6.9 North-span Decompression Cycles - Change in Tendon Stress (ksi)

	Decompression Load	
	1.9(LL+I)	2.6(LL+I)
Tendon 1a:	0 / 2 / 0.5	.5 / 3 / 0.5
Tendon 1b:	.5 / 3 / 0.5	1 / 4 / 1
Tendon 3:	1 / 2 / 1	1 / 3 / 1

key = (1,2)/(5,6)/(9,10)
 = ext.end/midspan/int.end

Table 6.10 Summary of North-span Decompression Cycles

$P_{applied}$:	Description:
DL only	-Start Test ($P_{rams}=0$)
DL+1.9(LL+I)	-Decompression Load
DL+2.6(LL+I)	-Maximum Applied Load

The change in the tendon stresses due to applied load appeared to be linear throughout the entire load cycle, with a maximum stress range of approximately 3.5 ksi at midspan.

6.6.1.3 Torsional Load Cycles. After completing the service load cycles, a final test series was conducted to investigate the torsional response of the structure. The exterior spans were each subjected to three cycles of applied load with the rams positioned directly over the west web. The maximum applied torsional load was representative of a single lane of traffic positioned directly over the west web. The load was applied in 0.16(LL+I) increments to a maximum applied load of 1.0(LL+I).

To measure the torsional response of a structure, rotations must be precisely measured at critical locations along the span. In the model, the rotations were measured by a pair of potentiometers at each support and midspan region, located symmetrically about the longitudinal axis of the structure, as described in Section 3.7. The rotation was calculated from the difference in measured deflection and the spacing between the potentiometers. The magnitude of the measured deflections were very small leading to considerable error in calculating the rotations

at a particular section. In addition, the load cell bearings, described in Section 3.6, were relatively flexible compared with the torsional stiffness of the box-section. This caused the torsional forces to distribute in the girder. Further uncertainty existed because the applied ram-force was less than 5 percent of the ram capacity. Therefore, the only observation that can be made from the torsional test is to confirm that the box-section has very high torsional stiffness.

6.6.2 Factored Load Cycles for North Span. After completing the service load tests of all three spans additional dead weight was erected onto the structure to simulate the factored dead load requirement. Loads were then applied to the dry joint north-span to simulate the factored live-load condition. A total of six factored load cycles were applied to the north-span. For the first three cycles, the load frame configuration (Section 6.2.1.2) induced longitudinal restraint to the top flange of the model. The longitudinal restraining forces induced lateral forces on the ram pistons which may have caused high friction.

The final three factored load cycles, and all subsequent tests, were conducted with a revised load frame which allowed relative movement between ram locations. The load was applied in approximately $0.16(LL+I)$ increments up to the factored design load of $1.3DL+2.86(LL+I)$. The applied load-deflection response was the same for all three factored load cycles, and cycle 1 is shown in Fig. 6.14. The measured reactions and the calculated joint-moments are plotted with respect to the applied load in Fig. 6.15.

1.4(LL+I) Decompression Load: In this case, with the structure preloaded with 30 percent more dead load, less applied force was necessary to cause tension at the extreme fiber. The decompression load is consistent with the previous estimation of the decompression load ($1.9(LL+I)$) determined without the additional dead weight. The difference between these two loads is equal to the test load that produces the same moment at the critical joint as 30 percent of the dead load, which is approximately $0.5(LL+I)$.

2.9(LL+I) Factored Live Load: The span was loaded to the factored live load level of $2.9(LL+I)$. Both the reactions and the calculated joint moments show linear behavior indicating minimal internal force redistribution. All tendons exhibited linear behavior with a maximum stress range at midspan of approximately

APPLIED LOAD vs DEFLECTION

Factored Load Tests of North Span - Pf Cycles

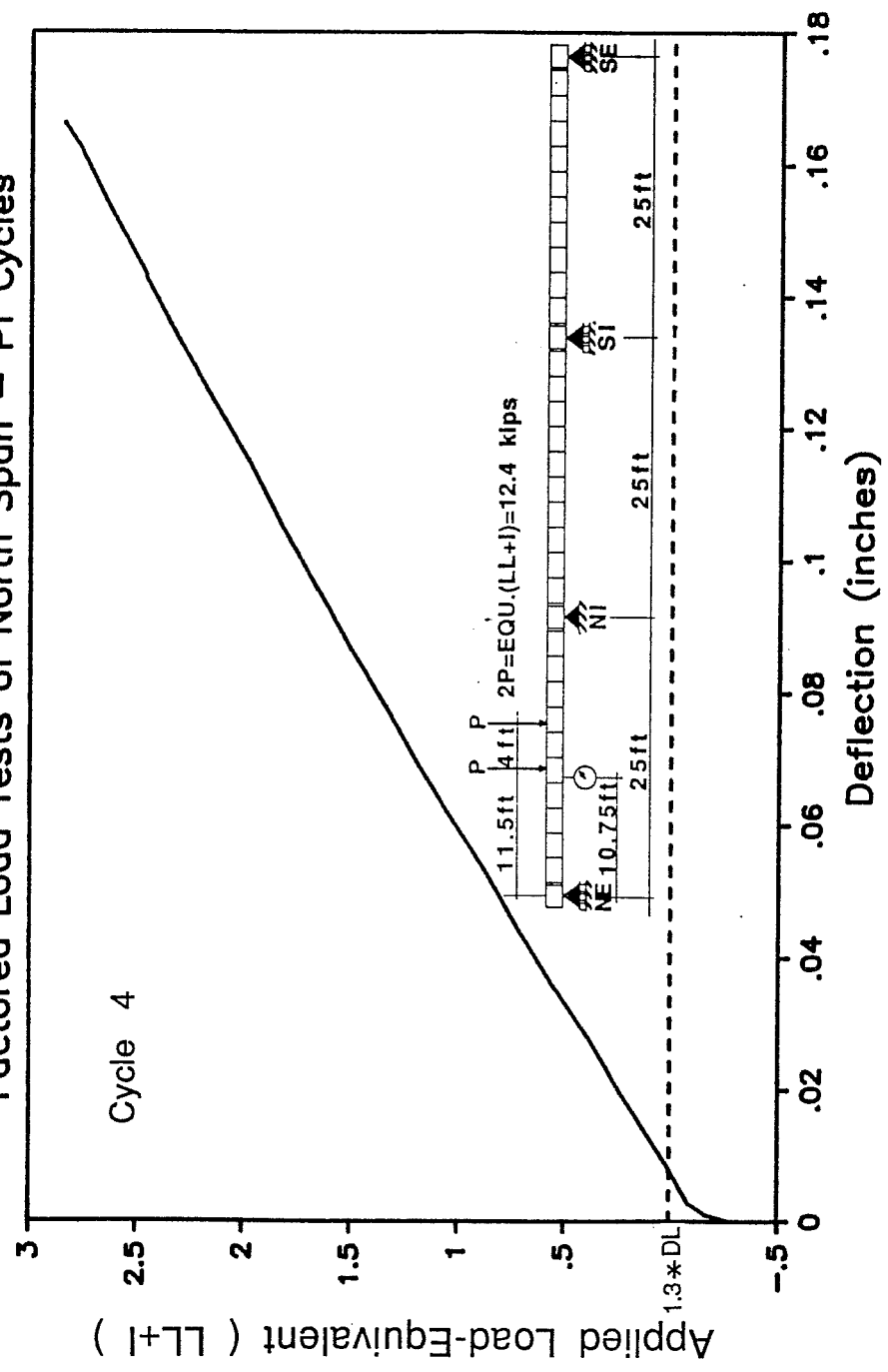


Figure 6.14 North Span Factored Load Cycles: Applied Load vs. Deflection

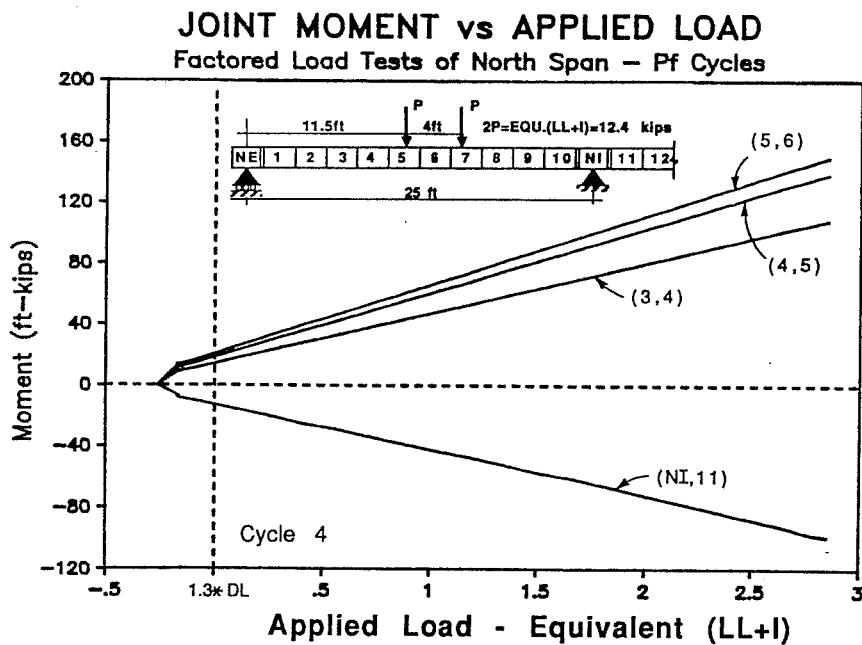
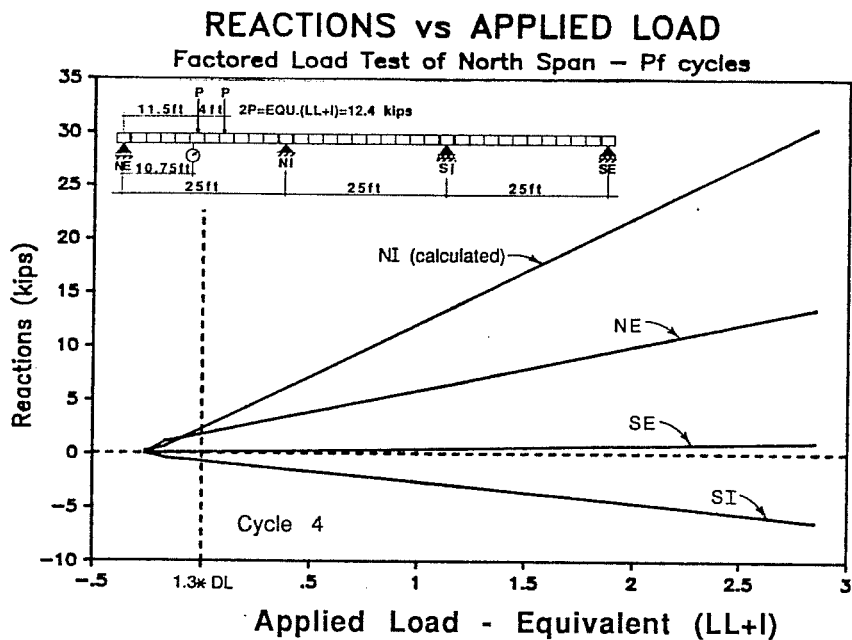


Figure 6.15 North Span Factored Load Cycles: Reactions and Joint Moments

Table 6.11 North Span Factored Load Cycle - Maximum Response Values at Factored Load = $2.9(LL+I)$

Deflections	0.17 inches (L/1764)
Reactions	30 kips at NI
Moments M +ve	150 ft-kips at (5,6)
M -ve	-100 ft-kips at (NI,11)

Table 6.12 North Span Factored Load Cycle - Change in Tendon Stress at Factored Load = $2.9(LL+I)$

	(1,2) ext.end	(5,6) midspan	(9,10) int.end
Tendon 1a:	1	4	1
Tendon 1b:	1	4	1
Tendon 3:	1	4	1

Table 6.13 Summary of North Span Factored Load Cycles

$P_{applied}$:	Description:
1.3DL-0.28(LL+I)	-Start Test ($P_{rams}=0$)
1.3DL	-Start Live Load application from the factored dead load condition
1.3DL+1.4(LL+I)	-Decompression Load
1.3DL+2.9(LL+I)	-Factored Load

4 ksi. The factored load cycles for the north-span are summarized in Tables 6.11, 6.12, and 6.13.

6.6.3 Flexural Strength Tests of North Span

6.6.3.1 Joint Opening Cycles for North Span. Load was then increased beyond factored load levels to investigate the ultimate flexural behavior of the system. The first stage of the flexural strength test was to apply load to the structure to visibly open a midspan joint. Load was applied in $0.32(LL+I)$ increments to the factored load level, $2.9(LL+I)$, and then in $0.16(LL+I)$ increments to a

maximum applied load of $4.7(LL+I)$. The corresponding joint opening at this load level was approximately 0.02 in., which translates into 0.08 in. in the prototype structure.

The applied load-deflection response for all three joint opening cycles is shown in Fig. 6.16. The measured reactions and the calculated joint-moments are plotted with respect to the applied load in Fig. 6.17. The change in tendon stress due to applied load is shown for all north-span tendons in Fig. 6.18. The measured joint openings are plotted with respect to applied load in Fig. 6.19.

1.4(LL+I) Decompression Load: The structure exhibited linear behavior up to the level of the decompression load, at $1.4(LL+I)$. Beyond this load, the load-deflection, reactions, and joint-moment response all diverge from linear behavior as applied load begins redistributing to the interior support.

1.8(LL+I): The midspan region of all the tendons in the north-span exhibited linear response up to approximately $1.8(LL+I)$. For load levels higher than $1.8(LL+I)$ the rate of change in tendon stress increased.

3.0(LL+I): Joints (4,5) and (5,6) began opening at approximately $3.0(LL+I)$. This resulted in rapidly reducing stiffness at midspan, increased deflections, and redistribution of internal forces towards the interior support.

The tendon stresses began increasing at a faster rate as the joint opened further. This increase in force caused Tendon 1a to begin to slip from the midspan region towards both ends of the span.

3.5(LL+I): Tendon 3 began slipping from both ends towards the midspan region.

4.2(LL+I): Slipping in tendon 1a began slowly at $3.0(LL+I)$ until major slip occurred at $4.2(LL+I)$. As tendon 1a slipped freely, the reactions and joint-moments indicated that "hinging" was occurring at the midspan region, and negative moments increased rapidly. Much larger elongations were necessary to develop the same force in the slipping tendon, leading to large rotations at the open joint region. Joints (4,5) and (5,6) opened at a faster rate as shown at the top of Fig. 6.19 for the first joint opening cycle.

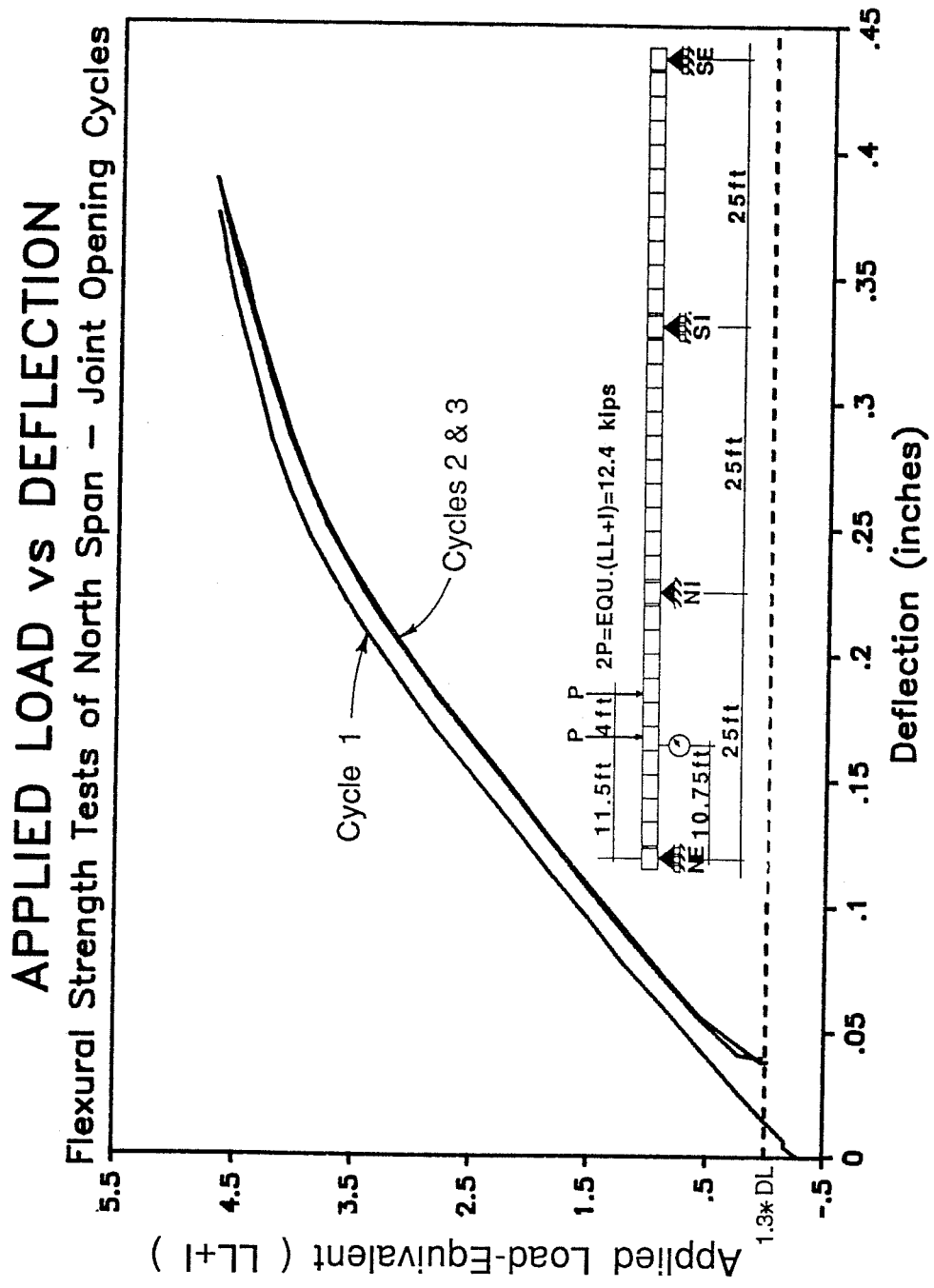


Figure 6.16 North Span Joint Opening Cycles: Applied Load vs. Deflection

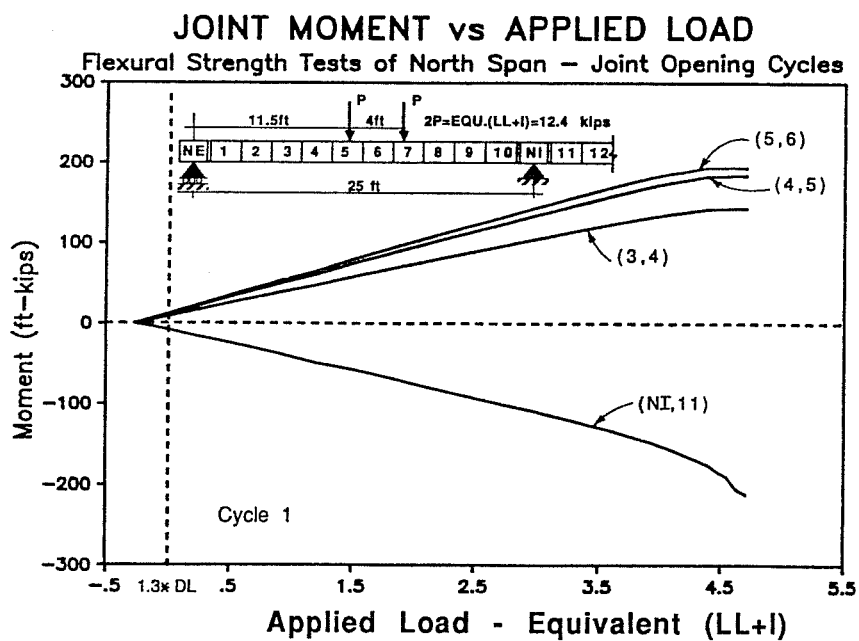
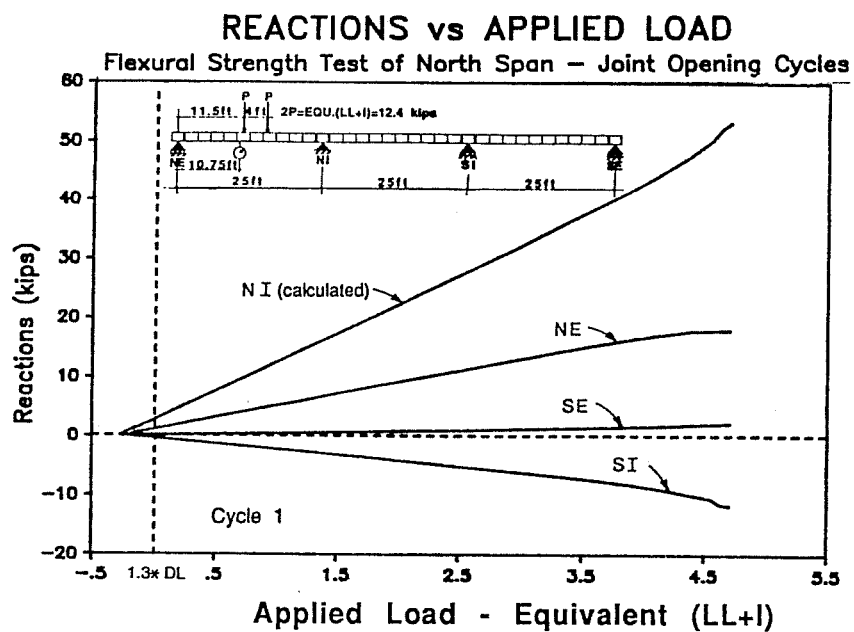


Figure 6.17 North Span Joint Opening Cycles: Reactions and Joint Moments

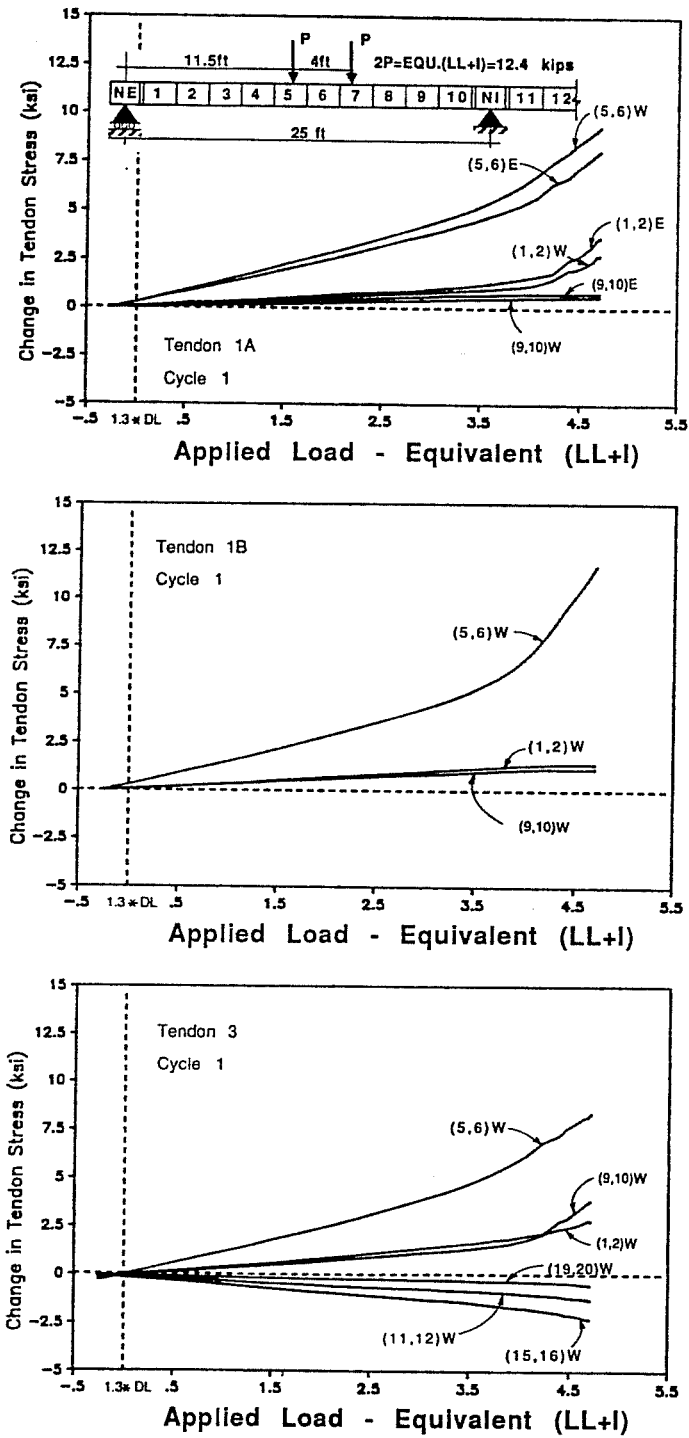
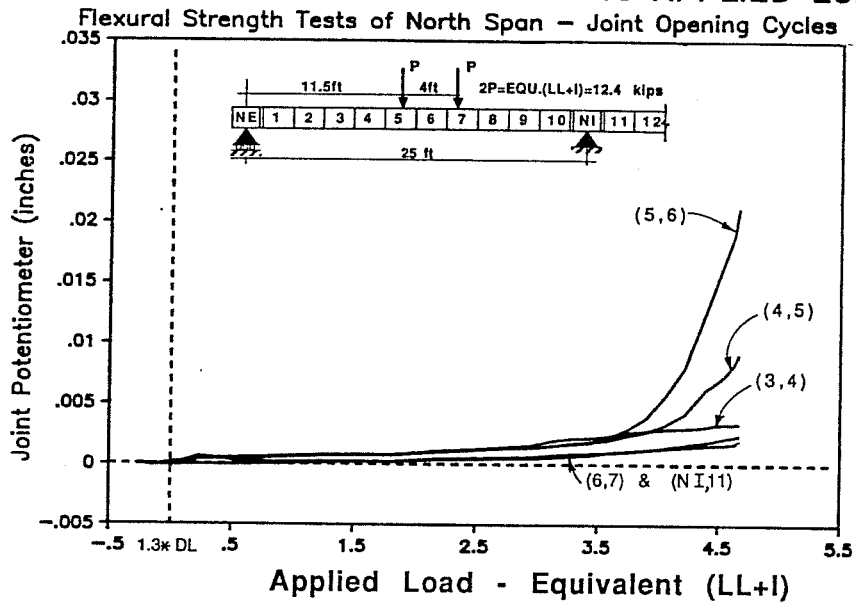


Figure 6.18 North Span Joint Opening Cycles: Change in Tendon Stress vs. Applied Load

JOINT OPENING POTENTIOMETER vs APPLIED LOAD



JOINT OPENING POTENTIOMETER vs APPLIED LOAD

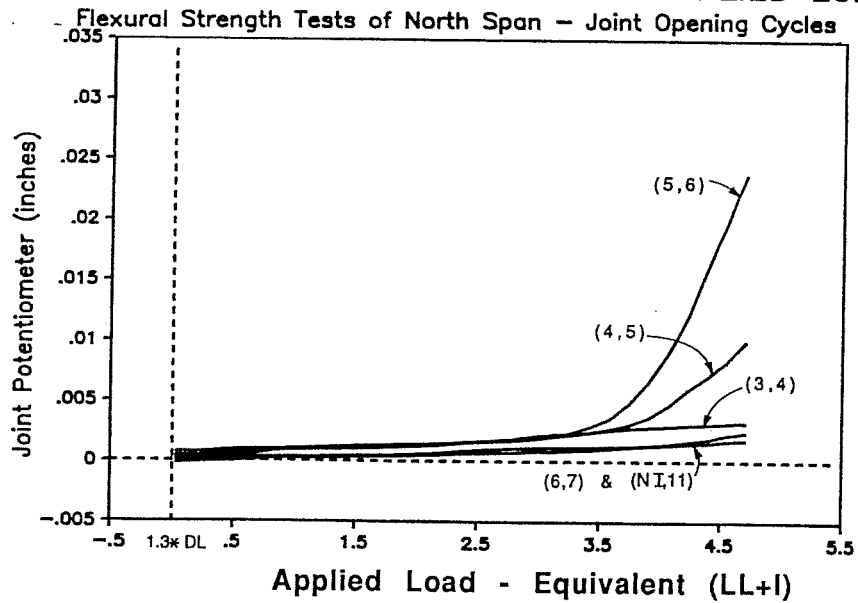


Figure 6.19 North Span Joint Opening Cycles: Joint Opening Potentiometer vs. Applied Load

4.7(LL+I): The applied load was increased until joint (5,6) was visibly open at a maximum load of 4.7(LL+I). The tangent stiffness at the beginning and end of the joint opening cycle was calculated as 18(LL+I)/inch and 5.9(LL+I)/inch, respectively. The joint opening cycles for the north-span are summarized in Tables 6.14, 6.15, and 6.16.

Table 6.14 North Span Joint Opening Cycles - Maximum Response Values at Load = 4.7(LL+I)

Deflections	0.37 inches (L/810)
Reactions	53 kips at NI
Moments M +ve	190 ft-kips at (15,16)
M -ve	-210 ft-kips at (NI,11)

Table 6.15 North Span Joint Opening Cycles - Change in Tendon Stress at Load = 4.7(LL+I)

	(1,2) ext.end	(5,6) midspan	(9,10) int.end
Tendon 1a:	4 *	10	1
Tendon 1b:	2	12	2
Tendon 3:	3 *	9 *	4

* denotes slip towards midspan

As mentioned above, tendon slip was noticed in tendons 1a and 3 during the first decompression load cycle. The applied load-tendon stresses are shown for the first two joint opening cycles in Fig. 6.20. The tendon stresses were set equal to zero at the start of the first cycle. After applying one cycle of load there was a net change in tendon stress at the start of the second cycle. The exterior-end stresses had increased and the midspan stresses had decreased. This is also illustrated by the tendon stress profile (Fig. 6.21) for the unloaded condition preceding each load cycle. With slip occurring towards the midspan section of the tendon, the “unstressed” length of that portion had increased, leading to decreased tendon stresses when the applied load was removed. Conversely, because the tendon had slipped away from

Table 6.16 Summary of North Span Joint Opening Cycles

$P_{applied}$:	Description:
1.3DL-0.28(LL+I)	-Start Test ($P_{rams}=0$)
1.3DL	-Start Live Load application from the factored dead load condition
1.3DL+1.4(LL+I)	-Decompression Load
1.3DL+1.8(LL+I)	-The midspan stresses of all the tendons begin to increase at a faster rate
1.3DL+3.0(LL+I)	-Joints (4,5) and (5,6) begin to open widely causing tendon stresses to increase at a faster rate -Tendon 1a begins to slip slowly from both ends towards the midspan region
1.3DL+3.5(LL+I)	-Tendon 3 begins to slip from both ends towards the midspan region.
1.3DL+4.2(LL+I)	-Tendon 1a begins to slip rapidly from the midspan section towards both ends. The resultant elongations cause "Hinging" to occur at midspan.
1.3DL+4.7(LL+I)	-Maximum Load for Joint Opening Cycles

the exterior region the "unstressed" length had decreased leading to increased tendon stresses when the applied load was removed.

The slip that occurred in the first cycle also changed the distribution of moments in subsequent cycles. Figure 6.22 is a comparison between the joint moments in the first two joint-opening cycles. In the first cycle, described above, the structure appears to hinge at the midspan region at approximately 4.2(LL+I). In subsequent cycles to the same load level the moment increased smoothly throughout the load cycle with a maximum moment equal to the first cycle.

The slip in the tendons during the first cycle also changed the behavior of the opening joints. In the first cycle, shown at the top of Fig. 6.19, the critical joint (5,6) (as predicted by the plastic mechanism analysis in Section 5.2) opened 0.021 inches, while the adjacent joint (4,5) opened 0.010 inches. All other joints remained visibly closed, with joint (3,4) measuring 0.003 inches. In the second cycle, shown at the bottom of Fig. 6.19, joint (5,6) opened widely at a lower load level and reached a

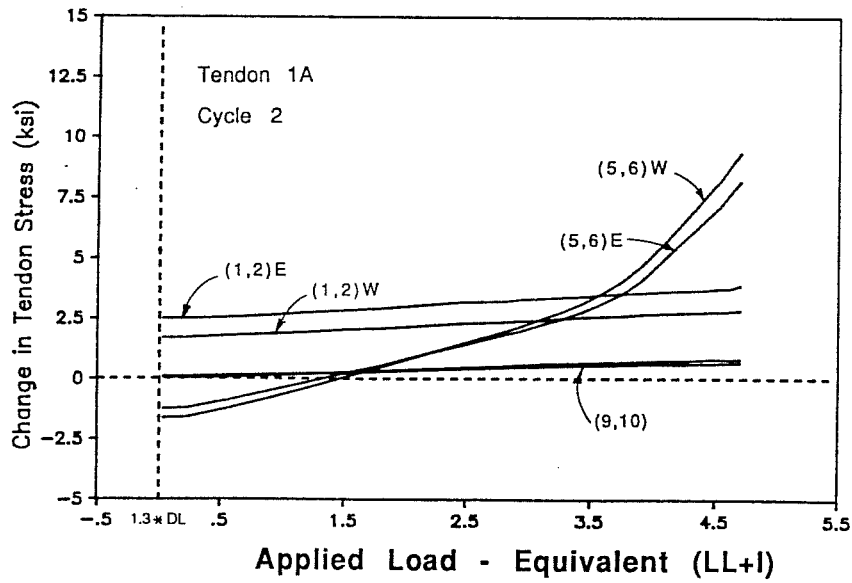
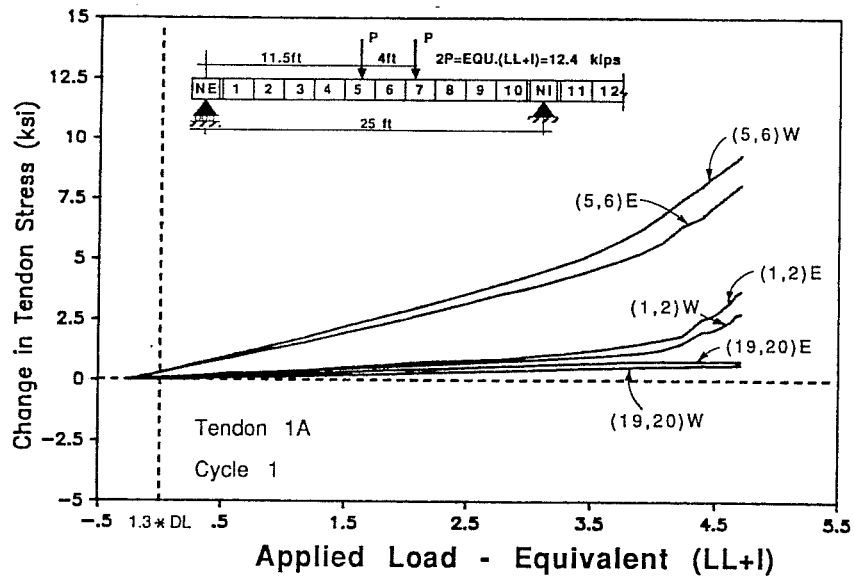


Figure 6.20 North Span Joint Opening Cycles: Comparison of Tendon Stresses of Cycles 1 & 2

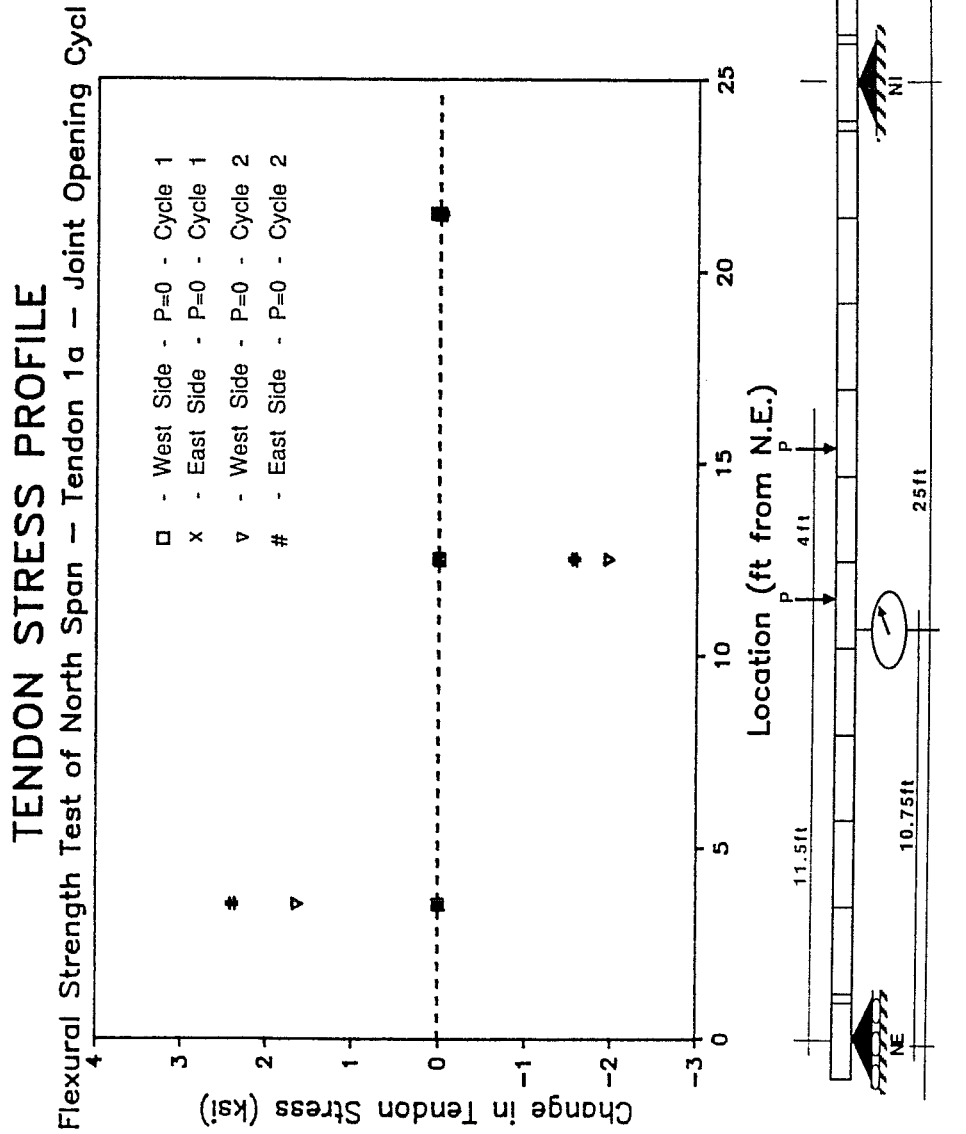


Figure 6.21 North Span Joint Opening Cycles: Tension Stress Profile

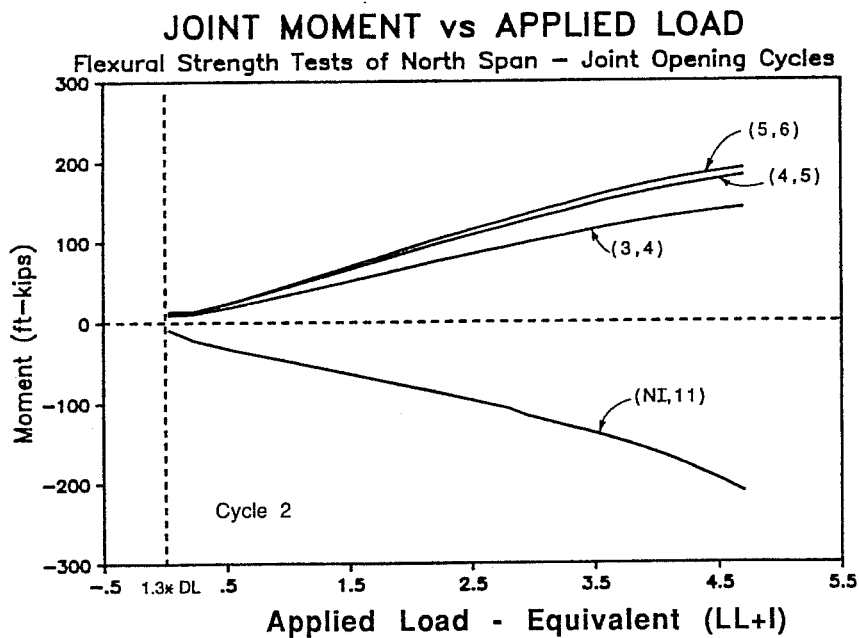
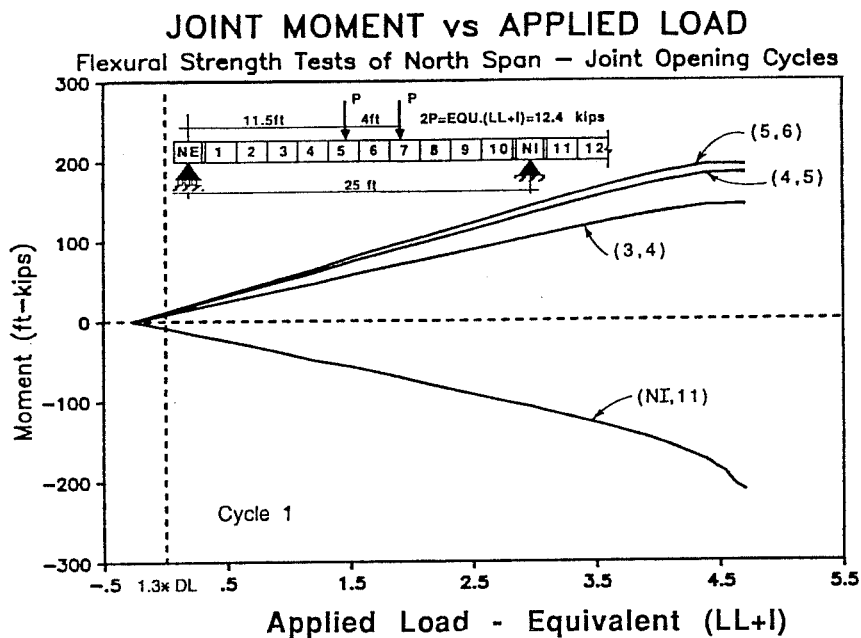


Figure 6.22 North Span Joint Opening Cycles: Comparison of Joint Moments for Cycles 1 & 2

higher maximum opening of 0.025 inches. joint (4,5) displayed more gradual opening to a maximum opening of 0.011 inches.

No cracking was visible in the concrete following the north-span joint-opening tests.

6.6.3.2 Flexural Strength Cycles for North Span. After completing the joint-opening cycles, the structure was loaded to higher levels to determine the flexural strength of the system. Because the strength of the structure could not be precisely determined, and because of the possible brittle nature of the failure mode, the load was increased above the previous joint opening load levels in very small increments (0.04 to 0.08(LL+I)). Subsequently, due to time constraints, the ultimate flexural strength test for the north-span was conducted in three sessions, each time to a higher load level. The flexural strength of the north-span (defined as when the tangent stiffness of the load-deflection response was reduced to 4% of the initial elastic stiffness) was measured to be 6.8(LL+I) with an ultimate midspan deflection of 1.62 inches.

The applied load-deflection response for all three flexural strength cycles is shown in Fig. 6.23 and the last cycle alone is shown in Fig. 6.24. The measured reactions and the calculated joint-moments for the ultimate cycle are plotted with respect to the applied load in Fig. 6.25. The change in tendon stress due to applied load is shown for all north-span tendons in Fig. 6.26. Because the critical negative-moment joint occurs on the interior side of the first interior pier segment (see plastic mechanism in analysis in Section 5.2), the change in tendon stress due to applied load is shown for all center-span tendons in Fig. 6.27. The joint behavior, as measured by potentiometer and grid crack-monitors, is illustrated in Fig. 6.28.

Response of the structure at load stages corresponding to 1.4(LL+I), 1.8(LL+I), and 3.0(LL+I) was essentially the same as that measured in the previous joint-opening cycles.

3.8(LL+I): Joint (4,5) began opening at approximately 3.8(LL+I) causing the tendon stresses in the midspan sections of tendons 1a and 1b to begin increasing at a faster rate. Tendon 3 began slipping from both ends towards the midspan region.

APPLIED LOAD vs DEFLECTION

Flexural Strength Tests of North Span – Ultimate Cycle

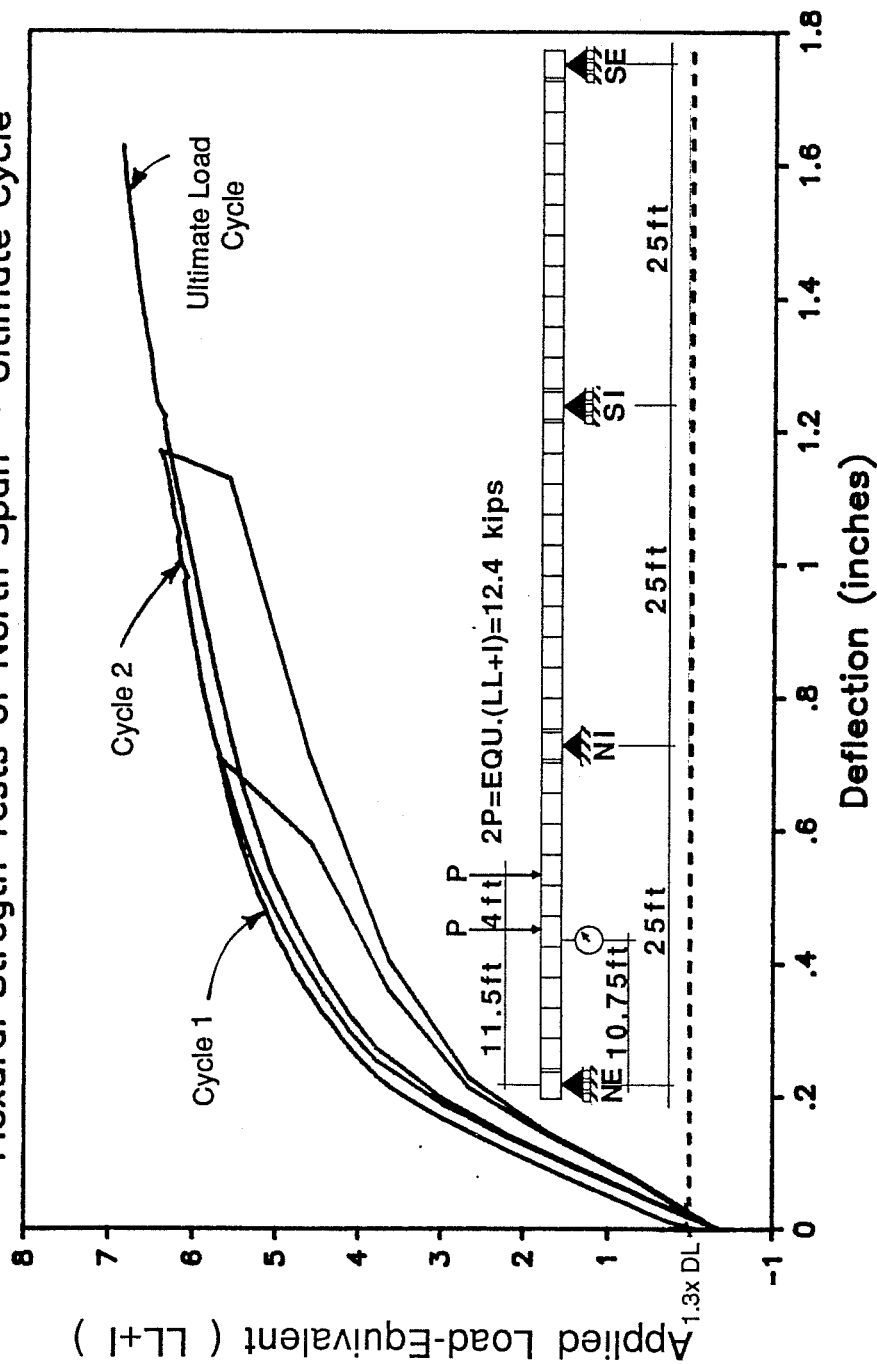


Figure 6.23 North Span Flexural Strength Test: Applied Load vs. Deflection

APPLIED LOAD VS DEFLECTION

Flexural Strength Tests of North Span – Ultimate Cycle

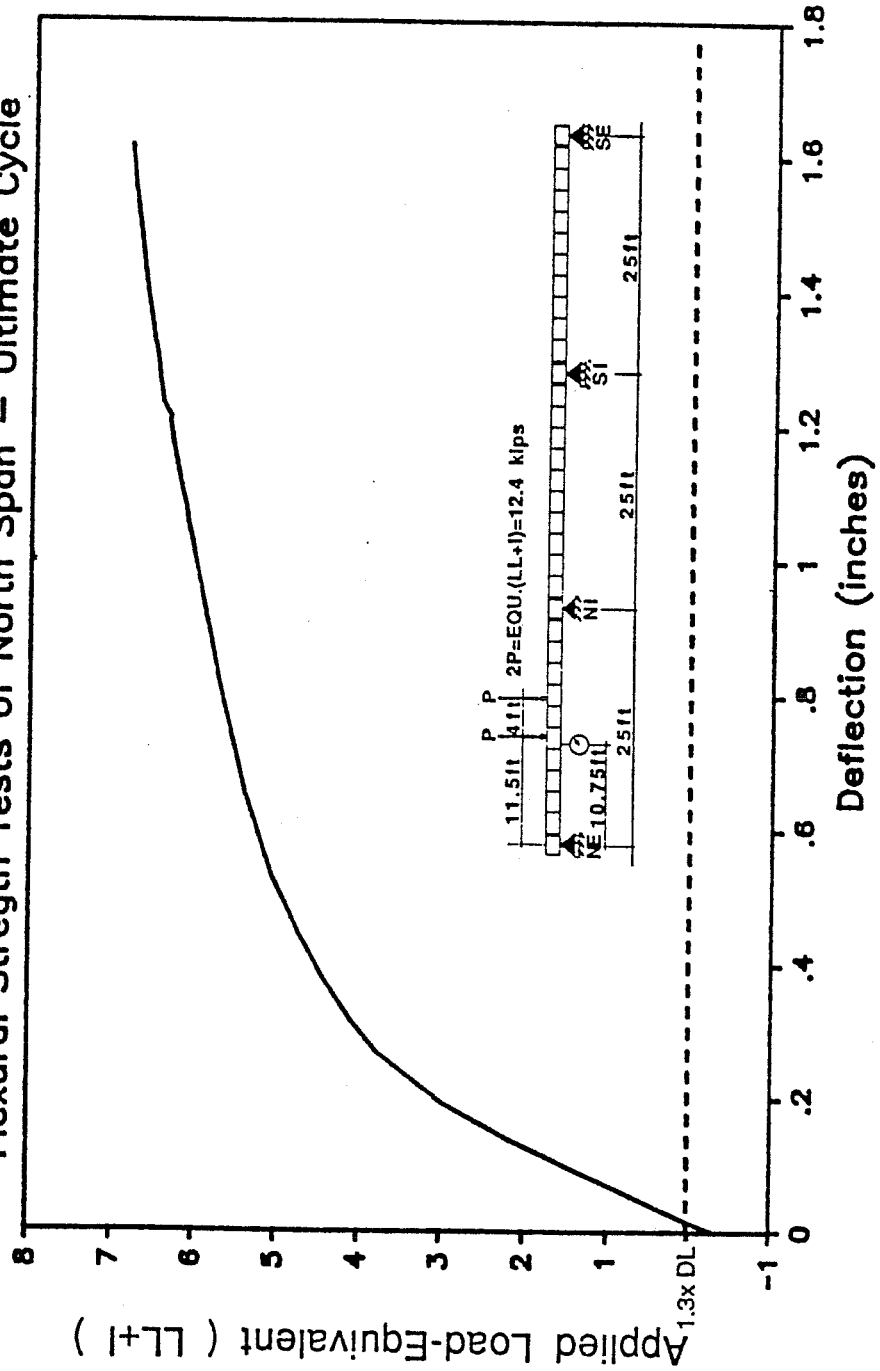


Figure 6.24 North Span Flexural Strength Tests: Applied Load vs. Deflection

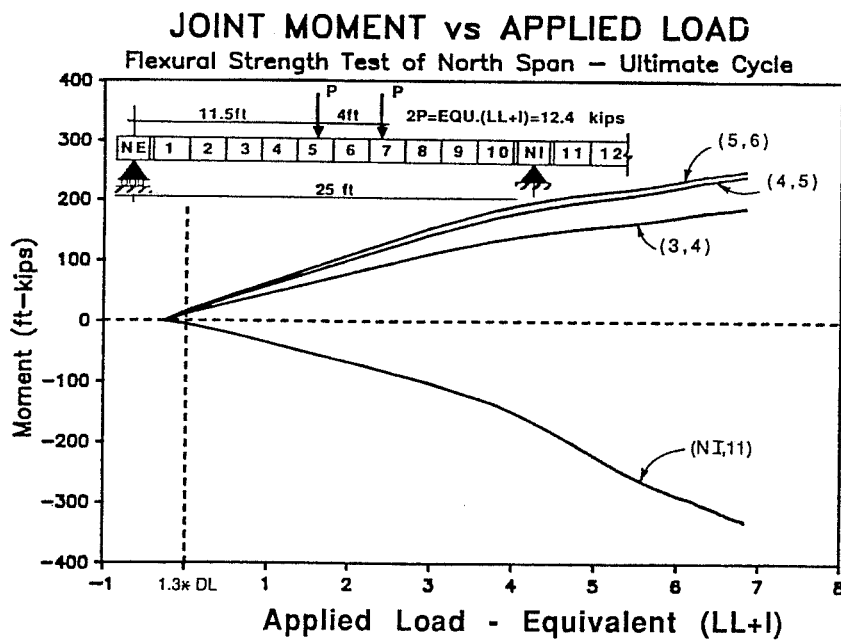
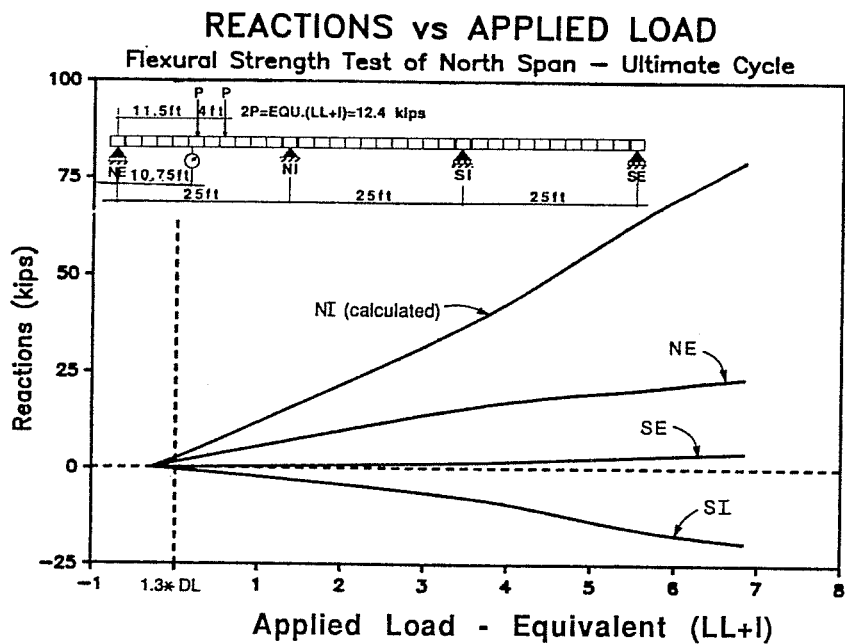


Figure 6.25 North Span Flexural Strength Tests: Reactions and Joint Moments

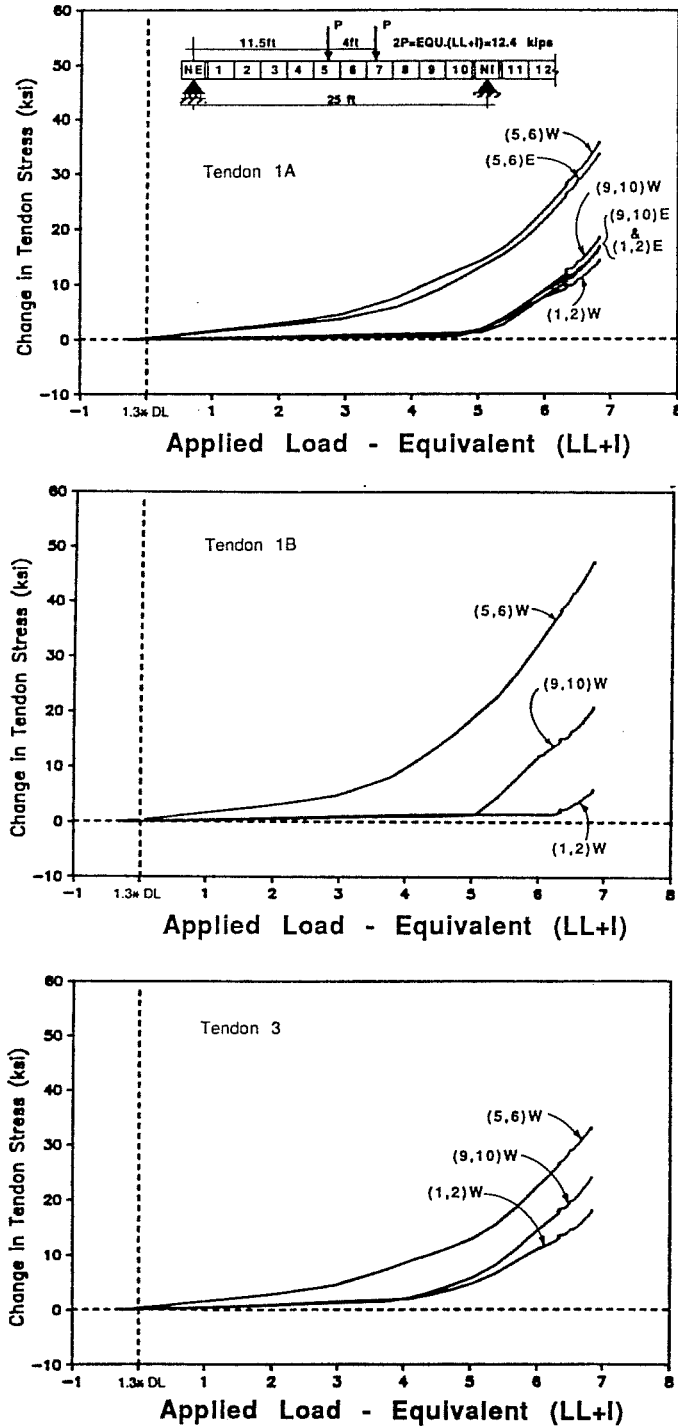


Figure 6.26 North Span Flexural Strength Tests: Change in Tendon Stress vs. Applied Load (North-Span Tendons)

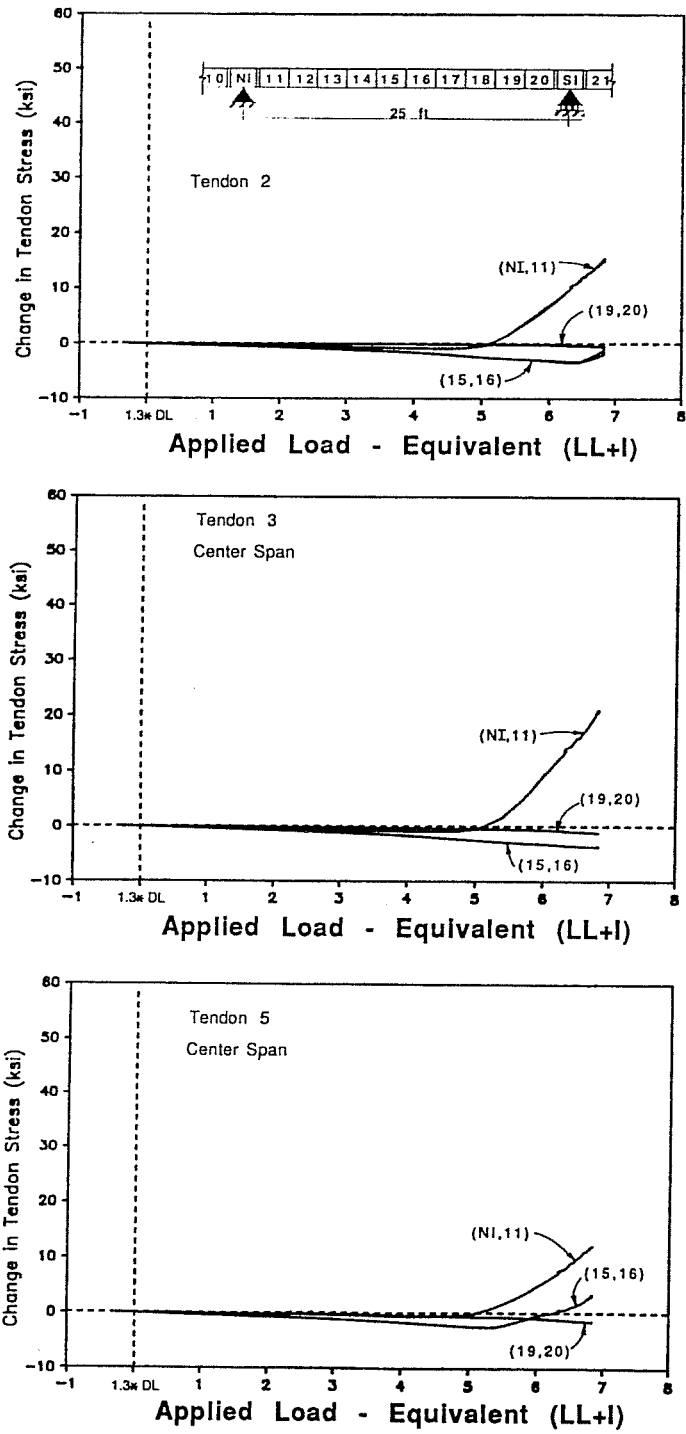
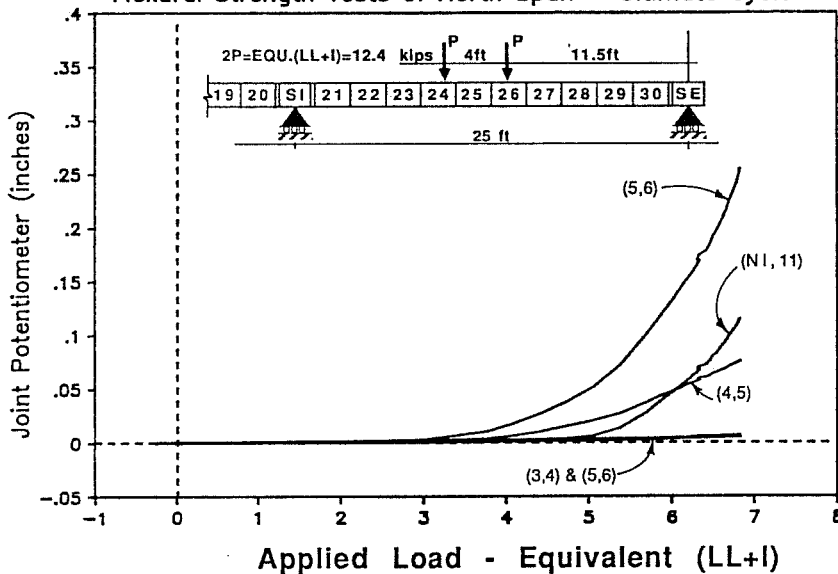


Figure 6.27 North Span Flexural Strength Tests: Change in Tendon Stress vs. Applied Load (Center-Span Tendons)

JOINT OPENING POTENTIOMETER vs APPLIED LOAD

Flexural Strength Tests of North Span - Ultimate Cycle



JOINT OPENING PROFILES

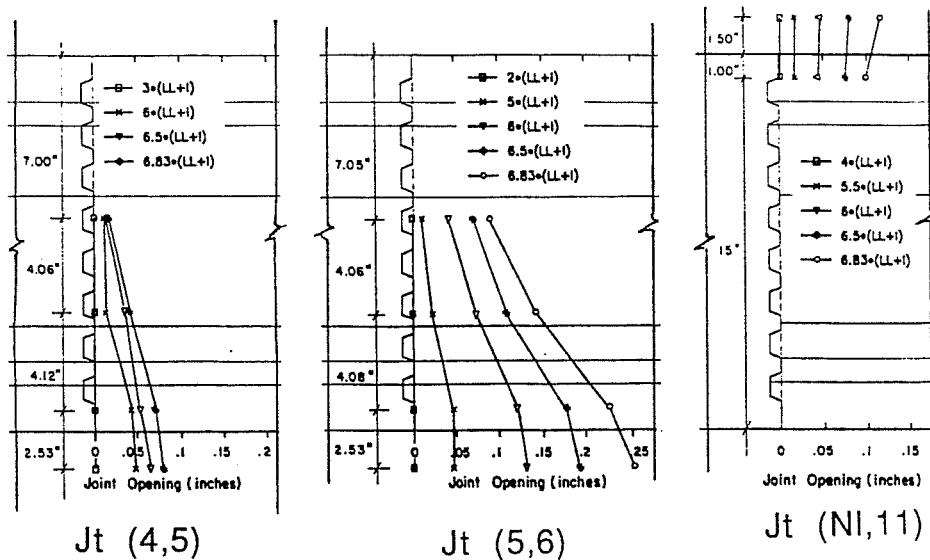


Figure 6.28 South Span Flexural Strength Tests: Joint Opening Behavior

4.8(LL+I): The support joint, (NI,11) began opening at approximately 4.8(LL+I). This shows up as the inflection point in the reaction and moment data (Fig. 6.26) indicating that the reduced stiffness at the support caused a redistribution of internal forces back towards the midspan region.

All the tendon stresses at the near end of the interior span (tendons 2, 3, and 5) increased as the support joint began opening at approximately 4.8(LL+I). Tendon 1a began slipping from both ends towards the midspan region.

5.0(LL+I): The support joint opened further, reducing stiffness at the support and redistributing the internal forces towards the midspan region. Tendon 1b began slipping from the interior end (9,10) towards the midspan region.

5.3(LL+I): Tendon 5 (interior span) began slipping from the midspan region towards the near end (11,12) of the interior span.

6.2(LL+I): Tendon 1b began slipping from the exterior end (1,2) towards the midspan region. Slipping continued from the interior end as well.

6.4(LL+I): Tendon 2 (Interior span) began slipping from the midspan region towards the near end (11,12) of the interior span.

6.8(LL+I) **Flexural Strength:** The test was discontinued before catastrophic failure when crushing was noticed on the top of a key in joint (5,6) (Fig. 6.29), and the tangent stiffness had reduced to 4 percent of the initial elastic stiffness. The tangent stiffness for increasing levels of applied live load was calculated from the load deflection curve, and is tabulated in Table 6.17. The flexural strength cycles for the north-span are summarized in Tables 6.18, 6.19, and 6.20.

The applied load-deflection response during the first two ultimate load cycles are also shown on Figure 6.23. The unloading portions of these cycles have also been shown. The structure exhibited non-linear elastic behavior with very small permanent deformations after loading to 82% and 93% of the ultimate strength. This was noticed for all cycles of testing with small permanent deformations caused by cracking and tendon slip.

The measured deflected shapes of the three-span structure for increasing levels of applied load are shown in Fig 6.30. At the service load (1.0(LL+I)) and the factored load (2.9(LL+I)) the deflections are small and the deflected shape is a

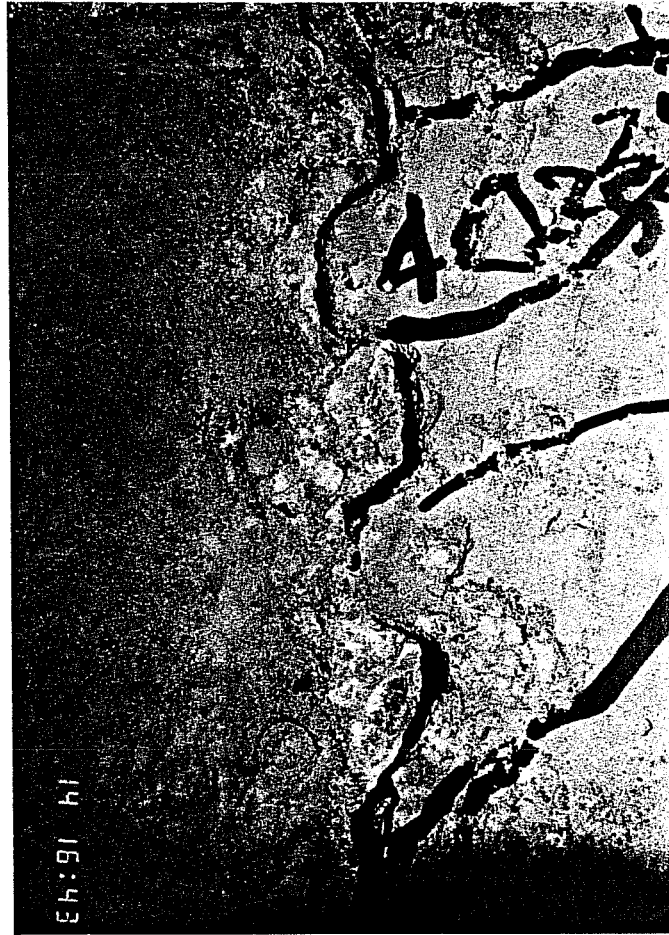


Figure 6.29 North Span Flexural Strength Test: Crushing on Top of Key at Joint smooth curve. The deflected shape remains smooth until the midspan joints begin to open at $3.0(LL+I)$. Beyond this load, “hinging” occurs at the opening joints, and the midspan deflections increase considerably. When the support joint opens at $4.8(LL+I)$ the mechanism forms and deflections begin to increase very rapidly. The final deflected shape of the structure clearly illustrates the mechanism behavior of the structure at ultimate load levels.

The reaction and joint-moment curves exhibit double curvature (slight S-shape). As the midspan joints open, the midspan stiffness reduces causing internal

Table 6.17 Instantaneous Stiffness During North-Span Tests (measured in (LL+I)/inch)

Applied Load	Flexural Test	Shear Test
1(LL+I)	18	18
2(LL+I)	16	17
3(LL+I)	13	11
4(LL+I)	6.2	4.7
5(LL+I)	4.3	3.1
6(LL+I)	1.6	1.3
6.8(LL+I)	.76	N/A
7.2(LL+I)	N/A	.82

Table 6.18 North Span Flexural Strength Cycles - Maximum Response Values - Flexural Strength Load = 6.8(LL+I)

Deflections	1.62 inches (L/185)
Reactions	82 kips at NI
Moments M +ve	250 ft-kips at (5,6)
M -ve	-320 ft-kips at (NI,11)

Table 6.19 North Span Flexural Strength Cycles Change in Tendon Stress (ksi) - Flexural Strength Load = 6.8(LL+I)

Exterior Span Tendons	Interior Span Tendons
Tendon 1a: 15 * 36 * 19	Tendon 2: 15 ** 0 / <0
Tendon 1b: 7 * 48 * 21	Tendon 3: 21 / ;0 / <0
Tendon 3: 18 * 33 * 25	Tendon 5: 12 ** 3 / <0
*denotes slip towards midspan key = (1,2)/(5,6)/(9,10) = ext.end/midspan/int.end	**denotes slip towards near end key = (11,12)/(15,16)/(19,20) = near end/midspan/far end

Table 6.20 Summary of North Span Flexural Strength Cycle

<i>P_{applied}</i> :	Description:
1.3DL-0.28(LL+I)	-Start Test ($P_{rams}=0$)
1.3DL	-Start Live Load application from the factored dead load condition
1.3DL+1.4(LL+I)	-Decompression Load
1.3DL+1.8(LL+I)	-Midspan tendon stresses begin to diverge from linear behavior.
1.3DL+3.0(LL+I)	-Joints (4,5) and (5,6) begin to open widely causing Reactions, Joint Moments and Tendon stresses to increase at a higher rate
1.3DL+3.8(LL+I)	-Tendon 3 (north-span) began slipping from both ends towards the midspan region
1.3DL+4.8(LL+I)	-The support joint begins to open causing the near-end interior-span tendon stresses to begin to increase -Tendon 1a began slipping from both ends towards the midspan section
1.3DL+5.0(LL+I)	-Support joint (NI,11) begins to open widely -Tendon 1b began slipping from the interior end towards the midspan region.
1.3DL+5.3(LL+I)	-Tendon 5 (interior span) began slipping from the midspan region towards the near end of the interior span
1.3DL+6.2(LL+I)	-Tendon 1b began slipping from the exterior end towards the midspan region
1.3DL+6.4(LL+I)	-Tendon 2 (interior span) began slipping from the midspan region towards the near end of the interior span
1.3DL+6.8(LL+I)	-Flexural Strength

Table 6.21 North Span Shear Test - Maximum Response Values -Shear Strength Load = 7.2(LL+I)

Deflections	2.19 inches (L/137)
Reactions	74 kips at NI
Moments M +ve	250 ft-kips at (5,6)
M -ve	-380 ft-kips at (NI,11)

Table 6.22 North Span Shear Test - Change in Tendon Stress -Shear Strength Load = 7.2(LL+I)

Exterior Span Tendons	Interior Span Tendons
Tendon 1a: 25 * 42 * 22	Tendon 2: 20 ** 0 / 0
Tendon 1b: 8 * 59 * 30	Tendon 3: 27 ** -1 / 0
Tendon 3: 27 * 41 * 30	Tendon 5: 15 ** 5 * 0.5
* denotes slip towards midspan key = (1,2)/(5,6)/(9,10) = ext.end/midspan/int.end	** denotes slip towards near end key = (11,12)/(15,16)/(19,20) = near end/midspan/far end

forces to redistribute towards the support. When the support joint opens, the support stiffness reduces and internal forces are redistributed back towards midspan.

The concentrated rotations that occurred at critical opening joints were measured with manually recorded crack-monitors distributed over the height of the joint, as described in Section 3.9. A profile of each opening joint during the flexural test of the north-span is shown at the bottom of Fig. 6.28. Large rotations occurred at two midspan joints (joints (4,5) and (5,6)), and one support joint (joint (NI,11)). The measured profiles indicate that the joint opened linearly with the compressive stresses gradually concentrating in the top flange. The neutral axis for all ultimate load cases can be extrapolated from the joint profiles, and was within the compression flange at all opening joints.

The concentrated angle changes that occurred at each joint mechanism can be roughly calculated from the joint opening profiles. The concentrated rotations that occurred at the midspan joints were approximately 0.3 degrees at joint (4,5) and 0.9 degrees at the primary joint mechanism (5,6) for a total midspan concentrated angle change of approximately 1.2 degrees. The concentrated angle change that occurred at the support joint (NI,11) was approximately 0.4 degrees. The total midspan angle change was approximately three times the magnitude of the concentrated angle change at the support. This is roughly consistent with the plastic mechanism rotations that occur in a propped cantilever beam, shown in Fig. 6.31, which for ideal conditions would predict the midspan-to-support angle changes of

Table 6.23 Summary of North-Span Shear Test

$P_{applied}$:	Description:
1.3DL-.30(LL+I)	-Start Test ($P_{rams}=0$)
1.3DL	-Start Live Load application from the factored dead load condition
1.3DL+1.4(LL+I)	-Decompression Load
1.3DL+1.8(LL+I)	-Midspan tendon stresses begin to diverge from linear behavior.
1.3DL+3.0(LL+I)	-Joints (4,5) and (5,6) begin to open widely resulting in increased deflections, redistribution of internal forces toward the interior support, and causing tendon stresses to increase at a higher rate.
1.3DL+3.9(LL+I)	-Tendon 3 (north-span) began slipping from both ends towards the midspan region.
1.3DL+4.4(LL+I)	-The support joint begins to open causing the near-end interior-span tendon stresses to begin to increase. -Internal forces begin to redistribute back towards midspan
1.3DL+4.6(LL+I)	-Tendon 1a began slipping from both ends towards the midspan region.
1.3DL+4.9(LL+I)	-Tendon 1b began slipping from the interior end (9,10) towards the midspan region.
1.3DL+5.5(LL+I)	-Tendon 5 (interior span) began slipping from the midspan region towards the near end (north) of the interior span.
1.3DL+5.7(LL+I)	-Joint (11,12) (support joint) begins to open widely causing the internal forces to shift back towards the midspan region, and an abrupt change in the reaction and joint-moment responses (Fig. 6.35).
1.3DL+6.2(LL+I)	-Tendon 2 (interior span) began slipping from the midspan region towards the near end of the interior span
1.3DL+6.4(LL+I)	-Tendon 1b began slipping from the exterior end (1,2) towards the midspan region.
1.3DL+7.0(LL+I)	-Tendon 3 (interior span) began slipping from the midspan region towards the near end (north) of the interior span.
1.3DL+7.1(LL+I)	-Tendon 5 (interior span) began slipping from the far end of the interior span (south) towards the midspan region.
1.3DL+7.2(LL+I)	-Ultimate strength limited by flexural capacity.

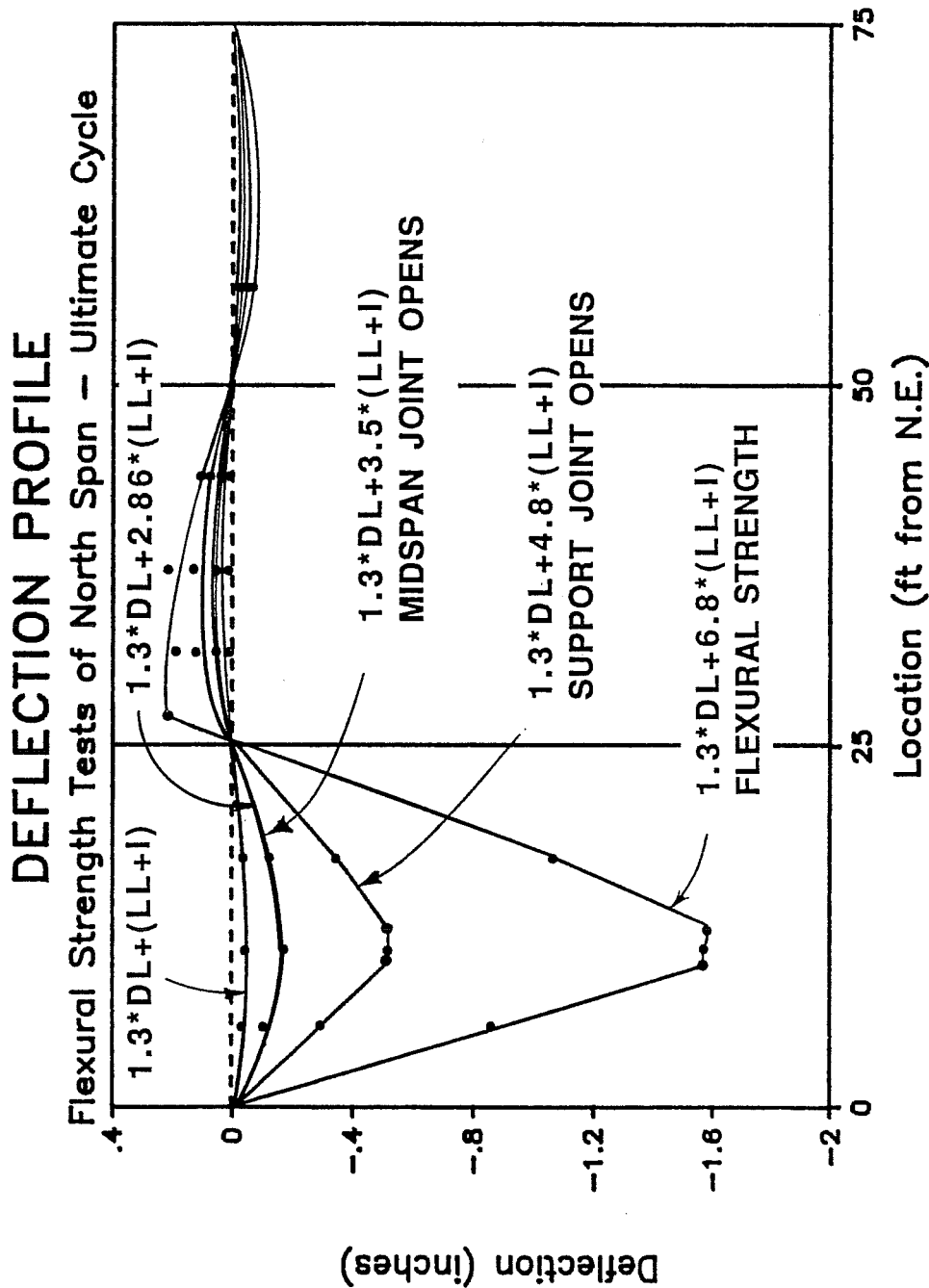


Figure 6.30 North Span Flexural Test: Deflection Profile

between 2 and 3. The relative magnitude of the plastic rotation at the support joint is a function of the critical mechanism for the load case, continuity with the adjacent span, and the initial deformations caused by secondary prestress effects.

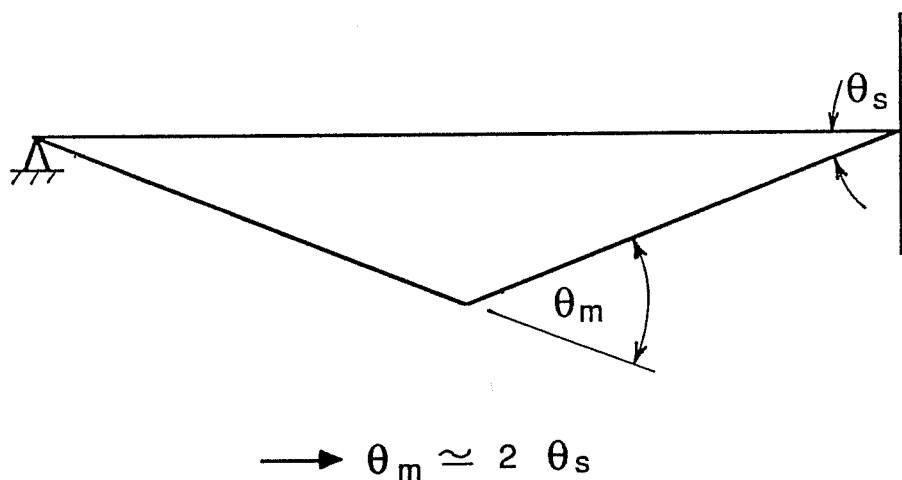


Figure 6.31 Plastic Mechanism Rotations for Propped Cantilever

The cracking behavior of the midspan region on the west and east sides of the north-span during the flexural strength test is summarized in Figure 6.32. The lines indicate the total length of cracks when the flexural strength ($6.8(LL+I)$) was reached. The initial extension and load at which the crack length was recorded are also indicated (as a multiples of $(LL+I)$). The shear transfer at the segment joints when the ultimate flexural moment was reached is also shown. The shear in segment 5 is distributed almost equally in both directions with a joint transfer shear of approximately $2.0(LL+I)$ at both joints.

The large rotations required for increased tendon stresses occurred primarily at the dry segment joints. Inclined web cracking first occurred in the second ultimate strength cycle at an applied load of approximately $5.8(LL+I)$. The cracking extended from the open joint and generally fanned towards the load point. The

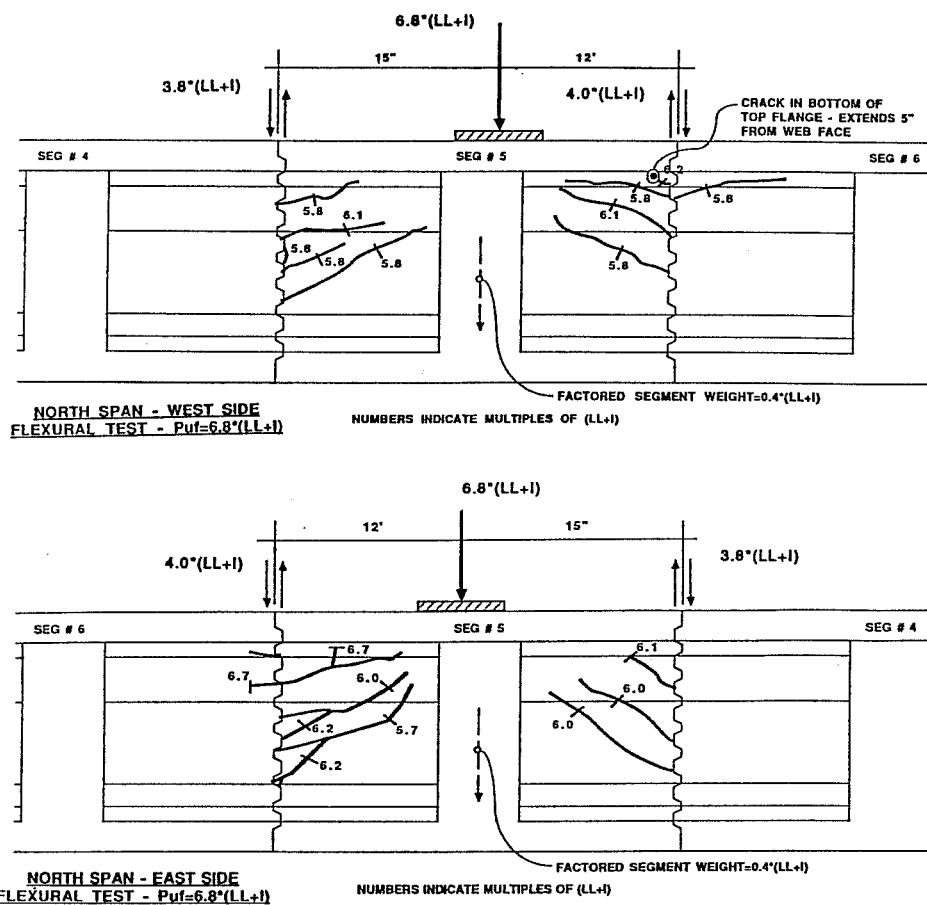


Figure 6.32 North Span Flexural Test: Cracking Summary

width of the inclined web cracks remained small throughout the flexural test. Horizontal cracking was also noticed at the web/top-flange junction at joint (5,6). At ultimate loads the neutral axis had shifted into the top flange as indicated by cracking in the bottom face of the top flange. The test was discontinued before crushing occurred in the top flange when the tangent stiffness of the load deflection response had reduced to 4% of its initial elastic value.

6.6.4 Shear Strength Test of North Span. The final test that was run on the north-span was a shear test in which the load was applied in such a way

that significant shear was transferred across an opening joint. One cycle of load was applied in $0.36(LL+I)$ increments up to $3.3(LL+I)$, $0.18(LL+I)$ increments to $4.7(LL+I)$, and $0.09(LL+I)$ increments up to a maximum load of $7.2(LL+I)$.

The applied load-deflection response for the shear strength cycle is shown in Fig. 6.33. The measured reactions and the calculated joint-moments are plotted with respect to the applied load in Fig. 6.34. The change in tendon stress due to applied load is shown for all north-span tendons in Fig. 6.35 and all center-span tendons in Fig. 6.36. The joint behavior, as measured by potentiometer and grid crack-monitors, is illustrated in Fig. 6.37.

1.4(LL+I) Decompression load: The test load that is equivalent to the service live load is calculated to cause the same moment at the critical joint as the design live load. The decompression load should therefore be approximately the same as for the flexural test load since the Equivalent (LL+I) adjusts for the load location.

The test was discontinued at $7.2(LL+I)$ before catastrophic failure when the tangent stiffness of the applied load-deflection response reached approximately the same stiffness as measured at the conclusion of the flexural strength test. The tangent stiffness at increasing levels of applied load is also tabulated in Table 6.17. The strength was ultimately limited by the flexural strength, although the shear transfer at the opening joints caused markedly different local behavior.

The measured deflected shape of the three-span structure for increasing levels of applied load is shown in Fig 6.38. At the service load, $1.0(LL+I)$, and the factored load, $2.9(LL+I)$, the deflections were small and the deflected shape is a smooth curve. The deflected shape remains smooth until the midspan joints begin opening at $3.0(LL+I)$. Beyond this load, "hinging" occurred at the opening joints and the midspan deflections increased considerably. When the support joint opened at $4.8(LL+I)$, the mechanism formed and deflections increased very rapidly. The final deflected shape of the structure clearly illustrates the mechanism behavior of the structure at ultimate load levels.

The reaction and joint-moment curves again exhibited double curvature (S-shape). As the midspan joints opened the midspan stiffness reduced causing internal forces to redistribute towards the support. When the support joint opened,

APPLIED LOAD vs DEFLECTION

Shear Strength Test of North Span

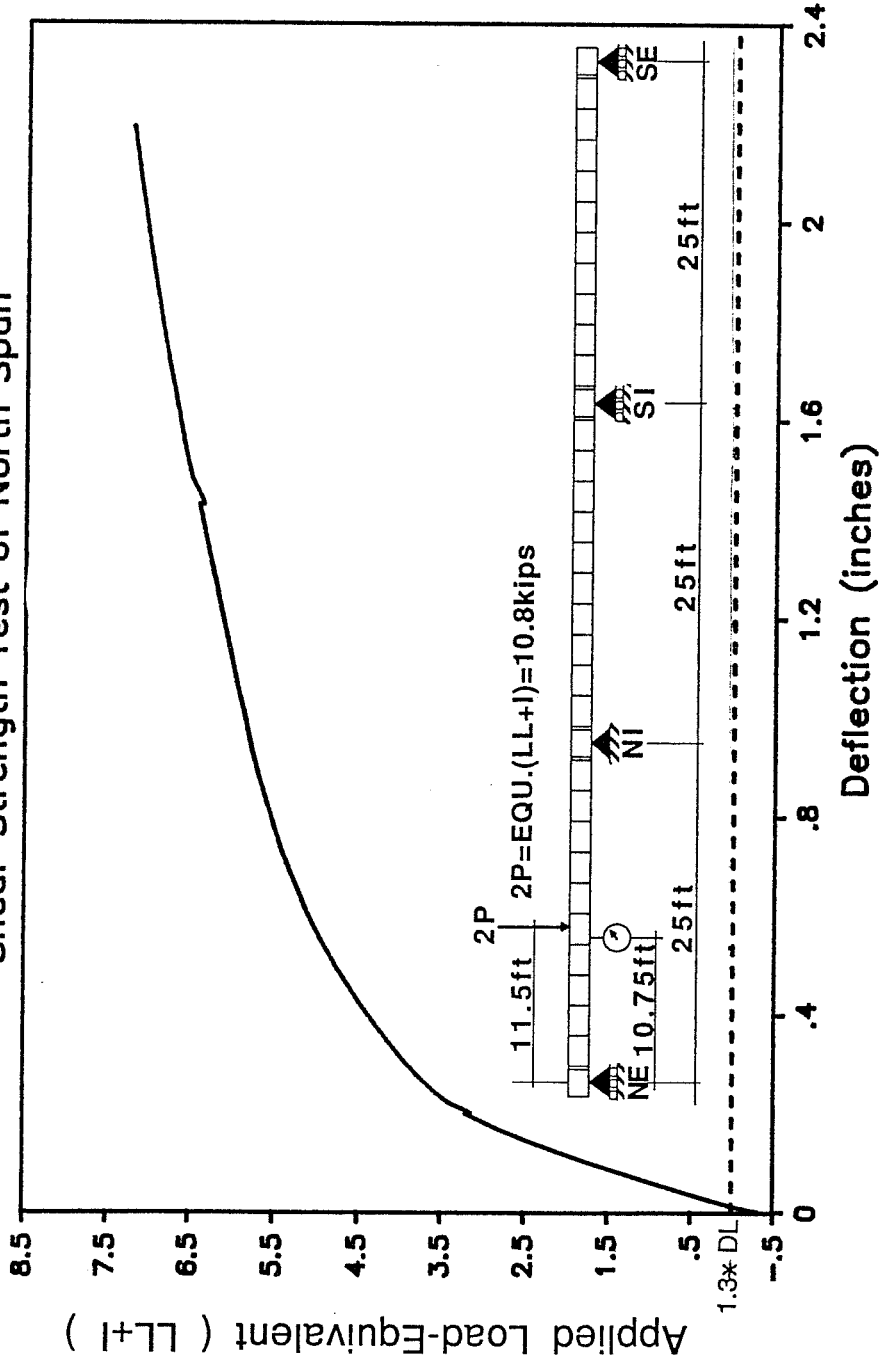


Figure 6.33 North Span Shear Strength Test: Applied Load vs. Deflection

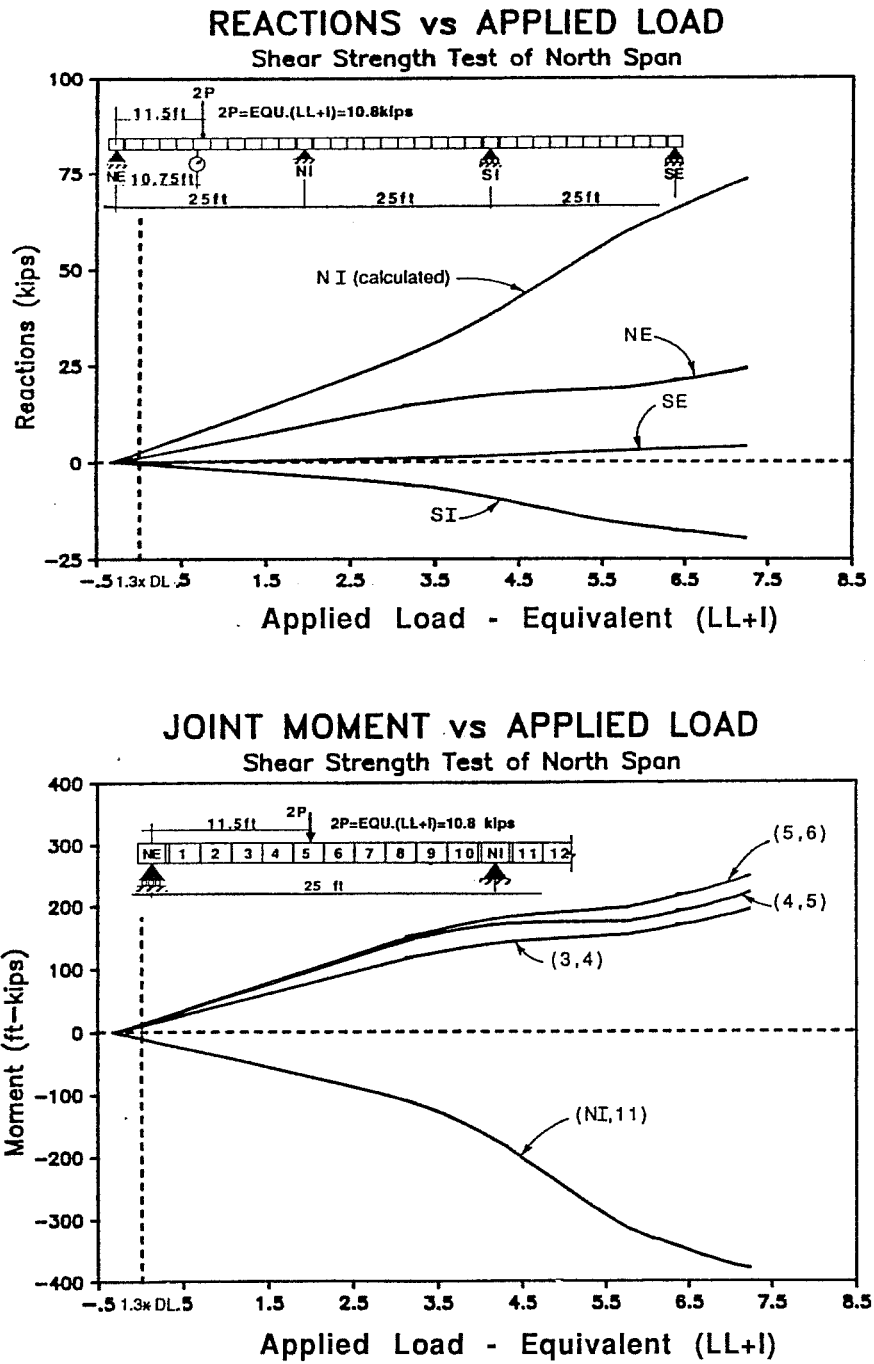


Figure 6.34 North Span Shear Strength Test: Reactions and Joint Moments

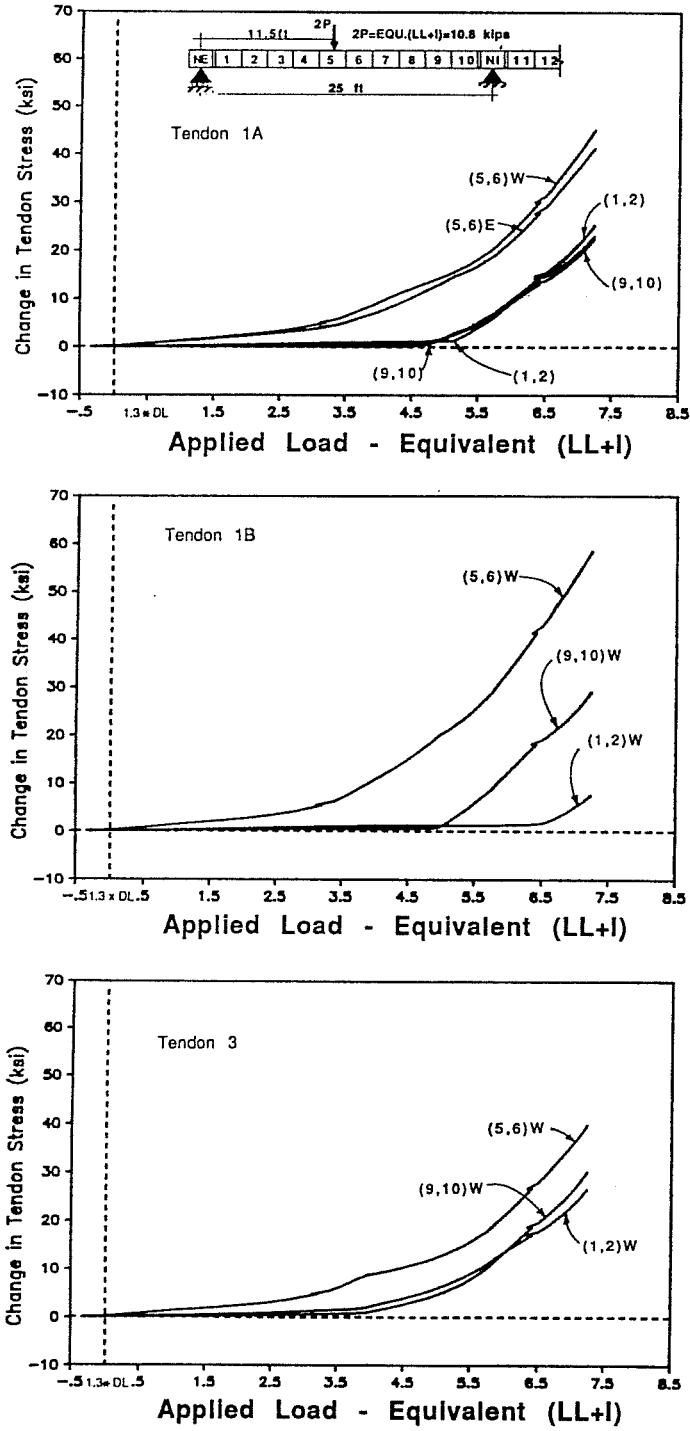


Figure 6.35 North Span Shear Strength Test: Change in Tendon Stress vs. Applied Load (North Span)

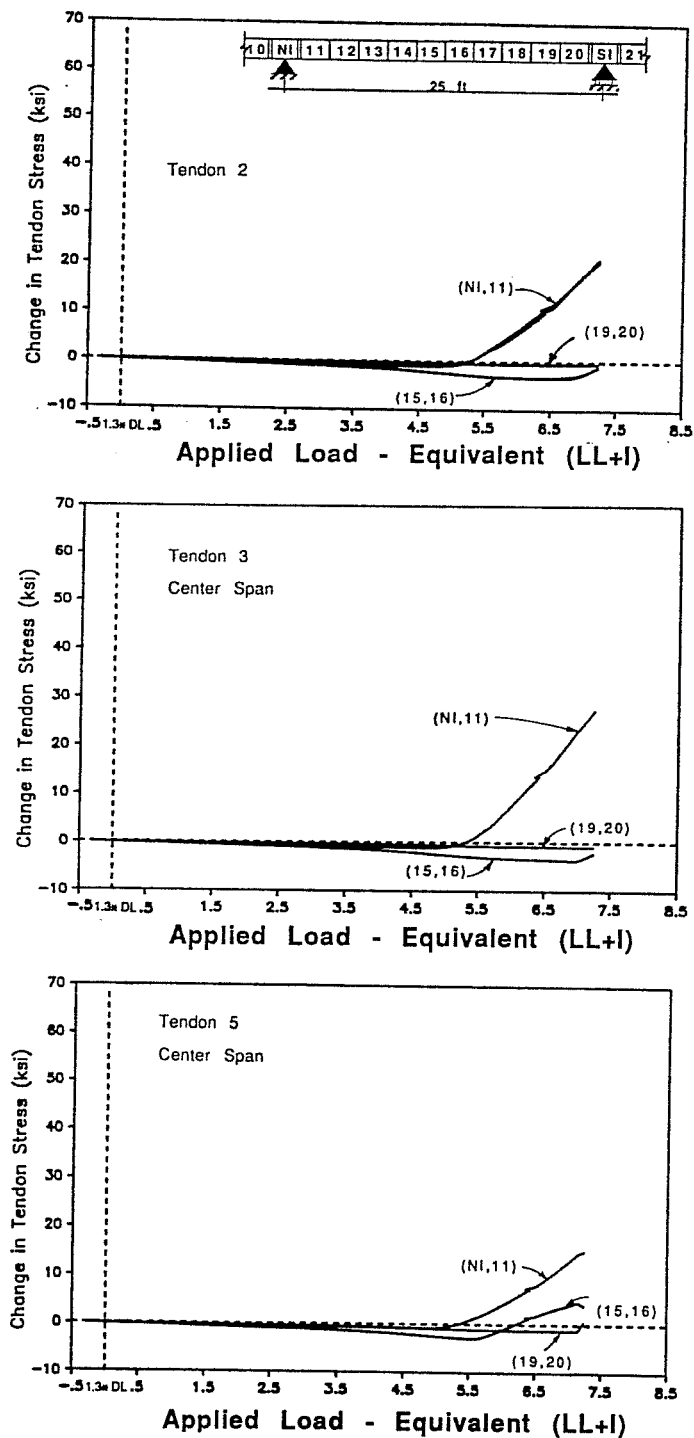
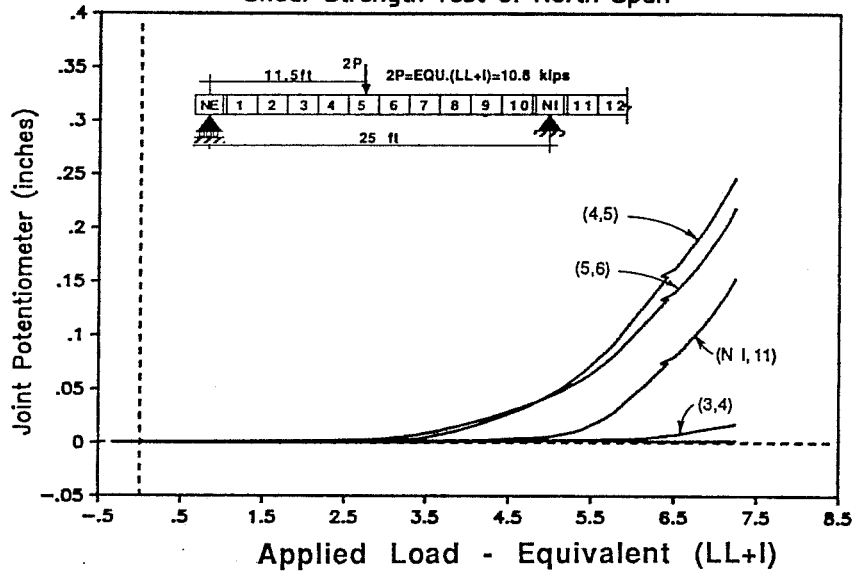


Figure 6.36 North Span Shear Strength Test: Change in Tendon Stress vs. Applied Load (Center Span)

JOINT OPENING POTENTIOMETER vs APPLIED LOAD
 Shear Strength Test of North Span



JOINT OPENING PROFILES

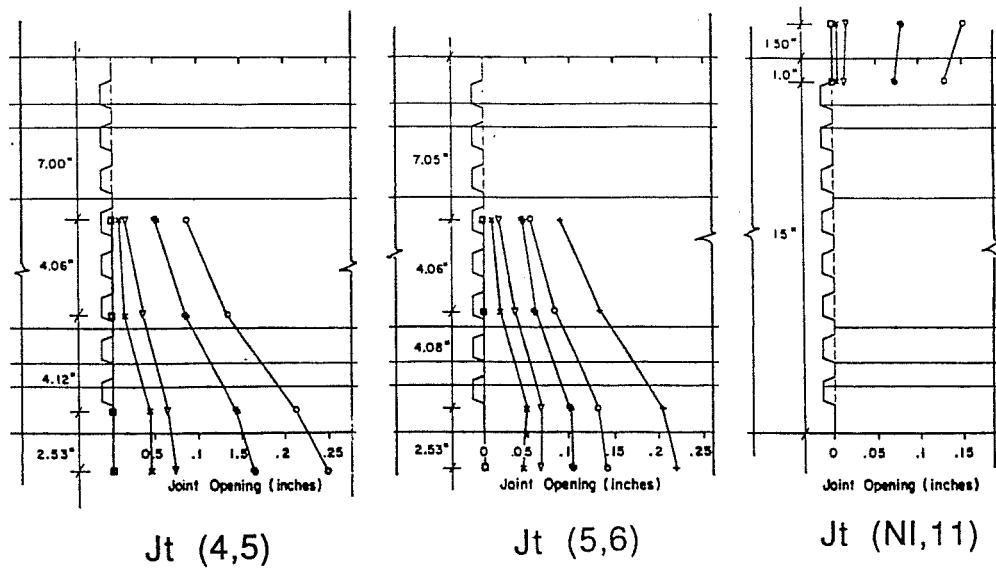


Figure 6.37 North Span Shear Strength Test: Joint Opening Behavior

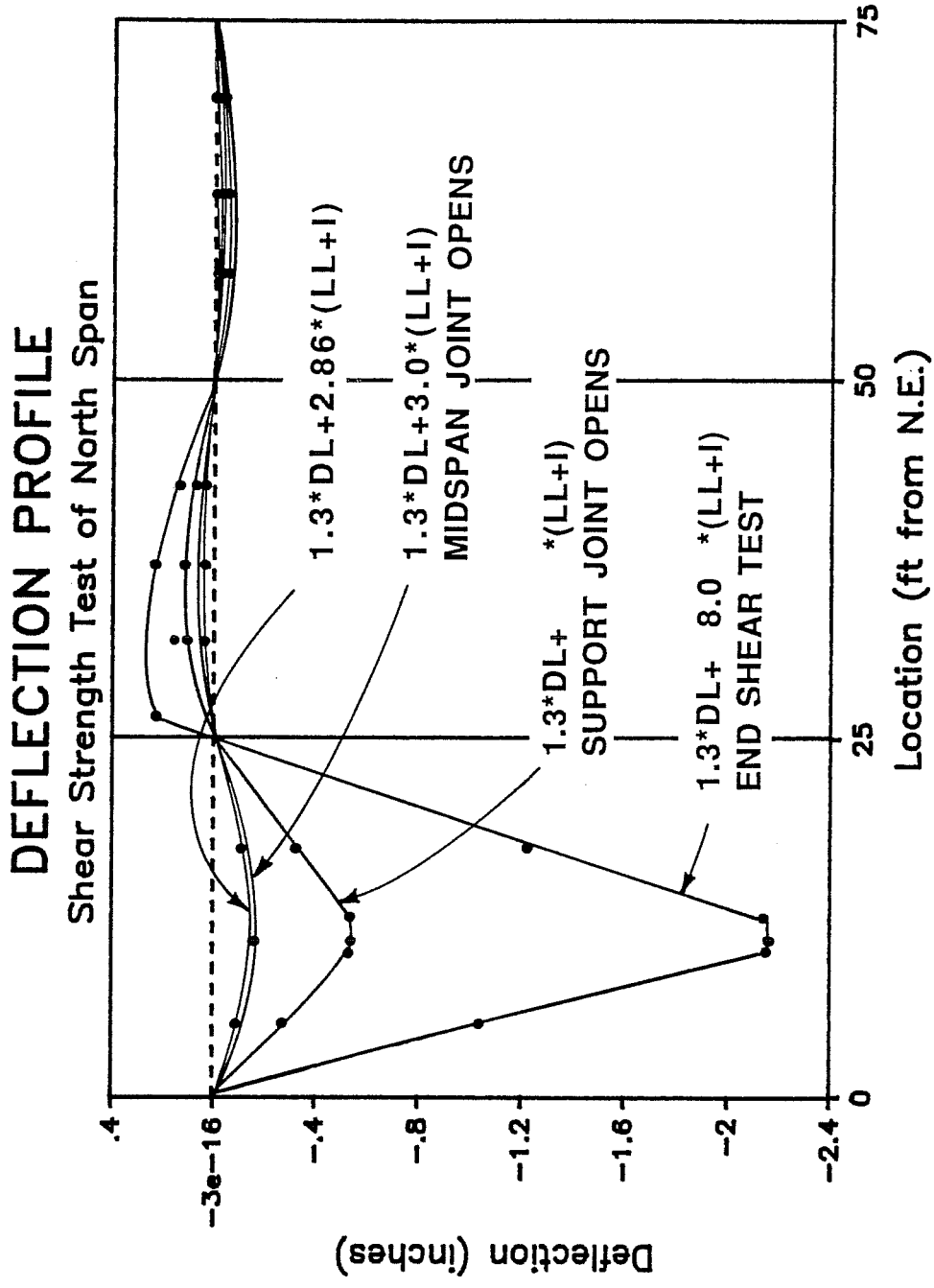


Figure 6.38 North Span Shear Test: Deflection Profiles

the support stiffness reduced and internal forces were redistributed back towards midspan.

A profile of each opening joint during the shear test of the north-span is shown at the bottom of Fig. 6.37. Large rotations occurred at two midspan joints, Joints (4,5) and (5,6) and one support joint, joint (NI,11). In this case, with significant shear transferred across the opening joint, the concentrated rotations occurred at an inclined crack which extended from the load point to the bottom of the web adjacent to the joint (shown in the cracking summary in Fig. 6.39). The apparent joint openings measured by the crack monitors occurred at cracks in the concrete section while the match-cast dry joints remained closed.

The concentrated rotations can again be calculated from the measured joint-opening profiles. The measured concentrated rotations were approximately 0.8 degrees at each of the two midspan joints (Joints (4,5) and (5,6)), and approximately 0.5 degrees at the support joint (NI,11). The ratio of total midspan rotation to support rotation is again approximately 3.

The cracking behavior of the midspan region on the west and east sides of the north-span during the shear test is summarized in Figure 6.39. The lines indicate the total length of the crack when the test was discontinued at $(7.2(LL+I))$. The previous cracking from the flexural tests is shown shaded, and the new cracking or opening of previous cracks is shown as solid lines. The initial extension and the load at which it first occurred are also indicated as multiples of $(LL+I)$. The shear transfer at the segment joints at the end of the test is also shown. The shear in segment 5 is distributed primarily towards the interior support with a joint shear transfer of $5.4(LL+I)$ at joint (5,6).

The cracks that formed during the flexural test began to reopen at approximately $4.1(LL+I)$. In addition, at joint (5,6), new cracks formed which extended from the base of the web at the match-cast joint up to a previous crack. At approximately $5.4(LL+I)$ an additional inclined crack formed on the west side of joint (5,6). This new crack crossed several of the cracks which had been formed during the flexural test. As load was increased, joints (4,5) and (5,6) opened at approximately the same rate, with the concentrated rotations occurring at the primary inclined cracks. At the conclusion of the test the dry match-cast joint was closed, with all of

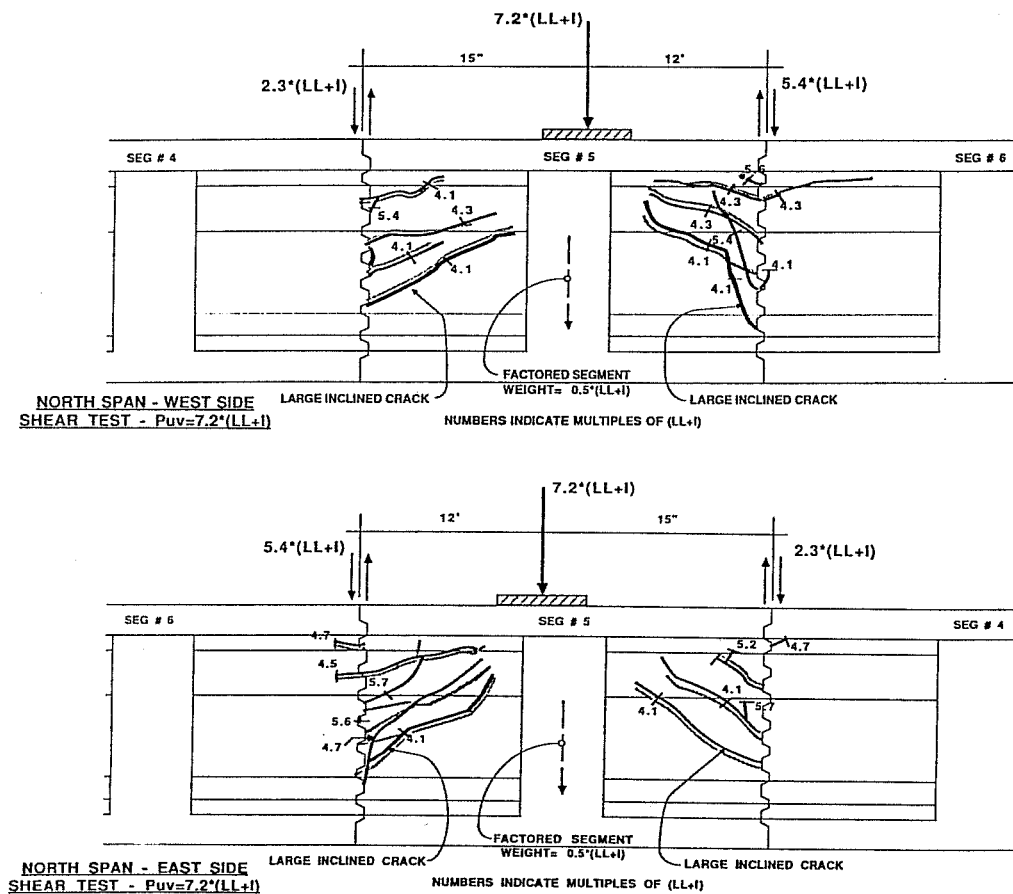


Figure 6.39 North Span Shear Test: Cracking Summary

the hinge rotations occurring at the inclined cracks. This allowed the shear forces to utilize the entire height of the web to transfer across the joint.

6.7 South-span Load Tests (Epoxy Joints)

6.7.1 Service Load Tests of South-Span.

6.7.1.1 Live Load Cycles for South-Span. Four cycles of service live load were applied to the epoxy jointed south-span using the load set-up shown

in the schematic of Fig. 6.40. For all four cycles the load was applied in $0.16(LL+I)$ increments up to the service live load $1.0(LL+I)$. Each of the four cycles provided approximately the same response to the applied loads.

The measured deflected shape of the three-span structure is shown in Fig. 6.40 for a typical service load cycle. The midspan deflection of 0.048 inches corresponds to a deflection/span ratio of $L/6250$. Also shown on Fig. 6.40 is the calculated deflected shape from the elastic analysis (see Section 5.4). The elastic analysis overestimates the measured deflection by approximately 29 percent.

The tendon data indicated a Live Load Stress range of about 1 ksi. No tendon slip was noticed at service-load levels.

6.7.1.2 Cracking Cycle for South-Span. After completing the live load cycles it was necessary to initially crack the epoxy-jointed south-span before the decompression load could be determined. The applied load was increased from zero to $3.2(LL+I)$ in $0.16(LL+I)$ increments, and from $3.2(LL+I)$ to a maximum load of $5.7(LL+I)$ at $0.08(LL+I)$ increments. The south-span cracked in segment 26 adjacent to joint (25,26) at approximately $5.4(LL+I)$. The crack was clearly through the concrete and the epoxy joint was uncracked.

The applied load-deflection response during the cracking cycle is shown in Fig. 6.41. The measured reactions and the calculated joint-moments are plotted with respect to the applied load in Fig. 6.42. The change in tendon stress due to applied load is shown for all south-span tendons in Fig. 6.43.

2.4(LL+I): As noticed in the epoxied center-span, the load deflection response exhibits bi-linear behavior with a reduction in stiffness at approximately $2.4(LL+I)$. This change in behavior is also noticed as a subtle change in the reactions, joint-moments, and tendon stress responses.

5.4(LL+I) Cracking Load: Cracking occurred through the concrete in segment 26 adjacent to joint (25,26). As for the north and center-spans, after cracking, the loads tended to redistribute towards the continuous support because of the reduced stiffness at midspan.

The midspan tendon stresses remained linear with applied load up to the point that the concrete cracked. As cracking occurred, the tensile force that was

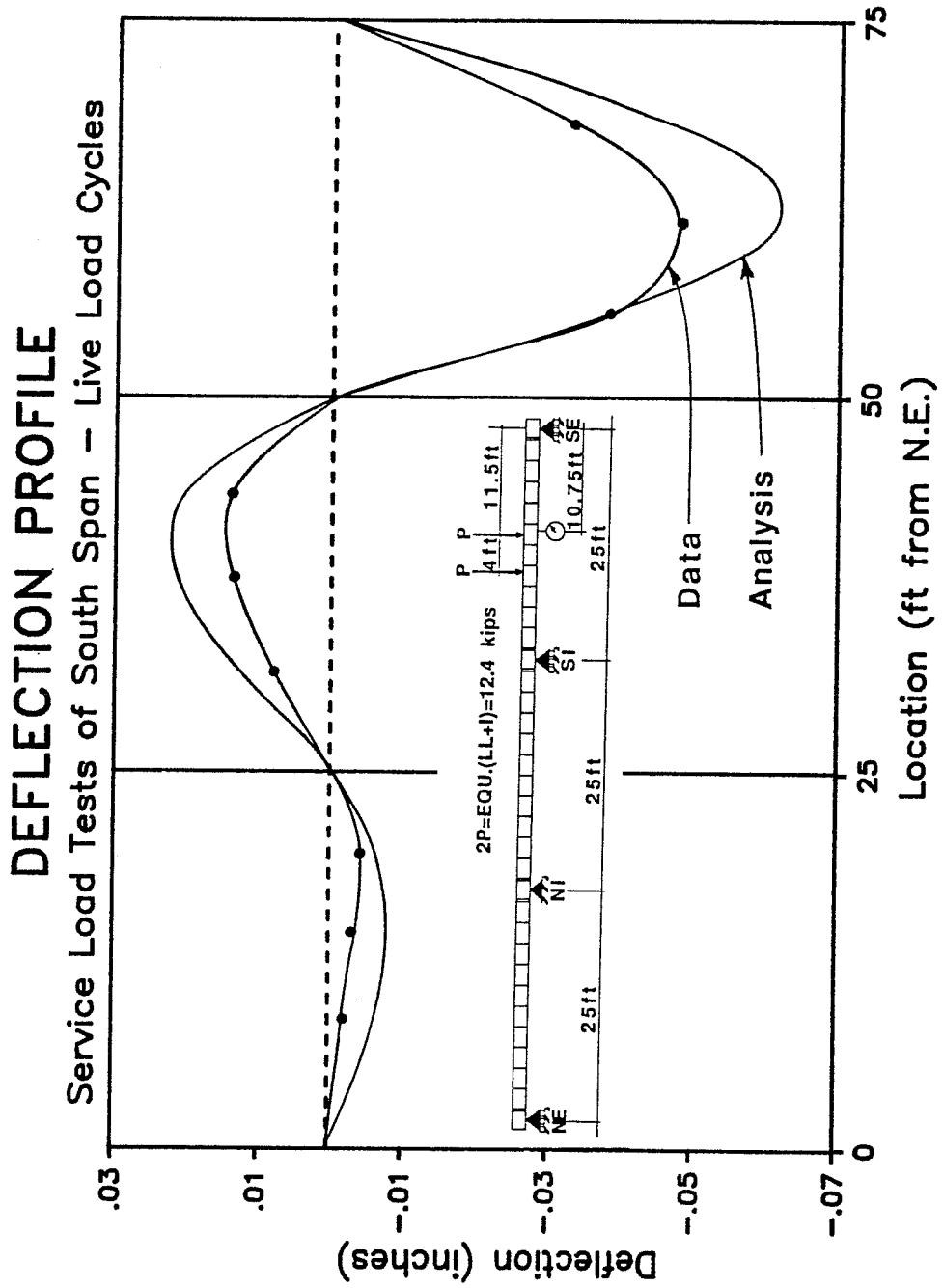


Figure 6.40 South Span Service Load Tests: Deflection Profile

APPLIED LOAD VS DEFLECTION

Service Load Tests of South Span - Cracking Cycle

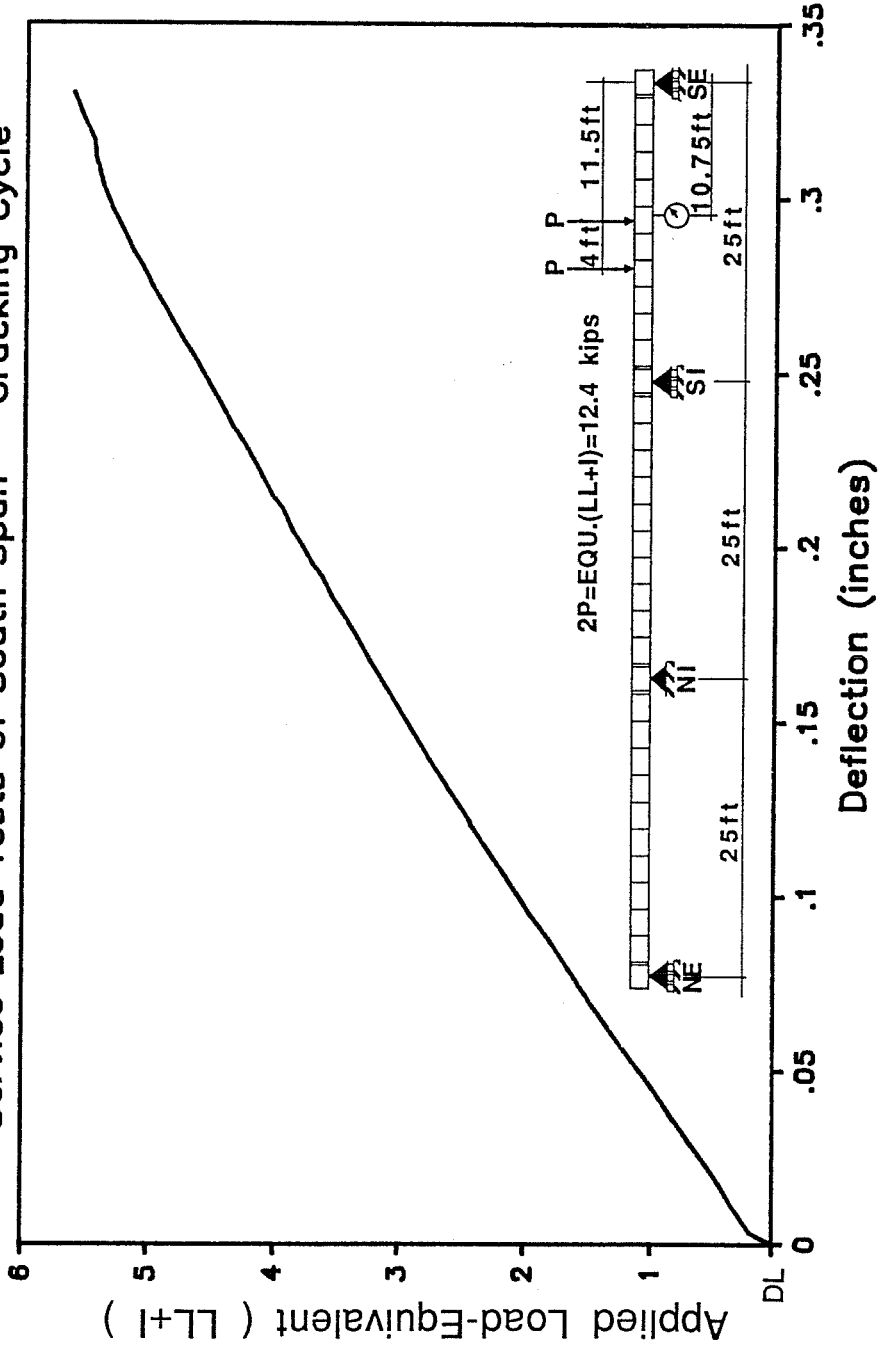


Figure 6.41 South Span Cracking Cycle: Applied Load vs. Deflection

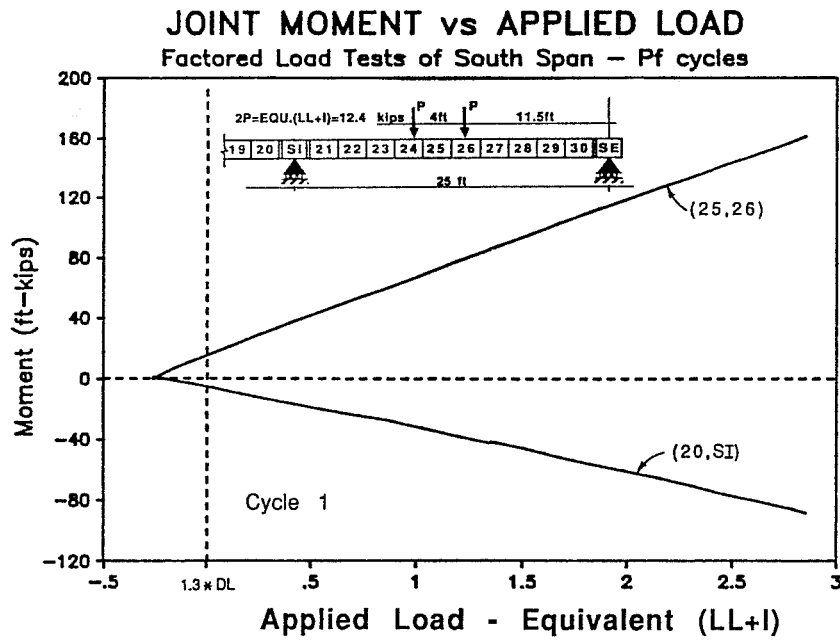
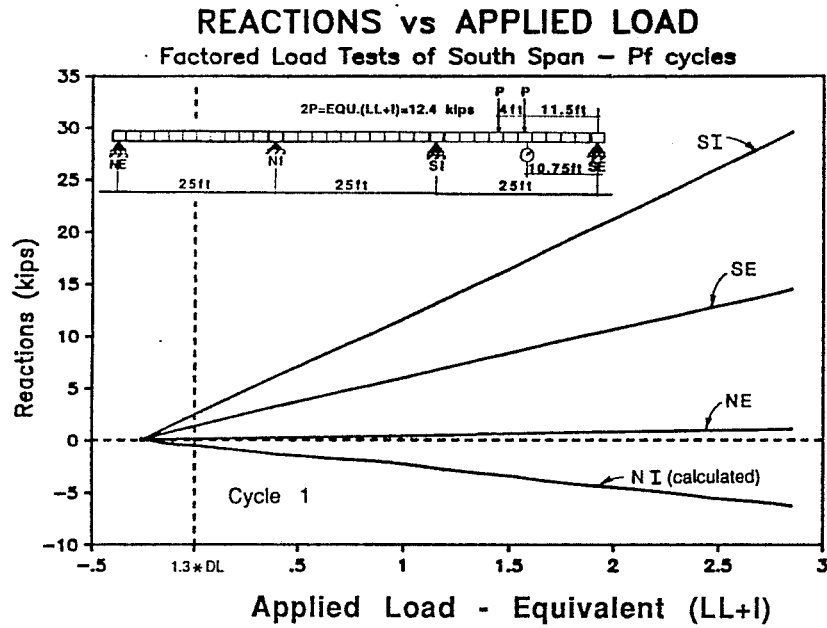


Figure 6.42 South Span Cracking Cycles: Reactions and Joint Moments

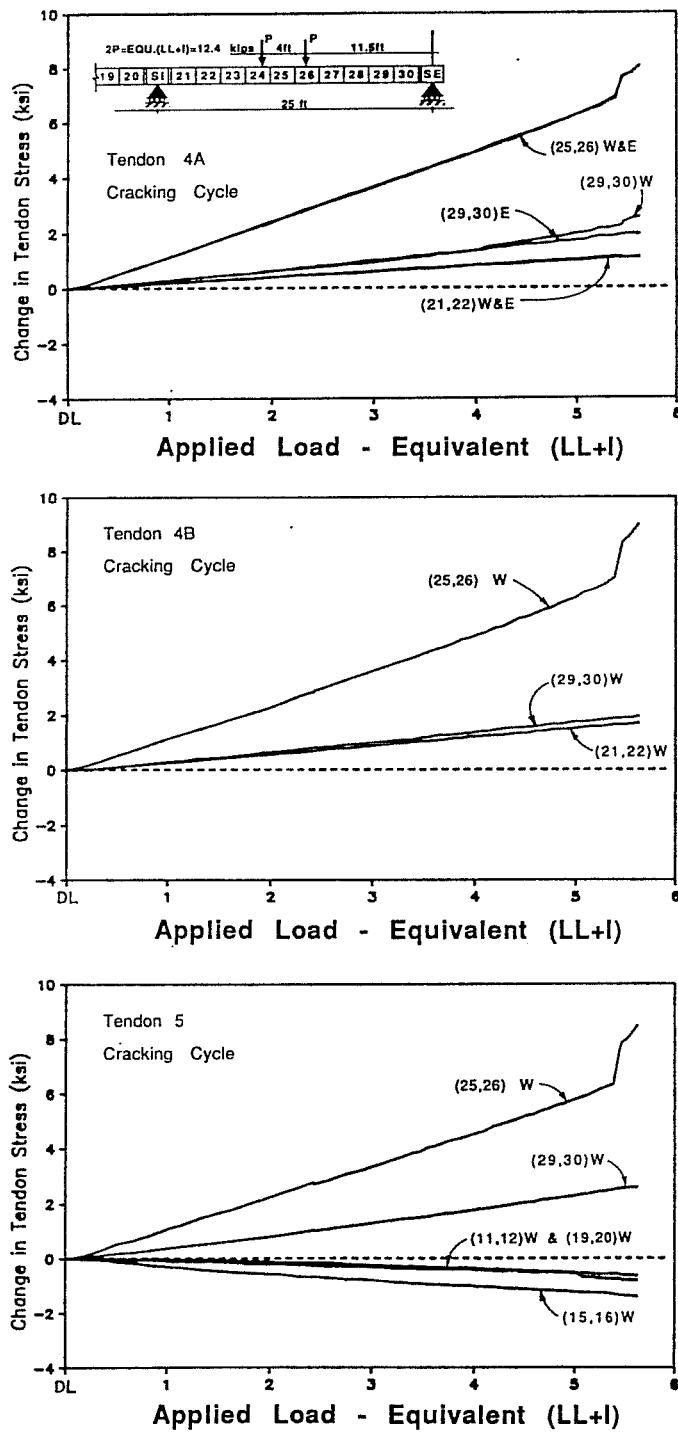


Figure 6.43 South Span Cracking Cycle: Change in Tendon Stress vs. Applied Load

previously carried by the concrete was transferred to the post-tensioning tendons. This caused a sudden increase in tendon stresses. For unbonded tendons, considerable elongation was necessary to develop the increased tendon forces. This caused concentrated rotations to occur at the crack and resulted in vertical deflection. The west side of tendon 4a slipped from the exterior end (29,30) towards the midspan region during cracking. Slip was not noticed at any other locations.

5.7(LL+I): The test was discontinued at 5.7(LL+I) at 10 percent above the cracking load. Although the bottom flange appeared to be cracked all the way through at the end of this cycle, subsequent testing to higher load levels indicated that only partial cracking had occurred at this load stage. The joint opening response, shown in Fig.6.44, also illustrates larger crack opening on the west side with only limited cracking on the east side. The cracking-load cycle for the south-span is summarized in Tables 6.24, 6.25, and 6.26.

6.7.1.3 Decompression Load Cycles for South-Span. After initial cracking at joint (25,26), three load cycles were applied to the south-span to determine the magnitude of the decompression load. The applied load was increased in 0.32(LL+I) increments to a load level of approximately 1.6(LL+I), and then in 0.16(LL+I) increments to a maximum load of 3.4(LL+I), or approximately 30 percent higher than the measured decompression load, 2.6(LL+I).

The applied load-deflection response during the cracking cycle is shown in Fig. 6.45. The measured reactions and the calculated joint-moments are plotted with respect to the applied load in Fig. 6.46.

2.6(LL+I) Decompression Load: The data was erratic throughout these cycles, perhaps as the result of friction in the rams. The decompression load was estimated from a large-scale plot of manually recorded data. This data showed a change in behavior at approximately 2.6(LL+I).

The reactions and joint moments show very subtle changes in response at the decompression load indicating only slight redistribution of internal forces towards the interior support.

3.4(LL+I): The maximum test load applied during the decompression load test of the south-span was 3.4(LL+I). The south-span decompression cycles are summarized in Tables 6.27, 6.28, and 6.29.

JOINT OPENING POTENTIOMETER VS APPLIED LOAD

Service Load Tests of South Span - Cracking Cycle

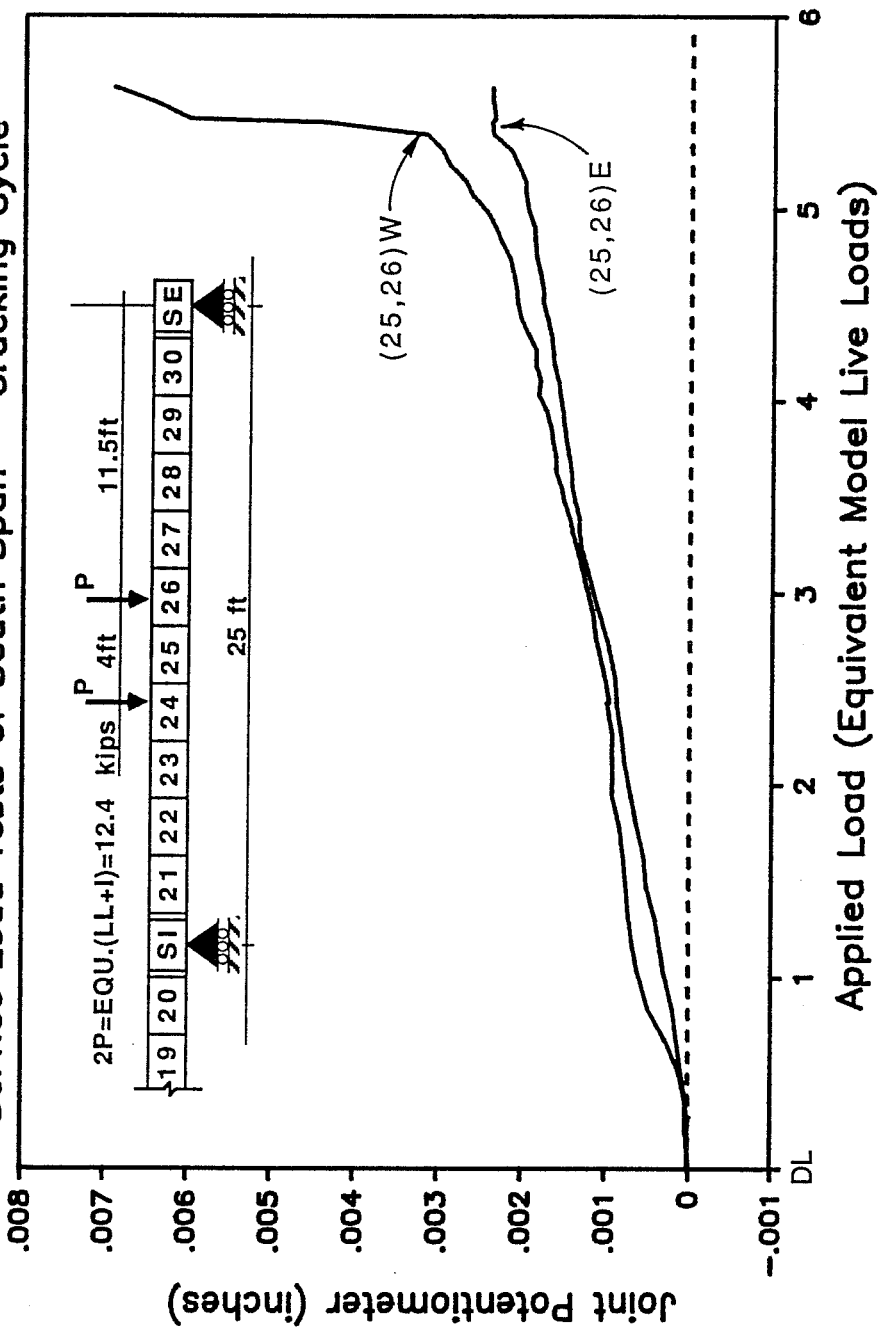


Figure 6.44 South Span Cracking Cycle: Joint Opening Potentiometer vs. Applied Load

Table 6.24 South-span Cracking Cycle - Maximum Response Values

	Cracking Load 5.4(LL+I)	5.7(LL+I)
Deflections	0.30 (L/1000)	0.33 inches (L/909)
Reactions	50 at SI	53 kips at SI
Moments M +ve	270 at (25,26)	280 ft-kips at (25,26)
M -ve	-150 at (20,SI)	-170 ft-kips at (20,SI)

Table 6.25 South-Span Cracking Cycle - Change in Tendon Stress

	Before Cracking 5.4(LL+I)	After Cracking 5.7(LL+I)
Tendon 4a:	2 * 7 / 1	2 * 8 / 1
Tendon 4b:	2 / 7 / 2	2 / 9 / 2
Tendon 5:	2 / 6 / X	2 / 8 / X

X: denotes inactive strain gage
 * denotes slip towards midspan
 key = (29,30)/(25,26)/(21,22)
 = ext.end/midspan/int.end

Table 6.26 Summary of South-Span Cracking Cycle

$P_{applied}$:	Description:
DL only	-Start Test ($P_{rams}=0$)
DL+2.4(LL+I)	-Stiffness reduces slightly as bottom of uncracked girder goes into tension
DL+5.4(LL+I)	-Cracking occurs in Segment 26 adjacent to joint (25,26)
DL+5.7(LL+I)	-Test discontinued

APPLIED LOAD vs DEFLECTION

Service Load Tests of South Span - Pd Cycles

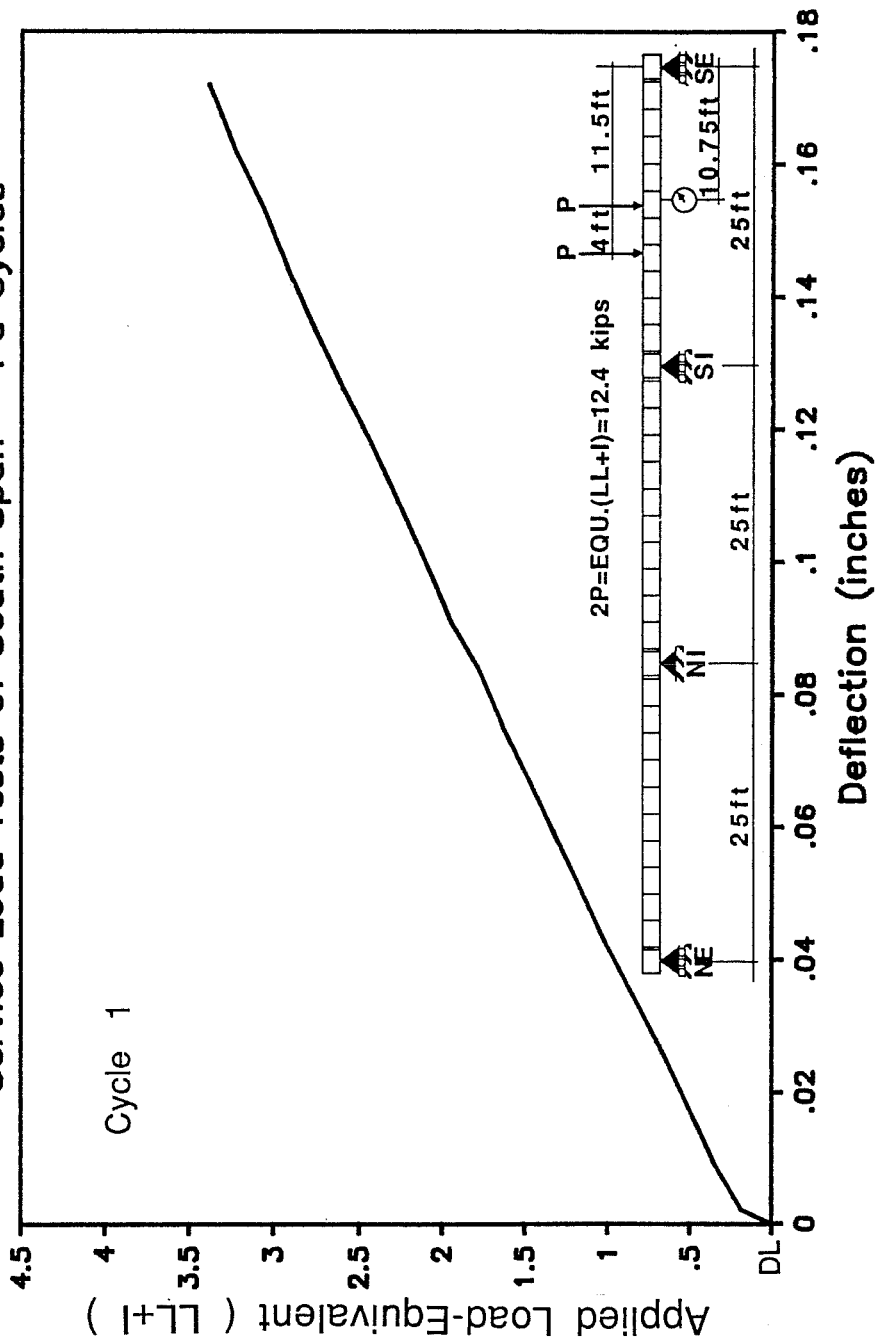


Figure 6.45 South Span Decompression Cycles: Applied Load vs. Deflection

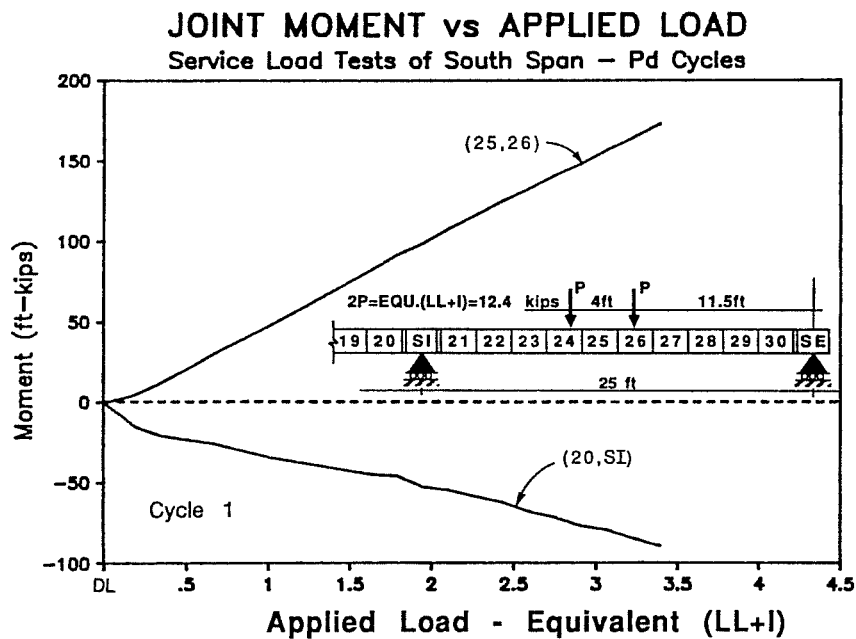
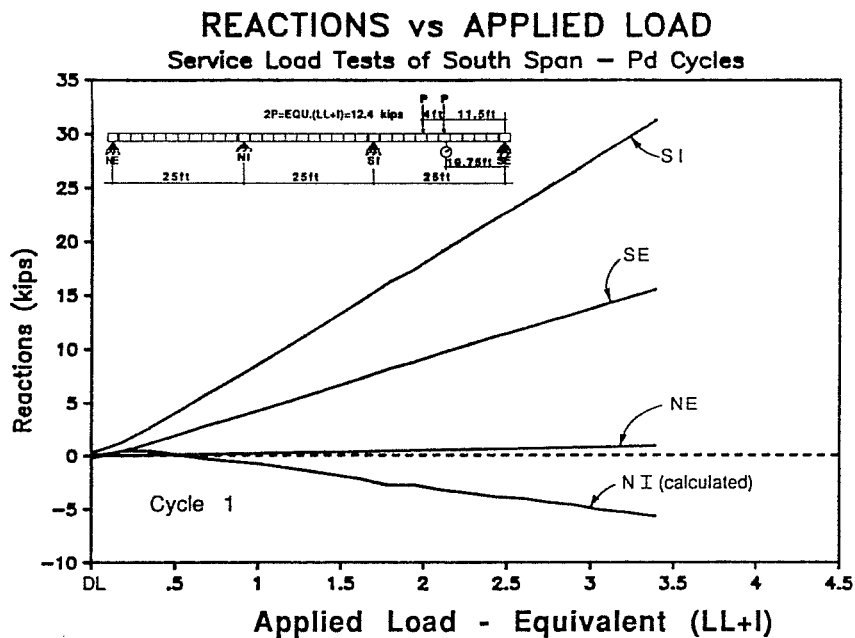


Figure 6.46 South Span Decompression Cycles: Reactions and Joint Moments

Table 6.27 South-Span Decompression Cycles - Maximum Response Values

	Decompression Load 2.6(LL+I)	3.4(LL+I)
Deflections	0.13 inches (L/2307)	0.14 inches (L/2142)
Reactions	24 kips at SI	32 kips at SI
Moments M +ve	130 ft-kips at (25,26)	120 ft-kips at (15,16)
M -ve	-70 ft-kips at (20,SI)	-75 ft-kips at (NI,11)

Table 6.28 South-Span Decompression Cycles - Change in Tendon Stress (ksi)

	Decompression Load 2.6(LL+I)	3.4(LL+I)
Tendon 4a:	1 / 3 / 0.5	1 / 4 / 0.5
Tendon 4b:	1 / 3 / 1	1 / 4 / 1
Tendon 5:	1 / 3 / X	1 / 4 / X

X: denotes inactive strain gage
 key = (29,30)/(15,16)/(21,22)
 = ext.end/midspan/int.end

Table 6.29 Summary of South-Span Decompression Cycles

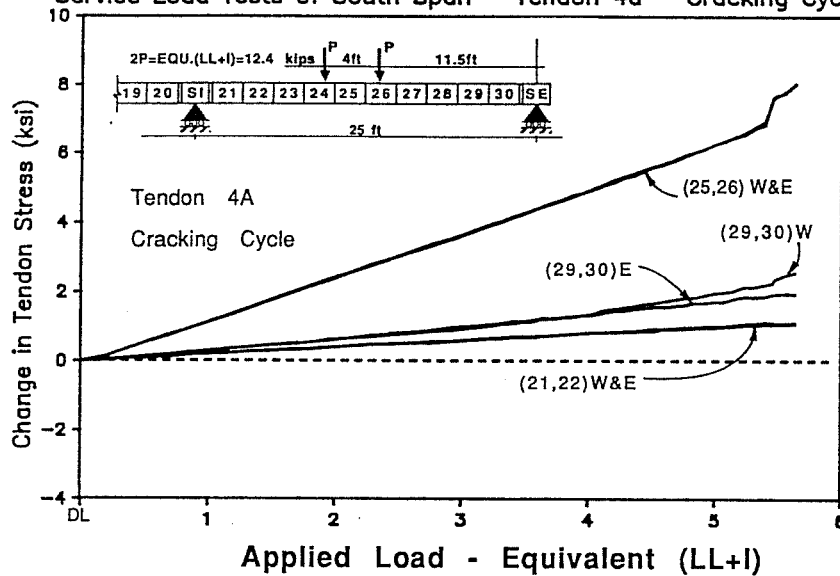
$P_{applied}$:	Description:
DL only	-Start Test ($P_{rams}=0$)
DL+2.6(LL+I)	-Decompression Load
DL+3.4(LL+I)	-Maximum load for Test Cycles

The change in the tendon stresses due to applied load appeared to be linear throughout the entire load cycle, with a maximum stress range of approximately 3.5 ksi at midspan.

Tendon slip in all tendons was noticed between the previous cracking cycle and the current decompression cycles. Figure 6.47 shows the applied load versus stress response in tendon 4a for the cracking cycle and the first decompression-load

CHANGE IN TENDON STRESS vs APPLIED LOAD

Service Load Tests of South Span – Tendon 4a – Cracking Cycle



CHANGE IN TENDON STRESS vs APPLIED LOAD

Service Load Tests of South Span – Tendon 4a – Pd Cycles

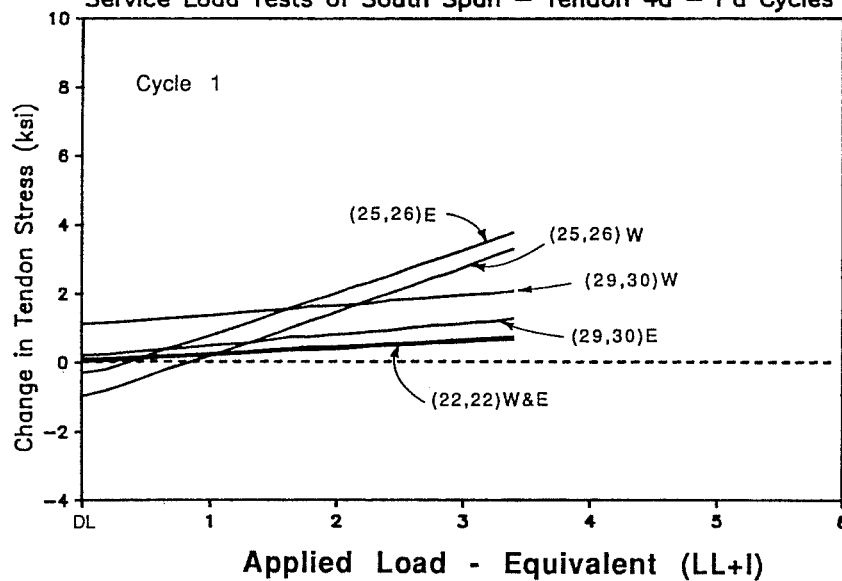


Figure 6.47 Comparison of South Span Cracking Cycle and Decompression Load Cycle Response for Tendon 4a

cycle. After the cracking cycle there was residual tension in the tendons. This is illustrated in the tendon stress profile (Fig.6.48) for the unloaded condition preceding each load cycle. The two-span continuity tendon (tendon 5) illustrates similar behavior with slip occurring across the pier segment (Figs. 6.49 and 6.50).

6.7.2 Factored Load Cycles for South-Span. After completing the service load tests additional dead weight was added to the structure to simulate the factored dead load requirement. Three factored load cycles were conducted on the south-span with loads applied in $0.16(LL+I)$ increments up to the factored design load of $1.3DL+2.86(LL+I)$.

The applied load-deflection response was the same for all three factored load cycles, and cycle 1 is shown in Fig. 6.51. The measured reactions and the calculated joint-moments are plotted with respect to the applied load in Fig. 6.52.

2.2(LL+I) Decompression Load: In this case, with the structure preloaded with 30 percent more dead load, less applied force was necessary to cause tension at the extreme fiber. The decompression force of $2.2(LL+I)$ is consistent with the previous estimation of the decompression load ($2.6(LL+I)$) determined without the additional dead weight. The difference between these two loads is approximately equal to the test load that produces the same moment at the critical joint as 30 percent of the dead load.

2.9(LL+I) Factored Live Load: The south-span was loaded to the factored live load level of $2.9(LL+I)$. The factored load cycles are summarized in Tables 6.30, 6.31, and 6.32.

Table 6.30 South-span Factored Load Cycles - Maximum Response Values at Factored Load = $2.9(LL+I)$

Deflections	0.17 inches (L/1765)
Reactions	29 kips at SI
Moments M +ve	160 ft-kips at (25,26)
M -ve	-90 ft-kips at (20,SI)

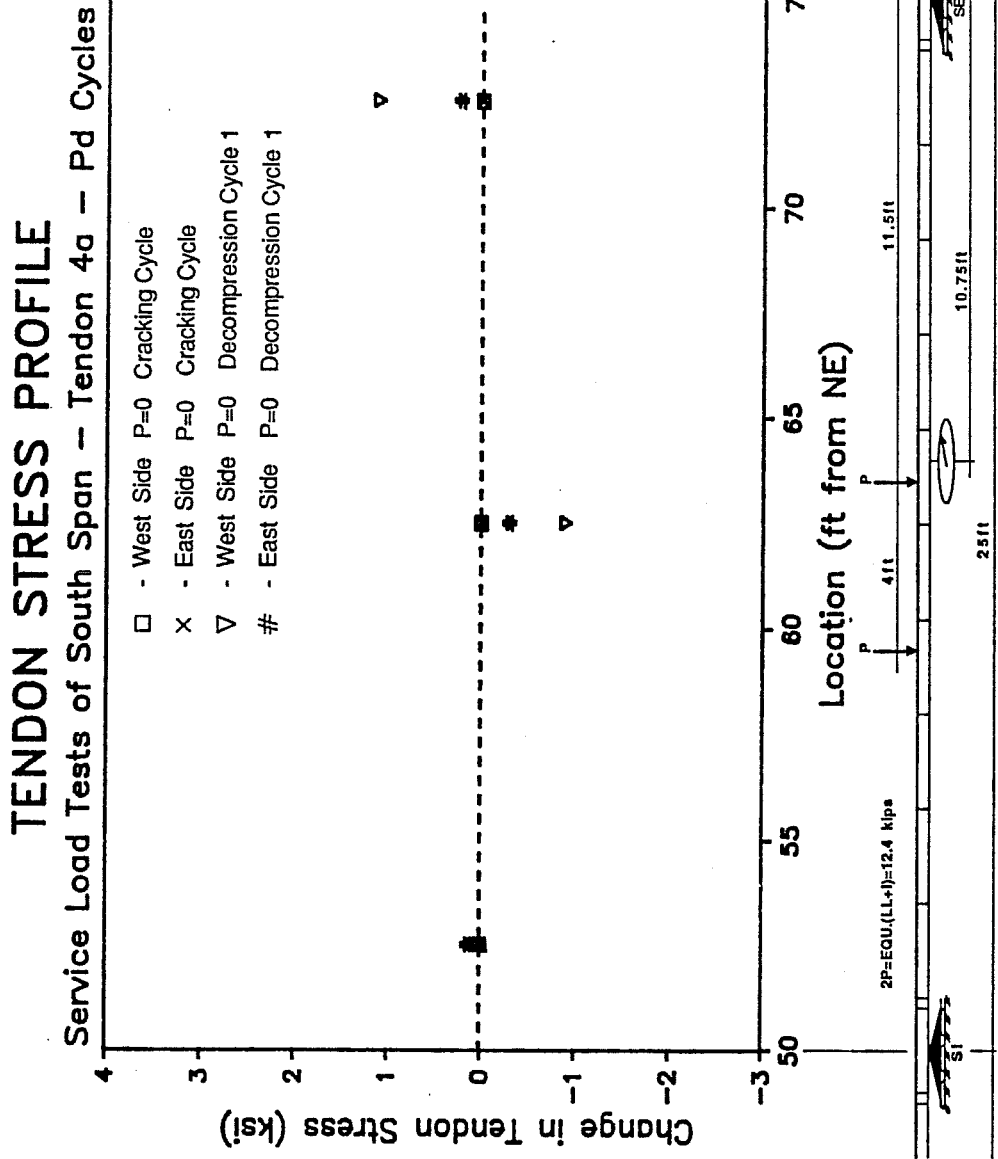


Figure 6.48 South Span- Tendon 4a Stress Profile

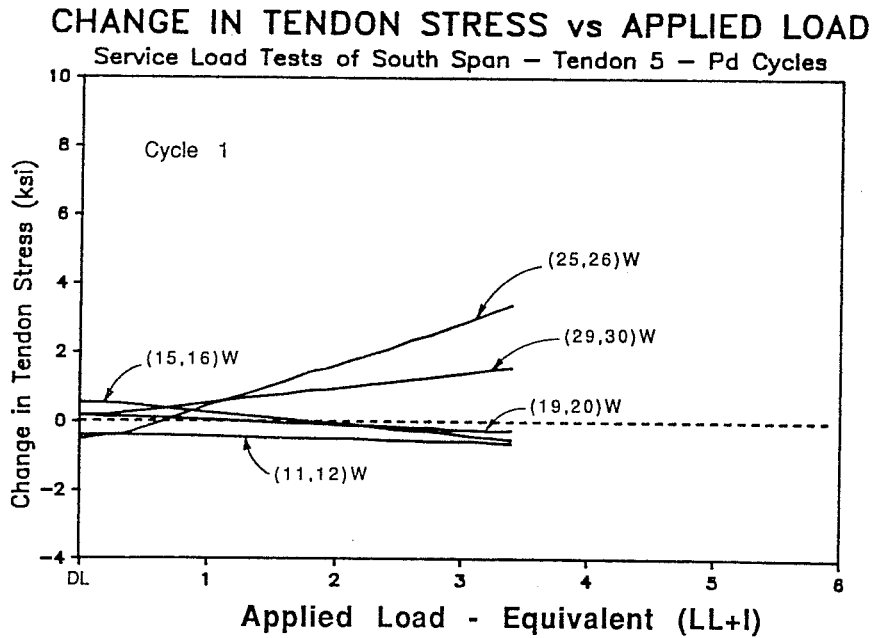
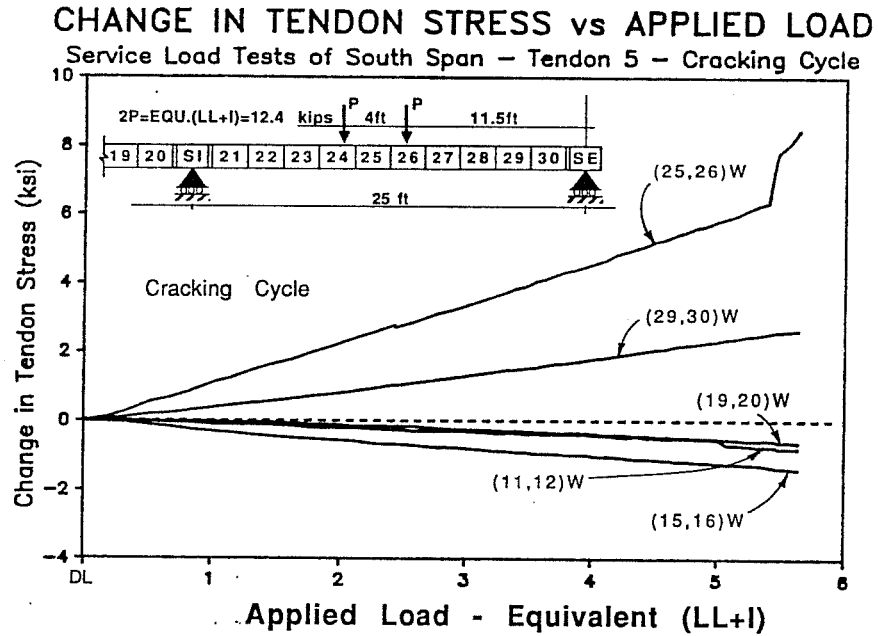


Figure 6.49 Comparison of South Span Cracking Cycle and Decompression Load Cycle Response for Tendon 5

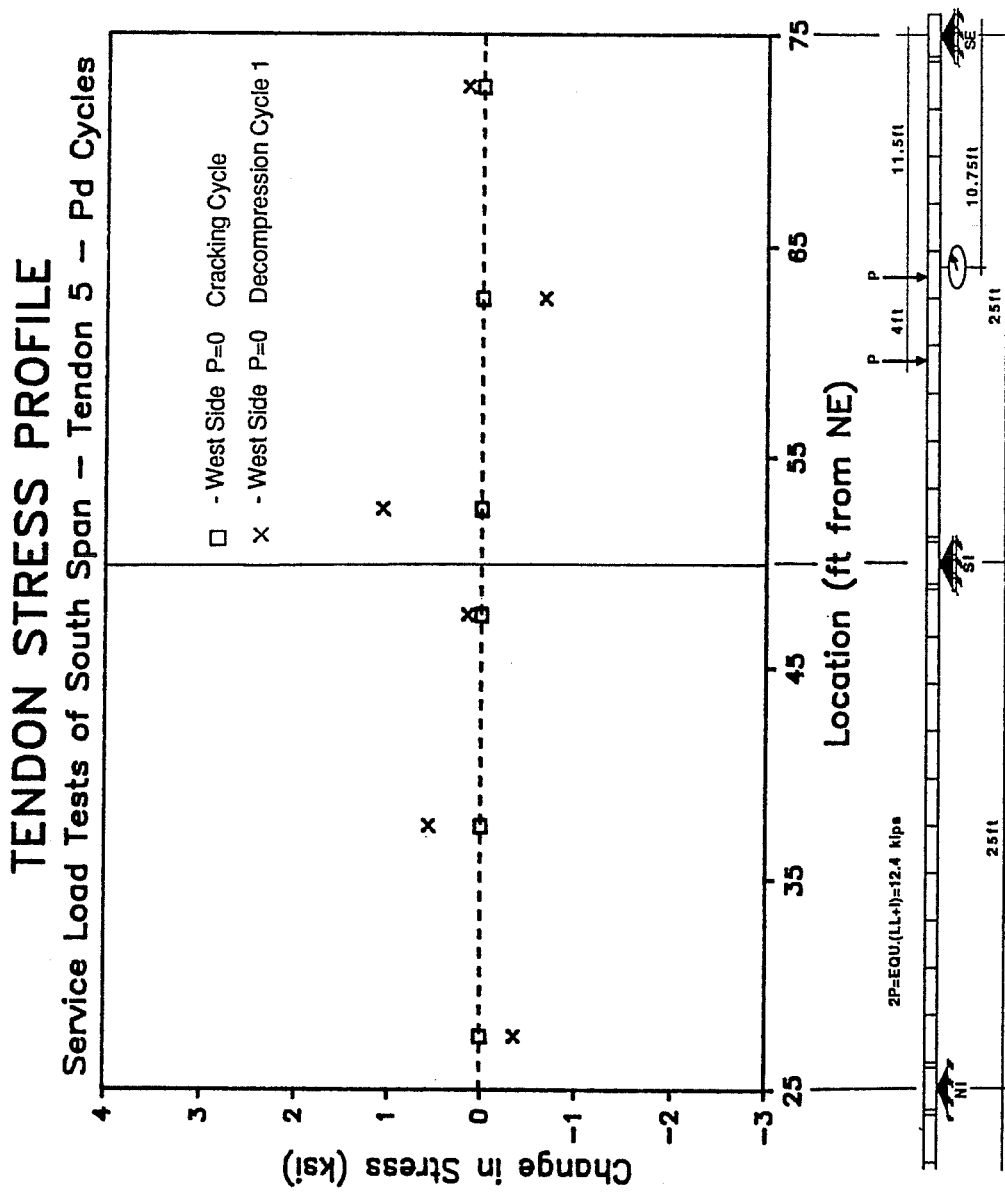


Figure 6.50 Tendon Slip after Cracking Cycle

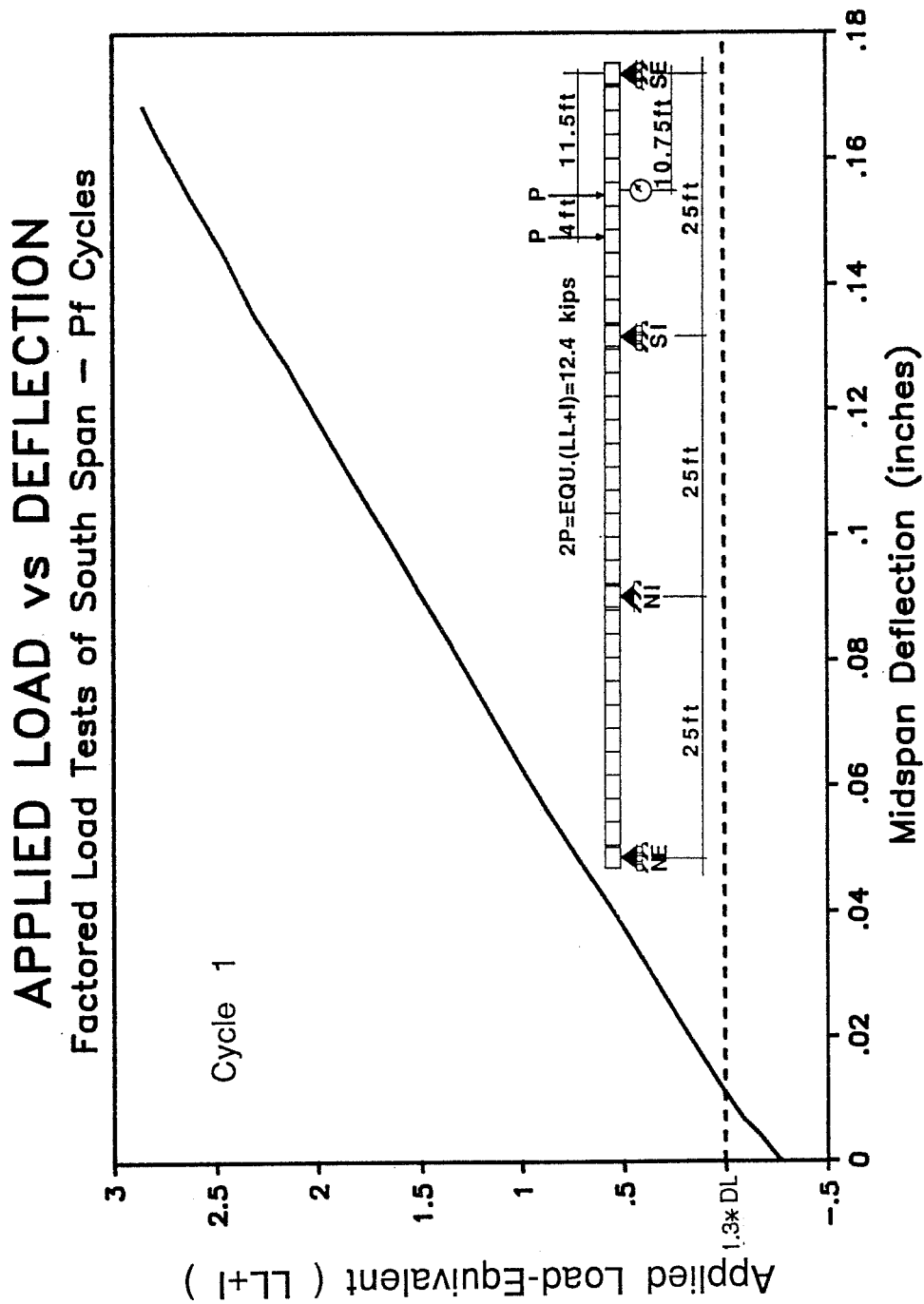


Figure 6.51 South span Factored Load Cycles: Applied Load vs. Deflection

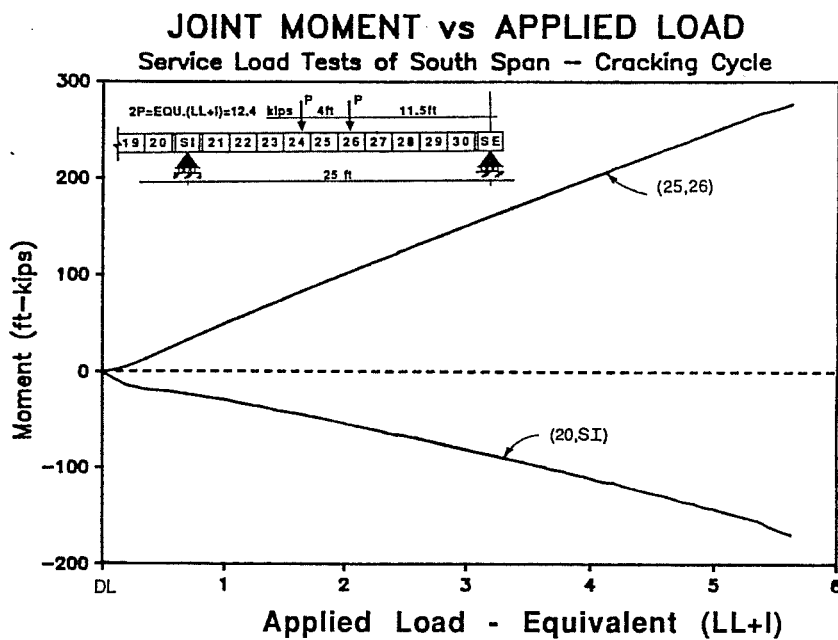
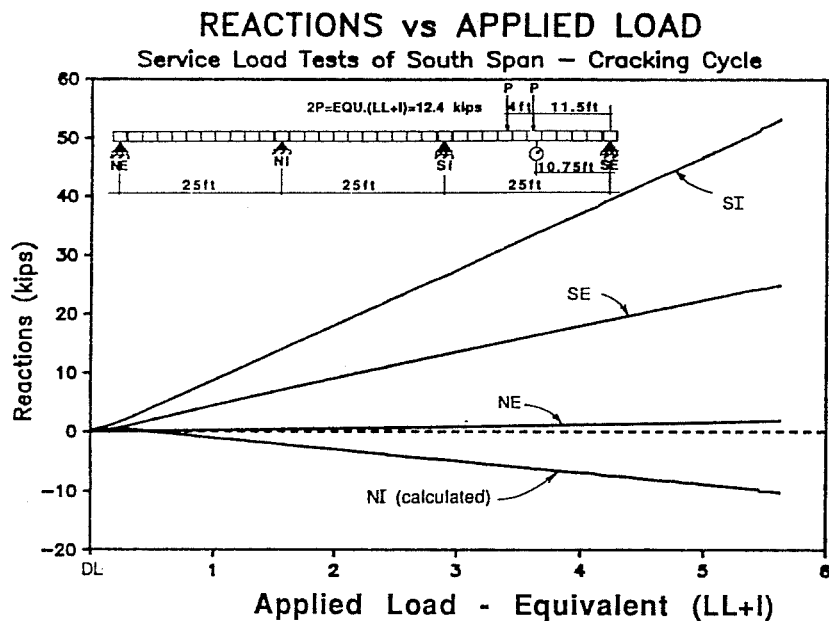


Figure 6.52 South Span Factored Load Cycles: Reactions and Joint Moments

Table 6.31 South-span Factored Load Cycles - Change in Tendon Stress (ksi) at Factored Load = 2.9(LL+I)

	(29,30) ext.end	(25,26) midspan	(21,22) int.end
Tendon 1a:	1	4	.5
Tendon 1b:	1	4	1
Tendon 3:	1	3	1

All gages are active.

Table 6.32 Summary of South-span Factored Load Cycles

$P_{applied}$:	Description:
1.3DL-0.28(LL+I)	-Start Test ($P_{rams}=0$)
1.3DL	-Start Live Load application from the factored dead load condition
1.3DL+2.2(LL+I)	-Decompression Load
1.3DL+2.9(LL+I)	-Factored Load Condition

Both the reactions and the calculated joint-moments show extremely linear behavior indicating minimal internal force redistribution. All tendons exhibited linear behavior with a maximum stress range of approximately 4.5 ksi.

6.7.3 Flexural Strength Tests Of South-Span

6.7.3.1 Crack Opening Cycles for South-Span. Load was increased beyond factored load levels to investigate the ultimate flexural behavior of the system. The first stage of the flexural strength test was to apply load to the structure to visibly open a midspan crack. Three cycles of load were applied to open the midspan crack. The load was applied in 0.32(LL+I) increments to the factored load level of 2.9(LL+I), and then in 0.16(LL+I) increments to a maximum applied load of 4.8(LL+I). Because the crack had only partially progressed during the initial cracking cycle (Section 6.7.1.2), additional cracking occurred during the first crack-opening cycle. The corresponding crack opening at this load level was approximately 0.03 in., which translates to 0.12 in. for the prototype structure.

After fully cracking the south-span in cycle 1, the structure behaved quite differently in the second and third crack-opening cycles. The flexural stiffness reduced for loads higher than the decompression load just as it did for the dry-jointed north-span.

The applied load-deflection response for the three crack-opening cycles is shown in Fig. 6.53. The measured reactions and the calculated joint-moments are plotted with respect to the applied load in Fig. 6.54.

2.2(LL+I) Decompression Load: At load levels higher than the decompression load the load-deflection, reaction, and joint-moment responses all exhibited the same behavior as observed for the dry-jointed north-span. After decompression, the midspan stiffness reduced and internal forces were redistributed toward the interior support.

2.4(LL+I): For cycles 2 and 3 the midspan region of all the tendons in the south-span exhibited linear response up to approximately 2.4(LL+I) with a corresponding stress range of approximately 3 ksi. For load levels higher than 2.4(LL+I) the tendon stresses increased at a higher rate.

2.8(LL+I): The crack-opening response near joint (25,26) for the first and second cycle is shown in Fig.6.55. For the first cycle, only the west side of the crack began opening at 2.8(LL+I). During the later two cycles, after fully cracking the joint, both sides of the crack opened symmetrically. The crack also opened slightly wider in the later cycles.

4.8(LL+I): The applied load was increased until the crack adjacent to joint (25,26) was visibly open at a maximum load of 4.8(LL+I). The tangent stiffness computed for the crack-opening response at the beginning and end of the crack-opening cycle was calculated as 18(LL+I)/inch and 7.8(LL+I)/inch, respectively. The crack-opening cycles for the north-span are summarized in Tables 6.33, 6.34, and 6.35.

The applied load tendon stress response for the south-span crack-opening cycles was similar for all tendons. The applied load-stress response during the first and second crack-opening cycles for Tendon 4a is shown in Fig. 6.56. In the first cycle the tendons remained linear to approximately the decompression load, and then the tendon stresses started increasing at a slightly higher rate. The tendon

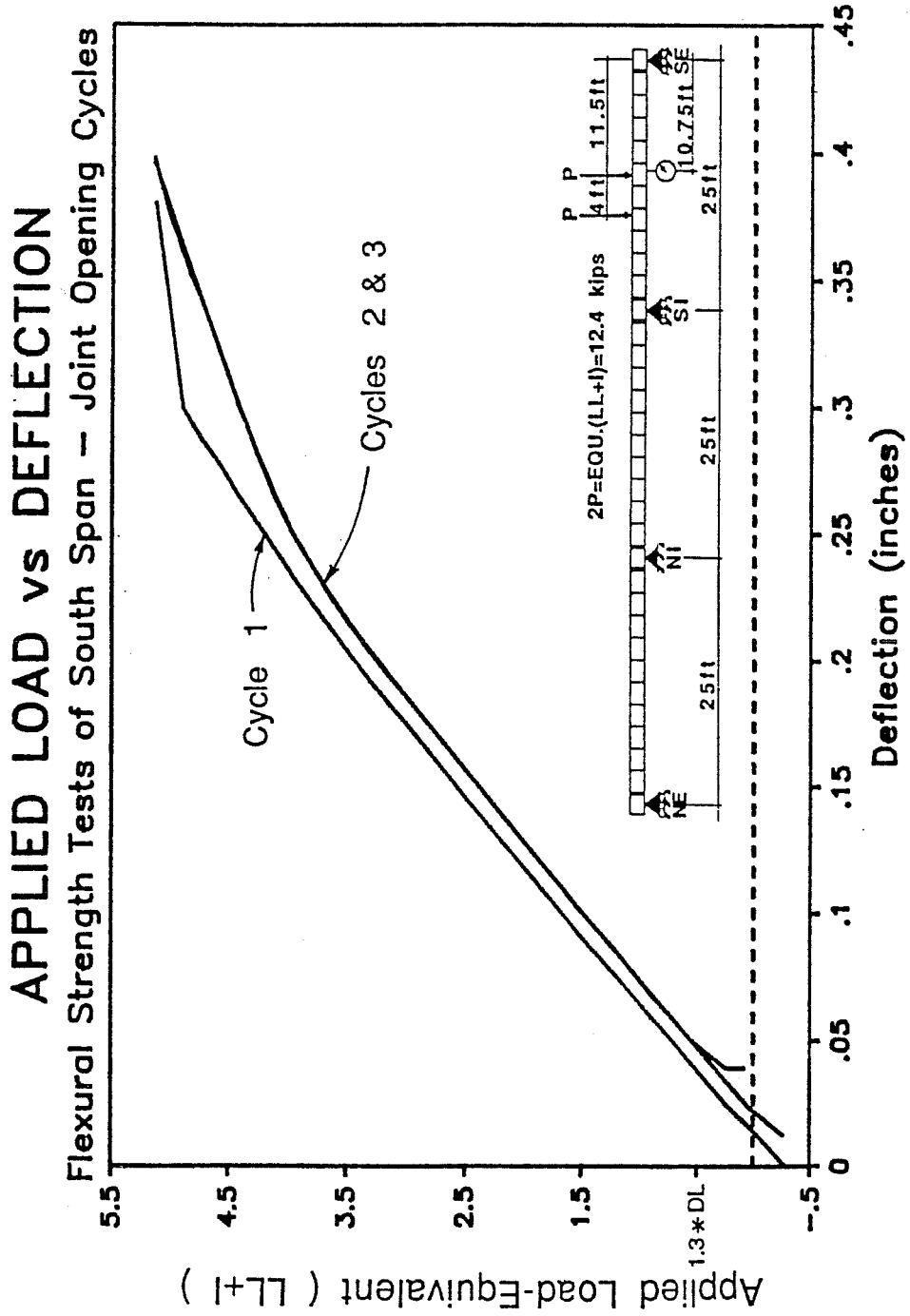


Figure 6.53 South Span Crack Opening Cycles: Applied Load vs. Deflection

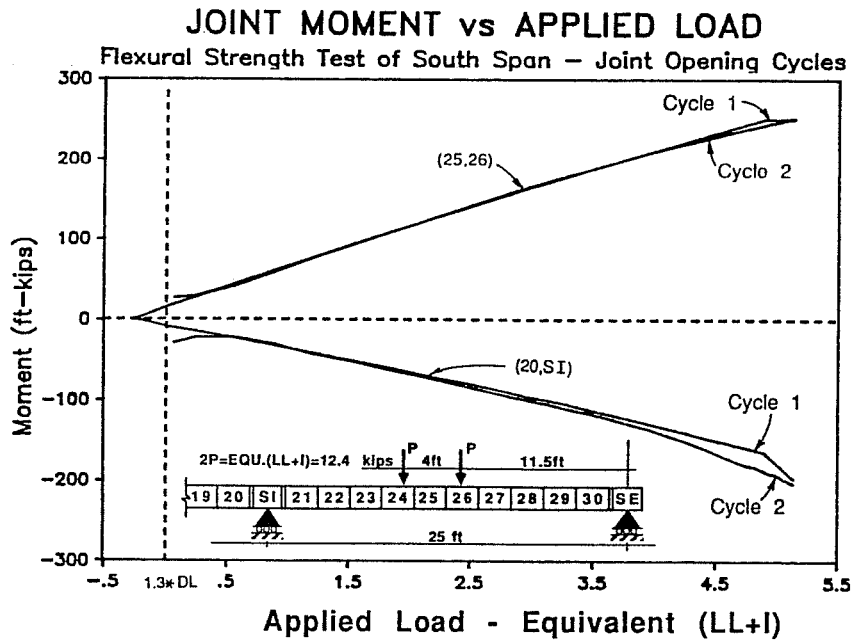
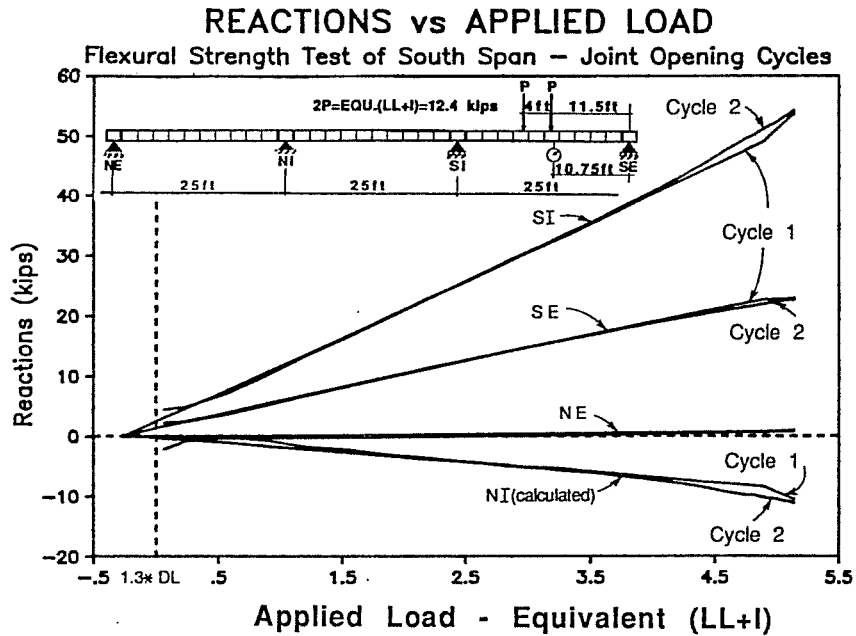
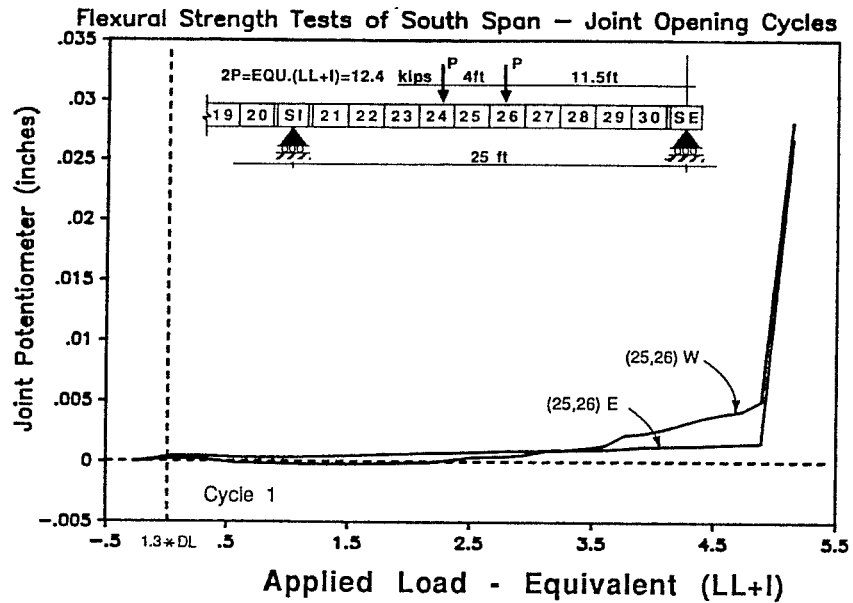


Figure 6.54 South Span Crack Opening Cycles: Reactions and Joint Moments

JOINT OPENING POTENTIOMETER vs APPLIED LOAD



JOINT OPENING POTENTIOMETER vs APPLIED LOAD

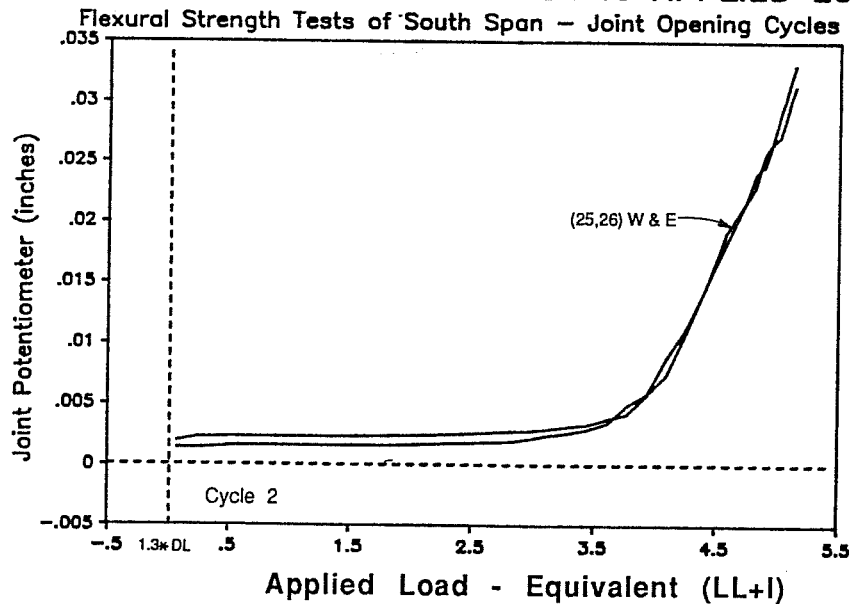


Figure 6.55 South Span Crack Opening Cycles: Joint Opening Potentiometer vs. Applied Load

Table 6.33 South-span Crack-Opening Cycles - Maximum Response Values at Load = 4.8(LL+I)

	(end of cycle 2)
Deflections	0.40 inches (L/750)
Reactions	54 kips at SI
Moments M +ve	250 ft-kips at (25,26)
M -ve	-200 ft-kips at (20,SI)

Table 6.34 South-span Crack-Opening Cycles - Change in Tendon Stress (ksi) at Load = 4.7(LL+I) Cycle 1

	(29,30) ext.end	(25,26) midspan	(21,22) int.end
Tendon 4a:	3	11	1
Tendon 4b:	2	13	2
Tendon 5:	2	13	2

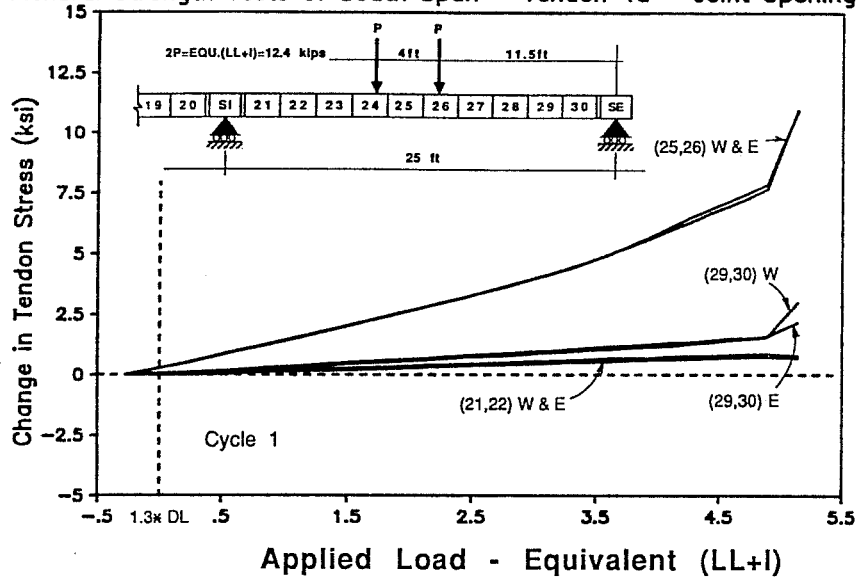
Table 6.35 Summary of South-span Crack-Opening Cycles

<i>P_{applied}</i> :	Description:
1.3DL-0.28(LL+I)	-Start Test ($P_{rams}=0$)
1.3DL	-Start Live Load application from the factored dead load condition
1.3DL+2.2(LL+I)	-Decompression Load
1.3DL+2.4(LL+I)	-The midspan stresses for all the south-span tendons begin to increase at a faster rate
1.3DL+2.8(LL+I)	-Crack near joint (25,26) begins to open
1.3DL+4.8(LL+I)	-Maximum Load for Crack-Opening Cycles

stresses increased suddenly to a maximum stress increase of approximately 11 ksi when the section cracked. Slip was also apparent from the exterior end towards the midspan region.

After applying one cycle of load there was a net change in tendon stress at the start of the second cycle. The exterior end stresses had increased and the midspan

CHANGE IN TENDON STRESS vs APPLIED LOAD
 Flexural Strength Tests of South Span – Tendon 4a – Joint Opening Cy



CHANGE IN TENDON STRESS vs APPLIED LOAD
 Flexural Strength Tests of South Span – Tendon 4a – Joint Opening Cy

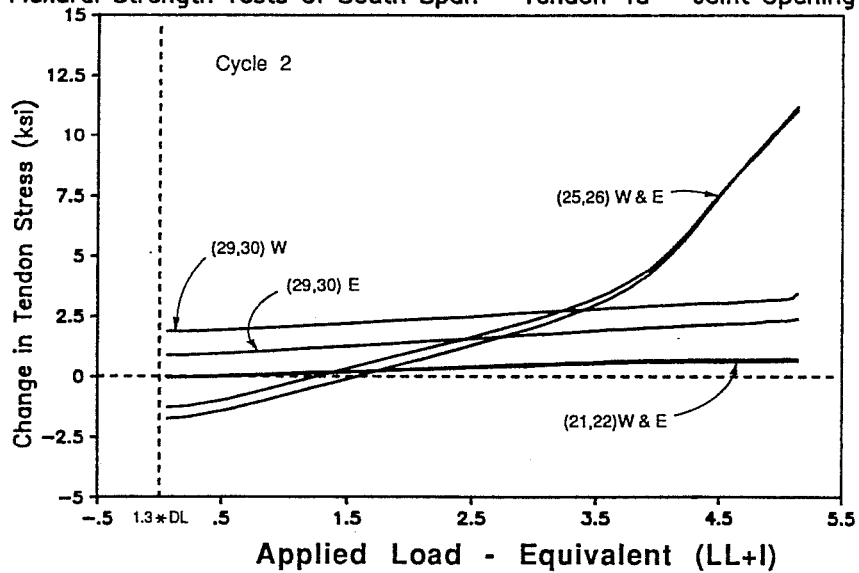


Figure 6.56 South Span Cracking Cycle: Joint Opening Potentiometer vs. Applied Load

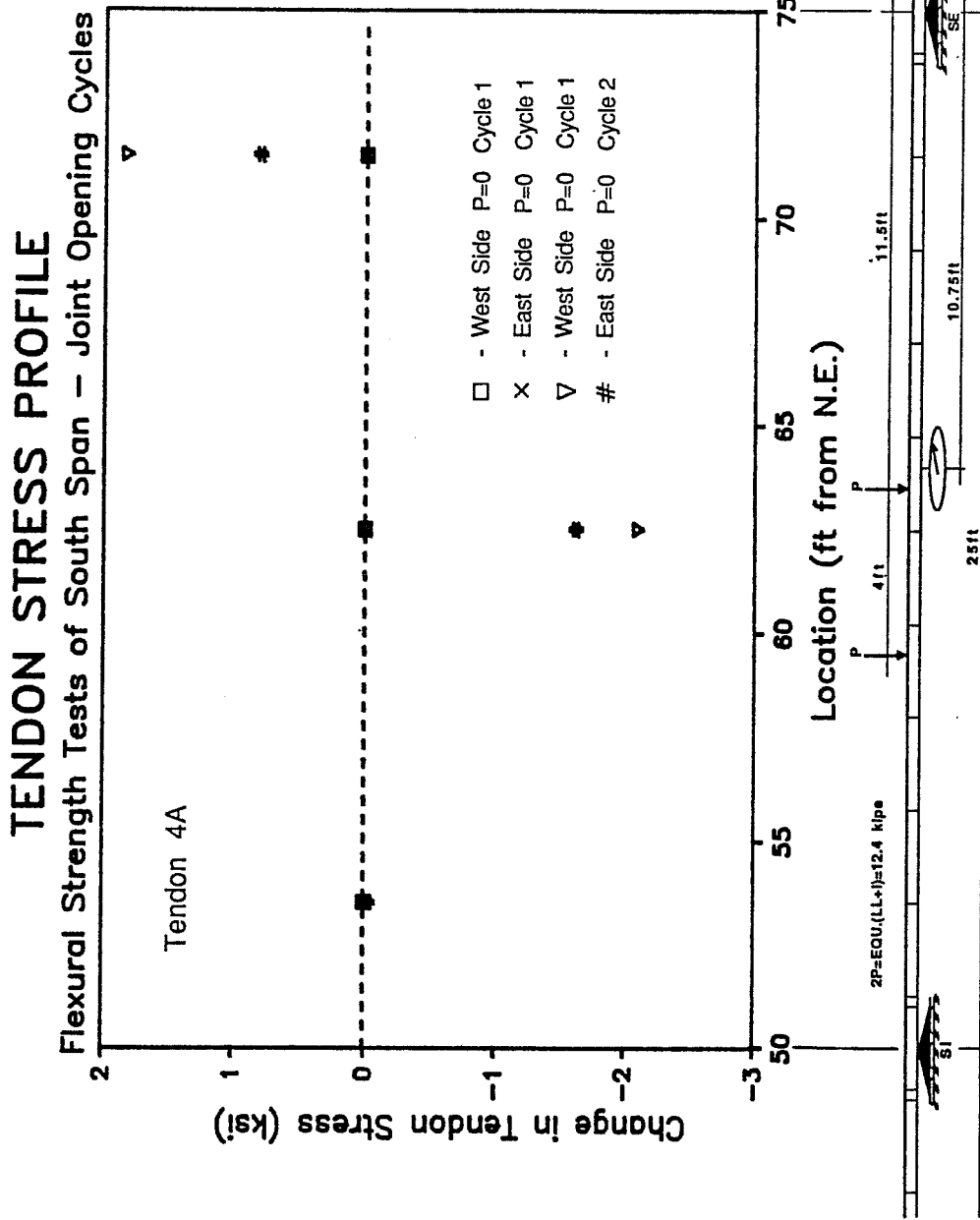


Figure 6.57 South Span Crack Opening Cycles: Tendon 4a Stress Profile Before Cycles 1 & 2

stresses had decreased. This is also illustrated by the tendon stress profile (Fig.6.57) for the unloaded condition preceding each load cycle. With slip occurring towards the midspan section of the tendon, the "unstressed" length of that portion had increased, leading to decreased tendon stresses when the applied load was removed. Conversely, because the tendon had slipped away from the exterior region, the "unstressed" length had decreased, leading to increased tendon stresses when the applied load was removed.

As load was applied for Cycle 2 the tendon-stress response histories had approximately the same initial slopes. At $2.4(LL+I)$ the stresses began deviating from the initial linear behavior, slowly at first and then at a higher rate at approximately $3.5(LL+I)$. Note also that stress range for the later crack-opening cycles was slightly higher in the midspan region and lower at the exterior end. However, the net stress increase from the start of the first cycle was the same for all cycles. No slipping was noticed in the later two crack-opening cycles.

Apart from the crack extension described above, there was no other cracking during the crack-opening cycles for the south-span. Only a single crack through the concrete adjacent to joint (25,26) was visible at the end of this cycle.

6.7.3.2 Flexural Strength Cycle for South-Span. After completing the crack-opening cycles the structure was loaded to higher levels to determine the flexural strength of the system. The load was applied in $0.81(LL+I)$ increments to the previous cracking load, in $0.16(LL+I)$ increments to $6.0(LL+I)$, in $0.08(LL+I)$ increments to $7.0(LL+I)$, and then $0.04(LL+I)$ increments until the flexural strength of the south-span was reached. The flexural strength test was conducted in one load cycle, and the strength was measured to be $7.7(LL+I)$ with an ultimate midspan deflection of 1.69 inches.

The applied load-deflection response for the flexural strength cycle is shown in Fig. 6.58. The measured reactions and calculated joint-moments are plotted with respect to the applied load in Fig. 6.59. The change in tendon stress due to applied load is shown for all south-span tendons in Fig. 6.60, and for all center-span tendons in Fig. 6.61. The joint behavior, as measured by potentiometer and grid crack-monitors, is illustrated in Fig. 6.62.

APPLIED LOAD VS DEFLECTION

Flexural Strength Tests of South Span -- Ultimate Cycle

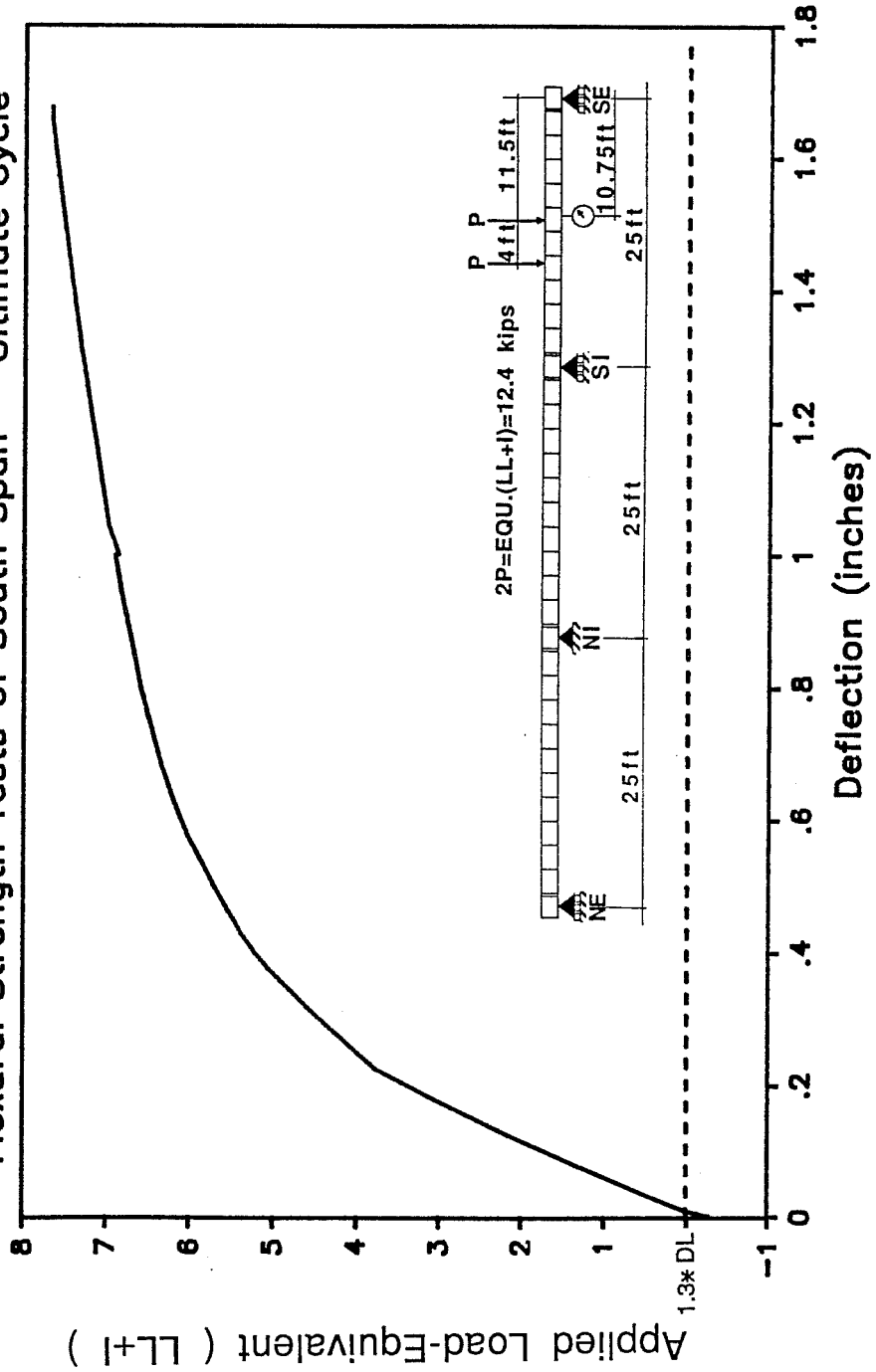


Figure 6.58 South Span Flexural Strength Test: Applied Load vs. Deflection

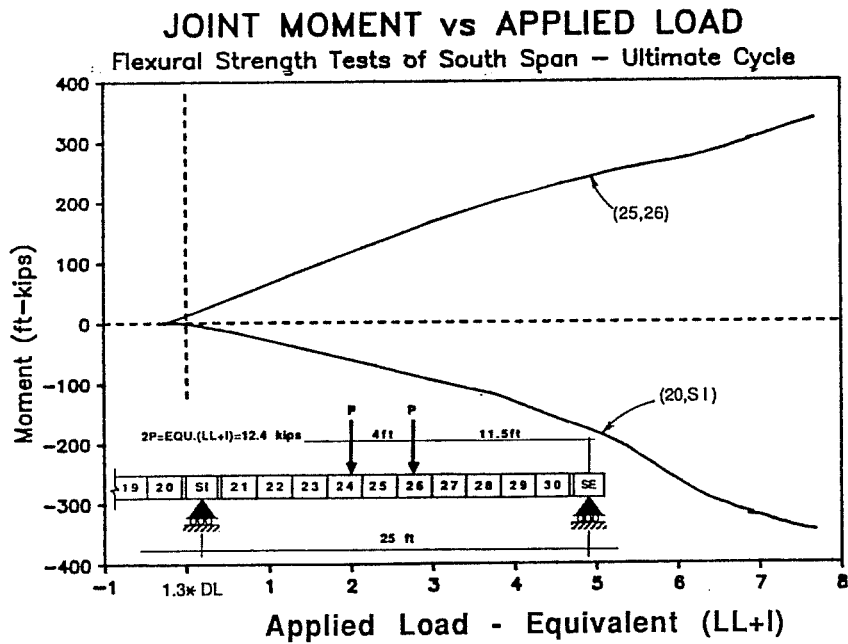
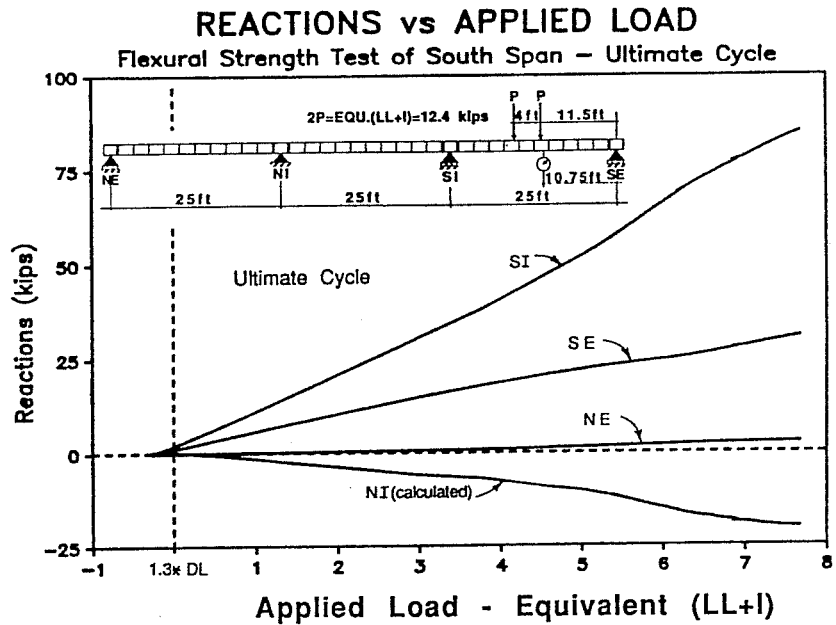


Figure 6.59 South Span Flexural Strength Test: Reactions and Joint Moments

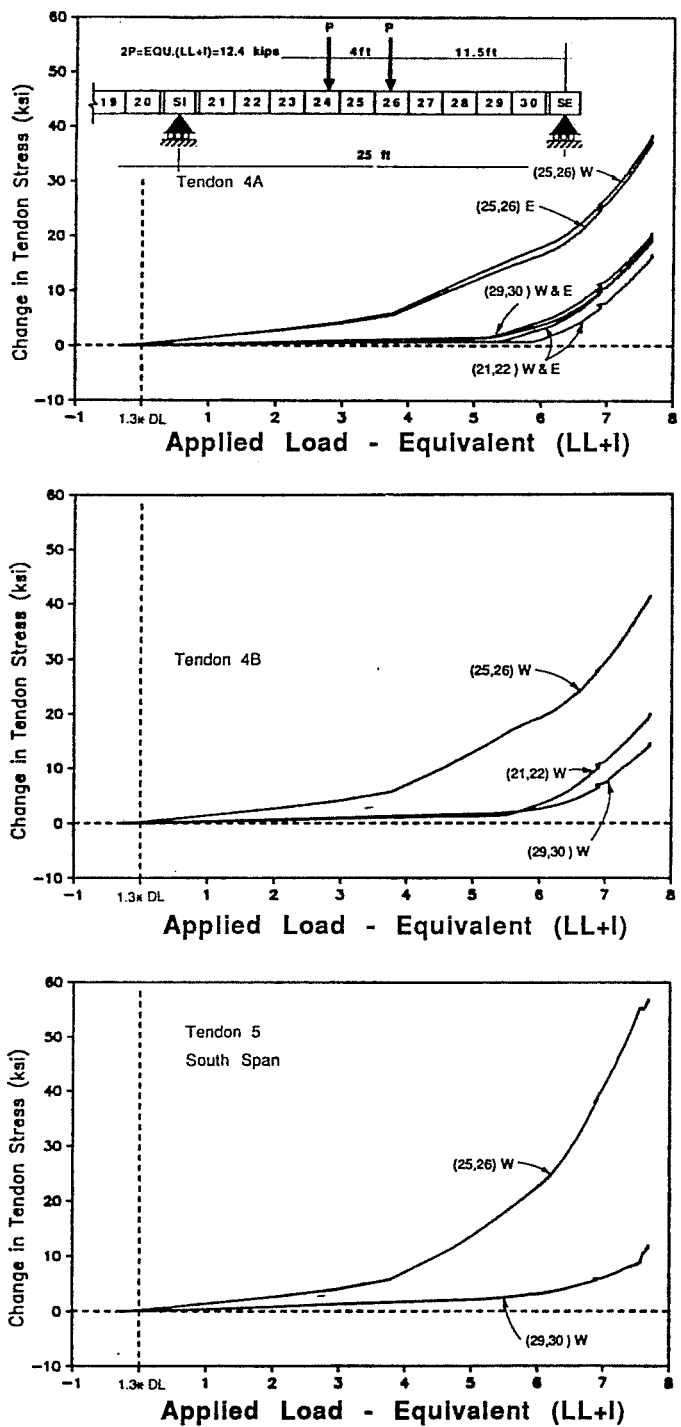


Figure 6.60 South Span Flexural Strength Test: Change in Tendon Stress vs. Applied Load South Span Tendons

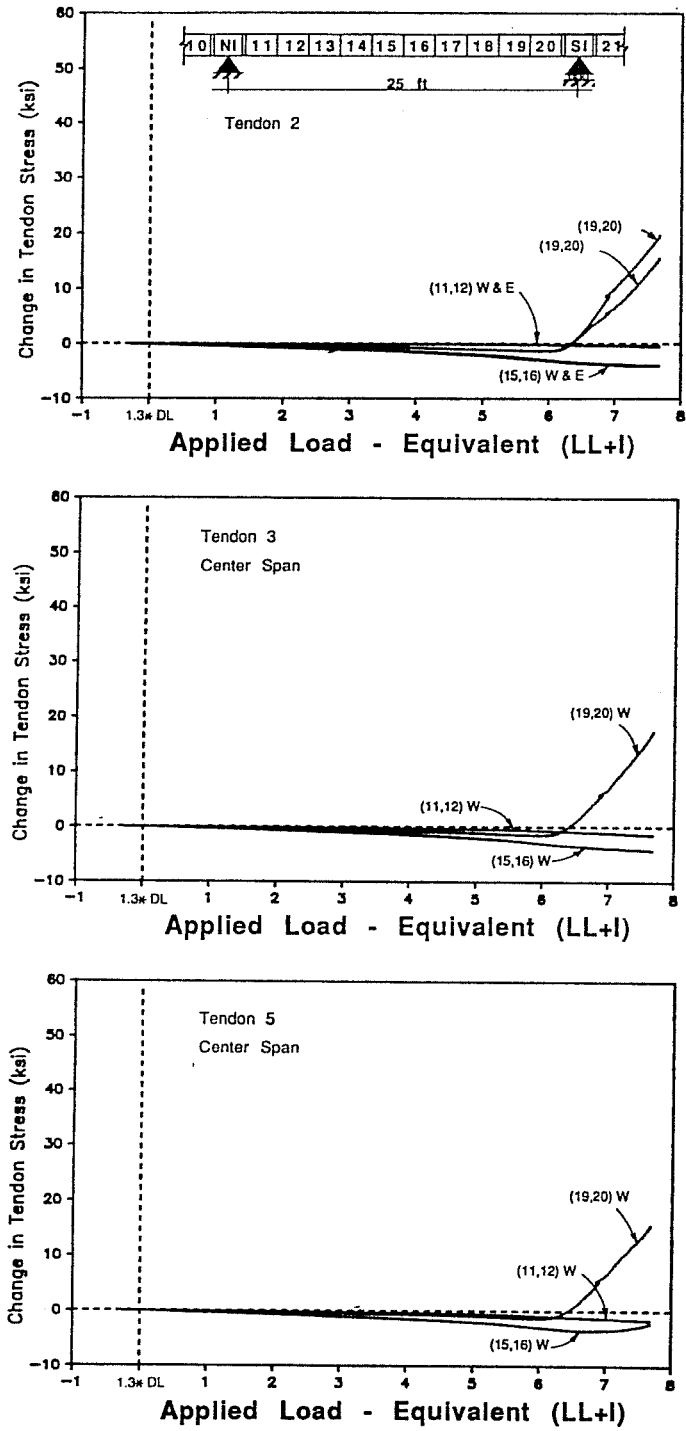
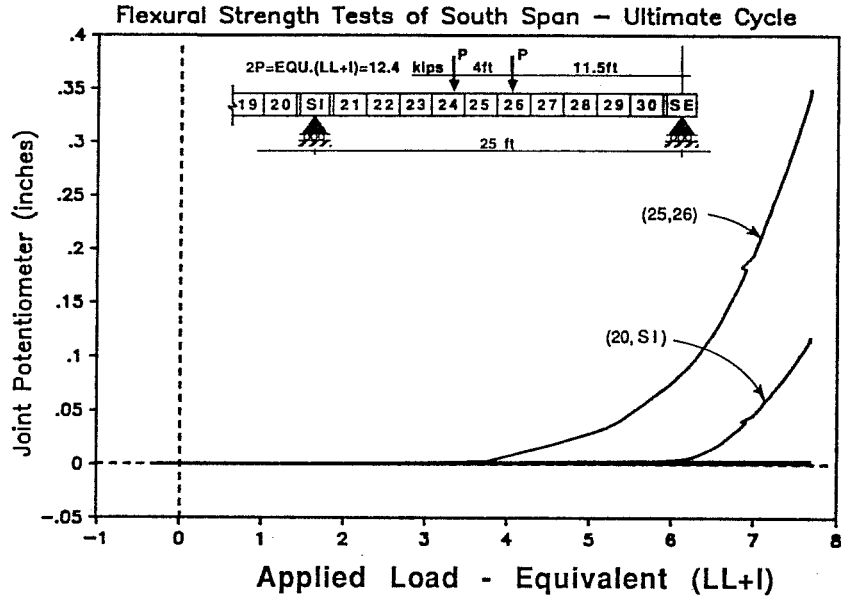


Figure 6.61 South Span Flexural Strength Test: Change in Tendon Stress vs. Applied Load South Span Tendons

JOINT OPENING POTENTIOMETER vs APPLIED LOAD



CRACK OPENING PROFILES

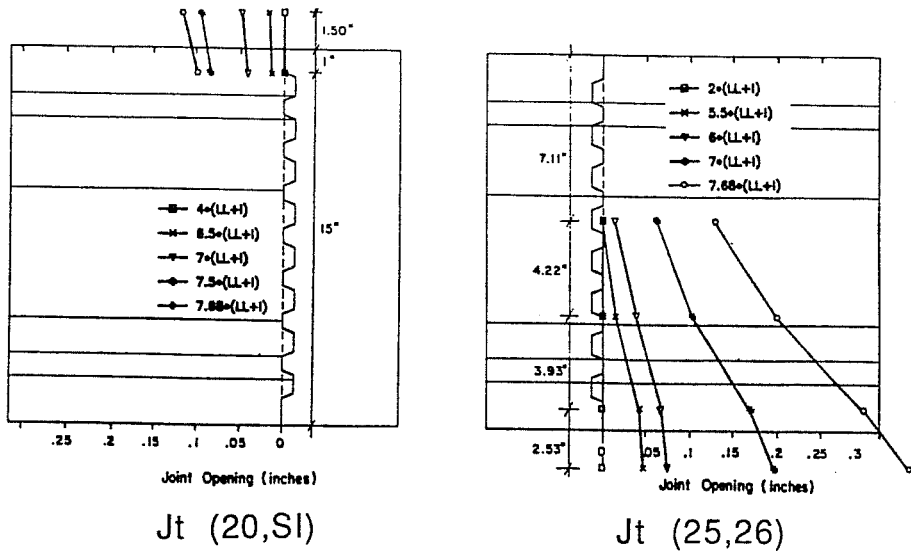


Figure 6.62 South Span Flexural Strength Test: Crack Opening Behavior

The south-span displayed essentially the same behavior for loads up to 2.4(LL+I) as was observed for the later cycles of the crack-opening load cycles.

3.8(LL+I): The crack adjacent to the midspan joint began opening widely causing internal forces to redistribute more rapidly and also causing all the tendon stresses in the midspan of the south-span to begin increasing at a higher rate.

5.2(LL+I): Tendon 5 (south-span) began slipping from the exterior end towards the midspan region.

5.3(LL+I): Tendon 4a began slipping from the exterior end towards the midspan region.

5.4(LL+I): Tendon 4a began slipping from the interior end towards the midspan region.

5.5(LL+I): Tendon 4b began slipping from both ends towards the midspan region.

5.8(LL+I): The crack adjacent to the support joint (20,SI) began to open at approximately 5.8(LL+I). This shows up as the inflection point in the reaction and moment data (Fig. 6.59) indicating that the reduced stiffness at the support caused a redistribution of internal forces back towards the midspan region.

All the tendon stresses at the near end of the interior span (tendons 2, 3, and 5) increased as the support crack began opening at approximately 5.8(LL+I).

6.2(LL+I): Tendon 5 (interior span) began slipping from the midspan region towards the near the south end of the interior span.

6.4(LL+I): The support crack began opening rapidly, reducing stiffness at the support, and redistributing internal forces back towards the midspan region. The tendon stresses for all tendons in the south- span began increasing at a higher rate.

7.6(LL+I): Tendon 5 (south-span) began slipping from the exterior end towards the midspan region.

7.7(LL+I) **Ultimate Flexural Strength:** The test was discontinued before catastrophic failure when the south-span experienced approximately the same

level of midspan deflection as the north-span. At this load level the tangent stiffness had reduced to 4 percent of its initial elastic stiffness and was approximately equal to the tangent stiffness at the conclusion of the north-span flexural test. The tangent stiffness for increasing levels of applied live load was calculated from the load-deflection curve, and is tabulated in Table 6.36. The flexural strength cycle for the south-span is summarized in Tables 6.37, 6.38, and 6.39.

Table 6.36 Tangent Stiffness During South-Span Tests – (measured in (LL+I)/inch)

Applied Load	Flexural Test	Shear Test
1(LL+I)	18	18
2(LL+I)	18	18
3(LL+I)	17	12
4(LL+I)	11	7.8
5(LL+I)	7.3	5.4
6(LL+I)	3.7	2.9
7(LL+I)	1.2	1.6
7.7(LL+I)	0.57	N/A
8.0(LL+I)	N/A	0.73

Table 6.37 South-Span Flexural Test - Maximum Response Values Flexural Strength Load = 7.7(LL+I)

Deflections	1.69 inches (L/178)
Reactions	93 kips at SI
Moments M +ve	340 ft-kips at (25,26)
M -ve	-350 ft-kips at (20,SI)

Table 6.38 South-span Flexural Test - Change in Tendon Stress (ksi) Flexural Strength Load = 7.8(LL+I)

Exterior Span Tendons	Interior Span Tendons
Tendon 4a: 20 * 38 * 17	Tendon 2: 18 / <0 / <0
Tendon 4b: 14 * 41 * 19	Tendon 3: 18 / <0 / <0
Tendon 5: 12 * 57 / X	Tendon 5: 16 ** <0 / <0
key = (29,30)/(25,26)/(21,22) = ext.end/midspan/int.end	key = (19,20)/(15,16)/(11,12) = near end/midspan/far end

X: denotes inactive strain gauge
 * denotes slip towards midspan
 ** denotes slip towards near end

The measured deflected shapes of the three span structure for increasing levels of applied load are shown in Fig 6.63. At the service load (1.0(LL+I)) and the factored load (2.9(LL+I)) the deflections are small and the deflected shape is a smooth curve. The deflected shape remained smooth until the midspan crack began opening at 3.8(LL+I). Beyond this load, “hinging” occurs at the opening crack, and the midspan deflections increase considerably. When the support crack opens at 5.8(LL+I), the mechanism forms and deflections begin to increase very rapidly. The final deflected shape of the structure clearly illustrates the mechanism behavior of the structure at ultimate load levels.

The reaction and joint-moment curves exhibit double curvature (slight S-shape). As the midspan crack opens, the midspan stiffness reduces causing internal forces to redistribute towards the support. When the support crack opens, the support stiffness reduces and internal forces are redistributed back towards midspan.

The concentrated rotations that occurred at critical opening cracks were measured with manually recorded crack-monitors distributed over the height of the crack. A profile of each opening crack during the flexural test of the south-span is shown at the bottom of Fig.6.62. Because of the presence of epoxy, large rotations occurred at only one midspan crack near joint (25,26) and one support crack adjacent to joint (NI,11). The measured profiles indicate that the crack opened linearly, with compressive stresses gradually concentrating in the top flange. The location of the

Table 6.39 Summary of South-span Flexural Strength Cycle

<i>P_{applied}</i> :	Description:
1.3DL-.28(LL+I)	-Start Test ($P_{rams}=0$)
1.3DL	-Start Live Load application from the factored dead load condition
1.3DL+2.2(LL+I)	-Decompression Load
1.3DL+2.4(LL+I)	-Midspan stresses for all south-span tendons begin to increase at a higher rate
1.3DL+3.8(LL+I)	-Crack adjacent to joint (25,26) began opening causing increased tendon stresses and redistribution of internal forces towards support region.
1.3DL+5.2(LL+I)	-Tendon 5 (south-span) began slipping from exterior end towards the midspan region.
1.3DL+5.3(LL+I)	-Tendon 4a began slipping from exterior end towards the midspan region.
1.3DL+5.4(LL+I)	-Tendon 4a began slipping from interior end towards the midspan region.
1.3DL+5.5(LL+I)	-Tendon 4b began slipping from both ends towards the midspan region.
1.3DL+5.8(LL+I)	-Crack adjacent to joint (20,S1) began opening causing redistribution of forces back towards midspan. -The tendons at the near end of the interior span begin to develop additional load.
1.3DL+6.2(LL+I)	-Tendon 5 (interior span) began slipping from the midspan region towards the near (south) end of the interior span.
1.3DL+6.4(LL+I)	-The support crack began opening rapidly. -The tendon stresses for all tendons in the south-span begin to increase at a higher rate.
1.3DL+7.6(LL+I)	-Tendon 5 (south-span) began slipping from the exterior end towards the midspan region.
1.3DL+7.7(LL+I)	-Ultimate Flexural Strength

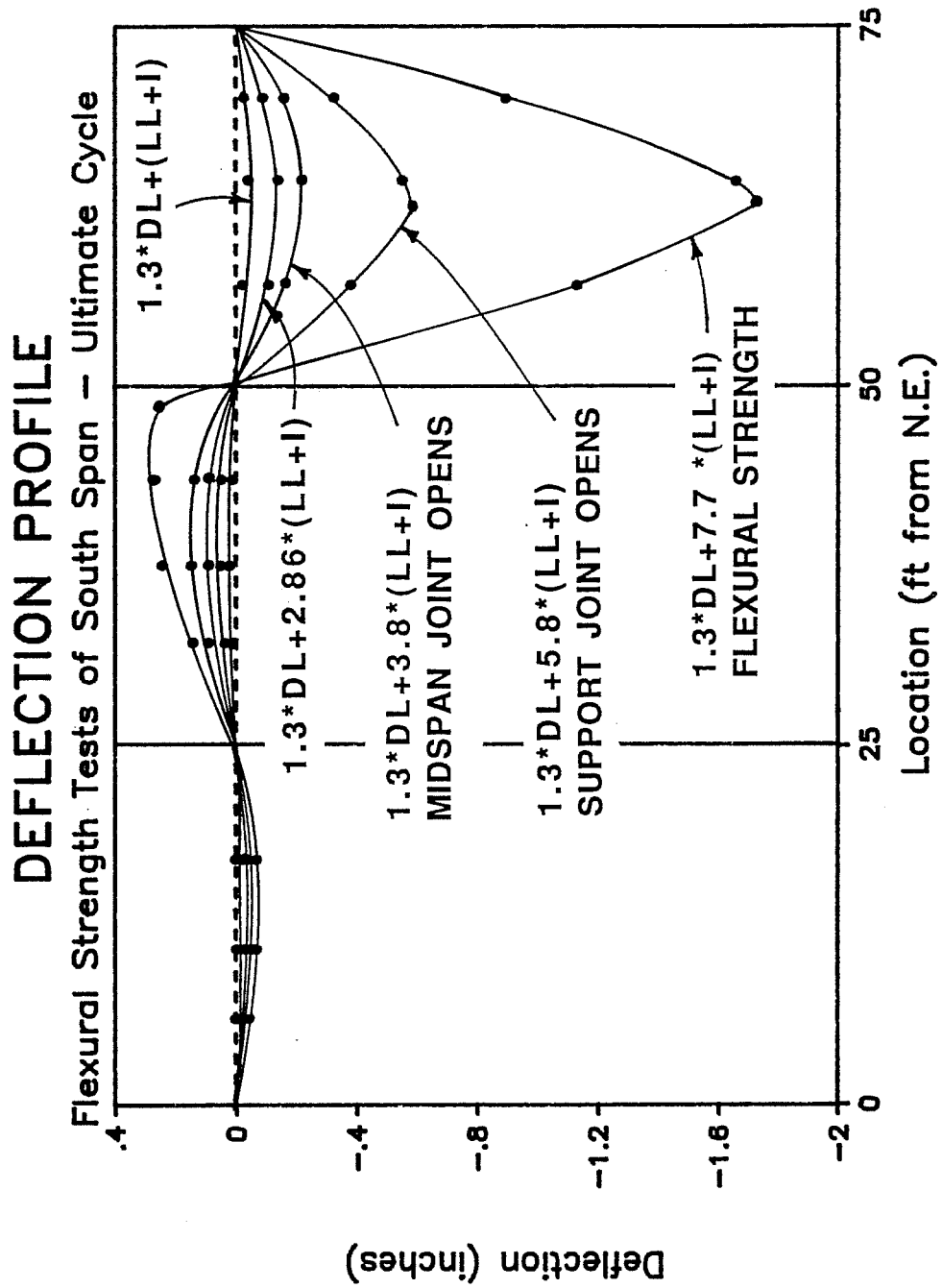


Figure 6.63 South Span Flexural Strength Test: Deflection Profiles

neutral axis at ultimate strength can be extrapolated from the crack profiles, and was within the compression flange at both opening cracks.

The concentrated angle changes that occurred at each mechanism can be calculated approximately from the crack opening profiles. The concentrated rotations that occurred at the opening cracks were approximately 1.1 degrees at the midspan crack near joint (25,26), and approximately 0.4 degrees at the support joint (20,SI). The midspan angle change is again approximately three times the magnitude of the concentrated angle change at the support.

The cracking behavior of the midspan region of the south-span during the flexural strength test is summarized in Fig. 6.64. The lines indicate the total length of the crack when the flexural strength ($7.7(LL+I)$) was reached. The initial crack length and load at which it was first observed are also indicated. The shear transfer at the segment joints when the ultimate flexural moment was reached is also shown. The shear in segment 26 was distributed primarily towards the exterior support with a shear transfer of approximately $1.6(LL+I)$ at the opening crack.

The rotations required for increased tendon forces occurred primarily at a crack through the concrete adjacent to joint (25,26). Inclined web cracking first occurred at an applied load of approximately $5.1(LL+I)$. The inclined cracking extended from the open flexural crack, and generally fanned towards the load point. The width of the inclined web cracks remained small throughout the flexural test. Horizontal cracking was also noticed near the web/top-flange junction near joint (25,26). At ultimate loads the neutral axis had shifted into the top flange as indicated by cracking in the bottom face of the top flange.

6.7.4 Shear Strength Cycle for South-Span. The final test that was run on the south-span was a shear test in which the load was applied so that significant shear would be transferred across an opening crack adjacent to a joint. One cycle of load was applied in $0.56(LL+I)$ increments to $4.1(LL+I)$, in $0.32(LL+I)$ increments to $5.6(LL+I)$, in $0.16(LL+I)$ increments up to $7.5(LL+I)$, and then in $0.08(LL+I)$ increments to a maximum load of $8.0(LL+I)$. The test was discontinued when the applied load-deflection stiffness had reached approximately the same level as for the flexural strength test. As in the dry-jointed north-span, the strength was ultimately

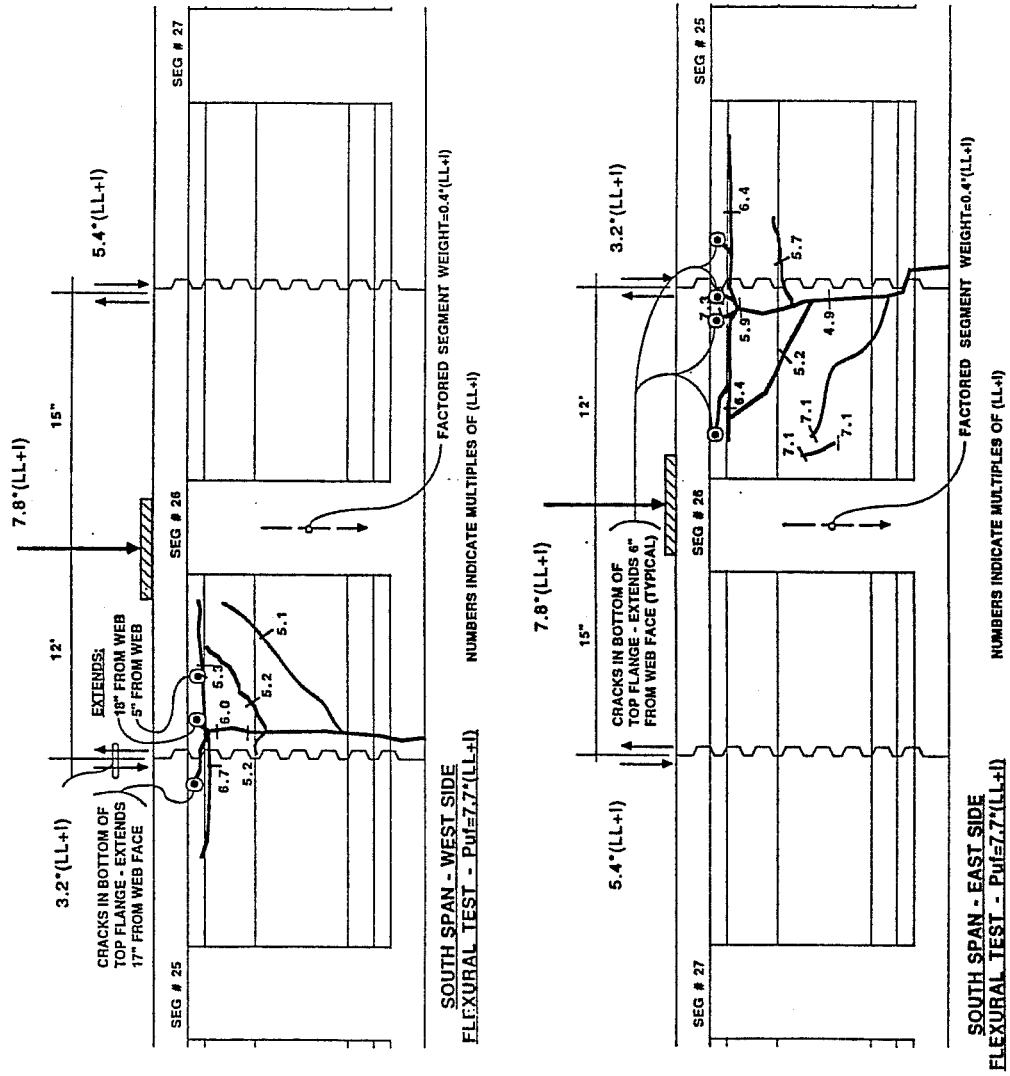


Figure 6.64 South Span Flexural Strength Test: Cracking Summary

limited by the flexural strength although the shear transfer at the opening crack caused markedly different local behavior.

The applied load-deflection response for the shear strength cycle is shown in Fig. 6.65. The measured reactions and calculated joint-moments are plotted with respect to applied load in Fig. 6.66. The change in tendon stress due to applied load is shown for all south-span tendons in Fig. 6.67, and for all center-span tendons in Fig. 6.68. The crack behavior adjacent to the joint, as measured by potentiometer and grid crack-monitors, is illustrated in Fig. 6.69.

The sequence of events during the south-span shear test was very similar to that outlined earlier for the flexural strength test (Sec. 6.7.3.2). Detailed highlights of the shear test are summarized in Table 6.42.

The test was discontinued before catastrophic failure at 8.0(LL+I) when the south-span had been subjected to the same level of midspan deflection as the north-span. At this load level the tangent stiffness had reduced to 4 percent of the initial elastic stiffness and was approximately equal to the tangent stiffness at the conclusion of the north-span shear test. The tangent stiffness at increasing levels of applied load is tabulated in Table 6.36. The strength was ultimately limited by the flexural strength although the shear transfer at the opening crack caused markedly different local behavior. The shear strength test of the south-span is summarized in Tables 6.40, 6.41, and 6.42.

Table 6.40 South-span Shear Test - Maximum Response Values Shear Strength Load = 8.0(LL+I)

Deflections	2.29 inches (L/131)
Reactions	74 kips at SI
Moments M +ve	350 ft-kips at (26,27)
M -ve	-340 ft-kips at (20,SI)

APPLIED LOAD VS DEFLECTION

Shear Strength Test of South Span

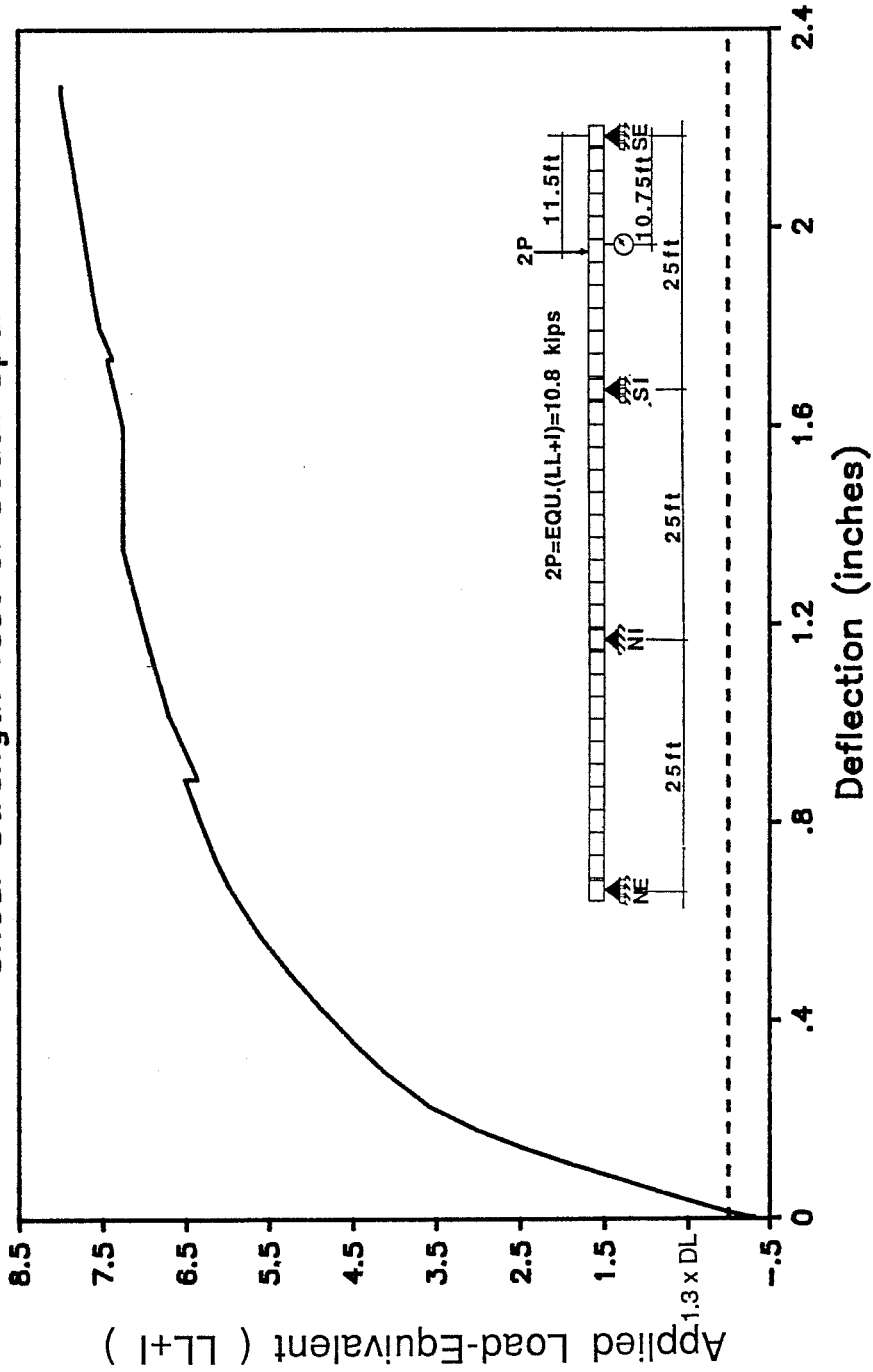


Figure 6.65 South Span Shear Test: Applied Load vs. Deflection

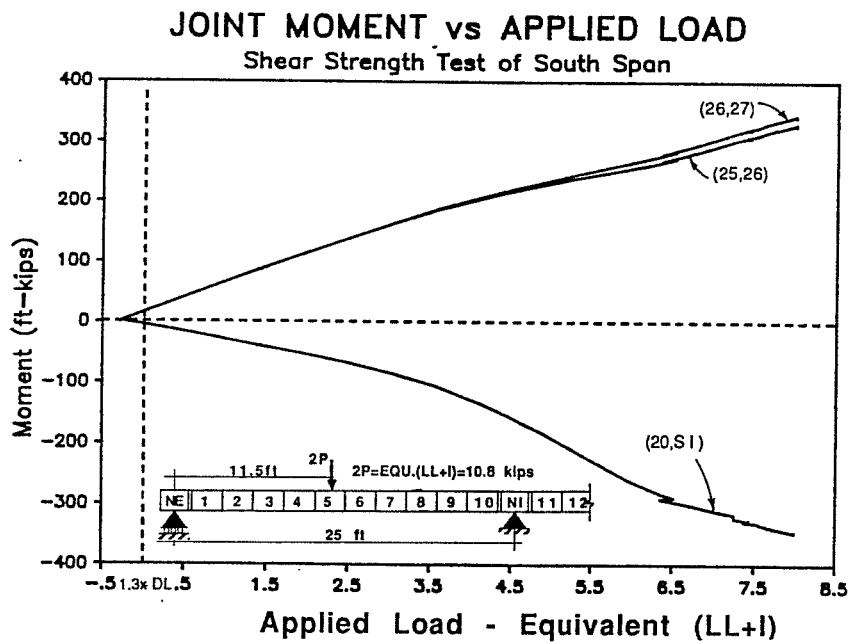
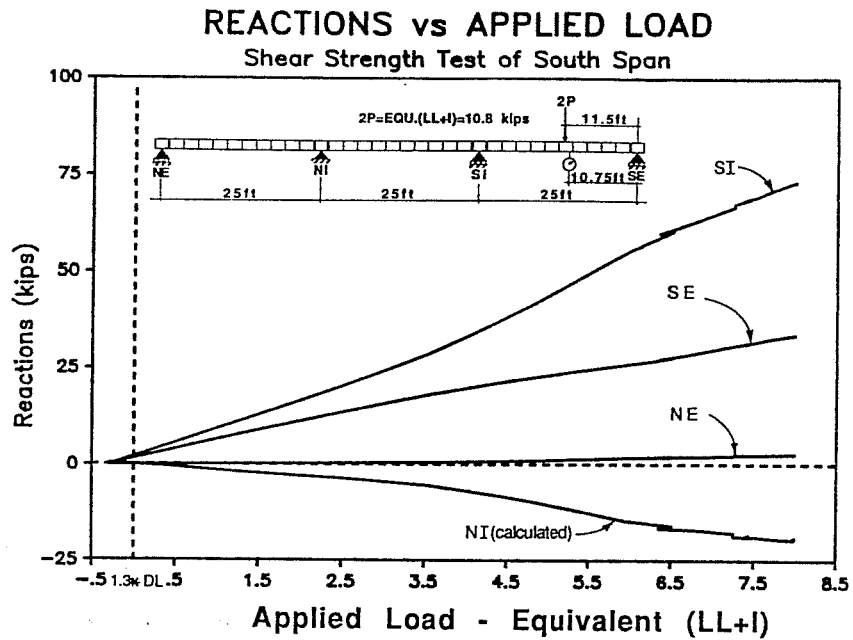


Figure 6.66 South Span Shear Test: Reactions and Joint Moments

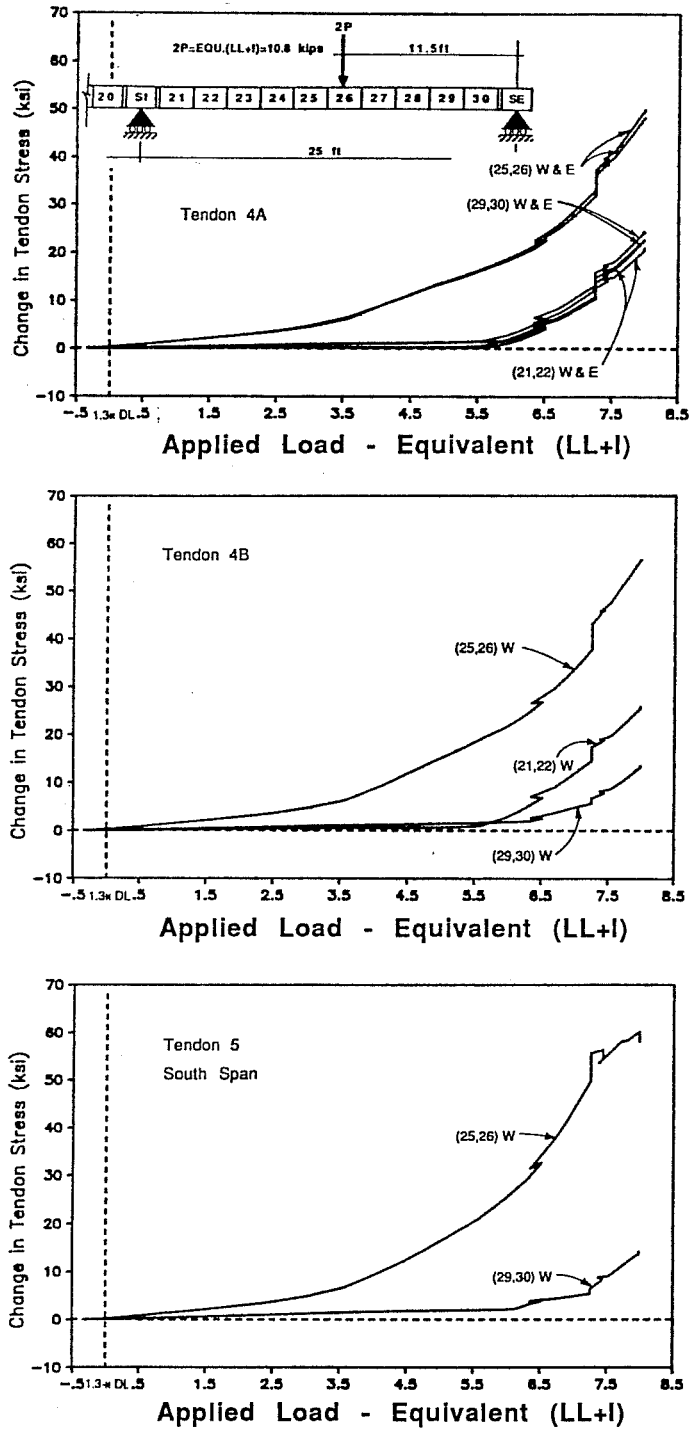


Figure 6.67 South Span Shear Test: Change in Tendon Stress vs. Applied Load- South Span Tendons

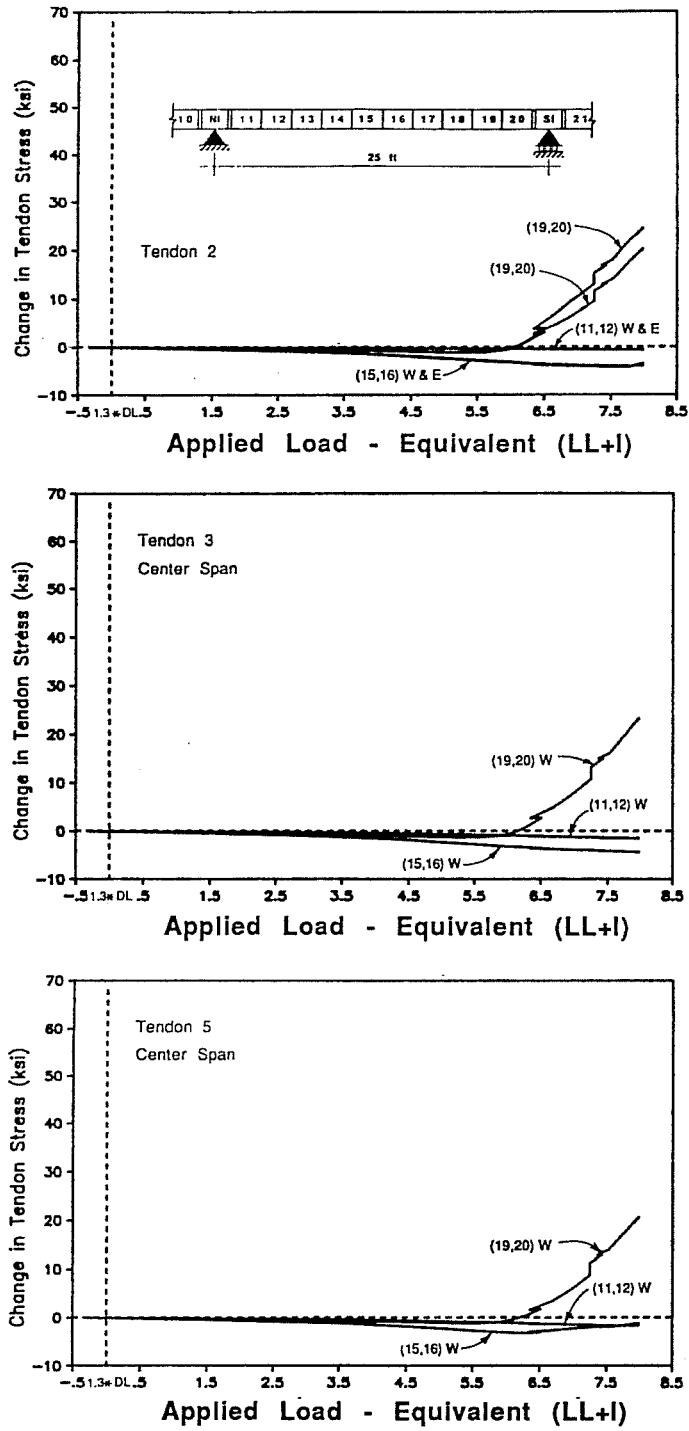
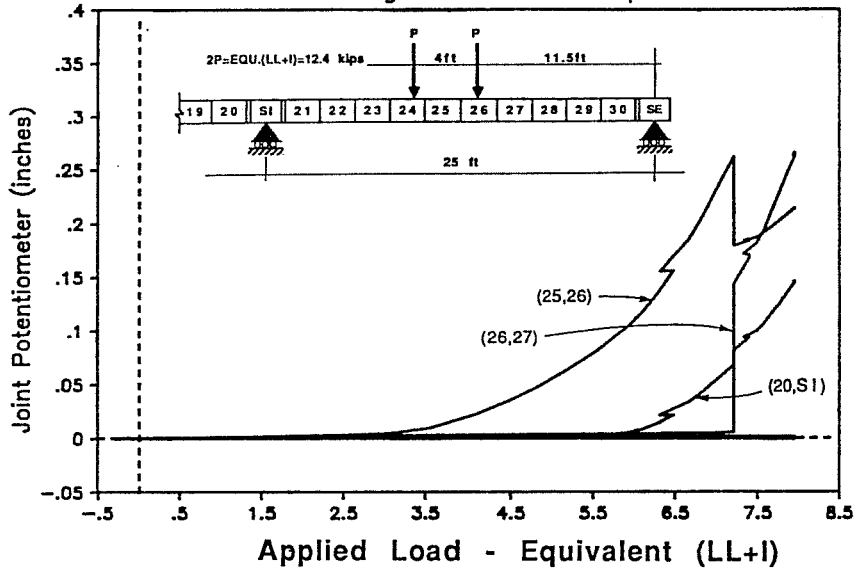


Figure 6.68 South Span Shear Test: Change in Tendon Stress vs. Applied Load-Center Span Tendons

JOINT OPENING POTENTIOMETER vs APPLIED LOAD

Shear Strength Test of South Span



CRACK OPENING PROFILES

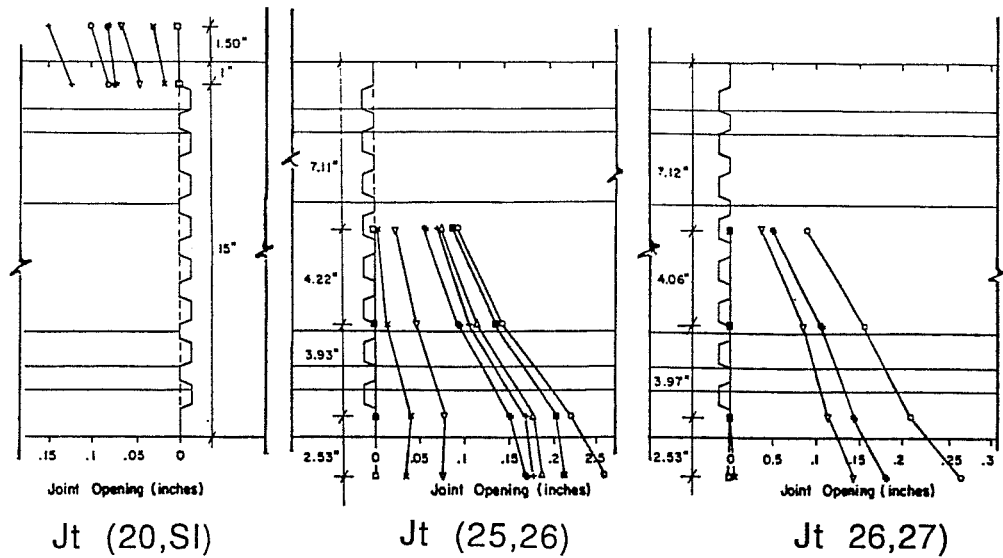


Figure 6.69 South Span Shear Test: Crack Opening Behavior

Table 6.41 South-span Shear Test - Change in Tendon Stress (ksi) Shear Strength Load = $8.0(LL+I)$

Exterior Span Tendons	Interior Span Tendons
Tendon 4a: 24 / 50 / 23	Tendon 2: 22 / -3 / 0
Tendon 4b: 14 / 57 / 27	Tendon 3: 23 / -3 / -1
Tendon 5: 17 / 60 / X	Tendon 5: 21 ** -1 / -1
key = (29,30)/(25,26)/(21,22) = ext.end/midspan/int.end	key = (19,20)/(15,16)/(11,12) = near end/midspan/far end

X: denotes inactive strain gauge
 * denotes slip towards midspan
 ** denotes slip towards near end

The measured deflected shapes of the three-span structure for increasing levels of applied load are shown in Fig 6.70. At the service load ($1.0(LL+I)$), and the factored load ($2.9(LL+I)$) the deflections were small and the deflected shape is a smooth curve. The deflected shape remains smooth until the midspan crack began opening at $3.5(LL+I)$. Beyond this load “hinging” occurred at the opening cracks, and midspan deflections increase considerably. When the support crack opened at $5.3(LL+I)$, the mechanism formed and deflections began increasing very rapidly. The final deflected shape of the structure clearly illustrates the mechanism behavior of the structure at ultimate load levels.

The reaction and joint-moment curves again exhibited double curvature (S-shape). As the midspan crack opened the midspan stiffness reduced causing internal forces to redistribute towards the interior support. When the support crack opened, the support stiffness reduced and internal forces were redistributed back towards midspan.

A profile of each opening crack during the shear test of the south-span is shown at the bottom of Fig. 6.69. Up to approximately $6.8(LL+I)$ the midspan rotations were concentrated at a single crack adjacent to joint (25,26). After cracking occurred near joint (26,27), the midspan rotations were equally distributed at the two cracks. Because a significant level of shear was transferred across the opening crack, concentrated rotations occurred at an inclined crack which extends from the load point to the bottom of the web, as shown in the cracking summary in Fig. 6.71

Table 6.42 Summary of South-Span Shear Strength Cycle

$P_{applied}$:	Description:
1.3DL-0.30(LL+I)	-Start Test ($P_{rams}=0$)
1.3DL	-Start Live Load application from the factored dead load condition
1.3DL+2.2(LL+I)	-Decompression load
1.3DL+2.4(LL+I)	-The midspan stresses for all south-span tendons begin to increase at a higher rate. The measured stress range of midspan was approximately 3 ksi.
1.3DL+3.0(LL+I)	-The cracks from the previous flexural test began to open.
1.3DL+3.5(LL+I)	-The crack adjacent to joint (25,26) began opening widely causing increased tendon stresses and redistribution of internal forces towards support region.
1.3DL+4.8(LL+I)	-Cracking occurs through the bottom flange approximately 9 in. south of joint (25).
1.3DL+5.3(LL+I)	-The crack adjacent to joint (20,S1) began opening causing redistribution of forces back towards midspan. -The tendon stresses at the near end of the interior span begin to increase.
1.3DL+5.6(LL+I)	-Tendon 4b began slipping from the interior end towards the midspan region.
1.3DL+5.7(LL+I)	-Tendon 4a began slipping from both ends towards the midspan region.
1.3DL+6.2(LL+I)	-Tendon 5 (south-span) began slipping from the exterior end towards the midspan region. Tendon 5 (interior span) also began slipping from the midspan region towards the near south end of the interior span.
1.3DL+6.3(LL+I)	-Tendon 4b began slipping from the exterior end towards the midspan region.
1.3DL+6.5(LL+I)	-An additional crack forms in the bottom flange of segment 26 at approximately 9 in. north of joint (26,27).
1.3DL+7.2(LL+I)	-Cracking occurs in 26 adjacent to joint (26,27).
1.3DL+7.7(LL+I)	-The primary inclined cracks form in segment 26. Rotations required for increased tendon stress concentrate at these inclined cracks.
1.3DL+7.8(LL+I)	-Tendon 2 (interior span) began slipping from the midspan region towards the near (south) end of the interior span.
1.3DL+8.0(LL+I)	-Ultimate strength limited by flexural capacity.

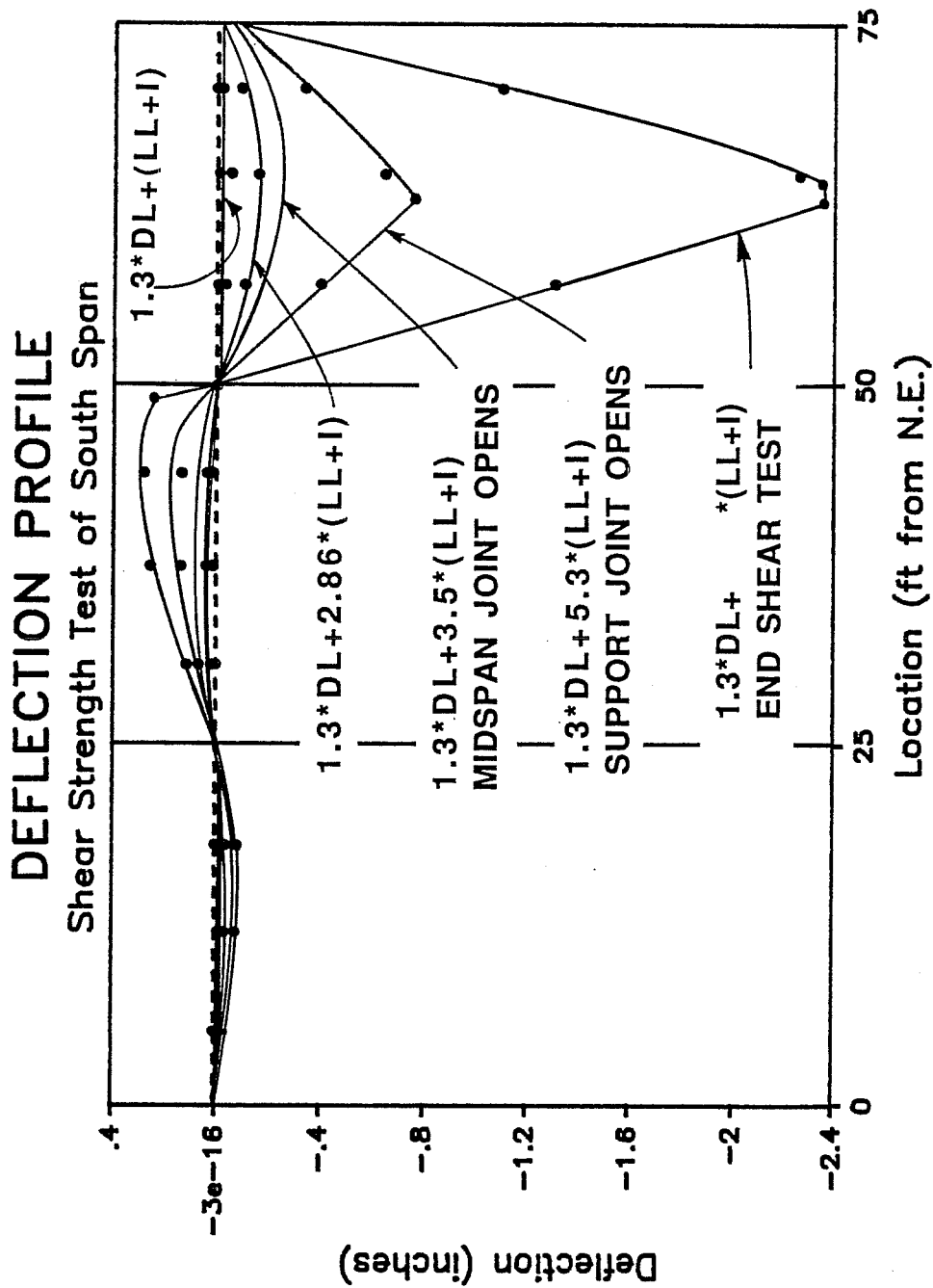


Figure 6.70 South Span Shear Test: Deflection Profile

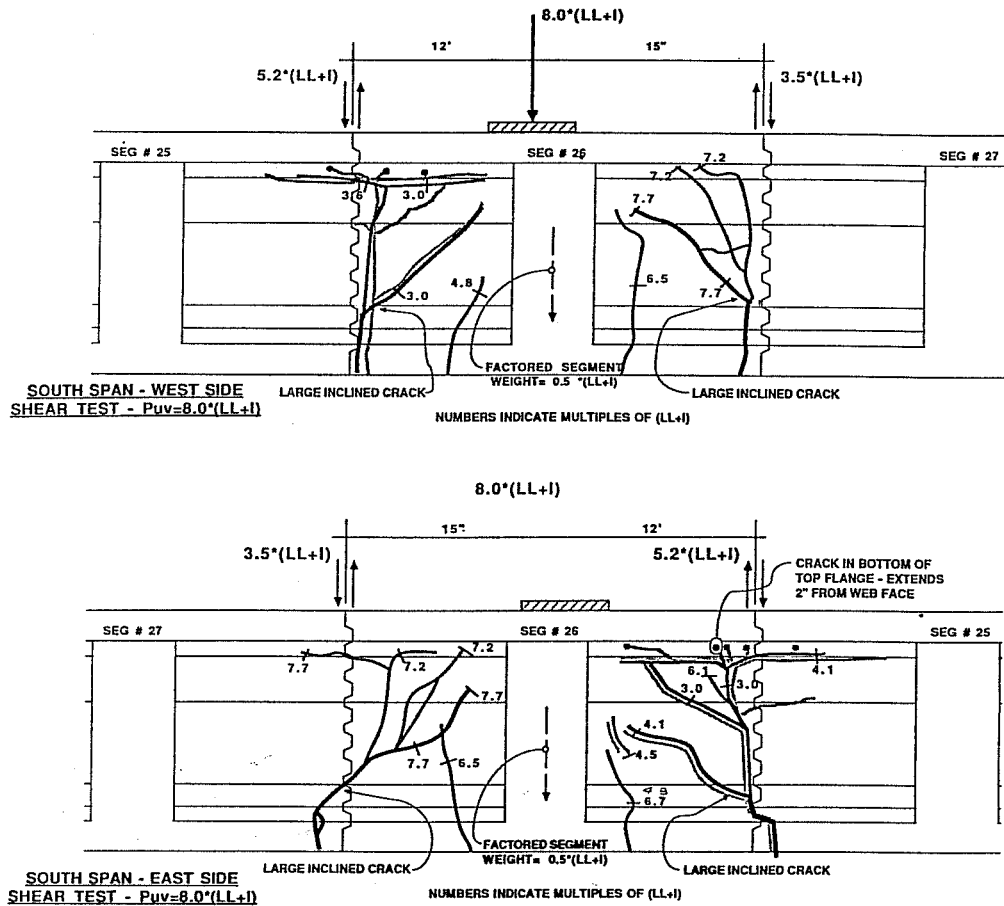


Figure 6.71 South Span Shear Test: Cracking Summary

Concentrated rotations were calculated from the measured crack-opening profiles. The measured concentrated rotations were approximately 0.8 degrees at each of the two midspan cracks (adjacent to joints (25,26) and (26,27)), and approximately 0.5 degrees at the support crack adjacent to joint (NI,11). The ratio of total midspan rotation to support rotation is again approximately 3.

The cracking behavior of the midspan region on the west and east sides of the south-span is summarized in Fig. 6.71. The lines indicate the total length of the crack when the test was discontinued at $8.0(LL+I)$. The previous cracking

from the flexural test is shown with shaded lines, and new cracks or previous cracks that reopen are shown as solid lines. The initial crack extension and the load at which the crack was first observed occurred are also indicated. The shear transfer at the segment joints at the end of the test is also shown. The shear in segment 26 was distributed primarily towards the interior support, with a shear transfer of $5.2(LL+I)$ at joint (25,26).

Cracks that formed during the flexural test reopened at approximately $3.0(LL+I)$. At approximately $4.8(LL+I)$ the bottom flange of Segment 26 cracked approximately 9 inches south of joint (25,26). At approximately $6.5(LL+I)$ the bottom flange of segment 26 cracked again, this time at approximately 9 inches north of joint (26,27). At an applied load of $7.2(LL+I)$ a major crack formed adjacent to joint (26,27). After this crack formed, the cracks located away from the joints closed slightly as the rotations concentrated at the crack which formed adjacent to the joints. As load was further increased, cracks adjacent to joints (25,26) and (26,27) opened at approximately the same rate, with concentrated rotations occurring at the primary inclined cracks. At the conclusion of the test the flexural cracks adjacent to the joints were effectively closed with all hinge rotations occurring at the inclined cracks. This allowed the transfer of shear across the joint over the entire height of the web.

7. INTERPRETATION OF TEST DATA

7.1 Observations from Load Tests

7.1.1 *Service Load Behavior.*

7.1.1.1 **Live Load Response.** The measured deflected shapes of the three span structure for typical service live load application on the dry-jointed north span, epoxy-jointed center span, and the epoxy-jointed south span are shown in Figures 6.5, 6.13, and 6.41 respectively. The measured maximum service live load deflections were $L/5660$ for the dry-jointed exterior span, $L/6250$ for the epoxy-jointed exterior span, and $L/7500$ for the epoxy-jointed interior span. The deflection in the dry-jointed exterior span was approximately 10 percent more than for the epoxy-jointed exterior span. This difference may be caused by a slightly smaller effective cross-section in the dry joints caused by differential shrinkage in the thin flanges of the precast segments. Differential shrinkage in segments, due to variable thicknesses, results in less than full contact between match-cast segments. Epoxy effectively filled any space left by differential shrinkage, and restored full contact between segments.

The live-load tendon-stress increases in the midspan region of the loaded span were measured to be less than 2 ksi in all spans. The stress response remained constant for five consecutive live load cycles indicating that the tendons did not slip at the deviators at service level loads.

7.1.1.2 **Comparison with Elastic Analysis.** The plane frame elastic analysis consistently overestimated the deflections of the model structure. Table 7.1 summarizes the maximum measured and calculated deflections for service load testing of each span. The elastic analysis overestimated the measured deflections by approximately 30 percent in the exterior spans and 20 percent in the interior span.

Some of the increase in measured stiffness might be caused by a higher insitu concrete modulus of elasticity. The concrete modulus used in the analysis was taken from concrete cylinders representative of each type of concrete used (Section 2.2.1). The reinforced concrete in the structure has a higher degree of confinement than the unreinforced cylinders, which may lead to a higher apparent modulus in

Table 7.1 Service Load Deflections

	Span Joint Type	North Dry	Center Epoxy	South Epoxy
Measured	Deflection (in.)	0.53	0.40	0.48
	Δ/L	1/5660	1/7500	1/6250
Calculated	Deflection (in.)	0.68	0.48	0.62
	Δ/L	1/4412	1/6250	1/4839
	$\frac{\text{Calculated}}{\text{Measured}}$	128%	120%	129%

the true structure. In addition, the neglect of the stiffening diaphragms and the relative size of the flange and web thickness, as compared to the thickness of the test cylinder, may contribute to increased stiffness.

Another possible cause for higher measured stiffness is the added stiffness of the secondary cable system. Applied loads are resisted by the combined action of bending stresses in the girder and by a suspension system with the draped external tendons, as shown in Fig. 7.1. The stiffness of each component system contributes to the overall stiffness of the structure. This effect may be further aggravated in the model by the relatively larger grouted ducts.

7.1.1.3 Torsional Response. The model structure exhibited high torsional stiffness with rotational deformations less than could be accurately measured with the instrumentation. The relative flexibility of the load-cell bearing assemblies caused the torsional forces to distribute to adjacent spans causing small distortions throughout the length of the structure.

7.1.1.4 Fretting Fatigue at Deviators. Although the live-load stress range was small, and slip was not apparent during live load cycles, there is need for research to assess the effect of fretting fatigue on external tendons at the deviation locations. The change in tendon force between two adjacent segments of an external tendon occurs by friction while undergoing a concentrated angle change at the deviators (Fig. 7.2). The force transfer occurs over a short length under high

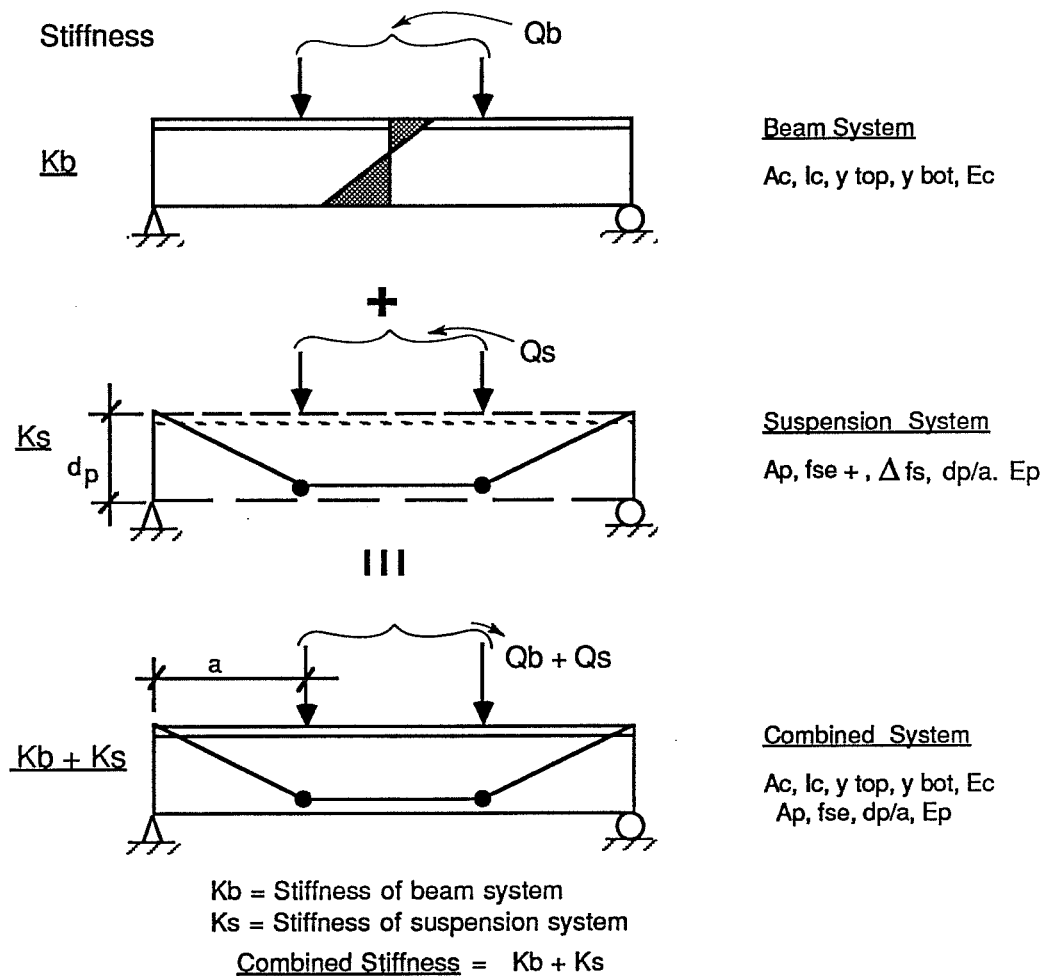
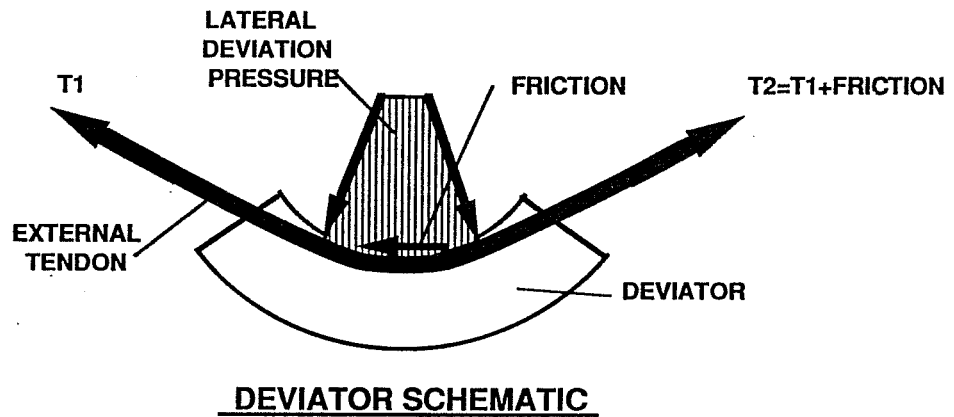


Figure 7.1 Beam and Suspension Systems

lateral deviation pressures. The friction force combines with the lateral pressure to induce a high surface shear on the strand wires that are in contact with the deviation hardware. Figure 7.3 shows the state of stress in an element of the strand in contact with the deviation hardware. As the lateral deviation stresses are increased with high curvatures or multiple strands, for example, the magnitude of the maximum



FRETTING CONCERN

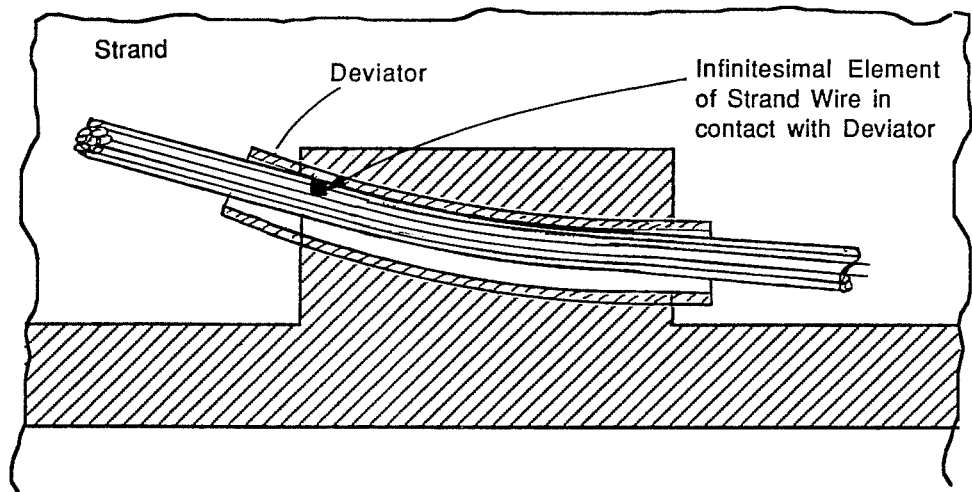
- HIGH LATERAL PRESSURE
- SURFACE SHEAR
- SLIP POTENTIAL

Figure 7.2 Deviator Force Components

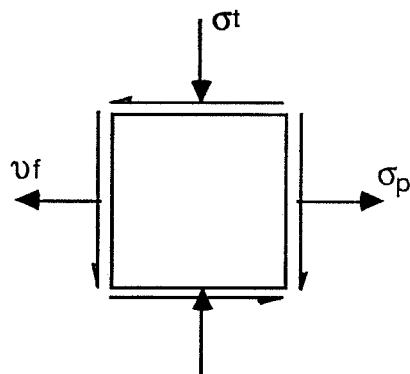
shear stress also increases. The magnitude of the maximum tensile stress remains constant.

The fretting problem is further aggravated by slip at the deviators, perhaps caused by the occurrence of a previous overload or inadvertent cracking. Slip was noticed in both exterior spans at approximately twice the load required for decompression. Once slip has occurred at a grouted deviator, then bond is lost and the potential for further slip is increased.

7.1.2 Factored Load Behavior. After completing the service load tests the three-span structure was loaded with additional weight to simulate the factored dead load condition of $1.3 \cdot DL$. Each of the exterior spans of the structure was then individually loaded with the factored design live load plus impact, $2.86 \cdot (LL+I)$. Factored load tests were not conducted on the interior span.



a. Section at Deviator

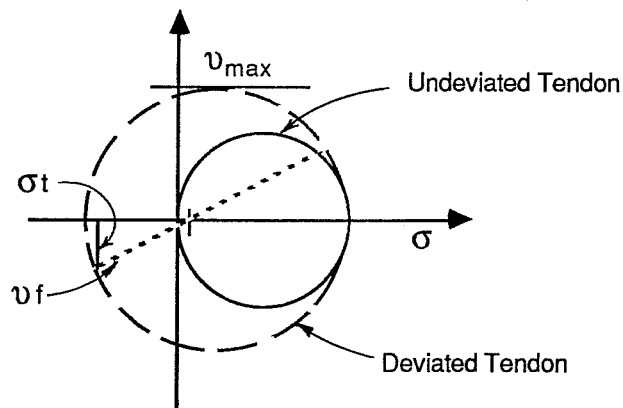


σ_p = tendon stress

σ_t = lateral deviation stress

ν_f = shear stress from friction forces

$\cong \mu \cdot \sigma_t$



b. Stress Condition

Figure 7.3 Stress Condition for Strand in Contact with Deviator

The structure behaved linearly throughout the load cycle with a slight reduction in stiffness when midspan joints decompressed. At these higher load levels the measured maximum factored live load deflections, as determined in different load cycles, were $L/1764$ for the dry-jointed exterior span and $L/2310$ for the epoxy-jointed exterior span. In this case the deflections in the dry-jointed span were approximately 25 percent more than in the epoxy-jointed exterior span, with the difference caused by the reduced effective cross-section in the dry joints and the tensile capacity in the uncracked regions of the epoxied joints.

The factored-load tendon-stress increases in the midspan region of the loaded span were measured to be less than 5 ksi in both exterior spans. The tendons did not appear to slip at the deviators for any of the factored load cycles.

7.1.3 Ultimate Flexural Behavior. The applied load is plotted versus the resultant midspan deflection for the ultimate load test of the dry-jointed north span in Fig. 7.4. The deflections represent the net deflection of the structure, after adjustment for support deflections at the location shown on the schematic. The deflections increase linearly with applied load up to the decompression load, P_d . As the midspan joints begin to open, stiffness reduces, and deflections increase at an escalating rate. The stiffness continues to decrease until the support joint opens and a mechanism forms. For load levels higher than the "mechanism load", P_m , the stiffness remains relatively constant with slight decreases as the ultimate strength is approached. The reduction in stiffness beyond the mechanism load is due primarily to slip in the external tendons at deviators.

The measured deflected shape of the three-span structure with factored dead load ($1.3*DL$) and increasing levels of applied load are shown in Fig. 7.5. At the applied service live load, $1.0(LL+I)$, and the applied factored design load, $2.9(LL+I)$, the deflections are small and the deflected shape appears as a smooth curve. The deflected shape remains smooth until the midspan joints open widely at $3.0(LL+I)$. Beyond this load, "hinging" occurs at the midspan joints, and the midspan deflections increase considerably. When the support joint opens at $4.8(LL+I)$ the mechanism forms and deflections begin to increase very rapidly. Due to reduced flexural requirements, the center span has less post-tensioning than the exterior spans. The support joint therefore opened on the interior side of the interior pier segment. The

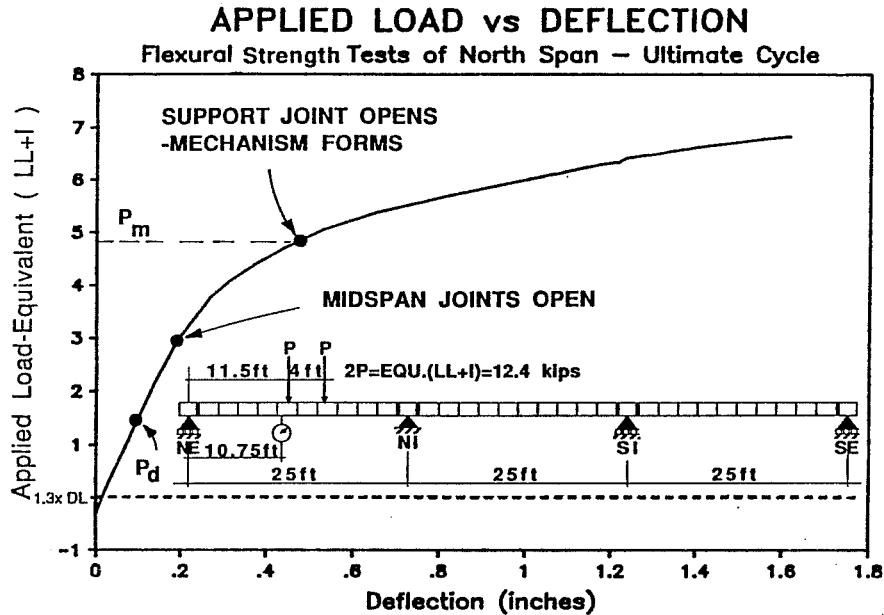


Figure 7.4 Stages of Flexural Behavior

final deflected shape of the structure clearly illustrates the mechanism behavior of the structure at ultimate load levels.

In section 5.2 a plastic mechanism analysis was conducted for each test load case. The plastic hinge capacities were calculated using first, the ACI formula for unbonded tendon stresses, and second, the tendon yield stress. The calculated mechanism capacity is dependent on the hinge capacity used. Using the ACI formula, the calculated mechanism capacity underestimated the measured capacity within 15 percent. Using the tendon yield stress, the calculated mechanism capacity overestimated the measured capacity by as much as 35 percent.

7.1.4 Shear Behavior. The local behavior of the segments near an opening joint was affected by the amount of shear that was being transferred across the joint. In the flexural tests, with the load applied as a series of forces along the longitudinal axis of the structure, small shears were transferred across the critical opening joints. In this case the concentrated rotations occurred either at the joints in the dry span or at a crack adjacent to a precast joint in the epoxied spans. At ultimate load levels

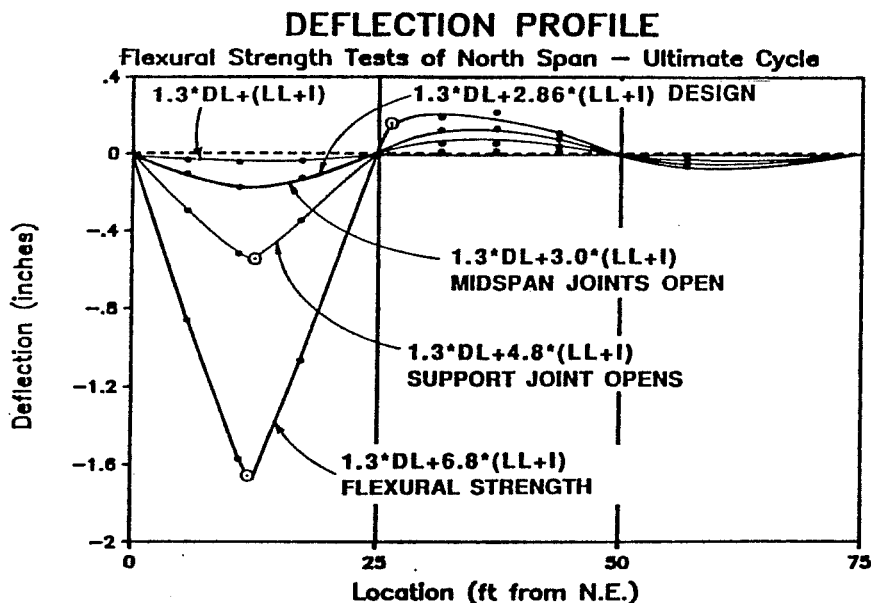


Figure 7.5 Ultimate Deflection Profile

joint/crack had opened into the top flange of the girder in both the dry-jointed and epoxy-jointed spans.

The local force transfer mechanism in the segments adjacent to the opening joints or cracks when flexural strength was reached is shown schematically in Fig. 7.6a. The joint/crack had opened into the top flange causing the load to arch across the segment joint. The small shears that were transferred across the open joints at this stage were carried by the vertical component of the "arch force" at the joint. The segment reinforcement transferred the shears from the load point to the edge of the segment, and then the arch action transferred the force across the joint.

In the shear tests, a concentrated force was applied to the structure so that significant shear would be transferred across opening joints or cracks. The ratio of shear at joint (5,6) during the flexural and shear tests was approximately 2.5:1. In this case after the joint had opened up through the bottom flange, an inclined crack formed from the load point to the bottom of the web at the edge of the segment, as shown in Fig. 7.6b. As load was increased to ultimate levels, the concentrated

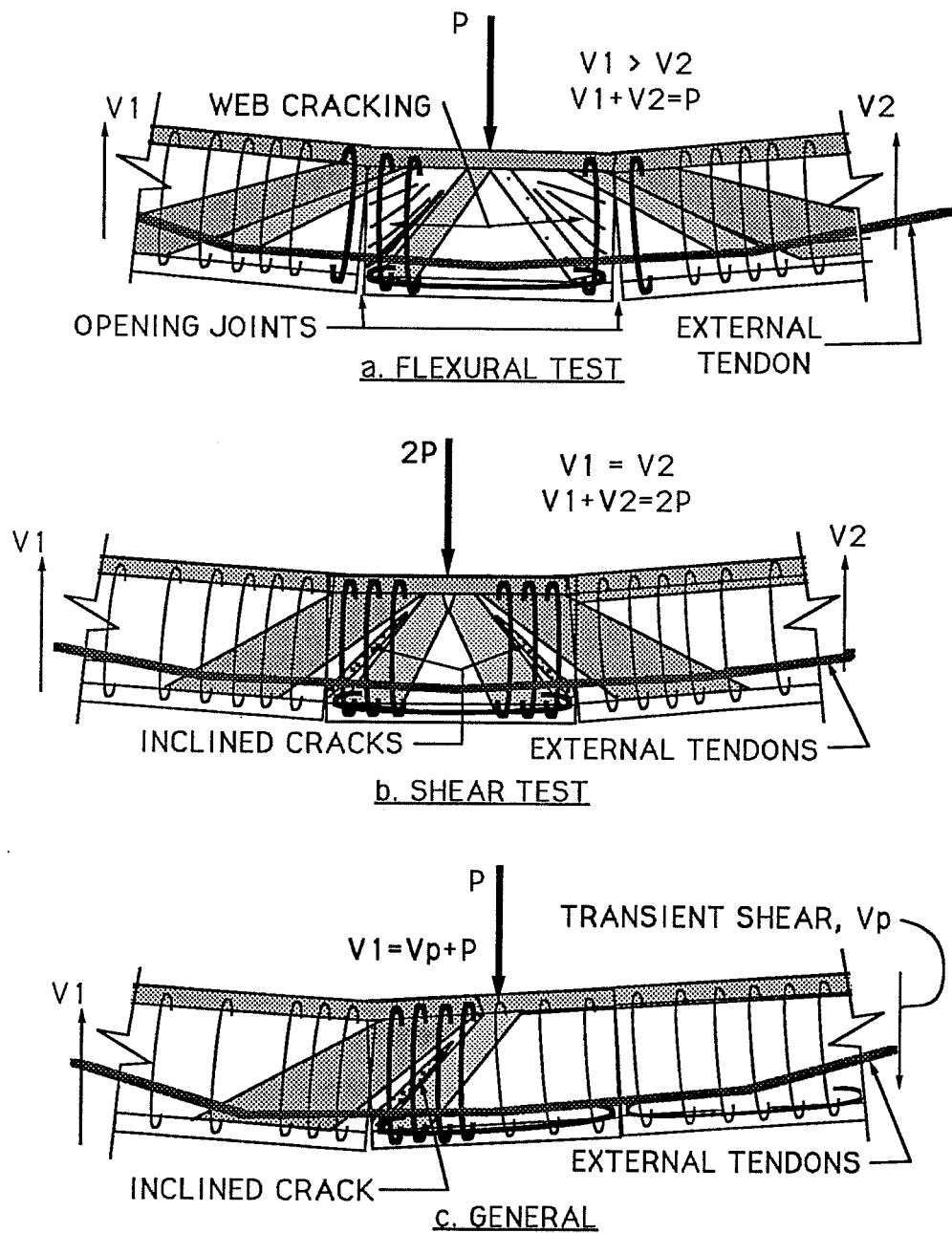


Figure 7.6 Shear Mechanisms at Opening Joints

rotations occurred at the inclined crack leaving the joint region in firm contact. This was true for both the dry-jointed and the epoxy-jointed spans.

The local force transfer mechanism in the segments adjacent to the opening joints/cracks when capacity was reached is also shown in Fig. 7.6b. A compressive strut formed from the load point to the lower corner of the segment. The segment web reinforcement transmitted this force across the inclined crack to the top of the segment. The shear force was then transferred across the joint utilizing much of the web depth.

The reinforcement for the concrete segments near opening joints must be properly detailed to allow the large rotations required for tendon stress increases. Local truss mechanisms, such as shown in Fig. 7.6c, should be developed for the critical segments to ensure that the shear transfer can be made across the joints. The bottom longitudinal reinforcement must be anchored close to the opening joint and must resist the horizontal component from the transient shears (Fig. 7.6c) plus the force in an inclined strut aligned between the load point and the bottom corner of the segment. The web reinforcement must be able to resist the transient shear from global loads plus the vertical component of the force in the inclined strut. The web reinforcement must be anchored under the bottom longitudinal reinforcement and high in the section so that anchorage is maintained when the neutral axis shifts to the top flange of the segment.

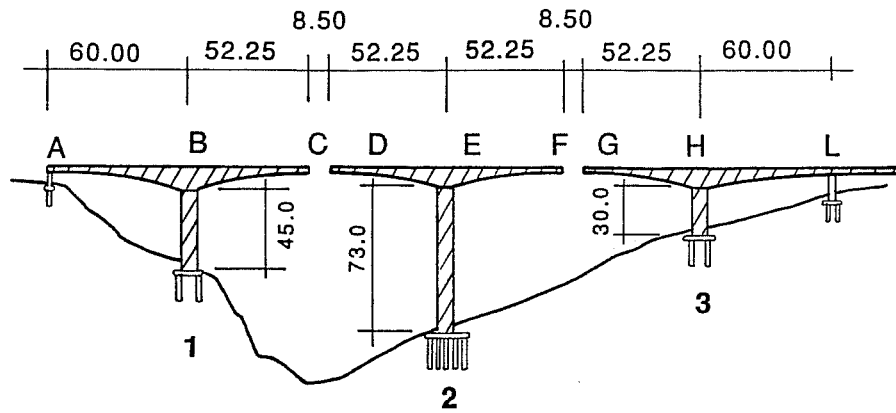
7.1.5 Ductility. Ductility of a structural member or system was defined by Naaman (39) as "a measure of the ability of a material, section, structural element, or structural system to sustain inelastic deformation prior to collapse, without substantial loss in resistance." Ductility is important in structural members so that warning is provided to the occupants of the structure of a possible impending failure. Brittle behavior in which ultimate failure occurs suddenly with little or no warning should be avoided in structural elements or systems.

The use of unbonded reinforcement in structural concrete can present a serious problem with respect to ductility. Because the reinforcement is not bonded to the concrete section, tendon elongations are distributed over the entire free length of the tendon. Large concentrated rotations and deflections are required for increases in tendon stresses.

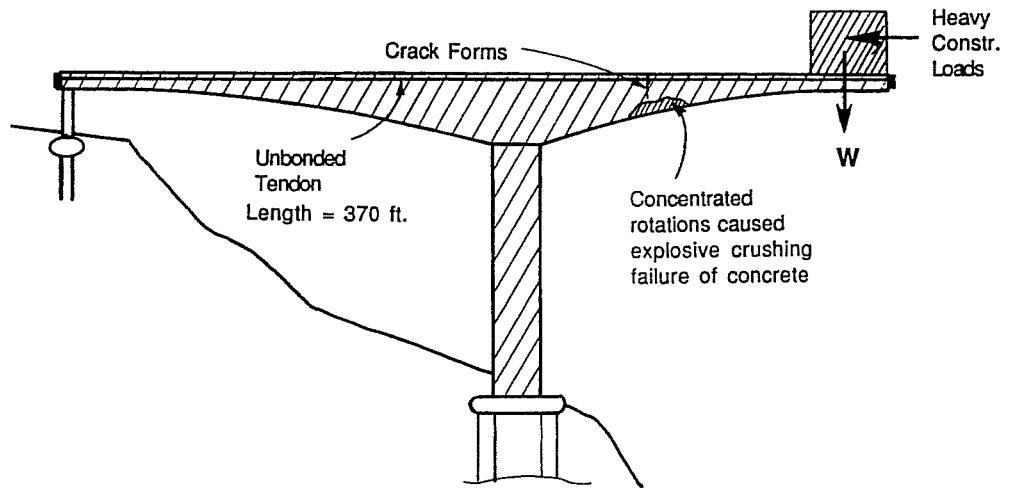
The following example illustrates the critical importance of ductility in unbonded systems. The structure shown in Fig.7.7a (40) was constructed by the balanced cantilever method. During construction, heavy loads were applied to the end of the cantilever which caused flexural cracking to occur at the location shown in Fig. 7.7b. After the concrete section cracked, the forces that were previously carried by tension in the concrete were transferred to the post-tensioning tendon. Because the internal tendons had not yet been grouted, the elongations required for increased tendon strain (and stress) were averaged over the entire length of the unbonded tendon. Large rotations were therefore necessary at the cracked section to develop the required tension forces. The large rotations caused the compressive stresses to concentrate in the top flange until the concrete exploded catastrophically and the segments dropped to the ground.

This example illustrates two important ductility considerations for unbonded tendons in structures. First, details should be provided to ensure that plastic hinges form in a ductile manner (40). This can be achieved by a number of methods, all of which involve providing bonded reinforcement at all locations in the structure. This requirement is especially critical in the case of single hinge mechanisms such as the cantilevered bridge example described. Further, formation of multiple-hinge mechanisms in redundant structures can lead to redistribution of loads and increased capacity. Second, if the moment capacity is less than the cracking moment, then an additional factor of safety on the required capacity should be provided.

Two general types of ductility are important for structural elements, global ductility and local ductility. In a global sense the structure should be able to withstand large deflections before strength is reached. In addition, the structure must have reserve capacity beyond load-levels that cause noticeable distress in the structure (cracking and/or large deflections). In a local sense, the structure must be able to withstand the necessary distortions required for global ductility. For unbonded systems, large concentrated rotations are required to develop increased tendon forces. The concrete in the vicinity of the "plastic-hinge" must be detailed properly to ensure that these large rotations can occur. Confinement of the concrete in the compressive zone at a hinge will allow higher ultimate concrete strains and larger induced



a) Condition of Bridge Prior to Collapse



b) Failure Condition

Figure 7.7 Bridge Collapse During Construction

rotations. In segmental construction, proper anchorage of the tension flange reinforcement in the segments will allow larger concentrated rotations at the critical opening joint.

The inherent flexural strength of the structural system is best reflected by examining moments at midspan. The midspan service load moments (DL+LL) are compared with the midspan ultimate load moments ($1.3DL+6.8(LL+I)$ or $1.3DL+7.7(LL+I)$) in Table 7.2. The difference between the ultimate applied-load moment in the dry and epoxy-jointed spans is caused primarily by a difference in the effective prestress in the two spans (see Section 7.2.2). Two indices of behavior are defined below:

Table 7.2 Factor of Safety and Safety Margin
Service and Ultimate Level
Midspan Moments

		Dead Load	Applied Load	Midspan Moments	
				Dry Joints	Epoxyed Joints
D	Dead Load	DL	0	101	115
S	Service Live Load	0	(LL+I)	50	48
Df	Factored Dead Load	0.3*DL	0	30	34
u	Ultimate Applied Load	0	6.8*(LL+I)	250	—
		0	7.7*(LL+I)	—	340
$\frac{D+Df+u}{D+S}$	Factor of Safety	—	—	2.5	3.0
$\frac{Df+u}{S}$	Safety Margin	—	—	5.6	7.8

1. The Factor of Safety is defined as the total ultimate moment divided by the total service load moment. The factor of safety exceeded 2.5 in the test structure. This means that the ultimate midspan moment was more than 2.5 times the midspan service-level moment.
2. The Safety Margin is defined as the ratio of the ultimate midspan applied-load moment to the service midspan applied-load moment. The safety

margin indicates the number of live-load multiples that can be applied to the structure above the service load condition. The safety margin was more than 5.6 for the model structure. The apparently large difference between the dry and epoxy spans is again due primarily to the larger effective prestress in the epoxy-jointed span.

7.2 Estimation of Insitu Forces

In order that conclusions can be drawn from the test data it is necessary to estimate the condition of the structure before testing. The concrete stress condition in the completed structure at the start of testing is a function of the sequential construction method. The analysis, described in Chapter 5, determined the final forces in the concrete by estimating the equivalent prestress forces from the measured tendon data and then applying these forces to the model structure. The construction process was tracked in a segmental manner with the equivalent prestress forces applied at each step of construction. Losses were accounted for by applying equivalent forces in the opposite direction. The analysis represents the best estimate of the forces which existed in the structure at the start of testing.

To provide a base for tendon stress increases, the effective prestress forces must also be determined. The effective prestress forces can be estimated from the decompression moment if the insitu dead load condition and the concrete section properties are known. This information can also be used to calibrate the analysis if the effective prestress is too dissimilar from the values used in the analysis.

7.2.1 Insitu Dead Load Forces. The reactions and moments from the analysis are compared with the reactions and moments measured with the load cells in Table 7.3. The analysis shears agree closely with the reactions measured at the north end of the structure. The measured reactions were adjusted as described in Section 4.4. At the south end of the structure, the analysis differs from the measured reactions by approximately 9 percent at the interior support and 6 percent at the exterior support. Because of the highly redundant system, a closure of less than 10 percent is considered acceptable.

7.2.2 Effective Prestress Forces at Critical Joints. A primary variable for estimating the ultimate strength of an unbonded system is the stress that exists in

Table 7.3 Insitu Dead Load Forces

Location	NEP	3:4	4:5	5:6	6:7	NIP	NIP	NIP	NIP	15:16	SIP	SIP	SIP	SIP	24:25	25:26	26:27	27:28	SEP	SEP	Units	
x:	0	0	8	10.3	12.5	14.8	24	25	25	26	37.5	49	50	50	51	60.3	64.8	67	75	75		
Dead Load Forces:																						
Analysis Shear (DL+PS2)	-1	18.0						-25.	23.0				20.	23.7							-20.	1 kips
Measured Reactions		19.5							49.6					40.2								22.4 kips
1.3* (Analysis Shear)	-1.3	23.4						-33.	29.9					-26.	30.9							1.3 kips
Analysis Moments (DL+PS2)	-5	-5	93.4	99.4	96.2	83.8	-64.	-89.	-89.	-66.	71.1	-32.	-51.	-51.	-28.	107.	116.	106.	106.			-5 ft-kips
Measured Moments			97.6	105.	103.	91.4			-60	99.5	19					133.	138.	134.	121.			ft-kips
1.3* (Analysis Moments)	-6.5	-6.5	121.	129.	125.	109.	-84.	-116	-115	-86.	92.5	-41.	-67.	-67.	-36.	139.	151.	151.	138.			-6.5 ft-kips

the tendon prior to loading the structure. The effective prestress should therefore be calculated for the model structure so that the strength prediction equations can be verified.

The total force in the prestressing tendons can be determined from the moment that causes decompression because the stress at the extreme fiber is known to be zero. The concrete stress resulting from application of the decompression load can be determined from the change in prestress forces and the change in forces resulting from applied load. If the change in prestress force is assumed to be small compared to the effective prestress force, and axial forces from loading are assumed to be zero, then the effective prestress force can be calculated. The effective prestress force is therefore estimated as the ratio of the stresses caused by dead loads, secondary prestress forces, and applied loading to an index which depends on the concrete cross-section and the tendon eccentricity. Note that the tendon eccentricity must include all the tendons crossing the joint.

Table 7.4 summarizes the calculation of the effective prestress forces at each midspan region and also at the interior face of the interior supports. Also shown is the average tendon stress at each location as determined from the tendon strain data. The tendon strain data were used for calculating the equivalent prestress forces for the analysis.

The effective prestress force from the decompression load agrees reasonably well with strain data for the midspan regions of the center and south spans. For the north span however, the decompression load yielded an effective prestress force that was considerably less than was determined from the tendon strain data. During testing, the north span decompressed at a lower load level than in the similar south span, which tends to verify the difference in the calculated effective prestress forces. This indicates that the equivalent prestress force in the north span may be less than was used for the analysis. The result of this is to increase the dead-load deflection in the north and south spans and decrease deflections in the center span.

The effective prestress force was also calculated at the opening joint on the interior face of the interior pier segment. In these cases, the magnitude of the decompression moment at the critical joint was determined from the factored dead load moment plus the applied load moment. These joints did not open until very

Table 7.4 Calculation of Effective Prestress Forces

Location:	5:6	11 NF	15:16	20 SF	25:26
x: (ft)	12.5	26	37.5	49	62.5
Ac: (in. ²)	450	450	450	450	450
S. top: (in. ³)	2512	2512	2512	2512	2512
S. bot.:	1757	1757	1757	1757	1757
(Ap) ext (in. ²)	2.04	1.53	1.53	1.53	2.04
(Ap) int	.68	.68	.68	.68	.68
(Ap)	2.72	2.21	2.21	2.21	2.72
(e) ext (in.)	6.01	-1.4	6.04	-1.4	6.01
Corrected (e) ext	5.76	-1.4	5.79	-1.4	5.76
(e) int	-5.35	-5.35	-5.35	-5.35	-5.35
(e) eff	2.983	-2.62	2.362	-2.62	2.983
$(A) = ((\frac{1}{A_c}) + (\frac{e}{S}))$.0039	.0033	.0036	.0033	.0039
<u>Dead Load Moments (M_{dl})</u>					
Analysis Moments	96.19	-66.1	71.14	-31.5	115.9
Measured Moments (from reaction data)	102.6	-60	99.51	19	137.9
1.3* Analysis Moments	125.1	-85.9	92.48	-41.0	150.6
1.3* Measured Moments	133.4	-78	129.4	24.7	179.3
<u>Decompression Load Moments (M_d)</u>					
Load Case	PDNd	PUNd	PDCd	PUSd	PDSd
Analysis Moments	91.5		90.2		129
Measured Moments	92	-190	90	-230	130
$(B) = \frac{(M_{dl} + M_d)}{S}$					
Analysis	1.282	-1.32	1.102	-1.29	1.672
Data	1.329	-1.28	1.294	-0.981	1.830
<u>Tendon Force and Stresses</u>					
$T_{pd} = \frac{(B)}{(A)}$					
Analysis	327.0	403.8	308.9	396.7	426.7
Data	339.1	392.3	362.9	300.5	466.8
$fpd = \frac{T_{pd}}{A_p}$ (ksi)					
Analysis	120.2	182.7	139.8	179.5	156.9
Data	124.7	177.5	164.2	136.0	171.6
fpd-fpe (ksi)	2.4	1	2	1	2.4
fpe (ksi)					
Analysis	117.8	181.7	137.8	178.5	154.4
Data	122.3	176.5	162.2	135.0	169.2
AVG =	120.0	179.1	150.0	156.7	161.8
fpe					
Tendon Strain Data					
Average Stress (ksi)	143.6	140.1	147.1	155.3	157.1

high loads were applied, and the exact magnitude of the moments was not as easily determined.

7.2.3 Service Load Tendon Stresses. A calculation procedure was presented in Chapter 1 for determining the service load tendon stresses. To calculate the tendon stress range the Curvature-Eccentricity diagram, $(M/E_c I_c) * e$, is plotted for all locations along the tendon. The elongation of a tendon between two anchored points is the area under the Curvature-Eccentricity diagram between the anchorages. The tendon strain is calculated by dividing the calculated elongations by the tendon length between the two anchorages.

The question arises as to what effective length should be used for calculating the service load tendon stresses. If no slip occurs at the deviators then the free length over which the tendon elongates is limited to the length between adjacent deviators. If no friction exists between the tendon and the deviator then the tendon can slide freely, and the elongations are averaged over the entire tendon length between the anchorages. From the test results the tendons did not begin slipping until load levels well above the service load condition. This was true for all load cycles including those in which the tendon had slipped during previous load cycles. The free length of tendon should therefore be taken as the length between adjacent deviators for calculation of the service load response. This is a conservative approach since this is the shortest free length that the tendon can have, and will lead to the largest service-load stress range.

The service load tendon stresses for the three tendons in the north span are calculated for the model bridge structure by integrating the Curvature-Eccentricity diagram between adjacent deviators. Since each tendon has a different profile and deviation locations, the service load stresses must be calculated separately for each tendon. The service-load tendon stress ranges are shown in Fig. 7.8 for each of the tendons of the north span. The measured stress ranges are also shown for comparison, and they agree closely with the calculated stresses at the support region, and were slightly less than calculated for all midspan locations.

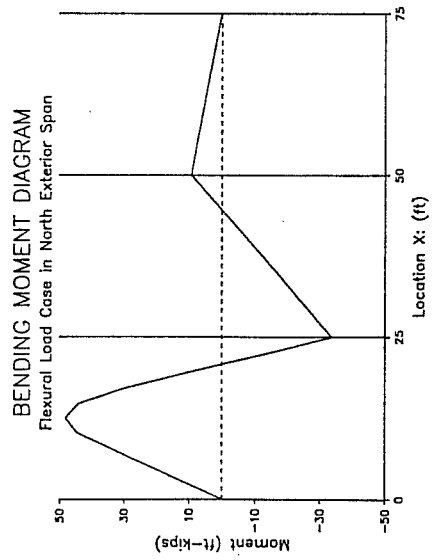
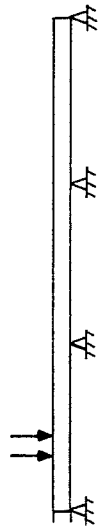
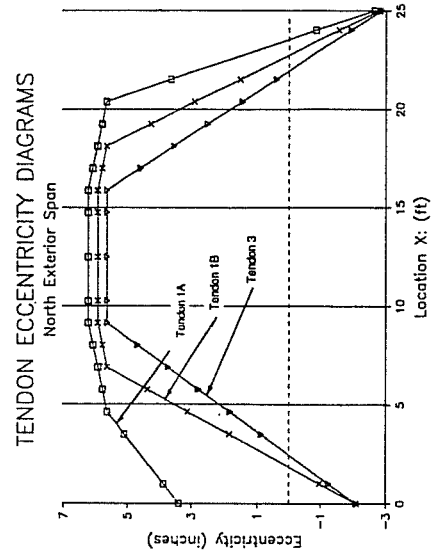
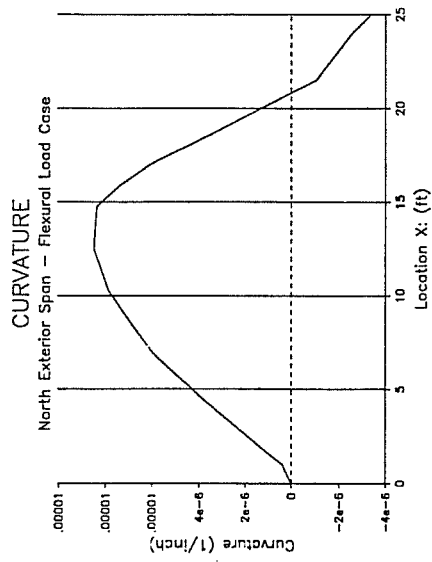


Figure 7.8 Service Load Tendon Stresses

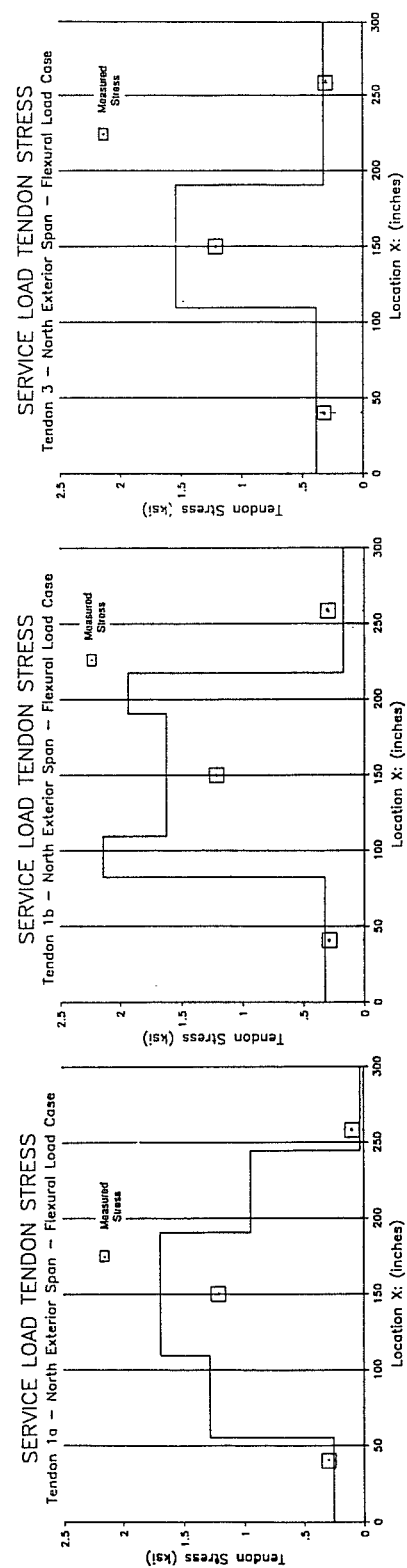
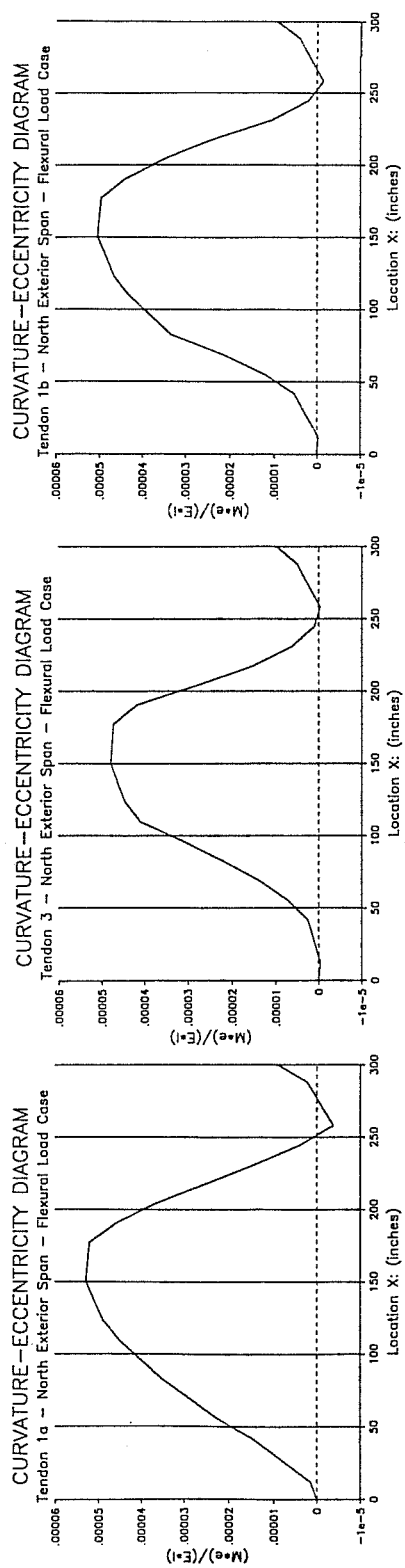


Figure 7.8 Service Load Tendon Stresses - continued

7.3 Effect of Epoxy on Model Behavior

7.3.1 Effect of Epoxy on Construction. The epoxy application process during erection of the center and south spans revealed several practical considerations concerning the handling of epoxy joining material. The epoxy should be delivered in clearly labeled, premeasured quantities of each component so they can be mixed directly without site measurement of quantities. This will ensure that the proper mix proportions are used and a minimum of material is lost in the mixing process. The epoxy supplier should also provide information regarding the necessary storage conditions and mixing techniques. In addition, the contractor should be experienced with epoxy and be able to recognize substandard materials.

A common argument for the use of epoxy in segmental construction is that it provides lubrication during closing of the match-cast faces. With the small segments of the model structure, lubrication did not appear to be necessary in the dry-jointed span of the structure. The matching faces were moistened with a cloth during closing. Lubrication during closing may be a more severe problem for full-size segments, however.

Finally, the epoxy application process must be planned carefully to ensure that all necessary tasks are completed within the usable life of the epoxy. The epoxy pot-life serves as a maximum time limit for completion of: epoxy measuring and mixing, application of the epoxy to both surfaces of a match-cast joint, joint closure, temporary post-tensioning, and cleaning of the epoxy from tendon ducts and equipment. Time studies were conducted to estimate the necessary manpower and the proper staging of the various tasks. The procedure was also practiced and timed during closing of the dry-jointed north span.

7.3.2 Effect on Service Load Behavior. A primary purpose for using epoxy at segment joints is to provide reserve capacity against joint opening for overload conditions. The cracking load and decompression loads for the two epoxied spans of the model structure are compared in Table 7.5. In each case cracking occurred through the concrete adjacent to a midspan match-cast joint at approximately twice the applied load required to decompress the flexural tension fiber and cause the cracked epoxy joint to begin to open. If zero tension is used as the limit for service

Table 7.5 Cracking and Decompression Loads

Cracking Loads in Epoxy Jointed Spans		
	Center Span	South Span
Cracking Load	DL+5.2 * (LL+I)	DL+5.4 * (LL+I)
Decompression Load	DL+2.4 * (LL+I)	DL+2.6 * (LL+I)
$\frac{\text{Cracking} - \text{DL}}{\text{Decompression} - \text{DL}}$	2.2	2.1

behavior, then the epoxy joints provided a potential factor of safety against joint opening of approximately 2.

In setting design criteria, however, it should be realized that the true factor of safety against cracking might be less than this because of traffic overloads, calculation inaccuracies, actual insitu epoxy behavior, and fatigue behavior of the concrete/epoxy joint. It would therefore be prudent to specify a small residual compressive stress in the extreme tension fiber for epoxy-jointed segments without bonded reinforcement crossing the joint. In dry joints without bonded reinforcement crossing the joint the beneficial tensile capacity offered by the epoxy is not present, so higher design residual compressive stresses are recommended.

7.3.3 Effect on Factored Load Behavior. In the epoxy-jointed south span the factored design load was less than was required to crack the span. The governing design criterion for the tendons of the model structure was the service load concrete-stress condition. Prestress was provided to induce a residual compressive stress in the extreme fiber where tensile stresses are caused by applied loads, as described in Section 2.1.3. The calculated extreme-fiber stresses for the dead load and service load conditions at the start of testing are plotted with respect to location along the structure in Fig. 5.10. The minimum residual compressive stresses under service load conditions were slightly greater than the PTI proposed limits for dry or epoxy joints without bonded reinforcement (see Table 2.2). In meeting the stress condition for design, significantly more prestress was provided than was required for ultimate strength. This was possibly aggravated in the model structure since the ratio of eccentricity to the distance from the neutral axis to the tension fiber (e/Y_b) was

less than the corresponding prototype value, thus reducing tendon efficiency with respect to stresses.

With the large reserve in ultimate strength, it would appear that smaller design stresses could be specified. This however would have a direct impact on the cracking load, thus reducing the factor of safety against cracking.

7.3.4 Effect on Flexural Strength. The primary influence of epoxy joints on the ultimate flexural behavior of the system was to concentrate the midspan rotations required for increased tendon stresses at a single joint. In the dry-jointed span, several midspan joints opened causing the rotations to be distributed over several joints. In the epoxy-jointed span, a single joint/crack opened causing the large rotations to be concentrated at a single location. If the ultimate strength is limited by the maximum rotation that can occur at a concrete-hinge, then the dry-jointed span may be able to withstand larger cumulative midspan rotations than the epoxy-jointed span. This may lead to a slightly higher ultimate flexural strength for spans with dry joints.

7.3.5 Effect on Shear Strength. As previously discussed in Section 7.1.4, the shear behavior at an opening joint was a function of the amount of shear crossing the joint, and was not noticeably affected by the epoxy. Under high shear the concentrated rotations required for increased tendon stresses occurred at an inclined crack with the match-cast joint region remaining in firm contact to transfer the shears. This behavior was similar for both exterior spans and has been subsequently investigated and confirmed by Ramirez (13).

One possible advantage of epoxy joints is that it provides a more direct flow of forces through the joint region. The shear transfer at the match-cast joint has the additional component of adhesion between the two matched faces. This component is in addition to the friction and shear key strength associated with dry joints.

7.3.6 Effect on Ductility. The epoxy did not provide any noticeable increase in ductility, and in some respects may cause some slight reduction. As was discussed earlier in Section 7.3.4, the epoxy tended to concentrate the hinge rotations at a single joint. This caused a severe strain gradient in the segments adjacent to the opening joint, and the ultimate capacity is limited by the maximum crushing

strain in these segments. If the hinge rotations are distributed to several joints, as for dry joints, larger total rotations may be possible with the same limiting strain gradient. The larger rotations would lead to larger deflections and more warning of impending failure.

Another reason that epoxy may reduce ductility was discussed earlier in Section 7.1.5. The epoxy prolongs elastic behavior until the tensile stress exceeds the modulus of rupture of the concrete or the tensile capacity of the epoxy joint. If the load that causes cracking is larger than the flexural strength of the system, then failure will occur suddenly with no warning. This form of brittle behavior requires direct treatment during the design process. If epoxy is used at segment joints, and the moment capacity is less than the cracking load, then additional factor of safety on the required capacity should be provided.

7.4 Flexural Strength Model

A structural member resists applied bending moments by an internal force couple between a compressive force, C , and a tension force, T , separated by a known lever arm, Z_p , as shown in Fig.7.9. For horizontal equilibrium of a beam member, the magnitude of C and T must be the same. Therefore, to predict the flexural capacity of a beam it is necessary to estimate either the maximum resultant concrete compressive force or the maximum tendon force and the distance between these two equal and opposite forces.

In a bonded-tendon girder the tendon strains are assumed to be compatible with the adjacent concrete, and as a result the tendon undergoes large strains. If the girder is detailed so that the tendons yield prior to failure, by specifying a maximum reinforcement ratio for example, then the simplest method for determining the ultimate flexural strength is by predicting the stress in the tendon when the ultimate strength is reached. This is the approach that is commonly taken for bonded-tendon girders.

In an unbonded-tendon girder, the tendon strains are not compatible with the adjacent concrete, and are instead averaged over the entire length of the tendon. In this case it is difficult to predict the tendon stress that corresponds with ultimate flexural strength. The tendon strains are a function of many different variables, all of

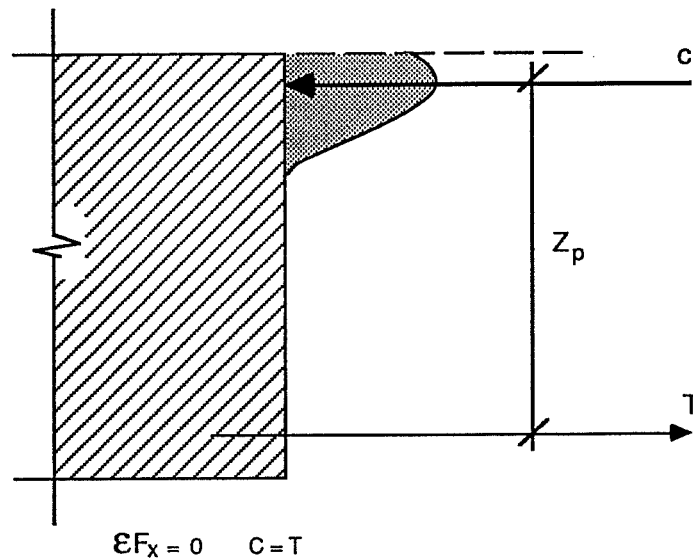


Figure 7.9 Flexural Model

which are difficult to predict and control during construction. The flexural behavior of unbonded systems is limited by the rotation capacity of the concrete at a plastic hinge. The tendon stress corresponding with ultimate flexural strength is therefore determined from the effective prestress in the tendons before applying load plus the change in tendon stress that occurs as the plastic hinges deform (open).

7.4.1 Observations from Load Tests. As loads are increased beyond service levels, the tendon stresses exhibit several stages of behavior, as shown in Fig. 7.10a. The concrete stress profile at the critical opening joint is shown in Fig. 7.10b for important stages of tendon stress development. Initially, before the joints begin to open, the tendon-stress increases are linearly related to the applied load. The tendon stresses remain linear until the neutral axis at the opening joint reaches the level of the tendon, Point B, at an applied load that is slightly greater than the decompression load, P_d . Beyond this load, the tendon stresses increase slowly at first as the increased moments are resisted primarily by an increased internal-force lever arm. When the resultant concrete compressive stresses are concentrated in the top flange of the section, Point C, then additional moments must be resisted by increased tendon forces. To develop the required tensile forces with

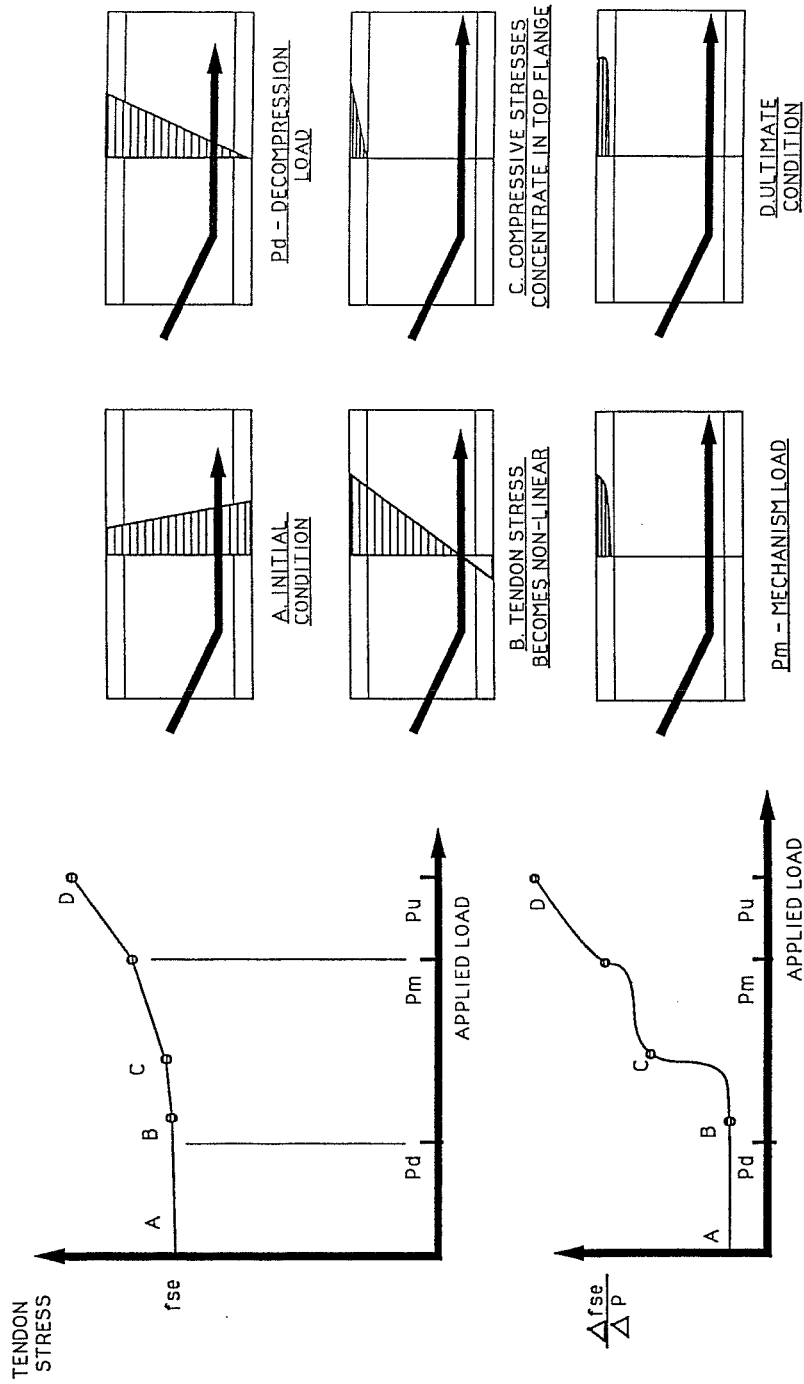


Figure 7.10 Tendon Stress Response to Applied Load

external tendons, large rotations must occur at opening joints resulting in increased deflections and joint openings.

The applied-load stresses for a typical tendon during the flexural strength load cycle for the north span are shown in Fig. 7.11. Tendon strain measurements were made at the exterior and interior ends of the span, joints (1,2) and (9,10) respectively, at midspan, and at joint (5,6). The midspan tendon stresses remained linear with applied load up to approximately $1.8(LL+I)$ when the concrete section had decompressed to the level of the external tendons. This load is slightly higher than the measured decompression load of $1.4(LL+I)$. The tendon stresses increased slowly at first until the midspan joints opened at $3.0(LL+I)$. At this load level the resultant compressive stress had concentrated in the top flange, and additional moments were resisted by a direct increase in tendon stress. Subsequently, as the support joint opened at approximately $4.8(LL+I)$, midspan moments increased and the rate of tendon stress development ($\Delta f_s/\Delta P$) also increased.

7.4.2 Factors Affecting the Unbonded Tendon Stress at Nominal Flexural Capacity

7.4.2.1 Effective Prestress Force. The effective stress in the prestressed reinforcement after allowance for all prestress losses, f_{pe} , is the most important parameter affecting the tendon stress at nominal strength. If friction losses are higher than expected during stressing, or the long-term relaxation and creep losses are higher than expected during the service life, then there is a direct reduction in the ultimate flexural strength. This dependency is clearly illustrated by comparing the ultimate flexural behavior of the two exterior spans of the model structure, as shown in Fig. 7.12. The load-deflection response of the two spans was virtually identical, except the south span response was offset by the difference between the decompression loads. As illustrated in Table 7.4, the effective prestress was higher in the south exterior span than in the north exterior span causing the decompression load to be lower for the north span. The difference in the decompression loads is approximately equal to the difference in the ultimate capacities. The effective prestress force, therefore, acts as a starting point from which the tendon stresses increase under applied loads.

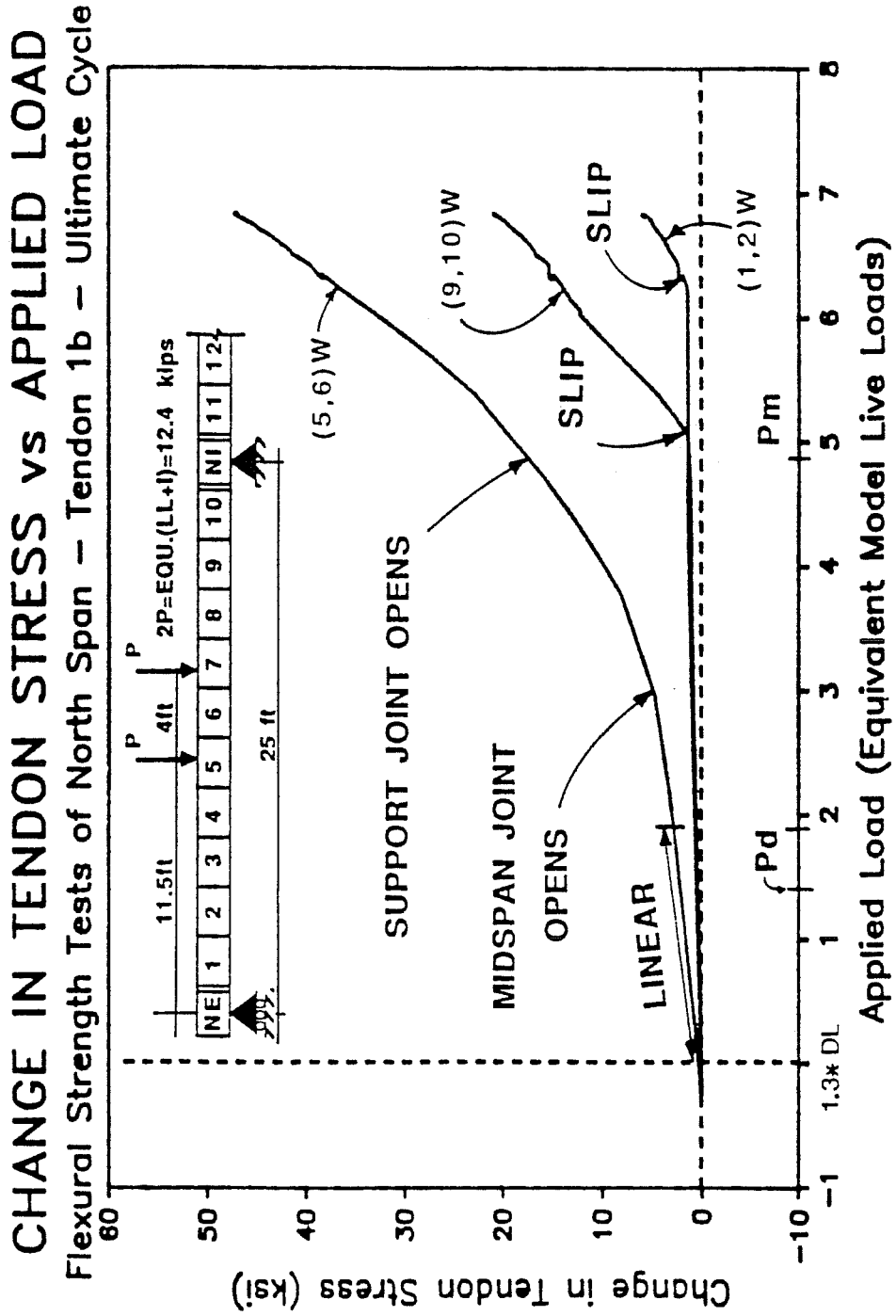


Figure 7.11 Typical Tendon Stress Response

Side Span Flexural Strength Tests

Applied Ram Force vs Midspan Deflection

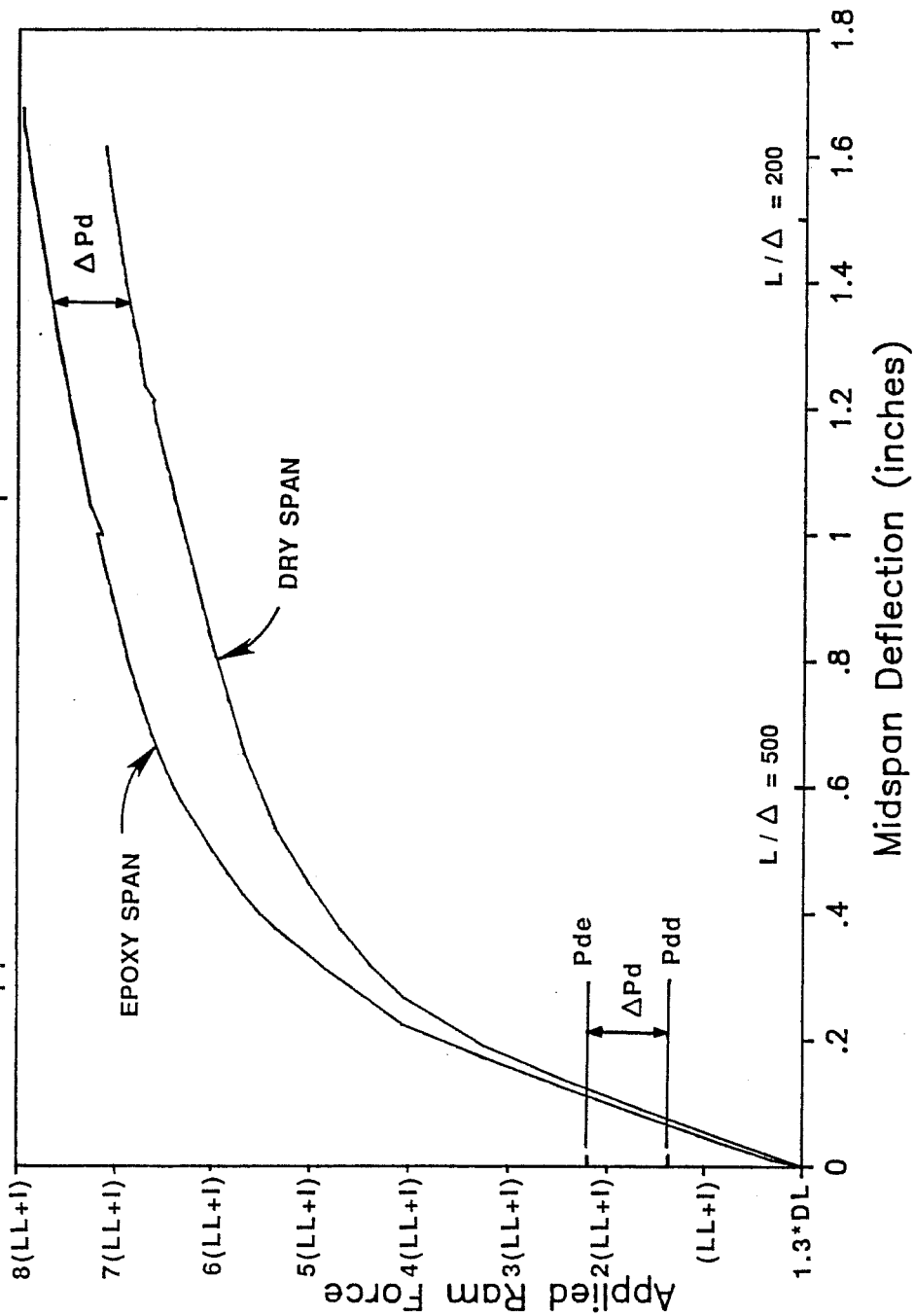


Figure 7.12 Comparison of Ultimate Flexural Behavior of Exterior Spans

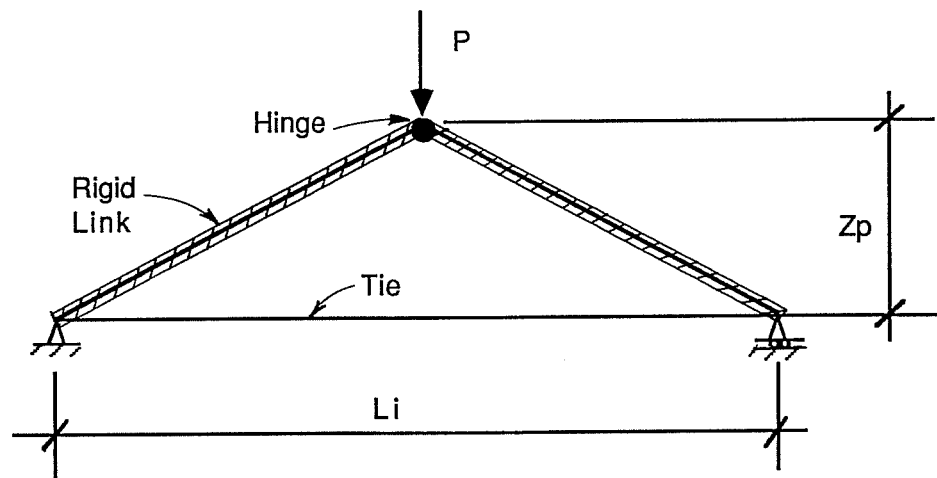
7.4.2.2 Ratio of Prestress Depth to Tendon Free Length. The ratio of the plastic depth of the prestress to the free length of the tendon segment (Z_p/L_i) is the most important factor affecting the increase in tendon stress above the effective prestress level. The elongations that occur at a plastic hinge are a direct function of the plastic depth, Z_p . Tendon strain is calculated from the tendon elongations divided by the free length of the tendon segment, L_i .

A simple truss model was presented by Mojtahedi and Gamble (31) to illustrate this effect on the development of tendon stress. The model, shown in Fig. 7.13a consists of two rigid links connected by a hinge and tied at the base by a flexible tie. A vertical deflection is induced on the hinge which results in elongation of the flexible tie. For a constant induced deflection the aspect ratio of the truss was varied. The resultant stress response, (Fig. 7.13b) illustrates the relationship between Z_p/L_i and the change in tendon stress. A large value of Z_p/L_i indicates a deep beam in which large tendon elongations are averaged over a short length, thus leading to large tendon-stress increases. A small value of Z_p/L_i indicates a slender girder in which small elongations are averaged over a long length, thus leading to small increases in tendon stress.

7.4.2.3 Neutral Axis Depth. It has been shown that the length of the plastic hinge region is a function of the depth to the neutral axis (5). A longer hinge length will allow larger hinge rotations, and therefore, larger tendon elongations. The neutral axis depth at ultimate is a function of several factors, including the amount of prestressed and nonprestressed reinforcement crossing the joint, the ultimate tendon stress, the concrete strength, and the shape of the concrete compression zone. Generally, larger reinforcement percentages and lower concrete strengths will lead to larger neutral axis depths and larger ultimate tendon elongations at ultimate.

7.4.2.4 Rotation Capacity at Precast Joints. In Section 1.2.2.2.1 the ultimate rotation capacity and the ultimate tendon elongations were shown to be dependant on the limiting strains in the concrete compression zone, and in the passive segment reinforcement on the tension side of the girder. Increases in either of these limiting strains will cause a direct increase in the hinge rotation at ultimate.

Confinement of the compression zone - It is well documented that the ultimate concrete strain is dependant on the degree of confinement of the



a. Simple Truss Model

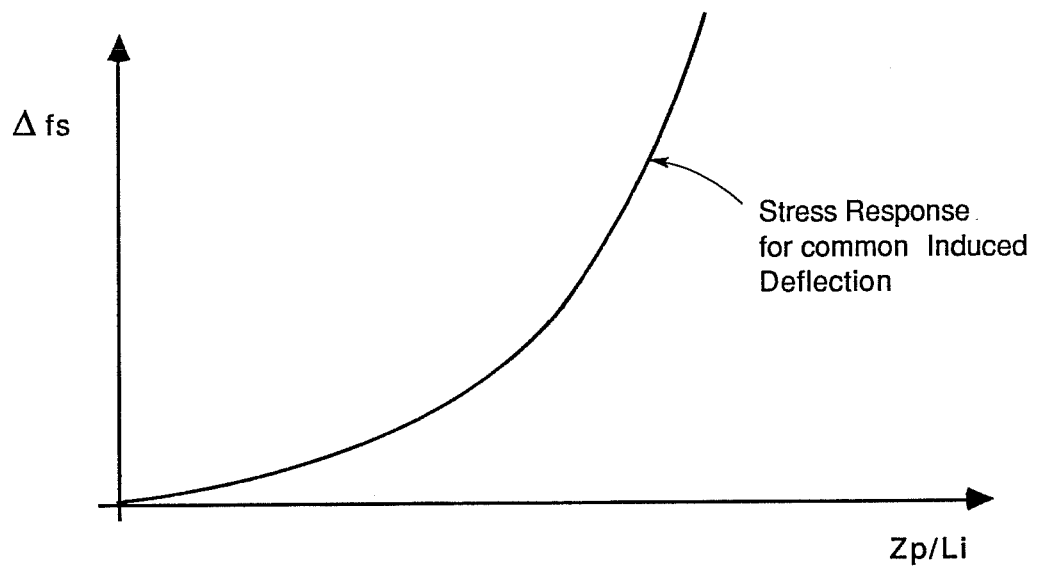
b. Change in Tendon Stress vs Z_p/L_i

Figure 7.13 Tendon Profile Slenderness Ratio

concrete compression zone (32, 33). The most direct method of increasing the concrete strain capacity is by providing reinforcement to confine the compression zone. This indicates that proper anchorage of the web reinforcement up to the extreme surface of the compression flange could possibly increase the rotation capacity at a flexural hinge.

Segment reinforcement - The ultimate rotation capacity at an opening joint was also believed to be a function of the passive segment reinforcement on the tension side of the girder. In order to develop the required strains, tension reinforcement must be properly anchored as close to the joint as possible. This requirement is especially critical at the tension flange-web interface. Segments should be detailed with well anchored reinforcement at each web-flange junction. In addition, observations made during testing indicate that well anchored and well distributed longitudinal web reinforcement may increase the ultimate rotation capacity by distributing distortions to several opening cracks.

7.4.2.5 Tendon Slip at Deviators. Substantial tendon slip was noticed in all tendons at all deviator locations for ultimate load levels. The tendon slip behavior can be illustrated by examining Fig. 7.11 which shows the change in stress in tendon 1b during the flexural strength test of the north span. The tendon began to slip from the interior end towards the midspan region at an applied load of $5.0(LL+I)$. Slip also occurred from the exterior end at approximately $6.2(LL+I)$. The tendon slipped through the deviator when the change in tendon force exceeded the maximum friction capacity.

When the tendon began to slip it did not suddenly slip and release stress in the midspan region. Instead, initial tendon slip was followed by continual slip as load was increased. For ultimate load levels the tendon was elongating over its entire length.

The maximum midspan stress that was achieved in the model tendons was affected by the load level at which slip began. If tendon slip began at a low load level then the ultimate midspan tendon stress was low. Conversely, if slip did not occur until higher load levels then the ultimate midspan tendon stress was increased. Therefore, before prototype extrapolation can be made, additional information is

required to determine the force transfer mechanism at deviators and the level of force at which tendons begin to slip at deviators.

7.4.3 Prediction Equations for Tendon Stress in Unbonded Tendons Corresponding to Nominal Capacity. Several methods are currently available to predict the stress in unbonded tendons at flexural strength. Each of the available methods calculates the ultimate tendon stress as the sum of the effective prestress and an increment occurring under applied load. Each of the methods is summarized below, and predicted and measured ultimate stresses are compared.

7.4.3.1 ACI. The current ACI Building Code equations (7) for ultimate tendon stress in unbonded beams (Fig. 7.14a) was originally proposed by Mattock et al (34) to provide a reasonable lower bound to the available test data for simply supported, unbonded post-tensioned beams having reinforcement ratios permissible under the ACI code. It was later noticed by Gamble and Mojtahedi (31) that slender girders developed unbonded tendon stresses at a much reduced rate which lead to the second ACI equation for slender beams with span-to-depth ratios greater than 35.

7.4.3.2 AASHTO. The ACI provisions described above were based on test data for 25 to 30-foot single and double-span girders. For large bridge structures it was not known whether the same level of stress increase could be attained. AASHTO therefore limited the stress increase to 15 ksi for bridge structures, as shown in Fig. 7.14b.

7.4.3.3 Tam and Pannell. The Tam and Pannell method was presented in Section 1.2.2.2.1 and was based on the elongations that occur at a plastic hinge. The length of the plastic hinge was experimentally related to the depth of the neutral axis. The ultimate curvature was calculated from the concrete crushing strain and the depth to the neutral axis. The ultimate elongation in the tendon at the plastic hinge was the product of the ultimate curvature, the length of the plastic hinge, and the plastic depth of the tendon. The increase in tendon stress at the plastic hinge is therefore calculated as shown in Fig. 7.14c.

In the equation for ultimate tendon stress, shown in Fig. 7.14c the solution is iterative because the depth of the neutral axis at ultimate, c_u , is a function of the ultimate tendon stress, f_{ps} .

Span/Depth ≤ 35

$$\left\{ \begin{array}{l} f_{ps} = f_{pe} + 10000 + \frac{f'_c}{100f_p} \\ = f_{pe} + 60000 \\ = f_{py} \end{array} \right\} \quad \text{use lesser of}$$

Span/Depth > 35

$$\left\{ \begin{array}{l} f_{ps} = f_{pe} + 10000 + \frac{f'_c}{300f_p} \\ = f_{pe} + 30000 \\ = f_{py} \end{array} \right\} \quad \text{use lesser of}$$

a. ACI Method

$$f_{ps} = f_{pe} + 15000$$

b. AASHTO Method

$$f_{ps} = f_{pe} + \left[\Psi \epsilon_{cu} E_p \left(\frac{d_p - c_y}{l_i} \right) \right]$$

Assume $\Psi = 10.5$ (determined experimentally)

c. Tam and Pannell Method

Figure 7.14 Methods for Calculating f_{ps}

$$f_{ps} = f_{pe} + 725 \left(\frac{d_p - c_y}{\ell_e} \right)$$

c_y = neutral axis depth assuming the tendons have yielded

ℓ_e = length of tendon between anchors divided by the number of plastic hinges required to develop a failure mechanism in the span under consideration.

d. CSA Method

$$f_{ps} = \frac{f_{se} + \phi_m Z_p Z_s E_p}{\ell_i}$$

$$\phi_m = \frac{\epsilon_{cm} + \epsilon_{sm}}{d_s}$$

ϵ_{cm} = limiting compressive strain in concrete

= 0.002 for design

= 0.003 for ultimate

ϵ_{sm} = limiting tensile strain in passive segment reinforcement

= 0.010 for design

= 0.020 for ultimate with proper anchorage

e. Virlogeux Method

Figure 7.14 Methods for Calculating f_{ps} – continued

7.4.3.4 Canadian Standards Association (CSA). The iterative solution of Tam and Pannel can be simplified by replacing the neutral axis depth at ultimate, c_u , with the neutral axis depth when the tendon yields, c_y . Since unbonded tendons generally remain within the elastic range, the value of c_y will always be slightly larger than the true neutral axis depth, c_u . This will lead to a conservative estimate of the maximum increase in tendon force.

This approach was adopted by the Canadian Standards Association CAN3-A23.3-M84 (37) for calculating the ultimate tendon stress in unbonded tendons (Fig. 7.14d). After making the appropriate simplifications to the Tam and Pannell formula, the result yields an equation very similar to the CSA code equation.

There appears to be a small conceptual error in the CSA equation for the reasons described in Chapter 1 for multiple hinge structures. The value of ℓ_e in the CSA equation is defined as "the length of the tendon between anchors divided by the number of plastic hinges required to develop a failure mechanism". This means that for an interior-span mechanism in which three hinges must form, the effective length is divided by three, or the elongations are multiplied by three. Because support hinges rotate only half of the midspan-hinge rotation, the elongations should only be multiplied by two. In addition, it must be checked whether the mechanism hinges all involved the same tendons. A correction to the CSA code equation is presented in Section 7.4.4.

7.4.3.5 Virlogeux. Virlogeux's method was presented in Section 1.2.2.2.1 and was based on the elongations that occur at a plastic hinge. The ultimate rotation capacity was determined from limiting strains in the concrete and the steel, and the length of the plastic hinge. The maximum elongation in the tendon at a plastic hinge was the product of the rotation capacity and the plastic lever arm of the unbonded tendon. The change in tendon stress above the effective prestress force is therefore calculated as shown in Fig. 7.14e. Virlogeux recommended limiting strains in the concrete and passive segment reinforcement corresponding to both the design and ultimate conditions.

7.4.3.6 Comparison of Prediction Equations with Test Data. The increase in midspan tendon stresses corresponding with flexural strength ranged from 36 to 60 ksi in the midspan region and from 15 to 27 ksi at the critical support

joint. Stress increases were generally larger for the shear test than for the flexural test. In Table 7.6 the measured tendon stress increases are compared with the calculated stress increases determined using the procedures described above. In general, the methods tend to underestimate the midspan tendon stress increases and overestimate the support tendon stress increases. This appears to indicate that the global behavior was governed primarily by the midspan strength with the support region not developing full capacity. This is consistent with the mechanism behavior in which the midspan region undergoes approximately twice the concentrated rotations induced at the support regions. It is important to note that if the total calculated tendon stress ($f_{pe} + \Delta f_p$) is compared with the total measured tendon stress, then the predicted-to-measured percentages will be substantially smaller than the percentages shown in Table 7.6.

The following specific observations can be concluded about each of the methods presented:

ACI Method - The ACI formula accurately predicted the measured tendon stress response in the midspan regions with predicted-to-measured ratios between 80 and 113 percent. This result is reasonable if it is remembered that the tests used to develop the ACI formula were conducted on specimens with short span lengths approximately equal to that used in the model bridge.

The average measured tendon stress increase at the critical support joint was overestimated by the ACI formula with predicted-to-measured ratios ranging between 127 and 172 percent. At these locations the effective depths of external tendons are reduced because of the drape from the support. An increased ratio of tendon depth to tendon free length leads to reduced stress development under applied loads.

AASHTO Method - The AASHTO formula predicted much lower tendon stress increases than measured in the midspan regions but implicitly assumes much longer spans. In the support regions the AASHTO formula predicted the ultimate stress increases relatively closely which would perhaps indicate a reduced level of safety in the negative moment regions.

Tam and Pannell Method - The Tam and Pannell iterative solution tended to slightly underestimate the maximum stress increases at midspan with the ratio of predicted-to-measured ranging between 60 and 81 percent. This conservatism is probably caused by the fact that the tendons do not begin to slip until considerable load has been applied. The effective length of the tendon can therefore be considered to be less than the length between anchorages, thus leading to increased stress.

The Tam and Pannell method tended to overestimate the tendon stress increases at the support with predicted-to-measured ratios ranging between 118 and 166 percent.

CSA Method - The CSA method generally overestimated the midspan tendon stress increases with predicted-to-measured ratios ranging between 97 and 128 percent. The larger predicted stresses are caused by the conceptual problem described earlier. The two hinges that form to cause a mechanism intersect different sets of tendons. The elongations occurring at each hinge are therefore independent and should not be added as is inherent in the CSA determination of effective tendon length. If the true tendon length is used the CSA-Corrected Method underestimates the tendon stress increases with predicted-to-measured ratios ranging between 49 and 64 percent. This conservatism is again caused by the delayed slip in the tendons as described for the Tam and Pannell method above.

Virlogeux Method - Virlogeux recommended two sets of assumptions for calculating the tendon stress increases for unbonded tendons. The first assumption was intended for design and assumed conservative values for the limiting strains in the concrete and steel. The design assumptions underestimated the tendon stress increases with predicted-to-measured ratios ranging between 24 and 32 percent at midspan and 45 and 64 percent at the support region. In the ultimate case, the limiting concrete and segment reinforcement strains were estimated using less conservative assumptions. In the ultimate case the predicted stress increases were less conservative at midspan with predicted-to-measured ratios ranging between 46 and 59 percent. At the support the ultimate limiting-strain assumptions predicted

the tendon stress increases fairly accurately with predicted-to-measured ratios ranging between 91 and 128 percent.

The Virlogeux method offers a convenient method by which local effects can be incorporated in the design. A series of tests could be run with varying degrees of confinement in the compression zone, and anchorage of the passive tension reinforcement in the segment. A series of design guidelines could then be developed in which limiting strains are prescribed depending on the level of confinement and anchorage.

7.4.4 Recommendation for Calculation of Flexural Strength. In light of the above discussion, a method similar to the CSA method is recommended for determining the stress increase in unbonded tendons at ultimate. It provides a convenient design method that incorporates most of the important factors described in Section 7.4.2. The effect of bonded reinforcement in the compression and tension zones can also be incorporated in the calculation of the neutral axis depth at ultimate.

Figure 7.15 summarizes the recommended design procedure. The equation is derived in the same way as the Tam and Pannell method with the neutral axis depth at ultimate, c_u , replaced by the neutral axis depth assuming yielding in the tension reinforcement, c_y . The neutral axis depth, c_y , can be calculated with only unbonded tendons crossing the critical joint, as shown in Fig. 7.16a, or with bonded compression and tension reinforcement as shown in Fig. 7.16b.

The free length of the unbonded tendon, ℓ_e , should be estimated from the length between anchorage locations and the number of hinges crossed by the tendon under question. Since support hinges undergo approximately half the concentrated rotation as the midspan hinges, elongations occurring at a support hinge will be approximately half the elongations occurring at midspan. The effective length of tendon should therefore be calculated as

$$\ell_e = \frac{\ell_i}{1 + .5N_s}$$

with ℓ_i equal to the length between anchorage locations and N_s equal to the number of support hinges crossed by the tendon. Note that this equation is true only for draped tendons in which the tendon is on the tension (opening) side at each

$$f_{ps} = f_{pe} + \psi E_p \epsilon_{cu} \left(\frac{d_p - c_u}{\ell_e} \right) \text{ (ksi)}$$

$$\psi = 10.5 \text{ (determined experimentally by Tam and Pannell)}$$

$$E_p = 28. \times 10^3 \text{ ksi (AASHTO)}$$

$$\epsilon_{cu} = 0.003 \text{ (ACI)}$$

$$\ell_e = \left(\frac{\ell_i}{1 + \frac{N_s}{2}} \right)$$

ℓ_i = length of tendon between anchorages

N_s = number of support hinges crossed by the tendon (draped tendons only)

Assume $c_u = c_y$

$$\therefore f_{ps} = f_{se} + 10.5 \times 28 \times 10^3 \times .003 \left(\frac{d_p - c_y}{\ell_e} \right)$$

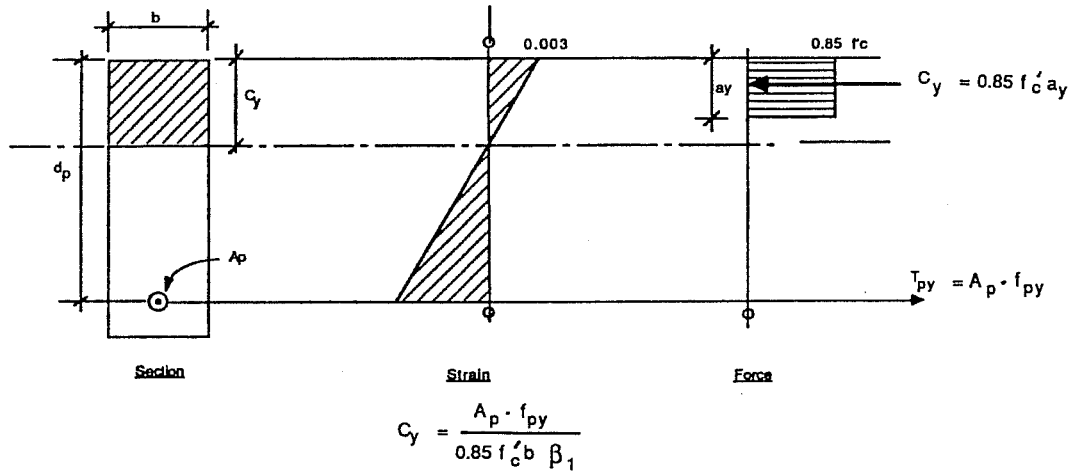
$$f_{ps} = f_{pe} + 882 \left(\frac{d_p - c_y}{\ell_e} \right)$$

\therefore Recommended Design Equation

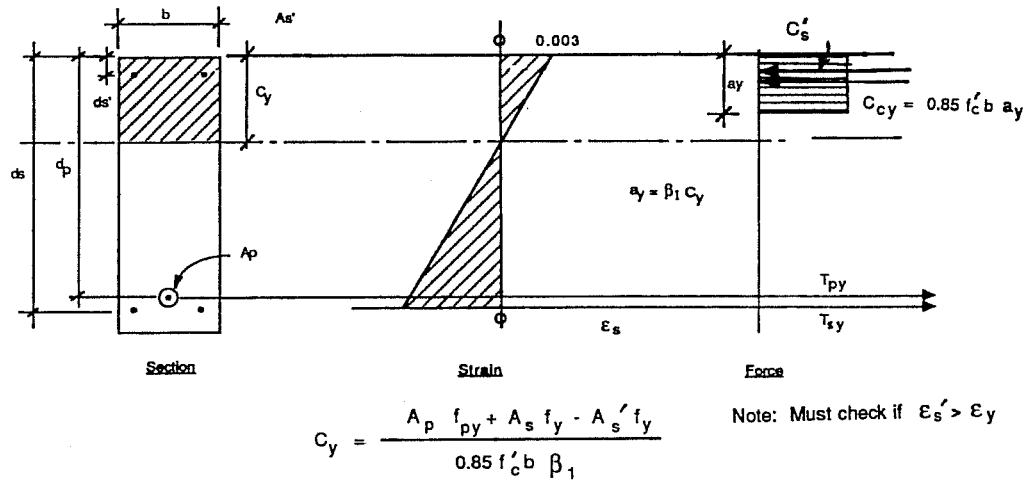
$$f_{ps} = f_{pe} + 900 \left(\frac{d_p - c_y}{\ell_e} \right)$$

Figure 7.15 Recommended Design Equation

Figure 7.15 Recommended Design Equation



(a) Unbonded tendons only



(b) With bonded reinforcement

Figure 7.16 Neutral Axis Depth, c_y

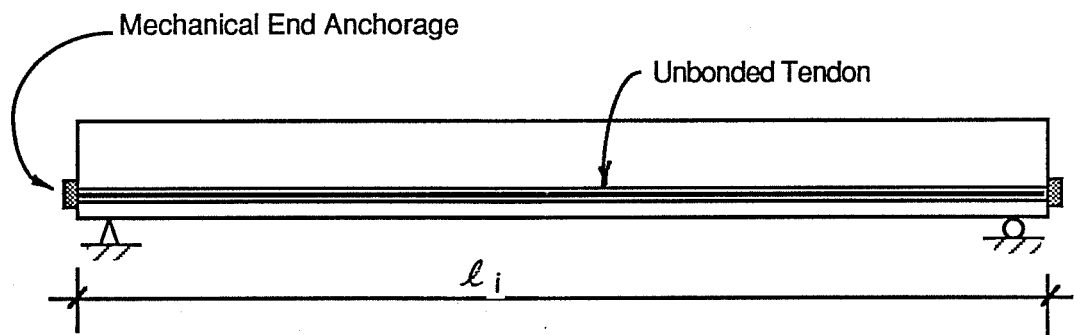
hinge location. The length between anchorage locations, l_i , may refer to the length between mechanical end anchorages as shown in Fig. 7.17a or the free unbonded length between regions in which the tendon is bonded and fully developed, as shown in Fig. 7.17b.

The calculated tendon stress increases using the proposed design procedure are also tabulated in Table 7.6. The proposed method generally underestimated the midspan tendon stress increases with predicted-to-measured ratios ranging between 62 and 80 percent. The conservatism is probably caused by the delayed slip in the tendons leading to a higher measured stress increase in the model structure.

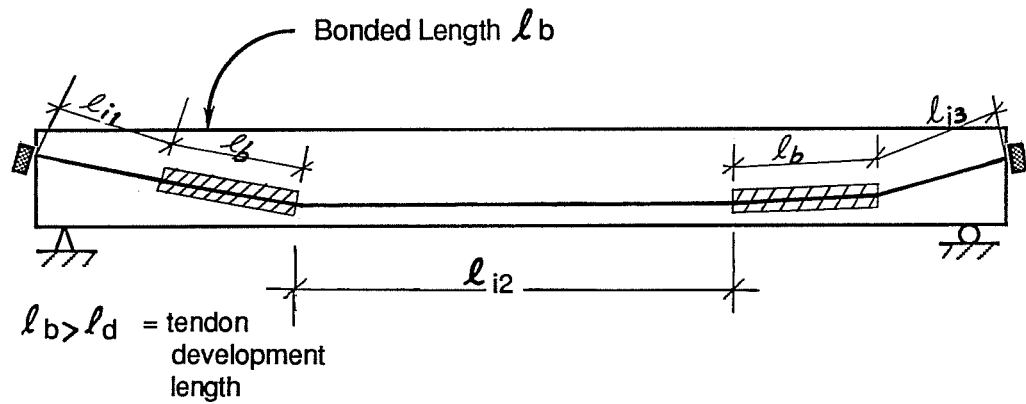
7.5 Load Rating Existing Structures

The AASHTO Manual for Maintenance Inspection of Bridges (38) requires that all bridges be inspected at regular intervals at a frequency not exceeding two years. For each inspection it is necessary to rate the structure at two load levels. The first level, called the Operating Load Rating, is the maximum permissible load level to which the structure can be subjected. This represents the factored ultimate strength of the structure, and load levels higher than the Operating Load will result in permanent deformation or damage. The second level, called the Inventory Load Rating, is the load level which can be safely applied to the structure for an indefinite period of time. This represents the service strength of the structure, and load levels higher than the Inventory Load will result in gradual deterioration of the load carrying capacity.

This need to rate existing bridges requires accurate methods for predicting the ultimate and service capacities of existing structures. For most structures these capacities can be accurately calculated from the section properties, either from the as-built drawings or from field measurements. For an unbonded prestressed system however the ultimate and service level behaviors are dependant on the effective prestress in the tendons. An accurate knowledge of existing tendon stress is therefore required to determine both ultimate strength and the limits to service level behavior. Overestimating the insitu tendon stresses will lead to a direct overestimation of structural strength.



a. Between Mechanical End Anchorages



b. Between Bonded Regions

Figure 7.17 Free Tendon Length

Two general methods are therefore available to rate an existing unbonded structure. By the first method the engineer must make a conservative estimate of the insitu tendon stresses. The insitu tendon stress must be calculated assuming artificially high stressing friction and long term losses. The rating engineer must be sure that the calculated tendon stress is an extreme lower bound to the true insitu stress.

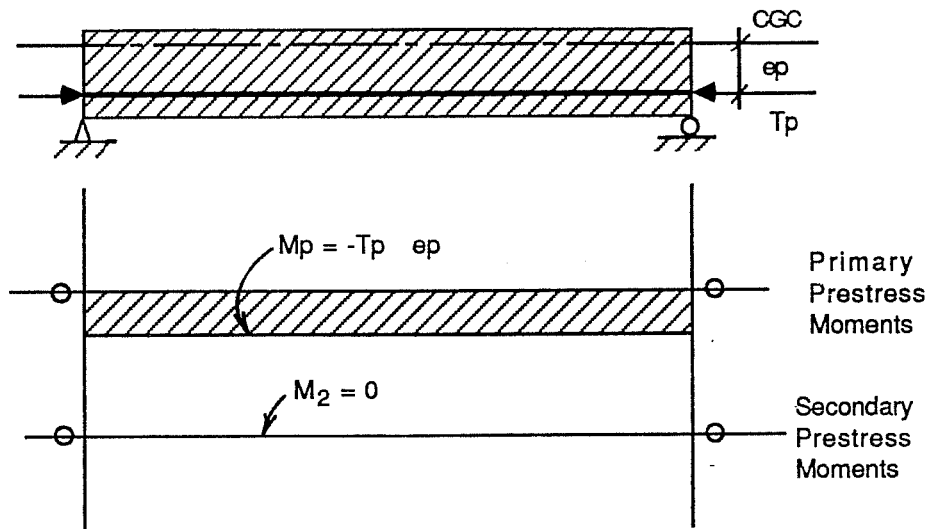
The second method for rating an existing structure is by load testing. The structure must be loaded and monitored in an attempt to determine the load that causes decompression at the extreme tension fiber. From this load an estimate of the effective prestress can be made.

7.6 Secondary Prestress Forces at Ultimate Load Levels

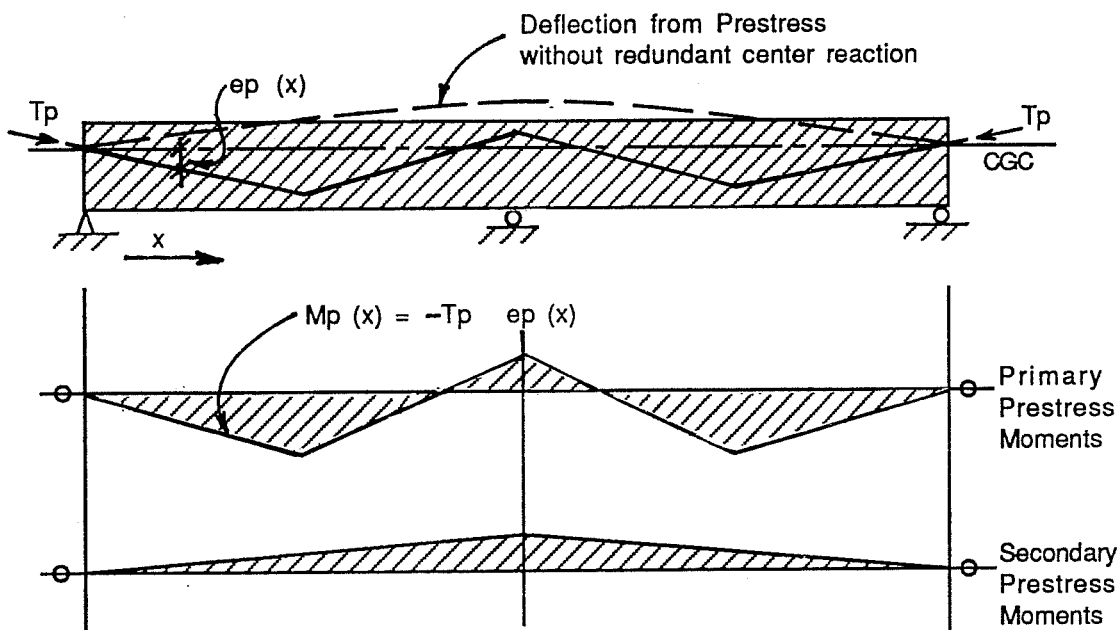
7.6.1 Background Information. Secondary prestress forces are caused by stressing a restrained structure. When prestress is applied to a structure, the structure will develop stresses to equilibrate the forces. The stresses cause strains that result in deflections in the structure. If these deflections are restrained in any way then the restraining forces will cause additional stresses to occur in the beam. These additional stresses are commonly known as the secondary prestress forces.

If prestress is applied to a statically determinate structure, as shown in Fig. 7.18a, the structure is free to deflect and the prestress forces are self-equilibrating. The prestress causes local changes in cross-sectional stresses but does not alter the global equilibrium of forces. The structure remains statically determinate externally but is determinate internally only if magnitude and location of the prestress force are exactly known. The local changes in cross-sectional stress are called the primary prestress forces and are calculated directly from the effect of the eccentric prestress at a section.

If prestress is applied to a statically indeterminate structure, as shown in Fig. 7.18b it is not free to deflect since restraint is provided by the redundant reaction. Global equilibrium is altered by the restraining reactions, called the secondary prestress reactions, which causes a redistribution of forces. In this case the structure is statically indeterminate with respect to both global and local forces. Global force distribution must consider both the girder stiffness and the secondary prestress



a. Statically Determinate Structure



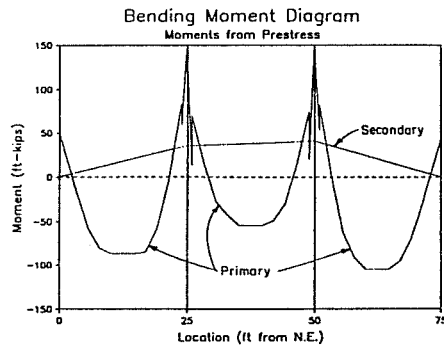
b. Statically Indeterminate Structure

Figure 7.18 Primary and Secondary Prestress Forces

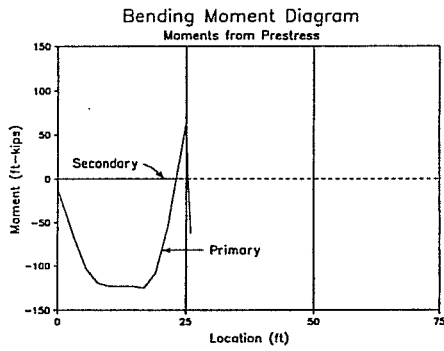
forces. The sectional stress distribution caused by the prestress at a particular location must consider the primary prestress forces as above plus the additional stresses caused by the secondary prestress forces.

7.6.2 Secondary Prestress Forces from Construction. The secondary prestress forces are dependant on the method and order of construction. Secondary forces develop during construction from the restraining forces that exist when a tendon is stressed. The restraining forces are therefore a function of the structural configuration at the time of stressing. This phenomenon can be illustrated by considering the primary and secondary prestress forces for two similar three-span beams. The first beam was stressed in its final three-span configuration, and the prestress forces are shown in Fig. 7.19a. Because tendons are symmetrical with respect to the center of the structure, the secondary prestress forces are also symmetrical. For the second beam, the structure was constructed in a sequential span-by-span manner by starting at one end-span and proceeding towards the other end. The prestress forces at the end of each stage of construction are shown in Fig. 7.19b. Since the one-span configuration is statically determinate, the prestress causes only primary prestress forces. In the two-span configuration the structure is restrained by one redundant reaction, and the secondary prestress forces develop as shown. When the tendons of the third span are stressed, the structure is restrained by two redundant reactions and the secondary prestress forces develop as shown. The final distribution of secondary forces is calculated from the addition of the secondary forces that occur during each stage of construction. Note that the final secondary prestress forces are not symmetrical with respect to the center of the girder, even though the tendon profiles are.

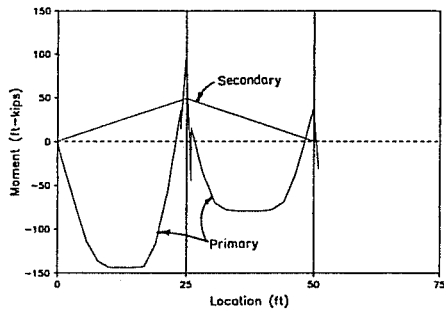
Attempts have been made in prototype construction to reduce the secondary prestress forces by using staged casting and stressing procedures. If rotations are allowed to occur at the ends of the span at the time the tendons are stressed, then the restraining forces and secondary prestress forces will be small or nonexistent. The staged casting procedure, shown in Fig. 7.20, has been used to reduce the secondary prestress forces in prototype span-by-span construction. The first span is erected normally with the tendons causing only primary prestress forces. The second span is then erected and the closure strip is cast only at the level of the bottom flange. The tendons are then coupled to the ends of the first-span tendons



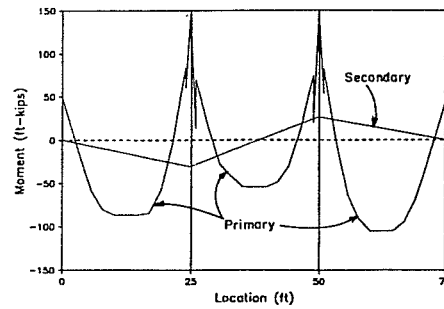
a. Stressed in Three-Span Configuration



One-Span Configuration



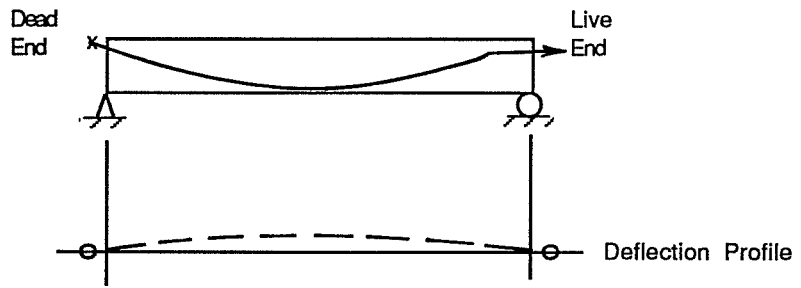
Two-Span Configuration



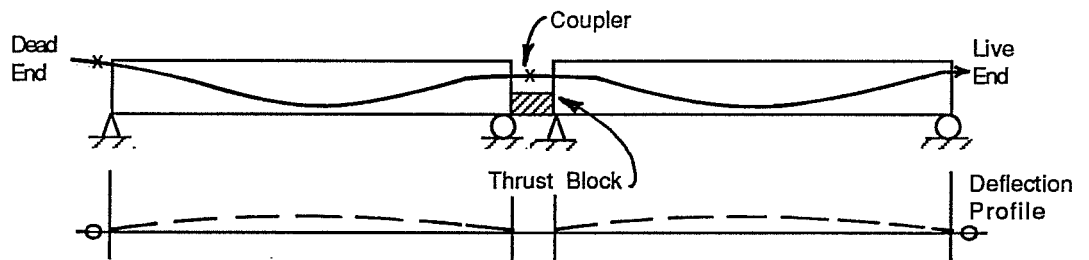
Three-Span Configuration

b. Structural Constructed Span-by-Span

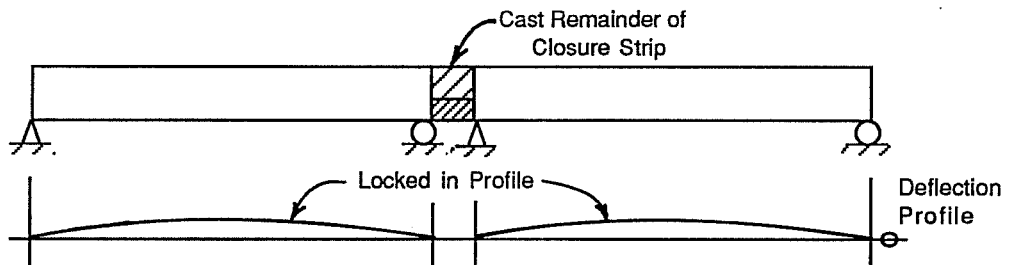
Figure 7.19 Secondary Prestress Forces from the Construction Method



a. Erect First Span



b. Erect Second Span, Cast Thrust Block, and Stress



c. Cast Remainder of Closure Strip

Figure 7.20 Staged Construction to Relieve Secondary Forces

(Fig. 7.20b) and then stressed. The thrust from the prestress forces is carried by the continuous bottom flange. Since only the bottom flange is in contact at the time of stressing, the ends of the second span are relatively free to rotate, and the resulting secondary prestress forces are small or nonexistent. The closure strip is then completed and the next span is erected in a similar manner.

This staged method of casting and stressing to reduce secondary forces has several critical problem areas, however, that must be carefully addressed during design. At the time of stressing, the bottom flange is the only concrete present for transferring the large prestress forces between spans. This causes relatively higher stresses to occur in the bottom flange which remain during the life of the structure. In addition to the high stress, the concrete must also undergo local deformations to allow the ends of the beam to rotate and relieve the secondary prestress forces. The high stresses combined with the induced rotations may cause distress in this concrete. Crushing of this concrete before the remainder of the closure strip is cast will cause a serious safety problem.

A final concern with this construction procedure is the effect of the tendon coupler at the location of maximum negative moment. The top part of the closure strip is cast after stressing the primary tendons, so the compressive stress in this region is minimal. Under applied loads the closure strip will crack allowing moisture to penetrate into the coupler region. In addition, the stress range in the coupler may be large at this cracked section. This indicates that a serious fatigue problem in the coupled tendon, which may be aggravated by moisture infiltration, could possibly develop.

7.6.3 Redistribution of Secondary Prestress Forces. Because the external tendons are bonded to the concrete section only at discrete locations along the span, large concentrated rotations must occur at opening joints to develop the large tendon elongations required for increased tendon stresses. These rotations allow the internal forces to redistribute to stiffer uncracked regions. This is apparent from the reaction and joint moment data for the flexural test of the north span, shown in Fig. 7.21. As the midspan joints begin to open at the decompression load, the resultant loss in stiffness causes a larger portion of the additional load to be carried at the interior support. As loading is further increased, the support joint opens causing a reduction in stiffness at the support. The internal forces then redistribute back towards the

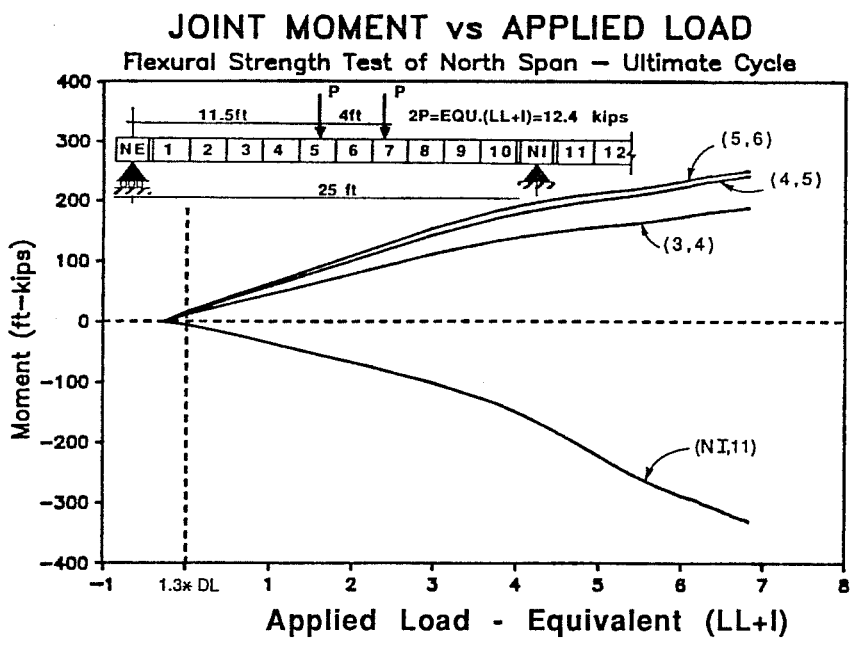
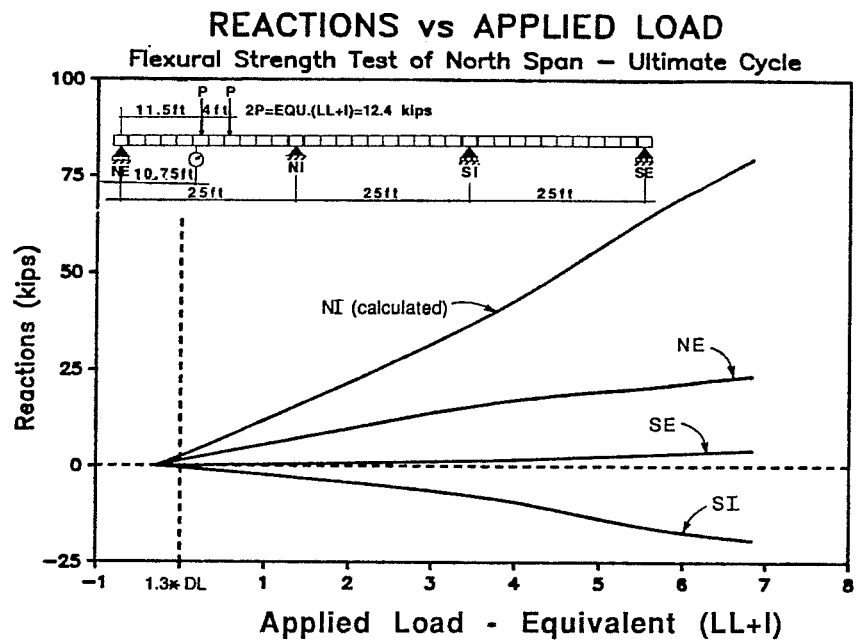


Figure 7.21 Reactions and Joint Moments

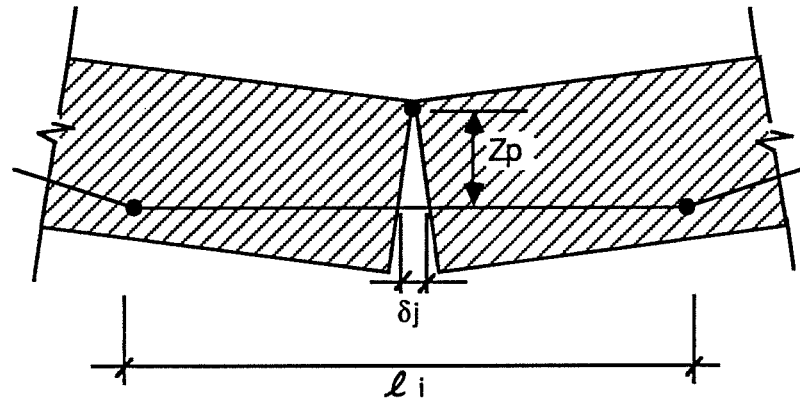
midspan region with the distribution of internal forces at ultimate being controlled by the relative stiffness of the support and midspan regions.

The distribution of applied loads becomes dependant on the relative rotational stiffness at the support and at midspan. As ultimate loads are approached the plastic hinges can be idealized by a rotational spring with a moment-rotation stiffness as described in Fig. 7.22. The idealized spring has a non-zero stiffness which is dependant on the effective depth of the prestress and the free length of the tendon. This behavior is quite different from the behavior of a plastic hinge that forms because of yielding of a bar, as is common in bonded construction.

From the equation for the rotational spring constant several observations can be made. First, the values of E_p and A_p are constant and known. The value of Z_p is smallest at the decompression load, and increases as the compressive forces concentrate in the top flange. After the hinge has fully developed, the value of Z_p remains approximately constant throughout the range of hinge behavior. Near ultimate loads, the rotational spring stiffness is almost entirely dependant on the free length of the tendon.

For low load levels before the tendon slips at the deviators, the length of the tendon segment is equal to the length between adjacent deviators. As load is increase the tendons begin to slip at the deviators, and the length of the tendon segment becomes larger, and the resultant rotational joint stiffness decreases. For ultimate load levels the tendon slip advances until the length of the tendon segment approaches the total length between end anchorages. This was evident during the test with tendons slipping at all locations as load approached the ultimate level.

The rotational joint stiffness, therefore, behaves as shown in Fig. 7.23. For load levels below the decompression load the joint remains in contact with no local joint rotation. This is analogous to having an infinite rotational spring stiffness. After the joint decompresses, the rotational joint stiffness decreases until the compressive forces are concentrated in the top flange at M_o . For moments larger than M_o , the rotational joint stiffness remains approximately constant. At some moment, M_{si} , the tendon begins to slip and the stiffness begins to decrease, with a stiffness reduction occurring each time the tendon slips. Finally at some moment, M_{sf} , the tendon is slipping at all locations and the length of the tendon segment is the length



$$K_{\Theta} = \frac{\Delta M}{\Delta \Theta}$$

$$\begin{aligned} \Delta M &= Z_p \cdot \Delta T = Z_p \cdot (\Delta \sigma_p \cdot A_p) \\ &= Z_p \cdot \left[\left(\frac{\delta_j}{\ell_j} \cdot E_p \right) \cdot A_p \right] \end{aligned}$$

$$\Delta \Theta = \frac{\sigma_j}{z_p} \quad \text{or} \quad \sigma_j = Z_p \cdot \Delta \Theta$$

$$\therefore \Delta M = Z_p \times \left[\left(\frac{Z_p \cdot \Delta \Theta \cdot E_p}{\ell_i} \right) \cdot A_p \right]$$

$$\text{or} \quad \frac{\Delta M}{\Delta \Theta} = K_{\Theta} = \frac{Z_p^2 E_p A_p}{\ell_i}$$

Figure 7.22 Rotational Stiffness at an Opening Joint

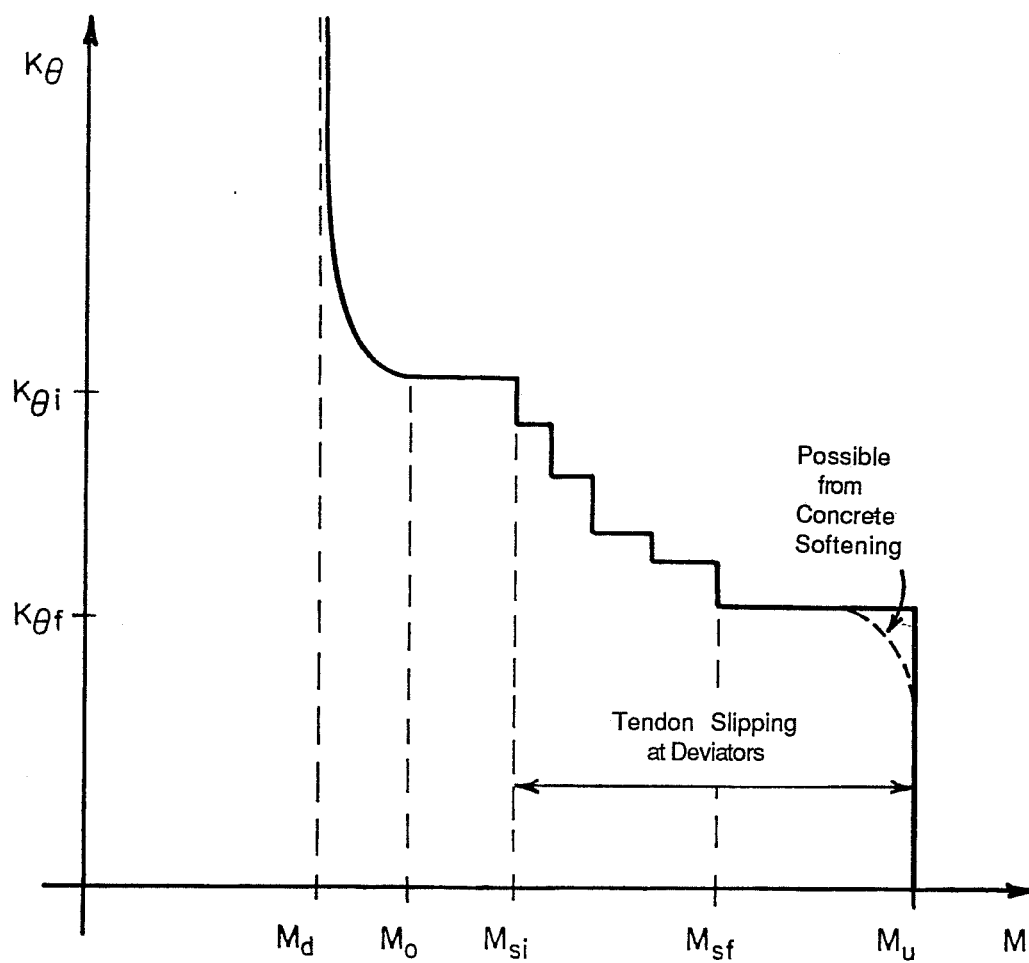


Figure 7.23 Rotational Joint Stiffness vs. Moment

between end anchorages. For moments above M_{sf} the rotational joint stiffness remains approximately constant with small decreases occurring due to softening in the concrete compression zone.

Figure 7.24 shows the relationship between the applied load and the bending moments at the midspan and support hinges for the flexural strength tests of the two exterior spans. Three separate expressions for bending moment are presented for each hinging joint. The first case, designated as "E", shows the theoretical response of the structure assuming elastic behavior and no secondary prestress moments. The second case, designated as "E+P2" shows the theoretical response of the structure assuming elastic behavior including the effects of the initial secondary prestress moments. The final case shows the measured response of the structure during the test.

As was described above for Fig. 7.21, the measured TEST response starts at the initial secondary moment and follows the E+P2 case. When the midspan joint begins to open, the load is redistributed to the stiffer support region. When the support joint begins to open, the internal forces are redistributed back towards the midspan region with the distribution of internal forces at ultimate controlled by the relative rotational stiffness at the support and midspan hinges.

Once the mechanism is fully developed and the ultimate load is approached, it appears that the Load - Moment response again becomes linear. The slopes of the resultant lines are dependant on the relative rotational stiffness of the midspan and support hinges. It also appears from the data that the moment response is asymptotic to a line which passes through a point defined by zero moment and the applied load at the start of the test (initial load was required to simulate the factored dead load condition as described in Section 6.2.3). This behavior is clearly visible in the south-span test data, although the north span data is inconclusive. This would appear to indicate that the internal force distribution at ultimate is dependant entirely on the rotational stiffness at the mechanism hinges, and is independant of initial conditions such as the secondary prestress forces.

The redistribution of internal forces, caused by "hinging" at the critical joint locations, causes redistribution of the secondary prestress forces near ultimate

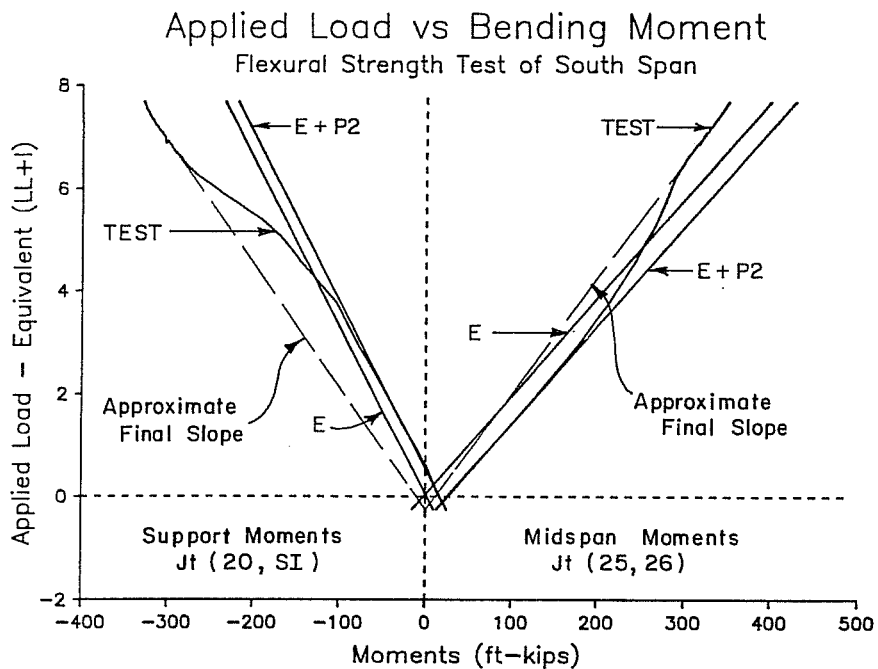
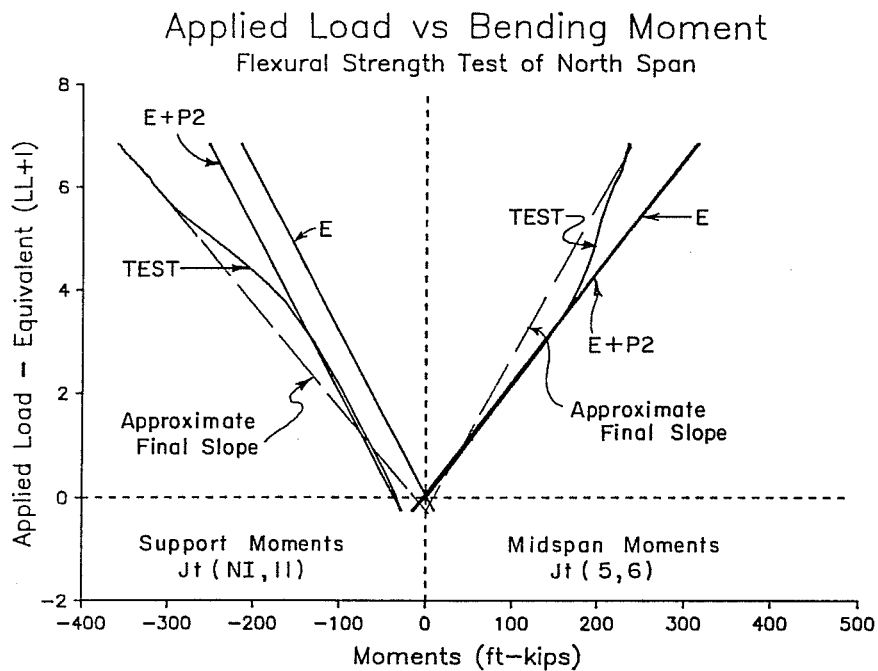


Figure 7.24 Applied Load vs. Bending Moment

load levels. As described above, the secondary prestress forces are caused by geometric constraints on the entire structure when the tendons are initially stressed. To develop the required tensile forces with external tendons, large rotations must occur at the segment joints. As joints "hinge" and a mechanism forms, the forces from the initial geometric constraints dissipate. If the segments are detailed to allow large rotations to occur at the segment joints, then the geometric constraints will no longer be valid. Therefore, the geometric constraints and the corresponding secondary prestress forces affect the service load behavior, while the conditions at ultimate load approach plastic mechanism behavior with small, non-zero rotational stiffnesses at flexural hinges.

8. CONCLUSIONS AND RECOMMENDATIONS

An experimental investigation was conducted to examine the service and ultimate load behavior of segmentally precast box-girder bridges with external post-tensioning tendons. A primary interest of this study was to examine the effect of joint type (dry versus epoxied joints) on the stiffness, strength, and ductility of the structure. A three-span reduced-scale segmental box-girder bridge model was constructed, then tested in three stages corresponding to service loads, factored design loads, and ultimate loads. Flexural behavior was examined first, then shear tests were conducted on the partially damaged structure. Test results and observations were presented in previous chapters.

The conclusions presented in this chapter are based on the tests of the model structure and hence their applicability may be limited to similar precast segmental bridges with external tendons, similar tendon anchorage, deviation, and segment joinery details. In this research program a realistic reduced-scale model of an externally post-tensioned box-girder bridge was constructed and tested. Results of the tests indicate that both dry and epoxy-jointed systems behave in a ductile manner with considerable reserve capacity beyond service and factored design load conditions. The joints remained closed and the structure uncracked for loads as high as the factored design load. For higher load levels the structure displayed considerable visible distortion before reaching ultimate strength.

In this chapter, observations and recommendations are summarized from all aspects of the research program. Important information concerning the fabrication and erection processes are presented to assist designers in constructing better structures. Behavior, design recommendations, and conclusions are then summarized from the test data and observations. Finally, additional research needs in areas related to externally post-tensioned bridge structures are presented.

8.1 Fabrication Conclusions and Recommendations

The following conclusions were drawn from experience gained during fabrication of the model bridge components:

1. Precasting match-cast box-girder bridge segments is a highly complex operation requiring thorough planning before production casting begins. The following is a partial list of important items to be considered before beginning precast operations of match-cast segments: concrete mix-design, concrete properties, concrete and cement supplier, aggregate availability and consistency, concrete batching, concrete approval methods, concrete placement and consolidation, concrete finishing, concrete curing and testing, form preparation, form operation, form stripping, debonding agent, geometric control of match-cast segments, quality control procedures, post-tensioning hardware support and preparation, post-tensioning hardware reinforcement, shear-key details, segment reinforcement,... All of these factors, plus others, will need to be assessed during the precast operation. Initial planning will help eliminate most construction problems (Chapter 2).
2. The post-tensioning anchorage details should be pretested prior to use in the prototype structure. The pretest can be conducted either by proof testing prototype anchorage regions or by load testing a mockup of the anchorage region (Section 7.3.2.2).
3. Unequal web reactions can be expected with segmental systems erected on shoring. Provision should be made in the bearing design and fabrication to equalize web reactions after erection (Section 4.4).

8.2 Erection Process

The following conclusions were drawn from experience gained during the erection of the model bridge structure:

1. The layout of the temporary post-tensioning is controlled by several factors: the workable life of the epoxy joining material, the weight of segments being joined, and the stiffness of the supporting falsework. Each factor must be considered independently, as well as its relationship to the other factors. The temporary post-tensioning equipment and procedure should also be tested before production erection begins (Section 2.4.3).

2. The epoxy should be delivered in clearly labeled, premeasured quantities of each component so they can be mixed directly without site measurement of quantities. The epoxy supplier should also provide information regarding the necessary storage conditions and mixing techniques. The contractor should also have experience with epoxy and be able to recognize substandard materials (Section 2.4.5).
3. The epoxy application process must be planned carefully to ensure that all the necessary tasks are completed within a required time frame. The epoxy pot-life serves as a maximum time limit for completion of: epoxy measuring and mixing, application of the epoxy to both surfaces of a match-cast joint, joint closure, temporary post-tensioning, and cleaning of the epoxy from tendon ducts and equipment. Time studies should be conducted to estimate the necessary manpower and the proper staging of the various tasks (Sections 2.4.3 and 2.4.5).
4. The use of superplasticizers is recommended in the cast-in-place closure strip to ensure proper workability of the concrete. The high surface-to-volume ratio in the closure strips requires that the forms and matching segment faces be moistened to reduce water loss due to absorption. The super-plasticizer is beneficial in providing a concrete with a high workability that is independent of water loss through absorption (Section 2.4.6).
5. Each post-tensioning ram should be operated independently with its own pump and pressure control system. Coupling of post-tensioning rams into parallel systems is not advised (Section 2.4.7).

8.3 Analysis

The following conclusions were drawn from experience gained by applying various analysis methods to the model bridge structure:

1. The model structure was adequately analyzed using a plane-frame elastic analysis to load levels as high as the factored design load (Section 5.3).

2. A plastic mechanism analysis can be used to reveal important information about the behavior of the structure near ultimate loads. Critical mechanism joints can be determined and an estimate of the ultimate flexural strength can be obtained. For the model structure, when the ACI formula for unbonded tendon stress was used in the calculation of hinge capacities, the mechanism analysis yielded calculated strengths less than, and within 15 percent of measured strengths (Section 5.2).
3. To properly predict the insitu condition of the structure it is necessary to analyze each structural configuration that occurs during construction of the structure. Dead loads, prestress forces, and construction or service live loads must be applied to each intermediate structure. The resultant internal forces and deflections from a particular configuration must be superposed with subsequent configurations (Section 5.3).

8.4 Behavior

The following conclusions are drawn from the tests which documented the full range of behavior of a segmental box-girder bridge model with external post-tensioning tendons erected in a span-by-span sequence:

1. The structure remained uncracked for service load conditions with live-load deflections of approximately $L/6000$ in the exterior spans and $L/7500$ for the interior span. The deflection of the dry-jointed exterior span was about 10 percent greater than for the epoxy-jointed exterior span. The reduced stiffness in the dry-jointed span is perhaps caused by differential shrinkage in segments, due to variable thicknesses, which results in less than full contact between match-cast segments. Epoxy effectively filled any space left by differential shrinkage, and restored full contact between segments. Additionally, lower concrete strengths in the north span may have lead to decreased stiffnesses (Section 7.1.1.1).
2. The live-load tendon-stress increases in the midspan region of the loaded span were measured to be less than 2 ksi in all spans. Tendon slip was not noticed during service load cycles (Section 7.1.1.1).

3. The box-girder shape used for the model structure exhibited high torsional stiffness with rotational deformations less than could be accurately measured with the instrumentation (Section 6.6.1.3).
4. The cracking load in the epoxy-jointed span was approximately twice the load required to decompress the flexural tension fiber and begin to open an existing flexural crack or a dry joint. Cracking occurred through concrete adjacent to an epoxied joint (Section 7.3.2).
5. The structure remained uncracked to load levels higher than the factored design load (Section 7.3.3).
6. The structure was quite stiff under the factored design load. While carrying 1.3 DL, the measured factored live load deflections were $L/1764$ for the dry-jointed exterior span and $L/2310$ for the epoxy-jointed exterior span. The approximately 25 percent higher stiffness in the epoxy-jointed span reflects the tensile capacity of the joints and the reduced effective cross-section in the dry-jointed span (Section 7.3.3).
7. The factored-load tendon stress increases in the midspan region of the loaded exterior spans were measured to be less than 5 ksi in both exterior spans. Tendon slip was not noticed for any of the factored load cycles (Sections 6.6.2 and 6.7.2).
8. Failure of the exterior span in flexure (defined as when the tangent stiffness of the load-deflection response was reduced to 4% of the initial elastic stiffness) occurred after development of a failure mechanism involving concentrated rotations in a joint or crack near midspan of the exterior span and subsequent opening at a joint at the interior face of the first interior pier segment (Section 7.1.3).
9. The total moment at midspan of the north span when flexural capacity was reached was approximately 2.5 times the total service-load moment in the north dry span and 3.0 in the epoxied south span. This indicates that the midspan moment has an overall factor of safety above the service load condition of approximately 2.5 in the dry north span and 3.0 in the epoxied south span. The difference in capacity was due to a larger effective prestress in the south span (Section 7.1.5).

10. The maximum applied-load moment at midspan of the north span when flexural capacity was reached was approximately 5.6 times the maximum applied service-load moment in the dry north span and 7.8 in the epoxied south span. This indicates that the midspan moment has an overall safety margin above the service load condition of approximately 5.6 in the dry north span and 7.8 in the epoxied south span. Again, the difference in capacity was caused by a larger effective prestress in the south span (Section 7.1.5).
11. Two important ductility requirements should be considered during design of externally post-tensioned girders.
 - i. Details should be provided to ensure that plastic hinges form in a ductile manner. Bonded reinforcement and multi-hinge mechanisms will lead to more ductile structures.
 - ii. If epoxy is used at segment joints, and the moment capacity is less than the cracking load then an additional factor of safety on the required capacity should be provided (Section 7.1.5).
12. The tendon stress corresponding to nominal flexural strength, f_{ps} , is dependant on many factors. The primary variable affecting f_{ps} is the effective stress in the prestressed reinforcement after allowance for all prestress losses, f_{pe} . Other factors that may influence f_{ps} are: the ratio of section effective depth to unbonded tendon length ((Z_p/ℓ_i)), the depth to the neutral axis (c_u), the amount of prestressed and nonprestressed reinforcement (ρ_p and ρ_s), the concrete strength (f'_c), the level of confinement in the compression zone, and detailing of the segment reinforcement (Section 7.4.2).
13. The tendon stress corresponding to nominal flexural strength, f_{ps} , is critically dependant on the effective stress in the prestressed reinforcement after allowance for all prestress losses, f_{pe} . To ensure adequate safety, the design should be based on conservative assumptions with respect to losses from friction, creep, and shrinkage (Section 7.4.2.1).
14. The following design method is recommended for design of post-tensioned girders with unbonded external tendons (Section 7.4.4):

$$f_{ps} = f_{pe} + 900 \left(\frac{d_p - c_y}{\ell_e} \right) \quad (ksi)$$

but not to exceed f_{py}

where:

- f_{ps} = the tendon stress corresponding to nominal strength (ksi).
- f_{pe} = effective stress in the prestressed reinforcement after allowance for all prestress losses (ksi).
- d_p = distance from the extreme compression fiber to center of prestressed reinforcement (in.).
- c_y = distance from the extreme compression fiber to the neutral axis calculated using factored material strengths and assuming the tension reinforcement, prestressed or mild, has yielded (in.).
- ℓ_e = effective length of the tendon for calculation of nominal strength

$$\ell_e = \left(\frac{\ell_i}{1 + \frac{N_s}{2}} \right) \quad (in.)$$

where:

ℓ_i = the length of the tendon between anchorages (in.).

N_s = the number of support hinges crossed by the tendon (draped tendons only).

15. Large concentrated rotations are required at opening joints to cause tendon stresses to increase with the applied load. These rotations allow the internal forces to redistribute to stiffer regions. The secondary prestress forces also redistribute as ultimate load levels are reached (Section 7.6.3).
16. Two general methods are available to rate an existing unbonded structure. With the first method, the engineer must make a conservative assumption of the insitu tendon stresses and be sure that the calculated tendon stress is an extreme lower bound to the true insitu stress. With the second method the structure must be loaded and monitored in an attempt to determine

the load that causes decompression at the extreme tension fiber. From this load an estimate of the effective prestress can be made (Section 7.5).

17. Tendon slip was observed for all tendons at all deviators during the ultimate strength cycles. Tendons also slipped during cracking and joint-opening cycles. When a tendon began to slip, it did not suddenly slip and release stress in the midspan region. Instead, the tendon started to slip and then continued to slip as load was increased. For ultimate load levels the tendons were elongating over their entire unbonded lengths between anchorages (Section 7.4.2.5).
18. The maximum midspan stress that was achieved in the model tendons was affected by the load level at which slip began. If tendon slip began at a low load level, then the ultimate midspan tendon stress was low. Conversely, if slip did not occur until higher load levels, then the ultimate midspan tendon stress was increased (Section 7.4.2.5).
19. The local transfer of forces across opening joints depended on the level of shear being transmitted across the joint. For opening joints with small shear transfer, the joint/crack opened in a flexural mode into the top flange of the structure with the concentrated rotations occurring at the joint. For opening joints with large shear transfer, an inclined crack formed from the load point to the lower corner of the segment adjacent to the joint. The concentrated rotations occurred at the inclined crack (Section 7.1.4).
20. The tests results indicated that there was a measured decompression load of 1.9(LL+I) in the dry-jointed north span. However, the design of this span provided substantial residual compression at service load levels only slightly above the recently recommended PTI-NCHRP-AASHTO recommended levels. In addition, the true factor of safety may be less because of traffic overloads, excessive prestress losses, or calculation inaccuracies. The epoxy joints offered substantial reserve against cracking. The use of epoxy joints is recommended for this type of construction (Sections 5.4, 7.1.4 and 7.3).

8.5 Research Needs

The goal of any research project is to obtain a better understanding of the research subject. Frequently, a better understanding of the subject will lead to an increased awareness of subject areas still requiring investigation. The following is a list of possible research topics which will improve understanding of externally post-tensioned box-girder bridge systems.

1. An important aspect of the behavior of externally post-tensioned systems is the shear behavior at a critical mechanism joint. This subject was partially studied with the scale model bridge project and was also studied independently by Ramirez (13) at the Ferguson Structural Engineering Laboratory of the University of Texas at Austin. Additional research is required to fully document all components of shear strength at an opening joint (Section 7.1.4 and 7.3.5).
2. During stressing of the scale model bridge structure it appeared there was substantial friction loss through the live-end anchor. This was also noticed by Quade (30) in another project at the University of Texas at Austin. Because the ultimate flexural strength of unbonded systems is critically dependant on the insitu tendon stress, research is needed to quantify the friction losses in standard industry anchorage hardware. Friction loss studies should also be conducted for deviator regions and regions of high duct curvature (Section 4.1).
3. The deviators provide the only positive connection between the prestressing tendons and the concrete box-girder. Complete understanding is therefore required for this critically important detail. Components contributing to deviator strength have been investigated by Powell and Beaupre (12). Other areas important to deviator behavior requiring study are (Sections 1.3.3, 7.1.1.4 and 7.4.2.5):
 - fretting fatigue
 - bond mechanism between the deviator and grouted external tendon.
 - possible improved details

4. The finite element program prepared by El-Habr (10) provides an excellent starting point for analyzing externally post-tensioned systems. The following refinements are suggested to make the program easier to use and more applicable to bridge structures (Section 1.3.2.1):
 - include a method for tracing the segmental construction process.
 - include the potential for slip between the tendons and deviators.
 - post-tensioned tendons rather than prestressed tendons.
5. The scale model bridge structure was designed and constructed with many features which could extend the testing program. The following is a list of additional studies that could be conducted on the model:
 - bond external tendons to intermediate diaphragms.
 - bond external tendons to the bottom flange with a secondary cast of concrete.
 - stress and grout internal tendons.
 - conduct direct shear tests.
 - investigate the fatigue behavior of the global system.
 - investigate the seismic behavior of externally post-tensioned structure.
 - investigate redistribution of secondary prestress forces.
 - develop and verify code equations for flexural strength of externally post-tensioned bridge structures.
6. Prototype testing can be used to verify and extrapolate model test data. The following is a list of possible research that could be conducted on prototype structures:
 - apply instrumentation to a prototype structure during construction to monitor true behavior under service loads.
 - apply strain gages to external tendons and monitor friction losses during stressing.
 - monitor long-term serviceability of dry-jointed structures.

APPENDIX A
Dimensional Analysis

Function, $f\Delta$:

$$\Delta = f\Delta (L, \gamma, R, f_p, v_p, E_c, G_c)$$

Dimensionless Parameters:

$$\frac{\Delta}{L} = \phi_{\Delta} \left[(\lambda), \left(\frac{R}{E_c L^2} \right), \left(\frac{f_p}{E_c} \right), \left(\frac{v_p}{v_p} \right), \left(\frac{E_c}{G_c} \right) \right]$$

Appendix A1 Variables Affecting Elastic Deflection

Function, fR :

$$R = fR (l, \lambda, \gamma, q, p, E_c, G_c)$$

Dimensionless Parameters:

$$\frac{R}{P} = \Phi_r \left[(\lambda), \left(\frac{P}{\gamma L^3} \right), \left(\frac{P}{qL} \right), \left(\frac{P}{EL^2} \right), \left(\frac{E_c}{G_c} \right) \right]$$

Appendix A2 Variables Affecting Section Forces

Function, fM_n :

$$M_n = fM_n (b, d_e, d_i, A_{pe}, A_{pi}, f_{pse}, f_{psi}, f_{pu}, f'_c)$$

Dimensionless Parameters:

$$\left(\frac{M_n}{M_u} \right) = \Phi_{M_n} \left[\left(\frac{A_{pe}}{bd_e} \right), \left(\frac{A_{pi}}{bd_i} \right), \left(\frac{A_{pe}}{A_{pi}} \right), \left(\frac{M_u}{F_{pse} A_{pe} d_e} \right), \left(\frac{M_u}{f_{psi} A_{pi} d_i} \right), \left(\frac{M_u}{f'_c b d_e} \right), \left(\frac{M_u}{f'_c b d_i^2} \right) \right]$$

Appendix A3 Variables Affecting Flexural Strength

Function, f_{psi} :

$$f_{psi} = f_{psi} \left(b, d_i, A_{pi}, f_{pu}, f_{py}, f'_c, E_c, E_p, \alpha \right)$$

Dimensionless Parameters:

$$\left(\frac{f_{psi}}{f_{pu}} \right) = \phi_{f_{psi}} \left[\left(\frac{A_{pi}}{bd_i} \right), \left(\frac{f_{pu}}{f'_c} \right), \left(\frac{f_{pu}}{f_{py}} \right), \left(\frac{E_p}{E_c} \right), (\alpha) \right]$$

ACI-318.83 Equation for Bonded Prestressing Tendons
- with no bonded mild reinforcement

$$\left(\frac{f_{psi}}{f_{pu}} \right) = \left[1 - \frac{\gamma_p}{\beta_i} \left(\rho_p - \frac{f_{pu}}{f'_c} \right) \right]$$

$$\gamma_p = f \left(\frac{f_{pu}}{f_{py}} \right)$$

$$\beta_i = f(f'_c)$$

$$\rho_p = \left(\frac{A_{pi}}{bd_i} \right)$$

Appendix A4 - Variables Affecting f_{psi}

Function, f_{pse} :

$$f_{pse} \left(b, d_e, A_{pe}, f_{pu}, f_{py}, f'_c, E_c, E_p, \alpha, l_i, M_d \right)$$

Dimensionless Parameters:

$$\left(\frac{f_{pse}}{f_{pu}} \right) = \phi_{f_{pse}} \left[\left(\frac{A_{pe}}{bd_e} \right), \left(\alpha \right), \left(\frac{d_e}{l_i} \right), \left(\frac{f_{py}}{f_{pu}} \right), \left(\frac{f_{pe}}{f_{pu}} \right), \left(\frac{f'_c}{f_{pu}} \right), \left(\frac{E_p}{E_c} \right), \left(\frac{M_d}{f_{pe}A_{pe}d_e} \right) \right]$$

Appendix A5 - Factors Affecting f_{pse}

APPENDIX B
Tendon Stress Data

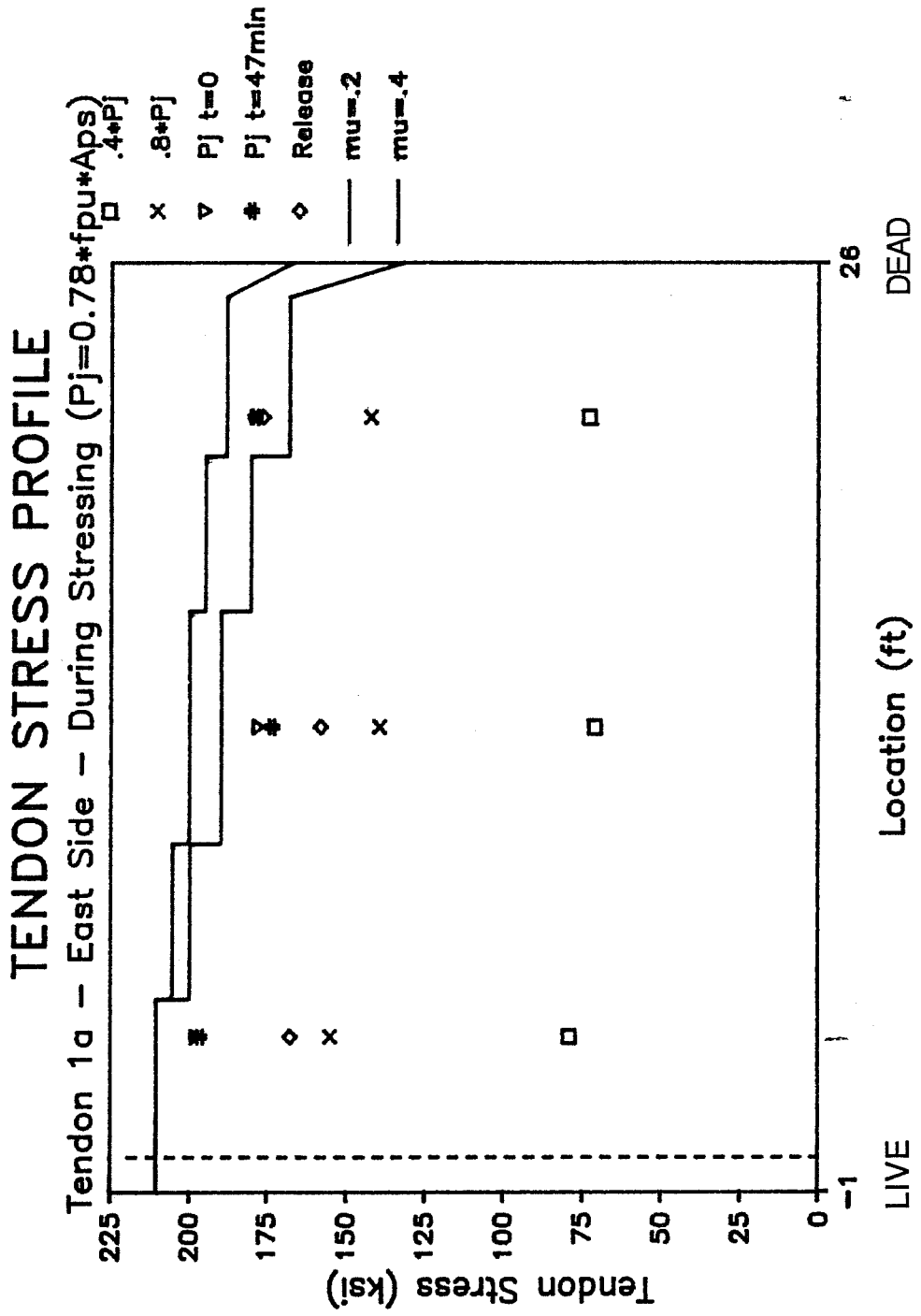


Figure B.1 Tendon Stress Profile During Stressing

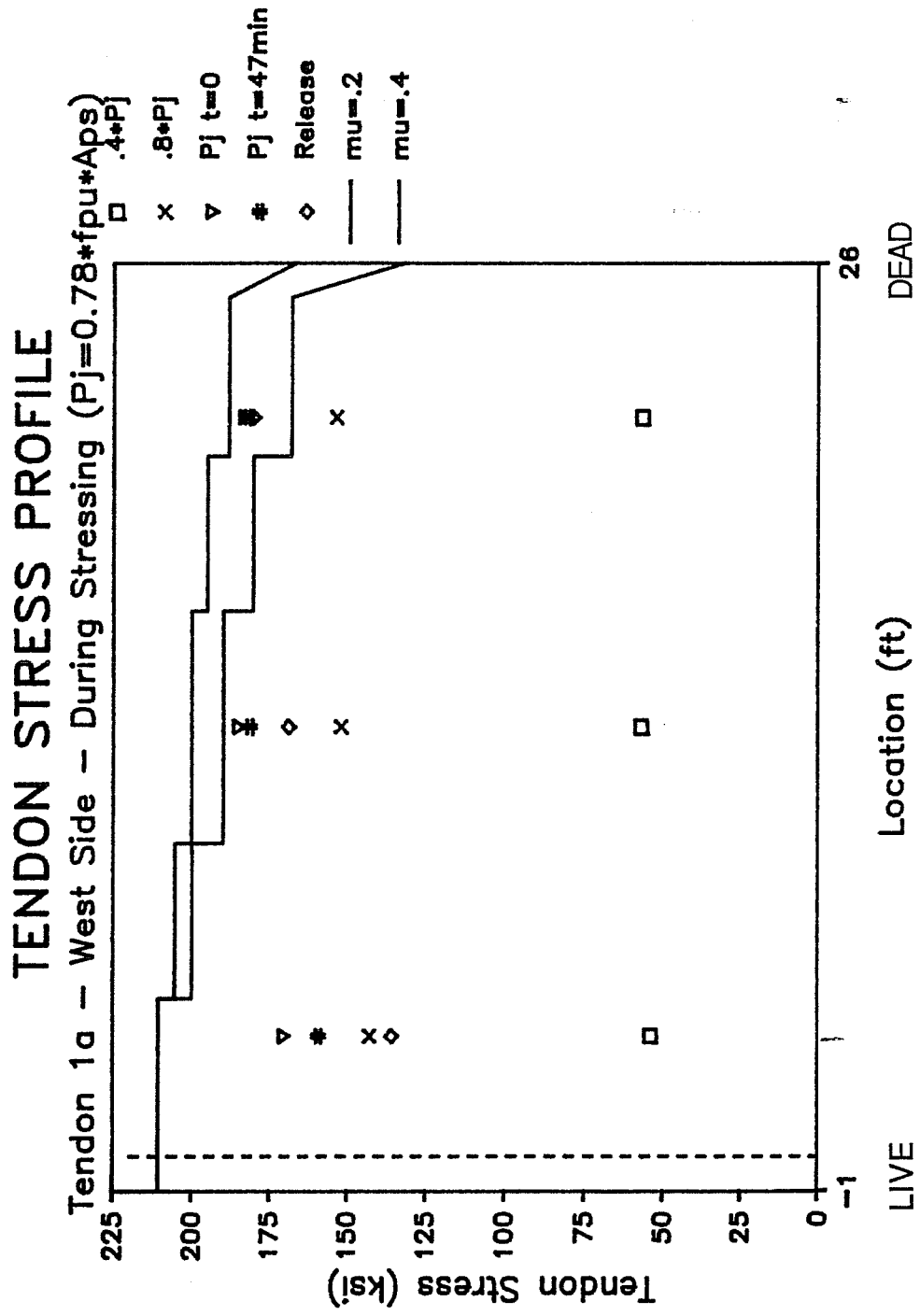


Figure B.1 Tendon Stress Profile During Stressing - continued

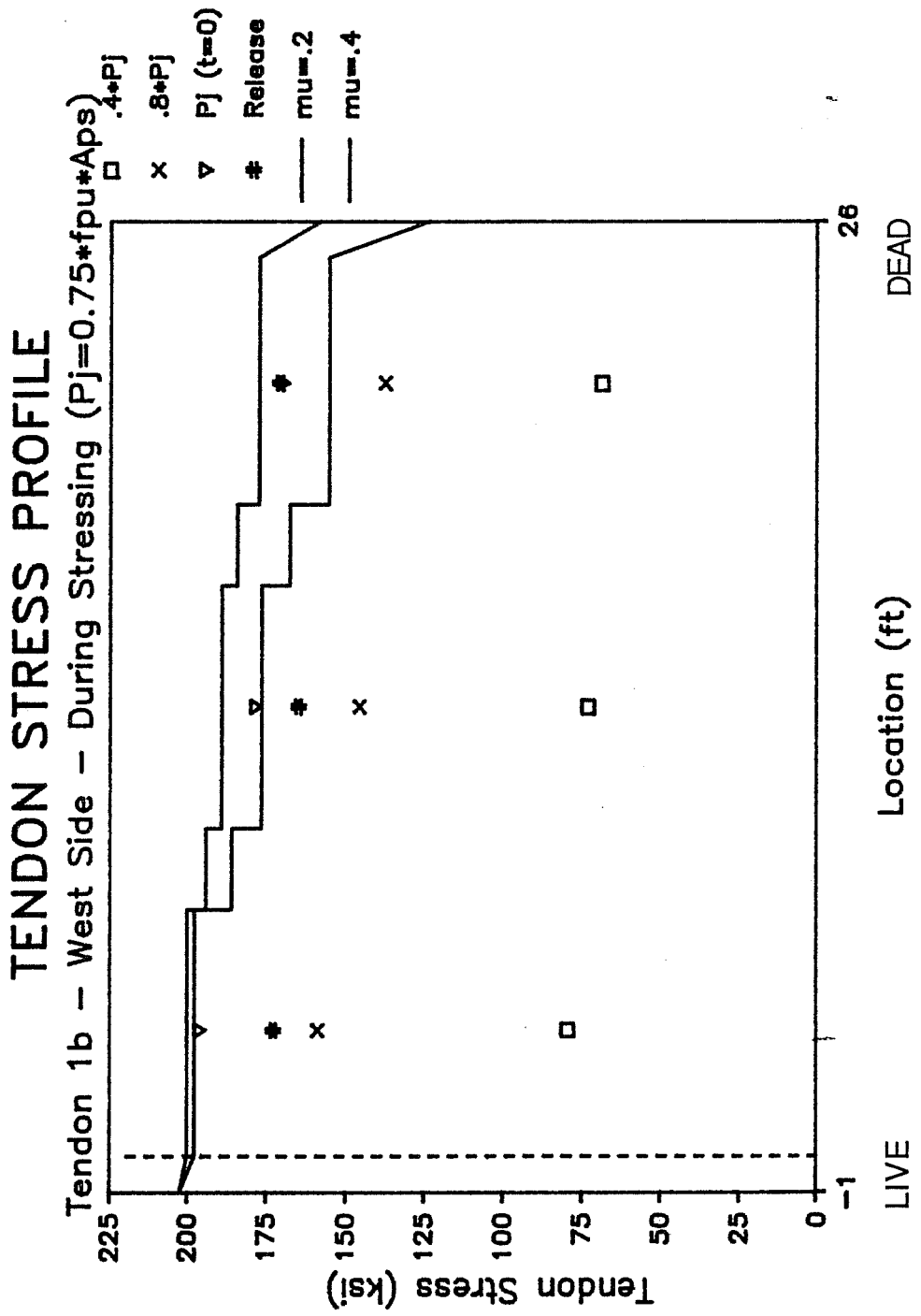


Figure B.1 Tendon Stress Profile During Stressing - continued

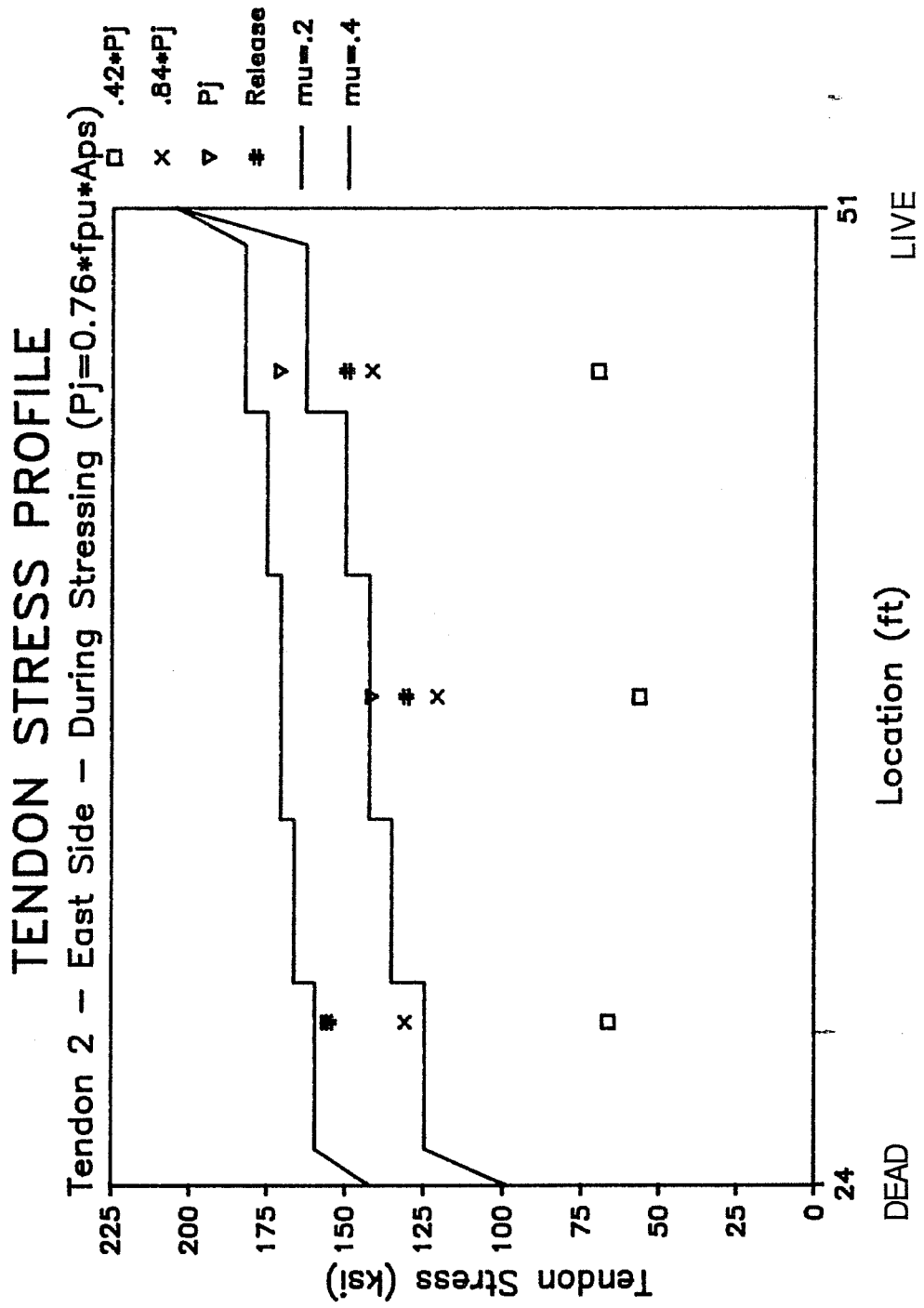


Figure B.1 Tendon Stress Profile During Stressing - continued

TENDON STRESS PROFILE

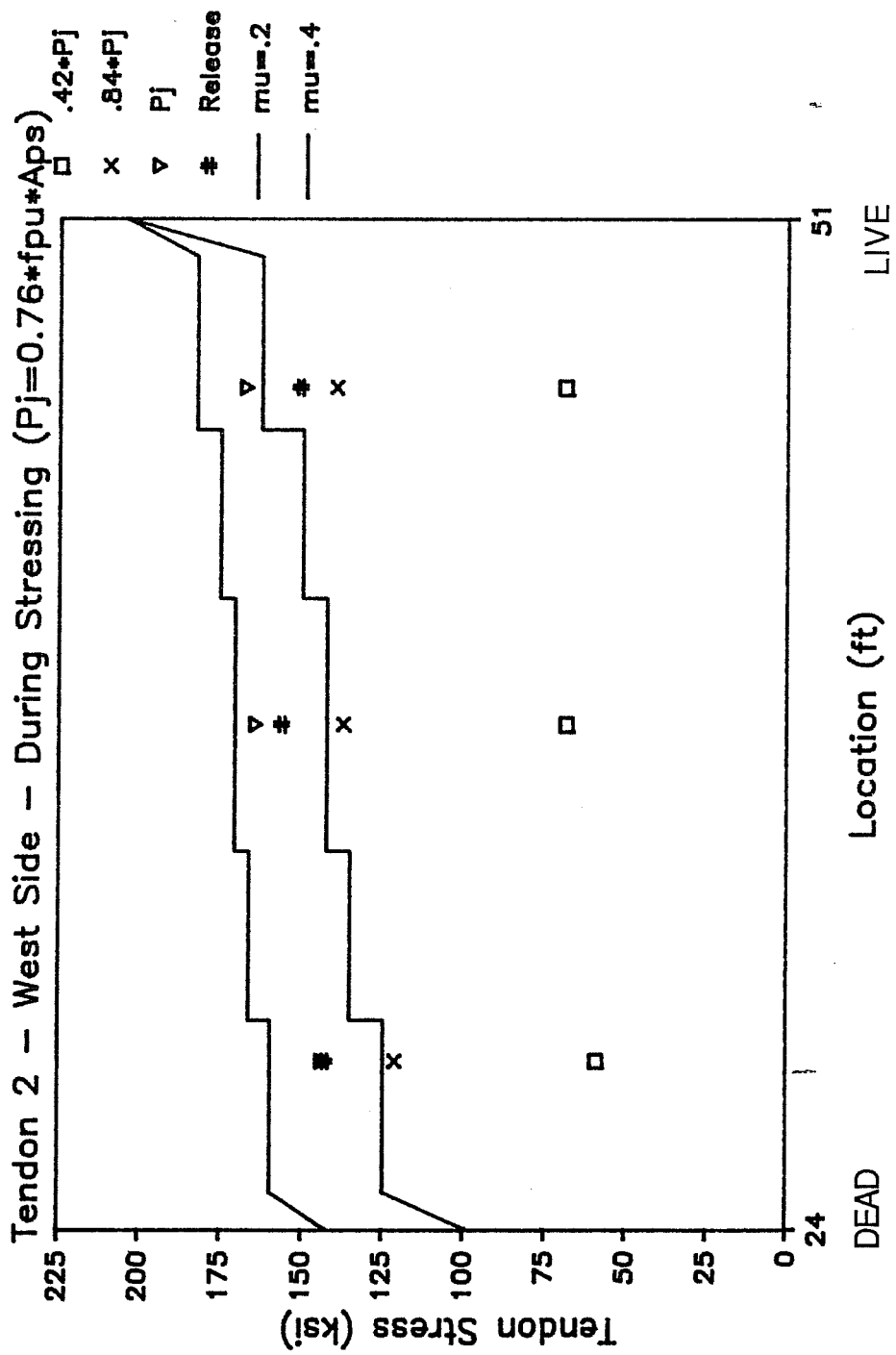


Figure B.1 Tendon Stress Profile During Stressing - continued

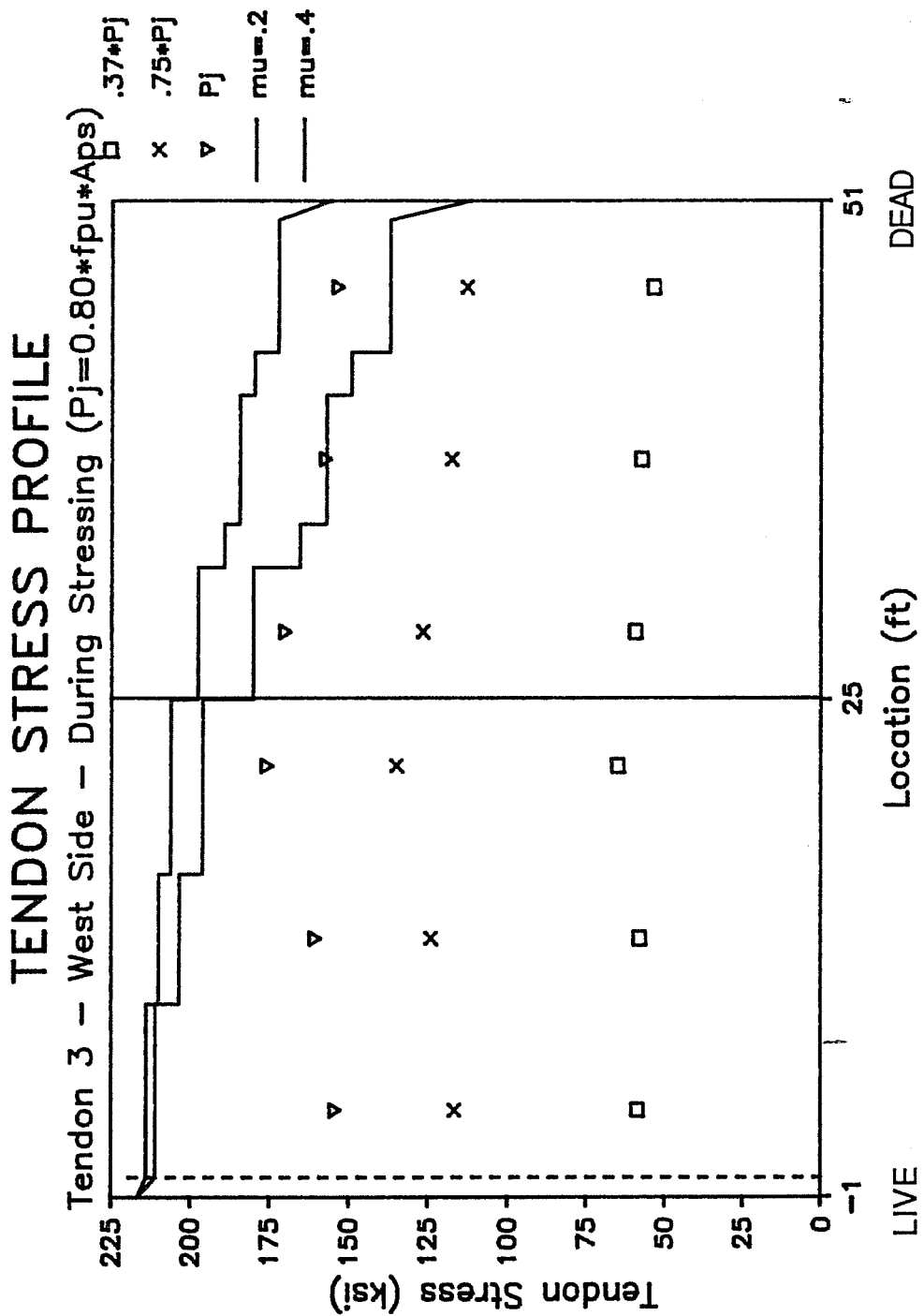


Figure B.1 Tendon Stress Profile During Stressing - continued

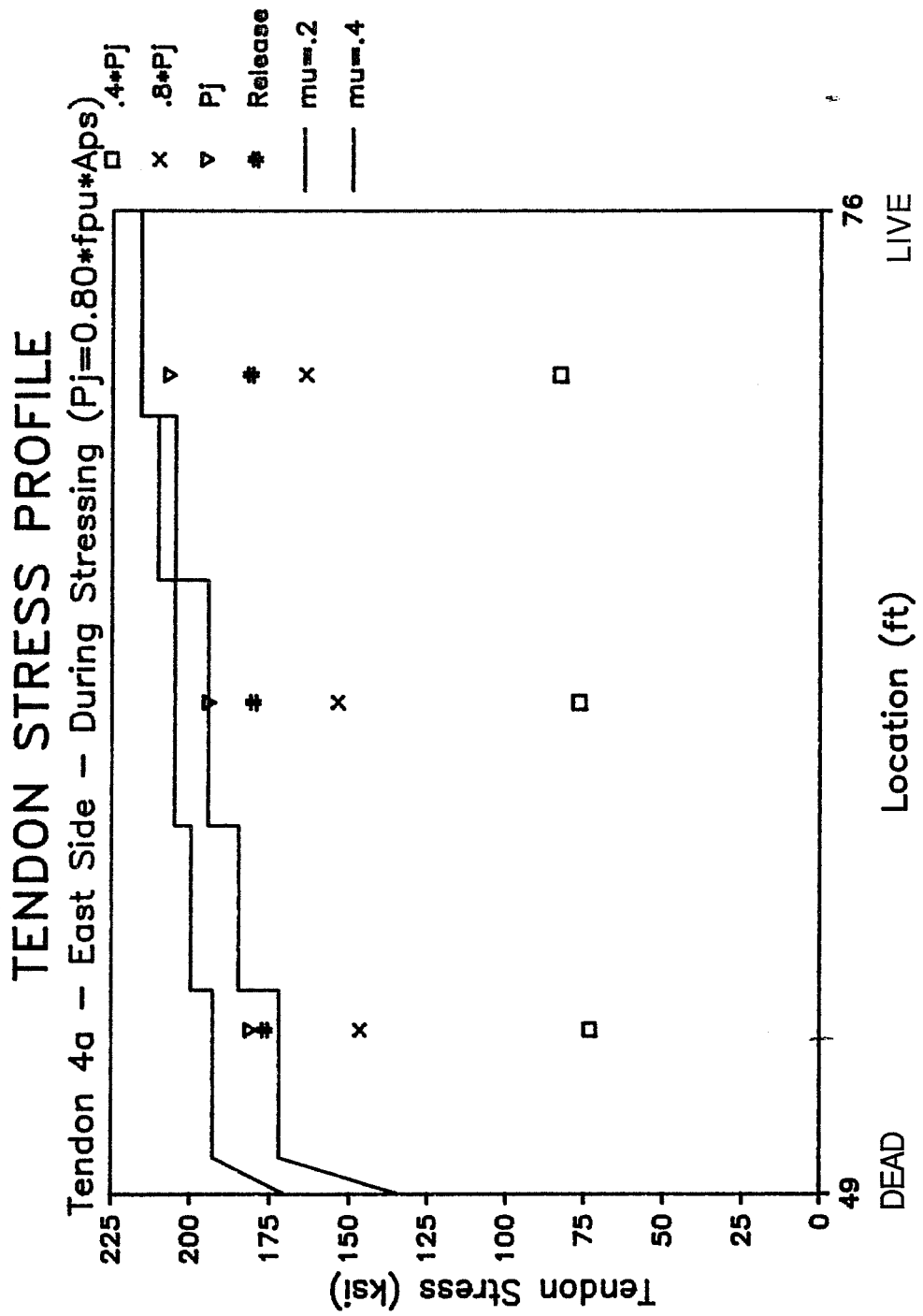


Figure B.1 Tendon Stress Profile During Stressing - continued

TENDON STRESS PROFILE

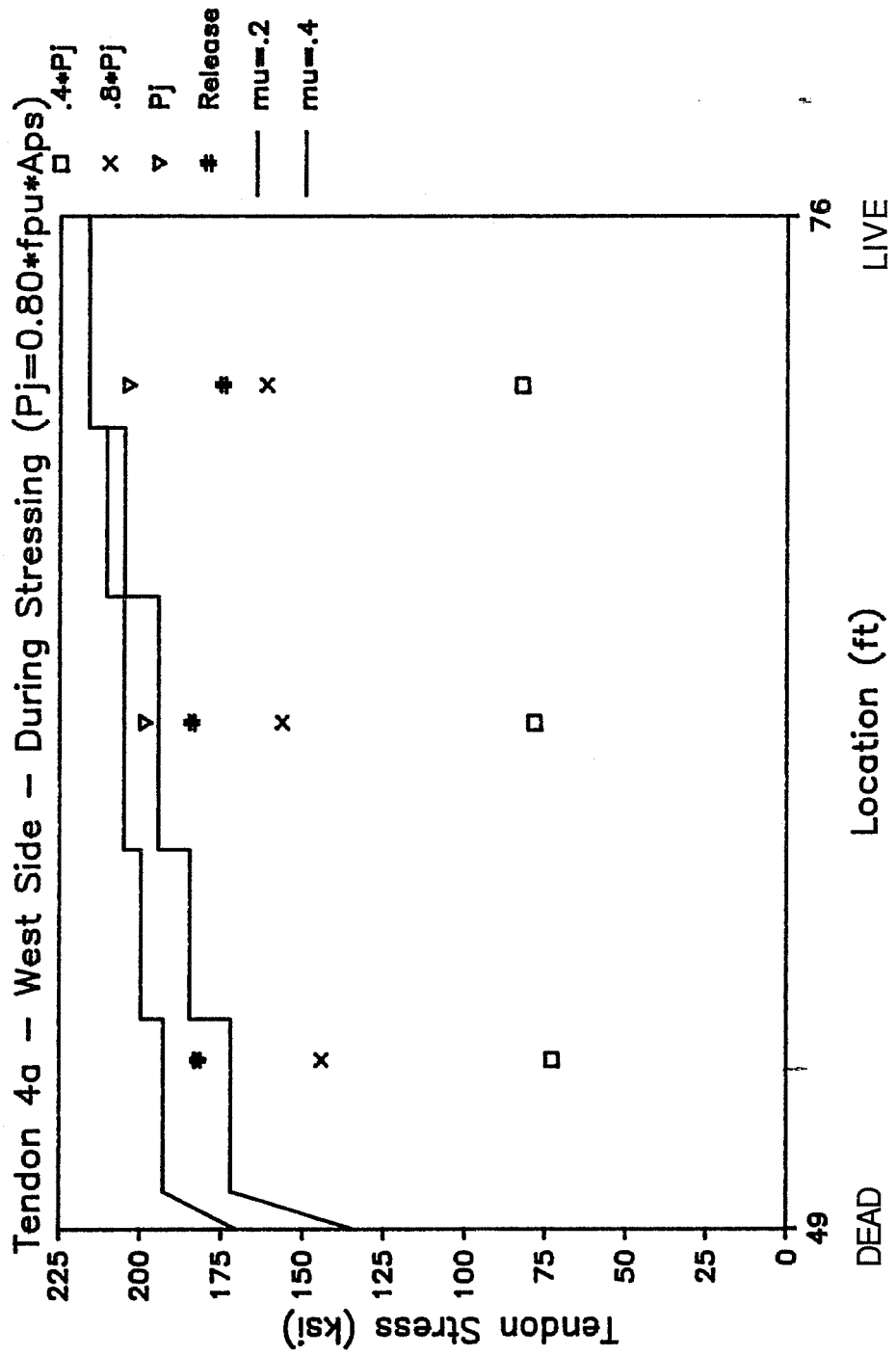


Figure B.1 Tendon Stress Profile During Stressing - continued

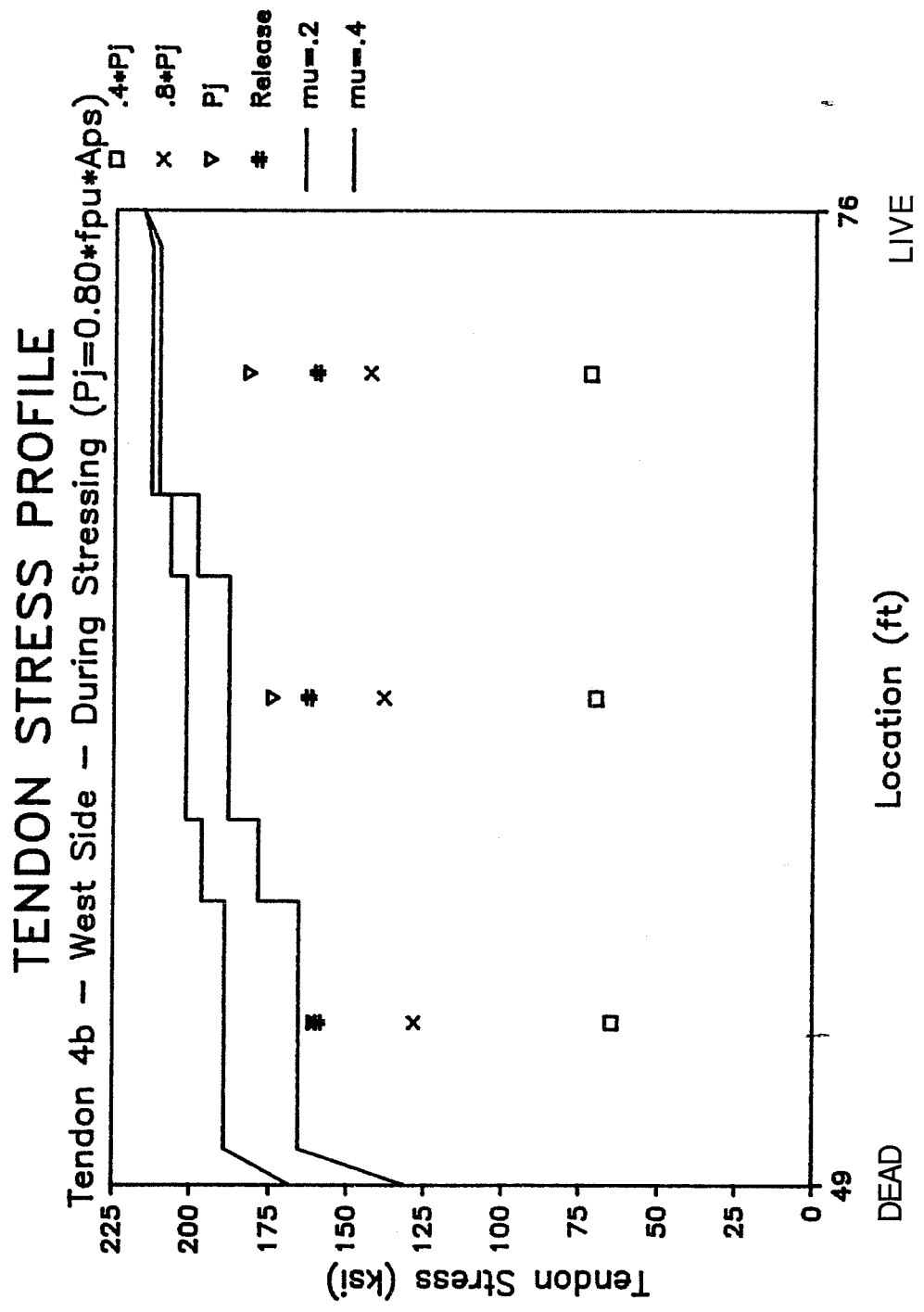


Figure B.1 Tendon Stress Profile During Stressing - continued

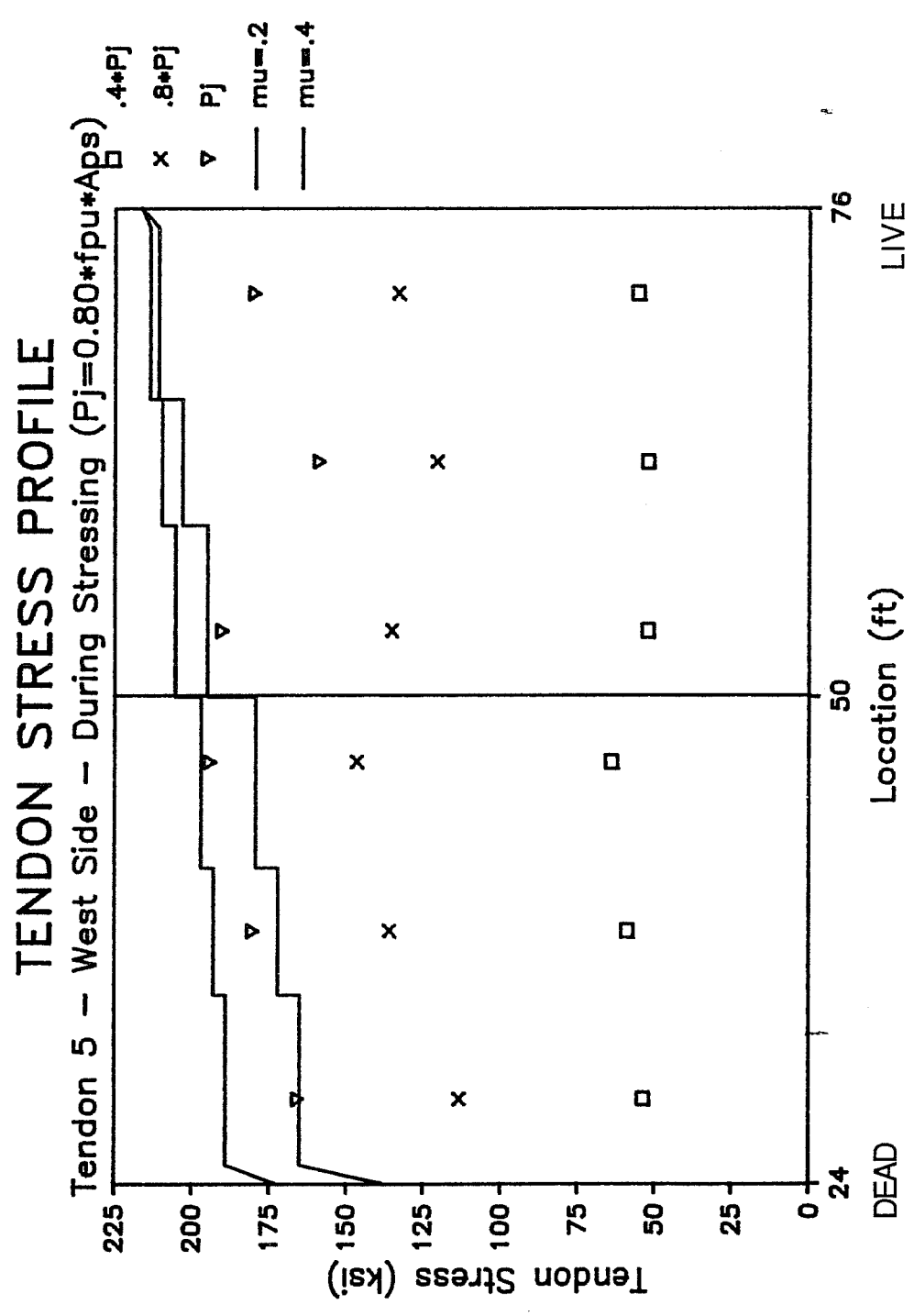


Figure B.1 Tendon Stress Profile During Stressing - continued

REFERENCES

1. Powell L.C., Breen J.E., and Kreger M.E., "State of the Art for Externally Post-Tensioned Bridges with Deviators", The University of Texas at Austin, Center for Transportation Research, Research Report 365-1, June 1988.
2. Mathivat J., "The Recent Evolution of Prestressed Concrete Bridges", Contributions of the French Group (English Translations), IABSE Symposium at Paris-Versailles - September 2-4, 1987, International Association of Bridge and Structural Engineering, 1987, pp. 75-86.
3. Virlogeux M., "La Precontrainte Exterieur", Annales de l'Institut Technique du Batiment et des Travaux Publics, Dec. 1983.
4. Baker A.L.L., "A plastic Theory of Design for Ordinary Reinforced and Prestressed Concrete including Moment Redistribution in Continuous Members", Magazine of Concrete Research, No.2, June 1949, pp. 57-66.
5. Tam A. and Pannel F.N., "The Ultimate Moment of Resistance of Unbonded Partially Prestressed Reinforced Concrete Beams", Magazine of Concrete Research, Vol.28, No.97, Dec.76, pp. 203-208.
6. Ritz P., "Biegeverhalten von Platten mit Vorspannung ohne Verbund" ("Flexural Behavior of Unbonded Post-Tensioned Slabs"), Dissertation, Institut fur Baustatik und Konstruktion, Swiss Federal Institute of Technology at Zurich, Bericht No.80, Birkhauser Verlag Basel und Stuttgart, May1978.
7. American Concrete Institute Committee 318, "Building Code Requirements for Reinforced Concrete (ACI 318-83)", American Concrete Institute, Detroit, Michigan, 1983.
8. Hoang L.H., and Pasquignon M., "Essais de Flexion sur des Poutres en Beton Precontraintes par des Cables Exterieurs", Volumes 1 and 2, Contrat SETRA-CEBTP 1985, Dossier de Recherche 91017, Nov. 1985.
9. Sowlat K., and Rabbat B.G., "Testing of Segmental Girders", Final Report to Figg and Muller Engineers, Inc., Project No. 0217, July 1984.

10. El-Habr K.C., "Finite Element Analysis of Externally Prestressed Segmental Construction", unpublished M.S. Thesis, The University of Texas at Austin, May 1988.
11. Muller J., and Gauthier Y., "Ultimate Behavior of Precast Segmental Box-Girders with External Tendons", Proceedings of the International Symposium on External Post-Tensioned Bridges, Houston, Texas, October 1988 (in press).
12. Beaupre R.J., Powell L.C., Breen J.E., and Kreger M.E., "Deviation Saddle Behavior and Design for Externally Post-Tensioned Bridges", The University of Texas at Austin, Center for Transportation Research, Research Report 365-2, July 1988.
13. Ramirez G., "Behavior of Unbonded Post-Tensioning Segmental Beams with Multiple Shear Keys", unpublished M.S. Thesis, The University of Texas at Austin, January 1989.
14. Taylor E.S., "Dimensional Analysis for Engineers", Clarendon Press, Oxford, 1974.
15. Murphy G., "Similitude in Engineering", The Ronald Press Company, New York, 1950.
16. Breen J.E., "Structural Models - Fabrication and Test Techniques", ASCE Structural Engineering Conference, The American Society of Civil Engineers, Seattle, Washington, May 8-12, 1967.
17. Podolny W., and Muller J., "Construction and Design of Prestressed Concrete Segmental Bridges", John Wiley and Sons, Inc., 1982.
18. AASHTO, "Standard Specifications for Highway Bridges", 13th Edition, American Association of State Highway and Transportation Officials, 1983.
19. Post-Tensioning Institute, "Design and Construction Specifications for Segmental Concrete Bridges", Final Report on NCHRP Project 20-7/32, Feb. 1988.

20. Post-Tensioning Institute, "Design and Construction Specifications for Segmental Concrete Bridges", Unpublished Draft No. 1, NCHRP Project 20-7/32, January 1987.
21. Hartman D. , "Shear Capacity of High Strength Prestressed Concrete Girders", unpublished M.S. Thesis, The University of Texas at Austin, May 1988.
22. MacGregor J.G., "Reinforced Concrete-Mechanics and Design", Prentice Hall, New Jersey, 1988.
23. Pucher A., "Influence Surfaces of Elastic Plates", 4th Edition, Springer-Verlag, New York, 1973.
24. Robertson I.N., and Durrani A.J., "Shear Strength of Prestressed Concrete T-Beams with Welded Wire Fabric as Web Reinforcement", Research Report No. 29, Department of Civil Engineering, Rice University, Houston Texas, January 1985.
25. Koseki K., "Shear Strength of Joints in Precast Segmental Bridges", unpublished M.S. Thesis, The University of Texas at Austin, May 1981.
26. Guyon Y., "Limit State Design of Prestressed Concrete - Volume 2 - The Design of the Member", John Wiley and Sons, New York and Toronto, 1974.
27. Stone W.C., and Breen J.E., "Analyses of Post-Tensioned Girder Anchorage Zones", The University of Texas at Austin, Center for Transportation Research, Research Report 208-1, June 1981.
28. Stone W.C., and Breen J.E., "Design of Post-Tensioned Girder Anchorage Zones", Journal of the Prestressed Concrete Institute, Vol.29, No.2, March-April 1984, pp. 28-61.
29. Yates D.L., "A Study of Fretting Fatigue in Post-Tensioned Concrete Beams", unpublished M.S. Thesis, The University of Texas at Austin, May 1988.

30. Quade C.E., "Distribution of Post-Tensioning Forces Prior to Grouting Tendons", unpublished M.S. Thesis, The University of Texas at Austin, May 1988.
31. Mojtahedi S. and Gamble W.L., "Ultimate Steel Stresses in Unbonded Prestressed Concrete", Journal of the Structural Division, ASCE, Vol.104, No.ST7, July 1978, pp. 1159-1165.
32. Corley W.G., "Rotational Capacity of Reinforced Concrete Beams", Journal of the Structural Division, ASCE, Vol.92, No.ST5, Oct.1966, pp. 121-146.
33. Kaar P.H., Fiorato A.E., Carpenter J.E., Corley W.G., "Limiting Strains of Concrete Confined by Rectangular Hoops", PCA Research and Development Bulletin - RD053.01D, Portland Cement Association, 1978.
34. Mattock A.H., Yamazaki J., and Kattula B.T., "Comparitive Study of Prestressed Concrete Beams With and Without Bond", ACI Journal, No.2, Vol.68, Feb.71, pp. 116-125.
35. Lin T.Y., and Thornton K., "Secondary Moment and Moment Redistribution in Continous Prestressed Concrete Beams", PCI Journal, Jan.-Feb. 1972, Vol.17, No.1, pp. 8-20.
36. Warwaruk J., Sozen M.A., and Siess C.P., "Strength and Behavior in Flexure of Prestressed Concrete Beams", Bulletin No. 464, Engineering Experiment Station, University of Illinois at Urbana, Aug. 1962, 105pp.
37. Canadian Standards Association Commitee A23.3, "Design of Concrete Structures for Buildings CAN3-A23.3-M84", Canadian Standards Association, Ottawa, Ontario, 1984.
38. AASHTO, "Manual for Maintenance Inspection of Bridges", 4th Edition, American Association of State Highway and Transportation Officials, 1983.
39. Naaman A.E., "Partially Prestressed Concrete: Review and Recommendations", PCI Journal, Vol. 30, No. 6, Nov-Dec 1985, pp. 30-71.
40. Wittfoht H., "Outstanding and Innovative Construction Methods in Concrete Structures: Recent and Future Trends", FIP OC/4.

VITA

Robert James Grierson MacGregor was born in Champaign, Illinois on November 10, 1957, the son of James Grierson and Barbara Ann MacGregor of Edmonton, Alberta, Canada. Robert was raised in Edmonton, where he received his Bachelors and Masters degrees in Civil Engineering from the University of Alberta. After working for a structural engineering consultant for five years, he attended the University of Texas at Austin to receive a Ph.D. in structural engineering. Currently Robert is a senior bridge engineer for Arvid Grant and Associates of Olympia, Washington. Robert married Mariann Andersen in 1980 and has two children, Lisanne and Anders.

Permanent Address: 229 Patricia Ct.
Olympia, WA 98503

This dissertation was typed by the author and TEX formatting was performed by Sharon Cunningham.